U.S.NRC
United States Nuclear Regulatory Commission
Protecting People and the Environment

NUREG/CR-7219
ANL-16/09

Cladding Behavior during Postulated Loss-of-Coolant Accidents

Office of Nuclear Regulatory Research

AVAILABILITY OF REFERENCE MATERIALS IN NRC PUBLICATIONS

NRC Reference Material

As of November 1999, you may electronically access NUREG-series publications and other NRC records at NRC's Library at www.nrc.gov/reading-rm.html. Publicly released records include, to name a few, NUREG-series publications; *Federal Register* notices; applicant, licensee, and vendor documents and correspondence; NRC correspondence and internal memoranda; bulletins and information notices; inspection and investigative reports; licensee event reports; and Commission papers and their attachments.

NRC publications in the NUREG series, NRC regulations, and Title 10, "Energy," in the *Code of Federal Regulations* may also be purchased from one of these two sources.

1. **The Superintendent of Documents**
   U.S. Government Publishing Office
   Mail Stop IDCC
   Washington, DC 20402-0001
   Internet: bookstore.gpo.gov
   Telephone: (202) 512-1800
   Fax: (202) 512-2104

2. **The National Technical Information Service**
   5301 Shawnee Rd., Alexandria, VA 22312-0002
   www.ntis.gov
   1-800-553-6847 or, locally, (703) 605-6000

A single copy of each NRC draft report for comment is available free, to the extent of supply, upon written request as follows:

Address: **U.S. Nuclear Regulatory Commission**
Office of Administration
Publications Branch
Washington, DC 20555-0001
E-mail: distribution.resource@nrc.gov
Facsimile: (301) 415-2289

Some publications in the NUREG series that are posted at NRC's Web site address www.nrc.gov/reading-rm/doc-collections/nuregs are updated periodically and may differ from the last printed version. Although references to material found on a Web site bear the date the material was accessed, the material available on the date cited may subsequently be removed from the site.

Non-NRC Reference Material

Documents available from public and special technical libraries include all open literature items, such as books, journal articles, transactions, *Federal Register* notices, Federal and State legislation, and congressional reports. Such documents as theses, dissertations, foreign reports and translations, and non-NRC conference proceedings may be purchased from their sponsoring organization.

Copies of industry codes and standards used in a substantive manner in the NRC regulatory process are maintained at—

The NRC Technical Library
Two White Flint North
11545 Rockville Pike
Rockville, MD 20852-2738

These standards are available in the library for reference use by the public. Codes and standards are usually copyrighted and may be purchased from the originating organization or, if they are American National Standards, from—

American National Standards Institute
11 West 42nd Street
New York, NY 10036-8002
www.ansi.org
(212) 642-4900

Legally binding regulatory requirements are stated only in laws; NRC regulations; licenses, including technical specifications; or orders, not in NUREG-series publications. The views expressed in contractorprepared publications in this series are not necessarily those of the NRC.

The NUREG series comprises (1) technical and administrative reports and books prepared by the staff (NUREG–XXXX) or agency contractors (NUREG/CR–XXXX), (2) proceedings of conferences (NUREG/CP–XXXX), (3) reports resulting from international agreements (NUREG/IA–XXXX), (4) brochures (NUREG/BR–XXXX), and (5) compilations of legal decisions and orders of the Commission and Atomic and Safety Licensing Boards and of Directors' decisions under Section 2.206 of NRC's regulations (NUREG–0750).

U.S.NRC
United States Nuclear Regulatory Commission
Protecting People and the Environment

NUREG/CR-7219
ANL-16/09

Cladding Behavior during Postulated Loss-of-Coolant Accidents

Manuscript Completed: March 2016
Date Published: July 2016

Prepared by: M.C. Billone, Y. Yan,* T.A. Burtseva, and R.O. Meyer

Nuclear Engineering Division
Argonne National Laboratory
9700 South Cass Avenue
Argonne, IL 60439

*Currently with Oak Ridge National Laboratory

H.H. Scott, NRC Project Manager

NRC Job Code Number V6199

Office of Nuclear Regulatory Research

ABSTRACT

A previous report by this laboratory provided results on cladding embrittlement, breakaway oxidation, and ballooning with rupture under conditions of loss-of-coolant accidents (LOCAs). This report updates those results, provides additional results in those areas, and adds results of mechanical testing of cladding after ballooning, rupture, oxidation at elevated temperature, and quench. Significant conclusions are as follows. Embrittlement of high-exposure cladding is accelerated by hydrogen that is absorbed during normal reactor operation (i.e., pre-transient) and the acceleration has been quantified as an oxidation limit vs. pre-transient hydrogen content in the cladding metal. Breakaway oxidation, which leads to excessive hydrogen pickup and embrittlement during a LOCA transient, can occur during times that are relevant for these accidents. Conditions that lead to breakaway are only partially understood. Factors that contribute to increased susceptibility to breakaway oxidation – especially surface finish and scratches – have been investigated. Ballooning strains increase as rupture temperature decreases within the temperature range explored in this work. Rupture temperature depends on alloy composition, pre-transient hydrogen level, internal gas pressure, and geometrical factors used to convert gas pressure to hoop stress. Four-point bend tests are effective for measuring post-quench failure limits for ballooned, ruptured, and oxidized cladding. The results indicate that strength and failure energy degrade significantly with increasing pre-transient hydrogen and transient oxygen levels, based on cross-section-average values for these parameters. Further, using the oxidation limit vs. hydrogen content derived for non-ballooned regions would ensure the preservation of strength for ballooned regions.

FOREWORD

Fuel rod cladding is the first barrier for retention of fission products, and the structural integrity of the cladding ensures coolable core geometry. In the early 1990s, new data from foreign research programs showed degraded cladding behavior for high-burnup fuel compared with low-burnup fuel in tests designed to simulate postulated accidents. Interim actions were taken, but it became clear that extrapolation from a low-burnup database needed to be reassessed more carefully for regulatory purposes.

One of NRC's central regulations used in plant licensing deals with postulated loss-of-coolant accidents (LOCAs). A portion of that regulation in 10 CFR 50.46(b) specified criteria that were derived from tests with non-irradiated Zircaloy cladding, and these criteria limit the peak cladding temperature and the maximum cladding oxidation during the accident. These two limits are known as embrittlement criteria. Their purpose is to prevent cladding embrittlement during a LOCA, thus ensuring that the general core geometry will be maintained and be coolable.

Since 1997, NRC has sponsored a research program at Argonne National Laboratory to reassess these limits for the possible effects of fuel burnup. Two formal NRC reports have been published, NUREG/CR-6967 and NUREG/CR-7139. The latter report discussed test methods to assess fuel-rod cladding behavior following a LOCA. For non-deformed cladding regions with uniform levels of hydrogen content and oxidation, and for irradiated cladding, the ring compression test (RCT) has been selected. The four-point bend test (4-PBT) has been selected for evaluating the performance of ballooned and ruptured regions of a fuel rod in LOCA analysis.

The purpose of this document is to (1) provide final results of tests performed and conclusions on hydrogen embrittlement of zirconium-based cladding alloys, and (2) support the technical bases for a revised regulation – now 10 CFR 50.46(c) – and Regulatory Guides 1.222, 1.223 and 1.224. It is considered appropriate to issue this document as a new report because it contains new data, as well as revisions to previously published results.

CONTENTS

FIGURES

TABLES

EXECUTIVE SUMMARY

Previous loss-of-coolant-accident (LOCA) acceptance criteria in 10 CFR 50.46(b) limited the peak cladding temperature to 2200°F (1204°C) and the maximum oxidation level to 17% of the cross-section-averaged cladding wall thickness. It had been assumed that ductility would be maintained in Zircaloys (Zr-Sn alloys) and ZIRLO (Zr-Sn-Nb alloy) if these criteria were satisfied. Data presented previously (NUREG/CR-6967) showed that the 17% oxidation level is not conservative for irradiated Zircaloy-4, ZIRLO, and M5 (Zr-Nb alloy) because the embrittlement oxidation level decreases with increasing hydrogen content picked up during normal operation. These data also showed that embrittlement can occur at even lower oxidation levels and lower temperatures due to excessive hydrogen pickup if breakaway oxidation occurs.

In work performed since publication of NUREG/CR-6967, the following were accomplished: (a) methodologies were improved for determining pre-transient hydrogen content and post-quench ductility, (b) high-temperature oxidation limits were established for high-exposure and pre-hydrided cladding with intermediate levels of pre-transient hydrogen (200-340 wppm), (c) minimum breakaway oxidation times were determined for as-fabricated ZIRLO and M5 cladding under near-isothermal conditions, (d) minimum transient breakaway oxidation times were determined for as-fabricated ZIRLO, (e) LOCA integral tests were conducted with as-fabricated and pre-hydrided ZIRLO to determine balloon size and rupture temperature, and (f) post-test integral samples were subjected to four-point bend tests (4-PBTs) to determine failure limits as functions of pre-transient hydrogen content and maximum oxidation level.

High-temperature embrittlement tests were conducted with pre-hydrided (180 to 280 wppm) and high-exposure (300 to 340 wppm) ZIRLO cladding oxidized to 8 – 11% CP-ECR at peak temperatures of 1200°C, quenched at 800°C, cooled to room temperature, and subjected to ring-compression tests at 135°C. CP-ECR is Equivalent Cladding Reacted (ECR) calculated using the Cathcart-Pawel (CP) weight gain correlation. It is used throughout this work to represent the oxidation level of cladding alloys. For pre-hydrided ZIRLO, ductile-to-brittle transition oxidation levels were 11% and 10% for pre-transient hydrogen contents of 200 wppm and 240 wppm, respectively. For high-exposure ZIRLO, the transition oxidation level was 9% for 300-wppm hydrogen and <8% for 340-wppm hydrogen. These transition oxidation levels correspond to borderline ductility as defined by the permanent-strain criterion (≥1%) and/or the corresponding offset-strain criterion. Past and current results are summarized in the following figure. The consistency in results for different cladding alloys and for pre-hydrided and high-exposure cladding materials indicates that the decrease in embrittlement threshold is due primarily to the pre-transient hydrogen content. No effects of alloy differences or irradiation were observed. The results also indicate that pre-hydrided cladding is a good surrogate for high-burnup cladding.

Based on previous results for as-fabricated ZIRLO cladding, the minimum breakaway oxidation time (3100±300 s) occurred for average hold temperatures of 970°C to 985°C. The criterion used by Argonne to determine breakaway-oxidation initiation is 200-wppm hydrogen pickup. The breakaway time was longer (4000±200 s) for 1000°C-oxidation tests. Using a different test apparatus, test methods, and breakaway criterion, Westinghouse (WEC) observed post-breakaway surface discoloration on ZIRLO samples after ≈4400 s at 1000°C. However, WEC data indicated no surface-oxide discoloration after ≈4400 s at <1000°C. Additional tests were conducted by Argonne and WEC using samples from the same cladding lots. The same differences were observed at <1000°C. These apparent differences may be due to the high temperature sensitivity of ZIRLO breakaway oxidation. Circumferential temperature variations in Argonne's radiant-heating furnace resulted in oxidation of samples at all temperatures from 970°C to 1000°C. WEC tests were conducted in a more homogeneous resistance furnace at discrete temperatures of 960°C, 980°C, and 990°C.

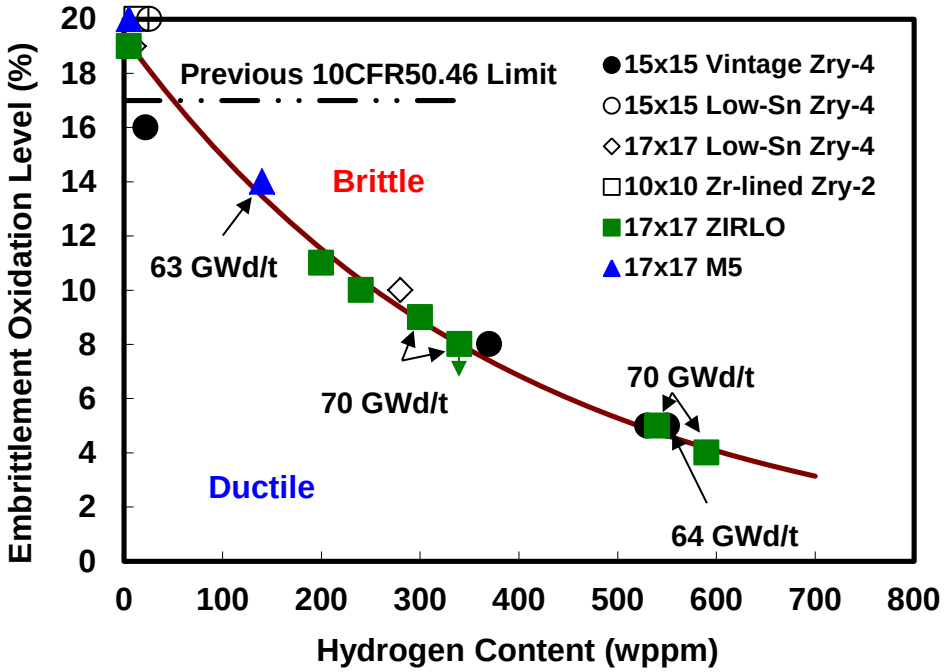

Embrittlement oxidation level as a function of pre-transient hydrogen content for peak oxidation temperatures of 1200°C for <400 wppm and 1130−1180°C for >400 wppm hydrogen.

Argonne also conducted four tests with as-fabricated ZIRLO oxidized under transient conditions, which included single step changes up and down in temperature and temperature cycling. The minimum breakaway oxidation time was determined to be 2800 s for these transient temperature tests. This time is within the data scatter for isothermal tests and the same as the breakaway oxidation time for a mildly scratched (20-microns deep) ZIRLO sample subjected to isothermal oxidation. These results suggest that temperature transients do not reduce the minimum breakaway oxidation time measured in isothermal tests. Two breakaway tests were conducted with as-fabricated M5 cladding oxidized at 985°C for 5000 s. Breakaway oxidation was not observed at 5000 s, nor was it observed in previous tests with M5 cladding oxidized at 1000°C for 4100 s. These results are consistent with CEA/Saclay results (≈6400 s breakaway time) for 1000°C-oxidized samples.

Long (≈300 mm), pressurized, as-fabricated and pre-hydrided ZIRLO samples were subjected to controlled heating at 5°C/s from 300°C to 1200°C, oxidation at 1200°C for various times, controlled cooling at 3°C/s to 800°C, and quench at 800°C. All samples ballooned and ruptured during the heating ramp. Rupture temperatures and hence ballooning strains for as-fabricated ZIRLO varied with the internal gas pressure, which remained relatively constant from 300°C up to the rupture temperature: (a) 843±6°C and 25±3% strain for 4.14 MPa and (b) 749±7°C and 46±4% strain for 8.28 MPa. Ballooning, rupture, and subsequent oxidation processes resulted in local areas with significant axial variation in diameter, wall thickness, hydrogen content, and oxidation level, as well as large circumferential variations in wall thickness and oxidation level within cross sections containing the rupture region. The effects of pre-hydriding (220 to 700 wppm) ZIRLO cladding prior to the heating transient were opposite to what was expected based on the effect of hydrogen on phase changes. At 8.28 MPa fill pressure, rupture temperatures were lower (670°C to 740°C) than anticipated and rupture strains were consequently higher (47% to 71%) than anticipated. These results suggest that hydrogen has a more significant effect on ballooning strains due to weakening of the cladding (resulting in lower rupture temperatures) than on shifting the phase-change temperature.

Four-point bend tests (4-PBTs) were used to determine post-quench failure location, maximum bending moment (measure of strength), failure energy (measure of toughness), and offset displacement (measure of plastic deformation). For 4-PBT loading, the bending moment is constant between the load application points, which were spaced far enough apart (150 mm) to include the ballooned region. With analysis, the 4-PBT bending moment can be related to an equivalent axial tensile load. Non-oxidized, ballooned and ruptured samples were strong and highly ductile, but oxidized samples exhibited decreasing strength with increasing oxidation level and pre-transient hydrogen content. However, no clear pattern was exhibited with regard to plastic deformation; most samples with high ballooning strain severed through the rupture cross section prior to accumulating offset strain. Thus, even though the rupture cross section contained highly ductile regions, cracks initiated in the brittle region (near rupture tips) and propagated rapidly through the locally ductile section of the cladding (i.e., near the thick back wall). For low ballooning strains, failure (i.e., severing of the cross section) occurred in the regions between the edge of the rupture opening and the balloon neck.

Strength results are shown in the following figure. Data include samples that failed within the rupture region and outside the rupture region. At 17% CP-ECR, the linearized fit to the data for as-fabricated ZIRLO (round blue dots) gives 6.4 N•m maximum bending moment, which corresponds to an axial-restraint failure load of ≈2600 N. This value is higher than maximum loads measured by the Japanese Atomic Energy Agency at Tokai (1200-2400 N) for ballooned, ruptured, oxidized and quenched Zircaloy-4 samples that survived conditions of full restraint during quench from 700°C to ≈100°C. Thus, as-fabricated ZIRLO cladding restricted to ≤17% CP-ECR would survive this severe loading. The strength of ZIRLO with 220-wppm hydrogen following oxidation to ≈13% CP-ECR (round red dot) is comparable to the strength of as-fabricated ZIRLO oxidized to 17% CP-ECR. Based on the oxidation embrittlement limit figure, the oxidation level would be limited to <12% for cladding with 220-wppm pre-transient hydrogen. Samples with more pre-transient hydrogen or higher oxidation levels had correspondingly lower strength. Thus, the hydrogen-dependent oxidation limit based on ring-compression tests (see previous figure) ensures preservation of cladding strength for the balloon region for as-fabricated cladding and cladding with pre-transient hydrogen, including irradiated cladding.

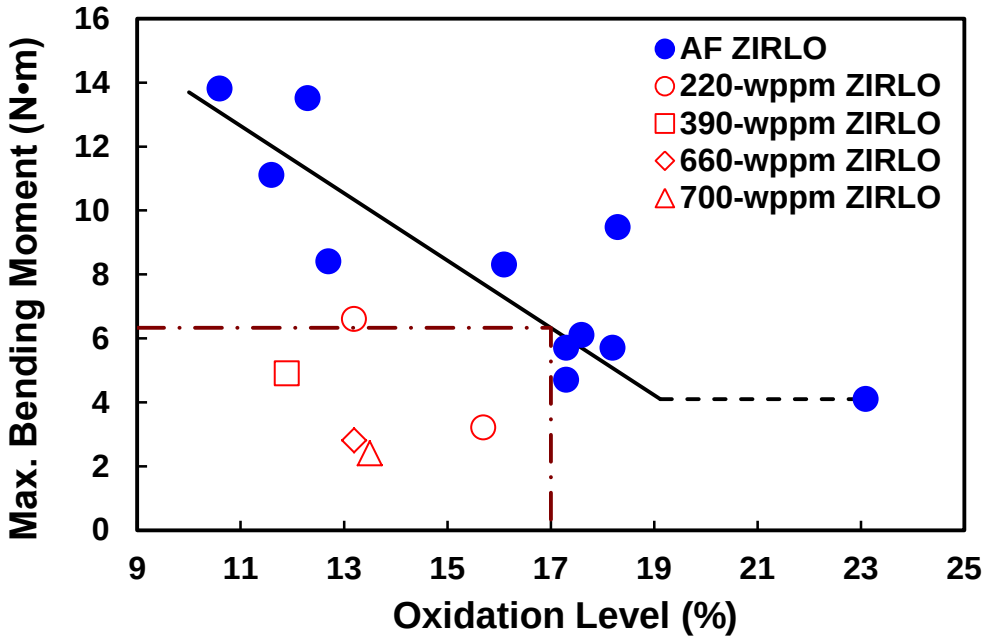

Maximum bending moment for ZIRLO LOCA integral samples with and without (AF) the addition of pre-transient hydrogen. Results are from 4-PBTs conducted at 1-2 mm/s and 135°C.

ACKNOWLEDGMENTS

The authors would like to express their appreciation to the Office of Nuclear Regulatory Research (RES) for support and management of this program. As Project Manager, Harold Scott provided programmatic and technical guidance. Michelle Bales (nee Flanagan) provided significant technical guidance with regard to data needs relevant to licensing issues.

Argonne technicians Jakub Dobrzynski, David McGann, and Kevin Byrne are acknowledged for their careful efforts in test setup, test conduct, and post-test measurements. The authors would like to express their appreciation to international colleagues Jean-Christophe Brachet and Valerie Vandenberghe of the Commissariat a l'Energie Atomique (CEA) at Saclay, Claude Grandjean and Georges Hache of the Institut de Radioprotection et de Surete Nucleaire (IRSN), and Fumihisa Nagase of the Japanese Atomic Energy Agency (JAEA) for sharing details, data, and insights regarding test methods and embrittlement mechanisms.

Many organizations, and individuals within those organizations, have contributed test materials, reviewed test plans, participated in program review meetings, shared experiences, and provided both guidance and technical expertise. The Electric Power Research Institute (EPRI), Global Nuclear Fuels (GNF), AREVA, and Westinghouse Electric Company (WEC) provided high-burnup commercial reactor fuel rods, as well as defueled M5 (Studsvik and AREVA) and ZIRLO (Studsvik and WEC) cladding from high-burnup fuel rods, to the program. These organizations, along with others, also supplied us with as-fabricated cladding and tubing. In particular, WEC is acknowledged for providing the ZIRLO cladding tubes used in the current study.

This report updates as necessary and includes all major results from the earlier work published in NUREG/CR-6967. Therefore, we also acknowledge those who contributed to that earlier report.

ACRONYMS AND ABBREVIATIONS

3-PBT	3-point bend test
4-PBT	4-point bend test
AF	As-fabricated
AGHCF	Alpha-Gamma Hot-Cell Facility
ANL	Argonne National Laboratory
BJ	Baker-Just
BP	Belt polished
Bu	Burnup
BWR	Boiling water reactor
CEA	Commissariat a l'Energie Atomique
CFR	Code of Federal Regulations
CP	Cathcart-Pawel
CP-ECR	ECR calculated using the CP weight-gain correlation
ECR	Equivalent cladding reacted
EdF	Electricitie de France
EPRI	Electric Power Research Institute
FEA	Finite Element Analysis
GWd/t	Gigawatt-days per metric tonne of uranium
HBR	H.B. Robinson reactors
HBU	High burnup
ID	Inner diameter
IML	Irradiated Materials Laboratory
IRSN	Institute for Radiological Protection and Nuclear Safety
JAEA	Japanese Atomic Energy Agency
LOCA	Loss-of-coolant accident
NA	North Anna reactors
NIST	National Institute of Standards and Testing
NRC	Nuclear Regulatory Commission
OCZL	Out-of-cell oxidation test for ZIRLO
OD	Outer diameter
ORNL	Oak Ridge National Laboratory
PCT	Peak cladding temperature
PH	Pre-hydrided
PQD	Post-quench ductility
PWR	Pressurized water reactor
R	Universal gas constant
RCT	Ring compression test
RES	Office of Nuclear Regulatory Research
RT	Room temperature
TC	Thermocouple
TMI-1	Three Mile Island Unit 1 Reactor
W	Westinghouse
WC	Westinghouse cleaned
WEC	Westinghouse Electric Company
Zry-2	Zircaloy-2
Zry-4	Zircaloy-4

SYMBOLS

a	Distance between applied load and support in 4-PBT
A	Cross-sectional area
A_{eq}	Equivalent cross-sectional area relative to the metal
A_g	Cross-sectional area for sample gauge section in axial tension test
A_m	Cross-sectional area of metal
A_{ox}	Cross-sectional area of oxide
$(A_{ox})_i$	Cross-sectional area of inner-surface oxide
$(A_{ox})_o$	Cross-sectional area of outer-surface oxide
C_H	Hydrogen content (in wppm) in sample measured prior to conducting oxidation tests
C_{Hi}	Hydrogen content (in wppm) in as-fabricated cladding
C_{HM}	Hydrogen content (in wppm) in cladding metal prior to conducting oxidation tests
C_m	Cladding mid-wall circumference
C_{mf}	Post-rupture value of cladding mid-wall circumference
C_{mi}	Pre-transient value of cladding mid-wall circumference
C_{oR}	Maximum post-rupture value of cladding metal outer circumference
C_{mR}	Maximum post-rupture value of cladding metal mid-wall circumference
$(C_H)_{POX}$	Hydrogen content (in wppm) in sample measured after oxidation tests
C_{oi}	Pre-transient value of cladding metal outer-wall circumference
c_o	Average oxygen concentration in the beta (β) layer
c_{oi}	Initial oxygen concentration in as-fabricated cladding
d_{ap}	Permanent displacement at loading positions in 4-PBTs
D_{avg}	Average diameter of ballooned cladding
D_{avgR}	Average diameter of ballooned and rupture cladding at about mid-span of rupture opening
D_i	Inner diameter of cladding
D_{max}	Maximum diameter at a cross section of ballooned cladding
D_{mi}	Inner diameter of cladding metal
D_{min}	Minimum diameter at a cross section of ballooned cladding
D_{mo}	Outer diameter of cladding metal
D_o	Outer diameter of cladding
d_p	Permanent displacement of RCT ring in loading direction
E	Young's modulus
E_g	Young's modulus for gauge material in axial tension test
E_m	Young's modulus for metal
E_{max}	Maximum applied energy in 4-PBT; equivalent to failure energy for failed samples
E_{ox}	Young's modulus for oxide
h	Wall thickness of cladding
H_B	Total mass of hydrogen in fuel-cladding bond layer
H_C	Total mass of hydrogen in corrosion layer
h_i	Wall thickness of as-fabricated cladding
h_R	Minimum wall thickness (averaged over cross section) of ballooned and ruptured cladding
H_M	Total mass of hydrogen in metal layer
h_m	Wall thickness of cladding metal
H_S	Total hydrogen mass in cladding sample
I	Area moment of inertia for bending
I_{eq}	Equivalent area moment of inertia relative to the metal
I_m	Area moment of inertia for metal
$(I_{ox})_i$	Area moment of inertia for inner-surface oxide

$(I_{ox})_o$	Area moment of inertia for outer-surface oxide
k	Temperature dependent coefficient
K	Stiffness; linearized loading slope of load-displacement curve
K_g	Stiffness of gauge section in response to axial load
K_{LC}	Calculated loading stiffness
K_{LM}	Measured loading stiffness
K_{mach}	Instron machine stiffness
L	Length
L_R	Axial length of rupture opening for ballooned and ruptured cladding
L_s	Distance between applied loads in 4-PBT
M	Bending moment
M_s	Total sample mass
M_B	Mass of fuel-cladding bond layer
M_C	Mass of corrosion layer
M_M	Mass of metal layer
M_{max}	Maximum bending moment
P	Load measured by load cell
P_{max}	Maximum load for 4-PBTs and JAEA tests
R	Ideal gas constant
R_{mid}	Mid-wall radius of cladding metal
R_{mo}	Outer radius of cladding metal
S_o	Solubility of oxygen in the beta layer
T	Temperature
T_R	Rupture temperature
W	Weight (mass) of sample
W_G	Weight gain due to oxygen pickup in mass units
W_g	Weight gain due to oxygen pickup in %
w_g	Weight gain due to oxygen pickup normalized to surface area (in g/cm^2 or mg/cm^2)
δ	Applied displacement
$\Delta C_m/C_{mi}$	Circumferential strain at the mid-wall location $([C_{mf} - C_{mi}]/C_{mi})$
ΔC_{HM}	Hydrogen pickup (in wppm) in cladding during oxidation normalized to pre-test metal mass
δ_b	Fuel-cladding bond layer thickness
δ_c	Corrosion layer thickness
δ_e	Elastic displacement
δ_m	Elastic displacement of machine, including all components outside gauge length
$(\delta_{ox})_i$	Thickness of inner-surface oxide
$(\delta_{ox})_o$	Thickness of outer surface oxide
δ_R	Maximum width of the rupture opening
δ_p	Offset displacement based on load-displacement curve
ε_p	Plastic hoop strain
ε_θ	Elastic hoop strain
ε_z	Elastic axial strain
ν	Poisson's ratio
ρ_p	Post-bend-test radius of curvature of the sample
σ_{max}	Maximum axial stress in cladding metal for samples subjected to 4-PBTs and JAEA tests
σ_θ	Elastic hoop stress
σ_z	Elastic axial stress

1 INTRODUCTION

By the mid 1990s, it was well known that significant cladding oxidation (corrosion) can take place during extended periods of normal operation, and that some of the liberated hydrogen from the interaction with water is absorbed in the zirconium alloy cladding material. It thus seemed likely that an oxide layer on the surface and hydrogen in the metal would affect the behavior of cladding under conditions of a loss-of-coolant accident (LOCA).

Several aspects of cladding behavior under LOCA conditions are involved in safety analyses: ballooning strains, flow area reduction, rupture conditions, axial distribution of heat sources, and cladding embrittlement. A previous report by this laboratory provided results on oxidation-embrittlement limits for non-ballooned cladding as a function of pre-transient hydrogen content, on minimum times and corresponding temperatures for breakaway oxidation, and on ballooning with rupture under LOCA conditions [1]. The present report updates those results, provides additional results in those areas, and adds results of mechanical testing of cladding after ballooning, rupture, oxidation, and quench.

Improved testing procedures and data-analysis methods have been developed and utilized in our work since the publication of Ref. 1. Step-by-step procedures for conducting breakaway-oxidation tests and post-quench-ductility tests, along with appropriate data-analysis methods, were provided to NRC and were then incorporated in regulatory guides [2-4]. In addition, an assessment of post-LOCA mechanical tests methods was performed to confirm that we were using the best available testing procedures [5].

Some of the material in the Introduction of Ref. 1 is repeated here in an effort to make the present report relatively self-sufficient. Although all the important results from Ref. 1 are summarized in the present report, the earlier report would have to be consulted for details. The background and regulatory significance of cladding behavior during postulated LOCAs can be found in Ref. 6.

1.1 Cladding Materials

Table 1 lists the dimensions (outer diameter, OD, and wall thickness, h) and major alloying elements of pressurized-water-reactor (PWR) cladding materials that have been tested in this program. In addition to the PWR alloys included in Table 1, two sizes of boiling-water-reactor (BWR) cladding were used in the previous study: 9×9 (11.18-mm OD and 0.71-mm h) and 10×10 (10.29-mm OD and 0.66-mm h) Zr-lined Zircaloy-2 (Zry-2) cladding, where the inner lining of Zr constitutes ≈10% of the total cladding thickness. The chemical composition of Zry-2 is similar to standard Zircaloy-4 (Zry-4) except for the addition of ≈0.06 wt. % Ni.

Wall thickness values of these cladding materials are important in the calculation of oxidation level as a percentage of wall thickness. The alloying elements have a significant impact on coolant-side corrosion and hydrogen pickup during normal operation and on phase-change temperatures during LOCA transients. In general, a reduction of Sn results in decreased corrosion levels and hydrogen pickup during normal reactor operation. Reactor coolant temperature is also an important factor in determining corrosion level and hydrogen pickup, as both decrease with decreasing coolant temperatures. For BWRs, the inlet and outlet coolant temperatures are about 278°C and 288°C, respectively. For PWRs, the inlet and outlet coolant temperatures are about 296°C and 328°C, respectively. Thus, corrosion and hydrogen pickup tend to be greater in PWR cladding than in BWR cladding. Additional details are provided in Chapter 2 for the as-fabricated and high-exposure (sometimes referred to as high-burnup) cladding materials used in the test program.

Table 1. Dimensions and compositions of PWR cladding alloys used in test program; OD is outer diameter and h is wall thickness.

Parameter	15×15 Zry-4 Vintage Cladding	15×15 Zry-4 Low-Sn Cladding	17×17 Zry-4 Low-Sn Cladding	17×17 ZIRLO Standard Cladding	17×17 M5 Standard Cladding
OD, mm	10.76	10.91	9.50	9.50	9.50
h, mm	0.77	0.67	0.57	0.57	0.57–0.61
Sn, wt. %	1.29–1.42	1.29	1.29	0.99	0.02
Nb, wt. %	---	---	---	0.98	1.02
O, wt. %	0.137	0.124	0.12	0.120	0.145
Fe, wt. %	0.21	≈0.21	≈0.21	0.11	0.05
Cr, wt. %	0.10	≈0.10	≈0.10	<0.01	<0.01

1.2 Transient Cladding Temperatures

In a LOCA transient, much of the coolant inventory could be lost, and the fuel cladding would begin to heat up due to stored heat and decay heat – coupled with the absence of sufficient cooling. Around 750ºC to 850ºC during the temperature rise, the pressurized cladding would reach its ultimate tensile strength, and a local plastic instability would produce a ballooning strain and a rupture. A modest temperature reduction would accompany this deformation in the vicinity of the balloon because of enhanced turbulent cooling, but the cladding temperature would then continue to rise. Eventually, the emergency cooling water would stop the temperature rise and begin to cool the cladding. The cooling rate would be gradual at first because of steam-blanketing around the hot cladding, but then rapid cooling, or quench, would take place, cooling the cladding to about 135ºC (saturation temperature at the expected reactor containment pressure). Such a temperature transient is shown schematically in Fig. 1.

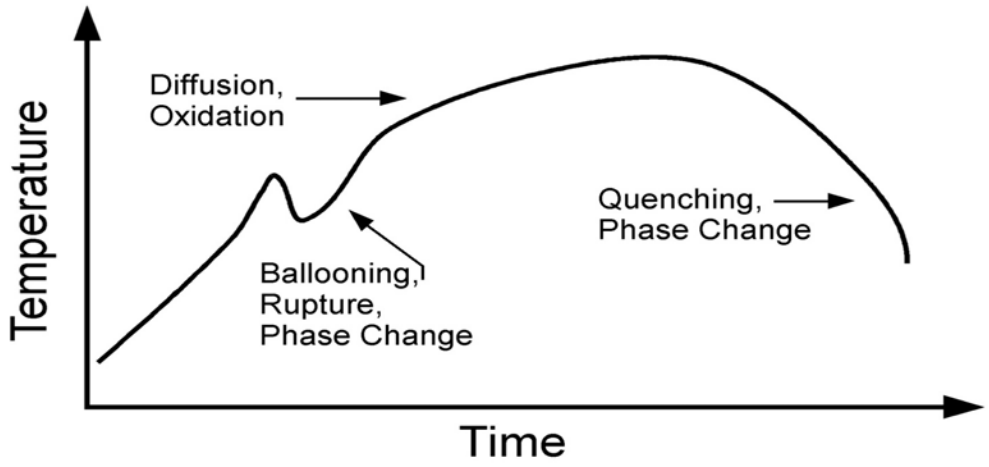

Figure 1. Schematic of cladding temperature history during a LOCA transient.

The calculated peak cladding temperature (PCT) for rods in a fuel assembly depends on fuel burnup, core location, and degree of conservatism used in the thermal analysis. Not all fuel rods will reach the cladding rupture temperature, nor will all rods that rupture reach a high PCT. The PCT and quench temperature can be lower for some LOCA transients, while the time at elevated temperature and pressure can be much longer. For those longer times at relatively lower temperatures, the normal oxidation process can become enhanced (so-called "breakaway oxidation") and accompanied by rapid hydrogen absorption, which leads to cladding embrittlement.

In the current work, no distinction is made between large- and small-break LOCAs because the experimental results and derived limits apply to both. PCT values in the range of 1000°C to 1204°C (licensing limit) were used to derive oxidation limits based on maintaining post-quench ductility. Tests were also conducted at 800°C to 1000°C PCT for times up to 5000 s to determine the minimum breakaway-oxidation time.

1.3 Transient Phase Transformations

During the heating phase of a LOCA transient, the zirconium-based cladding alloys of interest have a hexagonal crystal structure, the alpha phase, from room temperature up to about 650–800ºC. Above this temperature, there is a mixed-phase regime in which the crystal structure begins to change to a face-centered cubic geometry, the beta phase. For standard Zry-4 with 0.11 wt. % oxygen, the alpha to the mixed alpha-beta phase-change temperature is 810ºC, and the alpha-beta to beta phase-change temperature is 980ºC [7]. These phase-change temperatures increase with increasing oxygen content [7] and temperature ramp rate [8], and they decrease with increasing hydrogen content [8-13]. They also decrease with the substitution of Nb for Sn because Nb stabilizes the beta phase while Sn stabilizes the alpha phase [12]. Alloying elements Fe and Cr also stabilize the beta phase [12]. Thus, oxygen and Sn are alpha-stabilizers, while hydrogen, Nb, Fe and Cr are beta-stabilizers. The alpha to alpha-beta phase-change temperature is particularly sensitive to concentrations of these alloying elements, to hydrogen picked up during normal operation, and to the heating rate during the LOCA transient.

During the oxidation portion of a LOCA transient, alpha-phase Zr-based alloys have both high affinity for, and high solubility of, oxygen at high temperatures [13]. At LOCA-relevant temperatures, the oxygen-stabilized alpha phase is more thermodynamically stable than the oxide itself. Oxygen diffusion in the ZrO_2 oxide layer and in the Zr metal becomes rapid enough above 800ºC that measurable changes in metal oxygen concentration occur during the time period of a LOCA transient. Therefore, after some of the Zr alloy has transformed from the oxygen-rich alpha phase to the beta phase, the temperature is high enough that oxygen diffuses into the beta-phase metal, exceeding its solubility limit at the interface with oxygen-stabilized alpha layer. This oxygen-rich metal transforms back to the alpha phase, where the oxygen solubility limit is much higher than in the beta phase. Figure 2 is a qualitative representation of the oxygen content within the oxide, alpha phase, and beta phase for cladding heated to high temperature in flowing steam (outer surface only). Within a ruptured balloon, steam will also enter through the rupture and produce similar oxygen penetration from the inside surface of the cladding. Oxygen penetration can also occur from oxide and fuel bonded to the inside surface of high-exposure cladding. Upon cooling, the beta phase also converts back to the alpha phase, but this prior-beta region retains its low oxygen concentration and is ductile at 135ºC for average oxygen concentrations <0.6 wt. %. The prior oxygen-stabilized alpha region retains its relatively high oxygen concentration and is brittle, as is the oxide layer.

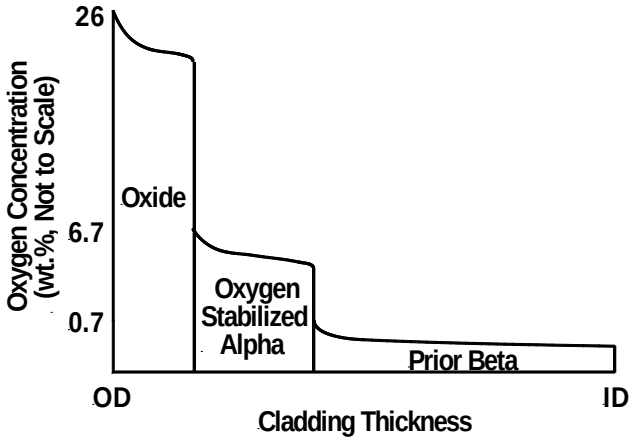

Figure 2. Qualitative diagram of oxygen concentration in Zircaloy cladding exposed at high temperature to steam on the outside surface and cooled to room temperature. OD and ID are outer and inner diameters, respectively.

1.4 Oxidation Equations

Although Baker-Just equations [14] have been used in many LOCA analyses, Cathcart-Pawel (CP) equations are more accurate for Zircaloys and will be used throughout this report. In their report [15], Cathcart et al. gave four related rate equations, one for each of the following: (a) the oxide layer thickness, (b) the alpha layer thickness, (c) the sum of the oxide-plus-alpha layer thickness, and (d) the total oxygen consumed, which was given as weight gain in grams per square centimeter of surface area. All these obeyed parabolic kinetics. The rate equation for weight gain, w_g (Cathcart et al. called it τ), is:

$$d(w_g)/dt = (k^2/2)/ w_g, \quad (1)$$

where k is a temperature-dependent coefficient (Cathcart et al. labeled it δ_τ). Under isothermal oxidation conditions, the integration of Eq. 1 is simply

$$(w_g)^2/2 = (k^2/2)\, t, \quad (2)$$

or

$$w_g = k\, t^{1/2}, \quad (2a)$$

which plots as a parabola.

The coefficient, k, is an Arrhenius-type function of temperature:

$$k = a\ \exp(-Q/[R\times T]), \quad (3)$$

where R is the universal gas constant, and the parameters "a" and "Q" are given by Cathcart et al. for each of the four rate equations reported. Using the Cathcart et al. values for "a" and "Q" for weight gain determined from metallographic results and the assumption of stoichiometric oxide, the isothermal CP equation becomes:

$$w_g = 0.602\ \exp(-1.005\times 10^4/T)\ t^{1/2}, \quad (4)$$

where w_g is in g/cm^2, T is temperature in K, and t is time in s. Thus, the weight gain increases as the square root of time at a given temperature, and the rate increases exponentially with temperature. The results of Eq. 4 should be multiplied by a factor of 10 to convert to SI units of kg/m^2. For convenience in the current work, the measured weight gain is expressed as mg/cm^2. In comparing the measured weight gain per unit surface area to the CP-predicted weight gain, results of Eq. 4 are multiplied by 10^3 to give units of mg/cm^2.

For steam oxidation at 1100ºC and 1200ºC, the agreement between calculated and measured weight gains was found to be excellent for the cladding materials (Zry-2, Zry-4, ZIRLO, M5, and E110) tested earlier in this program [1]. Differences among the alloys were observed at 1000ºC prior to breakaway oxidation: (a) measured weight gains for Zry-2 and Zry-4 remained in excellent agreement with calculated weight gains, (b) measured weight gains for Nb-bearing alloys (ZIRLO, M5, and E110) were considerably less than calculated weight gains due to slowing down of oxide-layer growth with increasing time, and (c) measured weight gains (based on oxide layer thickness) were considerably less for the Zr liner within Zry-2 [1]. However, as will be discussed later in this section, the post-quench ductility decrease and embrittlement with increasing oxidation time were similar for all alloys tested (even at 1000ºC) and correlated quite well with calculated weight gain normalized to cladding wall thickness.

A related parameter that is often used is ECR, or equivalent cladding reacted. ECR is defined as the percentage of the cladding thickness that would be oxidized if all the oxygen pickup stayed in the oxide layer as ZrO_2. This is an artificial parameter because some of the oxygen diffuses into the metal, but it is useful and is directly related to weight gain by simple geometric factors, along with the density of Zr (6500 kg/m^3 = 6.5 g/cm^3), the atomic mass of Zr (91.2 kg/kg-mole), and the atomic mass of diatomic oxygen (32.0 kg/kg-mole). The conversion is given in Eq. 5 for one-sided oxidation and Eq. 6 for two-sided oxidation.

$$\text{One-sided oxidation} \qquad ECR = 43.9\ [(w_g/h)/(1 - h/D_o)], \tag{5}$$

$$\text{Two-sided oxidation} \qquad ECR = 87.8\ w_g/h, \tag{6}$$

where ECR is in %, w_g is in g/cm^2, h is cladding thickness in cm, and D_o is cladding OD in cm.

1.5 Embrittlement Mechanisms

Six embrittlement mechanisms are described below. Data relating to these mechanisms are presented in subsequent sections of this report.

1.5.1 Beta-layer embrittlement by oxygen

At 1200ºC the oxygen solubility limit of beta-phase Zircaloy is about 0.6 wt% (0.57 wt. % [7]), and the solubility increases with increasing temperature. Above 1200ºC, oxygen solubility and diffusion rates in the beta phase become high enough in Zr-based cladding alloys that, when cooled, the prior-beta region is brittle after relatively short oxidation times. This mechanism was understood in 1973, and the 1204ºC (2200ºF) temperature limit in NRC's regulation precluded such rapid embrittlement in non-irradiated Zircaloy [6].

Oxygen solubility in the beta-layer is lower at 1100ºC (0.38 wt. %) and 1000ºC (0.24 wt. %) [7], and the prior-beta layer remains ductile at temperatures as low as room temperature (RT) even after the layer is saturated with oxygen. These solubility limits apply to as-fabricated cladding.

On the basis of the previous discussion, it would be more logical to correlate post-quench ductility with the average oxygen content in the prior-beta layer rather than with an ECR value. However, it is easier to calculate weight gain and CP-ECR, and there is a strong correlation between oxygen content in the prior-beta layer and CP-ECR. The layer-thickness correlations, oxygen concentrations at the metal-phase interfaces, and diffusion equations in Ref. 15 were used to calculate w_g, CP-ECR, and average oxygen content (c_o) in the beta layer as a function of oxidation time at 1200ºC for as-fabricated 17×17 Zry-4 cladding with an initial oxygen content (c_{oi}) of 0.12 wt. % and a solubility limit (S_o) of 0.57 wt. %. Figure 3 shows the near-linear relationship between the normalized oxygen pickup in the beta layer and CP-ECR in the range of interest (i.e., up to 18%, beyond which the beta layer is essentially saturated with oxygen). Therefore, using the CP-ECR value to characterize post-quench ductility of as-fabricated cladding is just as effective as using the prior-beta oxygen content.

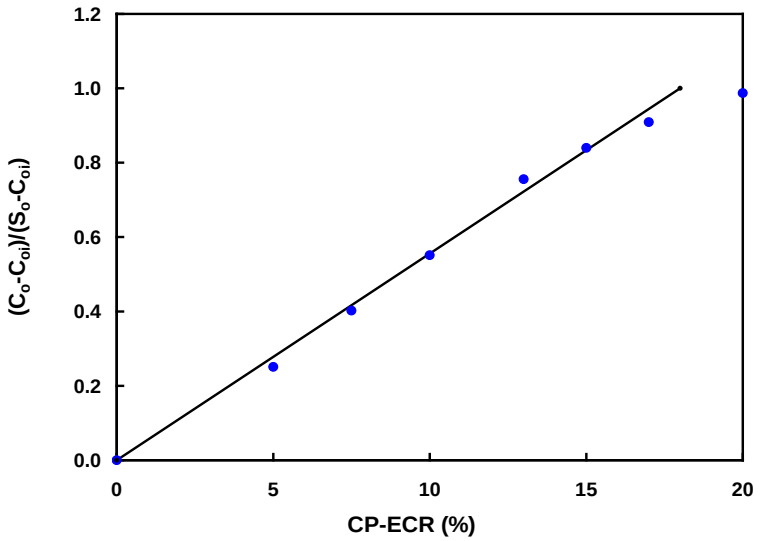

Figure 3. Average oxygen content (c_o) in the beta layer as a function of CP-ECR for isothermal oxidation at 1200ºC. The calculation was performed for 17×17 Zry-4 with 0.12 wt. % initial oxygen content (c_{oi}) and 0.57 wt. % solubility limit (S_o).

Notwithstanding this good correlation with calculated CP-ECR values, measured ECR values for Nb-bearing alloys (e.g., M5) did not correlate very well with ductility decrease for oxidation at 1000ºC [1]. The slow growth rate of the oxide layer resulted in low values of measured ECR for M5 with increasing test time. At oxidation times corresponding to about 20% CP-ECR, the measured ECR for M5 was only 13% (the measured ECR for Zry-4 [22%] was close to the CP-ECR value). However, the RT post-quench ductility value (3.2%) was essentially the same for M5 and Zry-4 [1]. The decreased weight-gain rate for M5 was predominantly due to the decreased rate of oxide-layer growth. This reduction would not affect the diffusion of oxygen into the beta-phase metal and hence the oxygen concentration in the beta phase. The average oxygen concentration in the beta phase increases at a diffusion-dependent rate, which depends on time at temperature. These are reflected in the CP-ECR correlation.

Calculated CP-ECR values and measured ECR are similarly independent of pre-transient hydrogen content, which increases the oxygen content in the beta layer and thus decreases post-quench ductility for a given oxidation temperature and time. Therefore, hydrogen content must be considered as an independent parameter in correlating ductility decrease with increasing CP-ECR.

1.5.2 Beta-layer thinning

With increasing time, diffusion of oxygen into the metal will convert more and more of the beta phase to the oxygen-stabilized alpha phase – the alpha layer grows and the beta region shrinks. For long times at temperature, the ductile prior-beta region becomes so thin that the macroscopic specimen exhibits brittle behavior. This mechanism was also understood in 1973 and was accommodated by the 17% ECR limit in NRC's regulation [6].

However, on the basis of previous test results [1], beta-layer thinning did not contribute to the embrittlement of as-fabricated cladding alloys within the range of oxidation levels (5% to 20%) included in the test program. For 17×17 Zry-4 (0.57-mm h) oxidized at 1100ºC, the RT post-quench ductility leveled off to ≈5% strain between 15% and 20% CP-ECR even though the beta-layer thickness continued to decrease to a minimum of 0.33 mm at 20% CP-ECR.

Nevertheless, beta-layer thinning does contribute to hydrogen-enhanced beta-layer embrittlement by oxygen. This subject is discussed in Section 1.5.4.

1.5.3 Localized hydrogen-induced embrittlement in the balloon region

Steam that enters through a rupture in a balloon causes oxidation inside the cladding. Hydrogen that is released during this reaction is not swept away as it is on the outside of the cladding, but is absorbed in the metal above and below the rupture opening. Beta-phase Zr-alloys have very high hydrogen solubility (e.g., $\approx 10^4$ wppm at 1200ºC), and hydrogen absorption results in enhanced embrittlement in the balloon region from the rupture edges to the balloon necks. This effect, which is neither burnup nor alloy dependent, was discovered earlier (see Ref. 6) and has been confirmed in the present research program.

For ballooned, ruptured, and oxidized Zry-2 cladding (as-fabricated and high-burnup), hydrogen peaks as high as 3000-4000 wppm were measured in the oxidized cladding [1]. In this previous work, only two post-quench four-point bend tests (4-PBTs) were conducted at RT with ballooned and ruptured as-fabricated Zry-2 samples oxidized to 9% and 15% CP-ECR, respectively. Neither test sample failed in the high-hydrogen region because the balloons were large and the weakest cross section was in the rupture region. However, in the current work, a large number of such LOCA oxidation and post-quench 4-PBTs were performed with as-fabricated and pre-hydrided ZIRLO cladding, and some did fail in the high-hydrogen region. These test results allowed us to better characterize degradation of mechanical properties as a function of pre-transient hydrogen content and oxidation level.

1.5.4 Hydrogen-enhanced beta-layer embrittlement

During normal operation, some hydrogen from the corrosion process is absorbed in the cladding metal. When that cladding is exposed to high-temperature LOCA conditions, the elevated hydrogen levels increase the solubility of oxygen in the beta phase and the rate of diffusion of oxygen into the beta phase. Thus, even for LOCA temperatures below 1204ºC, embrittlement can occur at times corresponding to less than 17% oxidation in corroded cladding with hydrogen pickup. Significant degradation can occur at hydrogen concentrations as low as 100 wppm. For high-burnup M5 with 140-wppm hydrogen, previous results showed that the ductile-to-brittle transition oxidation level for oxidation at 1200°C decreased from 20% (for as-fabricated M5) to about 14%. For high-burnup ZIRLO with 600-wppm hydrogen, the transition oxidation level decreased from 19% (for as-fabricated ZIRLO oxidized at 1200ºC) to 4% with a peak oxidation temperature of 1130ºC. In the current work, pre-hydrided and high-burnup ZIRLO

samples with intermediate pre-transient hydrogen contents of 200 to 340 wppm were used to determine oxidation embrittlement thresholds. These levels refer to hydrogen contents in the cladding metal.

During the oxidation portion of a LOCA transient, pre-transient hydrogen concentrates in the beta-phase metal, as this phase has a much higher hydrogen solubility and affinity for hydrogen than the oxygen-stabilized alpha phase. As the beta layer decreases in thickness, the hydrogen content in this layer increases correspondingly, along with the oxygen solubility [13]. Beta-layer thinning thus contributes to hydrogen-enhanced post-quench embrittlement of cladding at lower oxidation levels.

In addition to elevating oxygen solubility, there appears to be an intrinsic embrittlement effect of hydrogen dissolved in the beta phase [9-11]. During very rapid cooling from the oxidation temperature, hydrogen is essentially frozen in the low-oxygen prior-beta phase. For a fixed oxidation time (e.g., 50 s at 1200ºC and one-sided oxidation), Zry-4 samples with 600-wppm hydrogen were very brittle at CP-ECR values of ≈3%. For much slower cooling rates and lower quench temperatures (e.g., 600ºC and 700ºC), significant ductility was retained in these samples even though the oxidation level increased to ≈6% CP-ECR. The enhancement in ductility is attributed to small-scale diffusion of hydrogen out of the lower-oxygen regions of the prior beta phase to the interfaces between these lower-oxygen regions and higher-oxygen regions formed during pre-quench cooling. Although the cooling rates at which ductility was enhanced [9-11] were too slow to be LOCA-relevant, the results do support the hypothesis that there is an intrinsic embrittlement effect of hydrogen beyond the dominant effect of increasing the oxygen solubility.

1.5.5 General hydrogen-induced embrittlement from breakaway oxidation

Zirconium dioxide (ZrO_2) can exist in several crystallographic forms (allotropes) and has a monoclinic structure at normal operating temperatures. The tetragonal oxide that generally develops under LOCA conditions is dense, adherent, and protective with respect to hydrogen pickup. Although the monoclinic-to-tetragonal phase transformation temperature is nominally ≈1150°C, the tetragonal oxide phase can be stabilized at lower oxidation temperatures by compressive stress, hypostoichiometry, and to some extent grain size. There are, however, mechanical (e.g., local regions of tensile stress) and chemical (e.g., impurities at metal surface) conditions that promote a transformation to the lower-temperature monoclinic phase that is neither fully dense nor protective. When these conditions are present, the tetragonal-to-monoclinic transformation can begin in an unstable way at local regions of the metal-oxide interface and grow rapidly throughout the oxide layer due in part to the local volume increase (≈5%) associated with the phase transformation. Because this transformation results in an increase in oxidation rate, it is referred to as breakaway oxidation. Along with this increase in oxidation rate due to cracks in the monoclinic oxide, there is significant hydrogen pickup. Hydrogen that enters in this manner during a LOCA transient has a similar effect on embrittlement as hydrogen from the normal burnup process. Although breakaway oxidation was known in 1973, a connection to embrittlement was not made at that time.

In the previous work, a large test matrix was used to determine minimum breakaway times and corresponding isothermal oxidation temperatures for two variants of 15×15 Zry-4, for 10×10 Zry-2, for 17×17 ZIRLO, and for an older lot of Russian E110 (Zr-1Nb alloy). In the current work, isothermal tests were conducted with M5 cladding (up to 5000 s), the isothermal database for ZIRLO was expanded to include numerous tests within the narrow temperature range of 970ºC to 1000ºC, and tests were conducted with ZIRLO subjected to transient oxidation temperature histories.

1.5.6 Oxygen pickup from the cladding inner surface

For non-irradiated cladding, the oxygen source for diffusion into the metal is the ZrO_2 layer that forms during high temperature oxidation in steam. As burnup increases, normal corrosion will contribute to the outer-surface oxygen source. There will also be an oxygen source on the inner surface of irradiated cladding due to gas-phase UO_3 transport prior to gap closure, fuel-cladding-bond formation (UO_2 in solid solution with ZrO_2), and the oxide fuel bonded to this layer. Thus in high-burnup fuel under LOCA conditions, oxygen can enter the cladding from the inner surface even away from the balloon location. The situation is like a three-layer diffusion "couple" as illustrated in Fig. 4. The actual thicknesses of the OD and ID oxygen sources may be relatively unimportant at high burnup because they contain much more oxygen than will diffuse into the metal (see related tests by Hofmann and Politis [16]). However, if the ID oxide layer is the only source of inner-surface oxygen, it may be completely reduced by the cladding metal prior to high-temperature embrittlement and the effect would be limited. Nevertheless, if the inner-surface oxide layer or the oxide-bond-fuel layer is well developed (see Fig. 5), then two-sided oxidation would have to be accounted for in LOCA behavior away from the balloon region.

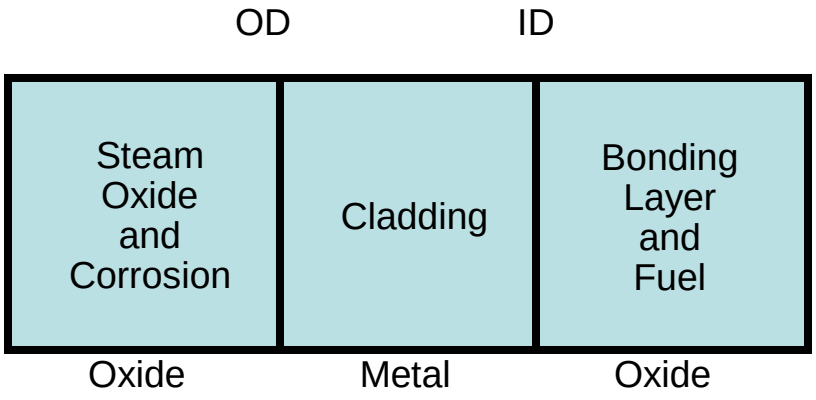

Figure 4. Three-layer diffusion "couple" character of oxygen sources and cladding metal.

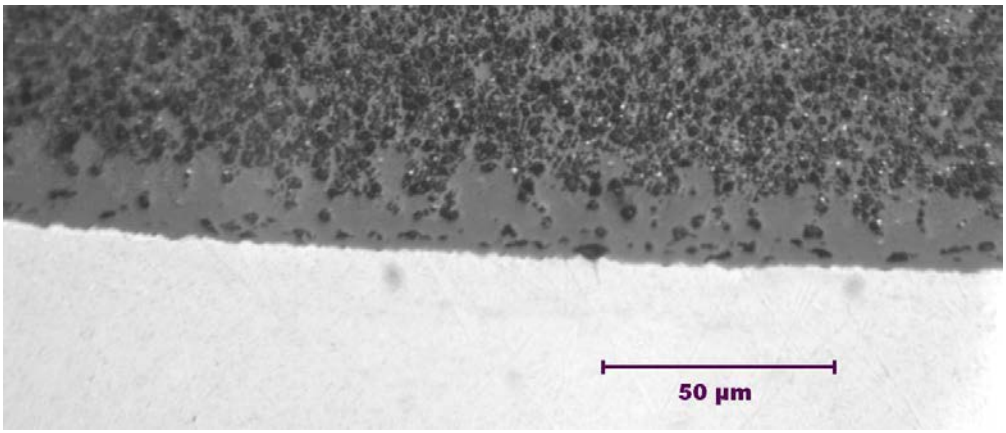

Figure 5. Well-developed fuel-cladding bond layer (gray) at the fuel mid-plane of a Zry-4-clad fuel rod irradiated to 67 GWd/t in the H.B. Robinson reactor.

1.6 Conventional Use of Equivalent Cladding Reacted (ECR)

The embrittlement mechanisms identified in Section 1.5 depend on oxygen diffusion into the cladding metal. It is clear from the work of Cathcart & Pawel and others that these diffusion-related processes have a form similar to the weight-gain relation (Eq. 4) for isothermal oxidation. Although it is not clear how to characterize the amount of oxygen diffusion that results in certain mechanical behavior of interest, it is convenient to empirically correlate this mechanical behavior with CP-ECR – a measure of time at temperature. In other words, mechanical behavior is correlated with the time it takes to produce a certain amount of oxygen pickup at a given temperature, as normalized to cladding dimensions. This practice has been used for 40 years and we continue to find it useful. For consistency, we will always use the CP weight-gain correlation to calculate w_g in Eqs. 5 and 6 and refer to that parameter as CP-ECR. As CP-ECR is independent of hydrogen content while ductility decrease is highly dependent on hydrogen content, the pre-transient hydrogen content will be treated empirically as an independent parameter such that the embrittlement oxidation level (CP-ECR) will be expressed as a function of this hydrogen content.

1.7 Pre-transient Hydrogen Content in the Cladding Metal (C_{HM})

The pre-transient hydrogen content in the cladding metal is easier to define than it is to measure for high-exposure, corroded cladding. Experimentally, C_{HM} is referred to as the pre-test (i.e., pre-LOCA-oxidation test) hydrogen content (in wppm) in the cladding metal. The methodology developed and applied in the current work (see Sections 3 and 5) used a combination of pre-test and post-test measurements to determine C_{HM}. Post-test hydrogen-content measurements were corrected to account for weight gain during the oxidation phase of the testing, the mass of the pre-test corrosion layer, and the mass of the pre-test fuel-cladding bond layer. As hydrogen in the corrosion and fuel-cladding-bond layers is driven off during the oxidation test, no additional correction factors were needed to account for this extra source of hydrogen.

The criterion used for initiation of breakaway oxidation (i.e., breakaway oxidation time) is 200 wppm hydrogen pickup (ΔC_{HM}). The parameter ΔC_{HM} refers to the increase in hydrogen content during the oxidation test referenced to the pre-test metal mass of the cladding sample. As pre-test cladding samples were non-irradiated and non-oxidized (see Section 4), correction factors were not needed for the masses of the corrosion and fuel-cladding bond layers. Post-test measurements of hydrogen content were corrected for weight gain, and the initial hydrogen content in as-fabricated cladding was subtracted to determine ΔC_{HM}.

2 MATERIALS, TEST METHODS, AND PROCEDURES

Testing in this work includes LOCA integral tests (heat-up, ballooning, rupture, oxidation, and quench) and separate tests for oxidation and embrittlement. Interpretation and application of LOCA-relevant data require an understanding of cladding materials used for test samples, test methods, test procedures, and data-analysis methods. These were described in detail in Ref. 1 for work performed through June 2008. For the convenience of the reader, some of these details are repeated in this section.

Also included in this section are refinements and improvements made during the course of the current work in sample preparation, data collection, and data analysis. During this time, draft procedures for conducting breakaway-oxidation tests [17] and post-quench ductility tests [18], along with data analysis methods, were documented and submitted to NRC in March 2009. These procedures were initially followed in the current work and later improved based on the practical experience of applying these procedures and data-analysis methods. Argonne also worked with NRC to improve, generalize, and formalize these documents into three regulatory guides needed for the planned performance-based LOCA acceptance criteria: RG 1.222 [2], RG 1.223 [3], and RG 1.224 [4]. These regulatory guides are readily accessible, and they contain additional improvements that were made since Refs. 17 and 18 were submitted to NRC.

2.1 Description of Cladding Alloys and High-Burnup Fuel Segments

As-fabricated cladding alloys were provided by Global Nuclear Fuels (8×8, 9×9, and 10×10 Zry-2), Westinghouse (17×17 low-Sn Zry-4 and ZIRLO), AREVA (1970s 15×15 Zry-4 tubing, 1980s 15×15 low-tin Zry-4, 15×15 low-tin Zry-4, 15×15 M5, and 17×17 M5), and Fortum (standard E110 tubing and cladding). Alloys, except for E110, listed above without a year are modern, belt- or wheel-polished (OD) and sand-blasted (ID) cladding alloys with reduced surface roughness and impurities. The 8×8 Zry-2 was used for early thermal and metallurgical benchmark testing of the LOCA integral apparatus. The 9×9 Zry-2 was fabricated by the same methods used to fabricate high-burnup Limerick fuel-rod cladding and had the same nominal composition and dimensions as the Limerick cladding. It was used in the previous test program to generate baseline LOCA integral data and one-sided, high-temperature steam oxidation data. The 1970s 15×15 Zry-4 tubing was close to being archival material for the high-burnup H. B. Robinson (HBR) cladding tested in this program. However, this tubing had ≈0.05-mm larger outer diameter and ≈0.025-mm thicker wall than the HBR cladding. The final finishing step after fueling the HBR tubing to convert it to cladding was pickling to remove ≈0.05 mm from the outer diameter. Because this tubing was not in final cladding form, it was not used to generate baseline data. Rather, the 1980s 15×15 low-Sn Zry-4 cladding, which had similar dimensions, oxygen content, and mechanical properties as the HBR cladding, was used in previous work to determine baseline HBR oxidation and post-quench ductility properties. This cladding is referred to as "HBR-type Zry-4" to distinguish it from more modern Zry-4 materials.

Some 15×15 and 17×17 M5 cladding was provided in 2002 by AREVA for benchmarking purposes but not for data generation. This 17×17 M5 (0.57-mm wall) was characterized in terms of chemical composition and used to develop and benchmark the two-sided oxidation test train. At a later date, AREVA provided 17×17 M5 with 0.61-mm wall thickness for data-generation purposes. The post-quench ductility of the 15×15 M5 and the 0.61-mm-wall 17×17 M5 was compared to confirm that post-quench ductility correlated with the calculated extent of oxidation (CP-ECR) at a given temperature independent of differences in cladding wall thickness and outer diameter.

For the post-quench ductility program, the primary alloys of interest were 10×10 Zry-2, 17×17 low-Sn Zry-4, 17×17 ZIRLO, and 17×17 M5 (0.61-mm wall). E110 was also added to the test program to determine why its steam-oxidation behavior was so poor as compared to M5, even though the compositions of both alloys were very similar. E110 tubing and final-form cladding were provided by Fortum (Finland). Results of previous tests performed with E110 material are well documented [1,19]. As such, these test results are not included in this report.

For breakaway-oxidation studies, the test plan called for the same alloys as used for the post-quench-ductility studies. However, due to the limited supply of 17×17 low-Sn Zry-4, wheel-polished 15×15 and HBR-type (rough surface) 15×15 low-Sn Zry-4 were used instead. This allowed the effects of surface roughness to be included in these studies for Zry-4 samples with similar geometry, Sn content, and oxygen content. The other three alloys (10×10 Zry-2, 17×17 ZIRLO, and 17×17 M5) used in the post-quench-ductility tests were also used in the breakaway oxidation tests. However, test results for the ZIRLO received in 2003 indicated early breakaway oxidation at the cladding inner surface for oxidation at 1000°C. Additional lots were received in 2006, 2008, and 2010. As none of these lots exhibited early breakaway oxidation on the cladding inner surface, it is hypothesized that there was a change in final treatment of the cladding inner surface to reduce surface roughness and impurities. Breakaway-oxidation test results are provided in Ref. 1 for ZIRLO–2006. ZIRLO–2008 was used in the current work for breakaway oxidation tests and post-quench ductility (PQD) tests with pre-hydrided cladding. LOCA integral tests were conducted in the current work with as-fabricated and pre-hydrided ZIRLO–2010.

Measurements were performed by Argonne to determine cladding OD, wall thickness, surface roughness, oxygen content, and hydrogen content. Nominal Sn contents for the cladding alloys were provided to Argonne by the fuel vendors. Some of the alloys were sent to an outside organization to determine chemical composition. For ZIRLO–2003 cladding, Westinghouse also performed chemical analysis on a sample from the cladding sent to Argonne. Some Argonne wall-thickness measurements were merely spot checks of this dimension at several axial locations. More detailed dimensional characterization was performed for HBR archive, for HBR-type Zry-4, for 17×17 M5 (0.61-mm h), and for lots of ZIRLO cladding received after 2003.

Table 2 summarizes characterization results for the Zr-lined Zry-2 used in the previous test program. The Zr liner was on the cladding inner surface (≈10% of the wall thickness). Chemical composition data listed in Table 2 refer to the final cladding product (≈90% Zry-2 and ≈10% Zr liner). They should not be interpreted as the composition of standard Zry-2.

Dimensions and chemistry of the Zry-4 used in the previous test program are listed in Table 3. Pickling was used for the inner-surface treatment of near-archive HBR tubing and HBR-type cladding. Based on 24 measurements for adjacent 25-mm long samples, wall thicknesses were determined to be 0.790±0.006 mm and 0.761±0.006 mm, respectively, for tubing and cladding.

Dimensions and chemistry for 17×17 ZIRLO (2003), 17×17 M5 (validation lot), 17×17 M5 (data lot), and 15×15 M5 (validation lot) used in the previous test program are listed in Table 4. Cladding OD and wall thickness values listed in Table 4 are nominal values provided by the vendor and spot checked by Argonne. Additional measurements were made for a 1-m-long segment of 17×17 M5 cladding used for data generation in both previous and current test campaigns. The OD was 9.48±0.00 mm (based on 24 measurements at 12 axial locations) and h was 0.062±0.01 mm (based on 12 measurements).

Table 2. Dimensions and chemistry of Zr-lined Zry-2 used in the Argonne test program (the "<" sign means below the detection limit and "---" means not measured).

Parameter	8×8 Zry-2	9×9 Zry-2	10×10 Zry-2
OD, mm	12.27	11.18	10.29
Wall Thickness, mm	0.82	0.71	0.66
ID Liner Thickness, mm	≈0.08	≈0.07	≈0.07
OD Surface Roughness, μm	---	0.14	0.11
Sn, wt.%	---	1.18	---
Nb, wt.%	---	<0.01	---
O, wt.%	---	0.11	---
Fe, wt.%	---	0.20	---
Cr, wt.%	---	0.12	---
Ni, wppm	---	550	---
S, wppm	---	30	---
C, wppm	---	250	---
Hf, wppm	---	<100	---
Si, wppm	---	≤100	---
N, wppm	---	45	---
H, wppm	---	6	13

Table 3. Dimensions and chemistry of Zry-4 used in the Argonne test program (the "<" sign means below the detection limit and "---" means not measured).

Parameter	15×15 Zry-4 HBR Tubing	15×15 Zry-4 HBR Cladding	15×15 Zry-4 Cladding	17×17 Zry-4 Cladding
OD, mm	10.84	10.77	10.91	9.50
Wall Thickness, mm	0.80	0.76	0.67	0.57
OD Surface Roughness, μm	0.36	0.32	0.10	0.14
Sn, wt.%	1.42	1.29	1.29	1.29
Nb, wt.%	---	---	---	---
O, wt.%	0.137	0.136	0.124	0.120
Fe, wt.%	0.21	---	---	---
Cr, wt.%	0.10	---	---	---
Ni, wppm	<35	---	---	---
S, wppm	---	---	---	---
C, wppm	140	---	---	---
Hf, wppm	<50	---	---	---
Si, wppm	92	---	---	---
N, wppm	54	---	---	---
H, wppm	12	22	26	5

Table 4. Dimensions and chemistry of ZIRLO and M5 cladding materials used in the Argonne test program (the "<" sign means below the detection limit "---" means not measured).

Parameter	17×17 ZIRLO–2003	17×17 M5 (Validation)	17×17 M5 (Data)	15×15 M5 (Validation)
OD, mm	9.50	9.50	9.50	10.91
Wall Thickness, mm	0.57	0.57	0.61	0.64
OD Surface Roughness, μm	0.11	0.12	0.12	0.11
Sn, wt.%	0.99	0.02	---	---
Nb, wt.%	0.98	1.02	---	---
O, wt.%	0.12	0.145	0.145	---
Fe, wt.%	0.11	0.05	---	---
Cr, wt.%	<0.01	<0.01	---	---
Ni, wppm	<100	<100	---	---
S, wppm	---	25±5	---	---
C, wppm	135	110	---	---
Hf, wppm	40	<100	---	---
Si, wppm	53	<100	---	---
N, wppm	46	55	---	---
H, wppm	5	6	5	---

Additional lots of ZIRLO were used in the previous and current work, and a comparison of the four lots of ZIRLO that have now been tested is shown in Table 5. Detailed chemistry values were not provided for the later quantities of ZIRLO, but more detailed dimensional characterization was performed by Argonne. Where one-sigma uncertainty ranges are shown in Table 5, multiple measurements were made (e.g., 90 data points over 11 m for the OD of ZIRLO–2008). Dimensions for each PQD and breakaway-oxidation sample were recorded and used to determine weight gain per unit surface area and CP-ECR.

Table 5. Characterization of the four lots of ZIRLO used in the Argonne test program.

Parameter	17×17 ZIRLO-2003	17×17 ZIRLO-2006	17×17 ZIRLO-2008	17×17 ZIRLO-2010
OD, mm	9.50	9.49	9.48±0.03	9.50±0.01
Wall Thickness, mm	0.57	0.57	0.59±0.01	0.58±0.01
OD Surface Roughness, μm	0.11±0.01	0.17±0.03	0.14±0.03	0.16±0.01
O, wt.%	0.119±0.003	0.116±0.003	≈0.12	≈0.12
H, wppm	5±0	11±3	17±2	22±2

Irradiated materials used in the Argonne test program are summarized in Table 6. The Electric Power Research Institute (EPRI) provided two fueled TMI-1 PWR rods at 48-50 GWd/t for validation of characterization and testing methodologies, seven fueled Limerick BWR rods at 54-57 GWd/t for LOCA data generation, and seven fueled H. B. Robinson PWR rods at 64-67 GWd/t. EPRI and AREVA provided two high-burnup fueled M5 rods at 63 and 70 GWd/t for LOCA integral testing of fueled-cladding samples. In addition, under agreements among NRC-Studsvik-AREVA and NRC-Studsvik-Westinghouse, high-burnup defueled M5 cladding from the European Ringhals PWR reactor and ZIRLO cladding from the North Anna (NA) PWR reactor, respectively, were supplied for post-quench ductility testing.

Table 6. Characteristics of high-burnup fuel rod segments and defueled high-burnup cladding for the Argonne LOCA test program. Burnup values are rod averaged.

Parameter	TMI-1	Limerick	H. B. Robinson	North Anna M5[a]	North Anna ZIRLO	Ringhals M5
Reactor	PWR	BWR	PWR	PWR	PWR	PWR
Enrichment, wt.%	4.00	3.95 (3.40-3.95)	2.90	4.20	≈4	≈4
Burnup, GWd/t	48-50	54-57	63-67	63-70	70	63
Discharge Date	1997	1998	1995	2004	2001	2003
Fast Fluence, 10^{25} n/m^2	9	11	14	Not Provided	Not Provided	Not Provided
Cladding	15×15 Low-Sn Zry-4	9×9 Zr-lined Zry-2	15×15 Standard Zry-4	17×17 M5	17×17 ZIRLO	17×17 M5
Initial Wall Thickness, mm	0.69	0.71	0.76	0.57	0.57	0.57
OD Oxide, μm	≤30	≈10 + ≈10 crud	≤100	<10	≈20-50	<15
Hydrogen Pickup, wppm	≤300	70	≤800	<100	≤650	≤140
Fueled	Yes	Yes	Yes	Yes	No	No

[a]Not tested because of closure of Alpha Gamma Hot Cell Facility to programmatic work.

For both the previous and current work, oxidation and PQD tests were conducted on defueled samples of ZIRLO cladding from NA Rod AM2-L17: (a) 40−50 μm corrosion layer thickness and 450−600 wppm hydrogen in cladding metal for previous work and (b) 25−30 μm corrosion layer thickness and 300−340 wppm hydrogen in cladding metal for current work.

2.2 General Description of Apparatus and Test Samples

The LOCA high-temperature apparatus was designed to perform both LOCA integral tests using long (≈300 mm) pressurized fueled cladding samples and oxidation-quench tests using short (25 mm) defueled cladding samples. An out-of-cell unit was used for thermal-benchmarking purposes and for generating data for as-fabricated and pre-hydrided alloys. Two in-cell units have been used in the Alpha-Gamma Hot-Cell Facility (AGHCF) and the Irradiated Materials Laboratory (IML) for testing high-burnup fueled and defueled cladding, respectively. When in operation, the units shared the same control and data acquisition systems used for the out-of-cell apparatus. The main difference in the apparatus between LOCA-integral and oxidation-quench tests is the test train holding the sample in position within the quad-elliptical, radiant-heating furnace and the connections required. Both use a quartz-tube steam chamber (48-mm ID and 610-686 mm long).

The radiant-heating furnace has four vertical bulbs, a reflecting inner surface, and a 250-mm-high uniform heating zone. LOCA integral tests were conducted with 300-mm-long samples initially under high internal pressure (≈8 MPa), which required connection to the high-pressure argon line, along with top and bottom pressure transducers. In the current work, the LOCA integral sample length was extended to 318 mm to minimize secondary ballooning in the top plenum region. Oxidation-quench-embrittlement tests with non-deformed cladding did not require the high-pressure connection or pressure transducers.

For both types of testing, steam, at near-atmospheric pressure, flowed up through the quartz-tube test chamber at 5.3 g/minute and exited the chamber into a condenser. The quartz tube length was initially 686 mm and later reduced to 610 mm for tests conducted in the IML. Following oxidation and slow-cooling phases, steam flow was turned off, and quench water was introduced (bottom flooding) to give very rapid sample cooling from 800ºC to about 100ºC at the selected test time.

During the course of the current work, two changes were made to pre-test sample characterization and cleaning: (a) the measured cladding thickness was used for as-fabricated and pre-hydrided cladding samples, rather than the nominal cladding thickness, in the CP-ECR calculation and (b) etching (i.e., pickling) with an HF-containing acid was used prior to gaseous charging of samples with hydrogen (i.e., pre-hydriding). Following pre-hydriding, the etched surfaces were polished (removal of ≈1 μm from etched surfaces) to remove surface impurities, especially fluorine. Argonne experience with pickling indicated that even a very light etch (e.g., 15 to 60 s in an acid bath containing 1% HF) can induce early breakaway oxidation and hydrogen pickup at 1000°C to 1200°C oxidation temperatures (e.g., 100 s ramp and 180 s hold time at 1200°C resulted in ≈500-wppm hydrogen pickup). Higher HF concentrations (2 to 4%) and longer etching times (120 to 240 s) did not result in early breakaway oxidation. As pickling has been used in some earlier experimental work [20,21] for sample cleaning, it is important to verify, in advance of data-generating tests, that this surface cleaning technique does not contribute to early breakaway oxidation due to the disruptive effects of fluorine on surface oxidation. In the Argonne program, the final cleaning methods consisted of sample submersion in an organic solvent (ethanol) within an ultrasonic water bath followed by a distilled-water rinse.

2.3 Oxidation and Quench Tests with Short Cladding Samples

Figure 6 shows the test train used in past and recent work for oxidizing and quenching samples prior to conducting post-quench ductility tests. Holes were drilled into the hollow Inconel holder below and above the sample to allow adequate steam flow inside the cladding sample. During the course of test-train development, the Inconel holder wall thickness and outer-diameter were reduced to decrease the thermal mass and the corresponding transient temperature lag of the holder.

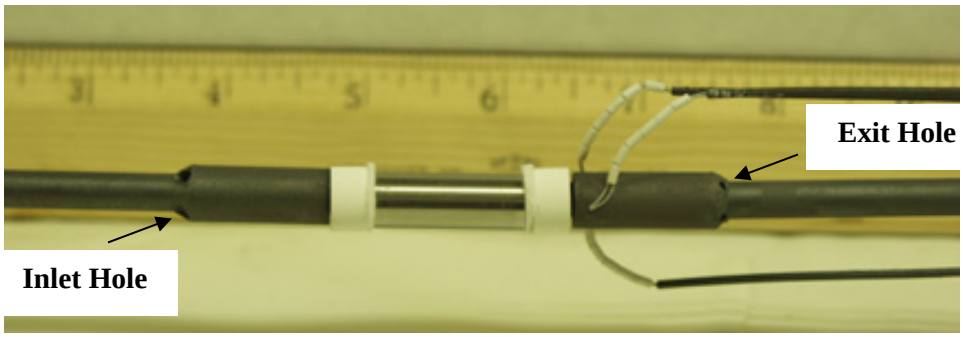

Figure 6. **Test train for two-sided oxidation tests with holes drilled into the Inconel holder below (left) the sample for steam ingress and holes drilled into the holder above (right) the sample for steam egress. Also shown are the three thermocouples permanently welded to the Inconel holder just above the sample (silver in appearance).**

Temperature control and monitoring are extremely important in conducting oxidation-quench tests, followed by post-quench ductility tests. As discussed in Section 1, the time-at-temperature for the transition between ductile and brittle behavior is a strong function of temperature. The furnace power and sample temperature are controlled by feedback from the designated control thermocouple (TC) output through a proportional-integral-differential controller to the furnace power. Because the sample has such low thermal mass per unit length, it is important to avoid temperature overshoot (due to the initially rapid heat generation from cladding oxidation) during the rapid temperature ramp to the hold temperature. In setting controller parameters, the requirements were that the temperature overshoot during the ramp be <20ºC relative to the target hold temperature for a short period of time (less than a few seconds), and that the average hold temperature be within 10ºC of the target temperature. The 10ºC deviation is reasonable given the uncertainty of a few degrees in the Type S thermocouple readings at the maximum oxidation temperature (1204ºC). Temperature overshoot is not much of an issue for long-time oxidation temperatures ≤1100ºC, but it can have a significant embrittlement effect for higher oxidation temperatures. For tests conducted at 1200ºC, temperature overshoot was minimized to <10ºC by slowing down the furnace heating rate (to 2–3ºC/s) at ramp temperatures within about 100ºC to 200ºC of the target temperature.

The following benchmarking procedure was established for each test train:

a) Calibrate purchased TCs to ANL-owned, NIST-calibrated TC wire (introduced in January 2006).

b) Weld two calibrated Type S TCs onto the sample outer surface; align one with the same orientation as the holder's control TC and align the other at ±120º from the control TC.

c) Use repeated testing with fresh and oxidized samples and same orientation for TCs welded to sample to determine optimum controller parameters for desired temperature ramp and hold temperature for test sample oxidized in steam from deionized water with ≈4 ppm dissolved oxygen.

d) Repeat test with new sample and TCs welded to sample. (See Refs. 1–3 for additional steps for larger-diameter cladding [e.g., BWR 9×9 and PWR 15×15].)

e) Perform metallographic examination to determine oxide-layer thicknesses at eight circumferential locations; compare measured and predicted average values to Cathcart-Pawel (CP) predicted values to ensure <10% difference; compare circumferential variation to ANL criterion (≤±3 μm).

f) Conduct oxidation test without TCs welded on the sample and compare measured sample weight gain at a time corresponding to about 10–13% CP-ECR to weight gain calculated with CP weight-gain correlation; also perform metallographic examination to determine average inner- and outer-surface oxide layer thicknesses, as well as variation. (Note: Zry-4 should be used for ≤1050°C oxidation temperatures.)

g) Begin data-generating oxidation tests if the following are satisfied: overshoot is <20°C for <3 s during temperature ramp, average hold temperature is within 10°C of target temperature, circumferential temperature variation is ≤20°C, measured weight gain is within 10% of predicted weight gain, average oxide layer thickness on inner and outer surfaces is within 10% of predicted thickness, and circumferential variation in oxide layer thickness is consistent with circumferential temperature variation.

h) Continue to run tests with benchmarked test train and controller parameters for specific hold temperature until measured weight gain and CP–predicted weight gain differ by ≥10%; repeated quench will cause test-train warping, which moves the sample away from the furnace focal point; generally, a test train should be good for ≈15 runs with quench and more without quench.

Figure 7 shows the thermal benchmark result for the as-fabricated 17×17 ZIRLO cladding used in the current program. The cladding sample temperature (TC4 and TC5) rise is very rapid to ≈1100°C. To prevent overshoot at 1200°C, controller parameters were set to slow down the heating rate. After 100 s from initiation of heating from 300°C, the average cladding temperature was 1200ºC. After 150 s, the cladding had essentially reached the 1202±7°C hold temperature. These temperatures and temperature variations were acceptable for proceeding to the weight gain benchmark test. The test was repeated with a fresh sample that did not have TCs welded to it.

As shown in Figure 7, the oxidation test is not isothermal. The significance of the weight gain during the initial heating ramp depends on the hold temperature and the hold time. For the temperature history shown in Figure 7, the CP-predicted weight gain was determined numerically by integrating Eq. 1 over the time-dependent temperature profile T(t), which was recorded every 0.1 s (i.e., 10 Hz):

$$(w_g)^2 = 0.362 \int_0^t \exp(-20100/T)\, dt, \qquad (7)$$

where w_g is in g/cm^2, T is in K, and t is in s. The integral in Eq. 7 was converted to an integral with respect to temperature, and the numerical integration for high-temperature oxidation tests (e.g., Fig. 7) was performed for T≥800ºC, where the predicted weight gain between 800ºC and 1000ºC was very small during the temperature ramp and negligible during the cooling ramp. Because of the parabolic nature of the weight gain correlation, the weight gain accumulated during the cooling ramp is usually insignificant. However, the calculation does include cooling to 800°C prior to quench. For the test conducted without TCs welded to the sample, the measured weight gain (7.91 mg/cm^2) was within 5% of the CP-calculated weight gain (8.27 mg/cm^2 with corresponding 12.7% CP-ECR), which was acceptable for conducting data-generating tests with this test train and set of control parameters. Also, the measured OD and ID oxide layers (40 μm) were in good agreement with CP-predicted values.

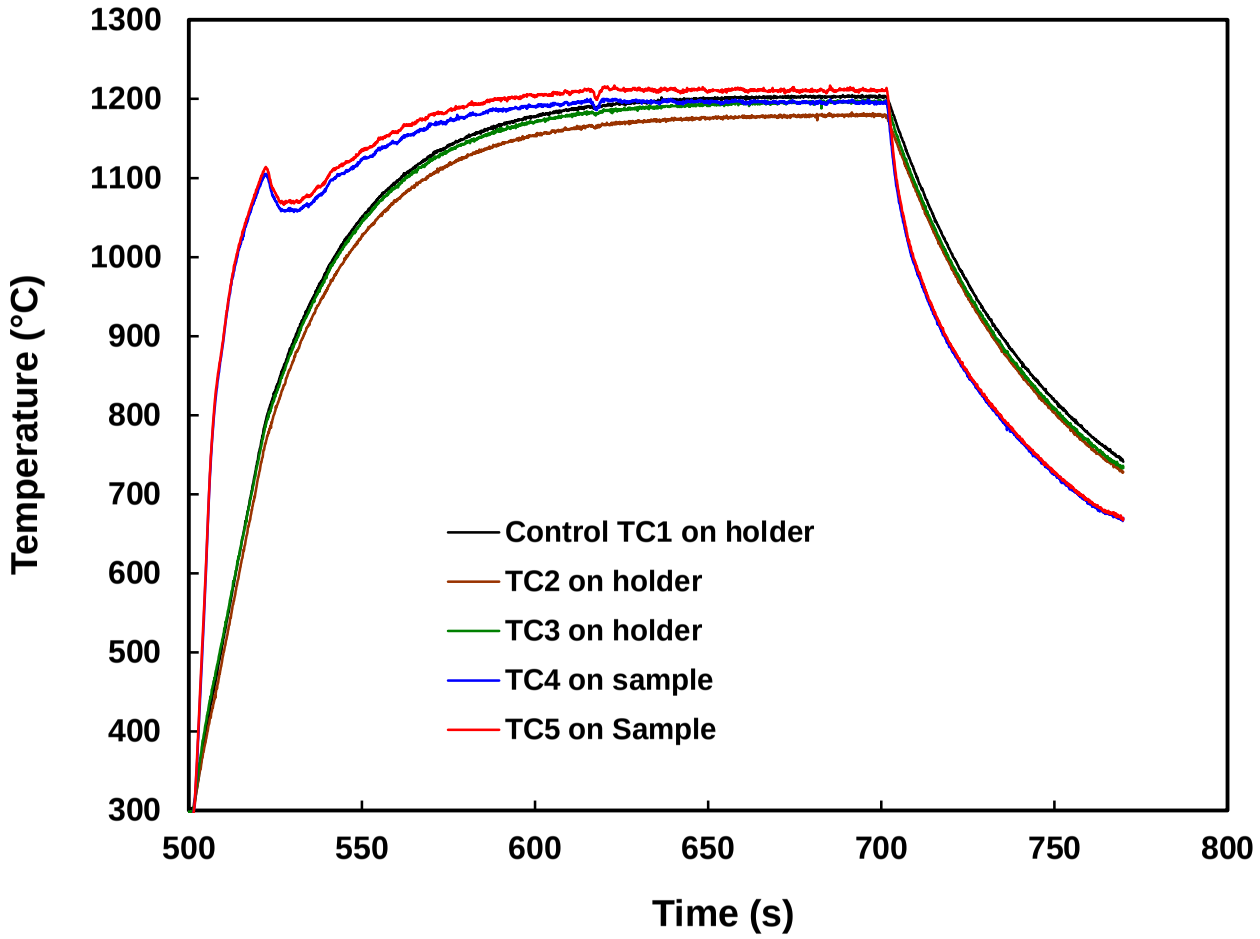

Figure 7. **Thermal benchmark results for bare ZIRLO cladding. At 100-s into the heating phase, the average sample temperature was 1200°C. After 150 s, the cladding temperature was 1202±7°C. Quench at 800°C is not shown in this figure.**

For oxidation and quench of as-fabricated and pre-hydrided samples used for post-quench ductility tests, the procedure is the same as the one used in the thermal and metallurgical benchmark tests:

a) Stabilize the system at 300ºC in flowing saturated steam for 500 s.

b) Initiate temperature ramp with feedback between the holder TC and the furnace power.

c) Hold at temperature for a predetermined time to achieve the desired CP weight gain and ECR.

d) Turn furnace power off while maintaining steam flow at the end of the hold time.

e) Stop steam flow and initiate bottom-flooding quench at a test time that will give rapid cooling at the desired cladding temperature. (Note: minimum temperature after quench was nominally 100ºC; for tests conducted after January 2006, minimum temperature was reduced to 80±10ºC.)

The procedure for conducting in-cell oxidation-quench tests with high-burnup cladding samples is similar to the one described above for out-of-cell tests with non-irradiated cladding samples. However, the corroded, irradiated samples were not benchmarked directly because Argonne does not have the in-cell capability to locally remove the corrosion layer and spot-weld TCs to the cladding metal surface. With respect to the temperature history shown in Figure 7 for bare, non-irradiated cladding, it is expected that pretest cladding corrosion would slow down the initial oxidation rate and the heating rate associated with the exothermic oxidation reaction. The presence of the corrosion layer would basically affect the peak temperature reached during the very rapid heating ramp. This effect has been confirmed in out-of-cell tests using the following procedure to determine the temperature profile for high-burnup ZIRLO cladding with a 30-μm-thick corrosion layer and a 10-μm-thick fuel-cladding bond layer. These conditions apply to the current work:

a) With TCs welded onto bare as-fabricated cladding, conduct the thermal benchmark test for a hold time selected to grow 10-to-40-μm-thick oxide layers on inner and outer surfaces of the cladding (see Fig. 7 for temperature history to grow 40-μm oxide layers).

b) Cool to 300ºC and repeat thermal benchmark test using the same controller parameters as were used in (a); compare the two sets of results (see Fig. 8 for 40-μm pre-oxide layers) with emphasis on the maximum temperature at the end of the rapid temperature rise (first peak), the time to reach the hold temperature, and the hold temperature.

c) If necessary, increase the holder control temperature to achieve the desired hold temperature for cladding with pre-transient oxide layers (not necessary for Fig. 8 results).

d) Install the calibrated test train in the in-cell furnace and conduct a metallurgical benchmark test with as-fabricated cladding without the TCs welded onto the cladding and with the hold time chosen to give a weight gain equivalent to about 10% CP-ECR; if the out-of-cell and in-cell weight gains and converted ECR values are in good agreement, then use of the test train in the in-cell furnace has been validated.

e) Use the results of the thermal benchmark in (b) or (c) – the one with oxide layers grown on the inner and outer surfaces prior to initiating the temperature ramp – to select test times to give the desired CP-ECR values and to interpret the experimental results for high-burnup cladding.

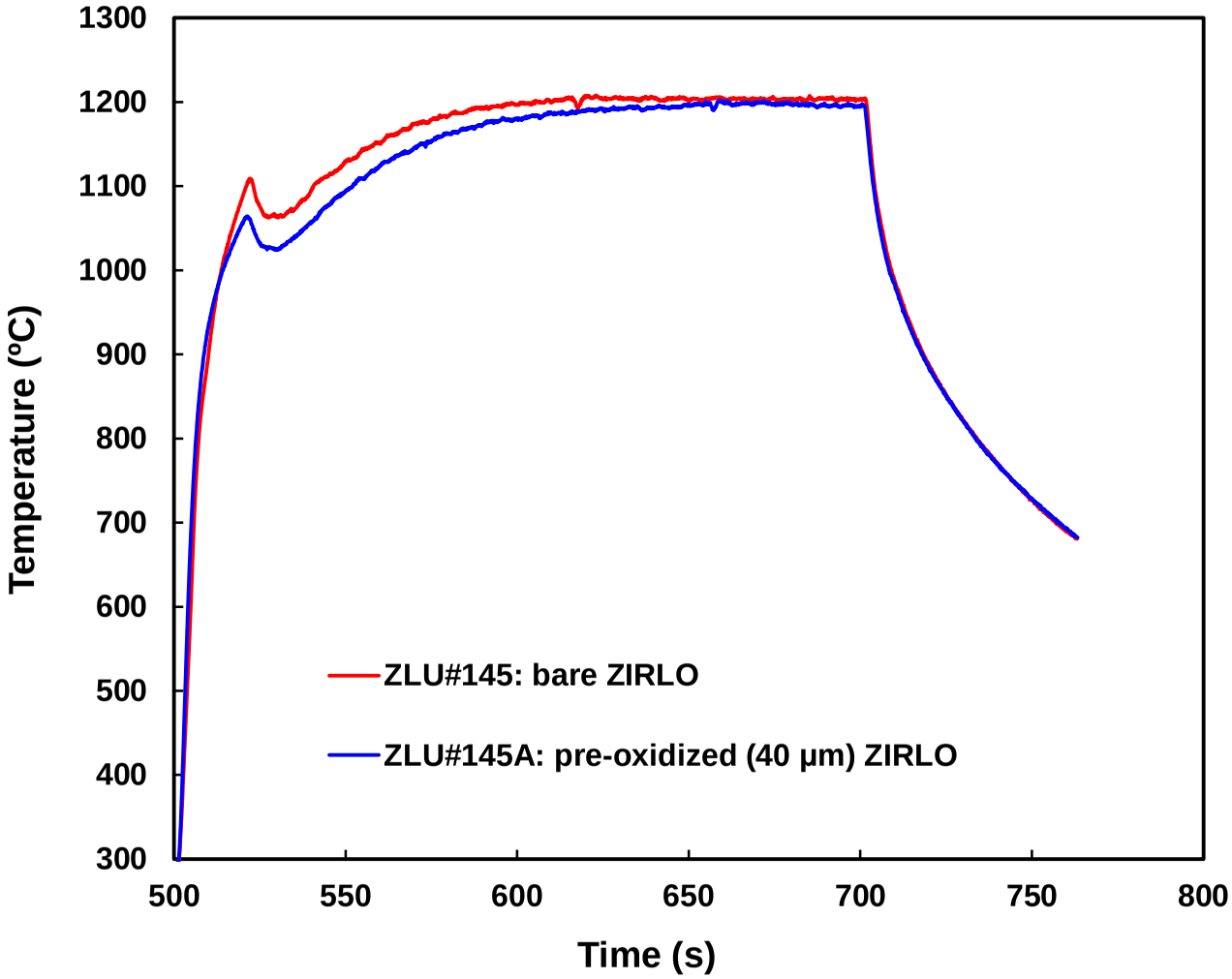

Figure 8. **Thermal histories for bare and pre-oxidized (40-μm) ZIRLO cladding tested in the same test train with the same control parameters. At 150-s into the heating phase, the average temperature for the pre-oxidized sample was 1200±3°C.**

Based on the results shown in Fig. 8, pre-oxidizing the cladding resulted in a 50°C decrease (from 1110°C to 1060°C) in the pre-1200°C peak and a longer time (150 s compared to 100 s) to reach 1200°C. Subsequently, it was verified that the results for 12-μm pre-oxide layers were essentially the same as the results for 40-μm pre-oxide layers (OD and ID). From a thermal perspective, it is likely sufficient to use a 10-μm pre-oxide layer in thermal benchmark tests for high-burnup cladding. This would reduce the oxidation rate and the rapid heating rate of bare cladding due to the effects of the heat of oxidation.

2.4 Ductility Determination Using Ring-Compression Tests

2.4.1 Background information and general description

The procedure for conducting ring-compression tests (RCTs) and the methodology for determining ductility are documented in Refs. 1–3. Reference 5 contains a detailed analysis of RCT loading and data interpretation. Some of this material is repeated below for the convenience of the reader.

Argonne has exposed as-fabricated, pre-hydrided, and high-burnup cladding samples to two-sided oxidation and quench. Short (≈8-mm-long) rings sectioned from these samples are subjected to ring-compression tests at RT and 135°C and at 2 mm/min (0.033 mm/s) displacement rate to determine the ductile-to-brittle transition oxidation level as a function of hydrogen content. With the limited amount of high-burnup cladding available for such tests, there is a practical advantage in using ring compression testing in that a large number of tests can be performed with a relatively small inventory of cladding.

Figure 9 shows a schematic of the ring cross section, loading, and displacement. The displacement (δ) is applied at a constant rate and the force (P) is measured by the load cell. Oxidized samples are compressed to failure, which may manifest itself as a single crack or multiple cracks through the sample wall and along the sample length. Ductility is determined from the permanent change (d_p) in ring diameter after unloading (for rings with ≤1 tight crack) and/or by the offset displacement (δ_p) method (for rings with ≥1 loose cracks). These displacements are normalized to the cladding metal outer diameter (D_o for as-fabricated and pre-hydrided cladding and D_{mo} for corroded cladding) prior to oxidation. For two-sided oxidized samples, cracking through the wall and along the length of the sample is equally probable at inner-surface locations under the load (12 o'clock position) and above the support plate (6 o'clock position). The maximum bending moment (M), tensile hoop stress (σ_θ), and tensile hoop strain (ε_θ) occur at these two locations. Bending stresses at these locations vary from tensile (inner surface) to compressive (outer surface). The bending moment and tensile hoop stress at positions ±90° (3 and 9 o'clock) from the loading axis are about 40% less within the elastic deformation regime. These stresses vary from compressive (inner surface) to tensile (outer cladding). Cracking seldom initiates and propagates at the 3 or 9 o'clock position, prior to cracking at the 12 and/or 6 o'clock position because of the lower tensile stress for intact rings. The primary bending stress is in the hoop direction. However, due to the large length-to-thickness ratio (L/h >10), a smaller axial stress is induced throughout the ring (excluding the free ends). This stress-inducing condition in the axial direction is referred to as plane-strain constraint.

Prior to conducting data-generating tests, RCTs are conducted with non-oxidized, as-fabricated cladding to ensure that the test machine is operating properly. Numerous benchmark tests have been conducted with 15×15 and 17×17 cladding rings at RT and 135°C to total displacements of up to 2 mm. As results for these homogeneous samples are easier to interpret, the data for one of these tests are used to illustrate methodology and measurement of key parameters. Figure 10 shows the RCT load-displacement curve for as-fabricated M5 cladding compressed to 1.7-mm displacement at RT. Dimensions of the ring were: L = 7.7 mm, D_o =9.48 mm, and h = 0.627 mm. Elastic properties for M5 at RT are: Young's modulus E = 91.9×10^4 MPa and Poisson's ratio ν = 0.37. Figure 10 is discussed further in the following subsections.

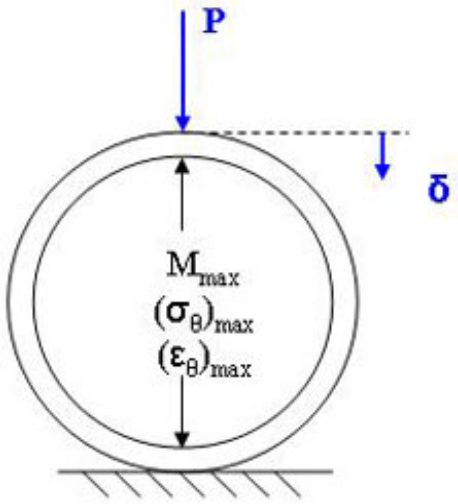

Figure 9. **Schematic of ring-compression test sample and loading. The displacement (δ) rate is controlled and the response force (P) is measured.**

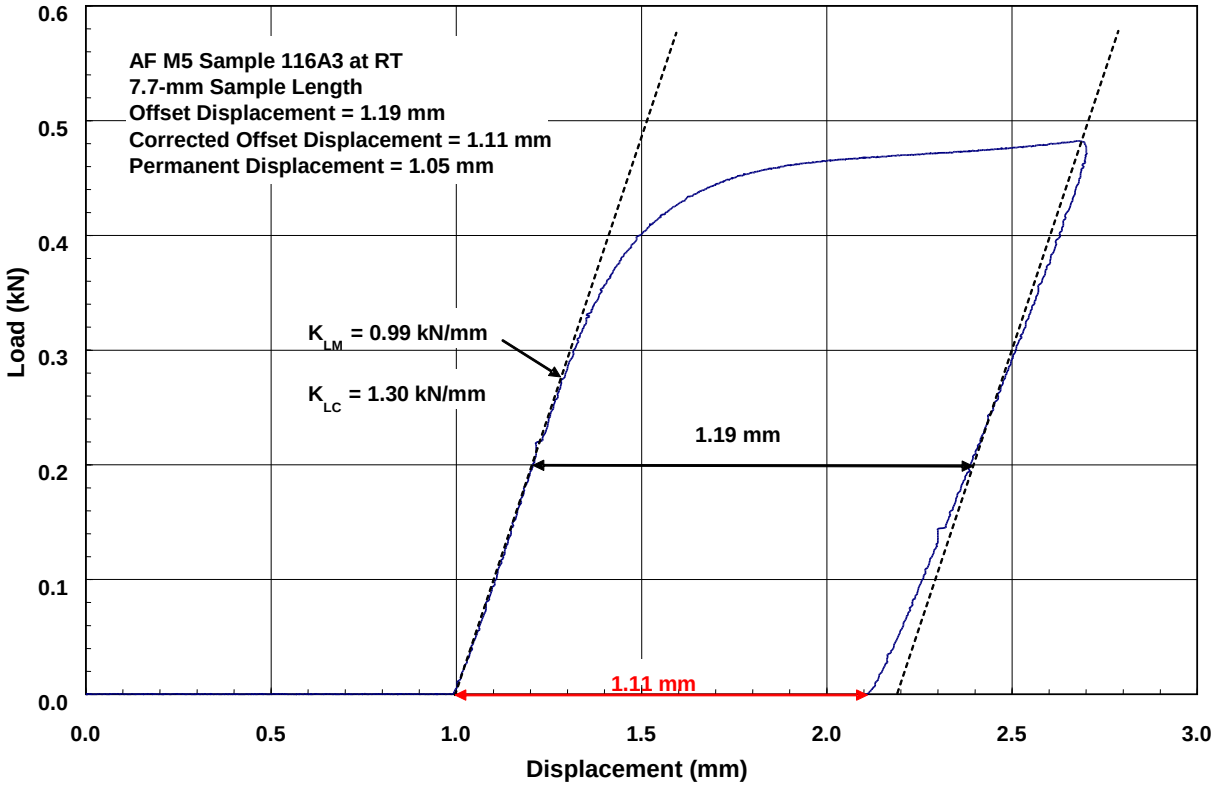

Figure 10. **Load-displacement curve for as-fabricated (AF) M5 cladding compressed at RT to 1.7-mm total displacement.**

2.4.2 Ductility and ductility criteria

The standard offset displacement methodology calls for mathematical unloading at the same slope as the measured loading slope (K_{LM}) just before failure or at the end of the test if no failure occurs. This is illustrated in Fig. 10 by the dashed black line at the end of the loading portion of the test. The distance between these two lines is the offset displacement (δ_p), which is 1.19 mm in Fig. 10. However, the unloading slope is not precisely equal to the loading slope for compressed rings, and the standard methodology gives a higher measured plastic displacement than the actual permanent displacement (d_p) measured after unloading (1.05 mm based on the difference between pre- and post-test micrometer measurements). For the load-displacement curve in Fig. 10, $\delta_p - d_p = 0.14$ mm. Normalizing δ_p and d_p to the initial outer diameter (9.48 mm), gives offset and permanent strains of 12.6% and 11.1%, respectively. Based on over 50 benchmark tests with as-fabricated cladding, the inherent error between offset and permanent displacements was found to be $\leq$0.2 mm for total displacements up to 2 mm. This equates to an absolute strain error of $\leq$2%. As the total displacement decreases, along with δ_p, the error decreases.

For oxidized cladding tested to failure, the RCT is manually terminated after the first significant load drop (>30%) in an attempt to preserve the ring geometry. If, upon unloading, the ring has a single tight crack, then the post-RCT diameter can be measured with reasonable accuracy and d_p can be determined from the difference between pre-test and post-test diameter along the loading direction. This situation is shown in the load-displacement curve (Fig. 11) for as-fabricated ZIRLO cladding oxidized (one-sided) at 1200°C to 17% CP-ECR prior to quench at 800°C. The test was conducted at reference temperature (135°C) and displacement-rate (0.033 mm/s) conditions. Offset and permanent displacements were 0.18 mm (1.9% strain) and 0.11 mm (1.2% strain). Based on the permanent-strain ductility criterion ($d_p/D_o \geq 1.0\%$) established in this program, the ring was classified as ductile. The 1.0% permanent strain criterion is based on an error assessment of post-RCT diameter readings, especially for corroded cladding with one tight crack. Corrosion-layer flake-off and mismatch of cracked surfaces during unloading account for most of the error in post-RCT diameter measurements for high-exposure cladding.

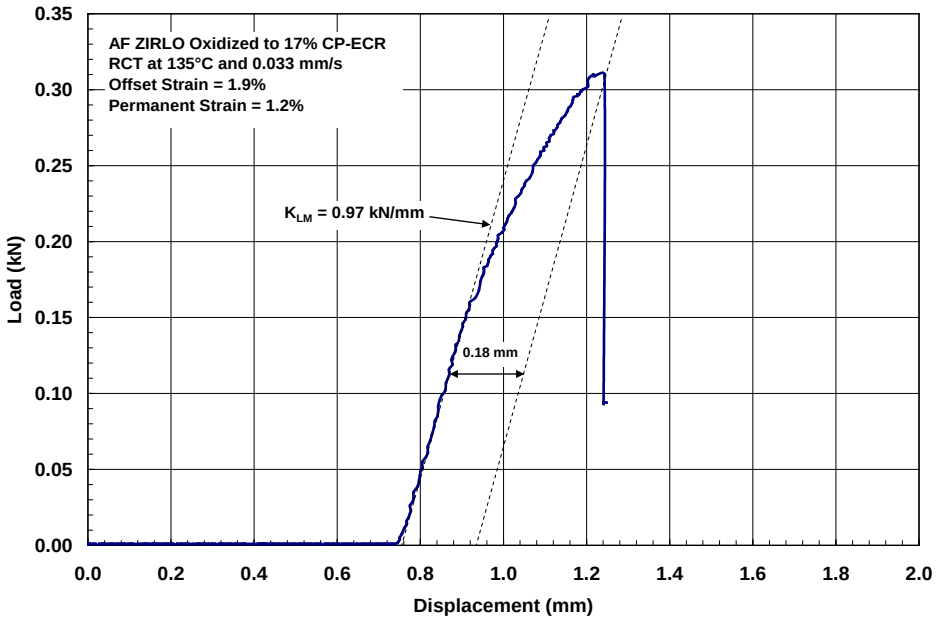

Figure 11. Load-displacement curve for as-fabricated ZIRLO oxidized (one-sided) at 1200°C to 17% CP-ECR. The sample had one tight through-wall crack at the 6 o'clock position.

Data trends were also considered in setting the permanent strain criterion for ductility. Figure 12 shows permanent-strain results for 17×17 Zry-4 cladding oxidized at 1200°C, quenched at 800°C, and compressed at RT and 135°C. The RT results show a sharp decrease in permanent strain from 20% at 5.5% CP-ECR to 2.2% at 7.8% CP-ECR. The permanent strain drops to 0.5% at 10% CP-ECR and then oscillates within the range of 0.5±0.02% from 10% to 20% CP-ECR even though the average oxygen content in the cladding continues to increase to about 0.57% at 18% CP-ECR. The observation that the permanent strain does not go to zero as the cladding continues to embrittle supports the approach of setting a 1% limit on permanent strain, as values below 1% appear to be in the "noise" of uncertainty. The RCT results for 135°C test temperature show a sharp decrease in permanent strain from 11% to 13% CP-ECR and a more gradual decrease from 13% to 19% CP-ECR. The average permanent strain is 1% at 17% and 19% CP-ECR. These results are consistent with the oxidation level at which the beta-layer oxygen content reaches the saturation level. The embrittlement oxidation level is assessed to be 19% for this material oxidized at 1200°C based on 3 data points at 17% and 2 data points at 19% CP-ECR. In Ref. 3, it is recommended that at least three RCT data points be generated at 17%, 18%, 19%, and 20% CP-ECR to better determine the transition oxidation level to within 1% CP-ECR for as-fabricated cladding.

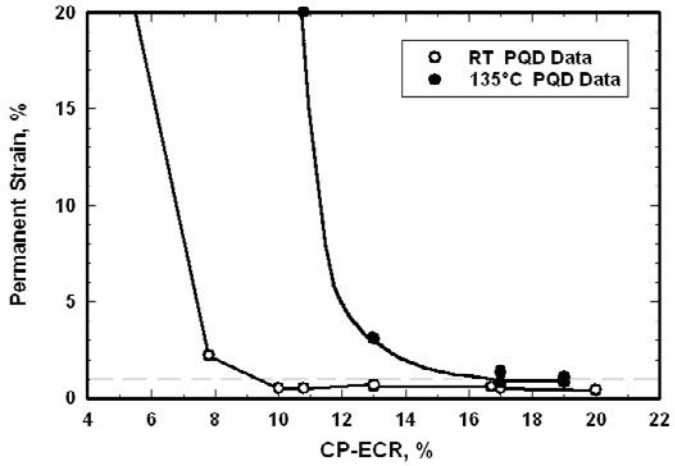

Figure 12. Permanent strain vs. CP-ECR for 17×17 Zry-4 oxidized at 1200ºC, cooled at ≈13ºC/s to 800ºC, quenched, and ring-compressed at RT and 135ºC.

For non-oxidized, as-fabricated cladding rings, the error between offset and permanent strain is negligible for small offset strain values (e.g., ≤3%). However, for oxidized-and-quenched cladding, the error increases with oxidation level. This deviation is shown in Fig. 13, which gives offset minus permanent strain ($\delta_p/D_o - d_p/D_o$) as a function of oxidation level (in % CP-ECR) for rings with permanent strains in the range of 1.0% to 2.3% (near ductility threshold). By setting d_p/D_o to the 1% ductility limit and adding it to the 1-σ upper bound in Fig. 13, the offset-strain ductility criterion can be expressed as:

$$\delta_p/D_o \geq 1.41\% + 0.1082 \text{ CP-ECR} \qquad (8)$$

In using Eq. 8, the average measured offset strain (rounded to the nearest 0.1%) at a particular hydrogen content and oxidation level should be greater than or equal to the right-hand side of Eq. 8 (rounded to nearest 0.1%) for the material to be classified as ductile. It should be noted that use of the offset-strain criterion (Eq. 8) may result in lower transition oxidation levels than would be determined based on the 1% permanent-strain criterion. The offset strains corresponding to Fig. 12 were 2.8% at 17% CP-ECR

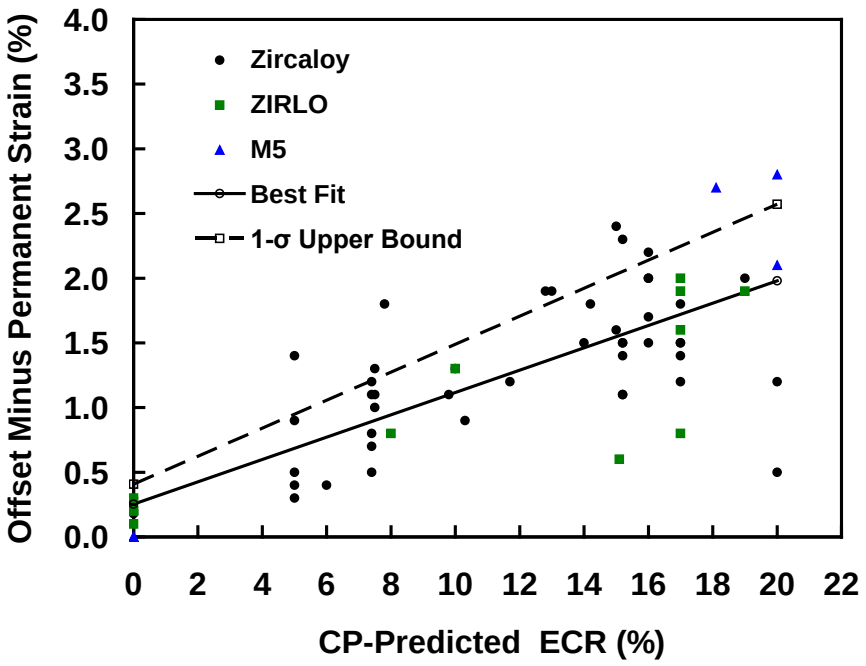

Figure 13. **Difference between offset and permanent strains as a function of oxidation level for as-fabricated, pre-hydrided, and high-exposure cladding alloys oxidized at 1200°C and compressed at 0.0333 mm/s. The dataset includes 15×15 Zry-4; 17×17 Zry-4, M5 and ZIRLO; and 10×10 Zry-2 compressed at RT and 135°C to permanent strains of 1.0−2.3%.**

(vs. 3.2% limit) and 2.5% at 19% CP-ECR (vs. 3.5% limit), which imply <17% transition CP-ECR. This conservatism is needed to accommodate the large data scatter seen in Fig. 13.

2.4.3 Measured vs. calculated loading slopes

The ring in Fig. 9 behaves like a spring in the elastic deformation regime with spring constant K_{LC} such that $P = K_{LC}\,\delta$. The spring constant can be calculated using advanced strength-of-materials methods:

$$K_{LC} = \{(E\,L)/[1.79\,(1-\nu^2)]\}\,(h/R_{mid})^3, \qquad (9)$$

where $R_{mid} = (D_o - h)/2$ is the mid-wall cladding radius. For the benchmark case shown in Fig. 10, K_{LC} = 1300 N/mm = 1.30 kN/mm. However, the stiffness measured from the load-displacement curve is less (0.99 kN/mm). While the measured load reflects the actual load on the sample, the measured displacement includes "machine" displacement, as well as sample displacement in the elastic deformation regime. The system acts like two springs in series. Let K_{mach} be the effective stiffness of the machine. The measured stiffness is:

$$K_{LM} = (K_{LC}/K_{mach} + 1)^{-1}\,K_{LC} \qquad (10)$$

For 0.99-kN/mm K_{LM} and 1.30 kN/mm K_{LC}, K_{mach} is calculated to be 4.1 kN/mm, which is close to the estimated 5 kN/mm for the Instron 8511 machine used in the current work. For stiffer machines and/or samples with lower stiffness values (e.g., 4-PBT samples discussed in Section 2.6), $K_{LM} \rightarrow K_{LC}$.

Using the standard methodology, the difference between measured and calculated stiffness values is not a factor in determining offset displacement and ductility. However, some caution should be exercised in integrating the area under RCT load-displacement curves to determine failure energy. Unless there is a correction to the measured slope, which is difficult to do for oxidized samples, the integration will result in higher calculated failure energy than is appropriate for the sample (e.g., as in Ref. 22).

2.5 LOCA Integral Tests with Pressurized Cladding Samples

Out-of-cell LOCA integral tests with as-fabricated and pre-hydrided cladding samples are relatively straightforward with regard to sample preparation and test conduct. Each cladding sample was partially filled with ≈25-mm-long zirconia pellets to simulate the heat capacity of the fuel. There was a clearance of about 13 mm between the top zirconia pellet and the inner surface of the top end fixture to prohibit contact during sample bending. The test train was supported at the top to minimize specimen bowing. The quartz tube encasing the test train provided an enclosed volume for steam flow and water quench, both of which were introduced through the bottom of the unit. The test train was centered within the quartz tube by means of two perforated spacer disks. Centering is very important as four vertical infrared lamps are focused within the furnace to heat the specimen. Swagelok fittings were used above the specimen to connect to the high-pressure gas line and top pressure gauge and below the specimen to connect to the bottom pressure-gauge line. The total gas volume above the fuel column was 10 cm^3, most of which was outside the heated zone. Four Type S TC lead wires were fed in through the top. Two of the TCs were spot-welded at the specimen mid-plane, 180° apart. The other two were spot-welded 50 mm above and 50 mm below the mid-plane at the same angular orientation as one of the mid-plane TCs. The signal from the top TC was used to control the furnace power to achieve the desired temperature ramp, hold temperature, and cooling rate prior to quench. Although the uniform heating zone of the furnace is nominally 250 mm, the actual uniform temperature region for a non-deformed sample ranged from 100-125 mm, centered on the sample mid-plane. For out-of-cell tests, hands-on assembly was used, and bare-wire TC beads were welded directly onto non-irradiated tubing. Reference 1 contains schematic diagrams, photographs, and a detailed description of the LOCA apparatus and integral test train.

During early-phase testing of 17×17 ZIRLO cladding in the current work, changes were made to sample length, pellet stack height, location of the TCs, and bottom pressure transducer. It was observed that a secondary balloon appeared near the top plenum region in some tests. In order to eliminate this secondary balloon, the plenum region was moved to a higher elevation above the heated zone by extending the sample length from 305 mm to 318 mm. An additional half pellet was added to increase the pellet stack height and to maintain the 13-mm-long plenum. Also, the survival rate for the two mid-plane TCs was low due to the disruptive effects of ballooning and rupture. For mid-plane TCs that did survive, results indicated that the circumferential temperature variation was greater than the axial temperature variation. As such, in the current work two TCs were welded onto the sample about 57 mm above the mid-plane at 0° and 180° orientations and two TCs were welded onto the sample at 44 mm below the mid-plane at 90° and 270°C. The TC above the mid-plane at 0° was used as the control TC. Also, the pressure transducer at the bottom of the test train was removed from the system. This pressure transducer was difficult to install, had a short lifetime, and was needed only for tests with fueled cladding samples in order to determine the gas communication between the top and bottom of the fuel column.

Real-time data of interest included pressure and temperature histories, rupture temperature, and pressure at which rupture occurred. Following a test, the sample was photographed (low and high magnification), micrometer measurements were made along the length of the sample at two orientations to determine the outer-diameter profile, the maximum outer circumference was measured, and the rupture opening was characterized in terms of axial location, width, and length. Prior to destructive examination, samples (with the pellets removed) were subjected to four-point bend tests at 135°C to determine maximum bending moment, failure energy, and plastic deformation (see Section 2.6). Destructive examinations were then performed to determine oxide and alpha layer thicknesses for inner- and outer-cladding surfaces (metallography), circumferential and axial distribution of oxygen (LECO oxygen analyzer), and circumferential and axial distribution of hydrogen (LECO hydrogen analyzer). Additional details about the LOCA integral test setup and data are provided in Sections 5 and 6.

2.6 Four-point-bend Tests (4-PBTs)

The 4-PBT (Fig. 14) was used in the current work to determine post-quench strength, failure energy, and plastic deformation of ballooned, ruptured, oxidized, and quenched LOCA integral-test samples. It is described in more detail in Ref. 5. The 4-PBT has advantages over the 3-PBT for cladding samples with axial variation in geometry, hydrogen content, and/or oxidation level. A uniform bending moment is applied along the span L_s between the two loading points. The sample will fail at its weakest location or locations. If the sample is very uniform and brittle (e.g., glass or ceramic rod), then simultaneous failure at multiple locations is likely to occur.

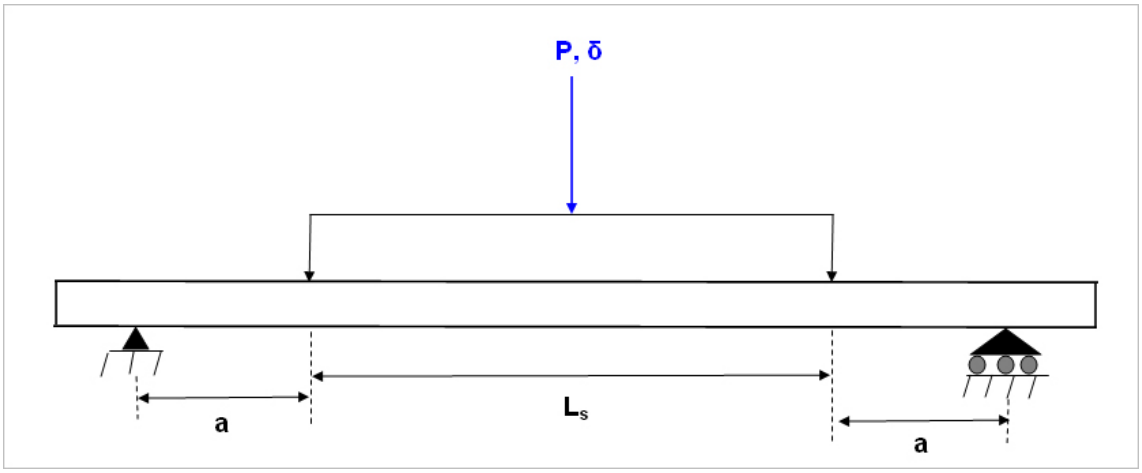

Figure 14. Schematic of four-point-bend test (4-PBT) loading. The bending moment is constant within the span L_s. The displacement (δ) rate is controlled and the force (P) is measured.

For the Argonne loading and support fixtures, L_s = 150 mm, a = 50 mm, and the distance between supports is 250 mm. The overhang regions beyond the supports are each 25 mm, but this length does not affect the loading. Thus, the uniform bending moment, M in N•m, is given in terms of the measured load, P in N, by M = (0.025 m) P. This bending moment results in maximum tensile stresses and strains at the bottom surface of the sample shown in Fig. 14, which would be convex during bending. The stresses and strains transition from maximum axial tension at the bottom surface to zero at the cross-section neutral axis to maximum axial compression at the top surface. The maximum stresses and strains are uniform within the span L_s for uniform geometry and material properties.

The 4-PBT sample is much more flexible than the RCT sample. Benchmark tests have been conducted at RT and 135°C with 15×15 Zry-4 (D_o = 10.77 mm and h = 0.76 mm) and 17×17 M5 (D_o = 9.50 mm and h = 0.57 mm). Calculated stiffness values varied from 246 N/mm (15×15 Zry-4 at RT) to 121 N/mm (17×17 M5 at 135°C). Measured values (248±2 N/mm and 121 ±1 N/m, respectively) were in excellent agreement with calculated values. Finite-element-analysis (FEA) calculations were also performed for 15×15 and 17×17 Zry-4 based on ANL-measured tensile properties for 15×15 Zry-4. The FEA-calculated load-displacement curves for the 15×15 Zry-4 benchmark tests at RT were in excellent agreement with the measured load-displacement curves.

Initially, the maximum elastic strain vs. displacement (δ) for the 4-PBT sample was set equal to the normalized RCT displacement (δ/D_o) to determine that the 4-PBT displacement rate should be 2 mm/s. This was later reduced to 1 mm/s on the basis of a direct comparison between calculated maximum elastic strain values for the RCT sample ($\varepsilon_\theta = 0.0305\ mm^{-1}\ \delta$) and the 4-PBT sample ($\varepsilon_z = 0.00104\ mm^{-1}\ \delta$). Thus, in order to conduct 4-PBTs at the same maximum elastic strain rate as was used in RCTs, the displacement rate was increased from 0.033 mm/s (RCT) to 1 mm/s (4-PBT).

Additional benchmark tests were conducted with 17×17 M5 cladding subjected to 4-PBTs at RT and 135°C. The displacement rate was 2 mm/s for these tests. Measured stiffness values were 131±1 N/mm at RT and 121±1 N/mm at 135°C. The measured values were in excellent agreement with the calculated values of 128 N/mm and 121 N/mm, respectively.

For one of the RT benchmark tests, 15×15 Zry-4 was subjected to a displacement of 10 mm at the loading points, which was large enough to induce plastic flow. Although loads were not measured during unloading, the subsequent reloading stiffness was measured and found to be within 1% of the original loading stiffness. It was concluded that the unloading stiffness was also the same and there would be no inherent error in determining 4-PBT offset displacement as there is for RCT offset displacement.

The permanent plastic strain can, in principle, be determined from the radius of curvature of the deformed sample by using elementary beam theory. However, the measurement of radius of curvature is tedious and cannot be done accurately for an oxidized sample tested to failure.

Another approach to determining plastic strain is to compare the offset displacement at several displacements beyond the elastic regime to FEA-calculated maximum plastic strains in an effort to determine the normalization length (L_n) to convert the measured plastic displacement to strain. The calculation was performed for both 15×15 and 17×17 Zry-4 geometries. The FEA results indicated that the normalization length varied with plastic strain. Unlike the RCT for which the outer diameter is used for normalization of plastic displacement, there is no equivalent normalization factor for the 4-PBT. For small plastic strains in the range of 0.l6% to 0.30%, the approximate value for L_n is 250 mm, which is the distance between supports in Fig. 14.

From a practical perspective, it is sufficient to use offset displacement as the metric for plastic deformation for the ANL 4-PBTs. Mathematically, $\delta_p > 0$ implies plastic deformation. Taking into account measurement errors, it is prudent to set a lower limit on offset displacement in the determination of plastic deformation: $\delta_p \geq 0.1$ mm implies plastic deformation. In addition to plastic deformation, material strength (as measured by the maximum bending moment) and failure energy (area under load-displacement curve) can be determined.

3 EMBRITTLEMENT OF NON-BALLOONED CLADDING

In the previous work, ductile-to-brittle transition oxidation levels were determined for as-fabricated cladding alloys, for pre-hydrided Zry-4, and for defueled Zry-4, ZIRLO, and M5 from high-burnup fuel rods. These results were documented in Ref. 1, and they are summarized in the following subsections. The terms "ductile-to-brittle transition" and "embrittlement" are defined as the highest CP-ECR value (rounded to the nearest percent) for which the cladding maintains borderline ductility. Oxidation to levels greater than these CP-ECR values leads to brittle cladding behavior. Samples were oxidized at 1200ºC and quenched at 800ºC, prior to determining post-quench ductility (PQD) using ring-compression tests conducted at 135ºC and 0.033 mm/s. For as-fabricated 17×17 cladding alloys, LOCA oxidation tests were conducted with and without quench at 800ºC to explore the effects of quench on PQD. The results indicated that quench at 800ºC had no significant effect on the ductility of as-fabricated cladding alloys. However, for pre-hydrided and irradiated cladding, quench at 800ºC significantly reduced ductility and the embrittlement oxidation level as compared to samples that were cooled without quench.

This previous work did not include testing of high-burnup cladding samples with pre-test cladding-metal hydrogen contents (C_{HM}) between 140 and 540 wppm. Thus, additional tests were conducted in the current work to determine the embrittlement oxidation level as a function of hydrogen content in the mid-range region of 200 to 400 wppm. These tests were performed with pre-hydrided, non-irradiated ZIRLO cladding and with defueled ZIRLO cladding from the same high-burnup rod used in the previous study.

3.1 Embrittlement of As-fabricated Cladding

Table 7 gives embrittlement oxidation levels (CP-ECR values) for as-fabricated cladding alloys based on the permanent-strain criterion (<1% implies embrittlement and ≥1% implies ductility). For multiple tests conducted at the same CP-ECR level, the average permanent-strain value was compared to 1%. If interpolation or extrapolation was required, the embrittlement CP-ECR was determined to the nearest 1% oxidation level. Table 7 only includes ductility data at oxidation levels close to the embrittlement CP-ECR levels. Offset-strain values are also provided such that they can be compared to the criterion in Eq. 8. These ductility data come from Ref. 1, where further details can be found at the locations indicated in the table. Where available, ductility data for slow cooling (i.e., no quench) were included to improve statistical significance because slow cooling in these tests had no observable effect on ductility.

With the exception of the vintage HBR-type Zry-4 cladding, the modern cladding alloys exhibited an embrittlement oxidation level in the narrow range of 19-20% based on the permanent strain criterion. These results are significant in that the embrittlement threshold for these different cladding alloys and cladding materials (e.g., two different designs for Zry-4) was independent of alloy type and fabrication differences. An extensive database was generated for HBR-type 15×15 Zry-4, not all of which was tabulated in Ref. 1. Its embrittlement oxidation level was determined to be 16% on the basis of data summarized in Table 7 and presented in Fig. 15a.

Except for 17×17 M5, use of the offset-strain ductility criterion (Eq. 8) resulted in an apparent decrease in embrittlement CP-ECR value: from 20% to 17% for 15×15 Zry-4, from 20% to 19% for 10×10 Zry-2, from 19% to 18% for 17×17 ZIRLO, from 19% to 16% for 17×17 Zry-4, and from 16% to 15% for HBR-type 15×15 Zry-4 (see Fig. 15b for offset strain vs. CP-ECR). For 17×17 Zry-4 additional offset-strain data (e.g., 7.5±3.1% offset strain at 13% CP-ECR) from Ref. 1 (Tables 11 and 43) were used to determine the 16% embrittlement oxidation level. Therefore, the use of offset strain in safety analyses to determine embrittlement threshold would appear to be conservative.

Table 7. Ductile-to-brittle transition oxidation levels (embrittlement CP-ECR values) for as-fabricated cladding alloys oxidized at 1200°C and ring-compressed at 135°C. Most data points used to determine ductility were for samples quenched at 800°C.

Cladding Material	Tested CP-ECR, %	Permanent Strain, %	No. of Data Points	Offset Strain, %	No. of Data Points	Embrittlement CP-ECR, %
17×17 M5 (34,45)[a]	16 20	2.8 1.0	1 2	7.6±2.8 3.5±0.5 (3.6%)[b]	4 2	 20
15×15 Zry-4 (16)[a]	17 20	1.8±0.4 1.1±0.4	2 2	3.3±0.8 2.4±0.4 (3.6)[b]	2 2	 20
10×10 Zry-2 (22)[a]	17 20	2.8 1.0±0.1	1 2	6.4±1.3 1.7±0.2 (3.6%)[b]	2 2	 20
17×17 ZIRLO (27,44)[a]	17 19	1.8±0.6 1.1±0.2	5 2	4.5±1.8 2.6±0.8 (3.5%)[b]	7 2	 19
17×17 Zry-4 (11,43)[a]	17 19	1.1±0.5 1.0±0.2	5 2	2.4±0.8 2.5±0.8 (3.5%)[b]	5 2	 19
15×15 Zry-4 HBR-type (current Fig. 15)	15 16	1.5±0.4 1.1±0.3	6 7	3.0±0.7 2.9±0.6 (3.1%)[b]	6 7	 16

[a]Table number(s) in Ref. 1 containing most of the data.
[b]Offset strain ductility criterion calculated with Eq. 8 at the indicated CP-ECR.

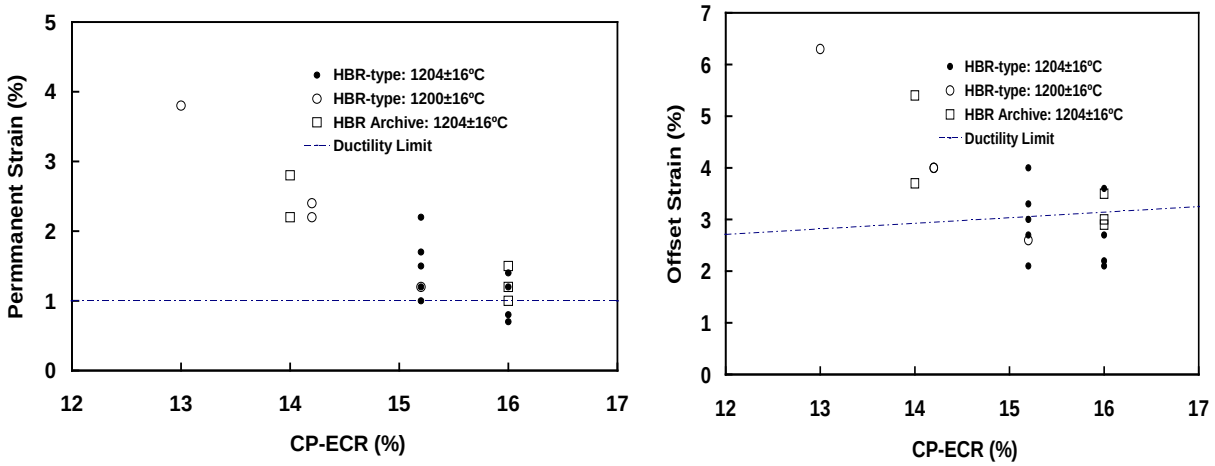

(a) Permanent strain **(b) Offset strain**

Figure 15. PQD results for 15×15 Zry-4 (HBR-type) following oxidation at 1200°C and quench at 800°C: (a) permanent strain and (b) offset strain.

3.2 Embrittlement of Pre-hydrided Cladding

3.2.1 Review of previous results

Table 8 summarizes previous PQD results for pre-hydrided 17×17 Zry-4 and HBR-type 15×15 Zry-4 oxidized at 1200°C to 5–10% CP-ECR followed by quench at 800°C. LOCA oxidation tests were conducted at fixed oxidation levels for samples with variable hydrogen content in the cladding metal (C_{HM}). For 17×17 Zry-4 oxidized to 10.3% CP-ECR, C_{HM} was between 274 and 335 wppm. Based on extrapolation of offset strain data for 209 and 274 wppm, the embrittlement C_{HM} was determined to be 280 wppm at about 10% CP-ECR. For 17×17 Zry-4 oxidized to 7.9% CP-ECR, the embrittlement C_{HM} was between 314 and 412 wppm.

At 7.7% CP-ECR, the embrittlement C_{HM} for HBR-type Zry-4 was between 360 and 386 wppm. Although results at about 8% CP-ECR were consistent for these two materials, the more extensive database for HBR-type Zry-4 was used to determine the embrittlement C_{HM} at about 8% CP-ECR: 370-wppm based on interpolation. PQD results depended on heating rate and time spent at elevated temperature. For example, HBR-type Zry-4 samples subjected to a fast heating rate with a brief overshoot to 1216°C (Fig. 109 [1]), were brittle with 335 wppm hydrogen following oxidation to 7.6% CP-ECR and quench at 800°C (Table 51 [1]).

Table 8. Embrittlement pre-test hydrogen content (C_{HM}) as a function of oxidation level (CP-ECR) for pre-hydrided Zry-4 cladding oxidized at ≈1200ºC and quenched at 800ºC.

Material	Tested CP-ECR, %	Pre-test C_{HM}, wppm	Permanent Strain, %	No. of Data Points	Offset Strain, %	No. of Data Points	Embrittlement C_{HM}, wppm
17×17 Zry-4 (46)[a]	10	209	3.3	1	5.5	1	
		274	–	0	2.8	1	
					(2.5)[b]		**280**
		335	0.4	1	0.6	1	
15×15 Zry-4 HBR-type (48)[a]	8	360	–	0	5.0	1	
					(2.3)[b]		**370**
		386	0.5±0.1	2	1.2±0.7	3	
15×15 Zry-4 HBR-type (47,53)[a]	5	470±8	–	0	4.2±1.5	4	
		500±16	–	0	3.0±2.3	3	
					(1.7)[b]		**530**
		636	0.4	1	0.5	1	

[a]Table number(s) in Ref. 1 containing the data. CP-ECR values include oxidation during cooldown.
[b]Offset strain criterion calculated with Eq. 8.

A large number of PQD tests were conducted with pre-hydrided, HBR-type 15×15 Zry-4 oxidized to 4.7–5.7% CP-ECR. The oxidation tests were conducted in four separate campaigns using different test trains and temperature control parameters. PQD results were sensitive to heating rate from 1000°C to 1180°C with higher heating rates causing enhanced embrittlement. In general, the target CP-ECR value was reached during the slow ramp rate from 1180°C to 1200°C. For 5% CP-ECR samples, the extrapolated C_{HM} leading to embrittlement was 530 wppm. This result is consistent with the embrittlement exhibited by the 5.2% CP-ECR sample with 636 wppm hydrogen.

At the time Ref. 1 was published, there was an apparent discrepancy between CEA (at Saclay) and Argonne data for pre-hydrided (about 600 wppm) Zry-4 samples oxidized to about 6% CP-ECR and quenched at 600°C or 700°C: CEA observed a significant enhancement in ductility while Argonne did not (see Table 54 in Ref. 1). Argonne speculated that the difference was due to the very slow cooling rates in the CEA furnace (e.g., about 1000 s to cool from 1200°C to 800°C) compared to the more typical fast cooling rates characteristic of the Argonne furnace (e.g., about 40 s to cool from 1200°C to 800°C). Argonne samples were sent to CEA for detailed characterization. Concurrently, CEA modified their apparatus by adding He cooling following steam oxidation to achieve cooling rates (10°C/s) comparable to Argonne's cooling rates. Using the faster cooling rate, CEA observed results comparable to Argonne results in that no enhancement in ductility was observed at the lower quench temperatures [11].

3.2.2 Current results

Oxidation and PQD tests were conducted with pre-hydrided ZIRLO samples after tests with high-burnup ZIRLO. However, results for pre-hydrided ZIRLO are presented before results are presented for high-burnup ZIRLO (see Section 3.3). Tests with pre-hydrided samples were also conducted after the draft procedure [18] was submitted to NRC for conducting PQD tests. Thus, there was a dual purpose to these tests: (a) to generate PQD data for pre-hydrided ZIRLO with hydrogen contents comparable to the high-burnup ZIRLO samples and (b) to test the adequacy of the detailed procedures documented in Ref. 18.

Materials and sample preparation

ZIRLO-2008 cladding was used to prepare pre-hydrided segments (≈80-mm long). Target hydrogen contents were 300±50 wppm. Based on trial efforts, it was very difficult to achieve these hydrogen levels with non-etched, belt-polished (outer surface), and sand-blasted (inner surface) segments. Hydrogen levels were either too low or too high. Although pre-etching segments with an HF-containing acid bath was not recommended in Ref. 18, additional trial runs were conducted with samples etched in a 1% HF solution (with equal parts of nitric acid and distilled water) for periods of 30 s to 120 s (reference time). This greatly improved the pre-hydriding process such that average hydrogen contents of 300 to 470 wppm (based on segment weight gain following pre-hydriding) were achieved. However, test samples (≈25-mm long) from etched as-fabricated cladding and pre-hydrided cladding experienced early breakaway oxidation and significant hydrogen pickup during relevant oxidation times at 1200°C. This artifact was eliminated by polishing the inner and outer surfaces of samples prior to conducting oxidation-quench tests. Polishing removed about 1 μm from these surfaces, which was sufficient to remove surface and near-surface fluoride impurities. As an extra caution, end caps were inserted into segments such that only the outer surface was exposed to the HF-containing bath. Both inner and outer surfaces were still polished to remove possible impurities that may have been picked up during the pre-hydriding process, which included a final long anneal in argon gas to achieve a more uniform hydrogen concentration. Based on the high purity levels of the gases used, polishing of the inner surface may have been unnecessary.

Parameters for hydrogen charging were modified over a five-year period to gain better control over the process. The hydrogen content of the gas was reduced from 100% to 30% (plus 70% He), and a transition was made from flowing to static hydrogen. The final process used to pre-hydride ZIRLO segments was: (a) evacuation of the system at RT, (b) out-gassing at elevated temperature (>400°C), (c) quick installation of cladding segment at RT, (d) purge of system at RT with flowing Ar gas (24 h), (e) evacuation at RT, (f) flowing hydrogen gas mixture through system at RT (4 h), (g) closure of valves to seal off hydrogen within furnace chamber, (h) controlled heating of furnace to 400°C hold temperature, (i) hold at 400°C in stagnant hydrogen mixture for target time, (j) turn off furnace at end of hold time, and (k) evacuation of system during initial cool down. Following pre-hydriding, cladding segments were

subjected to flowing Ar at 400°C for about 24 h with five temperature cycles between 400°C and 300°C to decrease axial and circumferential gradients in hydrogen concentration.

Pre-hydrided ZIRLO segments were sectioned as shown in Figs. 16a (A13) and 16b (A15) to produce oxidation test samples. Based on weight gain, average hydrogen contents were determined to be 302 wppm and 471 wppm for segments A13 and A15, respectively. As shown in Fig. 16, hydrogen contents measured at four axial locations per segment tended to be less than weight-gain values. Hydrogen-content measurements on both sides of the oxidation samples were mass-averaged to estimate the C_{HM} levels in the samples. Inner and outer sample surfaces were then polished. Length (L), outer diameter (D_o), wall thickness (h_m), and weight (W) were measured after polishing. Prior to weighing, the samples were thoroughly cleaned and dried. Table 9 summarizes the results of these measured parameters.

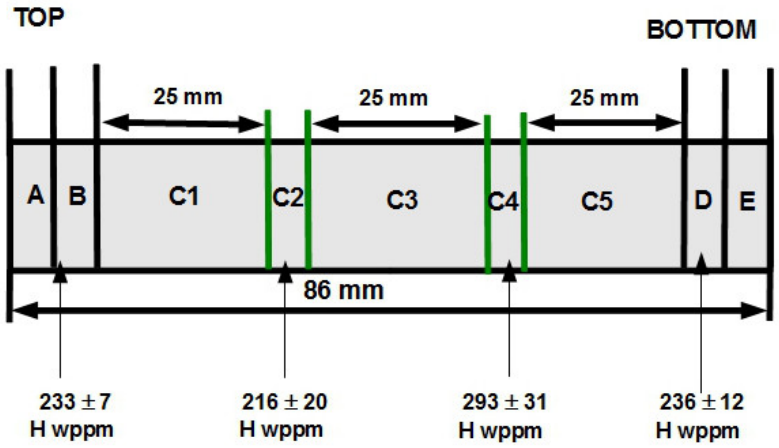

(a) Segment A13

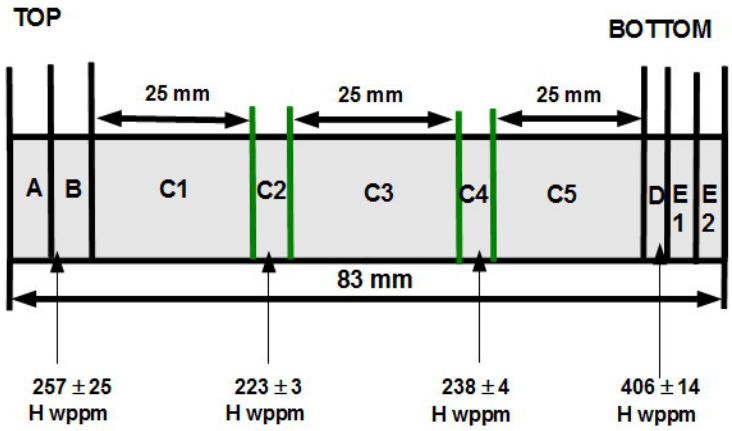

(b) Segment A15

Figure 16. Sectioning diagrams for pre-hydrided ZIRLO segments: (a) Segment A13 and (b) Segment A15. Nominal lengths are shown for the oxidation test samples.

Table 9. Pre-test estimates of C_{HM} levels, measured dimensions, and measured weights for pre-hydrided ZIRLO oxidation test samples.

Test ID ZLUP#	Sample ID	Estimated C_{HM}, wppm	L, mm	D_o, mm	h_m, mm	W, g
6	A13C1	226±16	23.6	9.48	0.567	2.4341
5	A13C3	256±46	22.7	9.48	0.567	2.3486
7	A13C5	263±36	27.3	9.50	0.560	2.8250
4	A15C1	245±23	23.8	9.47	0.564	2.4500
3	A15C3	231±8	22.0	9.47	0.565	2.2632
8	A15C5	314±91	22.8	9.47	0.560	2.3139

Thermal and weight-gain benchmark results

The standard procedure described in Section 2.6 was used to perform thermal and weight-gain benchmarks. Controller parameters were determined earlier for oxidation tests with irradiated ZIRLO (see Section 3.3). This was done to allow good comparison of PQD results for pre-hydrided and irradiated cladding samples. An as-fabricated ZIRLO sample, with two TCs welded onto the sample, was used for the thermal benchmark test. The temperature histories for the two welded TCs are shown in Fig. 17. After 151 s from the beginning of the temperature ramp, the average sample temperature was 1200±5°C. The test was repeated without the welded TCs. The measured weight gain (6.80 mg/cm^3) was only about 3% higher than the CP weight gain (6.62 mg/cm^3). The absence of temperature overshoot, the small circumferential temperature variation, and the excellent agreement between measured and calculated weight gain were well within limits established in Section 2.3.

Oxidation tests

Choosing test times and CP-ECR values to bracket ductile and brittle behavior was very challenging for pre-hydrided oxidation test samples because no two samples appeared to have the same average C_{HM}, the axial variation in C_{HM} was neither linear nor predictable, and because of the overall uncertainty in the estimated C_{HM}. The average (and 1–σ variation in) C_{HM} could not be determined accurately until after the oxidation test was completed. Given the post-oxidation sample weight gain and LECO-measured hydrogen content, C_{HM} was determined in the following manner for each cladding ring subjected to an RCT.

In general, the LECO-measured hydrogen content is: $C_H = (H_S/M_S) \times 10^6$, where H_S is the mass of hydrogen evolved from the sample and M_S is the mass of the sample. Therefore for pre-hydrided cladding samples before oxidation, the sample is all metal such that $H_S = H_M$, $M_S = M_M$ and $C_H = C_{HM}$. But for samples after oxidation, the sample mass is $M_S = M_M + W_G$, where W_G is the oxidation weight gain in mass units. Hence, the LECO-measured hydrogen content for pre-hydrided samples after oxidation is $(C_H)_{pox} = (H_M/[M_M+W_G]) \times 10^6$. This value can be multiplied by a mass-correction factor to determine C_{HM}: $C_{HM} = (1 + W_G/M_M)\,(C_H)_{pox} = (1 + W_g/100)\,(C_H)_{pox} = f_{Wg}\,(C_H)_{pox}$, where W_g is weight gain in percent and f_{Wg} is the weight-gain correction factor.

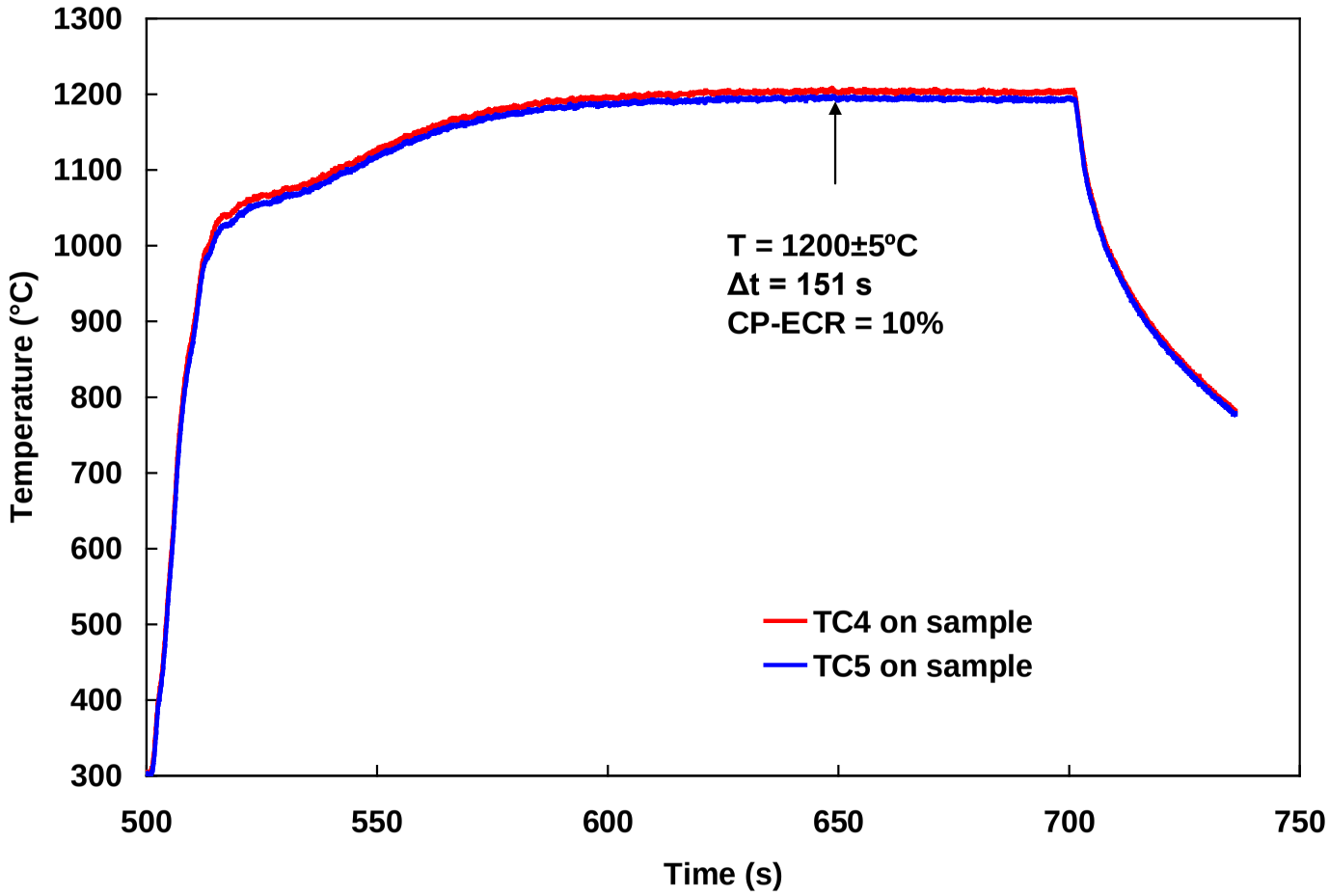

Figure 17. **Thermal history determined from benchmark test for oxidation tests to be conducted with pre-hydrided ZIRLO. Quench at 800°C, which was used for PQD tests, is not shown in this figure because benchmark samples are cooled without quench.**

Table 10 summarizes the six oxidation tests that were conducted in the CP-ECR range of 8 to 11%. RCT results are given in Table 11. Oxidation tests were run sequentially such that ductility and pre-test C_{HM} were determined for rings from the previous test prior to choosing the CP-ECR level for the subsequent test. Depending on sample length, short end pieces were removed and at least two RCT rings (6.7–8.6 mm long) were sectioned from each oxidation sample. Rings were subjected to RCTs at 135°C and 2 mm/min (0.033 mm/s) displacement rate. For 13 of the 16 rings, the permanent displacement could not be determined because simultaneous through-wall cracks occurred at multiple (2 to 4) circumferential positions. For the three RCT samples with only one through-wall crack, two were brittle and one was highly ductile. Thus, the ductile-to-brittle transition CP-ECR had to be determined based on the offset-strain criterion (Eq. 8).

The RCT data in Table 11 were reorganized and grouped according to CP-ECR and C_{HM} values. Results for 240-wppm and 200-wppm C_{HM} are given in Table 12. For LOCA samples oxidized to 8%, 9% and 11% CP-ECR, three rings (A13C3B, A15C5C, and A13C5B) had average hydrogen contents of about 240 wppm. Fourteen C_{HM} values (4 to 6 per ring) were mass averaged to determine C_{HM} for the three rings: 240±33 wppm. Minimum and maximum measured values were 169 and 287 wppm. Seven rings (A15C3B, A15C3C, A15C1B, A15C1C, A15C1D, A13C1B, and A13C1D) had average C_{HM} values of about 200 wppm. Thirty-eight C_{HM} values (4 to 6 per ring) were mass averaged to determine C_{HM} for the three rings: 200±7 wppm.

The RCT results for rings with 240 wppm are relatively straightforward to interpret. As shown in Table 12 and Fig. 18, rings oxidized to 8% and 9% CP-ECR were highly ductile, while the ring oxidized to 11% CP-ECR was very brittle. The transition CP-ECR is >9% and <11%. Based on the trend curve shown in Fig. 18, 10% is a reasonable transition oxidation level for ZIRLO with 240-wppm C_{HM}. If more samples had been available with 240 wppm C_{HM}, a confirmation test at 10% CP-ECR would have been conducted.

The RCT data set for 200-wppm ZIRLO is more robust at oxidation levels of 10% and 11% CP-ECR. The two high-ductility data points at 217 wppm and 8% CP-ECR can be included as a reasonable lower bound on the anticipated ductility of 200-wppm ZIRLO oxidized to 8% CP-ECR. On the basis of the data trend curve shown in Fig. 18, it is expected that 200-wppm ZIRLO would be brittle if it were oxidized to 12% CP-ECR. Thus, the transition CP-ECR for 200-wppm ZIRLO was chosen to be 11%. If additional 200-wppm ZIRLO samples had been available, then a test would have been conducted at 13% CP-ECR (severe embrittlement expected) and a confirmation test would have been conducted at 12% CP-ECR. It is possible that 200-wppm ZIRLO has a transition oxidation level of 12%, but a conservative approach was adopted in choosing 11% for which ductility was clearly established.

In addition to the ductile-to-brittle oxidation levels established for 200-wppm and 240-wppm ZIRLO, Table 11 includes one data point that indicates embrittlement at 286±33 wppm and 9% CP-ECR. Thus, ZIRLO with about 290-wppm pre-test C_{HM} has a transition CP-ECR <9%.

Table 10. Oxidation conditions and results for pre-hydrided ZIRLO samples. W_g is the measured change in sample weight (in %) and w_g is weight gain normalized to surface area.

Oxidation Test ID	Sample ID	Pre-test Estimated C_{HM}, wppm	Test Time[a], s	CP-ECR, %	Meas. ECR, %	W_g, %	w_g, mg/cm^3
ZLUPH#3	A15C3	231±8	166	11.0	11.8	4.23	7.56
ZLUPH#4	A15C1	245±23	145	10.0	10.4	3.73	6.69
ZLUPH#5	A13C3	256±46	166	11.0	11.5	4.11	7.41
ZLUPH#6	A13C1	226±16	166	11.0	11.5	4.12	7.40
ZLUPH#7	A13C5	263±36	110	8.0	8.3	2.95	5.34
ZLUPH#8	A15C5	314±91	127	9.0	9.5	3.47	6.13

[a]From beginning of temperature ramp to the end of the heating phase.

Table 11. Oxidation levels, RCT results, and C_{HM} values for pre-hydrided ZIRLO samples.

Oxidation Test ID (Sample ID)	CP-ECR, %	RCT Sample ID	RCT Sample L, mm	Permanent Strain, %	Offset Strain, %	$(C_H)_{POX}$, wppm	C_{HM}, wppm
ZLUPH#3	11						
(A15C3)		B	8.2	–	5.5	195±3	203±2
		C	8.1	–	1.8	189±3	197±1
ZLUPH#4	10						
(A15C1)		B	6.7	–	6.2	197±3	204±3
		C	7.7	–	7.6	194±9	201±9
		D	6.5	–	3.5	190±1	197±1
ZLUPH#5	11						
(A13C3)		B	7.7	0.4	0.5	232±23	242±24
		C	8.0	0.8	0.9	270±27	281±28
ZLUPH#6	11						
(A13C1)		B	7.6	–	3.6	195±5	202±5
		C	7.5	–	5.6	176±7	183±7
		D	6.4	–	4.4	184±10	192±11
ZLUPH#7	8						
(A13C5)		B	8.6	–	20	235±49	242±50
		C	8.2	–	31	210±20	217±21
		D	7.1	21	22	211±12	217±12
ZLUPH#8	9						
(A15C5)		B	7.6	–	1.6	276±22	286±23
		C	7.7	–	9.4	228±20	236±21
		D[a]	5.1	–	3.1	209±7	216±7

[a]Short end piece with oxidation on one face; excluded from data analysis.

Table 12. Analysis of PQD data to determine ductile-to-brittle transition CP-ECR and C_{HM} values.

CP-ECR, %	C_{HM}, wppm	Offset Strain, %	No. of Data Points	Ductility Limit, %	Embrittlement CP-ECR and C_{HM}
11	240±33	0.5	1	2.6	Based on data trend shown in Fig. 18 and interpolation of offset-strain data, embrittlement limit is 10% CP-ECR for 240 wppm hydrogen
(10)	(240)	(>2.5)	–	2.5	
9	240±33	9.4	1	2.4	
8	240±33	20	1	2.3	
(12)	(200)	(≈1.8)	–	2.7	Based on data trend shown in Fig. 18 and extrapolation of offset-strain data, embrittlement limit is 11% CP-ECR for 200 wppm hydrogen
11	200±7	3.8±1.6	4	2.6	
10	200±7	5.8±2.1	3	2.5	
8	217±6	27±6	2	2.4	

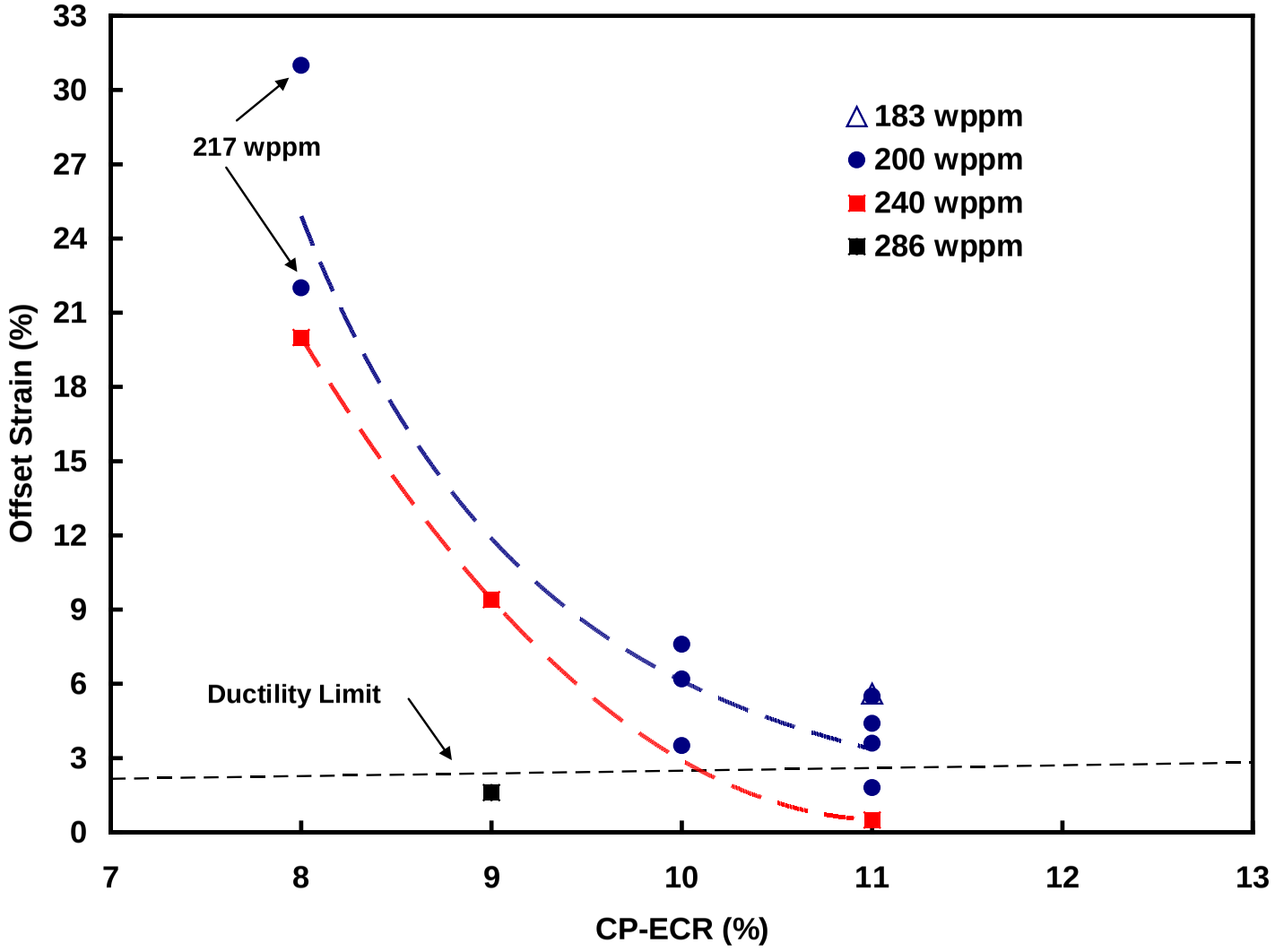

Figure 18. **RCT ductility (i.e., offset strain) results for pre-hydrided ZIRLO as a function of CP-ECR oxidation level.**

Clearly more than six oxidation tests would have to be conducted for samples sectioned from pre-hydrided ZIRLO segments with axial gradients in C_{HM}. Oxidation times and target CP-ECR values were chosen based on the estimated levels from interpolation of C_{HM} values determined for thin (about 2-mm) rings adjacent to the ends of oxidation samples. As shown in Table 13, there is enough variation between pre-test estimated and post-test-determined values of C_{HM} for PQD samples that about double (12) the number of oxidation tests would have to be conducted to determine transition CP-ECR levels at two pre-test C_{HM} levels. Based on recent results from an industry-coordinated round robin [23], it appears that significant improvements in pre-hydriding and oxidation test methods would be needed for some of the participating laboratories to reproduce the data documented in this report. Nevertheless, the combined industry results are consistent with our results.

Table 13. Comparison between pre-test estimated C_{HM} values for oxidation samples and C_{HM} values for RCT samples sectioned from oxidation test samples and determined from measured post-oxidation $(C_H)_{POX}$ values.

Test ID (Sample ID)	CP-ECR, %	RCT Sample ID	Pre-test Estimated C_{HM}, wppm	Determined from Measured $(C_H)_{POX}$ C_{HM}, wppm
ZLUPH#3 (A15C3)	11		231±8	
		B		203±2
		C		197±1
ZLUPH#4 (A15C1)	10		245±23	
		B		204±3
		C		201±9
		D		197±1
ZLUPH#5 (A13C3)	11		256±46	
		B		242±24
		C		281±28
ZLUPH#6 (A13C1)	11		226±16	
		B		202±5
		C		183±7
		D		192±11
ZLUPH#7 (A13C5)	8		263±36	
		B		242±50
		C		217±21
		D		217±12
ZLUPH#8 (A15C5)	9		314±91	
		B		286±23
		C		236±21
		D		216±7

3.3 Embrittlement of Irradiated Cladding

3.3.1 Review of previous results

Results are presented in Ref. 1 for characterization, thermal and weight-gain benchmark tests, oxidation tests, post-oxidation characterization, RCTs, and post-RCT characterization for Zry-4, M5, and ZIRLO cladding materials from high-burnup fuel rods. For convenience, these materials are referred to as "high-burnup" cladding in the following. After publication of Ref. 1 (2008), improvements have been made in the methodology used to determine the pre-oxidation hydrogen content in the cladding metal and in the offset-strain ductility criterion (see Eq. 8) used to determine the ductile-to-brittle transition CP-ECR. Thus, the results presented in Ref. 1 have been re-analyzed using these improvements.

The standard approach for determining hydrogen content in irradiated cladding is to section a thin ring, weigh it, heat it to melting, and measure the hydrogen evolved to give hydrogen content in wppm. For determination of oxidation embrittlement levels vs. C_{HM}, it is necessary to know the hydrogen content in the pre-test or pre-LOCA-transient cladding metal. However, there are several sources of uncertainty in standard approaches used to determine cladding hydrogen content. The dominant uncertainty is due to the large axial variation of hydrogen content, especially for hydrogen contents >400 wppm (see Table 8 in Ref. 1). Even if an accurate C_{HM} measurement could be made using short rings on both sides of a 25-mm-long pre-test oxidation sample, linear interpolation would not necessarily give an accurate result for the average hydrogen content of the test sample. Also, as the technique used to measure hydrogen is destructive, there is no way that this approach could be used to pre-determine the average C_{HM} values for an oxidation test sample or an 8-mm-long RCT sample used to determine PQD. For PQD determination, the average hydrogen content in RCT rings needs to be determined as accurately as possible. The only way to do this is to rely on post-oxidation and post-RCT measurements and to use mass correction factors to reference the hydrogen to the pre-test mass of the cladding metal.

With regard to the pre-test material (corroded and defueled cladding), the mass of the hydrogen-analysis sample consists of the corrosion-layer mass (M_C), the cladding metal mass (M_M) and the fuel-cladding bond mass (M_B). For higher-burnup cladding, the mass of the bond layer can be significant if the defueling process is poor. The mass of total hydrogen evolved from the sample consists of corrosion-layer hydrogen (H_C), cladding-metal hydrogen (H_M) and cladding-bond hydrogen (H_B). The bond layer can pick up hydrogen evolved from the nitric acid defueling process.

As before, C_H (in wppm) is the total hydrogen (H_S) evolved from the sample divided by the total mass of the sample (M_S). Equation 11 represents what is generally reported for the hydrogen content in corroded cladding:

$$C_H = (H_S/M_S) \times 10^6 = [(H_C + H_M + H_B)/(M_C + M_M + M_B)] \times 10^6 \qquad (11)$$

Based on Eq. 11, the hydrogen content in the cladding metal, $C_{HM} = H_M/M_M$, may be greater or less than what is measured for corroded, irradiated samples.

Argonne has made pre-test hydrogen-content measurements like this on short rings adjacent to locations from which oxidation test samples were sectioned, along with metallographic examination of one or two rings within each cladding segment (M5 and ZIRLO segments were 80-mm long). Such measurements were used in planning oxidation times and corresponding CP-ECR levels, but they were found to be not accurate enough to determine the hydrogen content in the cladding metal for oxidation samples and for PQD rings sectioned from post-oxidation samples.

The approach adopted by Argonne to determine C_{HM} for oxidation samples and PQD rings is similar to the one used in Section 3.2.2 for non-irradiated, pre-hydrided cladding samples except that an additional correction factor is required to account for the effects of the masses of the corrosion and fuel cladding bond layers. During the oxidation test, hydrogen that was in the corrosion and bond layers is driven off. Let M_S be the pre-test mass of the cladding sample, as defined in Eq. 11. The post-oxidation hydrogen measurement is then given by

$$(C_H)_{POX} = (H_M/M_S)\,(1 + W_g/100)^{-1} \times 10^{-6} = (H_M/M_S)\,(f_{Wg})^{-1} \times 10^{-6} \qquad (12)$$

An additional correction needs to be made to separate the cladding metal mass from the masses of the corrosion and bond layers. This can be performed by measuring the total mass and length of the pre-test oxidation sample to determine the mass per unit length (M_S/L) and by measuring the sample outer diameter (micrometer), the corrosion layer thickness (metallographic examination), the cladding metal wall thickness (metallographic examination), and the cladding bond-layer thickness (metallographic examination). From these measurements, as well as the densities for cladding metal and corrosion-bond oxide layers, the cladding metal mass per unit length (M_M/L) can be determined. Let the metal-mass correction factor be defined as $f_{MM} = (M_S/L)/(M_M/L)$. By inverting Eq. 12 and applying the metal-mass correction factor, C_{HM} may be determined from the measured $(C_H)_{POX}$ by:

$$C_{HM} = (f_{MM} \times f_{Wg})\,(C_H)_{POX} \qquad (13)$$

Based on Argonne experience, the metal mass correction factor is in the range of 1.06 to 1.10 for high-burnup ZIRLO with corrosion layer thicknesses of about 25 μm to 45 μm. The factors do not scale directly with the corrosion layer thickness because the mass of the fuel-cladding bond varies from defueled segment to defueled segment. For high-burnup M5 with a corrosion layer in the range of 10-15 μm, the factor can vary from 1.003 to 1.06, where the low value is for a segment whose inner-surface was wire brushed.

Two reasonable assumptions have been made in order to calculate C_{HM} from post-oxidation measurements. The first assumption was that no significant hydrogen pickup occurred during the oxidation test. Previous oxidation tests with bare, as-fabricated cladding materials indicated ≤14-wppm hydrogen pickup relative to the pre-test mass of the samples [1]. It is quite likely that this hydrogen pickup occurred during the initial oxidation of the bare cladding (i.e., during the heating ramp) prior to the formation of a protective tetragonal oxide layer. This level of hydrogen pickup is insignificant for the high-burnup Zry-4 and ZIRLO tested because of the high hydrogen content of these samples, as well as the large circumferential and axial variations within these samples. For high-burnup M5 with only about 100-wppm hydrogen, hydrogen pickup could represent 10 to 15% of the measured post-oxidation hydrogen content if hydrogen could easily diffuse through the corrosion and bond layers. If such hydrogen pickup did occur in high-burnup M5 cladding, it would be about the same as the axial and circumferential variations in hydrogen content.

The second assumption used was that the density of the cladding metal was not reduced by the presence of hydrides. This is a very good assumption for high-burnup M5 with low hydrogen content and a reasonable approximation for high-burnup Zry-4 and ZIRLO.

Previous results for high-burnup (HBU) Zry-4 cladding

Testing of 15×15 Zry-4 from HBU (63 GWd/t) HBR fuel rods was conducted in 2005. These samples were not thoroughly defueled. As the mass of the fuel adherent to the fuel-cladding bond was not known

and likely varied from sample to sample, pre-test hydrogen measurements at axial locations between oxidation samples, along with post-test hydrogen measurements, could not be used to determine reliable values for C_{HM}. An additional segment was sectioned from an axial location adjacent to the oxidation samples, carefully defueled, and sectioned into 8 rings for hydrogen determination. The hydrogen content (550±100 wppm) was relatively constant from ring to ring. Also, the total mass of the rings was 1.52 g. Thus, 550±100 wppm is a reliable characterization of the pre-test hydrogen content in the corroded cladding. The corrosion layer was ≈70-μm thick and the cladding metal wall was 710-μm thick. Including the bond layer, the metal-mass correction factor was calculated to be 1.09. However, the corrosion layer had about 10% porosity and may have contained a significant amount of hydrogen. As no reliable post-oxidation hydrogen data are available for the Zry-4 LOCA samples, it is assumed that the mass-correction factor and the corrosion-layer-hydrogen correction factor balance out to give 550±100 wppm of hydrogen in the cladding metal.

High-burnup Zry-4 samples with 550±100 wppm C_{HM} were oxidized to CP-ECR levels of 2.9% to 9.4% (includes oxidation during cooling). Samples were slow-cooled without quench. RCT results are summarized in Table 14. In selecting the transition CP-ECR level, the embrittling effects of quench on ductility were taken into account. Rings tested at 6.6% and 7.6% are expected to be brittle following quench based on results for pre-hydrided Zry-4 with comparable hydrogen contents. The 4.5% CP-ECR ring had enough ductility such that it should be ductile after quench. The transition CP-ECR is estimated to be 5% for the high-burnup Zry-4 tested. The peak oxidation temperature was ≈1180°C at 5% CP-ECR.

Table 14. RCT results for HBU Zry-4 samples oxidized at ≤1200°C and cooled without quench. C_{HM} was ≈550±100 wppm for these samples.

Oxidation Test ID[a]	CP-ECR, %	Maximum Oxidation T, °C	Offset Strain, %	Offset-Strain Ductility Limit, %	Permanent Strain, %
HBRI#2	2.9	1110	>45	1.7	>43
HBRI#1	4.5	1169	>12 ≈37	1.9	– –
HBRI#3	6.6	1196	4.0	2.1	2.6
HBRI#5	7.6	1197	4.0	2.2	2.9
HBRI#4	9.4	1198	0.5	2.4	0.6

[a]HBRI#6 sample (740 wppm) is not included because it was not used to determine the transition CP-ECR.

Previous results for high-burnup M5 cladding

M5 cladding samples from a fuel rod irradiated to high burnup (63 GWd/t) in one of the Ringhals Reactors were used for oxidation and PQD tests. Tests MI#1 to MI#4 were slow-cooled without quench to determine an upper-bound transition CP-ECR for samples cooled with quench. Tests MI#5 to MI#7 were cooled with quench at 800°C and were used to determine PQD. The corrosion layer thickness was 12 μm for one of two adjacent segments used to section oxidation test samples. Measured values for pre- and post-test hydrogen content for these test samples are listed in Table 15. Results for C_{HM} were higher than expected for six of the seven oxidation samples based on data given in Ref. 24.

Table 15. Determination of C_{HM} based on post-oxidation hydrogen measurements [$(C_H)_{POX}$] for high-burnup M5 samples used for oxidation tests; f_{Wg} is post-test-weight/pre-test-weight and f_{MM} is pre-test sample-mass/metal-mass. Sample masses are listed in parentheses.

Oxidation Test # (ID#)	CP-ECR, %	$(C_H)_{POX}$, wppm (mass, g)	f_{Wg}	Meas. Pre-test mass/L, g/cm	f_{MM}	C_{HM}, wppm	Measured Pre-test C_H, wppm (mass, g)
MI#1 (645A1)	13.4	85±7 (0.35)	1.040	1.036	1.028	91±8	101±21 (0.1 g)
MI#2 (645A4)	15.1	107±14 (0.38)	1.040	1.042	1.035	115±15	101±21 (0.1 g)
MI#3 (645A3)	17.0	128±19 (0.24)	≈1.045[a]	≈1.04	≈1.04	≈140±20	101±21 (0.1 g)
MI#4 (645B6)	18.1	109±9 (0.26)	1.052	1.066	1.059	122±10	108±5 (0.22 g)
MI#5 (645B2)	16.1	130±11 (0.33)	1.047	1.039	1.033	140±12	108±5 (0.22 g)
MI#6 (645C3)	15.1	138±15 (0.25 g)	1.047	1.044	1.025	148±14	108±10 (0.40 g)
MI#7 (645C6)	13.4	130±15 (1.31 g)	1.039	1.007	1.003	135±16	108±10 (0.40 g)

[a]Pre- and post-test masses were not measured. The f_{Wg} value was estimated by means of interpolation.

Post-oxidation and post-quench ductility results for high-burnup M5 are summarized in Table 16. Results for samples cooled without quench are interesting in that they show little effect of hydrogen content on the transition CP-ECR. Based on permanent strain, the transition CP-ECR is ≈18% for ≈120-wppm C_{HM}, as compared to 20% CP-ECR for as-fabricated M5 with only 5-wppm C_{HM}. However, for quenched samples the hydrogen content caused a significant reduction in the transition CP-ECR. On the basis of offset strains, quenched RCT samples were ductile (3 data points) at 13.4% CP-ECR and brittle (3 data points) at 15.1% CP-ECR. Using interpolation, the transition CP-ECR for HBU M5 is estimated to be 14.5% for 140-wppm C_{HM}. In order to be conservative in data interpretation and consistent with the embrittlement observed at 15.1% CP-ECR, 14.5% is rounded down to 14% for the transition CP-ECR. Consistent with the definition used for transition CP-ECR, embrittlement of M5 samples with ≥140 wppm C_{HM} is expected to occur for oxidation levels >14% CP-ECR.

Table 16. RCT results for HBU M5 samples oxidized at 1200°C and cooled without and with quench (see Table 74 in Ref. 1).

Oxidation Test ID	CP-ECR, %	C_{HM}, wppm	Average Offset Strain, %	Offset-Strain Ductility Limit, %	Permanent Strain, %
MI#1 Slow Cooled	13.4	91±8	12.0±0.2	2.9	6.5±0.3
MI#2 Slow Cooled	15.1	115±15	8.5±1.4	3.0	4.4
MI#3 Slow Cooled	17.0	140±20	5.8±0.6	3.2	1.3
MI#4 Slow Cooled	18.1	122±10	4.8±1.0	3.4	1.1
MI#5 800°C Quench	16.1	140±20	2.9±0.9	3.2	–
MI#6 800°C Quench	15.1	148±14	2.8±0.7	3.0	–
MI#7 800°C Quench	13.4	135±16	3.4±1.3	2.9	–

Previous results for high-burnup ZIRLO cladding

ZIRLO cladding samples from a fuel rod irradiated to high-burnup (70 GWd/t) in the North Anna Reactors were used for oxidation and PQD tests. Tests ZLI#1 to ZLI#3 were slow-cooled without quench to determine an upper bound on the transition CP-ECR. Tests ZLI#4 to ZLI#6 were cooled with quench at 800°C and were used to determine PQD. The corrosion layer thickness was measured to be 42±3 μm for one of two adjacent segments from which oxidation samples were sectioned [1]. Measured values for pre- and post-test hydrogen content for rings from the three oxidation tests with quench are listed in Table 17. The average C_{HM} values were about 50 wppm less than the hydrogen content measured for the corroded pre-test sample. This is less than the measured circumferential and axial variations.

Table 17. Determination of C_{HM} based on measured post-oxidation hydrogen content for high-burnup ZIRLO samples used for oxidation tests and PQD determination; f_{Wg} = post-test-weight/pre-test-weight, f_{MM} = pre-test sample-mass/metal-mass. Sample masses are given in parentheses.

Oxidation Test # (ID#)	CP-ECR, %	$(C_H)_{POX}$, wppm (mass, g)	f_{Wg}	Meas. Pre-test mass/L, g/cm	f_{MM}	C_{HM}, wppm	Measured Pre-test C_H, wppm (mass, g)
ZLI#4 (648F2)	6.3	505±107 (0.26)	0.996	1.074	1.074	540±114	620±140 (0.55)
ZLI#5 (648F6)	4.0	505±107 (0.27)	0.990	1.074	1.096	593±115	600±150 (0.36)
ZLI#6 (648E2)	5.1	414±115 (0.79)	1.004	1.073	1.080	451±101	500±120 (0.24)

Post-oxidation results for slow-cooled samples are presented in Ref. 1 (see Table 72). Although pre- and post-test sample weights were not measured for ZLI#1 through ZLI#3 test samples, pre- and post-test hydrogen contents were measured. As weight gain is expected to be negligible for these samples (see f_{Wg} in Table 17 for quenched samples), post-test hydrogen measurements are considered to be more reliable than pre-test measurements, especially as the masses of the post-test samples were generally larger than those for the pre-test samples. Offset strains indicated high ductility (19±10%) for the 540±100 wppm sample oxidized to 6.3% (1176°C peak oxidation temperature), moderate ductility (4.5±0.5%) for the 510±100 wppm sample oxidized to 8.1% (1191°C peak oxidation temperature), no ductility (1% offset strain and 0.3% permanent strain) for the 490±120 wppm sample oxidized to 10.2% (1200°C peak oxidation temperature). Given the expected decrease in ductility due to quench at 800°C, oxidation tests with quench (ZLI#4 through ZLI#6) were initiated at 6.3% CP-ECR. RCT results for these oxidized and quenched samples are summarized in Table 18.

Table 18. RCT results for high-burnup ZIRLO samples oxidized at <1200°C and cooled with quench at 800°C.

Oxidation Test ID (Sample ID)	CP-ECR, %	Maximum Oxidation T, °C	C_{HM}, wppm	Average Offset Strain, %	Offset-Strain Ductility Limit, %	Permanent Strain, %
ZLI#4 (648F2)	6.3	1176	540±114	0.8±0.4 (2 data points)	2.1	0.2 (1 data point)
ZLI#5 (648F6)	4.0	1132	593±115	>43 (2 data points)	1.9	>44 (2 data points)
ZLI#6 (648E2)	5.1	1162	451±101	40±27 (3 data points)	2.0	–

The PQD results for HBU ZIRLO with high-hydrogen content were more difficult to interpret than the PQD results for pre-hydrided ZIRLO with low-hydrogen content because: (a) only three oxidation with quench tests were conducted; (b) the average C_{HM} was not constant (about 90 wppm variation); (c) the circumferential variation in C_{HM} was large (about 100 wppm); and (d) the peak oxidation temperature decreased significantly as the target CP-ECR decreased. However, experience gained in testing pre-hydrided and high-burnup Zry-4 was used to assess and interpret the data in Table 18. The PQD sample with 540±114 wppm C_{HM} was very brittle at 6.3% CP-ECR based on both offset and permanent strains, while the PQD sample with higher C_{HM} (593±115 wppm) was highly ductile at 4.0% CP-ECR. It is reasonable to infer that the transition CP-ECR is about 5% for high-burnup ZIRLO with 540-wppm C_{HM} and a peak oxidation temperature of 1160°C. Conversely, the higher C_{HM} sample (593 wppm) would be very brittle at 6% CP-ECR and have lower ductility at 5% CP-ECR than the 540 wppm sample. Engineering judgment was used to assess the transition CP-ECR (to the nearest 1%) to be 4% for high-burnup ZIRLO with about 590 wppm C_{HM} and a peak oxidation temperature of about 1130°C.

Stronger conclusions could have been reached if all three LOCA samples had the same average C_{HM} (e.g., 540 wppm). However, cladding with high-hydrogen content has large axial and circumferential variations in C_{HM} over relatively short distances along fuel rods. ZLI#4 and ZLI#5 test samples were sectioned from the same 80-mm-long cladding segment with a mid-span to mid-span distance between of only 17 mm. The ZLI#6 LOCA test sample was from an adjacent 80-mm-long segment. Pre-test hydrogen-content measurements for the corroded cladding were 464±71 wppm and 563±145 wppm for 2-mm-long rings spaced 52 mm apart (see Table 68 [1]). These variations are very significant and should be accounted for in correlations for hydrogen pickup vs. corrosion layer thickness.

3.3.2 Current PQD results for high-burnup ZIRLO

Characterization

Figure 161 of Ref. 1 shows axial locations of ZIRLO Rod AM2-L17 irradiated to HBU (70 GWd/t) in the North Anna Reactors. Studsvik sectioned and defueled 80-mm-long cladding segments from this rod for ANL. Segments 5, 6, and 8 with high hydrogen concentrations were tested earlier and results are summarized in Section 3.3.1. Segments 1 and 2 with lower corrosion-layer thickness (25–30 μm based on eddy current) and expected medium hydrogen concentrations were selected for oxidation and RCT testing. Corresponding Argonne ID numbers for these segments are 648A and 648B, respectively.

Figure 19 shows micrographs at one of eight circumferential locations for: (a) cladding cross section; (b) corrosion layer; and (c) fuel-cladding bond layer. The measured thicknesses were 26±1 μm for the corrosion layer (δ_c), 551±5 μm for the metal wall (h_m), and ≈7±1 μm for the fuel-cladding bond (δ_b). However, as shown in Fig. 19c, local regions of the bond layer were about 20-25 μm thick. These thicker bond regions are consistent with the higher (factor of 2) gamma dose-rate readings for 648A and 648B, as compared to the dose rate reading for segment 648F (Segment 6) used in previous oxidation tests.

Figure 20 shows the hydride morphology at two circumferential locations adjacent to the sample with 318±30 wppm of hydrogen in the corroded cladding. As is typical of seven of the eight locations imaged, hydrides were primarily circumferential and clustered in a dense rim near the corrosion layer (Fig. 20a). Figure 20b shows one location that had long radial hydrides within the inner third of the cladding wall. For LOCA events, the radial variation in hydrogen content and hydride morphology are not important because hydrogen homogenizes quickly across the beta phase of the cladding.

Table 19 summarizes characterization results for δ_c, h_m, δ_b, and C_H. For the LECO hydrogen-content measurements (C_H), short cladding rings (≈2-mm-long) were sectioned and then snipped into four quarter rings. Hydrogen content and mass were measured for each quarter ring. The hydrogen content included the hydrogen evolved from the cladding metal and the corrosion layer, as well as the bond layer. The sample mass included masses of the corrosion layer, the cladding metal, and the fuel-cladding bond. The four measurements per ring were also used to determine the one-sigma (1-σ) circumferential variation in hydrogen content. The weight-averaged hydrogen contents of the two segments were 310±32 wppm for 648A and 366±30 wppm for 648B. Two oxidation samples were sectioned from 648A, and three oxidation samples were sectioned from 648B.

Pre-oxidation hydrogen data were used for choosing target oxidation levels (CP-ECR values). However, it was also realized that the hydrogen content in the cladding metal could be higher or lower than what was measured. LOCA samples were weighed before and after oxidation tests. Post-oxidation hydrogen contents were corrected for weight gain (1-2%). A final correction was made to account for the ratio of pre-test sample mass (measured) and metal mass (calculated from metallographic results). This factor (1.06 to 1.10) varied from sample to sample and reflected the added weight of the pre-test sample due to the fuel-cladding bond, which included fission products and actinides in or adherent to the fuel-cladding bond. The methodology for determining the metal hydrogen content (C_{HM}) is described in detail in Section 3.3.1. As indicated in Table 19, C_{HM} values were close to measured C_H values. Also, axial and circumferential variations in both C_{HM} and C_H were much smaller for these lower hydrogen-content samples than what was observed previously for high hydrogen-content samples. The results suggest that for 25–30 μm corrosion-layer thicknesses the additional hydrogen in the corrosion layer is compensated by the additional mass of the corrosion layer such that $C_{HM} \approx C_H$.

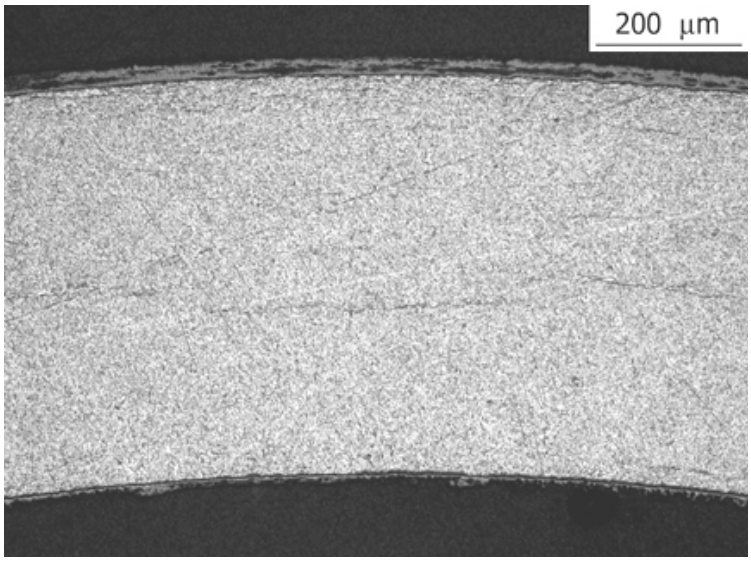

(a) Cladding cross section

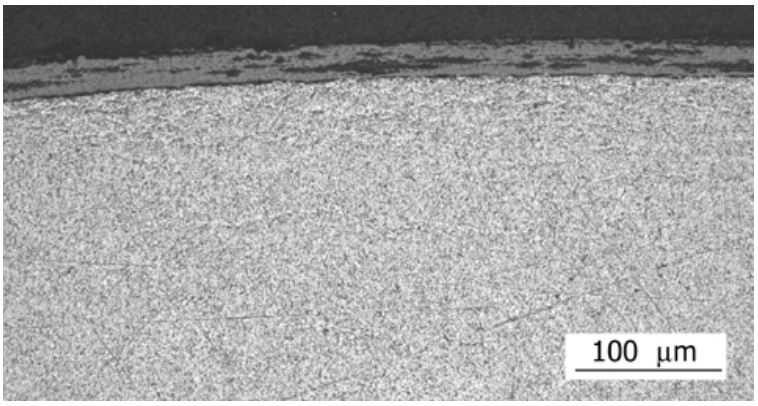

(b) Corrosion layer

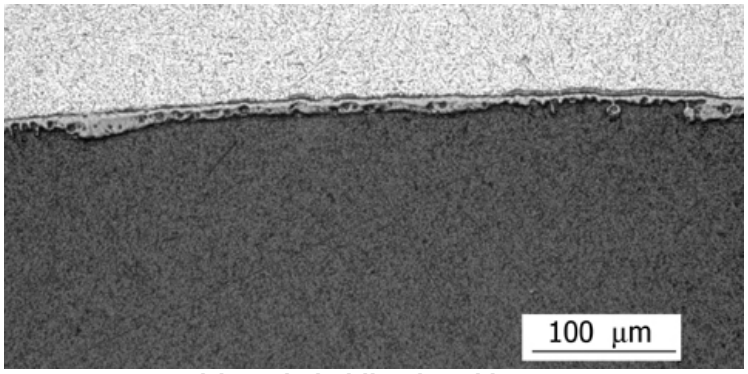

(c) Fuel-cladding bond layer

Figure 19. Micrographs taken from a sample sectioned near the middle of ZIRLO segment 648A: (a) cladding cross section; (b) corrosion layer; and (c) fuel-cladding bond layer.

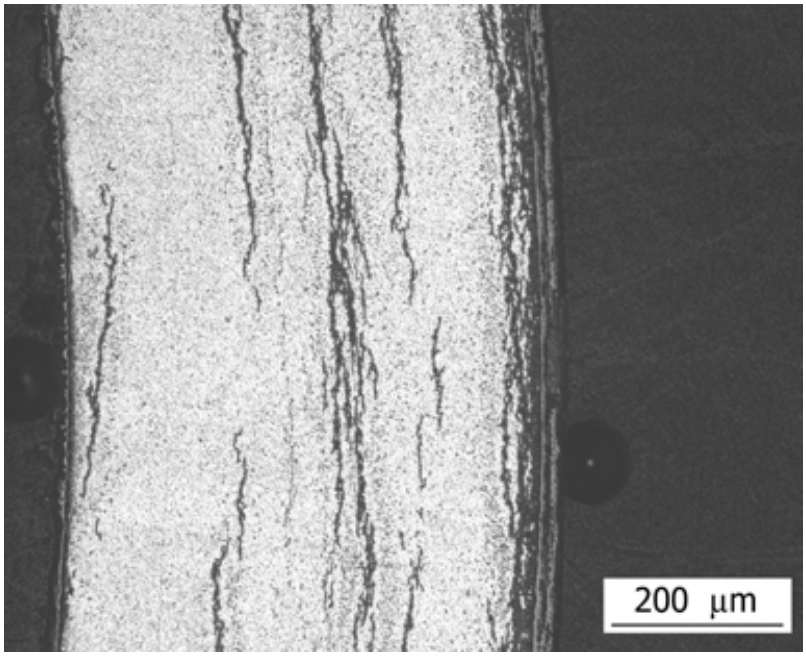

(a) Circumferential hydrides

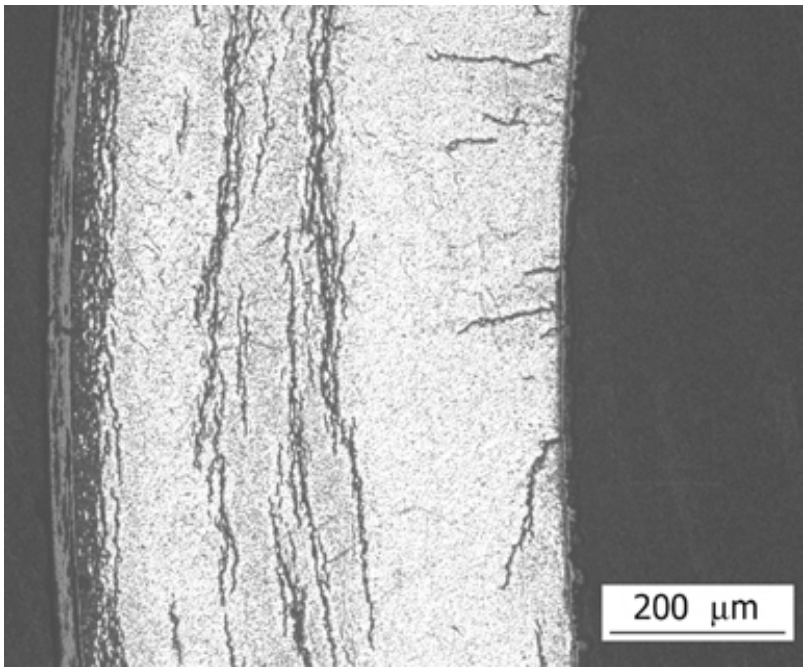

(b) Circumferential and radial hydrides

Figure 20. Hydride morphology for high-burnup ZIRLO sample 648A5: (a) circumferential hydrides (typical); and (b) circumferential and radial hydrides. Based on measured values for an adjacent ring (648A4), the C_H was 318±30 wppm.

Table 19. Characterization of high-burnup ZIRLO segments used for current oxidation tests.

ANL Segment ID	δ_c from Eddy Cur., μm	δ_c from Metallography, μm	h_m, μm	δ_b μm	Measured Pre-Test C_H, wppm	Estimated Pre-Test C_{HM}, wppm
648A	25-28	– 26±1 –	– 551±5 –	– 7±1[a] –	294±29 318±30 317±38	296±33
648B	25-30	– – –	– – –	– – –	361±36 367±29 370±33	340±34

[a]Local regions of bond layer were as thick as 20-25 μm.

Thermal and metallurgical benchmark tests for high-burnup ZIRLO

For in-cell tests with high-burnup ZIRLO, thermal benchmark tests were first conducted in the out-of-cell LOCA apparatus. Two thermocouples (TCs) were welded onto as-fabricated ZIRLO samples, in addition to the three TCs permanently welded to the Inconel holder just above the sample. Tests were repeated with fresh samples until furnace control parameters were established to give the desired temperature ramp and hold temperature. The results of benchmark test ZLU#145 with a bare ZIRLO sample are shown in Fig. 21. The time for the sample to reach 1200ºC was about 100 s. At 150 s, the average of the two sample TCs was 1202±7ºC. The heating phase of the test was 200 s. The corresponding CP weight gain and CP-ECR, including the cooling phase, were 8.27 mg/cm^2 and 12.7%, respectively. The CP-calculated oxide layer grown on the inner and outer surfaces of the cladding was about 40-μm thick.

For high-burnup ZIRLO cladding, the corrosion and bond oxide layers will result in a slower temperature ramp rate as compared to the rate for bare ZIRLO. At the completion of benchmark test ZLU#145, the oxidized sample was again ramped to the target temperature using the same control parameters as were used for ZLU#145. To distinguish these two tests, the one with the pre-oxidized sample was called ZLU#145A. Figure 22 shows the comparison between the average cladding temperatures for bare and pre-oxidized ZIRLO. The small temperature pre-peak was reduced from ≈1110ºC to 1060ºC. The average ramp rates (≈2.2°C/s) from 1080ºC to 1180 ºC were comparable. However, the time to reach 1200ºC was longer for the pre-oxidized cladding (150 s vs. 100 s for bare cladding). The average temperature of the pre-oxidized cladding was 1200±3ºC at 150 s during the heating phase. It was later verified that there was essentially no difference in the thermal response of pre-oxidized cladding samples with thin (≈12 μm) and thick (≈40 μm) oxide layers. Thus, the ZLU#145A thermal history was determined to be appropriate one for high-burnup cladding oxidation tests.

The test train benchmarked in the out-of-cell LOCA apparatus was installed in the in-cell apparatus located in Cell #4 of the IML with the same three holder TCs welded onto the sample holder. A weight-gain benchmark test was conducted in-cell with bare ZIRLO. The same temperature history and heating-phase shown in Fig. 21 were used to conduct this weight-gain benchmark test (ZLU#146). The measured weight gain (7.91 mg/cm^2) was within 5% of the CP-calculated weight gain (8.27 mg/cm^2). These results validated the use of the ZLU#145A thermal history for in-cell tests with high-burnup ZIRLO samples.

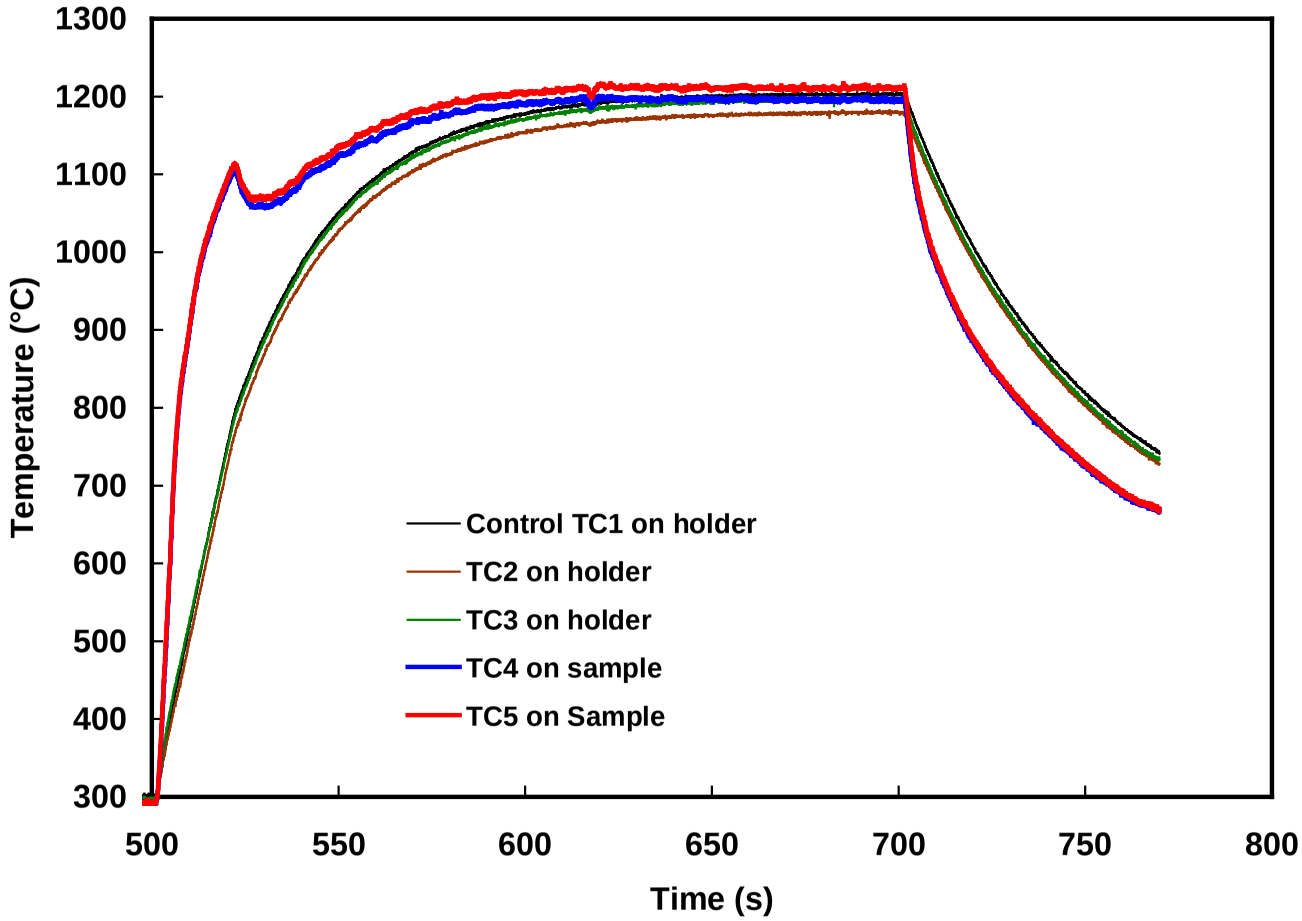

Figure 21. **Thermal history for bare ZIRLO cladding determined from test ZLU#145. At 150 s into the heating phase, the average sample temperature was 1202±7°C.**

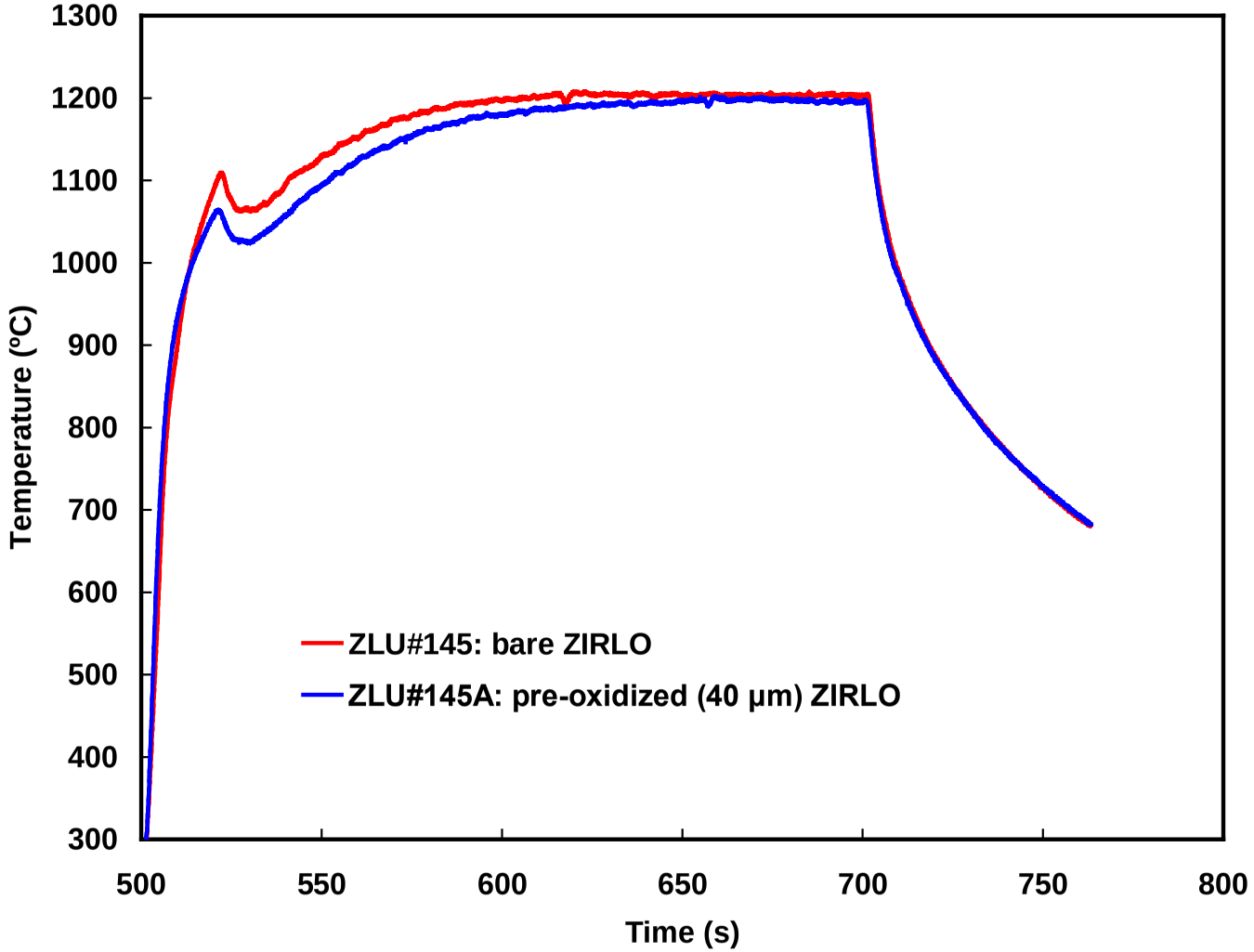

Figure 22. **Thermal history for bare ZIRLO (ZLU#145) and pre-oxidized (ZLU#145A) cladding. At 150 s into the heating phase, the average temperature for the pre-oxidized sample was 1200±3°C.**

Ductility Results for High-burnup ZIRLO

Four oxidation tests and 9 ring-compression ductility tests were conducted with samples sectioned from high-burnup ZIRLO segments 648A and 648B. Test conditions and PQD data, along with ductility data for one LOCA test cooled without quench, are summarized in Table 20.

For planning purposes, the measured cladding wall thickness (0.55 mm) was used to derive the relationship between CP-ECR (in %) and w_g (in mg/cm^2):

$$\text{CP-ECR} = 1.594\ w_g \qquad (14)$$

Test ZLI#7 was conducted without quench with a sample containing about 340 wppm C_{HM} to ensure adequate ductility at 10% CP-ECR. The heating-phase test time (153 s) and corresponding CP-ECR (10%) are shown in Fig. 23. The pre-test sample outer diameter was 9.50 mm. Subtracting twice the corrosion layer thickness measured at a neighboring location gave a pre-test cladding-metal outer diameter of about 9.45 mm. This pre-test metal diameter was used to normalize offset and permanent displacements to determine offset and permanent strains. As shown in Table 20, the offset and permanent strains at 135ºC were in the range of 10-13% and 5-9%, respectively. These results indicate significant ductility for the slow-cooled LOCA sample following oxidation to 10% CP-ECR. The results were used to plan the first test with quench.

For test ZLI#8, a lower hydrogen content (≈300 wppm) sample from segment 648A was used. The test time and CP-ECR were kept the same as for test ZLI#7. However, the sample was quenched at 800ºC. The effects of quench were significant in that the rings sectioned from the LOCA sample were brittle even though the sample had less hydrogen in the metal than the ZLI#7 sample. The offset strains (0.7% and 2.2%) were less than the ductility criterion (2.5%) at 10% CP-ECR. Permanent displacements and strains could not be determined because the rings cracked into two pieces.

In order to bracket the ductile-to-brittle transition oxidation level, test ZLI#9, also with ≈300 wppm hydrogen, was conducted for 118-s heating-phase time, which corresponded to 8% CP-ECR. As shown in Fig. 23, the peak oxidation temperature at the end of the heating phase was 1190ºC. The first two rings compressed at 135ºC also cracked at top and bottom locations with adequate offset strains of 2.9% and 4.6% indicative of ductile behavior (≥2.3%). In order to confirm ductile behavior, the load was terminated for the third ring before cracking occurred and after sufficient offset strain (≥2%). The offset and permanent displacements of the uncracked ring were 0.19 mm and 0.11 mm, respectively. These correspond to 2.0% offset and 1.2% permanent strains. The difference (0.8%) is less than the difference (1.3%) used for the offset-strain ductility criterion at 8% CP-ECR. These results are encouraging because the offset-strain criterion is based on the one-sigma upper bound for ductility.

Results in Table 20 indicate that the ductile-to-brittle transition oxidation level was 9% CP-ECR for 300-wppm C_{HM}. Following this determination, the remaining two oxidation samples with 340-wppm C_{HM} were used for oxidation tests. During the ZLI#10 ramp, the control thermocouple failed and the test was terminated after the other two thermocouples on the holder recorded temperatures above 1250ºC. The remaining sample was oxidized to 8% CP-ECR in test ZLI#11 and quenched at 800ºC. As indicated in Table 20, the two rings sectioned from this oxidation sample had very low offset strains (0.6–1.0%) indicating embrittlement. Although the ductile-to-brittle transition CP-ECR could not be determined precisely, the data point is useful in establishing that the transition CP-ECR is <8% for 340-wppm C_{HM}.

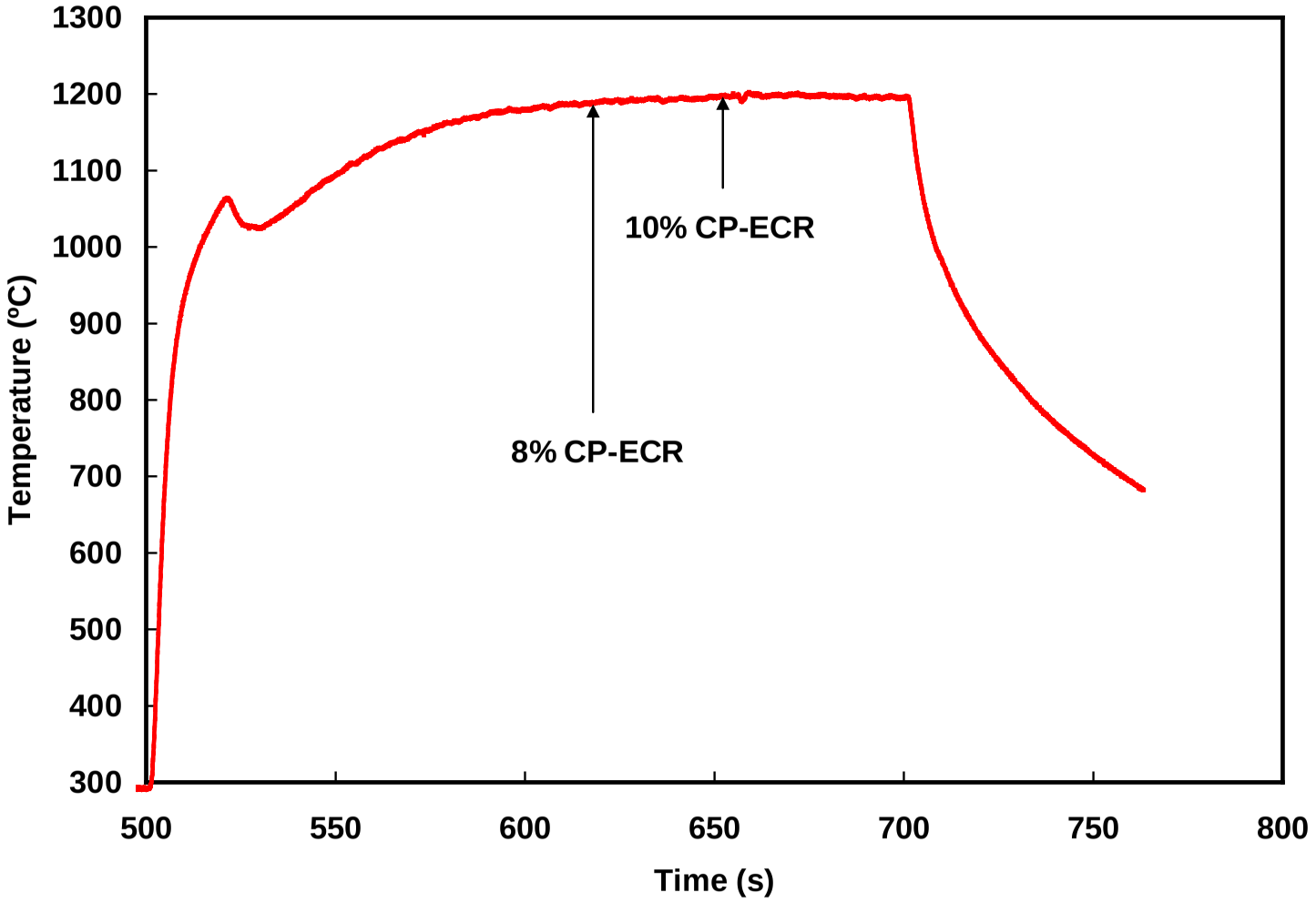

Figure 23. **Thermal history and test times for high-burnup ZIRLO tests conducted to 8% (ZLI#9 & 11) and 10% (ZLI#7 & 8) CP-ECR.**

Table 20. Post-test ductility results for high-burnup ZIRLO cladding oxidized at ≤1200ºC, cooled with or without (SC) quench at 800ºC, and ring-compressed at 135ºC.

Oxidation Test ID	C_{HM}, wppm (mass, g)	Test Time,[a] s	Peak T, ºC	CP-ECR, %	Offset Strain, %	Offset Strain Ductility Criterion, %	Permanent Strain, %
ZLI#7 SC	340±34 (0.28)	153	1200	10	9.9 13.4	2.5	5.0 9.4
ZLI#8 Quench	294±37 (0.76)	153	1200	10	0.7 2.2	2.5	--- ---
ZLI#9 Quench	296±35 (0.72)	118	1190	8	2.9 4.6 >2.0	2.3	--- --- >1.2
ZLI#11 Quench	340±34 (0.28)	118	1190	8	0.6 1.0	2.3	--- ---

[a]From beginning of ramp at 300ºC to end of heating phase.

3.4 Discussion of PQD Embrittlement Results

Figure 24 shows the oxidation embrittlement threshold vs. hydrogen content for as-fabricated cladding alloys, pre-hydrided Zry-4 and ZIRLO, and high-burnup Zry-4, ZIRLO, and M5. The bilinear fit to the data in Fig. 24 for high-burnup cladding alloys is more of a guide than a best fit. For $C_{HM} \leq 400$ wppm, it is based on one high-burnup M5 data point (140 wppm and 14% CP-ECR) and two high-burnup ZIRLO data points (300 wppm and 9% CP-ECR; 340 wppm and <8% CP-ECR). For $C_{HM} \leq 400$ wppm:

$$\text{CP-ECR} = 18.5 - 0.03125\, C_{HM} \qquad (15)$$

where C_{HM} is in wppm and CP-ECR is in %. Equation 15 gives 6% CP-ECR for 400 wppm. The choice of 400 wppm for the slope change is somewhat arbitrary as there are no data for high-burnup cladding between 340 wppm (1190°C peak temperature for high-burnup ZIRLO) and 540 wppm (1160°C peak temperature for high-burnup ZIRLO). As C_{HM} increases beyond 340 wppm, the peak oxidation temperature decreases to as low as 1130°C for high-burnup ZIRLO at 4% CP-ECR. For C_{HM} >400 wppm:

$$\text{CP-ECR} = 6.0 - 0.00865\,(C_{HM} - 400\ \text{wppm}) \qquad (16)$$

For as-fabricated cladding, the embrittlement oxidation level was found to be independent of quench temperature and of cladding alloy for modern belt- or wheel-polished materials. We speculate that the embrittlement threshold for as-fabricated cladding is also relatively insensitive to higher heating rates (>3°C/s from 1080°C to 1180°C) and slower cooling rates (<10°C/s) to quench. For pre-hydrided and high-burnup cladding alloys, the embrittlement threshold exhibited a high sensitivity to heating rate, peak oxidation temperature, cooling rate prior to quench, and quench temperature.

The results in Fig. 24 suggest that pre-hydrided cladding is a good surrogate for high-burnup cladding in terms of PQD. A second fit was performed by including all data points and using a decaying exponential function. In one curve fitting attempt, high-burnup data points were assigned a weight of 4 while all other data points were assigned a weight of 1. In a second curve fitting attempt, all data points were assigned a weighting factor of 1. The difference in curve-fitting parameters was negligible for these two approaches. The best-fit curve and data are shown in Fig. 25. The best-fit exponential function is given in Eq. 17.

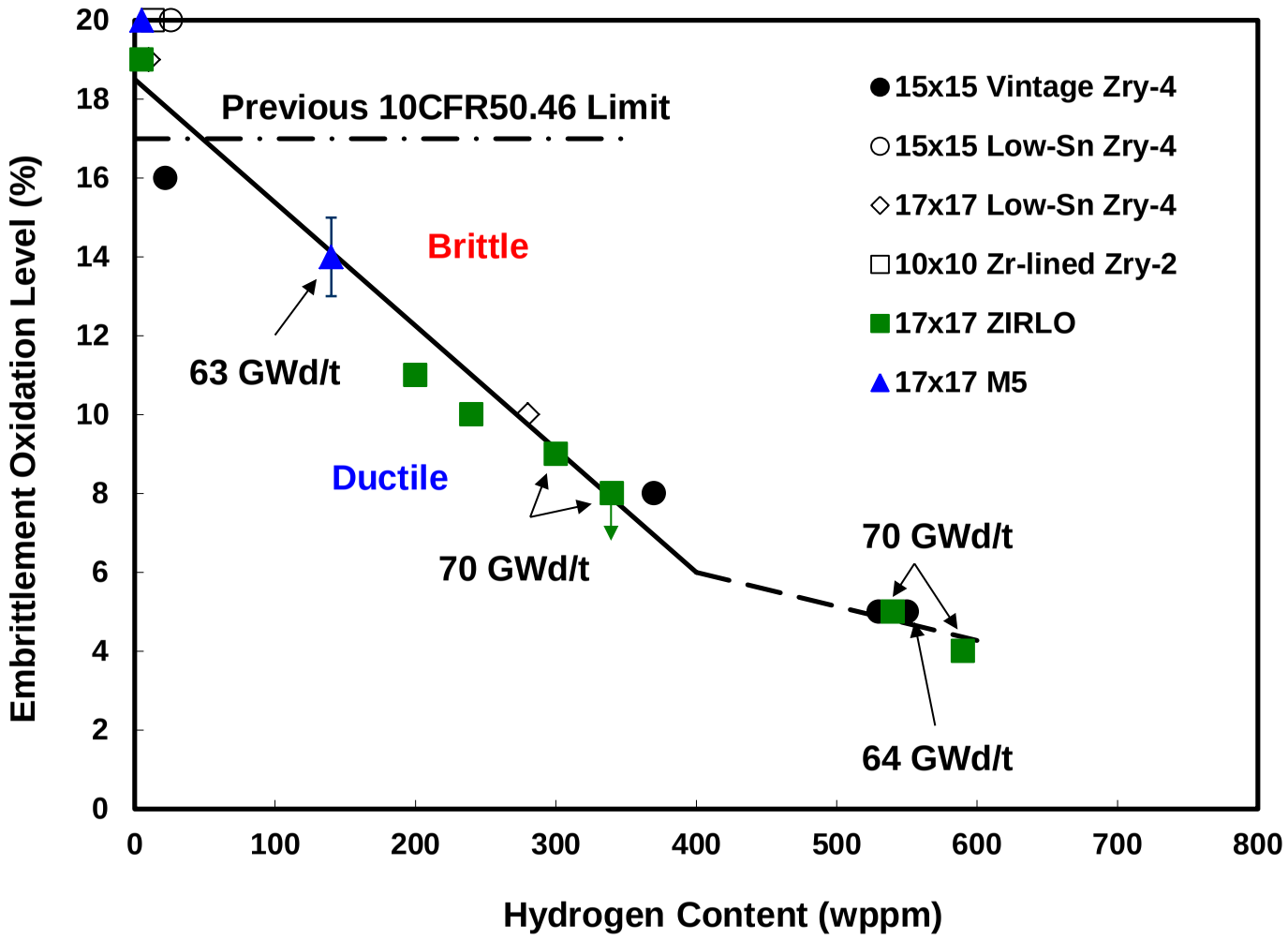

Figure 24. **Embrittlement oxidation level (CP-ECR) as a function of pre-transient hydrogen content in cladding metal for peak oxidation temperatures of 1190–1200°C for <400 wppm hydrogen content and 1130–1190°C for >400 wppm hydrogen content.**

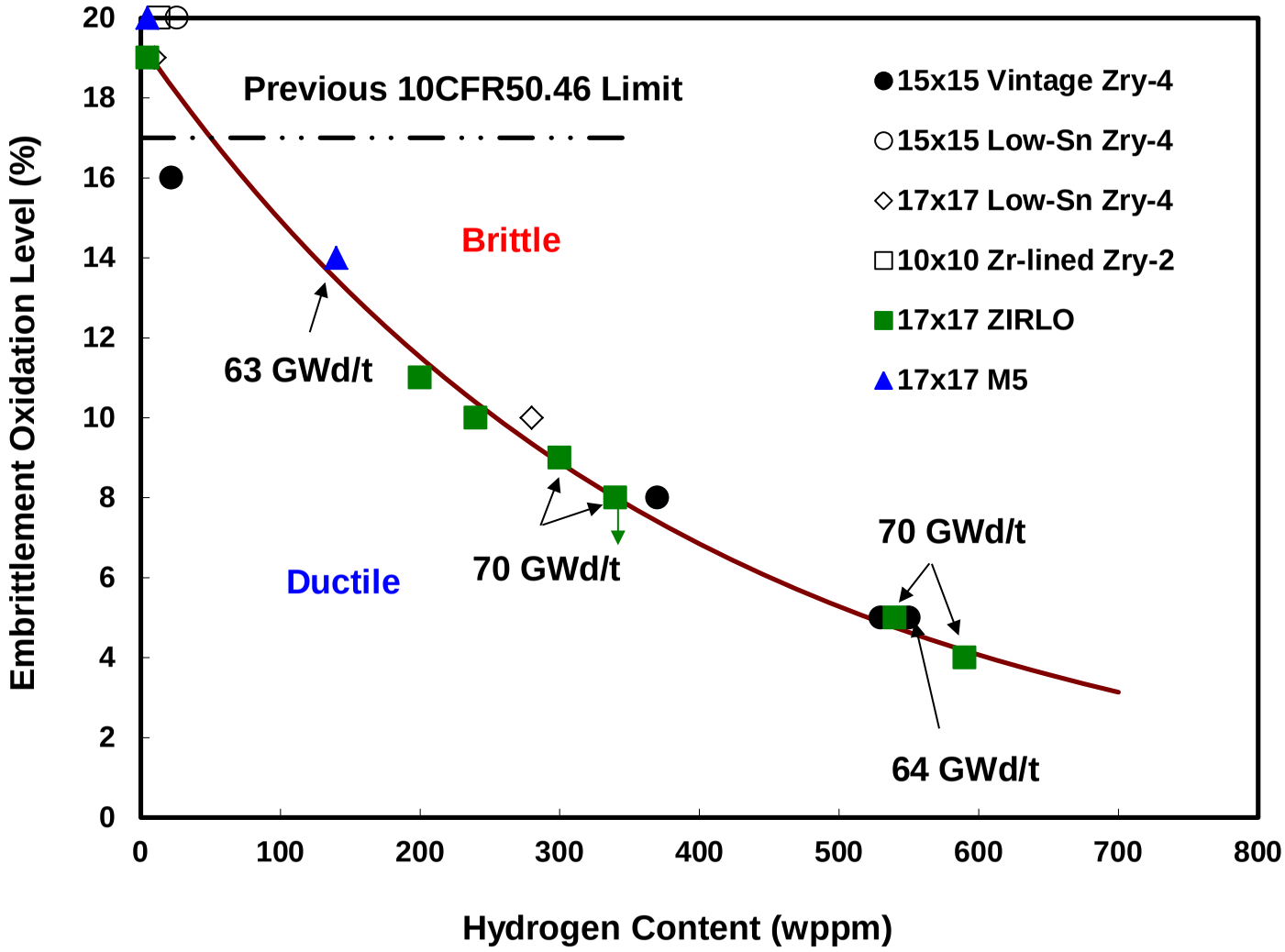

Figure 25. **Exponential fit to data for embrittlement CP-ECR as a function of pre-transient hydrogen content in cladding metal.**

$$\text{CP-ECR} = 19.38 \exp(-0.0026\, C_{HM}) \quad (17)$$

For the best-estimate curve using the weighted average of data points, in which high-burnup data were given a weighting factor of 4, the pre-exponential factor was 19.42 and the exponent factor was still -0.0026. The exponential fit (Eq. 17) gives better agreement with the data than the bilinear fit (Eqs. 15–16) and it is easier to use the continuous exponential equation. Also, the exponential fit is based on more data points by using the assumption that non-irradiated, pre-hydrided samples are a good surrogate for high-burnup samples for determining ductility and embrittlement threshold. The data generated in this program support the position that embrittlement is governed by hydrogen content in the cladding metal and oxidation level independent of whether the hydrogen pickup occurred during reactor operation or during the pre-hydriding process.

Equation 17 ignores the differences in peak cladding temperature for LOCA samples with high hydrogen content. Thus, it is not more mechanistic than the bilinear representation of the data. The 4% to 6% CP-ECR values attained for the double-sided oxidized samples with about 2°C/s temperature increase from 1000°C to the peak oxidation temperature <1200°C could have been obtained at 1200°C peak oxidation temperature by using faster heating rates, one-sided oxidation, and direct quench from 1200°C. CEA ran a number of tests with as-fabricated and pre-hydrided samples using these oxidation test parameters [9-11]. The hold time at 1200°C was as low as 50 s, which resulted in about 3% CP-ECR. Pre-hydrided (600 wppm) Zry-4 was found to be brittle after the CEA oxidation tests. However, the CEA test conditions were less LOCA-relevant than the Argonne test conditions.

For typical fuel management schemes, assemblies containing high-burnup fuel rods are placed closer to the edges of the core than the center of the core. It is unlikely that these high-burnup fuel assemblies would reach 1200°C during a LOCA. Thus, the decaying exponential curve (Eq. 17) is very useful for high-burnup fuel as long as the peak cladding temperature does not exceed 1130°C.

In order to allow independent assessment of the PQD data for high-burnup ZIRLO cladding, the RCT load-displacement curves are presented in Figs. 26–34.

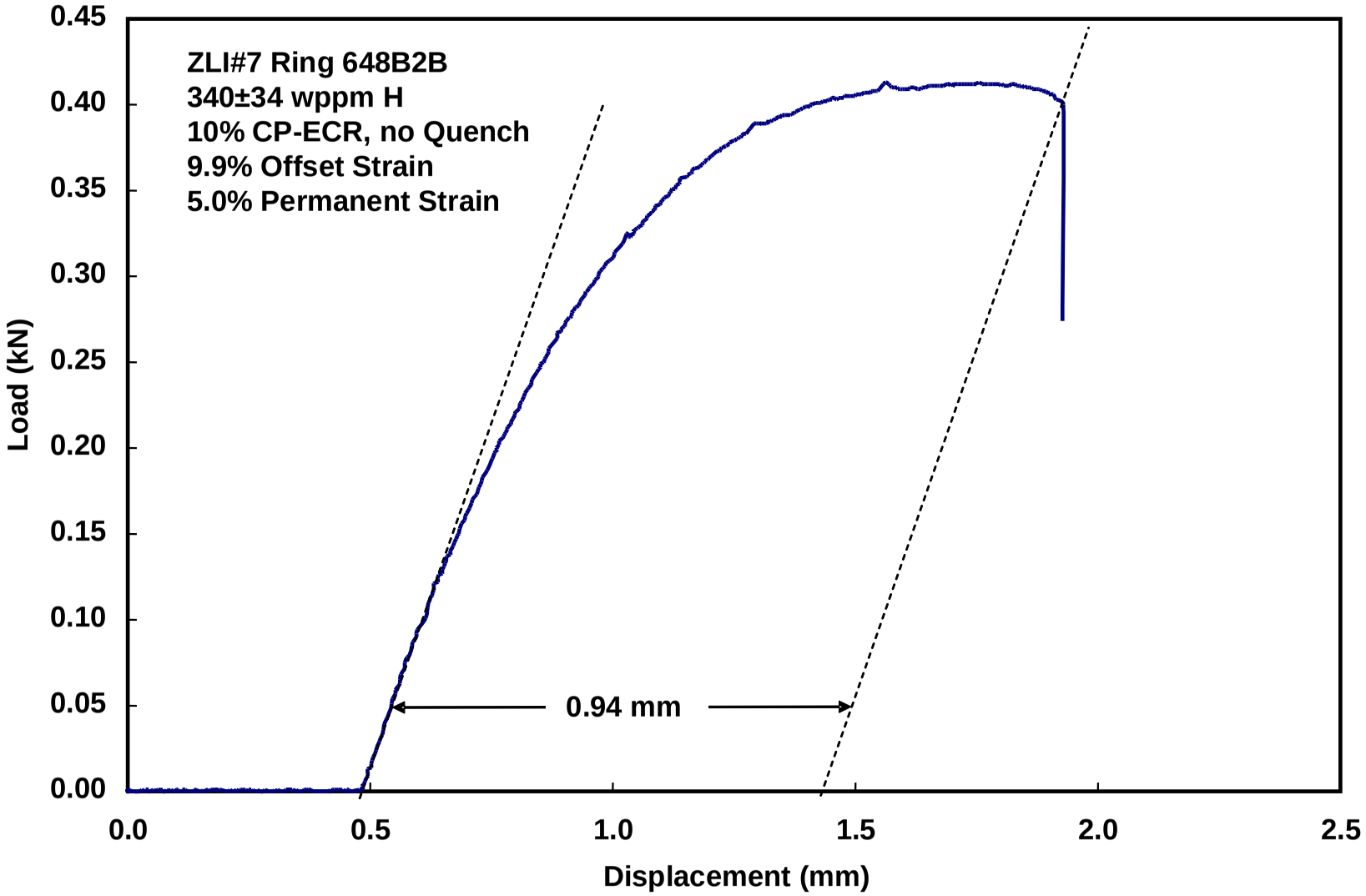

Figure 26. **Load-displacement curve for HBU ZIRLO cladding ring 648B2B oxidized to 10% CP-ECR and cooled without quench.**

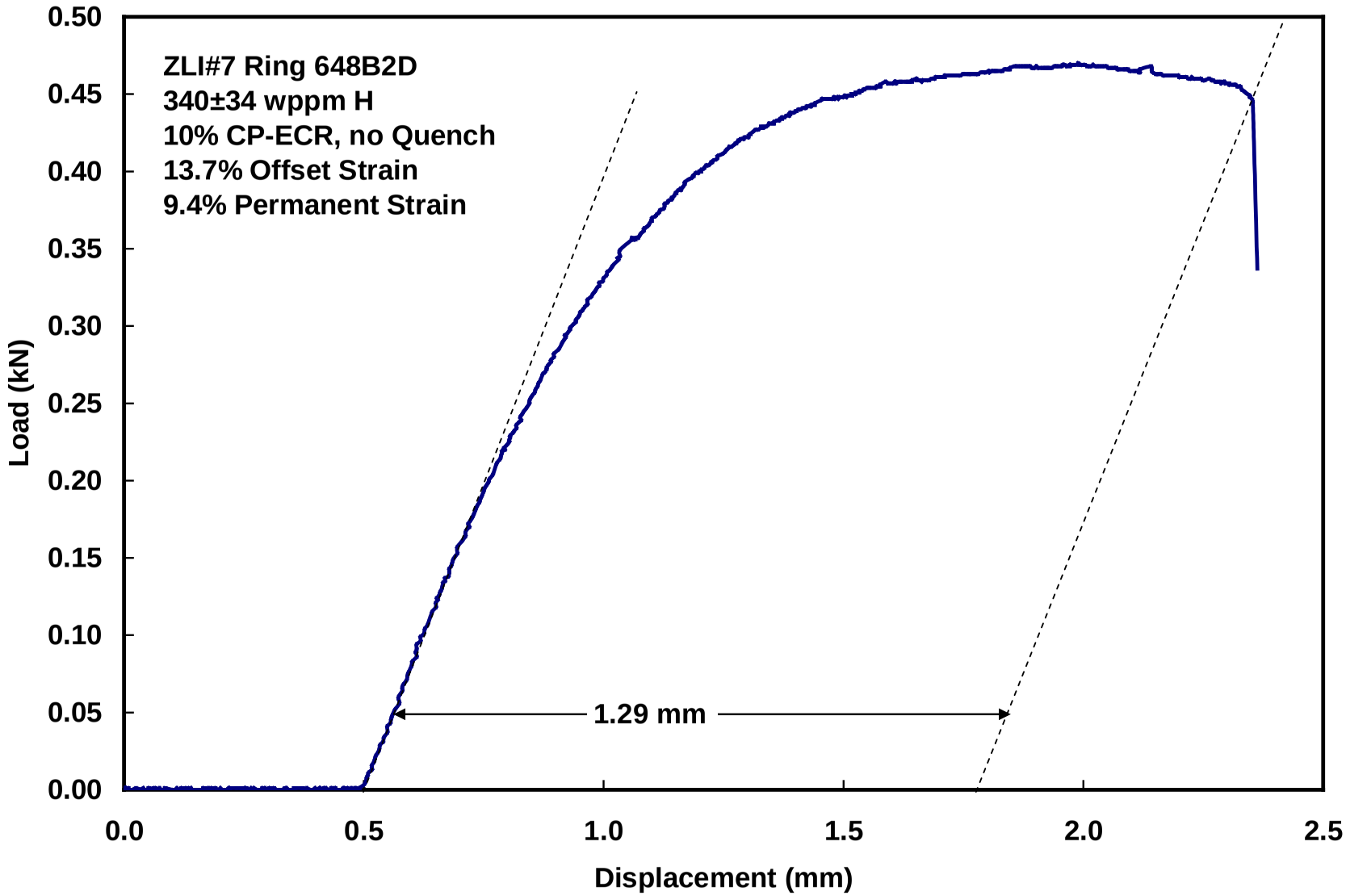

Figure 27. **Load-displacement curve for high-burnup ZIRLO cladding ring 648B2D oxidized to 10% CP-ECR and cooled without quench.**

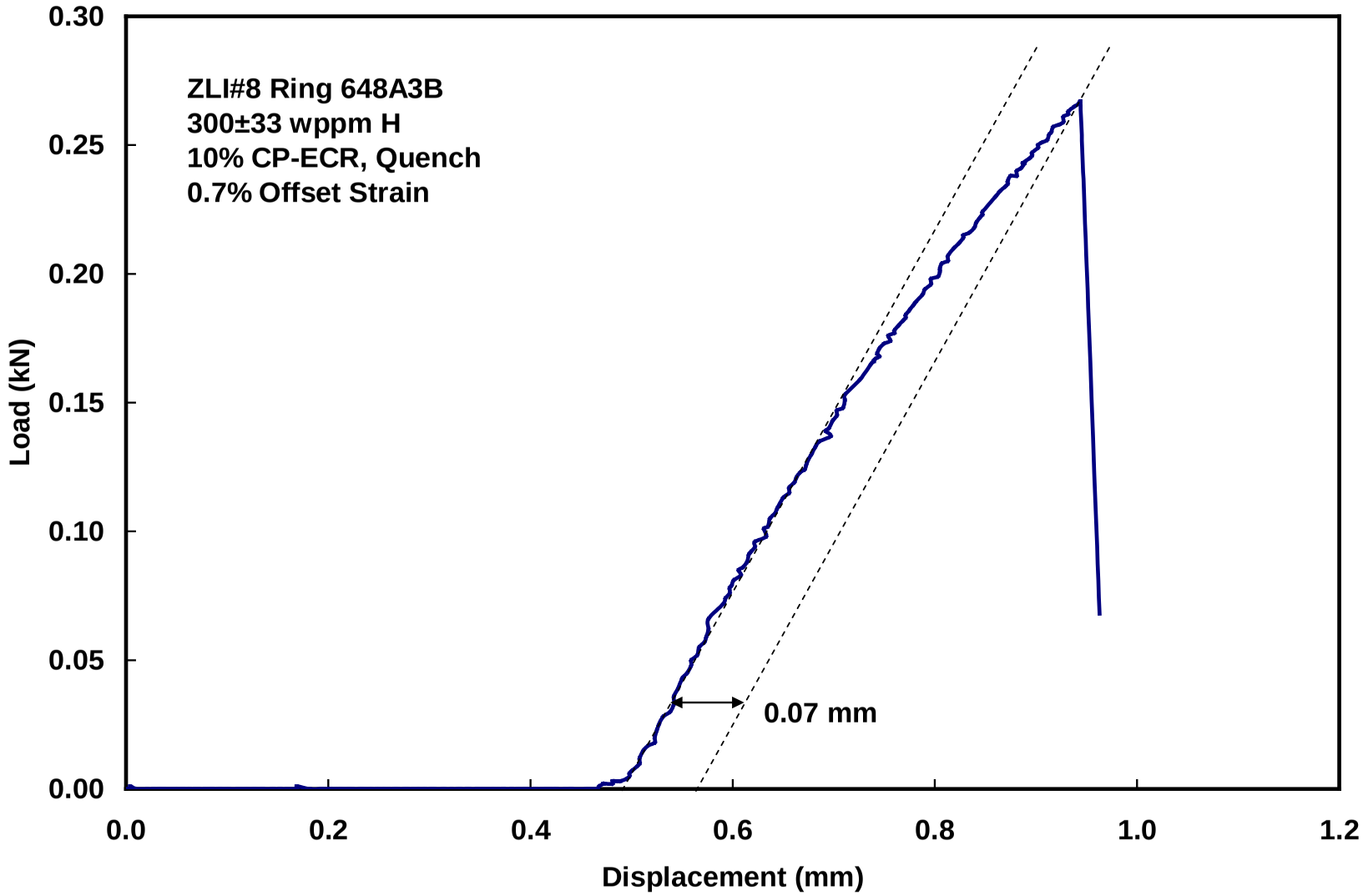

Figure 28. **Load-displacement curve for high-burnup ZIRLO cladding ring 648A3B oxidized to 10% CP-ECR and quenched at 800°C.**

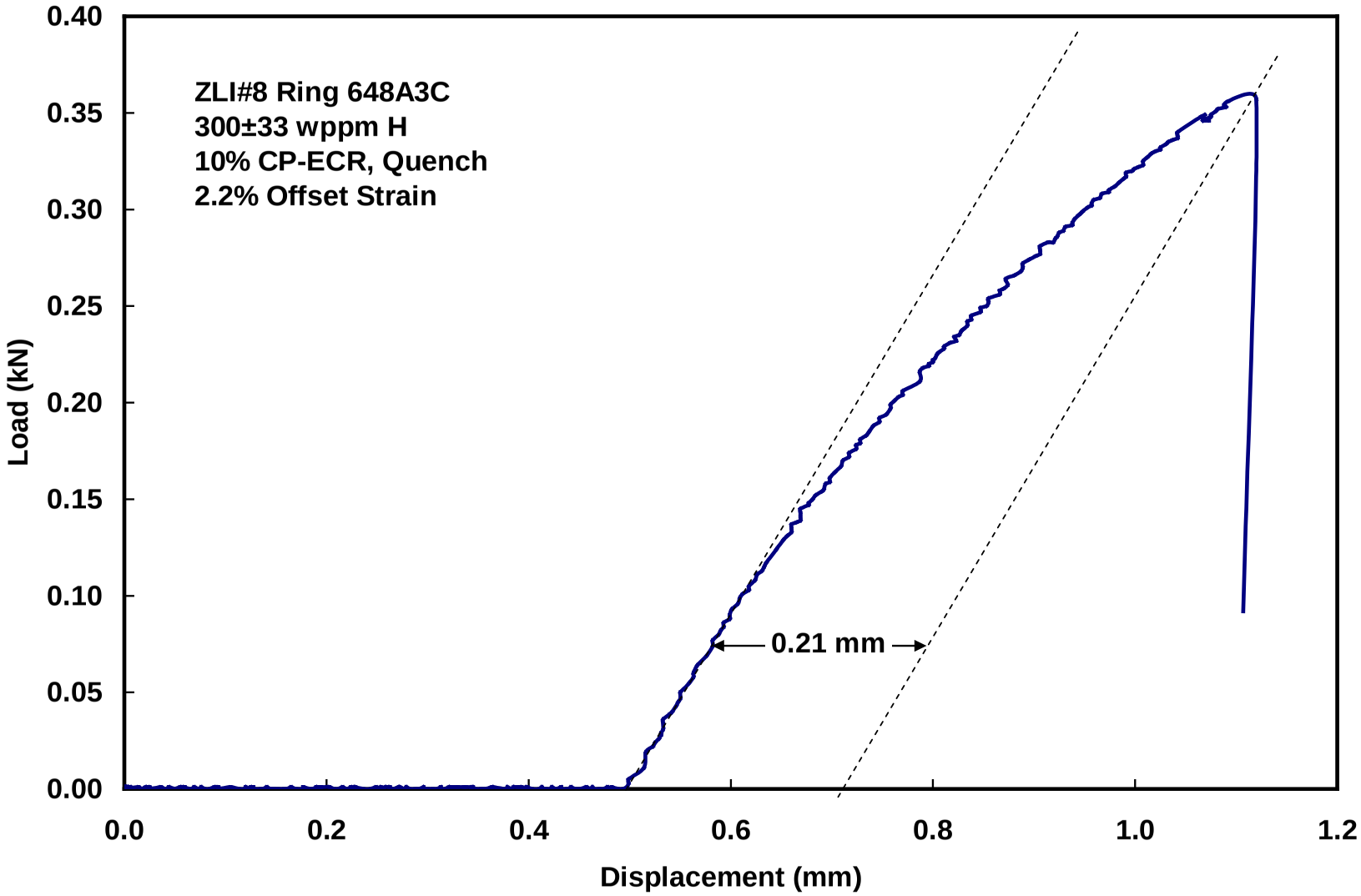

Figure 29. **Load-displacement curve for high-burnup ZIRLO cladding ring 648A3C oxidized to 10% CP-ECR and quenched at 800°C.**

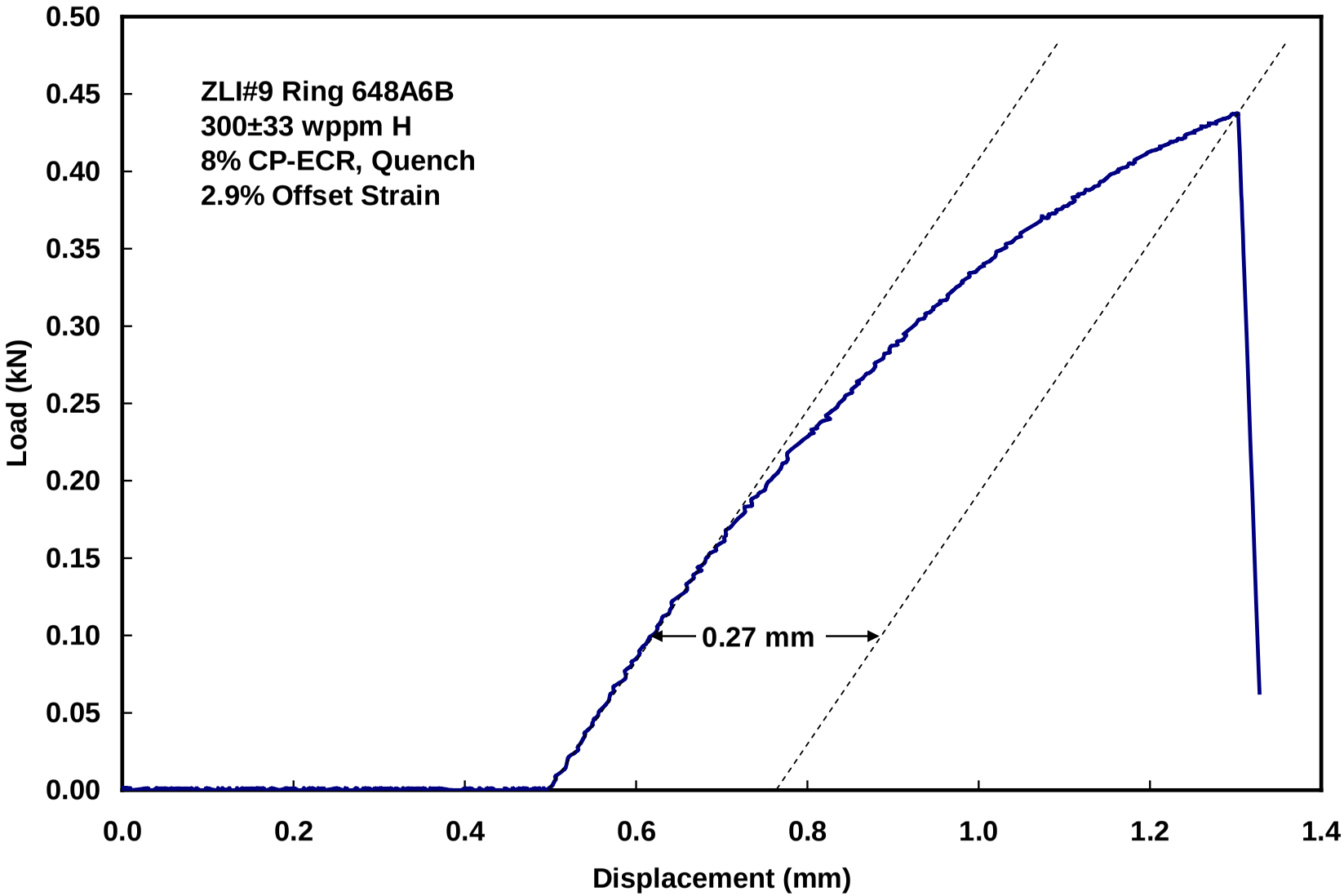

Figure 30. **Load-displacement curve for high-burnup ZIRLO cladding ring 648A6B oxidized to 8% CP-ECR and quenched at 800ºC.**

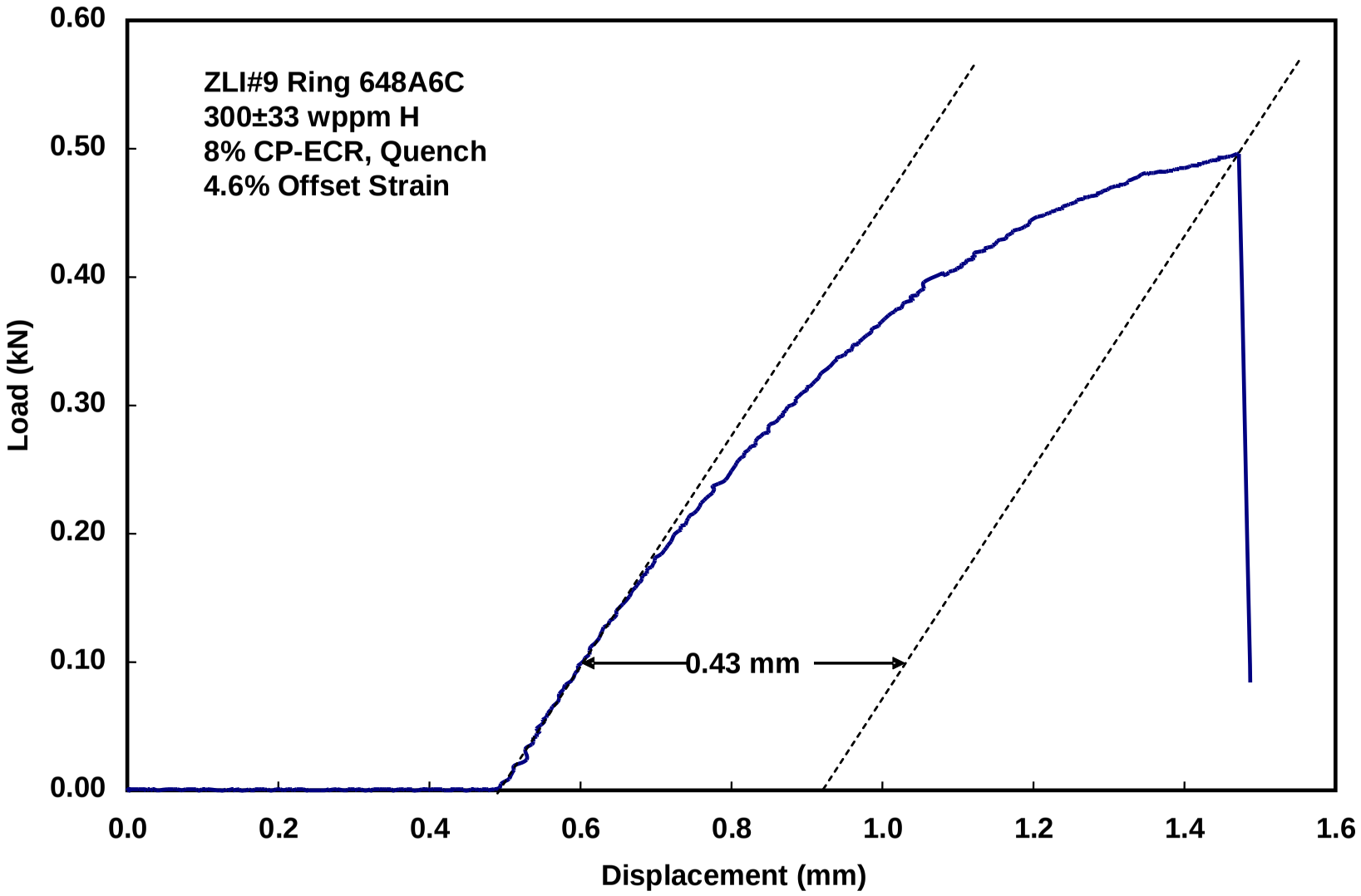

Figure 31. **Load-displacement curve for high-burnup ZIRLO cladding ring 648A6C oxidized to 8% CP-ECR and quenched at 800°C.**

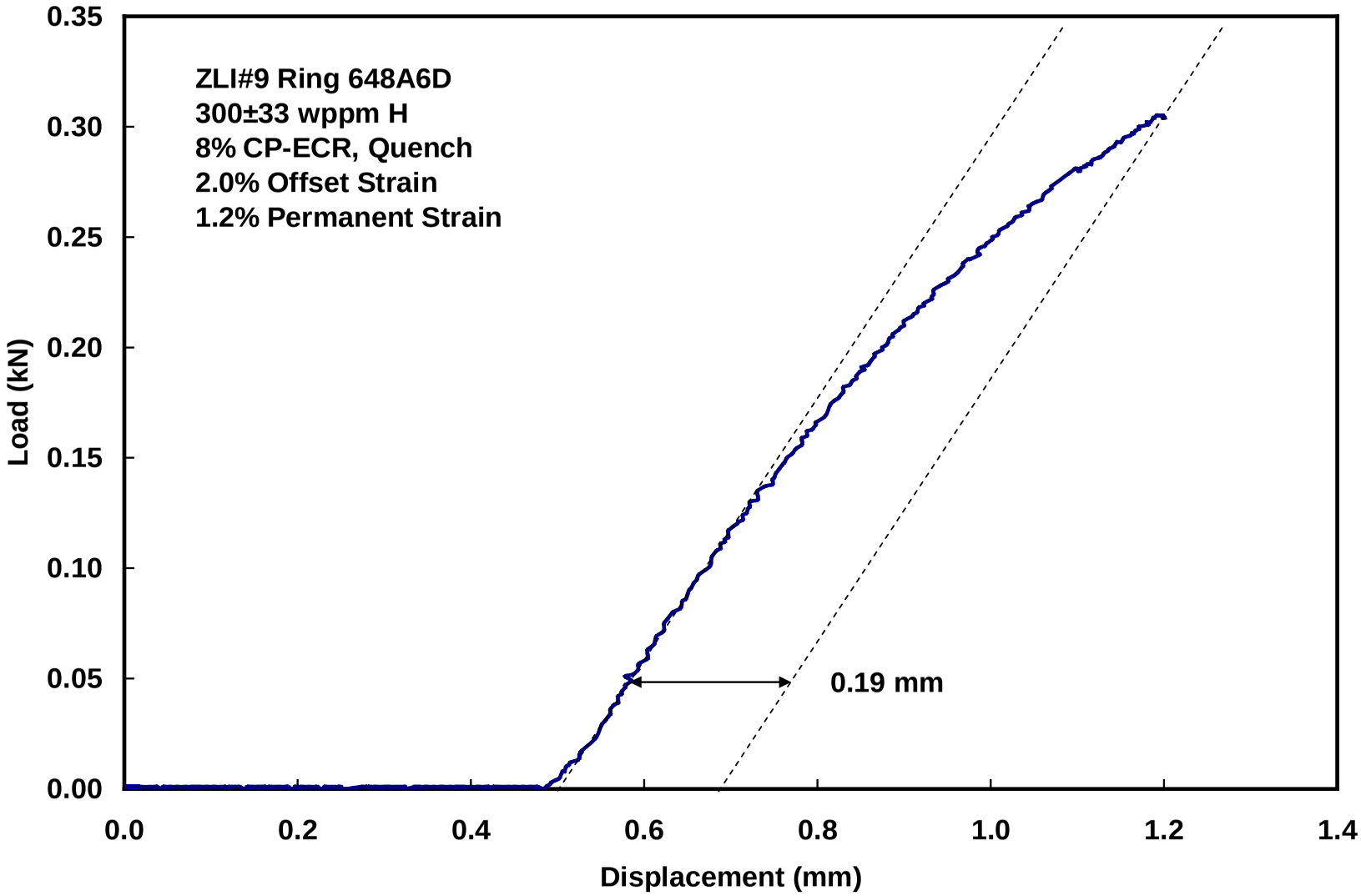

Figure 32. Load-displacement curve for high-burnup ZIRLO cladding ring 648A6D oxidized to 8% CP-ECR and quenched at 800°C.

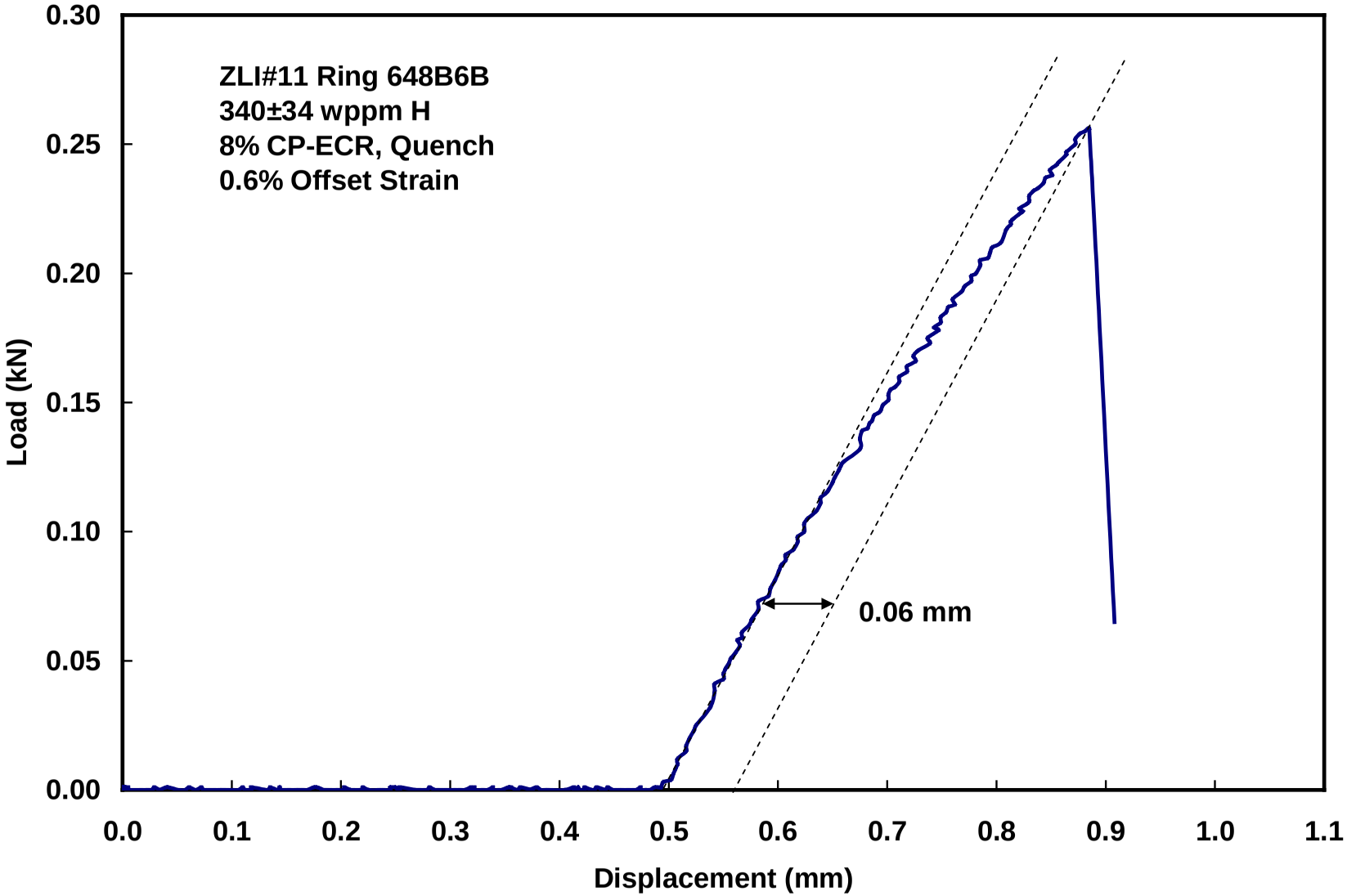

Figure 33. Load-displacement curve for high-burnup ZIRLO cladding ring 648B6B oxidized to 8% CP-ECR and quenched at 800ºC.

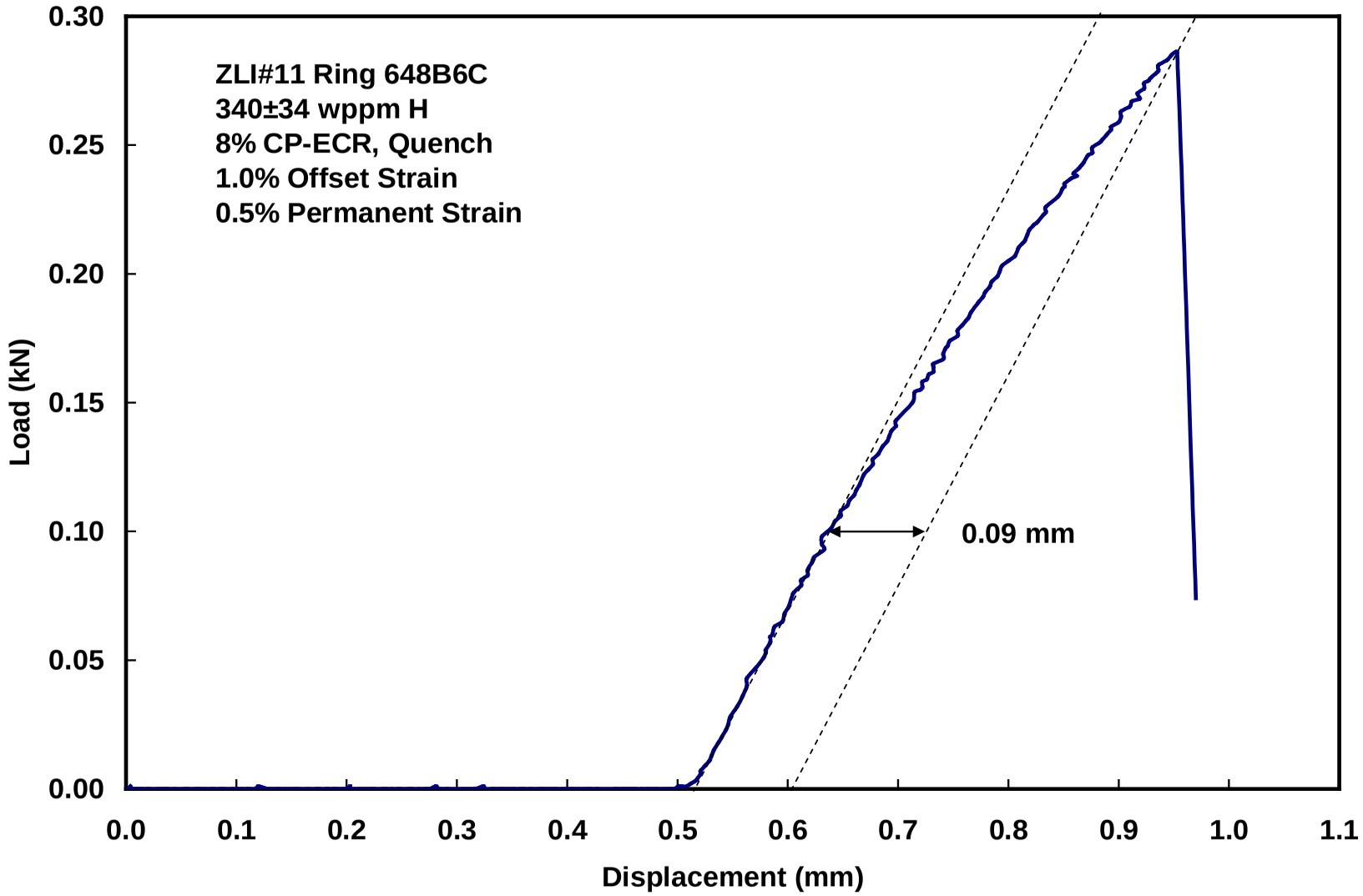

Figure 34. Load-displacement curve for HBU ZIRLO cladding ring 648B6C oxidized to 8% CP-ECR and quenched at 800ºC.

4 BREAKAWAY OXIDATION

Breakaway oxidation occurs in all zirconium-alloy cladding materials if the cladding is held for long times (minutes to hours) at constant temperatures between 650 and 1100°C. Under these conditions, the crystal structure of the zirconium dioxide can change to a form that is not protective, and hydrogen from the metal-steam reaction during LOCA oxidation can then be absorbed rapidly into the cladding metal thus affecting cladding embrittlement. Breakaway oxidation is often apparent from the visual appearance of the outer surface of the oxide layer. The time at which breakaway oxidation occurs is commonly determined from the increase in weight-gain rate. However, a more reliable and relevant indicator is the measured increase in hydrogen concentration. This is particularly true if breakaway oxidation is due to the presence of certain impurities such as fluorine or fluorides, which can result in high hydrogen uptake without appreciable increase in weight-gain rate [19]. In Ref. 1, 200-wppm hydrogen pickup was used to determine breakaway oxidation time. This metric is also used in the current work. Leistikow and Schanz [20] conducted a comprehensive study of breakaway oxidation during the 1980s, but its degrading effect on cladding ductility was not known at that time. Results are presented in Ref. 1 for cladding ductility decrease with increasing hydrogen pickup and for hydrogen levels at which embrittement was observed. Breakaway oxidation time has been shown to be sensitive to surface finish and methods used to produce zirconium ingots. Sensitivity to surface finish (i.e., roughness, scratches, impurities) was demonstrated in the Argonne test program [1]. Sensitivity to zirconium-ingot preparation was demonstrated in the Russian test program [25] sponsored by NRC and IRSN and in subsequent work [26].

Measured minimum breakaway-oxidation times were reported in Ref. 1 for a number of cladding materials. These are summarized in Table 21.

Table 21. Minimum breakaway oxidation times and corresponding oxidation temperatures reported in Ref. 1 for as-fabricated cladding alloys.

Cladding Material	Minimum Breakaway Time, s	Oxidation Temperature, °C
Zry-4 (vintage, unpolished)	3800	985°C
Zry-4 (modern, wheel polished)	≈5000	985°C
Zry-2 (modern, belt polished)	>5000	970–1000°C
ZIRLO (modern, belt polished)	3100±300	970–985°C
M5 (modern, wheel polished)	≈6400 [9]	1000°C
E110 (vintage, unpolished, pickled)	500-700	1000°C

In the current work, additional tests have been conducted with ZIRLO and M5 cladding oxidized at constant temperatures and with ZIRLO cladding oxidized under transient temperature conditions to improve understanding of these phenomena for conditions relevant to LOCA safety analyses.

4.1 Breakaway Oxidation for ZIRLO at Constant Oxidation Temperature

As the previously reported breakaway time for ZIRLO was relatively short compared with other modern cladding materials, additional measurements were performed along with careful reanalysis of data generated previously. New measurements were made with some ANL-cleaned specimens and some Westinghouse (WEC or W)-cleaned specimens, and these new tests will be highlighted below. To present the new measurements in the context of the older measurements, all relevant results are summarized in the following sections of this report.

The ANL criterion for breakaway oxidation is the time corresponding to 200-wppm hydrogen pickup (ΔC_{HM}), where the reference mass for this parameter is the pre-oxidation cladding metal mass. However, Zry-4 and ZIRLO materials retained ductility at higher hydrogen contents. Ring compression tests at 135ºC indicated ductility at ≤440±110 wppm ΔC_{HM} and embrittlement at ≥770±120 wppm ΔC_{HM}. The ± value represents one standard deviation based on hydrogen measurements for multiple arc segments of 8-mm-long compressed rings. Because of the rapid hydrogen pickup with time, the transition between ductile and brittle behavior was as short as 200 s at 1000ºC. Thus, 200-wppm hydrogen pickup is a reasonably conservative criterion for breakaway oxidation based on embrittlement.

The cladding materials used for previous studies included ZIRLO received from WEC in 2003 (ZIRLO-2003) and in 2006 (ZIRLO-2006), ZIRLO-2006 modified by ANL by machining a 20-μm deep scratch into the cladding wall along the length of the sample (ZIRLO-2006MS), and ZIRLO received from WEC with a thin (<1 μm) oxide film grown at low temperature in pressurized water (ZIRLO-PF). Results for ZIRLO-2003 are not included in this section because this material was highly susceptible to breakaway oxidation on the inner surface of the cladding. Excluding the short ballooned region of the cladding, only the outer surface of the cladding is exposed to steam oxidation. Thus, it is important to demonstrate that breakaway oxidation occurs at the cladding outer surface and that the measured hydrogen pickup includes only hydrogen absorbed at the cladding outer surface. All results reported in Ref. 1 were generated using a long quartz-tube steam chamber (686-mm long). At the time Ref. 1 was published, ANL was not able to demonstrate the early breakaway times for ZIRLO in a short (610-mm long) steam chamber, based on a very limited number of tests conducted.

At 1000ºC, the minimum breakaway time for ZIRLO was ≈4000 s based on tests at 3600s (60 wppm ΔC_{HM}), at 4000 s (130 wppm ΔC_{HM}), and at 4200 s (630 wppm ΔC_{HM}). As breakaway oxidation is an instability phenomenon due to local transformation from the protective, tetragonal oxide phase (lustrous black in appearance) to the non-protective, monoclinic oxide phase (yellow in appearance for ZIRLO), multiple tests under the same time-temperature conditions would have generated scatter of at least ±200 s at 1000ºC. Thus, the time for ZIRLO breakaway at 1000ºC was assessed to be 4000±200 s based on the limited data set generated. It should be noted that test times reported by ANL include the duration from the initiation of the temperature ramp at 300ºC to the end of the heating phase. Typical ANL heating curves consisted of a very fast ramp from 300ºC to 950ºC in <20 s and a slower ramp from 950ºC to 1000ºC in ≈60 s to limit the short-time temperature overshoot to ≤10ºC. Thus, breakaway oxidation times reported in Ref. 1 included about 80-s heating ramps from 300ºC to 1000ºC

Tests at higher (1015ºC) and lower (950-985ºC and 800ºC) temperatures were conducted to determine the temperature sensitivity of breakaway oxidation and the minimum breakaway oxidation time. Based on a more extensive data set for as-fabricated, machine-scratched, and pre-filmed ZIRLO, 3100±300 s was determined to be the minimum breakaway time within the temperature range of 970-985ºC. These earlier studies were conducted in two campaigns with separate test trains and associated thermal benchmarks: tests with ZIRLO-2006 and ZIRLO-2006MS within a wide temperature range and tests with ZIRLO-2006

and ZIRLO-PF within a narrow temperature range (970-985ºC). Results for two samples tested with a machined scratch indicated that local breakaway occurred early along the scratch, but the presence of the scratch had little effect on the reduction in breakaway time (<200 s) based on the 200-wppm criterion. Tests with ZIRLO-PF demonstrated that the presence of a thin oxide layer grown at reactor-relevant temperature had no significant effect on breakaway oxidation time.

WEC [27] generated independent data sets for 15×15 Zry-4 and 17×17 ZIRLO. The WEC-determined minimum breakaway oxidation times for Zry-4 (<4400 s at 980ºC for one bare sample and ≈4400 s at 1010ºC for one pre-filmed sample) were consistent with ANL results (3800 s for vintage material and 5000 s for modern material at 985ºC, both 15×15 Zry-4 manufactured by AREVA). WEC results for ZIRLO oxidized at 1000ºC were in agreement (within data scatter) with ANL results. However, WEC results indicated longer breakaway oxidation times than ANL results at <1000ºC. In an attempt to resolve the differences, WEC subsequently provided ANL with additional ZIRLO specimens that had been cleaned by WEC using their experimental procedures: chemical detergent (Alconox) treatment prior to water rinsing. ANL used an organic solvent (ethanol) prior to water rinsing. Although it was not anticipated that this would account for differences in results, it was the easiest factor to test and possibly eliminate. ANL had used ethanol, which never came in contact with the metal, to clean ZIRLO-PF samples prior to oxidation. Therefore, early breakaway times observed for ZIRLO-PF samples could not have resulted from an ethanol-metal surface reaction during cleaning.

WEC supplied ANL with ten samples of W-cleaned ZIRLO (ZIRLO-WC), as well as a new supply of ZIRLO (ZIRLO-2008). The following sections describe the results of new tests performed by ANL with both W-cleaned (Alconox) and ANL-cleaned (ethanol) ZIRLO samples. To help resolve the issue of long vs. short steam chambers, these new tests were conducted using both steam chambers.

4.1.1. ZIRLO materials for breakaway oxidation

Table 5 summarizes geometrical parameters, oxygen content and hydrogen content measured by ANL for the larger lots of W-supplied ZIRLO. The ten W-cleaned ZIRLO samples were very similar to the ZIRLO received in 2006 to 2010: 9.50-mm OD, 0.584±0.003-mm wall thickness, 0.16±0.01-μm OD surface roughness, and 22±2-wppm hydrogen.

4.1.2. Breakaway oxidation test parameters and results

Tests at 1000ºC in long steam chamber

Two new oxidation tests were conducted in the long steam chamber with a standard-length test train. W- and ANL-cleaned samples were oxidized for 4000 s at 1000ºC. The thermal benchmark for these tests is shown in Fig. 35. The benchmark was performed for a long-time hold temperature of 975±5ºC, a temperature at which additional tests were to be conducted. The actual test time (3100 s from ramp initiation to the end of the hold time) was longer than the time (1200 s) shown in Fig. 35. Temperature readings were recorded every 0.1 s and EXCEL has a limit (32000) on the number of data points that can be plotted for a single curve. The 10ºC circumferential temperature variation is based on readings of two TCs welded onto the sample. These TCs reached 975ºC in ≈80 s, experienced a 10ºC overshoot from 80 s to 160 s, and then decreased to a hold temperature of 975ºC for the time duration of about 1500 s. The slow decrease from 980 to 975ºC occurred during a period in which the control thermocouple on the sample holder had a constant reading. As such, in addition to ±5ºC circumferential temperature variation, there may have been a 5ºC uncertainty in long-time sample TC readings. For the current tests, the furnace power was increased to achieve a long-time hold temperature of 1000ºC.

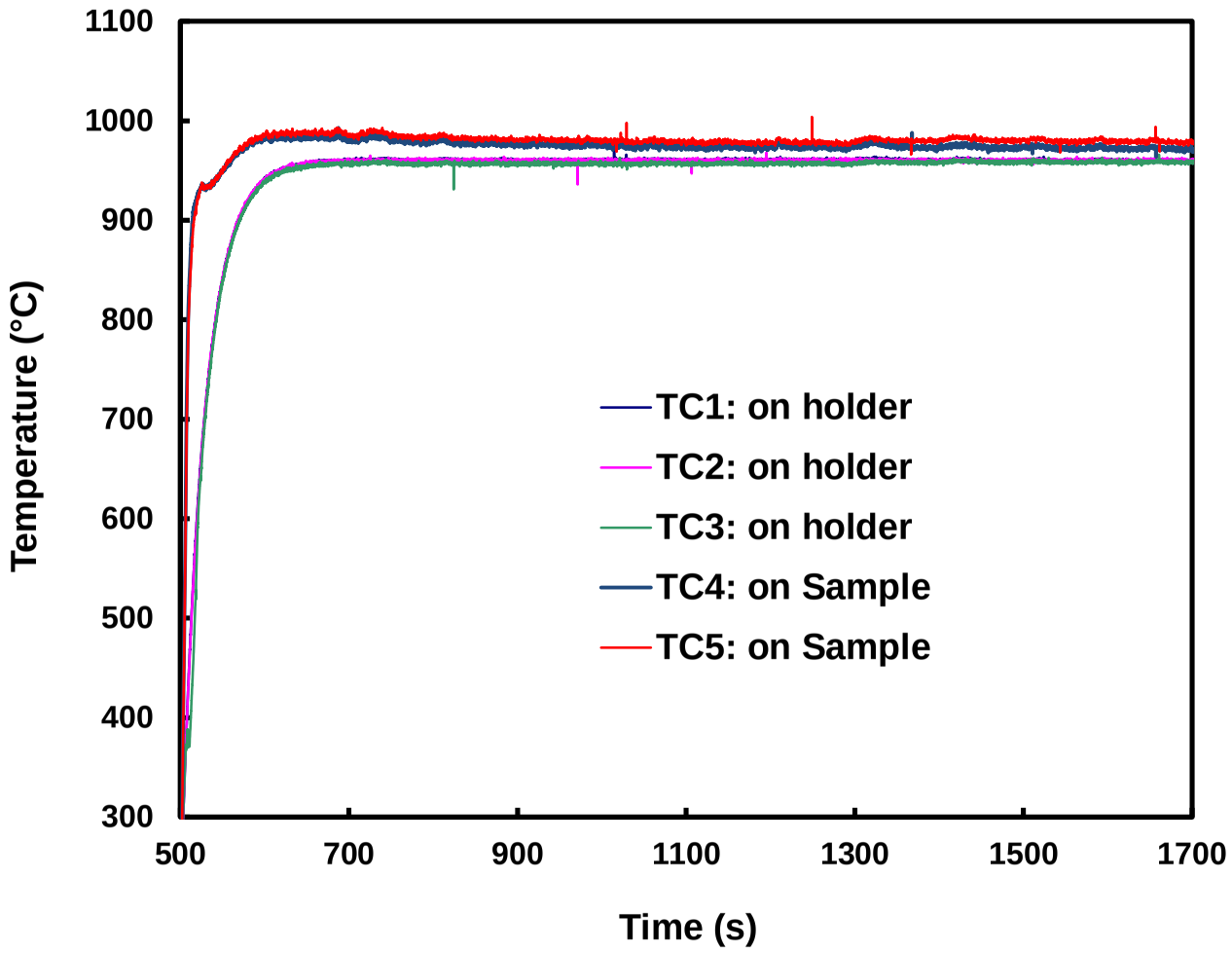

Figure 35. **Thermal benchmark results with two TCs welded onto as-fabricated, 17×17 ZIRLO-2008 cladding. The long-time sample hold temperature was 975±5°C. For data-generating tests, the furnace power was increased to give 1000°C oxidation temperature.**

Figure 36 shows the visual appearance of the two test samples. It is clear that the ANL-cleaned sample experienced more extensive breakaway oxidation than the W-cleaned sample. However, the W-cleaned sample had small yellow spots on the outer surface indicating the initiation of local breakaway oxidation.

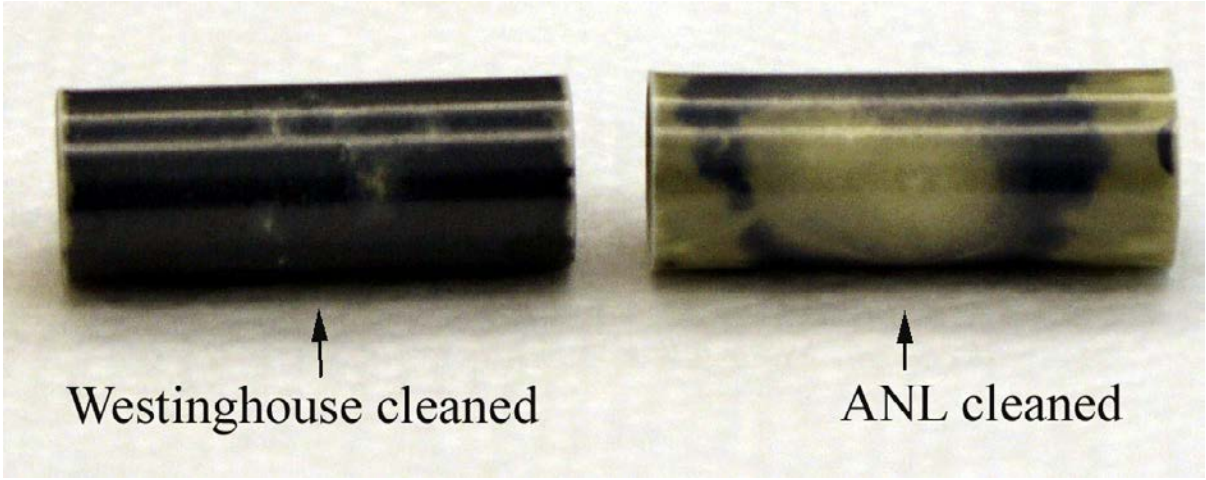

Figure 36. Surface appearance of W- and ANL-cleaned ZIRLO samples after 4000 s at 1000ºC.

The ANL-cleaned sample, with the extensive yellow regions, picked up 400±240 wppm hydrogen near the sample mid-span, while the W-cleaned sample picked up 120±110 wppm hydrogen near the mid-span. The hydrogen results for the W-cleaned sample indicated that local breakaway oxidation had occurred. Metallographic examination was performed to verify that local breakaway of the outer surface oxide was responsible for the hydrogen pickup in the W-cleaned sample. Images were taken at eight locations corresponding to angular orientations separated by ≈45º. One location indicated breakaway of the outer-surface oxide (Fig. 37a) which included both cracked monoclinic outer-surface oxide and tetragonal oxide. For the other locations, no tetragonal-to-monoclinic phase change was observed at the outer surface. For all images, the inner-surface oxide showed no signs of breakaway oxidation. The metallographic results are consistent with the local hydrogen readings: high hydrogen content under yellow spots and low hydrogen content in regions under lustrous black oxide. Based on ANL experience, the W-cleaned sample was <200 s away from picking up >200 wppm hydrogen. As shown in Table 22, this result is consistent with results previously obtained for ANL-cleaned samples. Thus, for an oxidation temperature of 1000ºC, no significant effects of Alconox vs. ethanol cleaning were observed.

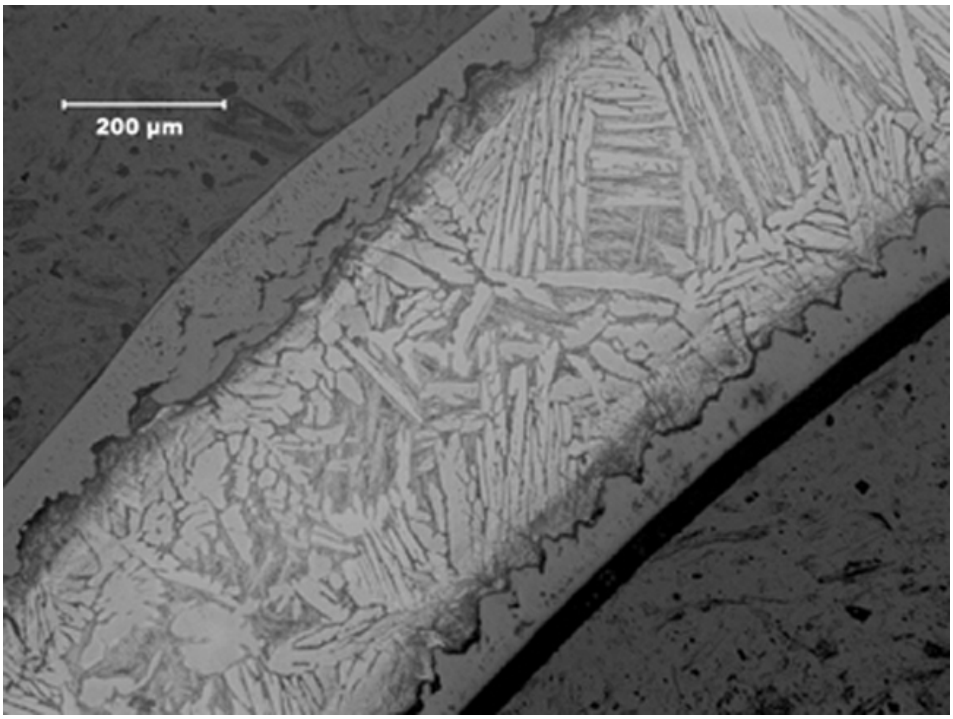

(a) Area 8: local hydrogen content >280 wppm under yellow outer-surface spot

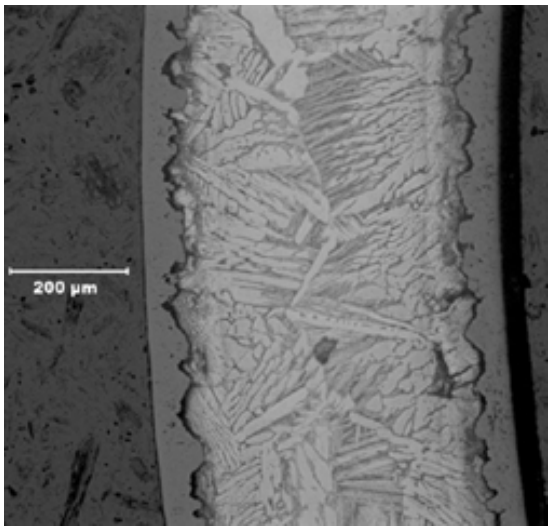

(b) Area 7

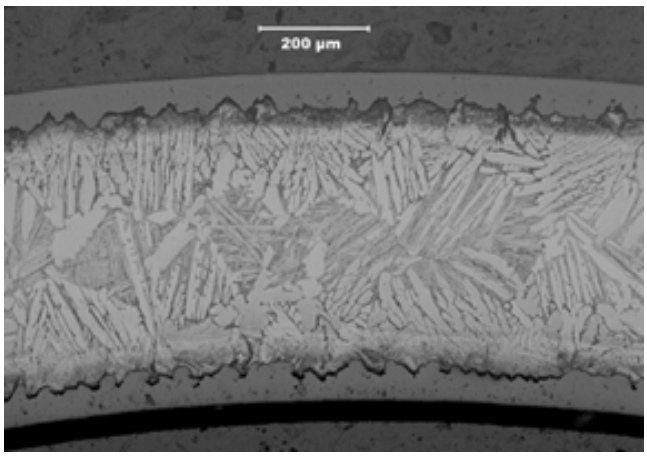

(c) Area 1

Figure 37. Metallographic images (at the same cross section) for W-cleaned sample oxidized for 4000 s at 1000ºC: (a) Area 8, which has outer-surface monoclinc oxide (≈0.4 mm long); (b) Area 7 with tetragonal oxide; and (c) Area 1 with tetragonal oxide.

Table 22. Results of ZIRLO breakaway oxidation tests at 1000ºC; new results are in bold font.

Material	Test Time[a], s	Measured w_g, mg/cm^2	Measured $(C_H)_{POX}$, wppm	ΔC_{HM} [b], wppm	Comment
ZIRLO-2006	1500	8.7	15	5	---
ZIRLO-2006	3600	11.4	68	60	---
ZIRLO-2006	4000	12.6	131±12	130±10	---
ZIRLO-2008	**4000**	**13.3**	**390±220**	**400±240**	**See Fig. 36**
ZIRLO-WC	**4000**	**12.6**	**130±100**	**120±110**	**See Fig. 36**
ZIRLO-2006	4200	14.3	610±370	630±400	

[a]Time from ramp initiation at 300ºC to end of hold temperature; ramp time is ≈80 s.

[b]ΔC_{HM} is referenced to as-fabricated sample mass: $\Delta C_{HM} = (1 + 5.4\times10^{-3}\ w_g)\ (C_H)_{POX} - C_{Hi}$, where C_{Hi} is the hydrogen content in as-fabricated ZIRLO.

The hydrogen content shown in Fig. 38 for the new ANL-cleaned sample was measured for a 2-mm-long ring sectioned from near the center of the sample. An 8-mm-long ring was sectioned from the adjacent area and subjected to a ring-compression test at 135ºC. The sample proved to be extremely brittle and failed at a much lower load than other samples tested. The hydrogen content measured for the 8-mm-long, compressed ring (555±133 wppm) was even higher than for the central 2-mm-long ring (390±220 wppm). The corresponding hydrogen pickup for the 8-mm-long ring was 600±150 wppm. This ring-compression data point is plotted in Fig. 39, along with the data in NUREG/CR-6967 Fig. 63, to better define the hydrogen range for ductile-to-brittle transition for breakaway oxidation samples. Based on Fig. 39, the ductile-to-brittle transition hydrogen level for samples oxidized at 970-1000ºC is between 440 and 600 wppm, which gives ≈500±50 wppm for the transition. Also, the circumferential variation in hydrogen content (greater than ±100 wppm) was very large for average hydrogen contents in this range (Fig. 40).

Breakaway oxidation tests were terminated by furnace cooling rather than quench at 800ºC. There were two reasons for conducting these tests with slow cooling from 800ºC: (a) for postulated LOCAs of long duration, the temperature range during which rapid cooling might occur due to wetting may be much lower than 800ºC and (b) the vibration and thermal stresses during quench might cause some oxide to flake off, particularly oxide that had experienced breakaway. From the experimental point of view, slow cooling was used to preserve the oxide layer for visual and metallographic examination. Based on the cooling method used for these tests, it is not clear if the data points shown in Fig. 39 for hydrogen levels >440 wppm would shift somewhat to the left if the samples had been quenched at 400 to 800ºC. Thus, it is recommended that the lower-bound value of ≈450 wppm be used for the ductile-to-brittle transition.

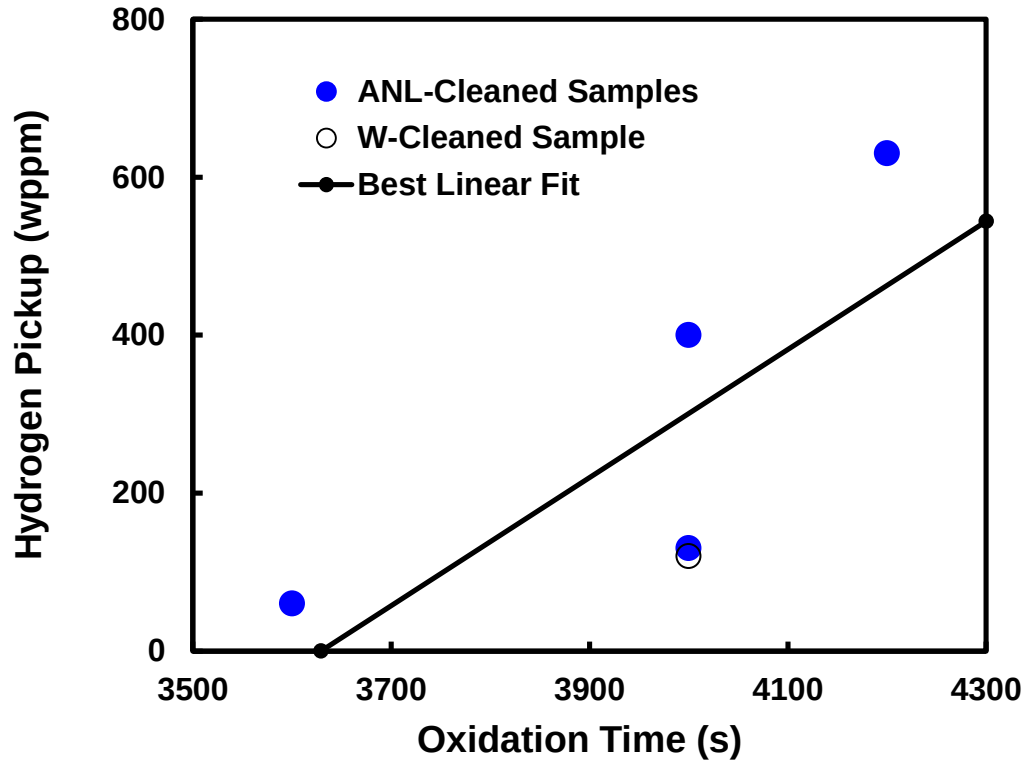

Figure 38. **Hydrogen pickup for ANL-cleaned and W-cleaned ZIRLO samples oxidized at 1000°C.**

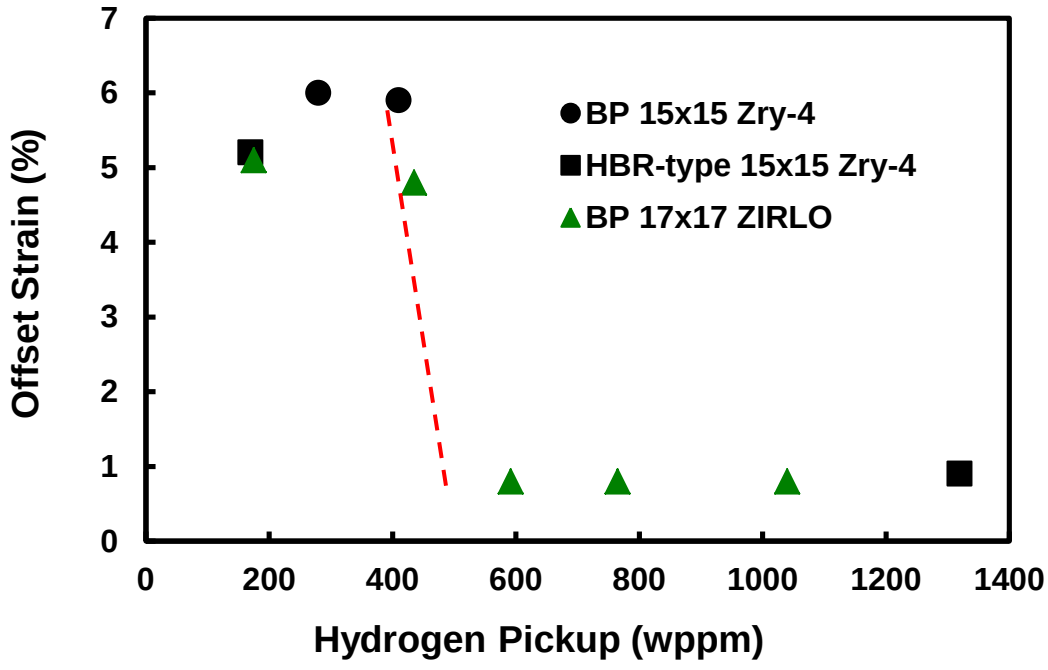

Figure 39. **RCT offset strains at 135°C for Zry-4 and ZIRLO rings following oxidation at 970-1000°C, local-to-global breakaway oxidation, and cooling without quench.**

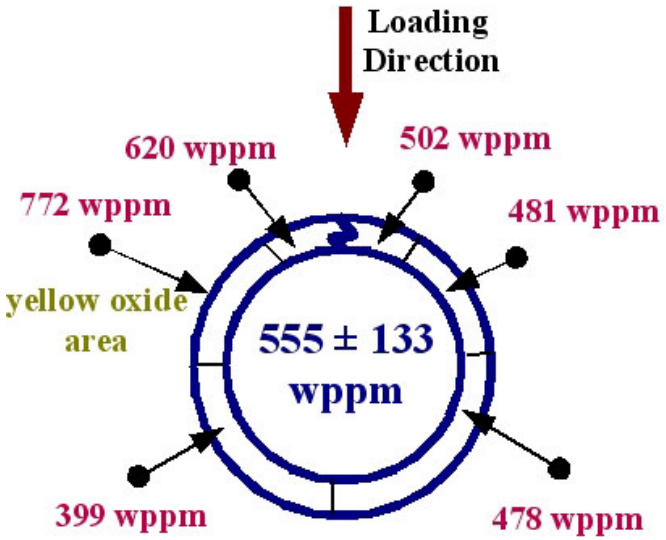

Figure 40. Circumferential variation in hydrogen content measured after ring-compression testing for an 8-mm-long ring sectioned from the ANL-cleaned ZIRLO sample oxidized at 1000ºC for 4000 s.

Tests at ≈980ºC in short steam chamber with temperature overshoot

Concurrent with the new breakaway oxidation studies, a test train for the shorter steam chamber was thermally benchmarked for a hold temperature of 1200ºC to conduct high-temperature embrittlement tests. It was time-consuming to switch back and forth between test trains and chambers for breakaway and high-temperature embrittlement studies. Therefore, the short test chamber was used for the next sequence of new breakaway tests, and the furnace power was scaled to give a long-time hold temperature of ≈985ºC. Two tests were run for 3200 s with W-cleaned samples, and one test was run for 3400 s with an ANL-cleaned sample. All three samples exhibited significant yellow areas on the outer surfaces indicating extensive breakaway. Following these tests, TCs were welded onto a fresh ZIRLO sample to determine more precisely the temperature history. As shown in Fig. 41, the scaling of furnace power resulted in a long-time hold temperature of 981±4ºC (≈980±5ºC). However, unlike other histories, this one had considerable overshoot early in the transient. The cladding temperature rose rapidly (18 s) to ≈1065ºC and was above 985ºC for ≈20 s. Other than a faster rise to high temperature, it is not clear what effect an early temperature excursion would have on breakaway oxidation occurring ≈3000 s later. As the purpose of the tests was to compare the performance of ANL- and W-cleaned ZIRLO samples exposed to the same steam flow and temperature conditions, the results from this series of tests are considered valid for that purpose. The hydrogen pickup was high (≈700 wppm) for the samples and well beyond the 200-wppm ΔC_{HM} criterion for breakaway. These three new results are significant because they showed no apparent difference between the W- and ANL-cleaned samples (Fig. 42). Also, for the first time at ANL, breakaway oxidation was observed using the short steam chamber.

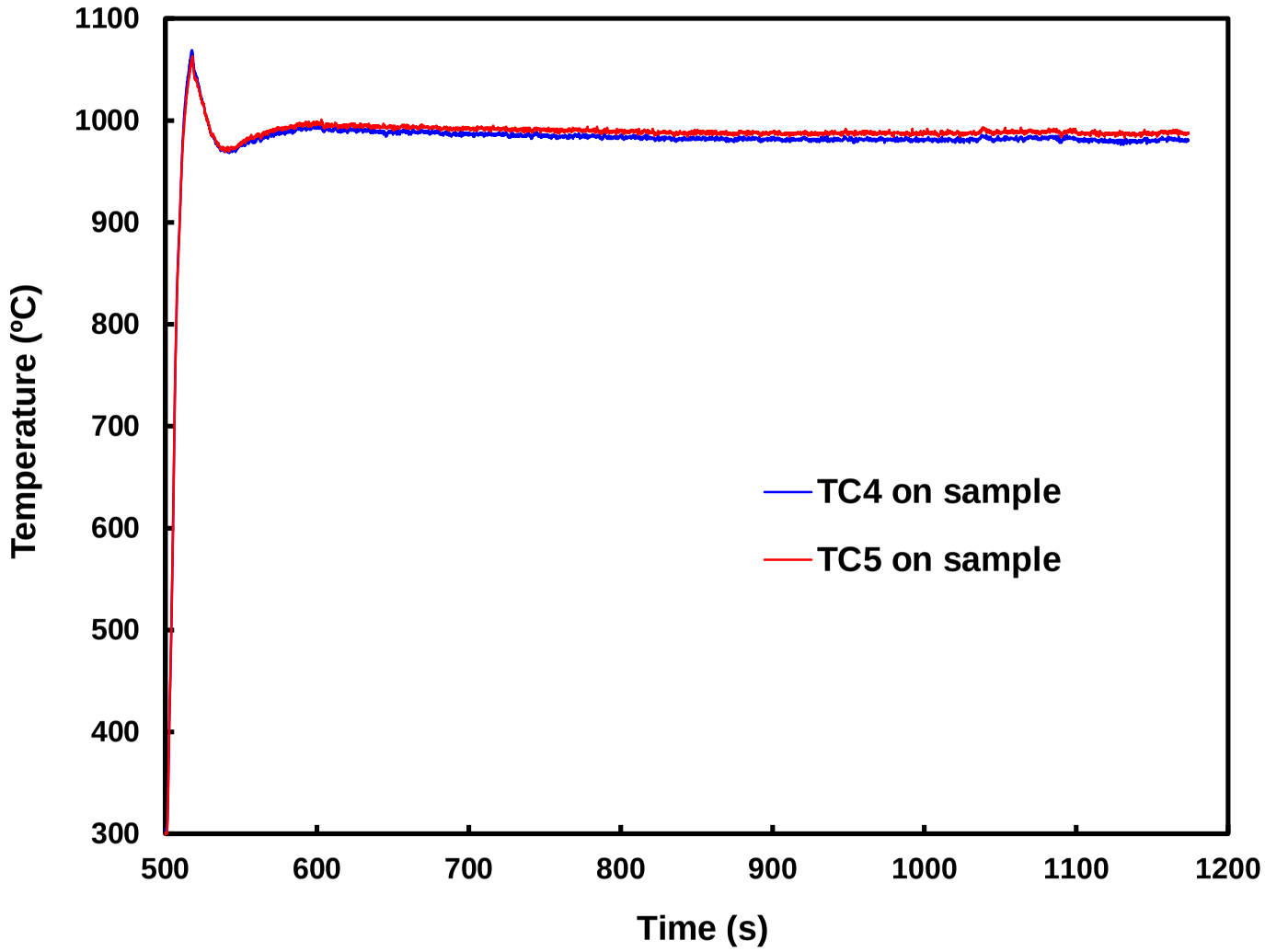

Figure 41. **Thermal benchmark results for test ZLU#129. Peak temperature was ≈1065ºC and long-time hold temperature was ≈980±5ºC.**

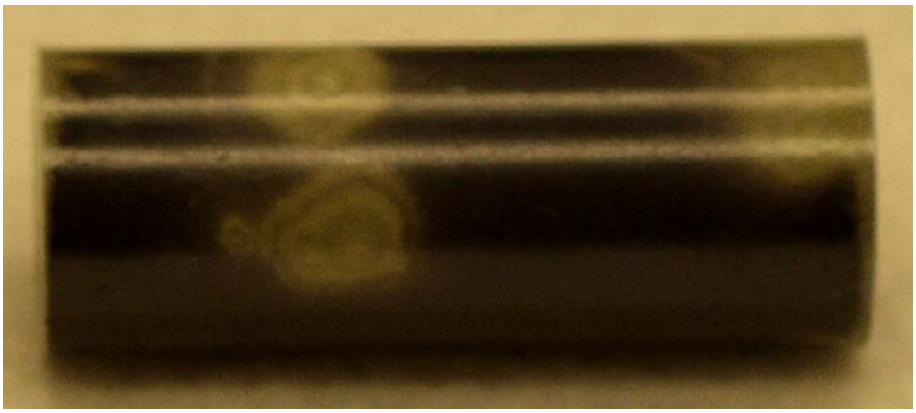

(a) ANL-cleaned sample after 3400 s at 980ºC

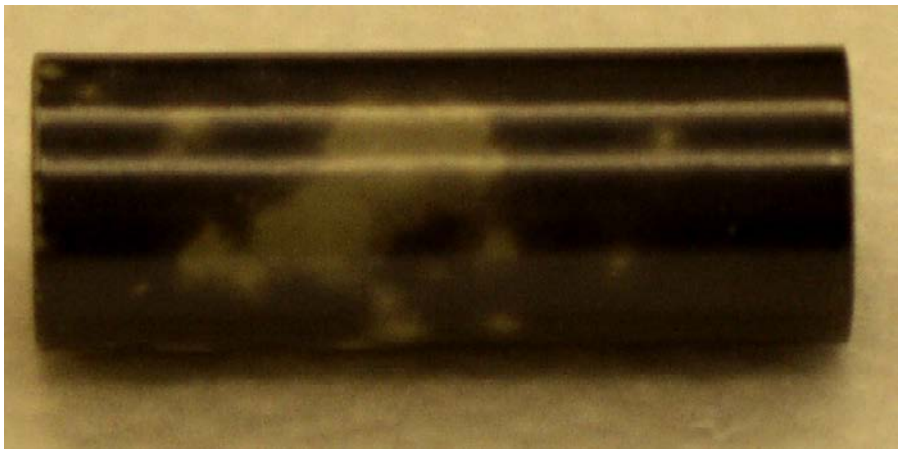

(b) W-cleaned sample #1 after 3200 s at 980ºC

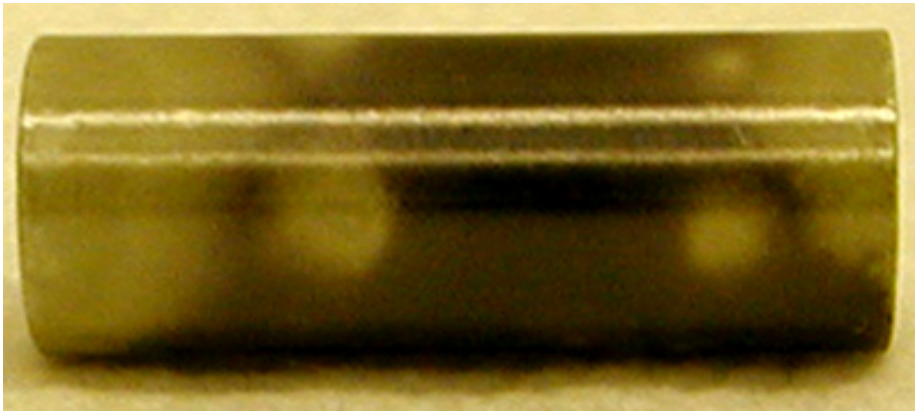

(c) W-cleaned sample #2 after 3200 s at 980ºC

Figure 42. **Surface appearance of ANL-cleaned and W-cleaned samples after oxidation at 980ºC: (a) ANL-cleaned sample after 3400 s; (b) W-cleaned sample #1 after 3200 s; and (c) W-cleaned sample #2 after 3200 s.**

Tests at 985ºC in short steam chamber with no temperature overshoot

An additional set of new tests was conducted with the same short test train and steam chamber as was used to generate the previous results. However, furnace control parameters were reset to eliminate temperature overshoot. The temperature history determined from the new thermal benchmark is shown in Fig. 43. The long-time hold temperature was 975±3ºC. Also shown in Fig. 43 are the histories of the control TC and one other TC, both welded to the sample holder. The control TC readings were only a few degrees lower than the sample readings. As the data-generating tests were to be conducted at 985ºC, the controller was adjusted to increase the control TC by 10ºC and to correspondingly increase the sample temperature to 985ºC (985±5ºC). One ANL-cleaned sample was oxidized for 3500 s and had a post-test hydrogen pickup of 720 wppm. The W-cleaned samples picked up 20 wppm after 3500 s and 270 wppm after 3800 s. Although breakaway oxidation was somewhat delayed for the W-cleaned samples, the results were within data scatter for this oxidation temperature.

Table 23 summarizes the six new results generated in the temperature range of 980-985ºC (short steam chamber), as well as previous results generated for as-fabricated, machine-scratched, and pre-filmed ZIRLO in the temperature range of 970-985ºC (long steam chamber). Hydrogen pickup values are plotted in Fig. 44 as a function of test time for all data in Table 23. Based on these results, as well as expected data scatter for an instability phenomenon such as breakaway oxidation, it is clear that there were no measurable effects of Alconox (WEC) vs. ethanol (ANL) pre-test cleaning.

In parallel with the ANL testing, WEC conducted a series of breakaway oxidation tests with ANL-cleaned samples and WEC-cleaned samples (ZIRLO-2008 and another lot of ZIRLO) [28]. WEC tests were performed in a resistance-heating furnace for which the circumferential temperature variation is expected to be small. Test temperatures were between 960ºC and 1020ºC based on measured sample-holder temperatures. Ramp times ranged from 60 to 270 s and hold times ranged from about 3700 to 4500 s. Breakaway oxidation was assessed based on the appearance of the cladding outer surface. For 1000ºC tests, breakaway was observed to have occurred for three samples at ≈4400 s (60 s ramp with 4330 s hold time), while no breakaway was observed at ≈4550 s (130 s ramp with 4410 s hold time). WEC samples oxidized with the faster ramp exhibited large discolored regions indicating that the minimum breakaway time was <4400 s. These results were consistent with ANL results for minimum breakaway oxidation time (4000±200 s). WEC speculated that there was a significant effect of temperature ramp rate on breakaway oxidation because the longer ramp-rate tests showed no evidence of breakaway at a total test time of 4550 s. However, for both “fast” and “slow” ramp times, the ramp rate was about the same up to 980ºC. It is difficult to comprehend why an extra 70 s to progress from 980ºC to 1000ºC would make a difference in results observed about 4000 s later. Also, it is not clear if apparent differences in three slow-ramp samples and three fast-ramp samples were due to data scatter or to differences in thermal history.

The WEC results for hold temperatures of 980ºC and 990ºC were quite different from ANL results. For the lower temperature regime, WEC observed no breakaway for total test times of 3800 to 4600 s. Based on a larger data set, ANL determined 3100±300 s for average hold temperatures of 970ºC to 985ºC. One possible explanation for these different observations is that ANL samples experienced the full range of temperatures between 965ºC and 990ºC while WEC samples were subjected to discrete temperatures. If the minimum breakaway time for ZIRLO is highly temperature sensitive, then this could explain why ANL and WEC data do not appear to be consistent in the lower temperature range. WEC did not measure sample temperatures directly nor did WEC perform weight-gain benchmarks prior to data generation. Weight-gain validation tests were performed successfully by WEC about two years later [29] after modifications were made to the furnace.

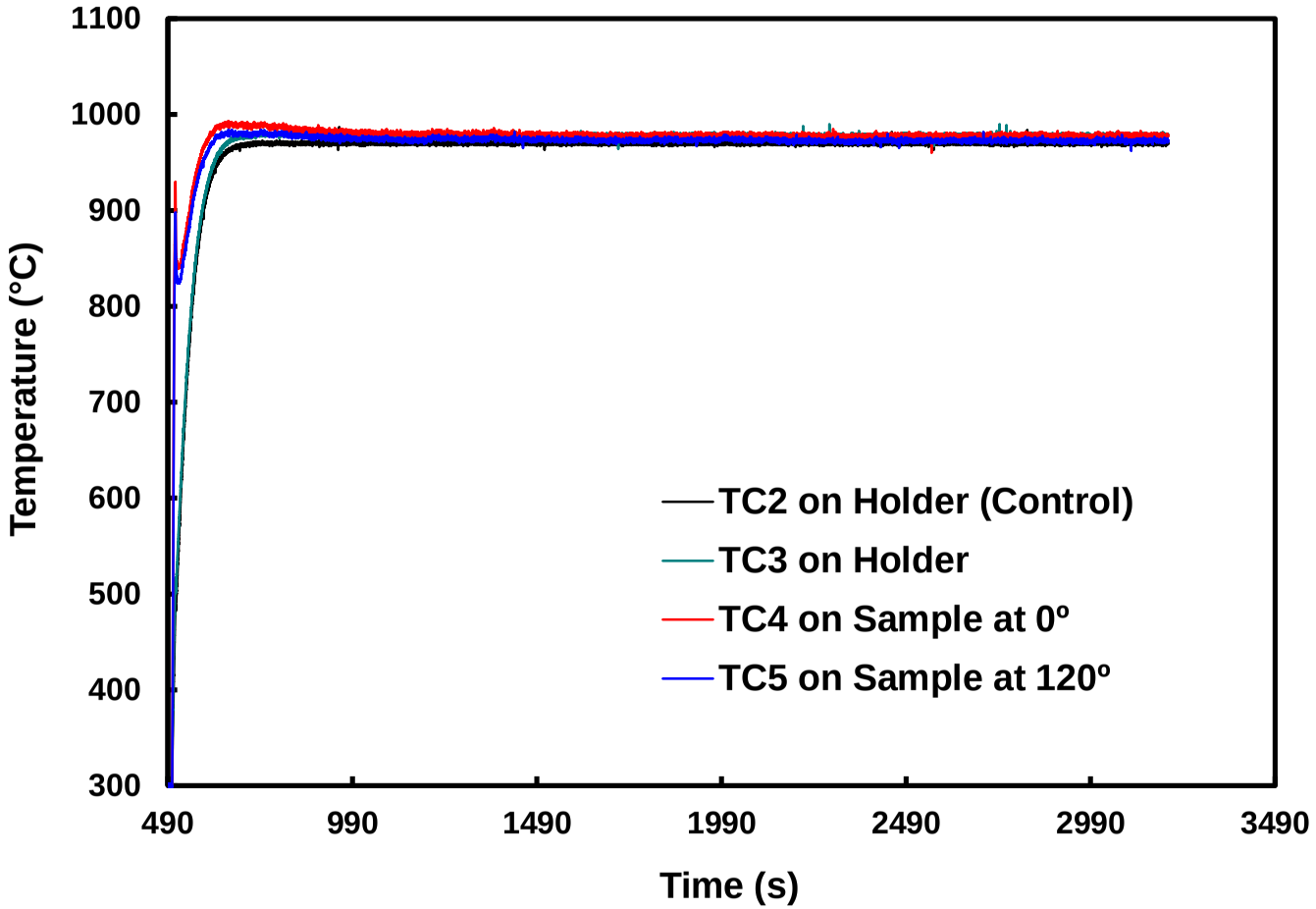

Figure 43. **Thermal benchmark results for test ZLU#132. Long-time hold temperature is 975±3ºC. The holder control temperature was increased by 10ºC for data generating tests, which increased the long-time sample temperature to 985±5ºC.**

Table 23. Results of ZIRLO breakaway oxidation tests at 970−985ºC; new results are in bold font.

Material	Test T ºC	Test Time[a], s	Measured w_g, mg/cm^2	Measured $(C_H)_{POX}$, wppm	ΔC_{HM} [b], wppm	Comment
ZIRLO-2006MS	970	2600	7.8	50	40	Scratched
ZIRLO-2006	970	3000	8.1	200±150	200±160	---
ZIRLO-2006	970	3400	8.6	570±90	580±90	
ZIRLO-2006	975	3000	9.0	40	30	---
ZIRLO-2006	975	3500	8.7	110±50	100±50	---
ZIRLO-2006	980	3000	11.8	350±120	370±130	
ZIRLO-PF	980	3200	8.7	130±120	120±120	
ZIRLO-PF	980	3200	8.8	100±100	100±100	
ZIRLO-WC	**980**	**3200**	**8.4**	**690±90**	**700±100**	**W-cleaned T-overshoot**
ZIRLO-WC	**980**	**3200**	**8.4**	**630±120**	**650±120**	**W-cleaned T-overshoot**
ZIRLO-2008	**980**	**3400**	**11.4**	**---**	**---**	**Breakaway T-overshoot**
ZIRLO-2006	985	3000	9.1	100±40	100±40	---
ZIRLO-PF	985	3000	9.0	60	50	Pre-filmed
ZIRLO-2006	985	3400	9.6	50	40	---
ZIRLO-2006MS	985	3400	9.9	180±140	170±150	Scratched
ZIRLO-2006	985	3400	9.4	300±160	310±170	
ZIRLO-PF	985	3400	9.3	260±140	260±150	Pre-filmed
ZIRLO-2008	**985**	**3500**	**9.5**	**700±120**	**720±120**	**---**
ZIRLO-WC	**985**	**3500**	**9.2**	**40**	**20**	**W-cleaned**
ZIRLO-2006	985	3600	10.0	280±160	280±170	---
ZIRLO-WC	**985**	**3800**	**8.9**	**280±60**	**270±60**	**W-cleaned**
ZIRLO-PF	985	4000	11.9	1070±90	1130±100	Pre-filmed
ZIRLO-2006	985	4000	11.8	850±140	890±150	---

[a]Time from ramp initiation at 300ºC to end of hold temperature; ramp time is ≈80 s.

[b]ΔC_{HM} is referenced to as-fabricated sample mass: $\Delta C_{HM} = (1 + 5.4\times10^{-3}\ w_g)\ (C_H)_{POX} - C_{Hi}$, where C_{Hi} is the hydrogen content in as-fabricated ZIRLO.

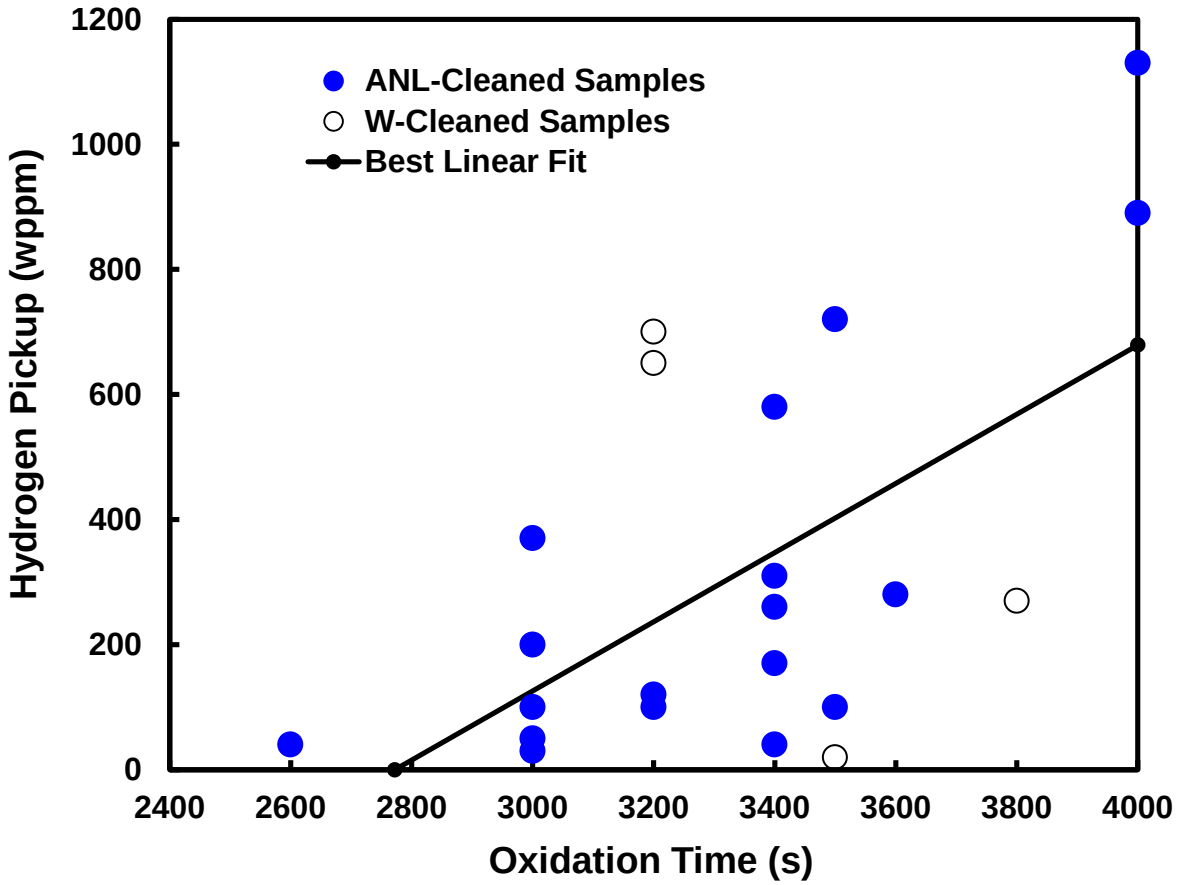

Figure 44. **Hydrogen pickup for ANL- and W-cleaned samples oxidized at 970−985ºC. ANL-cleaned samples included as-fabricated, MS (20-µm depth), and PF (<1-µm oxide) ZIRLO.**

4.2 Breakaway Oxidation for M5 Cladding

The purpose of these tests was to determine if as-fabricated M5 cladding would experience breakaway oxidation at ≤5000 s for oxidation temperatures in the range of 985-1000°C. ANL results for oxidation of M5 cladding at 1000°C for ≤4100 s are documented in Ref. 1. Based on the large data set generated by CEA at Saclay [9], the breakaway oxidation time (at ≈200-wppm H pickup) is ≈6400 s for M5 oxidized at 1000ºC. M5 exhibits very slow growth rate of inner- and outer-surface oxide layers at 1000ºC, which may contribute to the longer breakaway-oxidation time for M5 as compared to the CEA-value reported for Zry-4 (≈5400 s at 1000ºC). The Ref. 9 data were generated by very different testing methods (e.g., one-sided oxidation, fast heating ramp, etc.) than the ones used at ANL. Also, breakaway-oxidation times for M5 at <1000ºC oxidation temperatures have not been reported.

4.2.1 M5 materials for breakaway oxidation

Cladding materials used for the new ANL tests included as-fabricated 17×17 M5 tubing received from Framatome in 2003 (M5-2003) and M5 received from AREVA (formerly Framatome) in 2007 (M5-2007). Table 24 shows the comparison between the two materials based on ANL measurements.

Table 24. Characterization of 17×17 M5 cladding used in the ANL testing program.

Material	Outer Diameter, mm	Wall thickness, mm	OD Surface Roughness, μm	H Content, wppm	O Content, wppm
M5-2003	9.50	0.61	0.12	5	1450
M5-2007	9.50	0.57	--	17	--

4.2.2 Test parameters and results for M5 breakaway oxidation

Results for M5 oxidation tests conducted at 1000ºC for ≤4100 s are reported in Ref. 1. Three additional tests were conducted at ≈985ºC for 5000 s during the current test program.

Previous test results for M5 at 1000ºC

Thermal benchmark results for M5 (Validation Lot with 0.57-mm h) cladding are shown in Fig. 45 for 1000ºC tests. The results were used for M5-2003 with 0.61-mm h because the results for 0.57-mm cladding were so close to the holder temperatures. Table 25 lists the breakaway-oxidation test results for M5 cladding samples. For 1000ºC oxidation, M5 exhibited significantly lower weight gain and slower oxide-layer growth as compared to Zry-4 and to CP-predicted values. Also, above ≈10% CP-ECR (≈960 s equivalent isothermal time), weight gain did not increase in a consistent manner with either the oxidation time or with the square root of oxidation time (CP correlation). All samples had lustrous black outer surfaces. The measured hydrogen pickup was low. Breakaway oxidation was not observed at 1000ºC for test times ≤4100 s.

New Tests at 980ºC and 985ºC

During previous studies, minimum breakaway oxidation times were observed by Argonne for ZIRLO for temperatures in the range of 970-985ºC. Unlike results at 1000ºC, there was considerable scatter in hydrogen pickup vs. oxidation time within this highly sensitive temperature range. M5-2007 breakaway oxidation tests were therefore performed at 980ºC and 985ºC for 5000 s in parallel with those conducted using ZIRLO cladding.

Both ZIRLO and M5-2007 samples had the same outer-diameter (OD) and wall thickness. Therefore, thermal benchmark temperature histories determined for ZIRLO were also used for M5 (see Fig. 41 for test MU#80 and Fig. 43 for test MU#83). For test MU#81, control parameters were adjusted to give a slower ramp rate to the target temperature.

Table 26 lists the weight gain results for M5-2007 for long-time hold temperatures of 980ºC and 985ºC. Breakaway oxidation was not observed for test times as long as 5000 s, which was confirmed by metallographic examination of the MU#80 test sample (see Fig. 46).

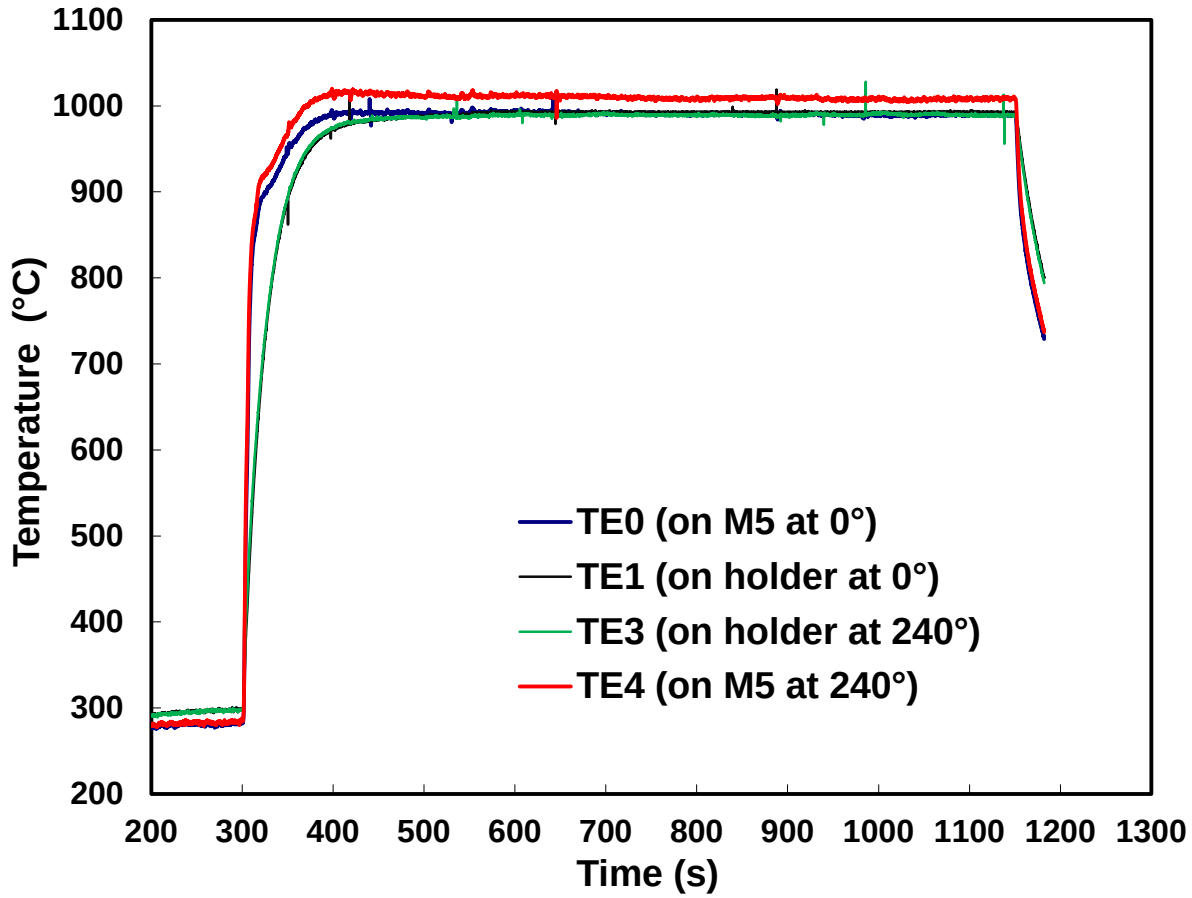

Figure 45. Thermal benchmark results for 17×17 M5 (Validation Lot) oxidation tests at 1000ºC.

Table 25. Results of previous M5 oxidation tests at 1000ºC in long test train.

Test ID	Material	Test Time[a], s	CP-predicted w_g, mg/cm^2	Measured w_g, mg/cm^2	$(C_H)_{POX}$, wppm	ΔC_{HM} [b], wppm
MU#52	M5-2003	207	3.3	3.0	---	---
MU#53	M5-2003	810	6.5	5.3	---	---
MU#54	M5-2003	1880	9.8	7.4	---	---
MU#55	M5-2003	2440	11.1	8.0	---	---
MU#56	M5-2003	3380	13.1	9.2	26	22
MU#61	M5-2003	4100	14.4	8.6	13	8

[a]Time from ramp initiation at 300ºC to end of hold temperature; ramp time is ≈80 s.

[b]ΔC_{HM} is referenced to as-fabricated sample mass: $\Delta C_{HM} = (1 + 5.4\times10^{-3}\ w_g)\ (C_H)_{POX} - C_{Hi}$, where C_{Hi} is the hydrogen content in as-fabricated M5.

Table 26. M5-2007 breakaway oxidation test results for long-time hold temperatures of 980ºC and 985ºC in the short test train.

Test ID	Long-Time Hold T, °C	Test Time[b], s	CP-predicted w_g, mg/cm^2	Measured w_g, mg/cm^2	$(C_H)_{POX}$, wppm	ΔC_{HM} [c], wppm
MU#80	985	5000	14.4	7.9	32	28
MU#81	980	5000	≈14.4	7.7	---	---
MU#83[a]	985	5000	≈14.4	7.4	---	---

[a]The ramp rate for this test was close to the one shown in Fig. 44.

[b]Time from ramp initiation at 300ºC to end of hold temperature.

[c]ΔC_{HM} is referenced to as-fabricated sample mass: $\Delta C_{HM} = (1 + 5.4\times10^{-3}\ w_g)\ (C_H)_{POX} - C_{Hi}$, where C_{Hi} is the hydrogen content in as-fabricated M5.

4.3 Discussion on Breakaway Oxidation under Isothermal Conditions

Leistikow and Schanz [20] observed a transition in the contour of the oxide-metal interface from stable, tetragonal oxide growth to breakaway oxidation. For Zry-4, the interface progressed from smooth to scalloped to smooth. Thus, they referred to the scalloped interface as a pre-cursor to breakaway oxidation. They further speculated that the oxide was growing stably under compressive stress in the thicker regions, while the thinner regions would become unstable under a tensile (or less compressive) stress because of the contour. Thus, destabilization or breakaway would initiate at the metal-oxide interface under the thin regions and propagate in the radial, circumferential and axial direction. However, the time between initiation of the scalloped interface and breakaway was not established. Additional metallographic examination was performed with Zry-4, ZIRLO, and M5 test samples to shed some light on the amplitude and frequency of scallops prior to breakaway oxidation or close to the initiation of breakaway oxidation.

Figure 47 shows the evolution of the outer-surface oxide-layer/metal interface for ZIRLO oxidized at 1000ºC. After 1500 s (Fig. 47a), the interface was relatively smooth with the appearance of very low-amplitude scallops. The amplitude of the scallops grew from 1500 s to 2440 s (Fig. 47b). At 3480 s, the high magnification image in Fig. 47c shows rather pronounced scallops. The image at 4000 s is from the W-cleaned ZIRLO sample that experienced local breakaway oxidation at a location about 140° from the location shown in Fig. 47d. Although not enough data were generated to directly correlate the amplitude of the scallops with initiation of local breakaway oxidation, the data trend shown in Fig. 47 is consistent with the Leistikow and Schanz speculation that scalloping is a precursor to breakaway oxidation. The trend is also consistent with the ANL hypothesis that breakaway initiation occurs at a critical scallop amplitude.

It should be noted that scalloping appears to result in measured weight gain and average oxide layer thickness values that are less than those predicted by the CP correlations. The results presented in Ref. 1 for ZIRLO-2003 were misleading because the inner surface (66 μm vs. 57 μm outer-surface oxide layer) experienced breakaway at 1000°C prior to 3480 s (20% CP-ECR). The measured weight gains for pre-breakaway ZIRLO oxidized at 970 to 1000ºC were less than CP-predicted weight gains.

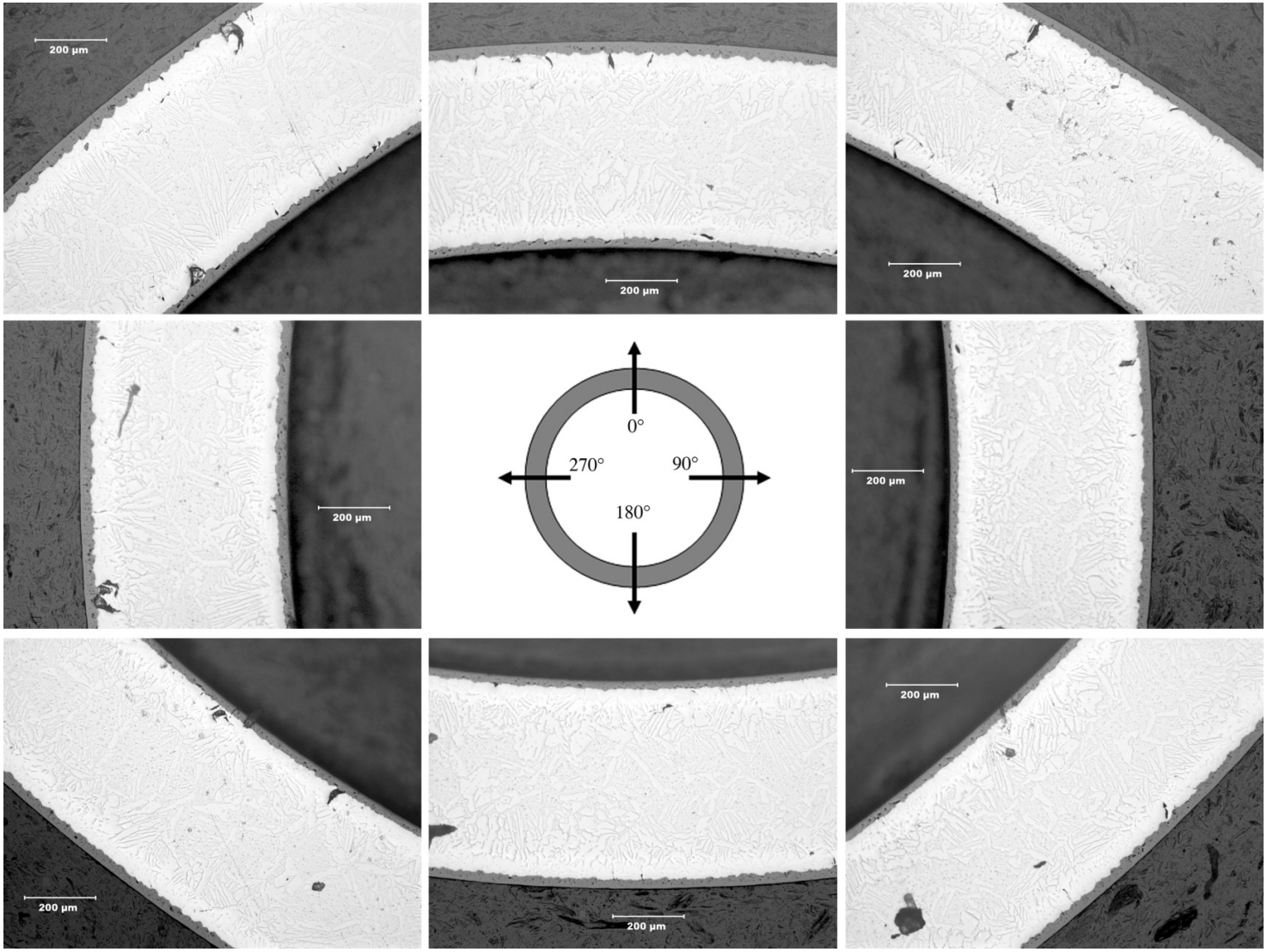

Figure 46. **Metallographic images around the cross section of the MU#80 test sample, which show wavy interfaces between oxide and metal layers. However, no local breakaway oxidation was observed after 5000 s at 985ºC.**

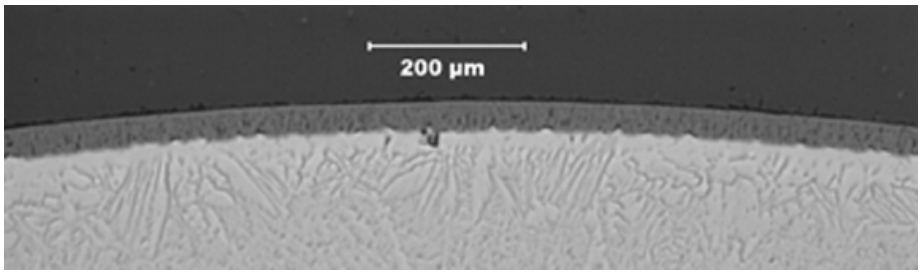

(a) 1500 s

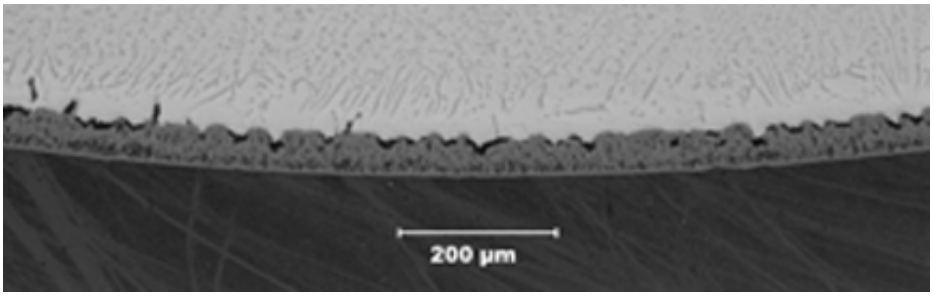

(b) 2440 s

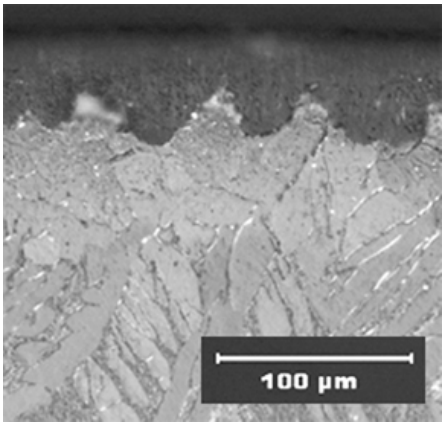

(c) 3480 s

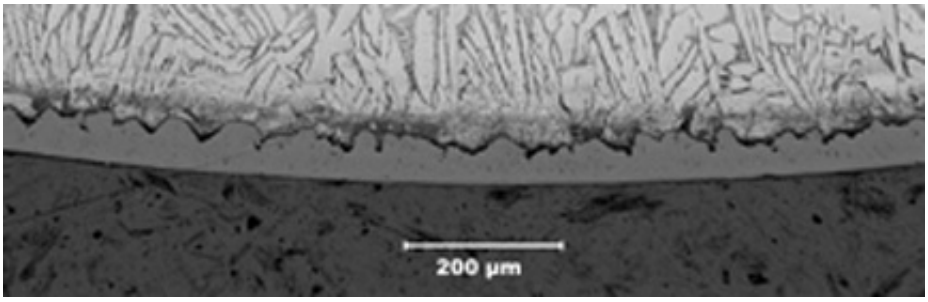

(d) 4000 s

Figure 47. Evolution of outer-surface oxide-layer/metal interface for ZIRLO oxidized at 1000°C for (a) 1500 s; (b) 2440 s; (c) 2480 s; and (d) 4000 s.

M5 exhibited slower oxide layer growth during oxidation at ≈1000°C relative to ZIRLO and Zry-4. Thus, the average thickness of the oxide layer, as well as the amplitude of the scallops at the oxide/metal interface, grew slowly with oxidation time within a temperature range of about 975°C to 1000°C. The slow oxidation kinetics appeared to contribute to the longer breakaway oxidation time for M5 relative to Zry-4 and ZIRLO. Figure 48 shows the oxide/metal interface for M5 oxidized at 1000°C for 3440 s (high-magnification image in Fig. 48a) and at 985°C for 5000 s (low- and high-magnification images in Figs. 48 b and c, respectively).

Based on hydrogen-content data in Ref. 9, it was estimated that the breakaway oxidation time (i.e., time to reach 200 wppm ΔC_{HM}) would be ≈6400 s at an oxidation temperature of 1000°C. More recently, CEA, EdF, and AREVA collaborated to do a more extensive study of the breakaway oxidation time for standard M5, as well M5 with variations in Nb, Fe, O, S, and Hf content [30]. For standard M5, the minimum breakaway oxidation time for 200-wppm hydrogen was in the range of ≈6500±500 s. Variations in alloy and impurity contents had little effect on breakaway oxidation time within the data scatter for standard M5. It was also observed that both the weight-gain and hydrogen-pickup rates were relatively slow during the transition between pre- and post-breakaway oxidation.

For polished Zry-4 oxidized at 1000°C, the outer-surface oxide-layer/metal interface was relatively smooth for test times up to ≈3400 s. Figure 49 shows the outer-surface oxide-layer/metal interface for Zry-4 oxidized for: (a) 3440 s at 1000°C and (b) 5000 s at 985°C. Pronounced scallops can be observed at the higher oxidation time for which local breakaway oxidation occurred at a location away from the one shown in the figure. The local breakaway oxidation is identified in Fig. 50 at one of eight metallographic images around the cross-section.

To develop a correlation between scallop amplitude and breakaway-oxidation initiation, additional oxidation tests would have to be performed at intermediate oxidation times. Also, metallographic samples would have to be prepared carefully (i.e., additional polishing steps with finer-grit paper) to avoid local fallout of the brittle oxide and/or oxygen-stabilized alpha material. Fallout tends to exaggerate the amplitude of the scallops. Examples of high-quality metallographic images are shown in Figs. 47a and c, Fig. 48a and the right half of Fig. 48c, and Fig. 49a.

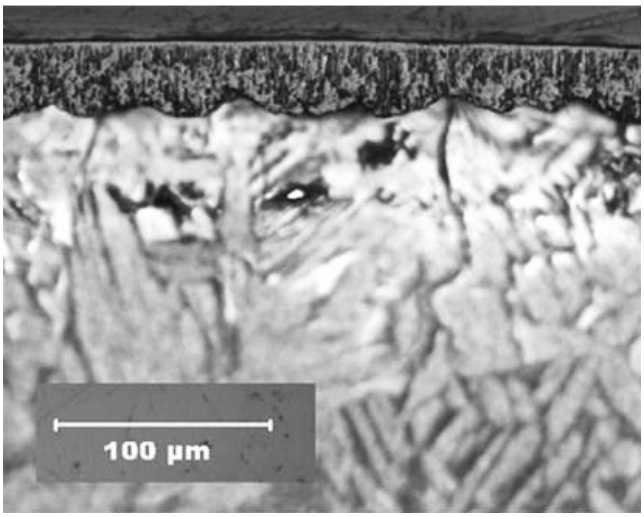

(a) 3440 s at 1000°C

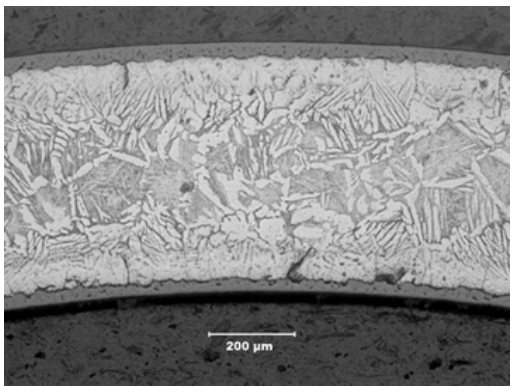

(b) 5000 s at 985°C (low magnification)

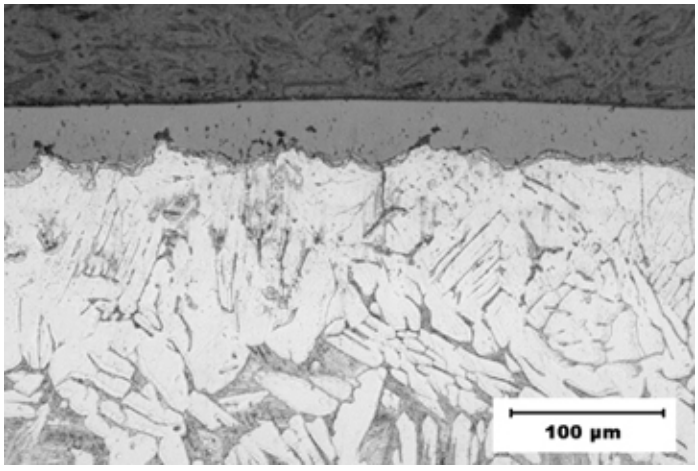

(c) 5000 s at 985°C

Figure 48. Evolution of outer-surface oxide-layer/metal interface for M5 cladding oxidized for: (a) 3440 s at 1000°C; (b) 5000 s at 985°C (low-magnification); and (c) 5000 s at 985°C.

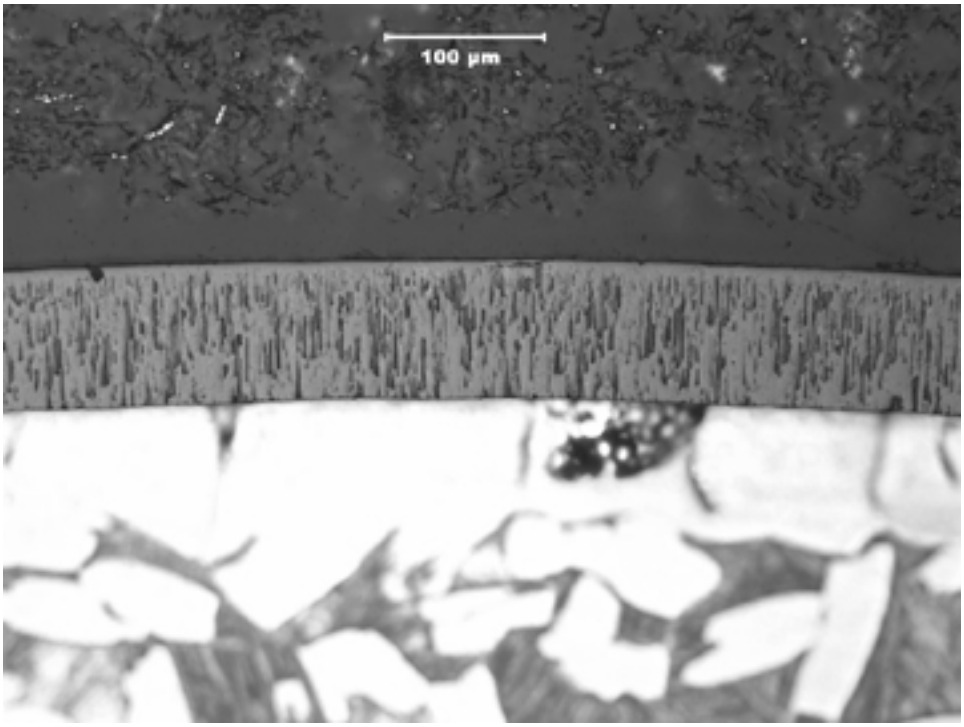

(a) 3440 s at 1000°C

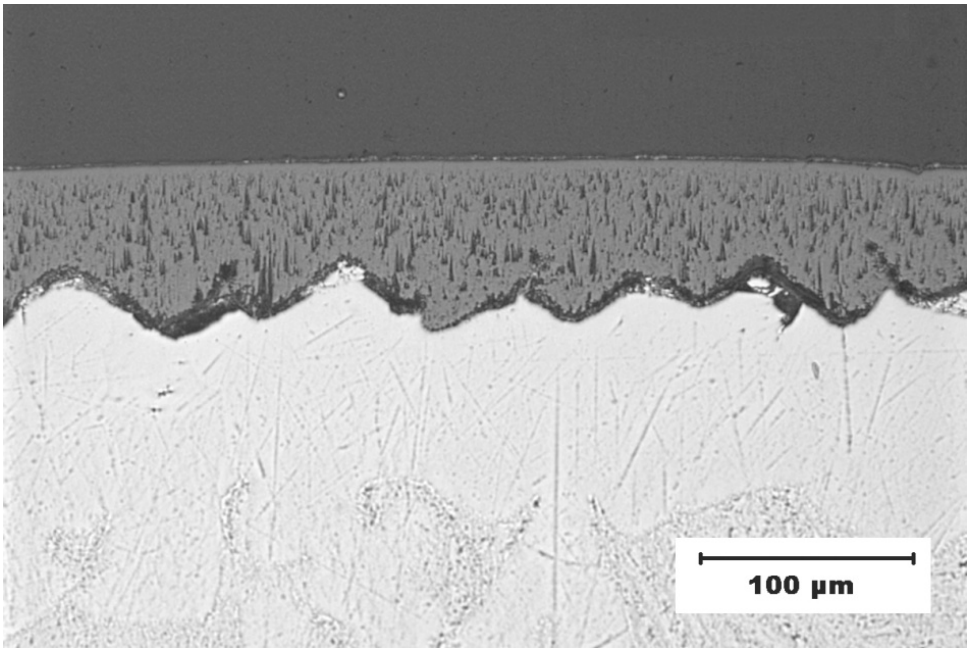

(b) 5000 s at 985°C

Figure 49. Evolution of oxide-layer/metal interface for polished Zry-4 oxidized for: (a) 3440 s at 1000°C and (b) 5000 s at 985°C.

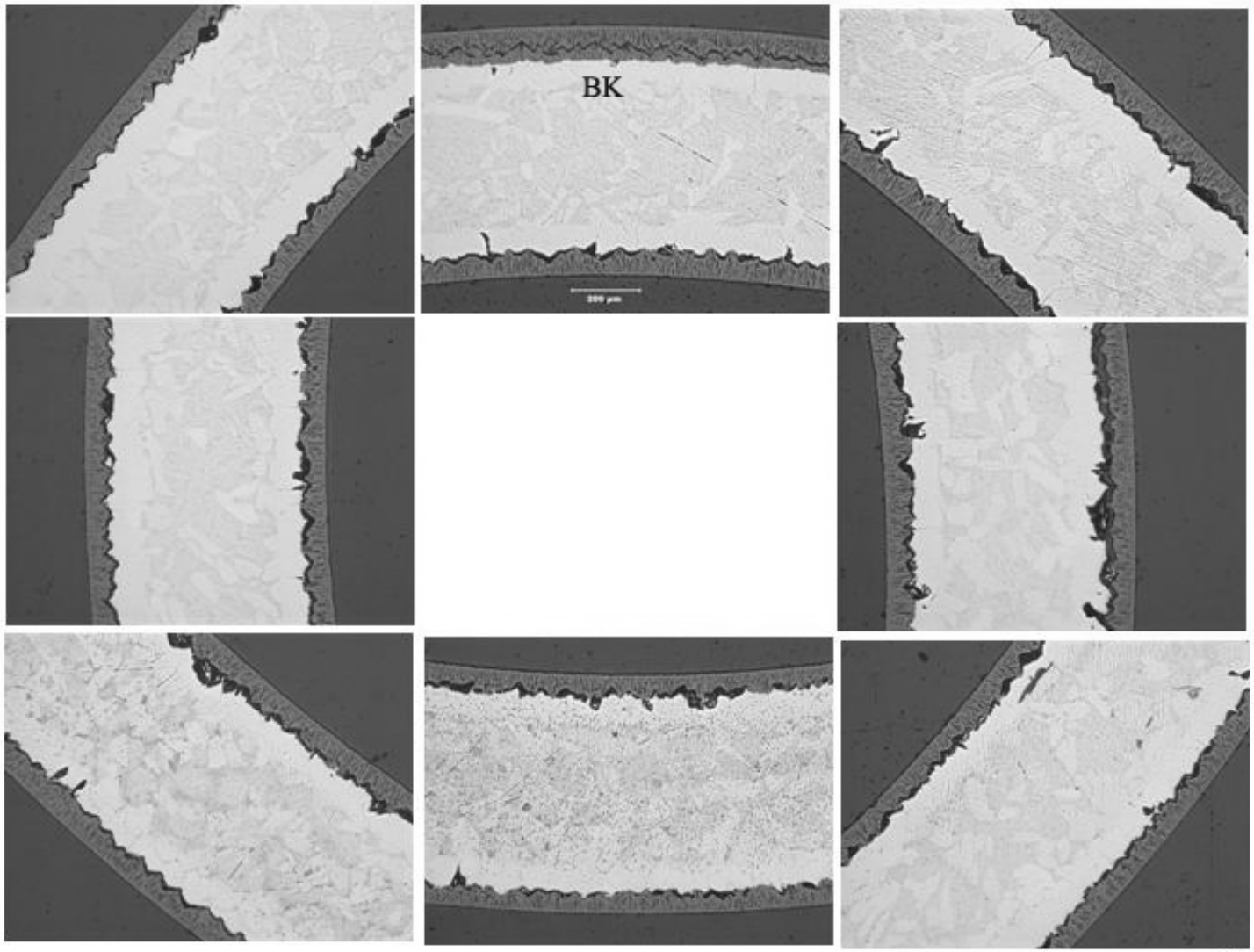

Figure 50. **Metallographic images at eight locations around the cross section of polished Zry-4 sample oxidized at 1000°C for 5000 s, which show scalloped (wavy) oxide-layer/metal interfaces. Local breakaway oxidation was observed in Area BK.**

4.4 Breakaway Oxidation under Transient Temperature Conditions

The purpose of the transient oxidation tests was to determine if temperature changes might decrease breakaway oxidation time. The study was not intended to simulate a temperature history for a particular LOCA, which would be difficult to do as there is no standard temperature history, especially for small-break LOCAs. As such, temperature histories were chosen such that they might disturb the stress state at the oxide-metal interface and thereby induce lower breakaway oxidation times. The approach was based on hypotheses of Leistikow and Schanz [20]: (a) the transition from a smooth oxide-metal interface to a wavy oxide-metal interface is a precursor to breakaway oxidation and (b) the variation in stress state from thick oxide regions (compressive) to thin oxide regions (less compressive and perhaps tensile) facilitates local breakaway oxidation in regions where the oxide layer is thin. The results of Argonne's isothermal tests support their hypotheses.

4.4.1 Transient temperature histories

Transient breakaway oxidation tests were conducted with three temperature profiles. Schematics of these three temperature profiles are shown in Fig. 51.

The first transient test was designed to have a temperature history corresponding to Transient #1 in Fig. 51. This history included a single step change from 1045°C to 980°C: (a) hold at 1045°C for ≈1000 s, (b) decrease temperature to 980°C and (c) hold for ≈3000 s at 980°C. Test ZLU#138 was conducted as a thermal benchmark with 2 TCs welded directly onto the ZIRLO sample outer surface. Benchmark results are shown in Fig. 52. The long-time hold temperatures were 1041±1ºC during the last 500 s of step (a) and 981±1ºC during the last 500 s of step (b). Except for the initial temperature ramp, the holder control TC measurements were only a few degrees lower than the sample TCs. The first 500 s (not shown) was the preconditioning phase to stabilize the temperature at 300ºC. The ramp time to 1045ºC was ≈80 s, the hold time was ≈920 s for step (a), the temperature-decrease duration was ≈40 s, and the lower-temperature hold time was ≈1960 s to give 3000-s total test time from ramp initiation at 300ºC to the end of the heating phase. The long-time step (b) temperatures were stable enough that the benchmark was terminated 1000 s earlier than what was specified for Transient #1. Data were recorded every 0.1 s. Due to the 32000 data point limit of EXCEL, the data were filtered at the end of the heating phase such that data are plotted every 50 s from 3200 s to 3500 s (see thinner lines in Fig. 52).

Prior to conducting Test ZLU#139, the furnace power was adjusted slightly to give long-time hold temperatures of 1045°C and 980°C and the total test time was extended to 4000 s. As Test ZLU#139 was a data-generating test, it was conducted without TCs welded directly onto the sample. Figure 53 shows the temperature history for the control TC welded to the sample holder. The thinner part of the temperature trace represents data points recorded every 50 s.

Test ZLU#140 was conducted with a temperature history corresponding to Transient #2 in Fig. 51. This was also a single step-change test: (a) hold at 975°C for 1500 s, (b) increase temperature to 1000°C, and (c) hold for 2500 s at 1000°C. In order to achieve long-time hold temperatures of 975ºC and 1000ºC, the furnace power was adjusted based on the benchmark relationships established among the furnace power, the holder control TC, and the sample TC. The control TC temperature history for Test ZLU#140 is shown in Fig. 54. As before the thinner parts of the temperature trace represent data plotted every 50 s.

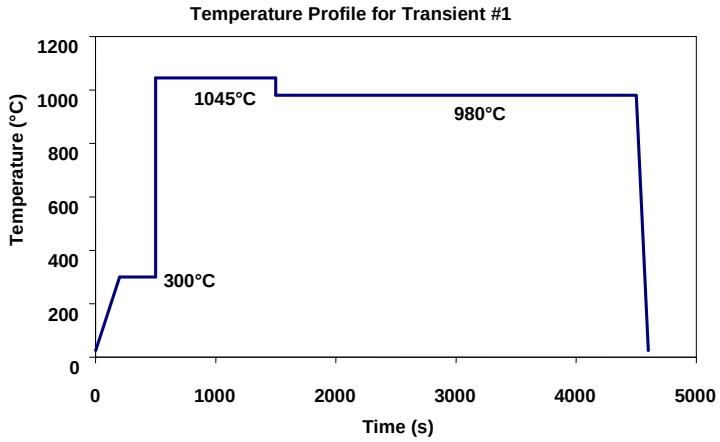

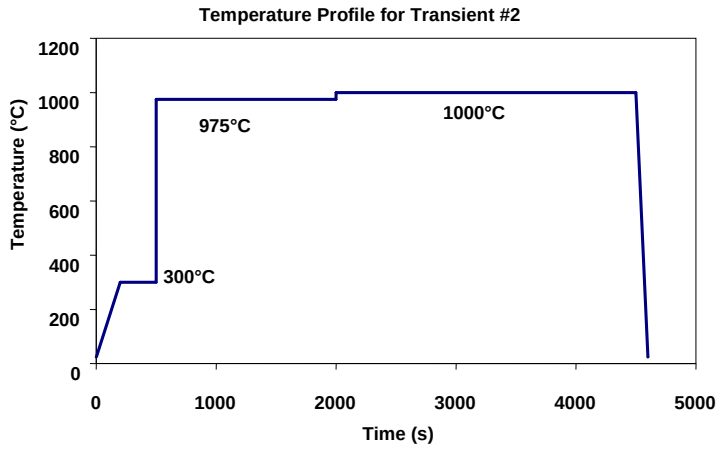

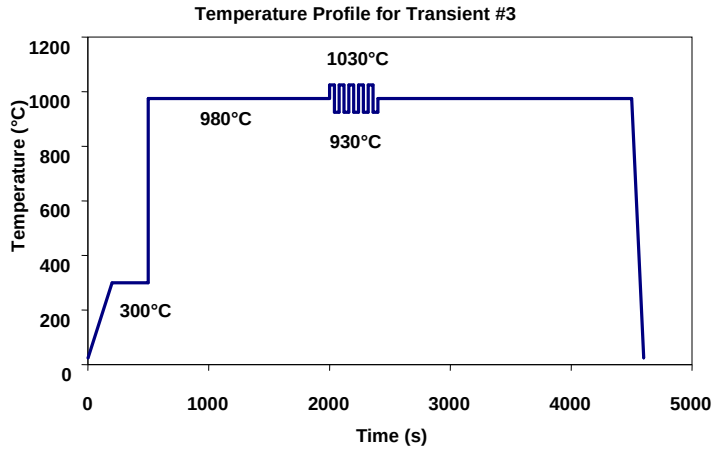

Figure 51. Schematics of transient temperature histories for breakaway oxidation tests with ZIRLO cladding samples.

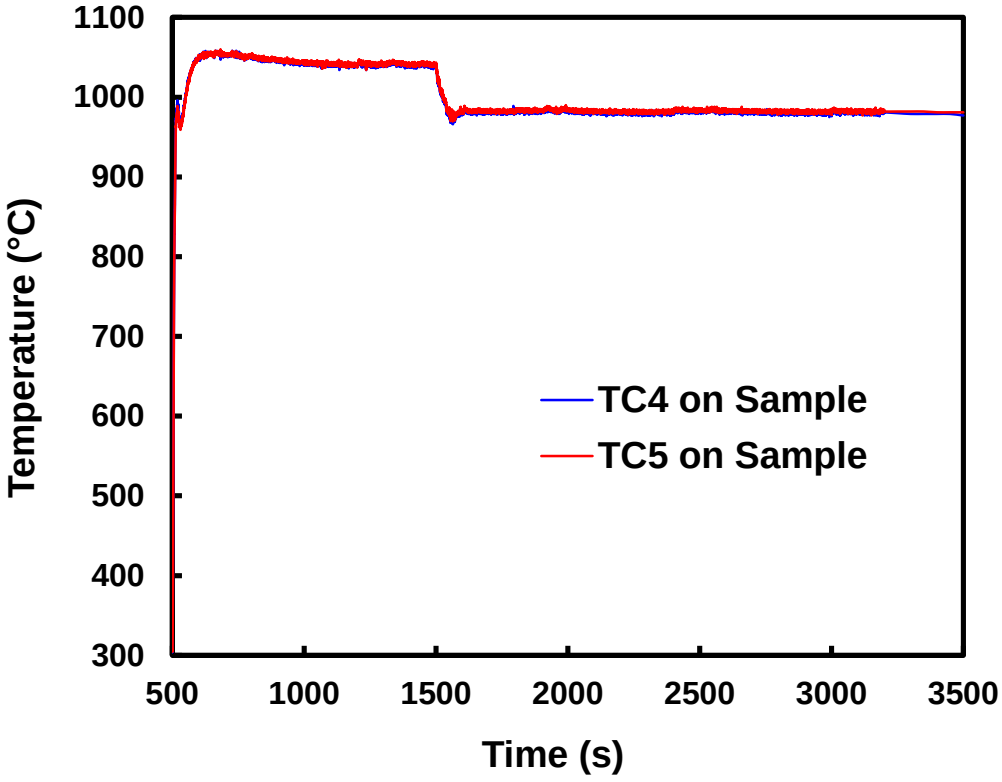

Figure 52. **Thermal benchmark results for Test ZLU#138 with as-fabricated ZIRLO-2008.**

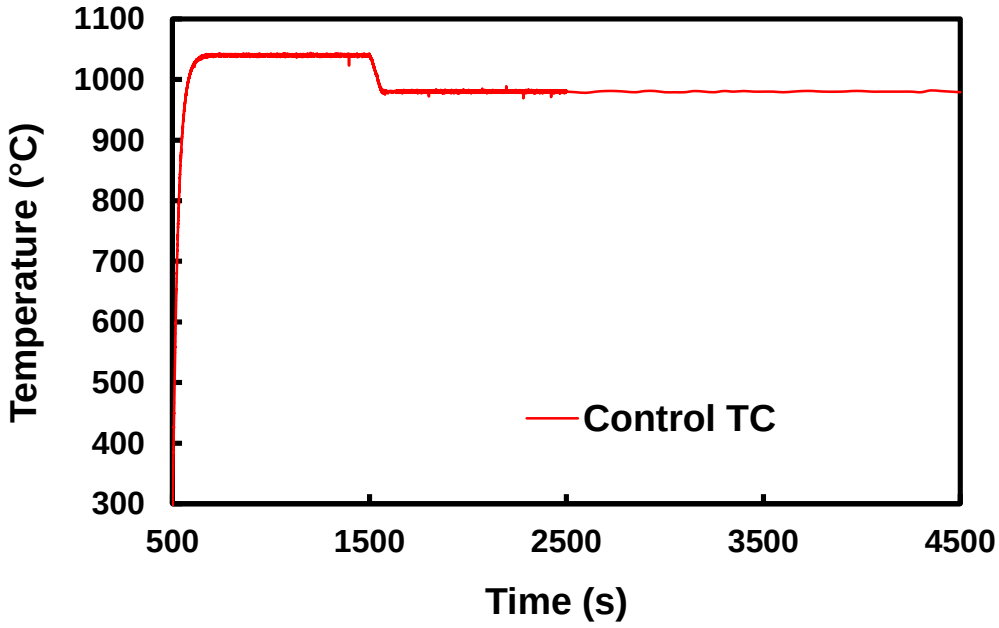

Figure 53. **Temperature history of the control TC for Test ZLU#139.**

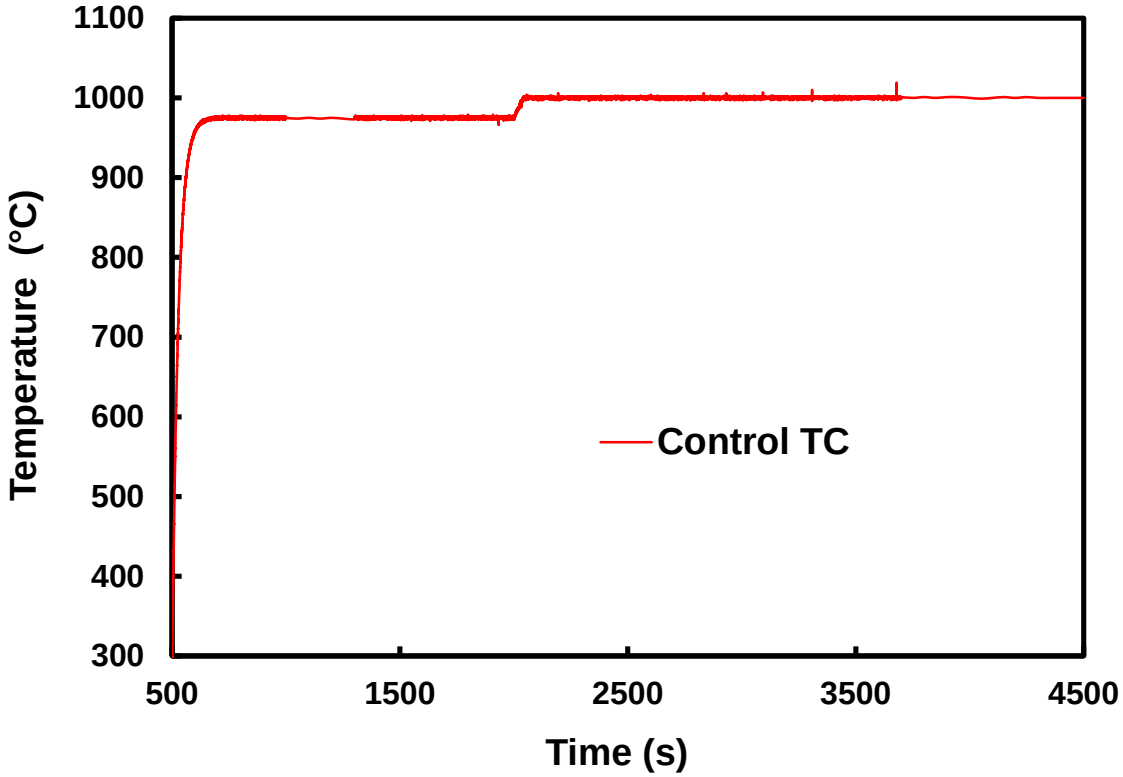

Figure 54. Temperature history of the control TC for Test ZLU#140.

Two thermal-cycling tests were performed for Transient #3. Test ZLU#142 was run with ZIRLO cladding under the following conditions: (a) 980°C for 1500 s, (b) 5 cycles from 930°C to 1030°C for about 400 s, and (c) 980°C for 1400 s. For ZLU#143, the temperature profile was modified slightly: the initial hold time at 980°C was increased from 1500 s to 2000 s, the temperature was cycled during the 2000-2400 s time interval, and the sample was held at 980°C during the remaining 2400-2800 s time interval. The control TC temperature histories for Tests ZLU#142 and ZLU#143 are shown in Figs. 55 and 56, respectively.

4.4.2 Outer-surface appearance of transient oxidation samples

The outer surfaces of the ZLU#139 and ZLU#140 samples were lustrous black (see Fig. 57a). There were no indications of breakaway behavior after 4000-s total oxidation time for these samples subjected to temperature decrease (from 1045°C to 980°C) and increase (975°C to 1000°C).

Outer surface discolorations were observed for both samples subjected to temperature cycling (see Figs. 57c and 57d). The ZLU#142 sample had small, but significant, yellow-gray areas on the outer surface and extensive (middle 75%) yellow-gray areas on the inner-surface after 3300-s total test time. The region just to the right of the ZLU#142 sample mid-plane had more discoloration than the mid-plane due to yellow-gray areas around the back of the sample, which are not visible in Fig. 57c. The reverse was true for the ZLU#143 sample after 2800-s total test time: extensive yellow-gray area on the outer surface and yellow-gray spots on the inner surface.

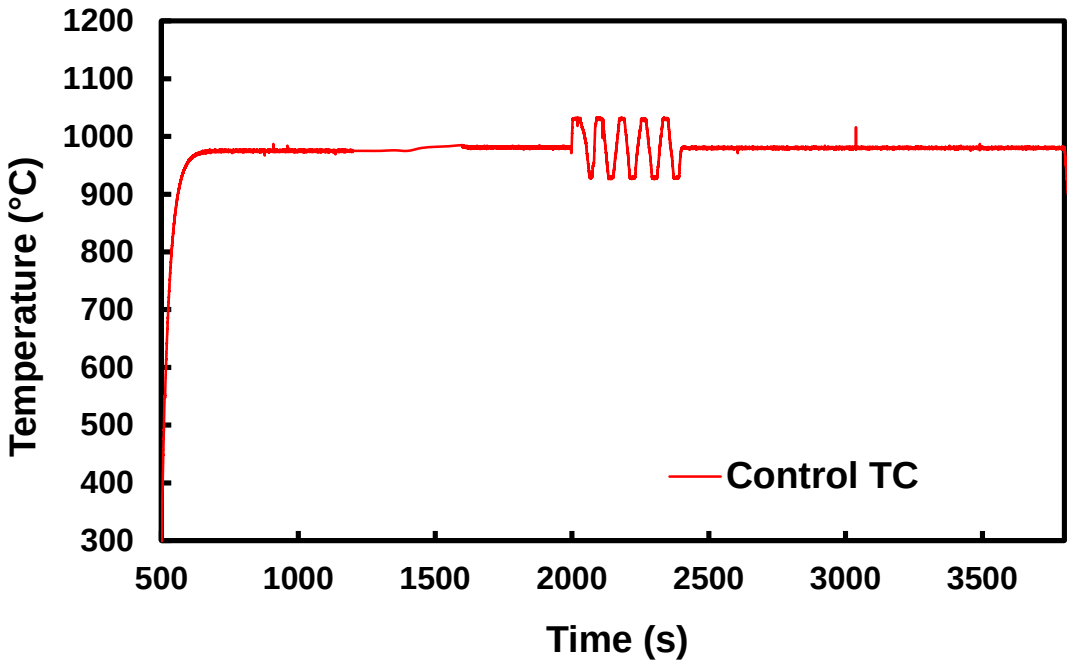

Figure 55. **Temperature history of control TC for Test ZLU#142. 1400-s hold time following cycling.**

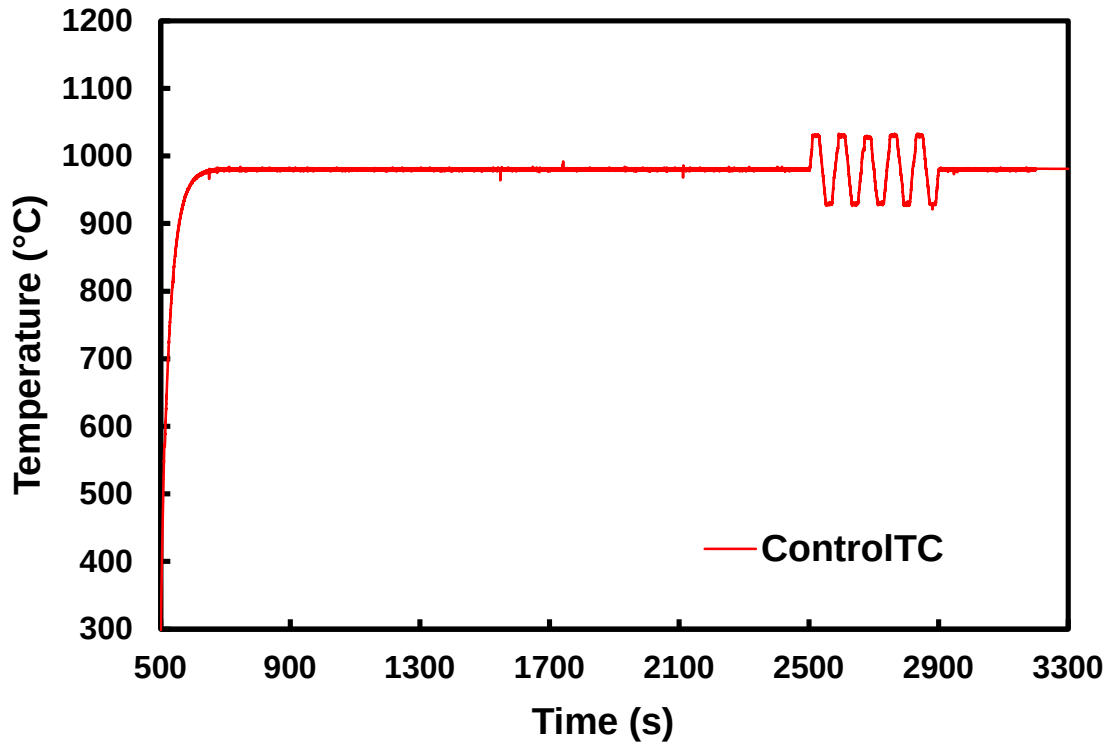

Figure 56. **Temperature history of control TC for Test ZLU#143. 400-s hold time following cycling.**

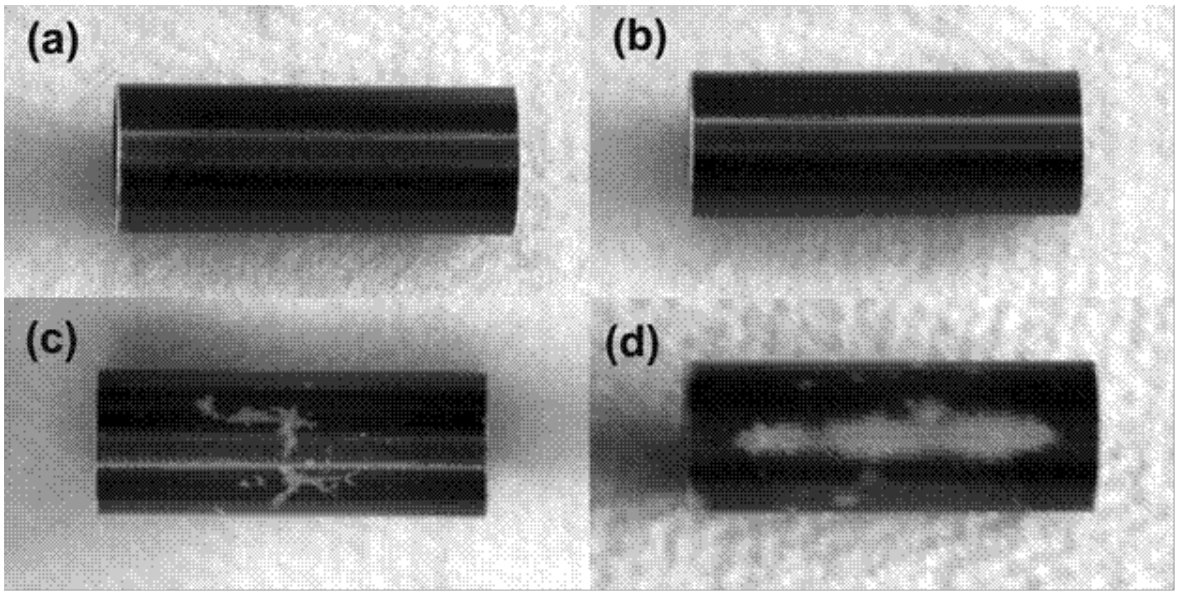

Figure 57. Appearance of as-received ZIRLO cladding outer-surface after steam oxidation tests (a) ZLU#139 for Transient #1, (b) ZLU#140 for Transient #2, (c) ZLU#142 for Transient #3, and (d) ZLU#143 for a modified Transient #3. Photos are in gray scale.

4.4.3 Weight gain and hydrogen pickup

As indicated in Table 27, the measured weight gains were less than the CP-predicted weight gains for all four samples oxidized under transient conditions. This is consistent with weight-gain results from isothermal oxidation tests conducted at 970 to 1000°C for long times. The hydrogen contents of ZLU#139 and ZLU#130 test samples were not measured because both outer and inner surfaces were lustrous black.

Breakaway oxidation for both temperature-cycled samples was confirmed by outer-surface discoloration and hydrogen pickup (see Table 27): 427±36 wppm after 3300-s total test time for the ZLU#142 sample and 225±79 wppm after 2800-s total test time for the ZLU#143 sample. However, some of the hydrogen in the ZLU#142 sample came from inner-surface breakaway oxidation. Previous results obtained for ZIRLO-2003 oxidized at 1000ºC [1] indicated that hydrogen pickup from inner-surface breakaway was lower than hydrogen pickup from the outer surface: 30 wppm after 2440 s and 100 wppm after 3480 s even though the inner surface was in full breakaway (see Table 29 and Fig. 55b in Ref. 1). Therefore, most of the hydrogen pickup for the ZLU#142 sample was from outer-surface breakaway.

4.4.4 Discussion of transient oxidation results

In general, breakaway oxidation of zirconium-based alloys is associated with local formation of monoclinic oxide at the metal-oxide interface during oxidation in steam. It has been reported that the monoclinic-to-tetragonal and tetragonal-to-monoclinic transformations do not occur at a fixed temperature [31]. The ranges of the transformation vary for both the forward and the reverse transformations, depending on impurities (type and concentration), grain size, stoichiometry, and thermal history. In addition, the transformation temperature can be reduced as the compressive stress increases.

Table 27. Results of ZIRLO-2008 transient breakaway-oxidation tests.

Test ID	Transient Type	Total Test Time[a], s	CP-predicted w_g, mg/cm^2	Measured w_g, mg/cm^2	Measured $(C_H)_{POX}$, wppm	ΔC_{HM}[b], wppm	Comment
ZLU#139	1	4000	14.3	9.5	---	---	Lustrous black OD
ZLU#140	2	4000	13.5	8.1	---	---	Lustrous black OD
ZLU#142	3	3300	11.6	8.5	425±35	427±36	Small OD yellow areas; extensive ID yellow area
ZLU#143	3	2800	10.8	8.2	232±76	225±79	Extensive OD yellow area: small ID yellow areas

[a]Total time from ramp initiation at 300ºC to end of hold temperature; ramp time is ≈80 s.

[b]ΔC_{HM} is referenced to as-fabricated sample mass: $\Delta C_{HM} = (1 + 5.4\times10^{-3}\, w_g)\, (C_H)_{POX} - C_{Hi}$, where C_{Hi} is hydrogen content in as-fabricated ZIRLO.

Although it is not clear at which temperature the oxide phase transformation takes place for the ZIRLO alloy, previous ANL breakaway oxidation results for ZIRLO cladding subjected to isothermal oxidation indicate minimum breakaway oxidation times occur within the range of 3100±300 s for isothermal oxidation temperatures of 970-985ºC. At a slightly higher oxidation temperature (1000ºC), the minimum breakaway oxidation time for ZIRLO was longer (4000±200 s). We also found that a rapid temperature rise with ≈60ºC overshoot for a very short time appeared to have some effect on long-time breakaway. However, no conclusions could be drawn because the hydrogen-pickup results were within data scatter for long-time temperatures of 970-985ºC. Therefore, it was of interest to determine if these step-change transients (i.e., Transients #1 and #2) could lead to shorter breakaway times. As indicated in Table 27, step changes from higher (1045ºC) to lower (980ºC) and from lower (975ºC) to higher (1000ºC) temperatures did not result in shorter breakaway oxidation times (>4000 s total test time).

The monoclinic-to-tetragonal transformation is accompanied by a sudden volume change and by anisotropic thermal expansion behavior of the lattice parameter, which disrupt the oxide. The purpose of the cycling tests under Transient #3 conditions was to determine whether localized stresses induced by the phase transformation and differential thermal expansion could disrupt the tetragonal layer near the metal-oxide interface, which in turn might reduce the breakaway time near the critical breakaway temperature. Test results listed in Table 27 indicate a marginal reduction (≈300 s) in breakaway time due to temperature cycling: 225±79 wppm ΔC_{HM} after 2800 s. Additional characterization of this sample from Test ZLU#143, along with the ZLU#142 samples, is presented in the following.

Figure 58 shows the yellow breakaway regions on the ZLU#143 sample outer surface. Some grayish/white areas were also observed, and some of these were in the center of the yellow areas. Since the oxide color is strongly influenced by stoichiometry, as well as impurities, this change might indicate an increase in the O-to-Zr ratio. A high-magnification image of a small yellow area (Fig. 58b) shows the morphology of the monoclinic phase on the ZLU#143 sample outer surface. The center area appears grayish/white surrounded by yellow areas. Figure 59 shows the transition area from black to yellow in the region marked “T” in Fig. 58a. The cladding longitudinal axis is delineated by an arrow in Figs. 58a and 59a. It is interesting to observe that the yellow areas have a rougher outer surface than the black areas. This feature was also observed within the small area of yellow, monoclinic oxide shown in Fig. 58b.

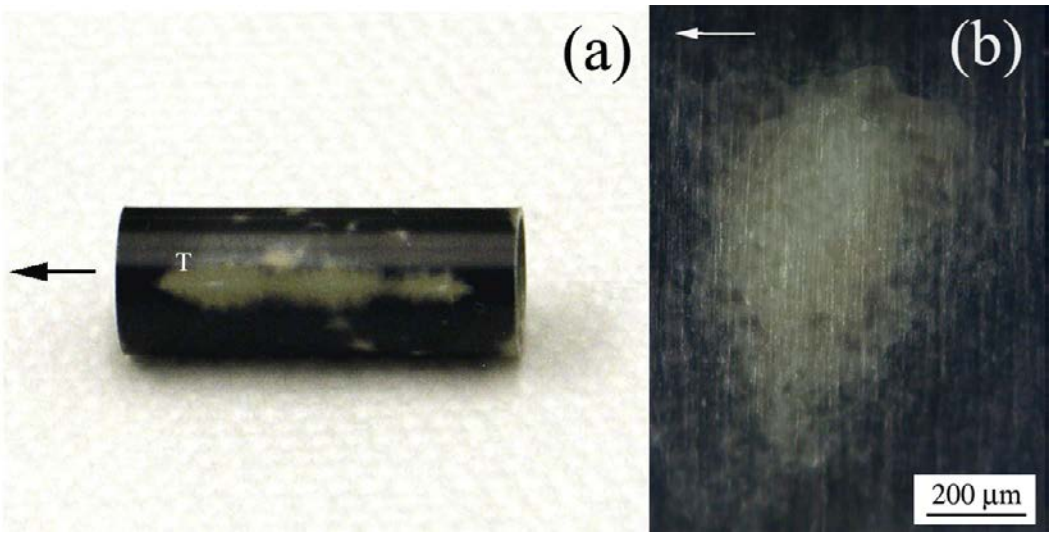

Figure 58. (a) ZIRLO sample after steam-oxidation at Transient #3 conditions for 2800 s total test time with cycling from 930°C to 1030°C (Test ZLU#143), and (b) high-magnification.

For the temperature-cycled ZLU#142 sample oxidized for longer time (3300 s), there was extensive discoloration within the middle 75% of the sample inner surface, and the additional 500 s allowed for more axial and circumferential diffusion of hydrogen (see Fig. 59). As shown in Fig. 60, rings were sectioned from an axial region that was ≈3 to 11 mm from the center of the sample. Hydrogen pickup values were determined to be 427±36 wppm, 312±31 wppm, 221±41 wppm, and 153±38 wppm, with the highest value for a thin ring closest to the center of the sample. The highest ΔC_{HM} value corresponded to an area with yellow-gray oxide over the whole inner surface and with yellow-gray oxide over about 40% of the outer surface. The lowest ΔC_{HM} value was for a ring near the end with lustrous black oxide on both inner and outer surfaces. Given the relatively small circumferential variation and the relatively large hydrogen content in the ring with black inner- and outer-surface oxides, it is clear that significant hydrogen diffusion occurred during the additional 500 s test time.

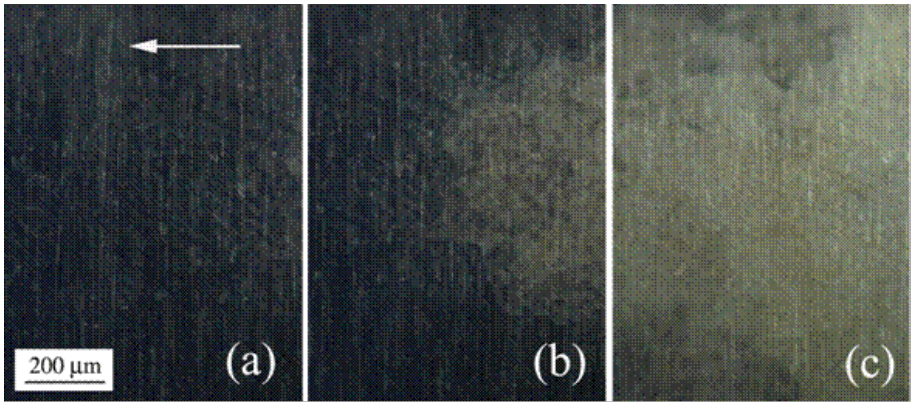

Figure 59. **High-magnification images of Area T in Fig. 58a showing different outer-surface areas of the ZLU#143 sample: (a) lustrous black area, (b) transition area from black-to-yellow, and (c) yellow area.**

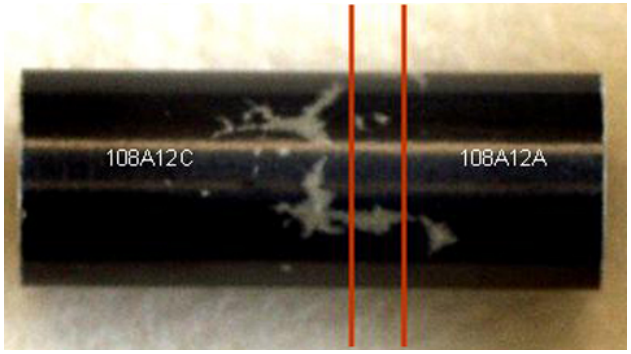

(a)

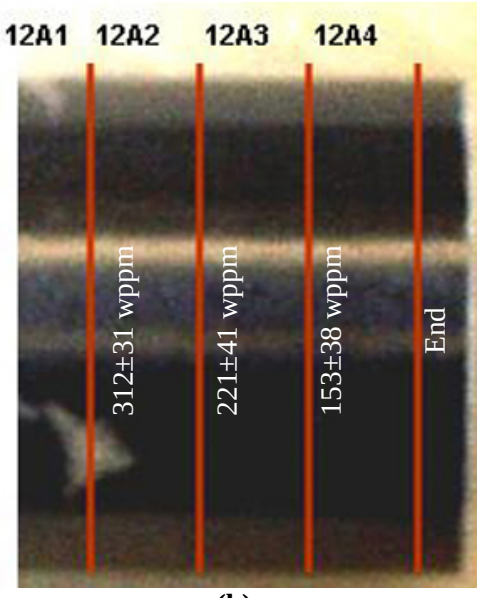

(b)

Figure 60. **Axial distribution of hydrogen pickup for the ZLU#142 test sample.**

The 2800-s breakaway time for temperature-cycled ZIRLO is comparable to the breakaway time for a pre-scratched ZIRLO sample oxidized under isothermal conditions at 970°C [1]. In the earlier testing, a 20-μm-deep, rectangular-shaped scratch was machined along the length of the outer surface. After oxidation, a yellow region was observed along the middle third of the scratch. The average hydrogen pickup at the sample mid span was 44 wppm. However, the local hydrogen pickup under the yellow scratched region was 440 wppm. Based on the large hydrogen-pickup data set for smooth cladding, it was estimated that the sample would have picked up >200-wppm hydrogen by ≈2800 s. Thus, the effects of temperature cycling on breakaway oxidation time appear to be comparable to the effects of a machined surface scratch. Each of these conditions reduced the average breakaway time by about 300 s, which is at the lower end of the data scatter.

The total data set for oxidation under isothermal and transient conditions, with long-time hold temperatures in the range of 970 to 985°C, is shown in Fig. 61. As can be seen, this larger data base confirms our earlier conclusion that breakaway oxidation of ZIRLO occurs at 3100±300 s (as determined by pickup of ≈200 wppm hydrogen) in the temperature range of 970 to 985ºC.

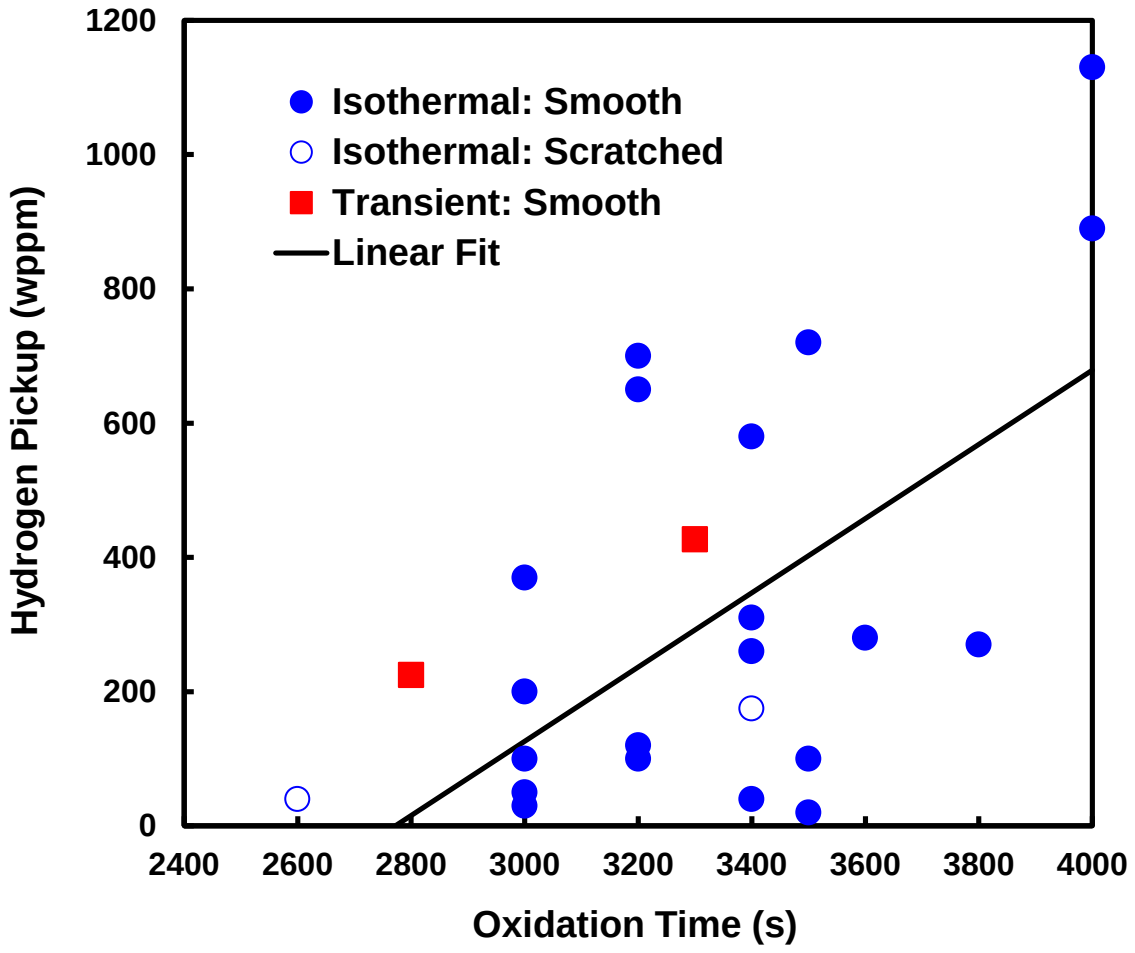

Figure 61. **Hydrogen-pickup vs. time data for ZIRLO oxidized in steam at 970−985°C: smooth samples (isothermal), pre-scratched (≈20-μm depth) samples (isothermal), pre-oxidized samples (isothermal) and smooth samples (transient) oxidized with five cycles from 930 to 1030°C for 400 s and 980°C isothermal temperature.**

5 BEHAVIOR OF BALLOONED AND RUPTURED CLADDING

Long, pressurized cladding samples subjected to a LOCA transient can balloon and rupture. Such samples will contain local areas that exhibit considerable axial variation in diameter, wall thickness, hydrogen content, and oxidation level. A substantial circumferential variation in wall thickness and oxidation level will also occur in cross sections containing a rupture opening [1]. Consistent with current licensing requirements in 10 CFR 50.46, all CP-ECR values reported in this section are for the rupture-region cross section with the minimum cross-section averaged wall thickness prior to oxidation.

Two 4-point bend tests (4-PBTs) were conducted previously at RT on as-fabricated Zry-2 specimens after LOCA integral testing [1]. Inferences were made from those results, but not enough tests were conducted to determine quantitative trends and effects of 4-PBT temperature. More recently, a large number of post-rupture 4-PBTs were performed at 135°C on ZIRLO specimens to evaluate results quantitatively.

LOCA integral tests were conducted with as-fabricated (AF) and pre-hydrided (PH) ZIRLO-2010 cladding samples. Methods for conducting these tests, along with sample geometry, are described in Section 2.5 and in Ref. 1. Following LOCA oxidation, 4-PBTs were conducted to determine the maximum bending moment (measure of strength), the applied energy prior to failure (measure of toughness), and the offset displacement (measure of plastic deformation). It was anticipated that all three of these metrics would decrease with increasing oxidation level and pre-test hydrogen content. Of particular interest was the determination of whether or not the embrittlement limits established for non-deformed cladding (see Fig. 25) would be sufficient to protect the ballooned and ruptured region from excessive degradation. The results of this investigation were documented in Ref. 5 for AF ZIRLO cladding. However, detailed results from LOCA integral tests (e.g., temperature and pressure histories) and 4-PBTs (e.g., load-displacement curves) were not documented in Ref. 5. This section presents a comprehensive documentation of test results for AF and PH ZIRLO cladding samples.

The testing sequence consisted of thermal and metallurgical benchmark tests, scoping tests generally conducted without quench and with variable internal gas pressures and oxidation test times, and data-generation tests. Relevant raw data are presented in the Appendices: (A) Temperature and Pressure Histories, (B) Axial Profiles of Post-Rupture Cladding Strains, (C) Photographs of Post-Oxidation LOCA Integral Samples, (D) 4-PBT Load-Displacement Curves, and (E) Photographs of Post-Bend LOCA Integral Samples.

Symbols used to describe measured and calculated geometrical parameters are defined as they are used throughout Sections 5.1−5.3. As a convenience to the reader, these symbols are also defined here with some of the more complicated ones illustrated in the Fig. 62 schematic. Dimensions of the AF cladding are used as reference pre-test parameters. Nominal dimensions for this cladding are indicated by the subscript "i" for initial condition: 9.50-mm outer diameter (D_{oi}), 0.57-mm wall thickness (h_i), 29.85-mm outer-wall circumference (C_{oi}), 28.05-mm mid-wall circumference (C_{mi}), and 16.0-mm^2 cross-sectional area (A_i). With the exception of A_i, these parameters change significantly during ballooning and rupture (R). Routinely measured and/or calculated parameters for the rupture cross section with the largest rupture strain are the (see Fig. 62): outer-surface diameter (D_{maxR}) measured from the rupture tips to the back of the rupture cross section, width (δ_R) of the rupture opening, outer-surface diameter (D_{minR}) measured at an orientation perpendicular to D_{maxR}, outer-surface circumference (C_{oR}) excluding δ_R, and mid-wall circumference (C_{mR}) excluding δ_R. The parameter D_{avgR}, which is used in correlations, is simply the average of D_{maxR} and D_{minR}.

$$D_{avgR} = \frac{D_{minR} + D_{maxR}}{2}$$

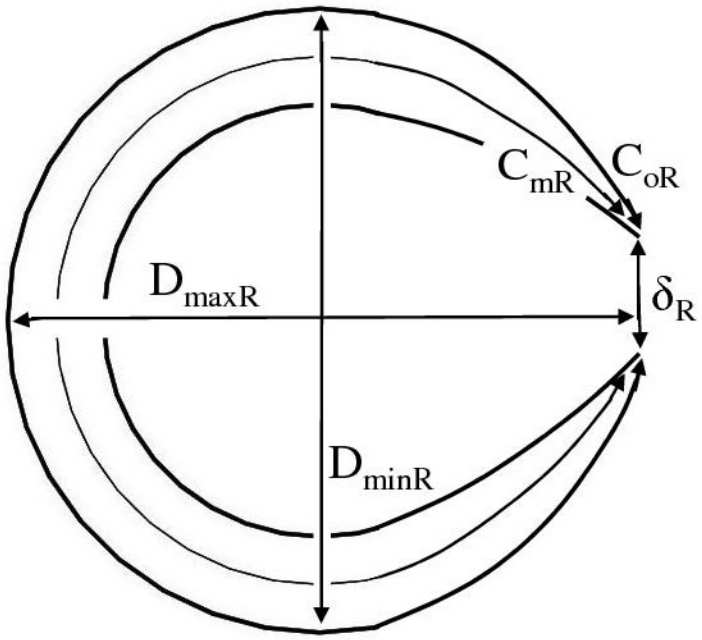

Figure 62. Schematic of ballooned and ruptured cladding, which includes the parameters routinely measured and/or calculated following a LOCA integral test. The sketch is not to scale.

5.1 Thermal and Metallurgical Benchmark Test Results

Prior to conducting tests with ZIRLO cladding, four tests were run with zirconia-filled Inconel tubing to optimize temperature control parameters for ramp rate and hold temperature, to examine the effects of sample axial location within the furnace, and to examine the effects of temperature ramp rate on axial and circumferential temperature variations during the heating ramp and the hold time. These tests were conducted with temperature ramp rates of 5°C/s and 10°C/s and hold temperatures of 1200°C and 1050°C. Multiple tests were conducted with a single Inconel tube because of its relatively low oxidation rate in steam. The TC positions and orientations were the same as used in the testing previously reported [1]. Relative to the sample mid-span, TCs were positioned at 0° orientation and axial locations of 51 mm, 0 mm, and -51 mm. In addition, a 4th TC was located at the mid-span (0 mm) at the 180° orientation. The reference heating rate was chosen to be 5°C/s because better temperature uniformity was achieved at this heating rate. The reference cooling rate was maintained at 3°C/s between the end of the hold time and 800°C. Also, because of the need for data at or near the licensing limit, 1200°C was chosen as the reference hold temperature. Given these test parameters, it was possible to conduct ramp-to-rupture tests at ≈0% CP-ECR and oxidation tests with ballooned-and-ruptured cladding at >10% CP-ECR. For ballooned-and-ruptured ZIRLO cladding with reduced wall thickness prior to oxidation, >10% CP-ECR was realized for temperature histories with essentially zero hold time because of oxidation during the heat-up and cool-down phases of the tests.

The 1st benchmark test with ZIRLO cladding (OCZL#5) was conducted without internal pressurization and without quench. The temperature history for this test is shown in Fig. A.1. During the temperature ramp, the variations in TC readings were quite small at average temperatures of about 700°C, 800°C, and 900°C. The programmed hold time was 60 s for this test. However, the temperature controller is programmed to slow down the ramp rate at about 1180°C as 1200°C is approached in order to avoid overshoot. On the average, the target temperature is reached after about 20 s to 25 s at the slow ramp rate. The average hold temperature was 1206±9°C about half way through the programmed 60-s hold time. These temperature values are well within acceptable ranges for LOCA integral tests.

The metallurgical part of the benchmarking consisted of measuring the outer-surface oxide layer thickness values at two axial locations and comparing them to the CP-predicted values for the corresponding temperature histories. On the basis of three measurements at each of eight circumferential locations at the mid-span (0 mm) and at 51 mm above the mid-span (location of control TC), the corresponding oxide layer thickness values were 41±2 μm and 40±3 μm, respectively, where the ± values represent one standard deviation in the data. The CP-predicted values for oxide layer thickness values at these locations were 39 μm and 42 μm for the two mid-span TC thermal histories and 38 μm for the TC history at 51 mm above the mid-span. The average of the 16 (times 3) data points was 40±2 μm. The average CP-predicted value for the four TC readings was also 40±2 μm. The oxide-layer-thickness data have an uncertainty of about ±1 μm. Thus, the agreement between measured and calculated values for oxide layer thickness was excellent, which confirmed the accuracy of the temperature measurements.

The 2nd thermal-metallurgical benchmark test (OCZL#6) was conducted with AF ZIRLO pre-pressurized to 8.28 MPa (1200 psig) and subjected to a 60-s hold time at a target hold temperature of 1200°C. It was anticipated that temperature uniformity would be good prior to ballooning initiation and that temperature variation would be more substantial after rupture. Ballooning and rupture cause a significant change in geometry, and they challenge the integrity of welded TCs. The temperature-pressure histories are shown in Fig. A.2, and a post-oxidation-test photograph is shown in Fig. C.1. Just prior to rupture, the mid-plane TC at 180° began to read higher than the other TCs. Figure C.1 shows that the rupture occurred at a location between the mid-span and the lower TC at -51 mm. The average rupture temperature was 750±30°C, with most of the variation due to the high reading of the 0-mm/180° TC. Half way through the hold time, there was excellent temperature uniformity for the three TCs at 0° orientation (1204±7°C). However, the corresponding 0-mm/180° TC reading was unacceptably high (1276°C). The average temperature for the effective hold time (82 s) was 1219±33°C. When one TC behaves significantly different from the other TCs, there is a distinct possibility that the measurement is unreliable. Measurements of outer-surface oxide-layer thickness at the mid-span cross section were used to confirm that all four TC readings were reliable. Oxide-layer thickness values varied from 50 μm at the orientation of the 0-mm/180° TC to 36 μm at the orientation of the 0-mm/0° TC. Corresponding CP-predicted values were 52 μm and 39 μm. Although the 0-mm/180° TC reading was unacceptably high from a temperature uniformity viewpoint, the accuracy of the temperature readings was confirmed.

Axial profiles of cladding diametral strain at two orientations are shown in Fig. B.1 for the post-oxidation OCZL#6 test sample. The designated orientations of 0° and 90° differ from TC orientations and are defined as follows: 0° corresponds to the caliper-measured diameter (D_{max}) along the length of the sample at the orientation defined by the line from the rupture-opening mid-span to the back of the cross section containing the widest rupture opening (δ_R) and 90° corresponds to the caliper-measured diameter (D_{min}) at an orientation perpendicular to D_{max}. Peak values within the cross section containing δ_R are labeled as D_{maxR} and D_{minR}. The average of these diameters, which is used in Section 5.3, is D_{avgR}. In Fig. B.1, as well as in subsequent Appendix B figures, the differences (ΔD_{max} and ΔD_{min}) between the post- and pre-test outer diameters were normalized to the pre-test outer diameter (D_{oi}) to give the plotted diametral

strains ($\Delta D_{max}/D_{oi}$ and $\Delta D_{min}/D_{oi}$). The diametral strains shown in Fig. B.1 are useful for identifying the presence of a secondary balloon at an axial location between the primary balloon and the top of the sample and for identifying a tertiary balloon near the top of the sample (i.e., gas-plenum region).

The presence of secondary and tertiary balloons observed in Fig. B.1 was undesirable, but it was decided to proceed with scoping tests to determine if these were trends or abnormalities. After completion of scoping and data-generation tests with AF ZIRLO cladding, additional benchmark tests (OCZL#36 and OCZL#37) were conducted with AF ZIRLO prior to testing PH ZIRLO. The temperature and pressure histories for these tests are shown in Figs. A.22 and A.23. Test OCZL#36 was essentially a repeat of OCZL#6, except that the sample length was increased from 305 mm to 318 mm to move the plenum region outside the heating zone of the furnace and the axial and circumferential positions for the TCs were modified. These modifications followed the scoping tests and are discussed in Section 5.2. Thermal benchmark results for test OCZL#37 are presented in the following paragraph.

As indicated in Fig. A.23, the longer hold-time test (150-s hold, 172-s effective hold) gave an average hold temperature of 1211±16°C. Although no TC was located at the sample mid-span, metallographic examination was performed to determine the outer-surface oxide layer thickness at this location. On the basis of images at 10 circumferential locations, the oxide layer thickness was measured to be 52±7 μm. The CP-predicted oxide layer thicknesses for the TC measurements above and below the mid-span were 51±3 μm. This good agreement justified the subsequent (for data-generation tests) relocation of the two TCs near the sample mid-span to locations above and below the mid-span with angular orientations of 0° (upper), 90° (lower), 180° (upper control TC), and 270° (lower). Also (see Fig. B.20), subsequent movement of the plenum region to a location above the furnace heating zone eliminated the tertiary balloon observed in the OCZL#6 sample.

5.2 Scoping Test Results

Seven scoping tests were conducted to determine the effects of internal gas pressure on the: (a) rupture strain ($\Delta C_{mR}/C_{mi}$) and temperature (T_R), (b) minimum wall thickness (h_R) for CP-ECR calculations, (c) TC durability and reliability, (d) temperatures (T_h and T_{he}) during programmed (t_h) and effective (t_{he}) hold times, and (e) 4-PBT performance. Four ramp-to-rupture tests, for which the furnace was shut down after rupture, were conducted. Three additional tests were heated to ≈1200°C for 60 s to 70 s, cooled at 3°C/s to about 800°C, and further cooled without quench. Table 28 summarizes test conditions and results for the scoping tests.

Ramp-to-rupture tests

Ramp-to-rupture tests were conducted with 300°C fill pressures of: 400 psig, 600 psig, 1400 psig, and 1600 psig. The determination of maximum rupture strains ($\Delta C_{mR}/C_{mi}$) and corresponding h_R is documented in Section 5.3. Data trends are comparable to what has been observed for AF Zry-4 [32]: (a) high rupture strains at 715°C (likely close to the temperature at which the peak strain is observed to occur in the alpha phase), (b) low rupture strains at 845°C (close to the mixed alpha-beta phase temperature at which the minimum strain is observed to occur) and (c) increasing rupture strains at >845°C.

Three ramp-to-rupture samples were subjected to 4-PBTs. None of the samples cracked during the 14-mm displacement, indicating high values for strength, absorbed energy, and plastic deformation for non-oxidized AF ZIRLO. The degree of out-of-plane bending and secondary-tertiary ballooning did vary from sample to sample following the ramp-to-rupture tests. For test OCZL#11 pressurized to 1400 psig,

Table 28. Summary of results for LOCA integral and post-LOCA-bend scoping tests with AF ZIRLO cladding. Fill pressures were at 300°C. Oxidation tests were conducted with a target hold temperature of 1200°C and without quench. 4-PBTs were conducted at 135°C and 2 mm/s displacement rate to 14-mm maximum displacement. Failure locations are referenced to the mid-span of the rupture opening.

Test ID OCZL#	Fill Pressure, psig (MPa)	$\Delta C_{mR}/C_{mi}$,% (T_R, °C)	h_R, mm	CP-ECR, % (T_{he}, °C)	Stress in Rupture Node	Failure Location	Max. Bending Moment, N•m	Max. Energy, J	Offset Displace., mm
7	800 (5.52)	**22** (810±30)	0.47	15.7 (1226±28)	–	–	–	–	–
8	600 (4.18)	22 (845±25)	0.47	0 (–)	Maximum tension	No cracking	20.9	>8.4	>7.7
9	400 (2.76)	33 (875±15)	0.43	0 (–)	Maximum tension	No cracking	20.6	>8.3	>7.8
10	1600 (11.0)	70 (715±10)	0.33	0 (–)	Maximum tension	No cracking	19.7	>7.7	>7.1
11	1400 (9.66)	**40** (750)	0.41	0 (–)	–	–	–	–	–
12	1000 (6.90)	33 (805±20)	0.43	14.5 (1191±17)	Maximum compression	-40 mm +33 mm	10.5	0.78	0.33
13	1200 (8.28)	42 (741±15)	0.40	14.4 (1162±21)	Maximum tension	0 mm	8.8	0.58	0.13

Figures B.6 (profilometry) and C.6 (photographs) show a pronounced secondary balloon that occurred near the top of the sample with a strain comparable to that of the primary balloon. A smaller tertiary balloon occurred below the primary balloon. Figure C.6a also shows the out-of-plane bending of the sample, which would cause alignment issues during the 4-PBT. On the basis of the limited results for ramp-to-rupture tests, 600-psig fill pressure at 300°C was chosen as the reference pressure for tests designed to achieve oxidation levels of 10% to 12% CP-ECR because of the relatively high h_R value for this pressure.

Metallographic examination was performed on the OCZL#11 sample to determine the rupture node cross-section shape, variation in cladding thickness around the circumference, and circumferential strain at the cladding mid-plane. Figure 63 shows the cross section at the rupture mid-span location. The circumference (C_{mR}) around the cladding mid-wall was 39.3 mm. Relative to the mid-wall circumference (C_{mi} = 28.05 mm) for AF ZIRLO, the rupture strain ($\Delta C_{mR}/C_{mi} = [C_{mR} - C_{mi}]/C_{mi}$) was 40%.

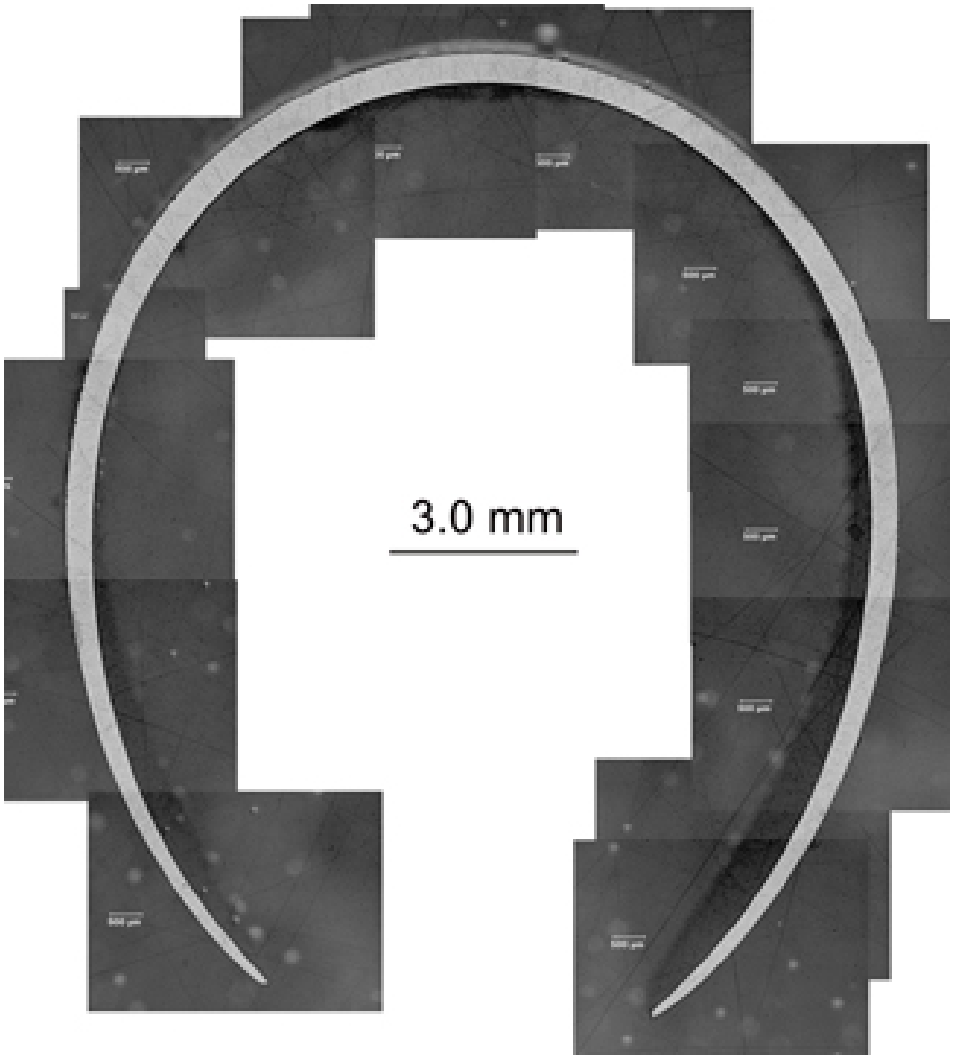

Figure 63. Image of ramp-to-rupture test OCZL#11 sample cross section through rupture-node mid-span. Rupture width (δ_R) was 6.2-mm and $\Delta C_{mR}/C_{mi}$ was 40%.

Scoping oxidation test results

Three oxidation tests were conducted at 300°C fill pressures of 800 psig (OCZL#7), 1000 psig (OCZL#12) and 1200 psig (OCZL#13) Temperature and pressure histories are presented in Figs. A.3, A.8, and A.9, respectively. For the OCZL#7 test sample, three of the four TCs survived ballooning and rupture. Half way through the 60-s hold time, the average of the mid-span and top TC readings, both at 0° orientation, was 1211±13°C. However, the temperature recorded by the mid-span TC at 180° (close to the edge of the rupture opening) was considerably higher (1260°C). The profilometry results shown in Fig. B.2 indicated a relatively small secondary balloon near the top of the sample. Low-magnification metallographic examination was performed to determine the rupture cross-section shape and the cladding mid-wall circumference at the mid-span of the rupture node. Figure 64 shows the rupture cross-section, along with the variation in metal wall thickness from very thin at the rupture tips to relatively thick at the back of the rupture node. The shape of the OCZL#7 sample is similar to the shape of the OCZL#11 sample shape shown in Fig. 63. However, the rupture strain (22%) for the OCZL#7 sample was lower.

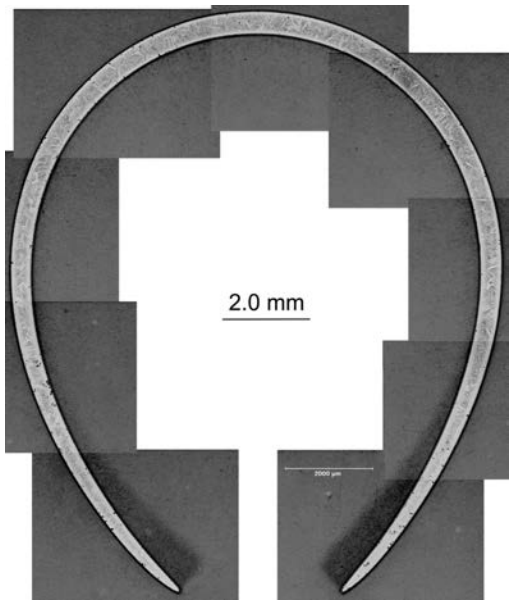

Figure 64. Low magnification image of the cross section through rupture-opening mid-span for the OCZL#7 sample with 22% rupture strain prior to 16% CP-ECR oxidation.

For the OCZL#7 sample, as well as the OCZL#11 sample, the cladding wall thickness varied from very small at the rupture tips to a maximum value near the back (top of figure) of the rupture node. In the Fig. 64 orientation, the thin rupture tips would be subjected to maximum axial tensile stresses in response to 4-PBT loading while the thicker back region of the cross section would be subjected to maximum compressive stresses. This reference orientation is conducive to crack initiation at the brittle rupture tips and rapid crack growth through at least half of the cross section. Whether or not the crack would blunt in the thicker “more ductile” back half of the cladding would depend on the fracture toughness of the material.

For the OCZL#12 test, all four TCs behaved well up until rupture. The temperature readings for the mid-span TC at 0° were unreliable after rupture. It is surprising that the control TC (51 mm/0°) behaved as well as it did. Figure C.7 shows that the top of the rupture tip was very close to this TC and at the same

orientation. Better temperature uniformity was achieved during the hold time for the three remaining TCs. Half way through the 60-s hold time, the average hold temperature was 1196±16°C, which is acceptable. The CP-ECR was about 15% (14.5%). However, as shown in Fig. B.7, there was a pronounced secondary balloon about 51 mm below the mid-span, which perhaps explains the failure of the TC at this location. The average diametral strain (23%) at this location was large compared to the average diametral strain (39%) at the rupture mid-span. Also, a tertiary balloon was observed near the top of the sample (close to the plenum region).

Following oxidation and cooling, the OCZL#12 sample was subjected to a "reverse" 4-PBT at 135°C with the maximum axial tensile stress occurring at the back of the rupture cross section and with the rupture tips in axial compression. The sample failed at two locations between the rupture edges and the balloon necks (see Fig. E.2) at relatively low failure energy and offset displacement compared to the ramp-to-rupture samples. The bending moment just prior to failure was about half of what was achieved by the ramp-to-rupture samples prior to test termination. Additional post-bend characterization was performed to determine the axial profile of hydrogen content (also known as secondary hydriding). Figure 65 shows the measured hydrogen content and CP-ECR at the rupture mid-span, as well as the hydrogen contents and measured ECRs (based on metallographic examinations) at the two failure locations. The hydrogen content at the rupture mid-span was only 25 wppm, as compared to 22 wppm for AF ZIRLO. As anticipated, the hydrogen pickup at the rupture mid-span was insignificant. However, the hydrogen content was 1700 wppm at the two failure locations. Figure 66 shows the hydrogen concentration vs. axial location relative to the rupture mid-span location, along with the hydrogen peaks (≈2400 wppm) near the balloon necks.

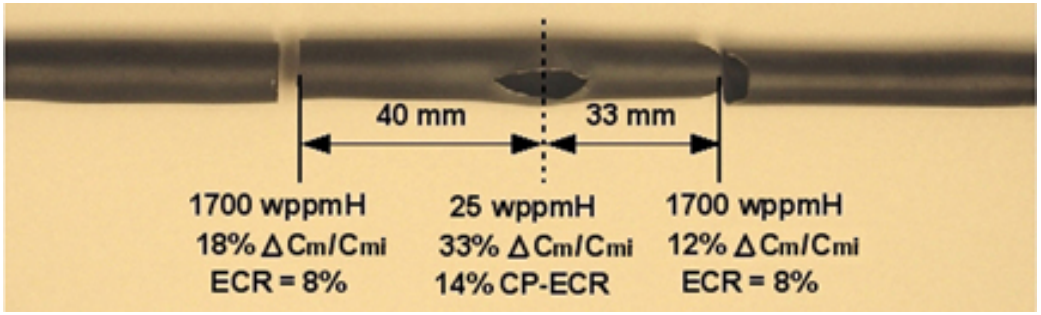

Figure 65. Hydrogen content, ballooning strain, and oxidation level at rupture mid-span (CP-ECR) and failure locations (measured ECR) for the OCZL#12 sample after the reverse 4-PBT.

For the OCZL#13 test, the sample was moved 13 mm higher in the furnace, the 300°C internal pressure was increased to 1200 psig and the hold time was increased to 70 s. The goals were to generate a 4-PBT sample exposed to oxidation temperatures closer to 1200°C and had less secondary ballooning. Previous experience with TC location and orientation suggested that circumferential variations in temperature were greater than axial variations. Thus, TCs were oriented at 4 circumferential orientations and positioned at ±51 mm from the center of the sample: 0° and 180° (both upper) and 90° and 270° (both lower). Figure A.9 shows that all four TCs responded reliably throughout the ramp, hold time, and cool down. The average temperature of the control TC was 1200°C during the 70-s hold time. However, the average temperature of the other three TCs was considerably lower (1150±8°C) during the same time period, such that the overall average was only 1162±21°C during the 92-s effective hold time. These results suggested

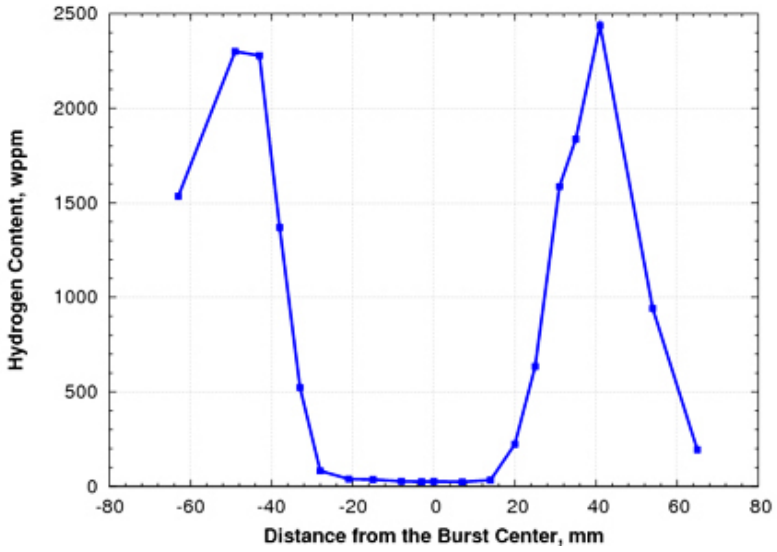

Figure 66. Axial profile of hydrogen content for the OCZL#12 sample following oxidation to 14.5% CP-ECR.

that additional refinements in axial location within the furnace were required before conducting data-generation tests. Some improvement was observed in the diametral strain profile. Movement of the plenum region about 13 mm higher appeared to eliminate secondary and tertiary ballooning near the top of the sample (see Fig. B.8). Another improvement was that no out-of-plane bending was observed, which is desirable for the 4-PBTs. Table 28 summarizes the results for the 4-PBT. The 4-PBT sample failed abruptly (see load-displacement curve in Fig. D.5) at the rupture mid-span (see Fig. E.3) with little evidence of offset displacement (0.13% measured compared to ≥0.1% criterion for plastic deformation).

Results from the scoping tests were used to refine sample length, axial position of the sample within the furnace, temperature control parameters, and TC locations. With respect to sample length, this was increased from 305 mm to 318 mm in order to relocate the short plenum region above the uniform heating zone of the furnace. The benchmark and scoping tests were also used to establish reference 300°C internal pressures of 600 psig and 1200 psig for the data-generation tests.

5.3 Determination of Rupture Strains and Post-Rupture Cladding Wall Thickness

For ballooned and ruptured cladding, the CP-ECR is based on the predicted average wall thickness (h_R) prior to oxidation for the cross section containing the rupture node. The instructions given in 10 CFR 50.46 for calculating h_R are: "…the unoxidized cladding thickness shall be defined as the cladding cross-sectional area, taken at a horizontal plane at the elevation of rupture…divided by the average circumference at that elevation. The average circumference does not include the rupture opening."

It is common to report rupture strain as the maximum post-test outer-surface circumference (C_{oR}) of non-oxidized cladding compared with the pre-test outer-surface circumference (C_{oi}):

$$\Delta C_{oR}/C_{oi} = (C_{oR} - C_{oi})/C_{oi} \quad (18)$$

To be consistent with 10 CFR 50.46, as well as to improve the accuracy in h_R determination, the mid-wall circumferential strain is used in the current work to calculate h_R. However, the measurement of cross-sectional area would be tedious for the cross sections shown in Figs. 63 and 64. A good approximation for determining h_R for CP-ECR calculations is:

$$h_R = h_i/(C_{mR}/C_{mi}) = h_i/(1 + \Delta C_{mR}/C_{mi}) \quad (19)$$

where h_i is the pre-test wall thickness (0.57 mm) and the subscript "m" indicates mid-wall values.

Equation 19 is consistent with observations from pressurized-tube tests for isotropic materials: (a) the axial plastic strain is negligible and (b) the cross-sectional area of the expanded tube is constant and equal to the pre-test cross-sectional area. For the AF ZIRLO cladding used in this study, the cross-sectional area (A_i) was 16.0 mm^2 and the outer and mid-wall circumferences were 29.85 mm and 28.05 mm, respectively. The product of C_{mi} and h_i agrees quite well with A_i, while $C_{oi} \times h_i$ over-predicts A_i by 6%. Although the expansion of the cross section with no change in area thins the wall and results in better agreement between C_{oR} and C_{mR} (e.g., 2% difference at 60% strain), we will use the more accurate mid-wall values.

The initial approach used in the current work was to develop a correlation for post-rupture circumference (i.e., C_{mR}) as a function of easily measureable parameters at the rupture mid-span: D_{minR}, D_{maxR}, D_{avgR}, and δ_R. During efforts to develop such a correlation, Argonne modeled the rupture-region cross section with two basic shapes with the same cross-sectional area: a partial circle and a partial ellipse with the arc length of the truncated portion associated with a cord of length δ_R subtracted from the full circle or ellipse. Neither approach gave good agreement with C_{mR} data determined from low-magnification images (e.g., see Figs. 63 and 64) or determined from direct measurements of C_{oR}. This is partly due to the wide range of rupture cross-section shapes and rupture-opening widths. Thus, it was determined that an empirical approach for determining C_{mR} from measured parameters would yield better results than a semi-analytical approach.

In addition to shapes shown in Figs. 63 and 64, Fig. 67 shows the post-oxidation, rupture mid-span cross section for data-generation test OCZL#18, which had a measured mid-wall circumference of 40 mm (43% rupture strain) and a 5.4-mm rupture opening. Data from these images were very useful in developing the empirical correlation because of the ranges of C_{mR} (34−40 mm) and δ_R (3.7−6.2 mm) values.

Concurrent with the LOCA integral testing at Argonne, Studsvik conducted similar tests with AF ZIRLO [33] and ZIRLO from fuel rods irradiated to high burnup [34]. Metallographic results for Tests 185 (AF ZIRLO) and 192 (irradiated ZIRLO with ≈230 wppm hydrogen) were analyzed by Argonne [35]. Rupture cross-section shapes for these two tests are shown in Figs. 68 and 69. The addition of the Studsvik data for correlation development expanded the databases for C_{mR} and δ_R to (34.1−43.5 mm) and (3.0−7.8 mm), respectively.

In addition to five mid-wall circumferences measured from low-magnification images, Argonne measured the post-oxidation C_{oR} values for seven AF and six PH ZIRLO test samples. The measurements were performed with a relatively stiff, thin string. The mid-wall circumference was calculated by solving a quadratic equation that included the subtraction of wall thickness from the diameter of an equivalent hollow-cylinder cross section. The quadratic equation comes from combining Eq. 19 with:

$$C_{mR} = C_{oR} - \pi h_R \quad (20)$$

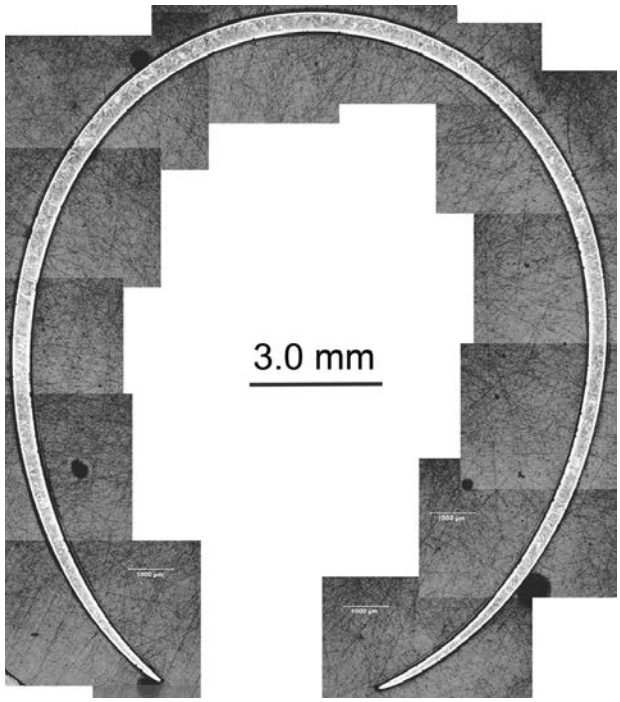

Figure 67. Low magnification image of cross section through rupture mid-span of the OCZL#18 test sample with 43% mid-wall circumferential strain oxidized to 12% CP-ECR.

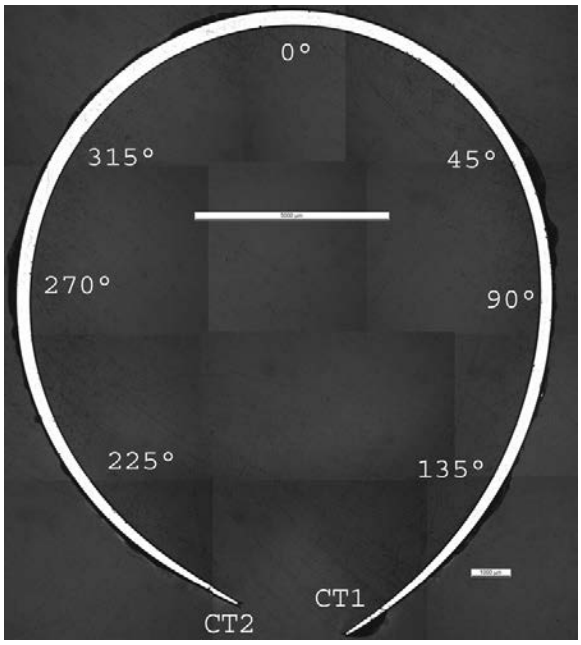

Figure 68. Rupture cross section for Studsvik Test 185 with AF ZIRLO sample pressurized to 1200 psig at 300°C.

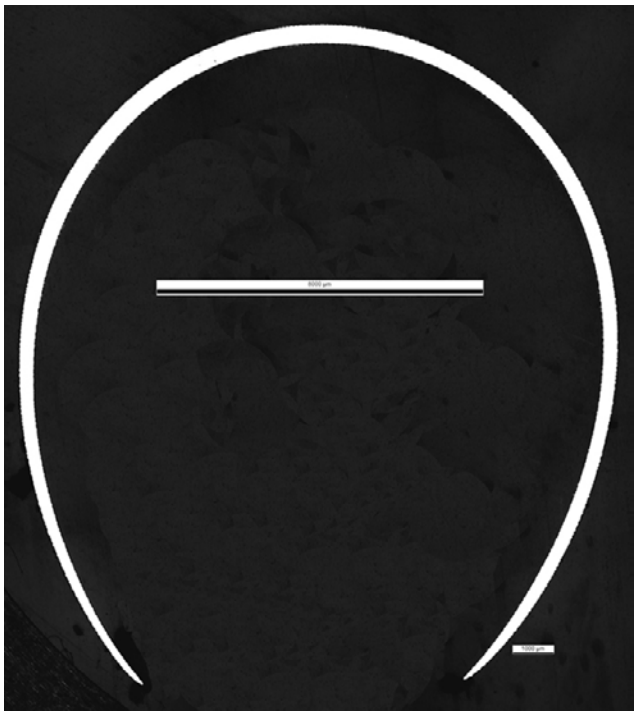

Figure 69. Rupture cross section for Studsvik Test 192 with irradiated ZIRLO pressurized to 1200 psig at 300°C. The central scale bar is 8 mm.

For large rupture strains, the mid-wall circumference was only 2−3% less than the outer-surface circumference. The oxide layer thickness, which has a very small effect on outer-surface circumference, was not accounted for in this correction.

Complete data sets are listed in Table 29. These data were used to develop a correlation for C_{mR} as a function of measured D_{avgR} and δ_R. The best linear fit to the decrease in $C_{mR}/(\pi D_{avgR})$ with the increase in δ_R/D_{avgR} is given by:

$$C_{mR}/(\pi D_{avgR}) = 1.00 - 0.207\ (\delta_R/D_{avgR}) \quad (21)$$

Although Eq. 21 is the best fit to both the AF and PH ZIRLO data, it is not accurate as δ_R/D_{avgR} approaches zero. For ballooned cladding outside the rupture region, δ_R is zero and $C_{mR}/(\pi D_{avgR})$ should be <1. Also, for very small values of δ_R and large values of D_{avgR}, $C_{mR}/(\pi D_{avgR})$ should be <1.

As is shown in Fig. 70, the data points for PH ZIRLO are higher, relative to predicted values, than the data points for AF and irradiated ZIRLO. An alternate fit to the AF and irradiated ZIRLO data is given by Eq. 22 and shown as the solid line in Fig. 70.

$$C_{mR}/(\pi D_{avgR}) = 0.980 - 0.225\ (\delta_R/D_{avgR}) \quad (22)$$

As the correlation is needed in the current work only for AF ZIRLO samples for which no direct circumferential measurements were made, Eq. 22 was chosen to calculate rupture strain and minimum cladding wall thickness for these samples. The correlation can be rewritten as:

Table 29. Summary of data for cross sections at rupture mid-spans for ZIRLO samples subjected to ramp-to-rupture tests and samples subjected to LOCA oxidation tests.

OCZL# ID	Cladding	C_{mi}, mm	D_{avgR}, mm	δ_R, mm	C_{oR}, mm	C_{mR}, mm	h_R, mm
7	AF	28.05	12.45	3.7	–	34.1[b]	0.47
11	AF	28.05	14.26	6.2	–	39.3[b]	0.41
18	AF	28.05	14.60	5.4	–	40.0[b]	0.40
185[a]	AF	28.05	14.85	3.0	–	43.5[b]	0.37
192[a]	Irrad.	≈28	15.64	7.8	–	41.0[b]	0.38
25	AF	28.05	14.95	8.7	41.0	39.7[c]	0.40
29	AF	28.05	14.82	5.9	43.0	41.8[c]	0.38
30	AF	28.05	14.51	4.5	41.0	39.7[c]	0.40
32	AF	28.05	14.90	7.2	43.0	41.8[c]	0.38
36	AF	28.02	15.04	10.2	44.0	42.8[c]	0.37
37	AF	28.02	14.35	5.2	40.9	39.7[c]	0.39
43	AF	27.99	14.04	6.1	43.0	42.8[c]	0.38
39	PH	28.02	13.98	1.9	45.2	44.1[c]	0.36
40	PH	27.99	13.51	4.2	42.3	41.1[c]	0.39
41	PH	28.02	13.83	3.0	44.8	43.6[c]	0.37
42	PH	28.02	14.88	1.2	49.0	48.0[c]	0.33
44	PH	27.99	14.25	8.2	44.8	43.6[c]	0.37
45	PH	27.99	14.94	5.0	48.0	46.9[c]	0.34

[a]Studsvik tests [33−35].
[b]Measured from low-magnification met images.
[c]Calculated from C_{oR} data.

$$C_{mR} = [0.980 - 0.225\ (\delta_R/D_{avgR})]\ (\pi D_{avgR}) \quad (23)$$

Figure 71 shows the comparison of the C_{mR} values determined from measurements and the calculated values (from Eq. 23). Given the inherent scatter in the database, the agreement is reasonably good for 10 data points while the correlation-predicted values are low by about 4 mm for two data points.

Table 30 lists the test ID#, initial fill pressure at 300°C, calculated or measured (in **bold** font) rupture strain, rupture temperature, average wall thickness calculated from rupture strain, and CP-ECR for tests conducted by Argonne with AF and PH ZIRLO. The CP-ECR values agree to within a fraction of a percent to previously published values [5] based on an older correlation. The CP-ECR values should be rounded to the nearest percent, as temperatures for calculating CP-predicted weight gain and wall thickness values are not accurate enough to justify three significant figures for CP-ECR. The purpose of listing CP-ECR values in Table 30 to the nearest 0.1% is to distinguish data points in subsequent plots of parameters vs. CP-ECR.

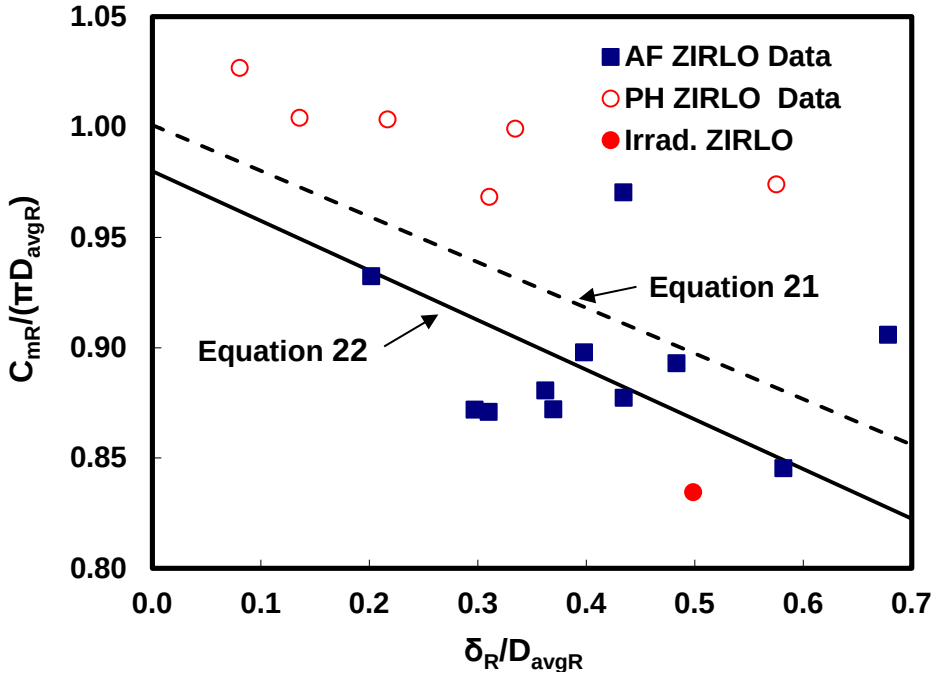

Figure 70. **Variation of $C_{mR}/(\pi D_{avgR})$ with δ_R/D_{avgR} for AF, PH, and irradiated (Irrad.) ZIRLO subjected to pressurized ramp-to-rupture tests and LOCA oxidation tests.**

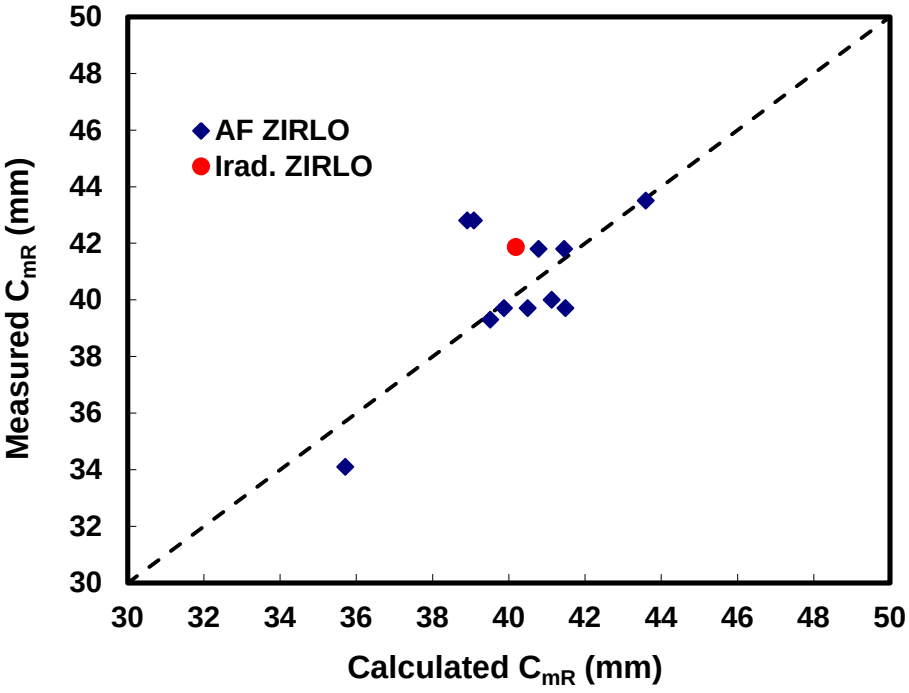

Figure 71. **Measured and calculated (Eq. 23) mid-plane circumferences in the rupture region for AF and irradiated (Irad.) ZIRLO following ramp-to-rupture and oxidation tests.**

Table 30. Internal pressure (P_i[300°C]), rupture strain ($\Delta C_{mR}/C_{mi}$, measured values in bold font), rupture temperature (T_R), wall thickness (h_R), and CP-ECR for AF and PH ZIRLO tests.

OCZL# (Cladding)	P_i(300°C), psig	$\Delta C_{mR}/C_{mi}$, %	T_R, °C	h_R, mm	CP-ECR, %
6 (AF)	1200	42	750±30	0.40	18.2
7 (AF)	800	**22**	810±30	0.47	15.7
8 (AF)	600	22	845±25	0.47	≈0
9 (AF)	400	33	875±15	0.43	≈0
10 (AF)	1600	70	715±10	0.33	≈0
11 (AF)	1400	**40**	750	0.41	≈0
12 (AF)	1000	33	805±20	0.43	14.5
13 (AF)	1200	42	741±15	0.40	14.4
14 (AF)	1200	48	735±6	0.39	18.3
15 (AF)	1200	52	755±23	0.37	18.4
16 (AF)	1200	35	734±15	0.42	13.9
17 (AF)	1200	**45**	750±17	0.39	12.7
18 (AF)	1200	**43**	748±4	0.40	12.3
19 (AF)	600	25	840±12	0.46	17.3
21 (AF)	600	28	850±10	0.44	10.6
22 (AF)	600	23	837±12	0.46	11.6
25 (AF)	1200	**42**	757±21	0.40	16.1
26 (AF)	1200	34	765±39	0.42	15.9
27 (AF)	1200	43	760±23	0.40	17.8
29 (AF)	1200	**49**	746±19	0.38	17.3
30 (AF)	1200	**42**	746±32	0.40	—
32 (AF)	1200	**49**	748±8	0.38	15.9
36 (AF)	1200	**53**	750±30	0.37	18.3
37 (AF)	1200	**46**	755±30	0.39	23.1
43 (AF)	1200	**50**	738±16	0.38	17.6
39 (PH)	600	**57**	742±15	0.36	13.2
40 (PH)	1200	**47**	690±10	0.39	11.9
41 (PH)	1200	**56**	730±32	0.37	15.6
42 (PH)	1200	**71**	682±5	0.33	14.4
44 (PH)	1200	**56**	673±2	0.37	13.5
45 (PH)	1200	**68**	737±11	0.34	13.2

The rupture-strain data in Table 30 are plotted against rupture temperature in Fig. 72. With the exception of two tests (OCZL#16 and OCZL#26), neither of which is included in Fig. 72, the agreement between correlation-calculated values and data is quite satisfactory for AF ZIRLO. For Test OCZL#16, the control TC experienced some electrical noise during ballooning and after rupture (see Fig. A.12) leading to rupture-temperature uncertainty. Also, the sample failed during disassembly just above the rupture region. OCLZ# 26 test results were excluded because of high uncertainty (about ±40°C) in rupture temperature.

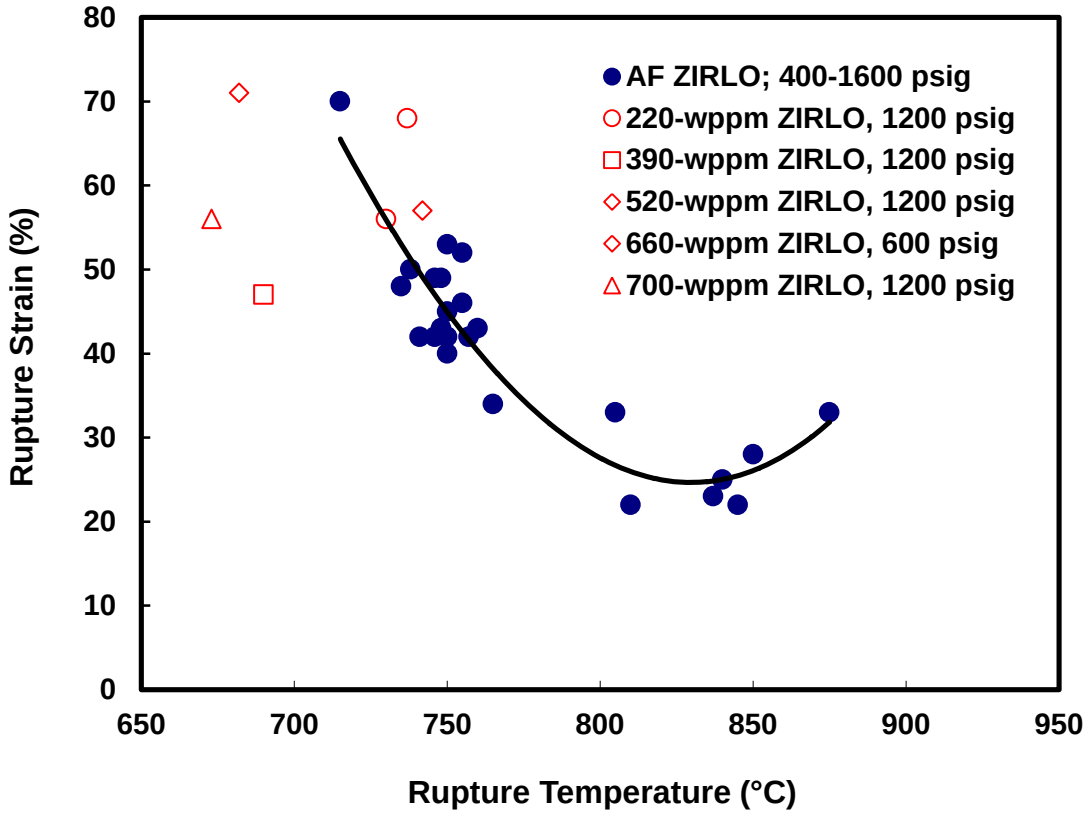

Figure 72. Rupture strain vs. rupture temperature following ramp-to-rupture tests (AF ZIRLO) and post-rupture oxidation at ≈1200°C (AF and PH ZIRLO).

For AF ZIRLO heated at 5°C/s, the maximum rupture strain (70%) occurred at the minimum rupture temperature (715°C). For Zry-4, this temperature would correspond to the alpha phase regime. The alpha to alpha-beta transition temperature for standard (≈1.5 wt.% Sn) Zry-4 is about 810°C for equilibrium conditions [7]. This transition temperature decreases with decreasing Sn, oxygen, and hydrogen content, and it increases with increasing heating rate. Brachet et al. [36] report the following for the phase-transition temperature of low-Sn (1.3 wt. %) Zry-4: 790°C under equilibrium conditions and 860°C for a heating rate of 10°C/s. The alpha-phase transition temperature is lower for M5 (Zr-1Nb) with 0.14 wt.% oxygen: estimated equilibrium phase change temperature as low as 650°C and 840°C for a heating rate of 10°C/s. Although the phase change temperature for ZIRLO (Zr-1Nb-1Sn) is not reported in the literature, it is expected to be between the phase-change temperatures for low-tin Zry-4 and M5 because of the intermediate tin content (1 wt. %). For the 5°C/s heating rate used in the current test program, 715°C could be within the alpha phase for ZIRLO where the peak rupture strain is expected to occur. The

rupture strain shown in Fig. 72 decreases monotonically for rupture temperatures <800°C, levels off at ≈830°C, and increases for temperatures >840°C. Similar behavior has been observed for Zry-4 [32] although the transition temperatures are different due to differences in phase-change temperatures. For the reference fill pressures (at 300°C) used in this test program, there is remarkable consistency in results: (a) 46±4% at 749±7°C based on 14 data points for 1200-psig fill pressure and (b) 25±3% at 843±6°C based on 4 data points for 600-psig fill pressure.

Considerably higher rupture strains and lower rupture temperatures were observed for PH ZIRLO with 220−700 wppm hydrogen. For the PH (660 wppm) sample with 600-psig fill pressure: the rupture strain was 57% (significantly higher than the 25% for AF ZIRLO) and the rupture temperature was 742°C (significantly lower than the 843°C for AF ZIRLO). Although the presence of hydrogen lowers the phase transition temperature (36), the results for PH ZIRLO cannot be explained based on phase change temperature alone. It appears that the presence of hydrogen weakens the non-oxidized cladding relative to the strength of AF ZIRLO such that the PH ZIRLO ruptures at a lower temperature and higher strain.

While the trends shown in Fig. 72 are instructive, the values of rupture strain are likely particular to the parameters of the sample and the LOCA integral apparatus used. Although the uniform heating zone of the furnace is 254 mm, the axial extent for which the cladding temperatures are relatively "uniform" is only 100−125 mm. The axial temperature distribution along the test sample would limit the axial extent of the balloon region and likely reduce the rupture strain. Also, circumferential temperature variations just prior to and at rupture were as high as ±32°C. These circumferential temperature variations would also limit the extent of rupture strain. It is highly likely that tests with longer uniform temperature regions, more uniform temperatures, and lower temperature ramp rates would result in considerably higher ballooning strains, as indicated in Ref. 32. However, in the current work, the purpose of generating rupture-strain data was to determine the wall thickness values for CP-ECR calculations. Thus, the rupture strain data in Table 30 and Fig. 72 have high significance for CP-ECR determination even though the data may not be applicable to what would be obtained using different sample lengths tested in different furnaces.

Although there are uncertainties in the data used to determine h_R, the values presented in Table 30 are much more accurate than those determined from modeling codes, which assume symmetrical balloons and which use empirical correlations to determine rupture time. Ballooning and rupture codes cannot predict the cross-section shapes shown in Figs. 63−64 and 67−69. As the current effort is experimental rather than analytical, it was appropriate to determine h_R as accurately as possible in order to establish data trends such as the variation of 4-PBT data with CP-ECR, which is based on h_R.

In addition to the data already presented in this section, metallographic examinations were performed to verify that the cross-sectional area remained constant during plastic deformation associated with ballooning and rupture. This assumption is the basis for Eq. 19. An example of the results of this effort is given in the following. For the OCZL#18 sample, the low-magnification image shown in Fig. 67 is very useful for measuring C_{mR}, but it is inadequate for measuring h_R. Higher magnification images are needed to measure the cladding metal thickness (100X) and the oxide layer thicknesses (200X). About 40 100X images would be needed to cover the whole cross section for this sample. As a compromise, Argonne did extensive metallographic examinations at 10 circumferential locations covering 25% of the cross section. On the basis of the 100X images, the average metal wall thickness was measured to be 0.35±0.12 mm. The inner- and outer-surface oxide layers were relatively uniform at 29±1 μm (0.058 mm total oxide thickness). For a Pilling-Bedworth ratio of 1.56, the cladding metal thickness prior to oxidation would be 0.39±0.12 mm. Using the measured C_{mR} value and the area-conservation assumption, Eq. 19 predicted h_R = 0.40 mm, which is in excellent agreement with the data. The data for average cladding metal thickness

prior to oxidation could be improved by analyzing 40 images, which would cover the whole cross section. However, the results for 10 images were adequate to demonstrate conservation of area.

5.4 Bend-Test Results for AF ZIRLO

Samples used for 4-PBT data generation were subjected to the full LOCA integral test sequence, including quench. Reference conditions for LOCA integral tests were: 1200 psig or 600 psig pre-pressurization at 300°C, 5°C/s temperature ramp rate from 300°C to the target temperature of 1200°C (based on the control TC output), hold at temperature T_h (based on average of TC readings) for specified times (t_h), 3°C/s temperature cooling rate from 1200°C to 800°C (based on control TC output), and quench at 800°C. Reference conditions for 4-PBTs were: (a) sample positioned such that the rupture tips were exposed to the maximum axial bending stress, (b) 135°C test temperature, (c) 2 mm/s (subsequently reduced to 1 mm/s) displacement rate, and (d) 14-mm maximum displacement. Under these LOCA integral test conditions, CP-ECR values of about 11% to 23% were achieved. 4-PBT parameters of interest were the maximum bending moment (M_{max}) prior to failure, maximum applied energy (E_{max}) prior to failure, and offset displacement (δ_p) prior to failure. 4-PBT failure is defined as the complete severing of one or more cross sections and is easily discerned by the load drop to zero. M_{max} is a measure of post-quench strength, E_{max} is a measure of post-quench toughness, and δ_p is a measure of post-quench plastic deformation (for $\delta_p \geq 0.1$ mm).

Raw data for all LOCA integral tests conducted are given in Appendices A (temperature histories), B (axial profiles of post-test outer diameters), and C (photographs of post-test samples). The raw data for 4-PBTs are presented in Appendices D (load-displacement curves) and E (photographs of post-bend samples). In addition to these data, hydrogen-content measurements and metallographic examinations were routinely performed at the failure locations. For some test samples, both metallographic examination and oxygen-content measurements were conducted. For two of the data-generation test samples, the axial profile of hydrogen content was measured, and the axial profile of oxygen content was measured for one of these samples.

On the basis of scoping-test results, it is evident that several regions of the post-quench sample were vulnerable to failure during the 4-PBT: (a) the rupture mid-span with the smallest average cladding thickness and the highest oxidation level and (b) locations on either side of the rupture mid-span, between rupture edges and balloon necks, with sufficient oxidation and hydrogen pickup. As an aid to understanding phenomena relevant to the 4-PBT results presented in this section, it is useful to know the: (a) ballooning and rupture geometrical parameters, (b) effective oxidation hold time (t_{he}), (c) effective oxidation hold temperature (T_{he}), and (d) CP-ECR (values given in Table 30). These parameters are listed in Table 31 for the 11 tests conducted under reference conditions, for one 4-PBT test conducted at RT, and for one reverse 4-PBT conducted with the rupture tips subjected to maximum compressive stress.

The effective time (t_{he}) during which significant high-temperature oxidation occurs is longer than the programmed hold time because the controller slows down the temperature rate when the control temperature is within about 20°C of the target temperature. For a target temperature of 1200°C, t_{he} is the time for which the control TC reads ≥1180°C to the time corresponding to the end of the heating phase. T_{he} is the average temperature during t_{he}.

Ballooning and rupture parameters of interest are the: (a) maximum circumferential strain ($\Delta C_{mR}/C_{mi}$ values are given in Table 30), (b) maximum width of the rupture opening (some δ_R values are given in Table 29), (c) axial length (L_R) of the rupture opening, and (d) axial length (L_B) of the balloon region.

Table 31. Summary of LOCA integral post-quench parameters that may affect AF-ZIRLO cladding performance during 4-PBTs.

OCZL#	$\Delta C_{mR}/C_{mi}$, %	δ_R, mm	L_R, mm	L_B, mm	t_{he}, s	T_{he}, °C	CP-ECR, %	Comments
14	48	3.8	11	150	77	1194±5	18.3	Large control TC noise during ramp between rupture and hold
15	52	4.4	18	160	89	1199±19	18.4	Reverse bend test
17	45	5.7	19	170	30	1192±7	12.7	–
18	43	5.4	18	160	30	1191±9	12.3	–
19	25	3.3	12	140	141	1200±11	17.3	–
21	28	4.9	13	160	22	1183±13	10.6	Low control TC noise
22	23	5.2	10	130	29	1216±11	11.6	–
25	42	8.7	26	160	89	1202±11	16.1	2 reliable TCs after rupture
29	49	5.9	21	150	99	1197±7	17.3	–
32	49	7.2	22	170	84	1181±11	15.9	RT 4-PBT; no significant effects of test temperature
36	53	10.2	24	180	68	1215±18	18.3	Higher than expected M_{max} and E_{max}
37	46	5.2	19	160	172	1211±14	23.1	–
43	50	6.1	19	160	74	1210±21	17.6	–

L_B is defined as the axial span for which the average diametral stress is ≥5% (see Appendix B for diametral strain data). L_R is significant because of the high oxygen and low hydrogen pickup for this region. Also, all failure locations given in this section are referenced to the mid-span of L_R. L_B is significant because the highest hydrogen pickup occurs between the edges of the rupture opening and the necks of the balloon region.

The results of the 4-PBTs are summarized in Table 32 for the 11 data-generation tests conducted under reference conditions, for the one reverse-bend test conducted with the rupture tips under axial compression, and for the one test conducted at RT. Results for the three metrics selected to characterize 4-PBT performance are discussed in the following.

Table 32. Summary of results for LOCA integral tests terminated with quench at 800°C and post-quench 4-PBTs with AF ZIRLO cladding. The 4-PBT displacement rate was decreased from 2 mm/s to 1 mm/s after OCZL#21 sample test.

OCZL#	Rupture Strain, %	CP-ECR, %	4-PBT Failure Location, mm	M_{max}, N•m	E_{max}, J	Offset Displace., mm	Comment
14	47	18.2	≈0	5.7	0.24	0	
15	51	18.3	No Failure	9.0	>1.9	>10	Reverse 4-PBT
17	45	12.7	≈0	8.4	0.65	>0.5	
18	43	12.3	≈0	13.5	1.28	0	
19	25	17.3	-23, +23	5.7	0.23	0	
21	28	10.6	-29, +33	13.8	1.17	0	
22	23	11.6	-27, +25	11.1	0.83	0	
25	42	16.1	-26,+26	8.3	0.50	0	
29	49	17.3	≈0	4.7	0.40	>9	<10% intact
32	49	15.9	≈0	6.7	0.26	0	RT 4-PBT
36	53	18.3	-40, +32	9.5	0.56	0	
37	46	23.1	-40, +35	4.1	0.13	0	
43	50	17.6	≈0	6.1	0.24	0	

Maximum Bending Moment (M_{max})

Results for the three ramp-to-rupture scoping tests (see Table 28 and Figs. D.1 to D.3) indicate that AF ZIRLO with essentially no oxidation has an average M_{max} value of about 20 N•m. Although none of these samples failed through 14-mm displacement, it appears that the bending moment leveled off at M_{max} and began to decrease slowly. M_{max} was relatively independent of rupture strain for values from 22% to 70%. As shown in Table 32, M_{max} decreased significantly with increasing oxidation level (i.e., CP-ECR).

The 4-PBT results indicate that samples failed either near the rupture node mid-span (0 mm) or at two locations between the rupture edges and the balloon necks. M_{max} results are plotted separately in Fig. 73 for these two cases. With the exception of the high M_{max} value for the OCZL#36 sample, which appears to be an outlier, results for both cases appear to be essentially the same within expected data scatter. Excluding the OCZL#36 result, the best linear fit to the data for 10% to 19% CP-ECR is:

$$M_{max} = 13.70 - 1.053\ (\text{CP-ECR} - 10\%),\ \text{N•m} \qquad (24)$$

After about 19% (19.1% to be precise), the maximum bending moment appears to level off at 4.1 N•m on the basis of results at 23% CP-ECR. Although no data were generated in the oxidation range of >0% to 10%, results from the ramp-to-rupture scoping tests (20 N•m) and the Eq. 24 value of about 14 N•m at 10% CP-ECR can be used to estimate the effects of increasing oxidation level in this regime.

For the previous licensing limit (17% CP-ECR), Eq. 24 gives a M_{max} value of 6.3 N•m. Data in the oxidation range of 17±1% CP-ECR give experimental values in the range of 5.8±1.4 N•m. It is interesting to note that the result (6.7 N•m) for the 4-PBT conducted at RT with a 17% CP-ECR sample is within this range. Although one RT data point does not constitute a trend, it appears that the maximum bending moment, which is the metric for maximum strength, is insensitive to 4-PBT temperature in the range of 20°C to 135°C. The results for maximum strength are quite different from the RCT ductility results for which there was a very high sensitivity of ductility to RCT temperature.

The OCZL#12 sample (see Table 28) was cooled without quench prior to the 4-PBT. It is interesting to note that the sample failed at a cross section that included the mid-span of the rupture opening with a maximum bending moment of 8.8 N•m. Equation 24, which is based on data for post-quench samples predicts 9.1 N•m for M_{max}. For this one sample, which failed in the high oxidation region with little hydrogen pickup, the absence of quench did not improve the maximum strength of the sample.

The 4-PBT results for OCZL#17 and #18 are interesting to compare because the two samples had essentially the same ballooning and rupture parameters (see Table 31), the same effective hold temperature, and the same oxidation level (12.7% and 12.3% for OCZL#17 and #18, respectively). Also, both samples failed along cross sections that included the rupture opening. However, the maximum bending moments (8.4 N•m vs. 13.5 N•m) were quite different. The average of these experimental results (11 N•m) is in excellent agreement with the value predicted by Eq. 24 (11 N•m). The deviation of the data (about ±23%) is about the same as the ±24% for four tests conducted with samples that were oxidized to 17±1% CP-ECR.

For the reverse-bend-test sample from test OCZL#15 (18% CP-ECR), partial-wall cracking and crumbling were observed to occur in the compressive-stress region around the rupture opening. Concurrent with this degradation, the load decreased (see Figs. D.7a and D.7b) and the thicker regions of the cross section continued to deform plastically without cross-section failure (see Fig. E.5).

The 4-PBT strength results, based on M_{max}, appear to be a meaningful measure of cladding performance in that the strength exhibits the expected decrease with increasing oxidation level. However, application of these results to LOCA acceptance criteria is not straightforward. In Section 5.6, post-quench bending strength results are compared to JAEA results for tests with a restraint-induced axial force during quench to assess the adequacy of the cladding strength determined from bend tests.

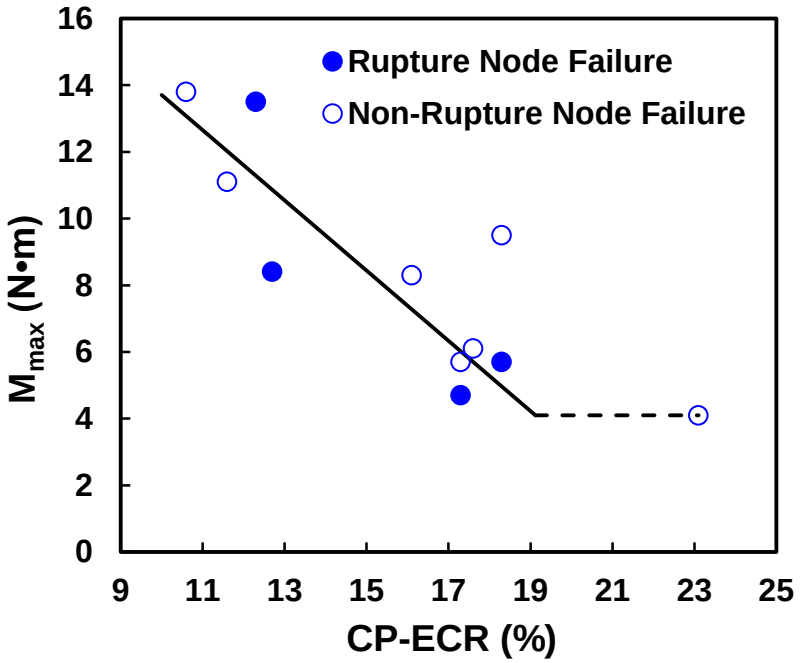

Figure 73. Maximum 4-PBT bending moment (M_{max}) vs. oxidation level (CP-ECR) for AF ZIRLO following ballooning, rupture, oxidation, and quench.

Significant insight into failure locations and modes can be gleaned from metallographic evaluation of layer thicknesses and from axial distributions of diametral strain, hydrogen content, and oxygen content. Detailed results are available for the OCZL#18 (12% CP-ECR) and OCZL#19 (17% CP-ECR) samples. The OCZL#18 sample severed along a cross section through the rupture node, while the OCZL#19 sample severed at two locations that were between rupture edges and balloon necks.

The OCZL#18 sample had large rupture strain (43%), thinner pre-oxidation cladding (0.40 mm average), and thinner metal wall (0.35 mm average) following oxidation. Outer- and inner-surface oxide layers were 29-μm thick. Figure 67 shows a low magnification image of the rupture-node cross section. Figures 74a and 74b, respectively, show the thickest (0.44 mm) and thinnest (0.14 mm) metal wall thicknesses after oxidation, quench, and 4-point bending. During the 4-PBT, there was an abrupt load drop from 540 N to zero, indicating very rapid crack growth (see Fig. D.9). The sample failed near the axial center of the rupture opening. The results are interesting in that the local CP-ECR at the back wall was <10% and the hydrogen pickup was very small (see Fig. 75). If this segment had been tested in isolation, it would have behaved in a very ductile manner. However, it appears that this region, along with the whole cross section, did not have high enough toughness to blunt crack growth. Also, the cross section was weaker than regions between the rupture edges and the balloon necks, which had high hydrogen pickup (up to 1800 wppm) and lower oxidation.

The OCZL#19 sample had low rupture strain (25%) and thicker pre-oxidation cladding (0.46 mm average). The sample failed at locations that were 24 mm above and 24 mm below the rupture-opening mid-span (see Fig. 76). Both hydrogen and oxygen contents were measured along the sample (see Fig. 77). It is clear from Figs. 76−77 that the failure occurred in regions where the combination of hydrogen and oxygen was high enough to weaken the material relative to the highest-oxygen/lowest-hydrogen rupture-node cross section and the lower-oxygen/highest hydrogen regions closer to the balloon necks.

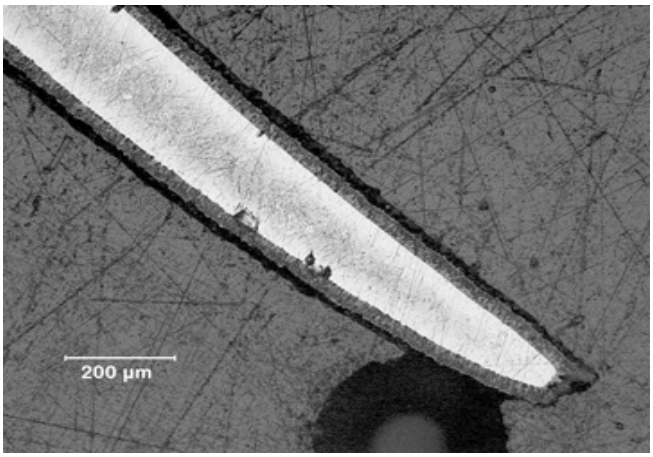

(a) Rupture tip

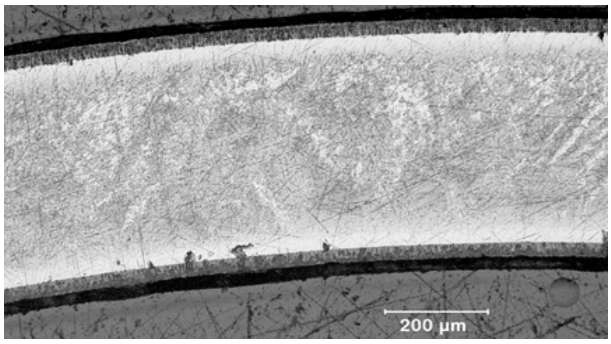

(b) Back side of cross section

Figure 74. Metallographic images of the OCZL#18 severed cross section following oxidation to 12% CP-ECR, quench, and 4-point bending: (a) rupture tip (0.14-mm metal wall) and (b) back side of cross section (0.44-mm metal wall).

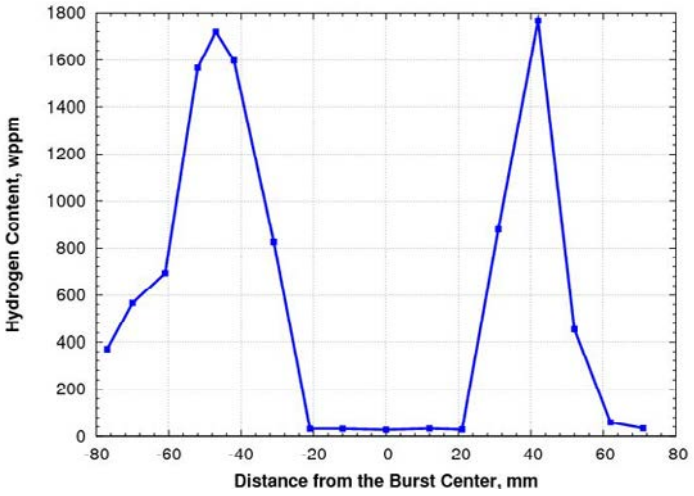

Figure 75. Axial profile of hydrogen content in OCZL#18 sample after oxidation to 12% CP-ECR.

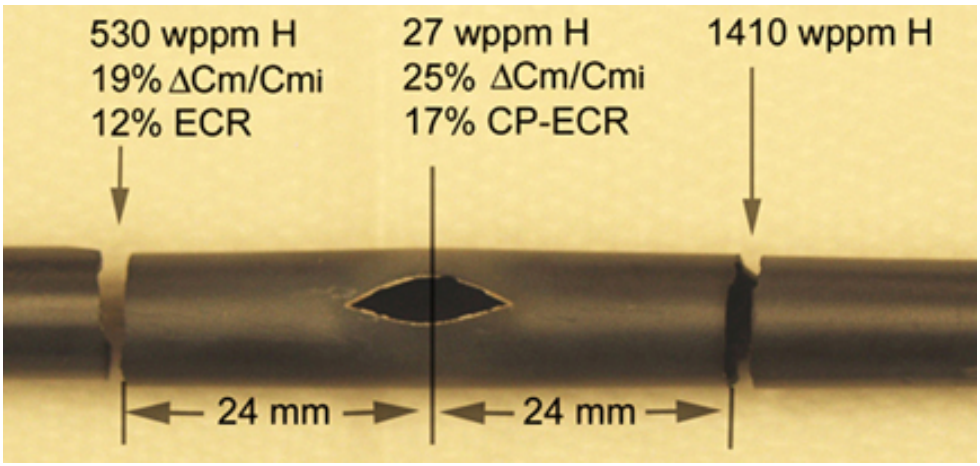

Figure 76. 4-PBT failure locations for the OCZL#19 sample after oxidation to 17% CP-ECR.

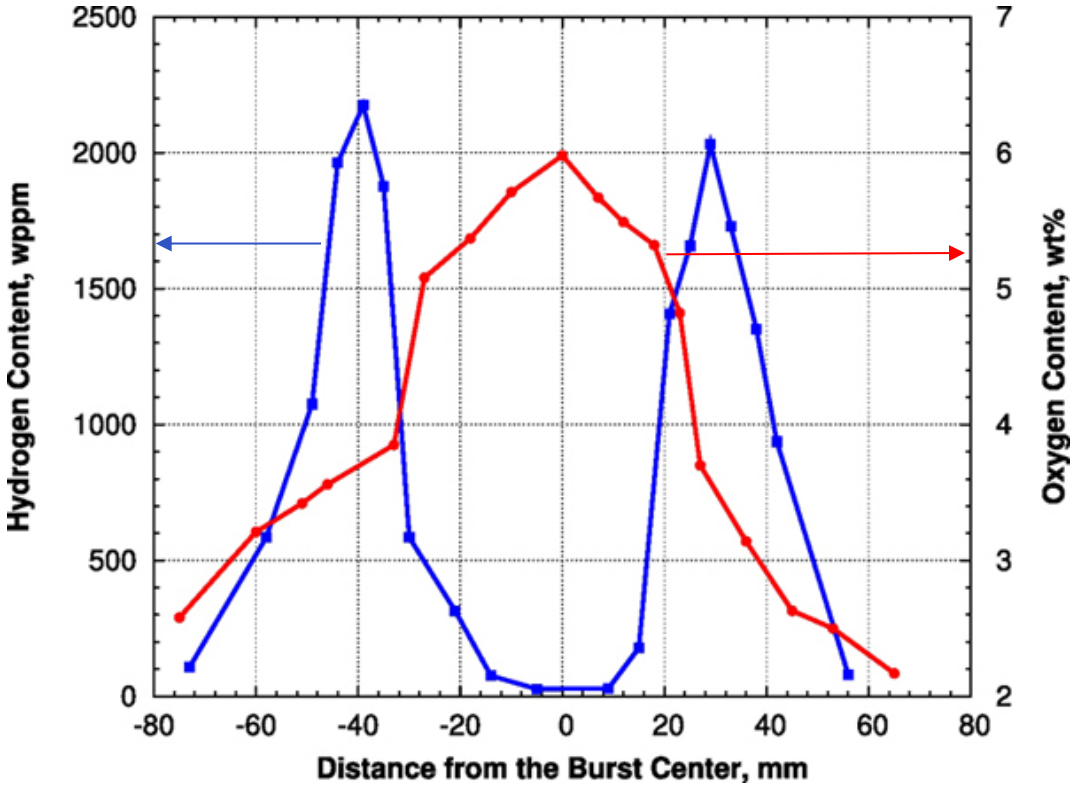

Figure 77. Axial profiles for hydrogen and oxygen content along the OCZL#19 sample after oxidation to 17% CP-ECR and 4-point bending.

Metallographic examination was performed for the failure cross section 24 mm below the rupture opening. The average outer- and inner-surface oxide layers were 50-µm and 35-µm thick, respectively, and the metal wall was 0.46-mm thick. The pre-oxidation metal thickness was calculated to be 0.51 mm, which is thicker than the 0.46-mm average value calculated for the rupture-node cross section. The differences in pre-oxidation wall thicknesses between the failure cross section and the rupture cross section would suggest that the rupture cross section would be weaker. However, high-hydrogen/lower-oxygen contents at ±24 mm from the rupture-opening mid-span had a larger effect on weakening the cladding at the failure locations than the strengthening effect of a thicker wall.

Failure Energy

The failure energy or maximum energy (E_{max}) when failure does not occur is plotted vs. oxidation level in Fig. 78, with data for failures within the rupture node cross section indicated by solid circles and data for non-rupture-node failures indicated by hollow circles. The load-displacement results from ramp-to-rupture scoping tests (0% CP-ECR) were used to determine upper-bound energies of ≈8 J for unfailed samples through 14-mm displacement. Although this value does not represent the maximum energy that such samples could accumulate prior to failure, it does represent the maximum that these samples accumulated through 14-mm displacement. The maximum energy decreased sharply from about 8 J for 0% CP-ECR to about 1.2 J for 10% CP-ECR. Figure 78 shows that E_{max} decreased by a factor of ≈10 from 10% CP-ECR to 19% CP-ECR and then leveled off at 0.13 J from 19% to 23% CP-ECR.

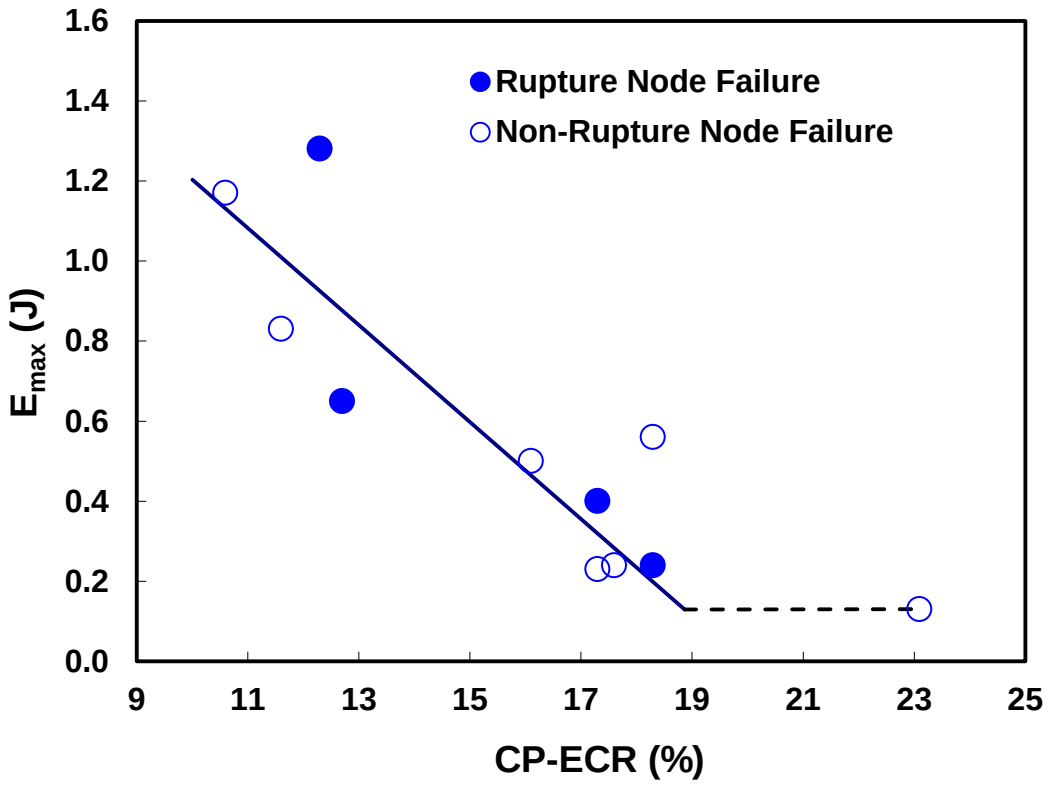

Figure 78. Maximum (failure) 4-PBT energy (E_{max}) vs. oxidation level (CP-ECR) for AF ZIRLO following ballooning, rupture, oxidation, and quench.

Within the scatter of the data, there was no significant difference between failure energies for samples that failed in the rupture-opening cross section and samples that failed between the rupture edges and the balloon necks. At about 12% CP-ECR, the failure energies for the OCZL#22 and the OCZL#18 samples were both about 1 J (0.83 J and 1.28 J, respectively). The best-fit linear correlation (excluding the suspected outlier OCZL#36 data point of 0.56 J at 18.3% CP-ECR) for failure energy vs. CP-ECR in the range of 10 to 19% CP-ECR is given by:

$$E_{max} = 1.204 - 0.1211\ (\text{CP-ECR} - 10\%),\ \text{J} \qquad (25)$$

The failure energy vs. CP-ECR shows the same trends as does the maximum bending moment vs. CP-ECR. Namely, it shows a significant decrease in failure energy with oxidation level up to about 19% (18.9% to be precise). For a triangular load-displacement curve with linear rise in load up to the failure load followed by a very abrupt load drop, E_{max} gives about the same failure characterization as M_{max}. However, it gives more information for samples that do not sever completely at the maximum load (e.g., see Figs. D.15a and D.15b for the OCZL#29 test sample) and continue to deform plastically at a decreasing load.

Offset Displacement

Offset displacement is a measure of plastic deformation. For the three ramp-to-rupture scoping-test samples (0% CP-ECR), there was a smooth transition between the constant load-displacement slope in the elastic bending regime and the decreasing slope after initiation of plastic flow in the axial direction (see Figs. D.1 to D.3). Measured offset displacements were in the range of 7 to 8 mm for these samples. The loading stiffness values were reasonably close, but they appeared to increase somewhat with decreasing rupture strain: 120 N/mm for 70% rupture strain, 130 N/mm for 33% rupture strain, and 135 N/mm for 22% rupture strain.

The load-displacement curves for oxidized and quenched samples were quite different from the ones for ramp-to-rupture samples. Most samples (9 out of 11 quenched samples) severed with an abrupt load drop during the linear portion of the loading ramp. These samples exhibited no offset displacement prior to crack initiation and propagation through the cross section. Six of the nine brittle samples failed outside the rupture node and the remaining three failed in the rupture node.

The six quenched samples that severed outside the rupture node with zero offset displacement had hydrogen contents and oxidation levels at the failure locations that would qualify them as brittle based on RCT results (Eq. 17) for non-deformed cladding samples. Metallographic imaging and analysis were performed at one of two severed cross-section locations for the post-bend OCZL#19 sample, and hydrogen content was determined from rings sectioned close to the severed cross-section (see Fig 76).

The three quenched samples that severed in the cross section containing the rupture-opening node with zero offset displacement had oxidation levels of 12% CP-ECR and 18% CP-ECR (2 samples). Counting the 16% CP-ECR sample tested at RT, four samples severed in the rupture-opening node.

Figure 79 shows the post-bend appearance of the OCZL#15 sample that was tested with the rupture tips in compression. This sample had an oxidation level of 18% CP-ECR. It was subjected to loading, unloading, and re-loading. As indicated in Figs. D7a and D7b, there was evidence of some offset displacement prior to the gradual load drop. As Fig. 79 shows, the sample continued to deform with significant plasticity as the partial cross-section crack grew.

Figure 79. Post-bend appearance of the OCZL#15 sample oxidized to 18% CP-ECR, quenched, and subjected to a reverse 4-PBT with the rupture tips in compression.

Figure 80 shows the pos-test image of the OCZL#17 sample (13% CP-ECR), which was subjected to reference 4-PBT conditions. The back region of the cladding remained intact after 10-mm displacement with an offset displacement of about 9 mm. Figure D.15a shows that the maximum load was 335 N and the load appeared to drop abruptly to zero at a total displacement of about 3.4 mm. The test was terminated at 4-mm displacement to allow for examination of the sample. It was observed that the sample was partially intact. The sample was then reloaded. The measured loads during the reloading were very low (3N to 13 N) as the ligament at the back of the cladding continued to deform plastically. This plastic deformation region contributed about 10% to the maximum energy. The images shown in Fig. 80 were taken after the reloading test was completed.

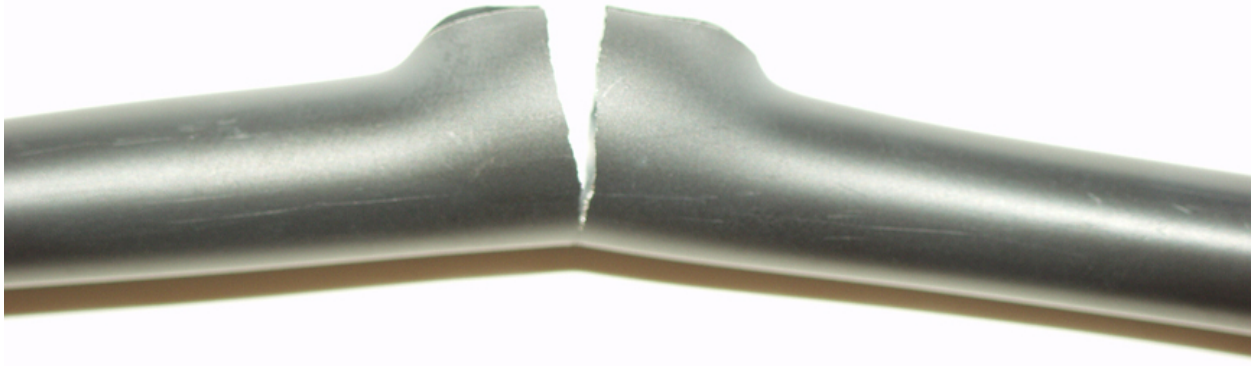

(a) Side view

(b) Rupture view

Figure 80. Post-bend-test images of the OCZL#17 sample oxidized to 13% CP-ECR, quenched, and subjected to bending at 135°C: (a) side view and (b) rupture view.

The OCZL#29 sample (17% CP-ECR) was also subjected to the reference 4-PBT. This test was terminated after ≈3-mm displacement (see Fig. D.15a) and reloaded (see Fig. D.15b). Cracking began at a relatively low load (188 N) and bending moment (4.7 N•m). The load dropped abruptly from 188 N to 107 N and again from 124 N to 85 N. At the end of these two load drops, the crack had propagated across more than half the cross section (see Fig. 81a). After reloading, the crack continued to propagate in a plastic manner leaving only the back region intact (see Fig. 81b).

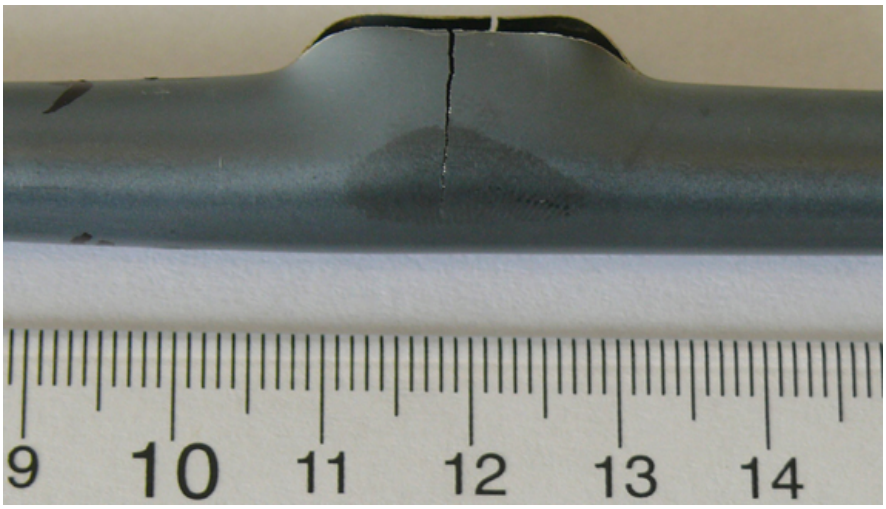

(a) Side view after 1st loading-unloading cycle

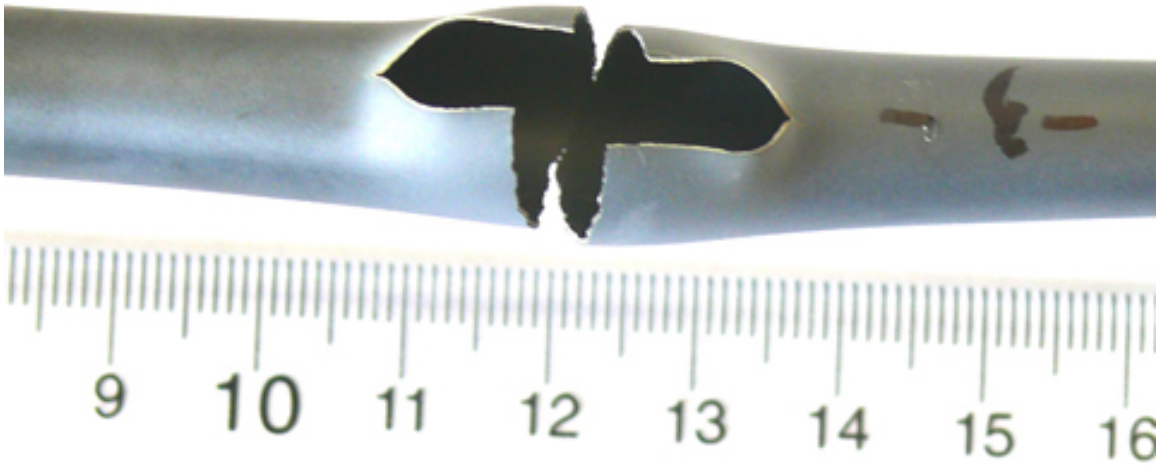

(b) Rupture view after 2nd loading-unloading cycle

Figure 81. Post-bend-test images of the OCZL#29 sample (17% CP-ECR) after 4-PBTs conducted under reference conditions: (a) side view after 1st loading-unloading cycle and (b) rupture view after 2nd loading-unloading cycle.

The use of offset displacement as a measure of plastic deformation was found to be meaningful only for samples that did not partially or fully sever following achievement of the maximum load. These samples included AF cladding alloys (no oxidation) used for benchmark testing and ramp-to-rupture scoping test samples, also at 0% CP-ECR. In most cases, the AF ZIRLO samples exhibited rapid crack growth and no offset displacement following oxidation and quench. For two of the samples tested under reference bend conditions, more than 50% of the cross section cracked during the first load drop. This was followed by crack extension through most of the cross section and plastic flow of a ligament of the cladding at very low load. Given that it can only be correlated with plastic flow of the structure prior to crack initiation, offset displacement was not a very meaningful metric for post-quench samples with CP-ECRs in the range of 11% to 23%. The use of offset displacement may be a meaningful metric for samples oxidized within the range of 0% to 10% CP-ECR, as there is clearly a transition from high (>8 mm) to low (≈0 mm) offset displacements in this oxidation range.

5.5 Bend-Test Results for PH ZIRLO

The pre-hydriding process is described in Section 3.2.2 for shorter (75−100 mm long) samples. The same process was used for 318-mm long ZIRLO LOCA integral samples. However, it was well recognized that axial variations in hydrogen content would be larger for the longer samples. The target hydrogen content for the mid-section of the cladding was 250±50 wppm. A number of practice samples were pre-hydrided and weighed to estimate average hydrogen content. Some of these were sectioned near the ends and mid-regions to get some idea of axial distribution of hydrogen. For some samples, hydrogen contents near the ends of the samples were higher than near the mid-regions. For other samples, the reverse was true. Also, most measured peak hydrogen contents were significantly higher than average values determined from weight-gain measurements. Reproducibility was also poor as there was wide variability in average hydrogen content for samples subjected to the same conditions for the same pre-hydriding time.

Engineering judgment was used to select six pre-hydrided samples for LOCA integral testing and 4-PBTs. Hydrogen contents near the cross section containing the rupture mid-span could only be determined by measuring local hydrogen content after ballooning, rupture, oxidation, quench and bending. As discussed in Section 3.2.2, these post-test hydrogen contents were corrected for oxygen-induced weight gain to determine pre-test and pre-rupture hydrogen content. For two of the samples, the pre-test hydrogen content (220 wppm) in the rupture-node cross section was within the target range. For the other samples, the hydrogen content (390−700 wppm) was higher than the target range.

Table 33 lists the PH ZIRLO samples tested, the hydrogen contents, and other parameters of interest such as those listed in Table 30 for AF ZIRLO. Five of the six PH ZIRLO samples survived disassembly and were available for 4-PBTs. The OCZL#42 sample failure near the rupture-opening mid-span during disassembly. For four of these five samples, there was very good temperature control during the heating ramp, the hold time and the cooling ramp. For LOCA integral test OCZL#41, the control TC reading fluctuated significantly during the heating ramp and during the cooling ramp just before and just after the hold time. As the output of the control TC determined the furnace power, the other TCs fluctuated significantly during this same time period. The last test (OCZL#45) was the best one in terms of temperature control, absence of secondary ballooning region, and rupture-opening orientation and width.

Results of the 4-PBTs are listed in Table 34 for PH ZIRLO samples subjected to the reference LOCA integral test sequence, including quench. The results in Table 34 show a clear trend of decreasing M_{max} and E_{max} with increasing hydrogen content, as well as with increasing oxidation. This trend can be see more clearly in Figs. 82 (M_{max}) and 83 (E_{max}), which show the comparison between results for PH and AF ZIRLO cladding samples.

Table 33. Summary of LOCA integral post-quench parameters that may affect PH-ZIRLO cladding performance during 4-PBTs.

OCZL# (wppm)	$\Delta C_{mR}/C_{mi}$, %	δ_R, mm	L_R, mm	L_B, mm	t_{he}, s	T_{he}, °C	CP-ECR, %	Comments
39 (660)	57	1.9	7.3	120	20	1195±19	13.2	2 reliable TCs after rupture; Large secondary balloon (>50%) 50 mm above primary balloon
40 (390)	47	4.2	16	130	14	1196±14	11.9	3 reliable TCs after rupture; Regular rupture opening
41 (220)	56	3.3	15	150	20	1212±52	15.6	Large control TC noise after rupture during heating and cooling ramps; Slanted rupture opening relative to axial orientation
42 (520)	71	0.8	7.5	140	22	1202±39	14.4	Control TC noise during hold time; Very small rupture opening; Sample failed in rupture node during disassembly
44 (700)	56	8.2	18	130	23	1201±19	13.5	3 reliable TCs; Large rupture opening with a flap of metal remaining
45 (220)	68	5.0	17	150	14	1188±9	13.2	Very good test

Table 34. Summary of results for LOCA integral tests terminated with quench at 800°C and post-quench 4-PBTs with PH ZIRLO cladding. 4-PBT displacement rate was 1 mm/s.

OCZL#	Rupture Strain, %	CP-ECR, %	4-PBT Failure Location, mm	M_{max}, N•m	E_{max}, J	Offset Displace., mm	Comment
39 (660)	57	13.2	≈0	2.8	0.05	0	–
40 (390)	47	11.9	≈0	4.9	0.16	0	–
41 (220)	56	15.6	≈0	3.2	0.07	≈0	–
44 (700)	56	13.5	≈0	2.4	0.11	≈0	Some offset displ. after >50% cracking
45 (220)	68	13.2	≈0	6.6	0.28	0	–

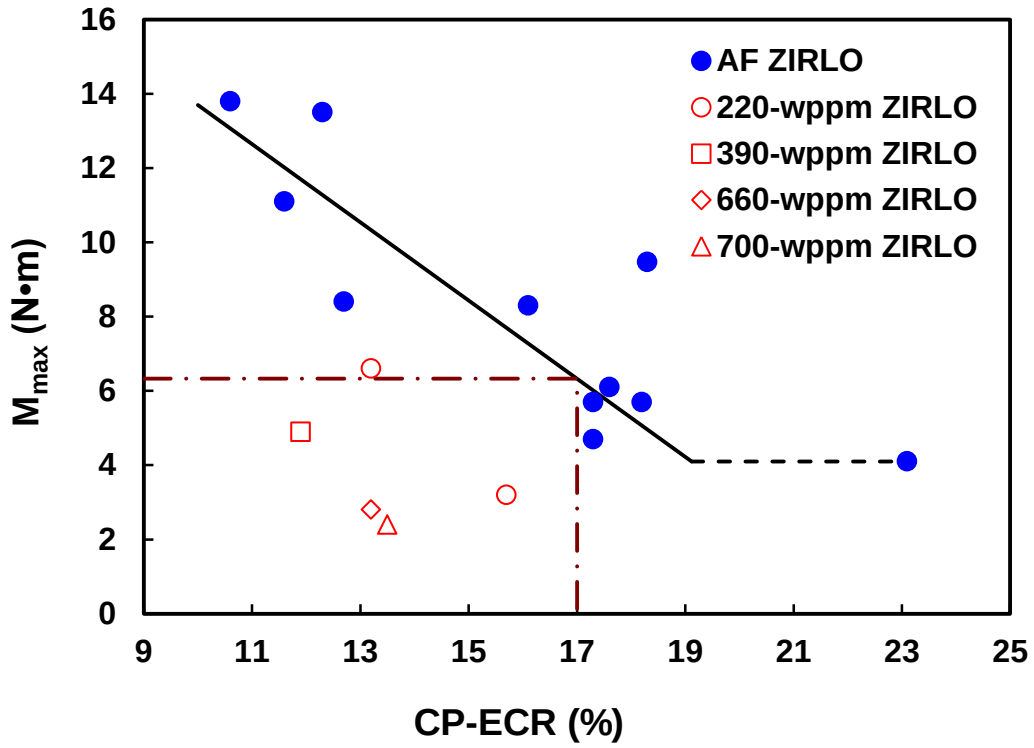

Figure 82. Maximum 4-PBT bending moment (M_{max}) vs. oxidation level (CP-ECR) for AF and PH ZIRLO following ballooning, rupture, oxidation, and quench.

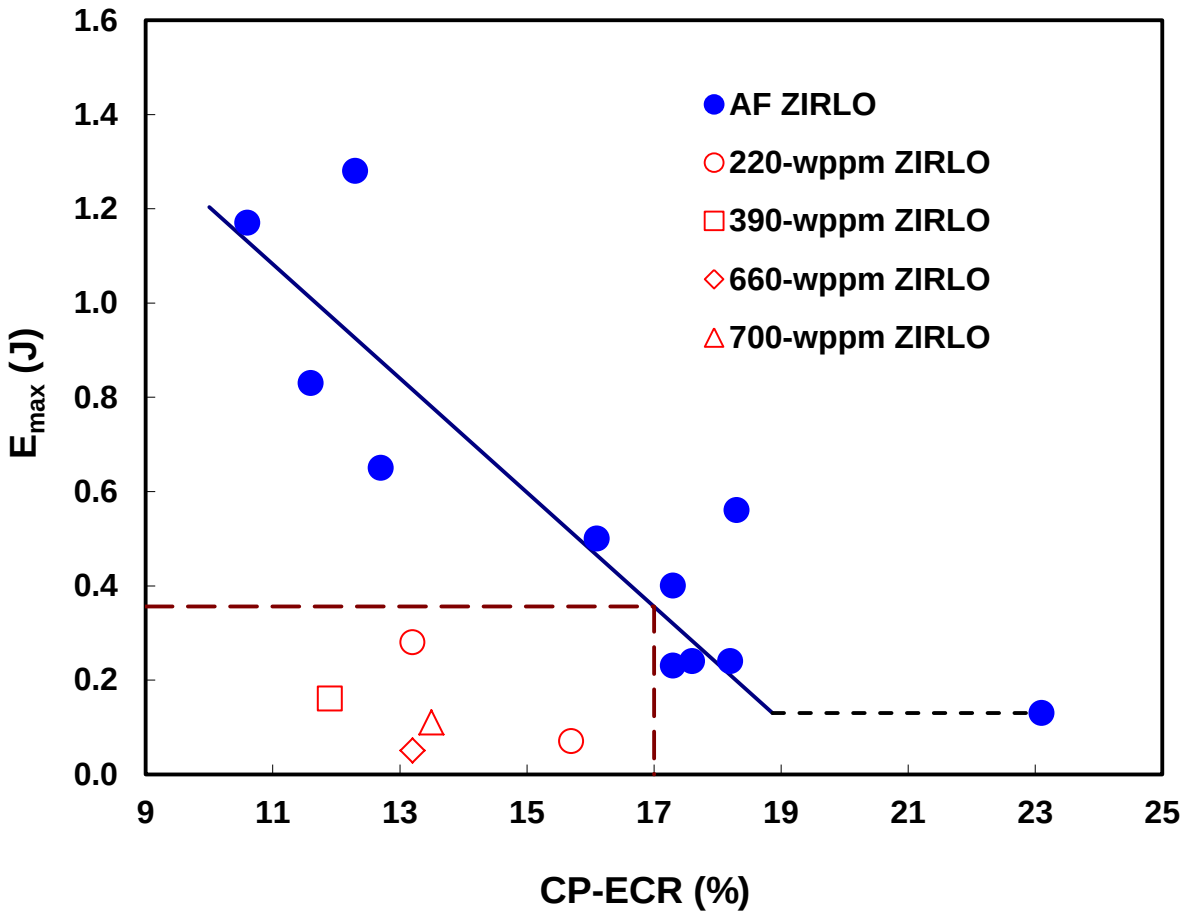

Figure 83. Maximum (failure) 4-PBT energy (E_{max}) vs. oxidation level (CP-ECR) for AF and PH ZIRLO following ballooning, rupture, oxidation, and quench.

The M_{max} and E_{max} data points for ZIRLO samples with 220 wppm are of particular interest in assessing whether or not such samples have sufficient values of M_{max} and E_{max} if the oxidation level were limited. In Section 5.4, it is established that the correlation value (Eq. 24) for the M_{max} of AF ZIRLO is 6.3 N•m at 17% CP-ECR. The corresponding value (Eq. 25) for E_{max} is 0.36 J at 17% CP-ECR. The 220-wppm sample at 13.2% CP-ECR had a maximum bending moment of 6.6 N•m, which is marginally above the 17% CP-ECR for AF cladding. However, if the oxidation level were limited based on retention of ductility (Fig. 25 and Eq. 17), then the CP-ECR would be limited to 11%. On the basis of linear extrapolation, the 220-wppm ZIRLO sample would have M_{max} and maximum E_{max} values of 9.6 N•m and 0.46 J, both of which are greater than the corresponding values for AF ZIRLO cladding oxidized to 17% CP-ECR. Thus, it appears that limiting oxidation level based on ductility retention for non-deformed cladding would be adequate to ensure that cladding with pre-test hydrogen had M_{max} and E_{max} levels at least as high as levels for AF cladding at 17% CP-ECR. The PH ZIRLO sample at 220-wppm and 13.2% CP-ECR was of high quality because temperatures were well controlled during the oxidation phase of the LOCA integral test. The sample at 220-wppm and 15.6% was of much lower quality because of significant temperature fluctuations (due to electrical noise) just before and just after the hold time. A more conservative approach for estimating M_{max} and E_{max} at 11% CP-ECR for 220 wppm pre-test hydrogen is to use the slopes in Eqs. 24 and 25 for extrapolation. This approach leads to values of 8.9 N•m M_{max} and 0.55 J E_{max}, which are still above the 17% CP-ECR values for AF ZIRLO.

Considerable characterization work was conducted after the 4-PBTs to determine the hydrogen and oxygen content within the rupture-node cross sections near the failure region, as well as the thickness of the outer-surface oxide layer in this region. The oxygen content was used to determine weight gain, which was then used to calculate pre-test hydrogen content.

Figure 84 shows results of hydrogen- and oxygen content measurements for the OCZL#39 sample following severing through a rupture-node cross section during the 4-PBT. Also shown in Fig. 84 is the secondary balloon that formed about 50 mm above (to the right in the figure) the primary balloon. The outer-surface oxide-layer thickness was measured for the metallographic-sample cross section containing the rupture opening near the bottom edge of this opening. The measured value (30±3 μm) was about 7% higher than the CP-predicted value (28±3 μm, based on two TCs). Agreement to within 10% is considered acceptable. Also, the circumferential variation in oxide layer thickness is consistent with the measured circumferential variation in the effective hold temperature (1195±19°C).

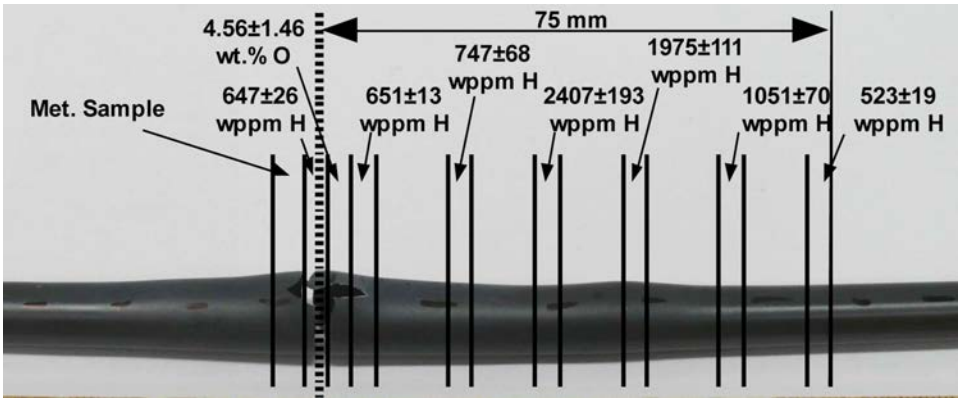

Figure 84. Sectioning diagram and characterization results for the OCZL#39 post-bend sample with 660-wppm pre-test hydrogen oxidized to 13.2% CP-ECR.

Figure 85 shows the hydrogen and oxygen contents measured for rings close to the severed cross section of the OCZL#40 sample. Three TCs remained reliable through the temperature history for this test. Measured (26±4 μm) and CP-predicted (27±2 μm) values for outer-surface oxide layer thickness were very close and the circumferential temperature variation (1196±14°C) was relatively mild.

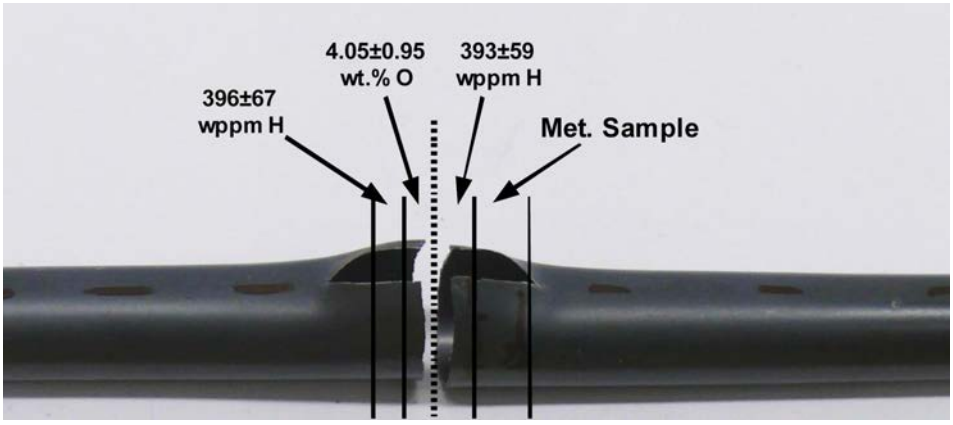

Figure 85. Sectioning diagram and characterization results for the OCZL#40 post-bend sample with 390-wppm pre-test hydrogen oxidized to 11.9% CP-ECR.

The sectioning diagram and characterization results for the post-bend OCZL#41 sample are shown in Fig. 86 for regions close to the severed cross section. The measured (31±4 μm) and calculated (33±6 μm) outer-surface oxide layer thicknesses were closer than expected given the temperature fluctuations before and after the hold time. The effective hold temperature was 1212±52°C with significant uncertainty in the ±52°C, which would have lead to larger variation in measured oxide layer thickness,

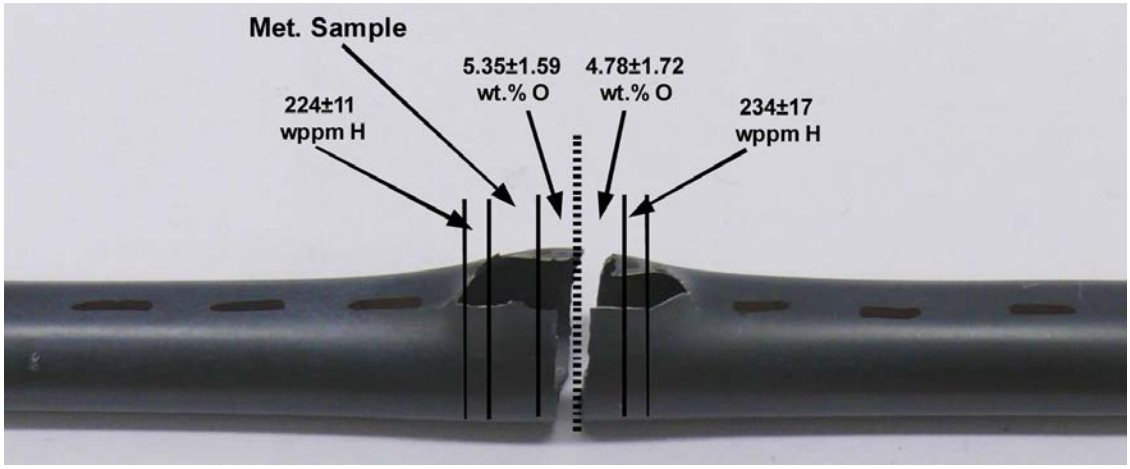

Figure 86. Sectioning diagram and characterization results for the OCZL#41 post-bend sample with 220-wppm pre-test hydrogen oxidized to 15.6% CP-ECR.

The OCZL#42 sample could not be subjected to a 4-PBT because the sample severed at a location within the rupture opening during disassembly. Hydrogen and oxygen measurements were made on rings sectioned from just above and just below the severed cross section to determine the pre-test hydrogen content (520 wppm).

Figure 87 shows the sectioning diagram and characterization results for the OCZL#44 test sample following the 4-PBT. The rupture opening was rather unique for this sample (see pre-bend photo in Fig. C.29) as it was bounded by a flap of metal resembling a partially opened door.

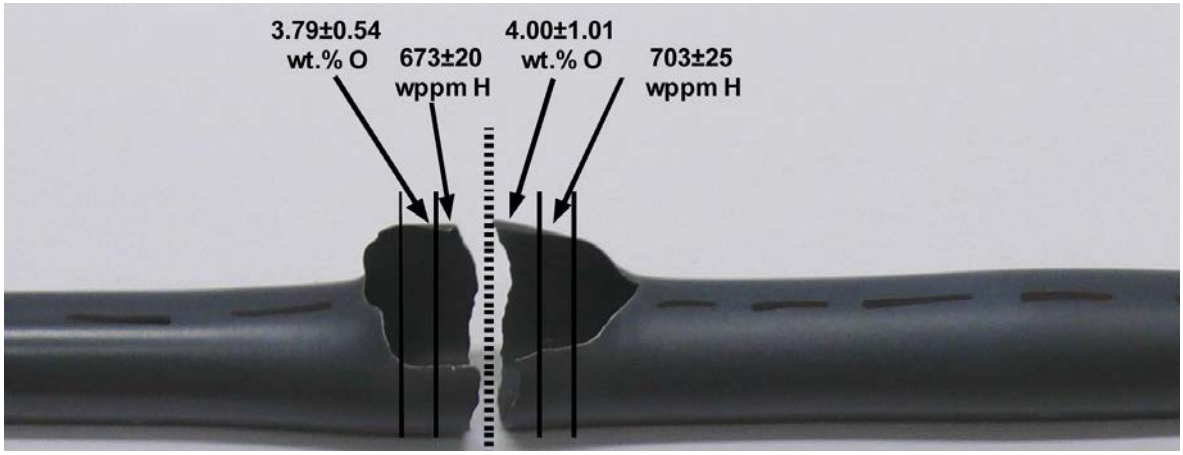

Figure 87. Sectioning diagram and characterization results for the OCZL#44 post-bend sample with 700-wppm pre-test hydrogen oxidized to 13.5% CP-ECR.

Figure 88 shows the sectioning diagram and characterization of the OCZL#45 sample after the 4-PBT. This was perhaps the most reliable PH ZIRLO sample because the four TCs remained intact during the thermal history and the circumferential temperature variation (1188±9°C) was low.

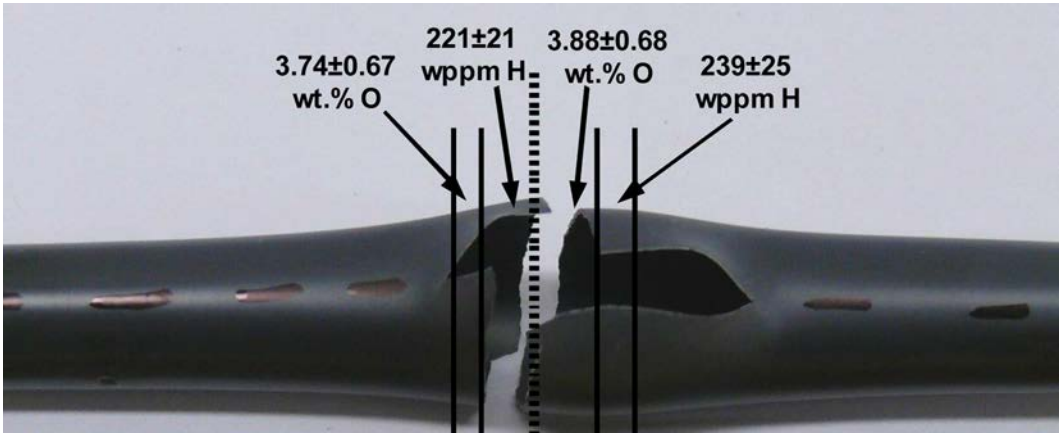

Figure 88. Sectioning diagram and characterization results for the OCZL#45 post-bend sample with 220-wppm pre-test hydrogen oxidized to 13.2% CP-ECR.

5.6 Discussion of Strength of Ballooned and Ruptured Cladding

Sections 5.4 and 5.5 establish maximum bending moments and failure energies for AF and PH ZIRLO cladding, respectively, as a function of oxidation level and pre-test hydrogen content. Both 4-PBT metrics decreased with increasing oxidation level (CP-ECR) and increasing pre-test hydrogen content. In order to determine oxidation-level and hydrogen-content limits to retain "adequate" post-quench strength, the term adequate needs to be quantified. Two approaches were considered for quantifying adequate strength.

The first approach comes from observations made in Section 5.5. If oxidation is limited according to Eq. 17 (see Fig. 25), then M_{max} and E_{max} for PH ZIRLO are at least as high as for AF ZIRLO with oxidation limited to 17%. It was also shown in Section 3.4 that pre-hydrided cladding is a good surrogate for high-exposure cladding with the same hydrogen content. It is further known that M_{max} and E_{max} are measures of strength and toughness, respectively. Therefore, it can be concluded that the strength and toughness of high-exposure and ruptured cladding containing hydrogen is at least as high as that of fresh cladding at 17% CP-ECR. Because the 17% limit has been used as a measure of adequacy for fresh cladding by the NRC for more than 40 years, it can be concluded that the same level of adequacy for high-exposure cladding would be maintained using Eq. 17 to limit the oxidation level based on the pre-LOCA-transient hydrogen content.

The second approach, which is more quantitative, comes from considering axial loading during quench that results from partial restraint of axial contraction during quench cooling due to bonding of the cladding to the grid spacers. JAEA and others have estimated limits for the axial restraint load due to this phenomenon. In addition, JAEA has generated a large data set for failure/non-failure loads for AF Zry-4, PH Zry-4, and irradiated Zry-4 under conditions of full restraint (AF and PH) and load-limited restraint (PH and irradiated) [37−40]. For the load-limited restraint cases, loads of 735 N, 540 N, and 390 N were used. The load limit of 540 N was adopted as the reference case for testing irradiated material even though it was argued by JAEA that this was a very conservative upper bound on the restraint load that could be imposed by cladding bonded to grid spacers. In the JAEA tests, the cladding was restrained from contracting during slower cooling from the oxidation temperature to the quench temperature (700°C) and

during rapid quench cooling until the load limits were reached. For the remainder of the quench to 100°C, the axial load on the cladding was maintained at the load limit.

In this section, the JAEA results for fully restrained AF 17×17 Zry-4 are compared to the Argonne 4-PBT results for AF 17×17 ZIRLO. In both types of tests, the cladding was exposed to axial stresses. The maximum stress for which Argonne samples did fail is compared to the maximum stress for which JAEA fully constrained cladding did not fail. Thus, adequate strength in this approach is defined as the strength needed to survive full axial constraint during quench cooling.

The description of the JAEA test parameters and results is documented in Refs. 37−40 and summarized in Ref. 5, which also includes the detailed analytical method for relating the maximum axial tensile stress in 4-PBT samples to the maximum axial tensile stress in fully restrained samples during cooling. For the convenience of the reader, the analytical method and results are repeated below.

Traditional axial tension tests are conducted either in the displacement-controlled mode or the load-controlled mode. In the displacement-controlled mode, the displacement rate (and hence displacement) is the independent parameter and the load is measured as a function of displacement. The RCTs and 4-PBTs used in the current work were displacement-controlled tests. The JAEA LOCA integral samples were not tested in the traditional way. The cooling rate from the oxidation temperature (e.g., 1200°C) to the quench temperature (700°C) and end-of-quench cladding temperature (≤100°C) were controlled; the load was measured as a function of time. For fully constrained tests, the displacement was zero. The purpose of these tests was to determine: the fracture/no-fracture boundary as a function of hydrogen content and oxidation level and the fracture load for tests in which fracture occurred.

The JAEA-measured loads were relatively low during cooling from the oxidation hold temperature to the 700°C quench temperature due to the low yield strength and high plasticity of the cladding metal at elevated temperatures and the relatively low cooling rate. However, the load increased rapidly during quench cooling because the metal yield strength increased with decreasing temperature and the metal did not have time to flow plastically to relax the axial thermal stresses induced by the restraint.

ANL 4-PBT results can be compared to JAEA axial-restraint results as both tests induce axial stresses. The stress distributions are different: (a) for the JAEA tests, the stress acting on a cross section is tensile and (b) for the 4-PBT, the axial stress acting on a cross section varies from tensile to compressive across the cross section. However, failure of a brittle material is governed by the maximum tensile stress. Given the failure bending moment for a 4-PBT, the equivalent axial force that gives the same maximum tensile stress can be determined. This determination can be made more easily for 4-PBT samples that failed outside the rupture region. The 4-PBT results for the OCZL#19 test sample are used for this comparison because: (a) the temperature control during the oxidation phase was excellent (1200±11°C), (b) the CP-ECR was about 17% (17.3%), (c) the oxidation level and hydrogen content were well characterized at one of two failure locations, and (d) metallographic examination was used to determine oxide-layer and metal-wall thicknesses at one failure location. Figure 89a (repeat of Fig. 76) shows the failure locations and some of the characterization results for the failure cross sections that occurred 24-mm below the rupture mid-span. Figure 89b shows a low magnification image of the severed cross section, which is nearly circular in shape. Table 35 defines the geometric and material properties needed for analyses and lists properties and dimensions determined from diameter measurements, lower-magnification (100X) metallographic images, and higher-magnification (200X) metallographic images.

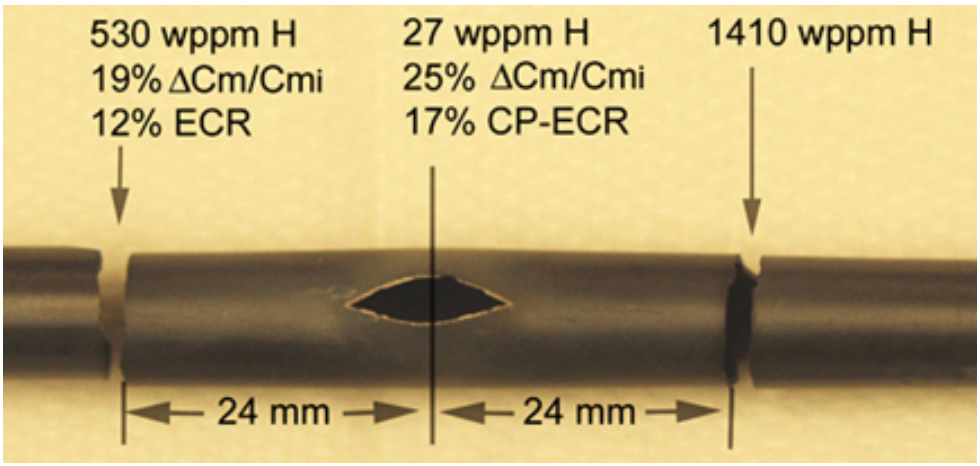

(a) Failure locations

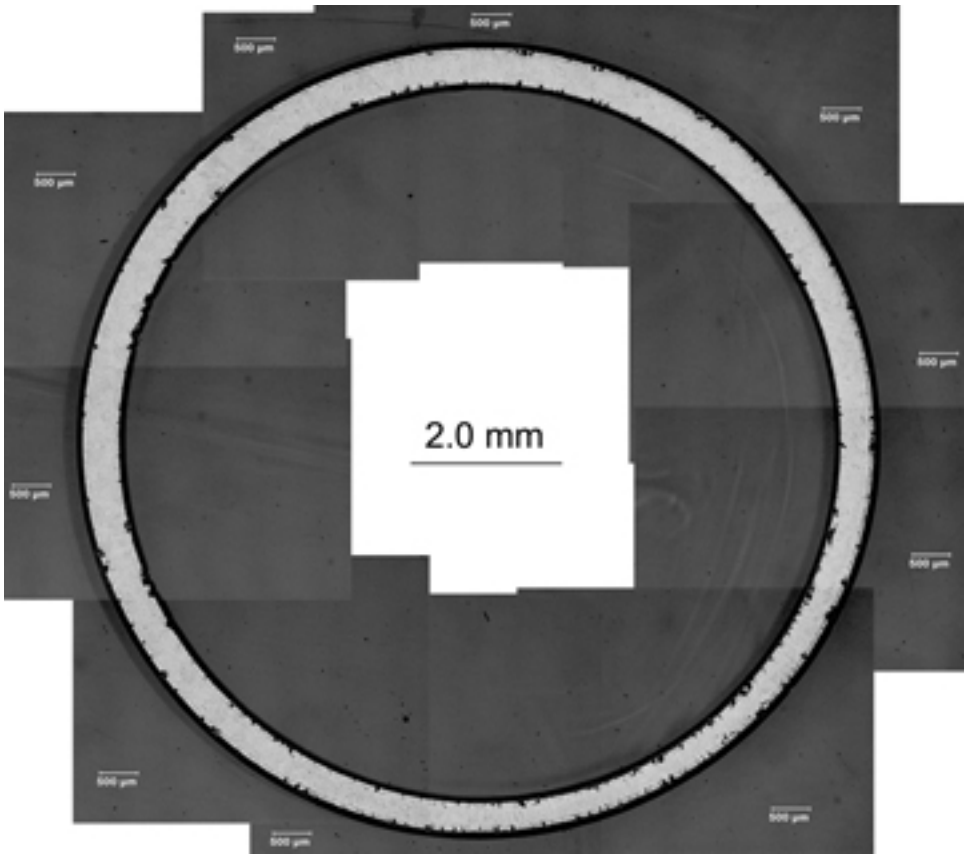

(b) Severed cross section at 24-mm below (left) the rupture mid-span

Figure 89. Images for the post-bend OCZL#19 sample oxidized to 17.3% CP-ECR and quenched: (a) failure locations and (b) severed cross section at 24-mm below the rupture mid-span.

Table 35. Dimensions, properties, and failure bending moment at severed location for the OCZL#19 test sample with 17% CP-ECR in the rupture node and 12% measured ECR at the severed location 24-mm below the rupture mid-span.

Parameter	Value	Comment
Outer Diameter (D_o), mm	10.67	Measured
OD Oxide Thickness $(\delta_{ox})_o$, μm	50±6	Measured
Metal OD (D_{mo}), mm	10.57	$D_{mo} = D_o - 2\,(\delta_{ox})_o$
Metal Wall Thickness (h_m), mm	0.46±0.04	Measured
Metal ID (D_{mi}), mm	9.65	$D_{mi} = D_{mo} - 2\,h_m$
ID Oxide Thickness $(\delta_{ox})_i$, μm	35±6	Measured
Inner Diameter (D_i), mm	9.58	$D_i = D_{mi} - 2\,(\delta_{ox})_i$
Cross-sectional Area (A), mm^2		
OD Oxide $(A_{ox})_o$	1.67	$(A_{ox})_o = (\pi/4)\,[(D_o)^2 - (D_{mo})^2]$
Metal (A_m)	14.61	$A_m = (\pi/4)\,[(D_{mo})^2 - (D_{mi})^2]$
ID Oxide $(A_{ox})_i$	1.06	$(A_{ox})_i = (\pi/4)\,[(D_{mi})^2 - (D_i)^2]$
Area Moment of Inertia (I), mm^4		
OD Oxide $(I_{ox})_o$	23.5	$(I_{ox})_o = (\pi/64)\,[(D_o)^4 - (D_{mo})^4]$
Metal (I_m)	187.1	$I_m = (\pi/64)\,[(D_{mo})^4 - (D_{mi})^4]$
ID Oxide $(I_{ox})_i$	12.2	$(I_{ox})_i = (\pi/64)\,[(D_{mi})^4 - (D_i)^4]$
Young's Modulus (E) at 135°C, MPa		
Oxide (E_{ox})	14.8×10^4	MATPRO [41]
Metal (E_m)	8.65×10^4	MATPRO [42]
Equivalent A (A_{eq}) Relative to Metal, mm^2	19.3	$A_{eq} = A_m + (E_{ox}/E_m)\,A_{ox}$
Equivalent I (I_{eq}) Relative to Metal, mm^4	248	$I_{eq} = I_m + (E_{ox}/E_m)\,I_{ox}$
Maximum Bending Moment (M_{max}), N•m	5.7	Measured

For the 4-PBT sample, the maximum tensile stress (σ_{max}) in the metal is related to the maximum bending moment (M_{max}) according to:

$$\sigma_{max} = M_{max}\,R_{mo}/I_{eq} \tag{26}$$

where R_{mo} is the outer radius ($R_{mo} = D_{mo}/2$) of the metal wall (5.285 mm in this case). This is the location of the outer surface of the oxygen-stabilized alpha layer, which has low strength and is more brittle than the tetragonal oxide layer and the beta layer.

The maximum tensile stress in the metal is thus, σ_{max} = 5.7 N•m (5.285 mm)/248 mm^4 = 121.5 MPa.

For the axial tensile test, the maximum load (P_{max}) is related to the maximum tensile stress (σ_{max}) in the metal according to:

$$P_{max} = \sigma_{max}\,A_{eq} \tag{27}$$

Setting σ_{max} to 121.5 MPa and A_{eq} to 19.3 mm^2 gives P_{max} = 2345 N. If the correlation value (see Eq. 24) of 6.3 N•m at 17% CP-ECR had been used, then P_{max} would be equal to 2591 N.

For the JAEA fully restrained samples [37,38], the maximum load measured for AF samples that survived quench from 700°C to ≤100°C was in the range of 1200 N to 2400 N. For samples oxidized at 1200°C to >12% Baker-Just-ECR, the maximum load was 1200 to 2000 N for PH samples that survived quench. These results are for cladding with pre-test hydrogen contents ≥100 wppm. Thus, even under these conditions, it is evident that the OCZL#19 test sample would have enough strength to survive the JAEA fully restrained quench without failure. As the ANL bend tests were performed at 135°C, it would be more proper to say that the 17% CP-ECR OCZL#19 sample would have survived the JAEA full-constraint test with quench from 700°C to 135°C. However, based on one 4-PBT conducted at 20°C, the result for M_{max} was not sensitive to test temperature. Thus, the Argonne 4-PBT results would apply to the end-of-quench temperature (≤100°C) achieved in the JAEA tests.

Equations 26 and 27 can be combined to give the JAEA tensile failure load (P_{max}) as a function of the ANL failure bending moment (M_{max}):

$$P_{max} = M_{max} R_{mo} (A_{eq}/I_{eq}) \quad (28)$$

In principle, Eq. 28 can be used for samples that severed in the rupture node (e.g., OCZL#29 at 17% CP-ECR). However, determination of the equivalent area, the location of the neutral axis, and the equivalent area moment of inertia would require numerical integration for cross sections containing a rupture node.

The E_m (86.5 GPa) used for cladding metal was calculated from the MATPRO correlation for as-fabricated, recrystallized-annealed cladding at 135°C. This requires validation because the Young's modulus ($E_{m\beta}$) in the prior beta-phase is 75.6 GPa, and it increases with oxygen content in the oxygen-stabilized alpha layer from 95.6 GPa (alpha/beta boundary) to 115 GPa (alpha/oxide boundary). The analysis was repeated by assuming that the ID/OD alpha layer thicknesses were the same as the ID/OD oxide layer thicknesses and the Young's modulus ($E_{m\alpha}$) was 105 MPa. Using 75.6 GPa for $E_{m\beta}$ and 105 GPa for $E_{m\alpha}$ resulted in a change in P_{max} of only <0.5%. Thus, the use of 86.5 GPa for E_m is justified.

Argonne's test samples with 220-wppm hydrogen would also have survived the JAEA fully restrained quench tests as long as the oxidation were limited to <17%. The M_{max} data reported in Section 5.5 for these two samples are: 6.6 N•m at 13.2% CP-ECR and 3.2 N•m at 15.6% CP-ECR. It appears as if the sample with 220-wppm and 13.2% CP-ECR would have survived the JAEA fully restrained quench test whereas the sample with 220-wppm and 15.6% CP-ECR might not survive. However, if the oxidation limit for 220 wppm hydrogen were based on data shown in Fig. 25 and the Eq. 17 correlation value for ductility retention in non-deformed samples, this oxidation limit would be 11%. As shown in Section 5.5, extrapolation of the 220-wppm data to 11% CP-ECR gives M_{max} in the range of 8.9 N•m to 9.6 N•m. Although clearly conservative, it appears that adequate strength of PH samples can be preserved if Eq. 17 is used to limit the oxidation level. This result is fortuitous as Eq. 17 is based on retention of ductility for uniformly oxidized non-deformed cladding rings subjected to RCTs.

For the other three PH samples tested, hydrogen contents were ≥390 wppm, which would limit oxidation levels to ≤7 % CP-ECR, as well as the peak oxidation temperature for >400 wppm. Although no data could be generated for CP-ECR values of >0% to 10% at 1200°C peak temperature, it is speculated that these samples would survive the JAEA fully restrained test if oxidation levels were limited by Eq. 17.

Upper-bound conservatism has been incorporated in the quantification of adequate strength. Quantification is based on the assumption that the cladding must be strong enough to survive full axial restraint during quench cooling. It is highly unlikely that the cladding/grid-spacer bond and the grid spacer springs could support such high loads.

6 REFERENCES

Documents issued by USNRC are shown with accession numbers (e.g., ML082130389), and these documents can be found using USNRC's web-based ADAMS search engine at www.nrc.gov or Google. Journal of Nuclear Materials articles can be found online at www.sciencedirect.com.

1. M. Billone, Y. Yan, T. Burtseva, and R. Daum, *Cladding Embrittlement during Postulated Loss-of-Coolant Accidents*, NUREG/CR-6967, ML082130389, July 2008.

2. USNRC, *Conducting Periodic Testing For Breakaway Oxidation Behavior*, RG 1.222, ML15238B044, 2016.

3. USNRC, *Testing For Postquench Ductility*, RG 1.223, ML15238B079, 2016.

4. USNRC, *Establishing Analytical Limits For Zirconium-Based Alloy Cladding*, RG 1.224, ML15238B155, 2016.

5. M.C. Billone, *Assessment of Current Test Methods for Post-LOCA Cladding Behavior*, NUREG/CR-7139, ML12226A182, August, 2012.

6. G. Hache and H.M. Chung, "The History of LOCA Embrittlement Criteria," *Proceedings of the Twenty-Eighth Water Reactor Safety Information Meeting*, NUREG/CP-0172 (Segment 2), ML011370559, April 30, 2001, 205-237.

7. H.M. Chung and T.F. Kassner, "Pseudobinary Zircaloy–Oxygen Phase Diagram," *J. Nucl. Mater.* **84** (1979) 327–339.

8. Jean-Christophe Brachet, Laurence Portier, Thierry Forgeron, Jacky Hivroz, Didier Hamon, Thomas Guilbert, Thierry Bredel, Pascal Yvon, Jean-Paul Mardon, and Patrick Jacques, "Influence of Hydrogen Content on the α/β Phase Transformation Temperature and on the Thermal-Mechanical Behavior of Zy-4, M4 (ZrSnFeV), and M5™ (ZrNbO) Alloys During the First Phase of LOCA Transient," *Zirconium in the Nuclear Industry*, ASTM STP 1423 (2002) 673-701.

9. J. P. Mardon, J.C. Brachet, L. Portier, V. Maillot, T. Forgeron, A. Lesbros, and N. Waeckel, "Influence of hydrogen simulating burn-up effects on the metallurgical and thermal-mechanical behavior of M5™ and Zircaloy-4 alloys under LOCA conditions," *13th International Conference on Nuclear Engineering*, ICONE13-50457 (2005).

10. Laurence Portier, Thierry Bredel, Jean-Christophe Brachet, Valerie Maillot, Jean-Paul Mardon, and Anne Lesbos, "Influence of Long Service Exposures on the Thermal-Mechanical Behavior of Zy-4 and M5™ Alloys in LOCA Conditions," *J. ASTM Intl.*, **2**, No. 2, Paper JAI12468 at www.astm.org (2005).

11. V. Vandenberghe, J.C. Brachet, M. Le Saux, D. Gilbon, M. Billone, D. Hamon, J.P. Mardon and H. Hafidi, "Influence of the Cooling Scenario on the Post-Quench Mechanical Properties of Pre-Hydrided Zircaloy-4 Fuel Claddings after High Temperature Steam Oxidation (LOCA Conditions)," *Proc. 2010 LWR Fuel Performance/TopFuel/WRFPM*, Orlando, FL, Sept. 26-29, 2010, Paper 096.

12. J-C. Brachet, C. Toffolon-Masclet, D. Hamon, T. Guilbert, G. Trego, J. Jourdan, A. Stern, and C. Raepsaet, "Oxygen, Hydrogen and Main Alloying Chemical Elements Partitioning Upon Alpha ↔ Beta Phase Transformation in Zirconium Alloys," *Solid State Phenomena*, **172-174** (2011) 753-659 (www.scientific.net).

13. C. Toffolon-Masclet, C. Desgranges, C. Corvalan-Moya, and J-C. Brachet, "Simulation of the β→α(O) phase transformation due to oxygen diffusion during high temperature oxidation of zirconium alloys," *Solid State Phenomena*, **172-174** (2011) 652-657 (www.scientific.net).

14. Louis Baker, Jr. and Louis C. Just, *Studies of Metal-Water Reactions at High Temperatures; III. Experimental and Theoretical Studies of the Zirconium-Water Reaction*, ANL-6548, ML050550198, May 1962.

15. J. V. Cathcart, R. E. Pawel, R. A. McKee, R. E. Druschel, G. J. Yurek, J. J. Campbell, and S. H. Jury, *Zirconium Metal-Water Oxidation Kinetics IV. Reaction Rate Studies*, ORNL/NUREG-17, ML052230079, August 1977.

16. P. Hofmann and C. Politis, "Chemical Interaction Between Uranium Oxide and Zircaloy-4 in the Temperature Range Between 900 and 1500˚C," *Zirconium in the Nuclear Industry (Fourth Conference)*, ASTM STP 681 (1979) 537-560.

17. USNRC, *Procedure for Conducting Breakaway Oxidation Tests with Zirconium-based Cladding Alloys*, ML090840258, March 23, 2009.

18. USNRC, *Procedure for Conducting Oxidation and Post-Quench Ductility Tests with Zirconium-based Cladding Alloys*, ML090900841, March 31, 2009.

19. Y. Yan, T.A. Burtseva, and M.C. Billone, "High-temperature steam-oxidation behavior of Zr-1Nb cladding alloy E110," *J. Nucl. Mater*. **393** (2009) 433-449.

20. S. Leistikow and G. Schanz, "Oxidation Kinetics and Related Phenomena of Zircaloy-4 Fuel Cladding Exposed to High Temperature Steam and Hydrogen-Steam Mixtures under PWR Accident Conditions," *Nucl. Eng. Des.* **103** (1987) 65-84.

21. J. H. Baek and Y. H. Jeong, "Breakaway phenomenon of Zr-based alloys during a high-temperature oxidation," *J. Nucl. Mater.* **372** (2008) 152-159.

22. Z. Hozer, C. Gyori, L. Matus, M. Horvath, "Ductile-to-brittle transition of oxidized Zircaloy-4 and E110 claddings," *J. Nucl. Mater.* **373** (2008) 415-423.

23. Yueh, H.K., Comstock, R.J., Dunn, B., Le Saux, M., Lin, Y.P., Lutz, D., Park, D.J., Perez-Fero, E. and Yan, Y., "Loss of Coolant Accident Testing Round Robin," *Proc. LWR Fuel Performance Meeting*, Charlotte, NC, Sept. 15-19, 2013.

24. J.P. Mardon and N. Waeckel, "Behavior of M5™ alloy under LOCA conditions," *ANS-Top-Fuel*, Wurzburg, March 17-19, 2003.

25. L. Yegorova, K. Lioutov, N. Jouravkova, V. Smirnov, V. Chesanov, and A. Goryachev, *Experimental Study of Embrittlement of Zr-1%Nb VVER Cladding under LOCA-Relevant Conditions*, NUREG/IA-0211, ML051100343, March 2005.

26. B. Somfai, Z. Hozer, I. Nagy, T. Novotny, E. Perez-Fero, A. Vimi, and P. Windberg, "High temperature Behavior of E110 Cladding Produced by New Technology," 7-th Intl. Conf. Safety Assurance of NPP with VVER, OKB GIDROPRESS, Podolsk, Russia, 17-20 May, 2011.

27. J.A. Gresham, *Updated Westinghouse Breakaway Oxidation Testing/Behavior (Non-Proprietary)*, LTR-NRC-08-29, ML081700587, June 12, 2008.

28. J.A. Gresham, *Westinghouse Results from Study on Impact of Specimen Preparation on Breakaway Oxidation (Non-Proprietary)*, LTR-NRC-09-24, ML091350581, May 7, 2009.

29. J.A. Gresham, *Weight Gain Data for Zircaloy-4 and ZIRLO Breakaway Tests (Non-Proprietary)*, LTR-NRC-11-10, ML110800046, March 10, 2011.

30. V. Vandenberghe, J.C. Brachet, M. Le Saux, D. Gilbon, J.P. Mardon, and B. Sebbari, "Sensitivity to Chemical Composition and Heating/Oxidation Mode of the Breakaway Oxidation in M5® Cladding Steam Oxidized at 1000°C (LOCA Conditions)," Trans. TopFuel-2012, Manchester, UK, Sept. 2-6, 2012, pp 214-220.

31. G.M. Wolten, "Diffusionless Phase Transformations in Zirconia and Hafnia," J. Amer. Ceram. Soc. 46, 418 (1963).

32. D.A. Powers and R.O. Meyer, Cladding Swelling and Rupture Models for LOCA Analysis, NUREG-0630, ML053490337, April 1980.

33. Mika Helin and Johan Flygare, *NRC LOCA Tests at Studsvik: Design and Construction of Test Train Device and Tests with Unirradiated Cladding Material*, Studsvik/N-11/130, ML12212A431, Jul. 2, 2012.

34. Michelle E. Flanagan, Peter Askeljung, and Anders Puranen, *POST-Test Examination Results from Integral, High-Burnup, Fueled LOCA Tests at Studsvik Nuclear Laboratory*, NUREG-2160, ML13240A256, Aug. 2013.

35. M.C. Billone, "Analysis of Data from Studsvik LOCA with High-Burnup ZIRLO," ANL Letter Report to NRC, ML113640255, Mar. 10, 2011.

36. J.-C. Brachet, V. Vandenberghe-Maillot, L. Portier, D. Gilbon, A. Lesbros, N. Waeckel, and J.-P. Mardon, "Hydrogen Content, Preoxidation, and Cooling Scenario Effects on Post-Quench Microstructure and Mechanical Properties of Zircaloy-4 and M5® Alloys in LOCA Conditions," J. ASTM Intl., Vol. 5, No. 5 (2008), at http://www.astm.org as JAI101116.

37. Fumihisa Nagase and Toyoshi Fuketa, "Effect of Pre-Hydriding on Thermal Shock Resistance of Zircaloy-4 Cladding under Simulated Loss-of-Coolant Accident Conditions," JNST, Vol. 41, No. 7 (2004) 723-730.

38. Fumihisa Nagase and Toyoshi Fuketa, “Behavior of Pre-hydrided Zircaloy-4 Cladding under Simulated LOCA Conditions,” JNST, Vol. 42, No. 2 (2005) 209-218.

39. Fumihisa Nagase and Toyoshi Fuketa, “Fracture Behavior of Irradiated Zircaloy-4 Cladding under Simulated LOCA Conditions,” JNST, Vol. 43, No. 9 (2006) 1114-1119.

40. Fumihisa Nagase, Toshinori Chuto, and Toyoshi Fuketa, “Behavior of High Burn-up Fuel Cladding under LOCA Conditions,” JNST, Vol. 46, No. 7 (2009) 763-769.

41. L.J. Siefken, E.W. Coryell, E.A. Harvego, and J.K. Hohorst, *MATPRO – A Library of Materials Properties for Light-Water-Reactor Accident Analysis*, in SCDAP/RELAP5/MOD 3.3 Code Manual, NUREG/CR-6150, Vol. 4, Rev. 2, ML010330424, January 2001.

42. Geelhood K J, Luscher W G, and Raynaud P A, *Material Property Correlations: Comparison Between FRAPCON-3.5, FRAPCON-1.5, and MATPRO*, NUREG/CR-7024, Rev. 1, ML14296A063, Oct. 31, 2014.

APPENDIX A: TEMPERATURE AND PRESSURE HISTORIES

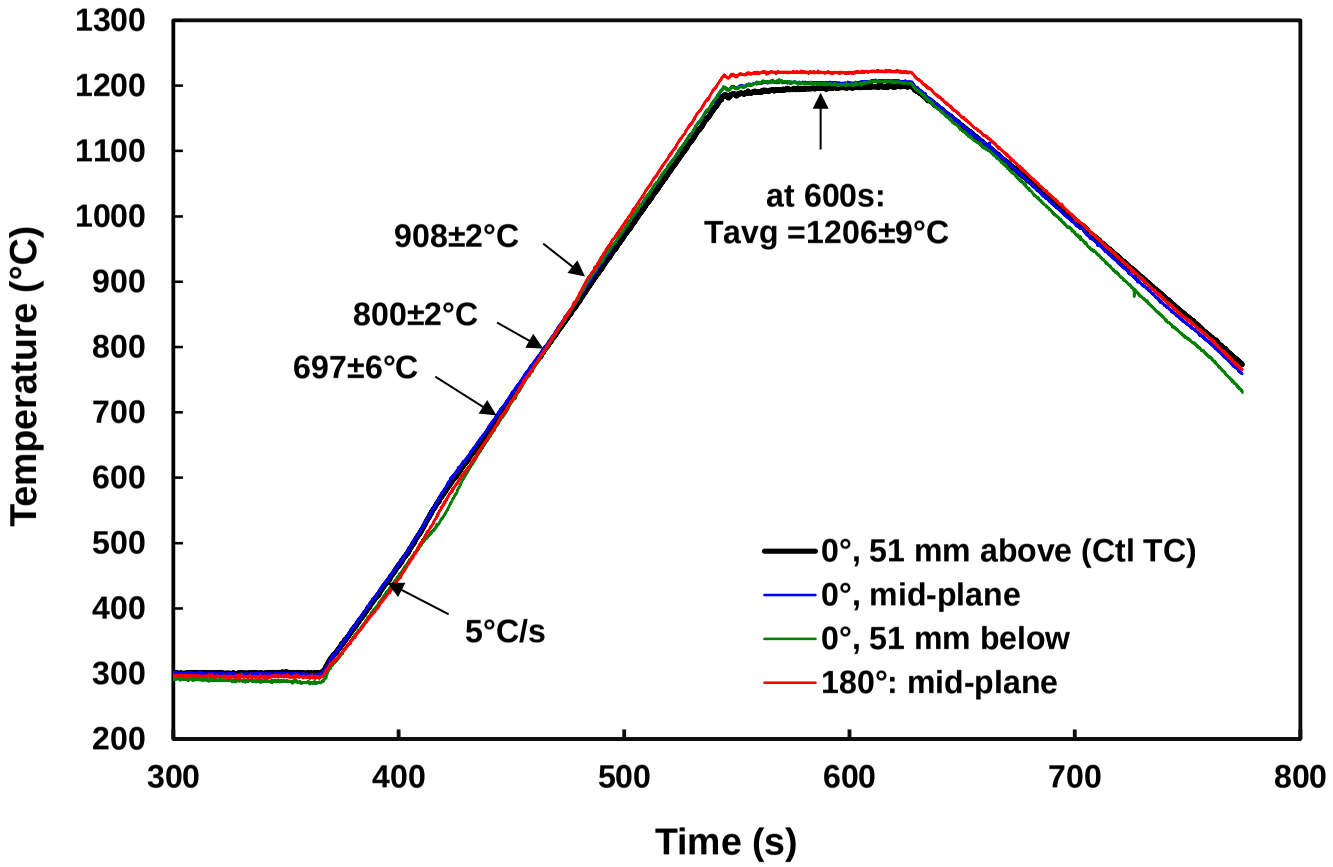

Figure A.1: **Temperature histories for the OCZL#5 thermal benchmark test with unpressurized ZIRLO cladding filled with zirconia pellets. Sample was subjected to outer-surface oxidation with 40 ± 2 µm predicted and measured oxide layer thicknesses at the TC locations.**

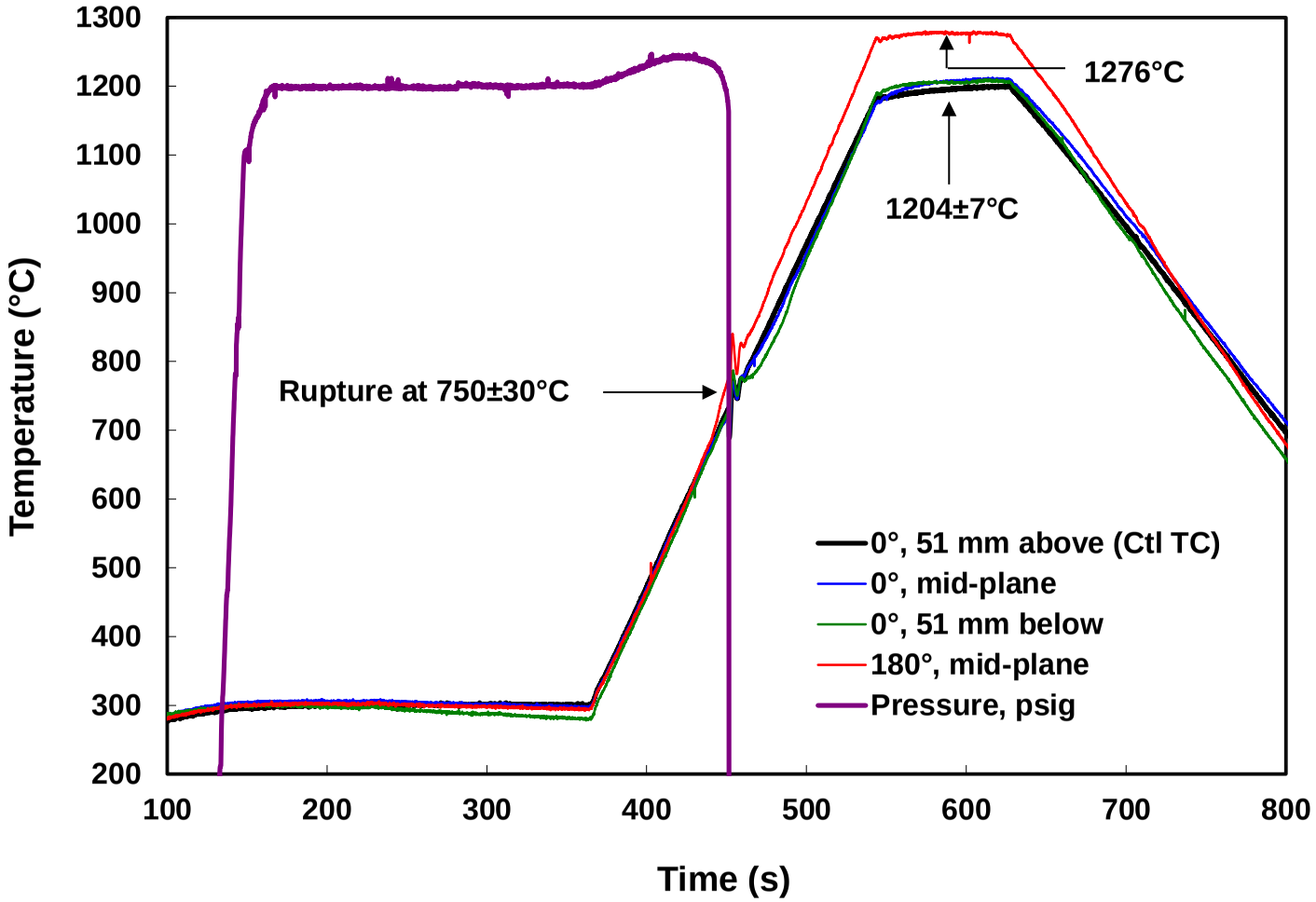

Figure A.2: **Temperature and pressure histories for thermal benchmark test OCZL#6 pressurized to 1200 psig, oxidized to 18% CP-ECR, and cooled without quench. The control TC orientation was about 180° from the rupture opening. The high temperature recorded on the rupture side was confirmed by oxide-thickness measurements.**

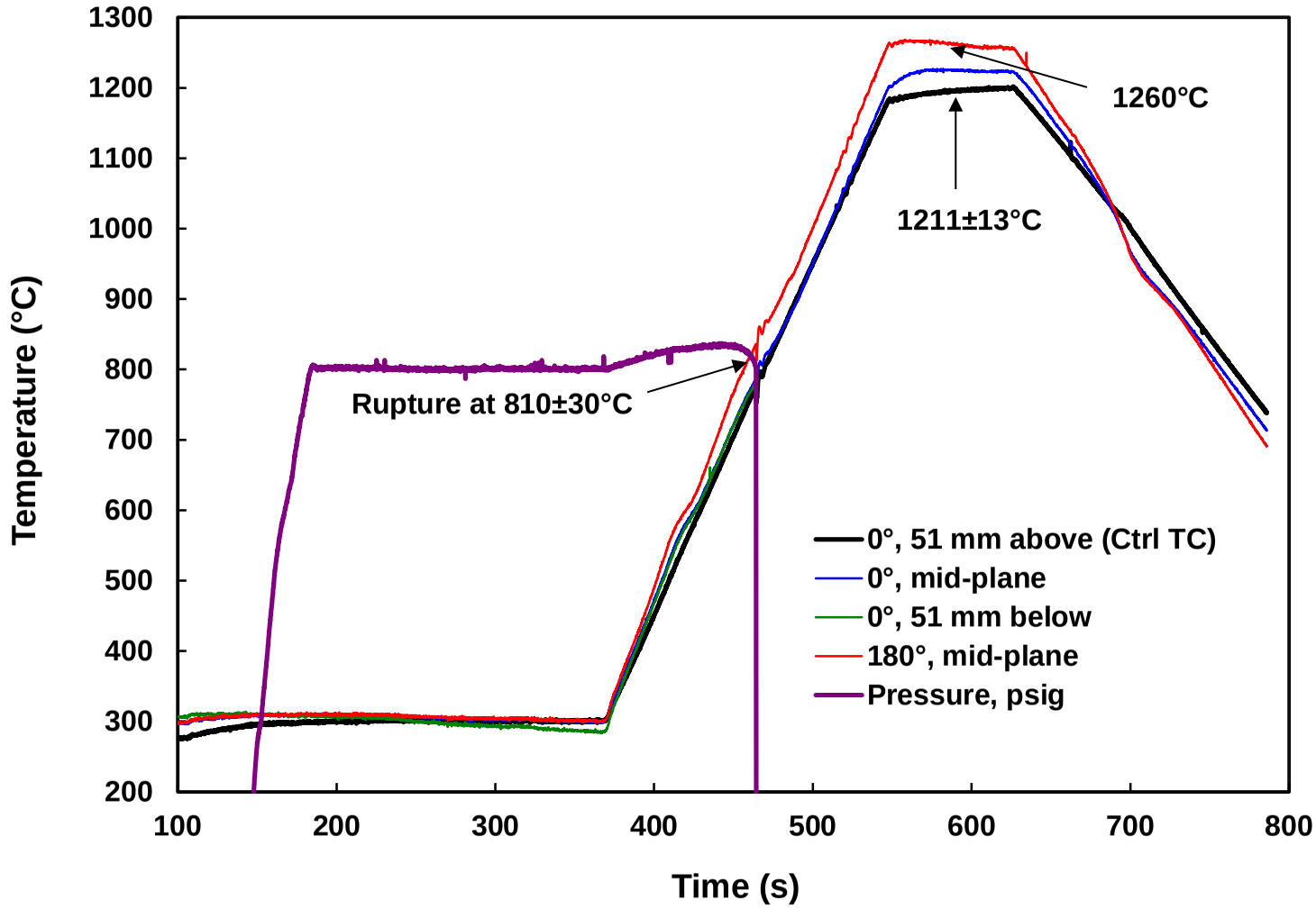

Figure A.3: **Temperature and pressure histories for thermal-benchmark/4-point-bend test OCZL#7 pressurized to 800 psig, oxidized to 16% CP-ECR, and cooled without quench. The control TC orientation was about 180° from the rupture opening.**

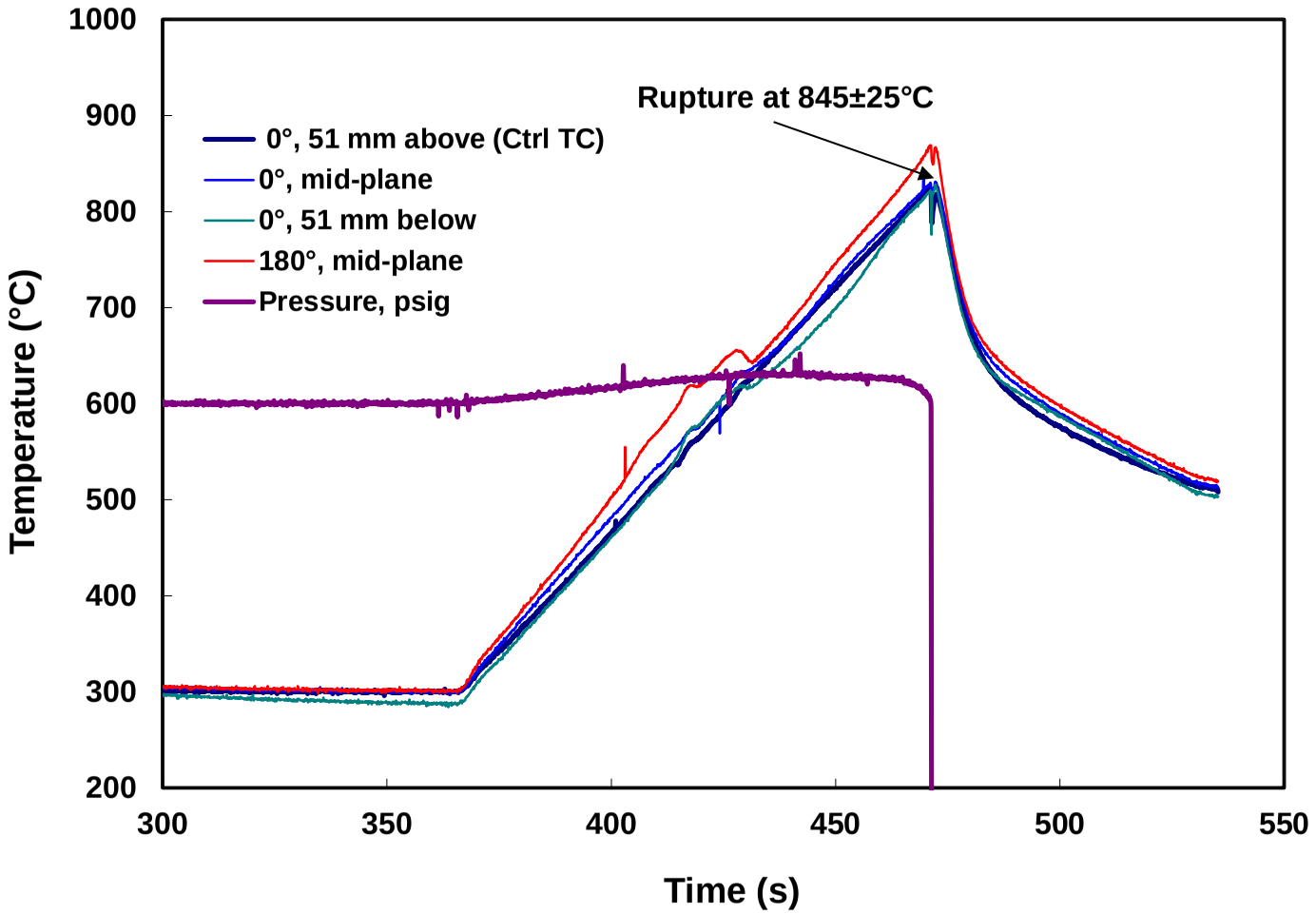

Figure A.4: **Temperature and pressure histories for ramp-to-rupture scoping test OCZL#8 pressurized to 600 psig and cooled without quench.**

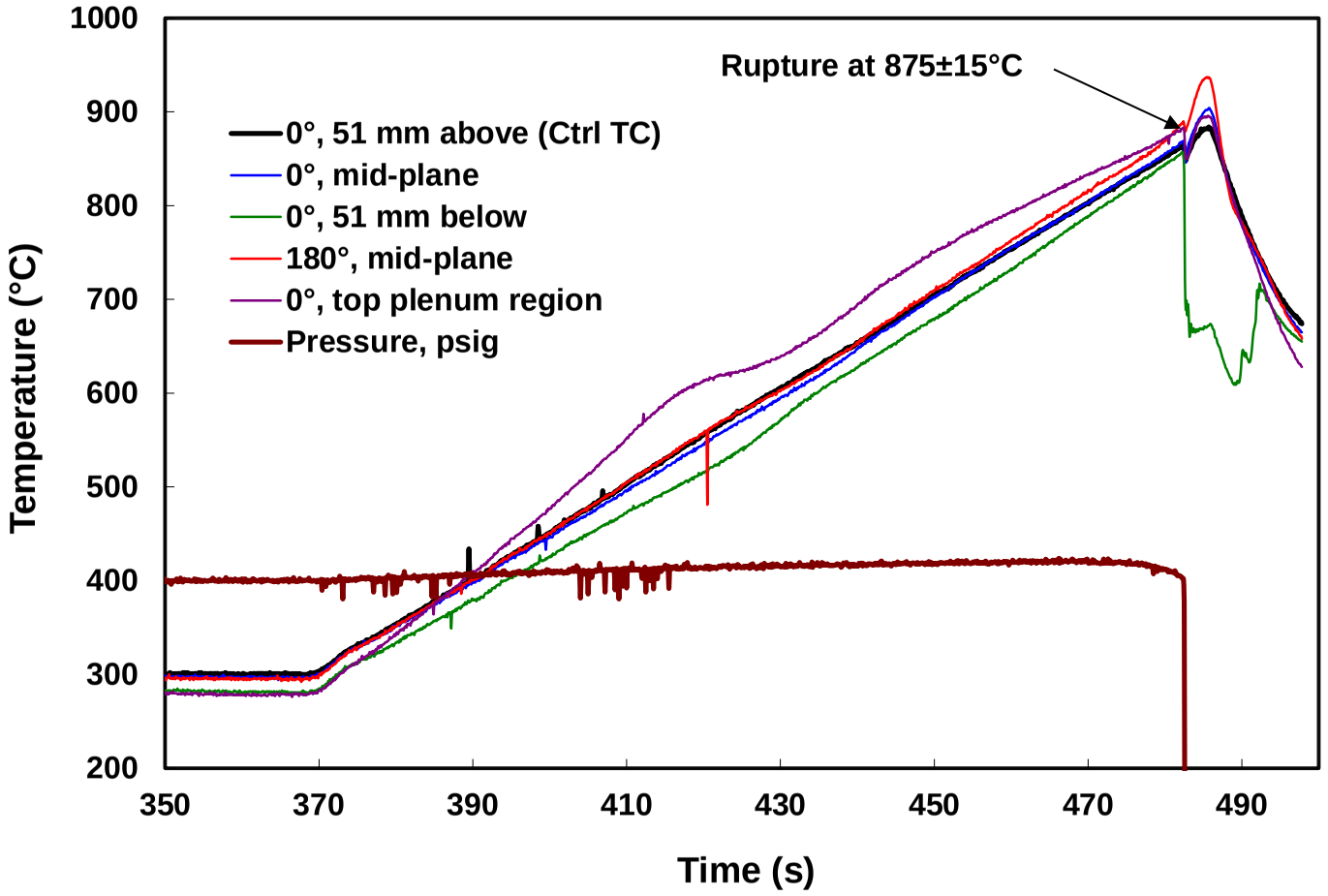

Figure A.5: **Temperature and pressure histories for ramp-to-rupture scoping test OCZL#9 pressurized to 400 psig and cooled without quench.**

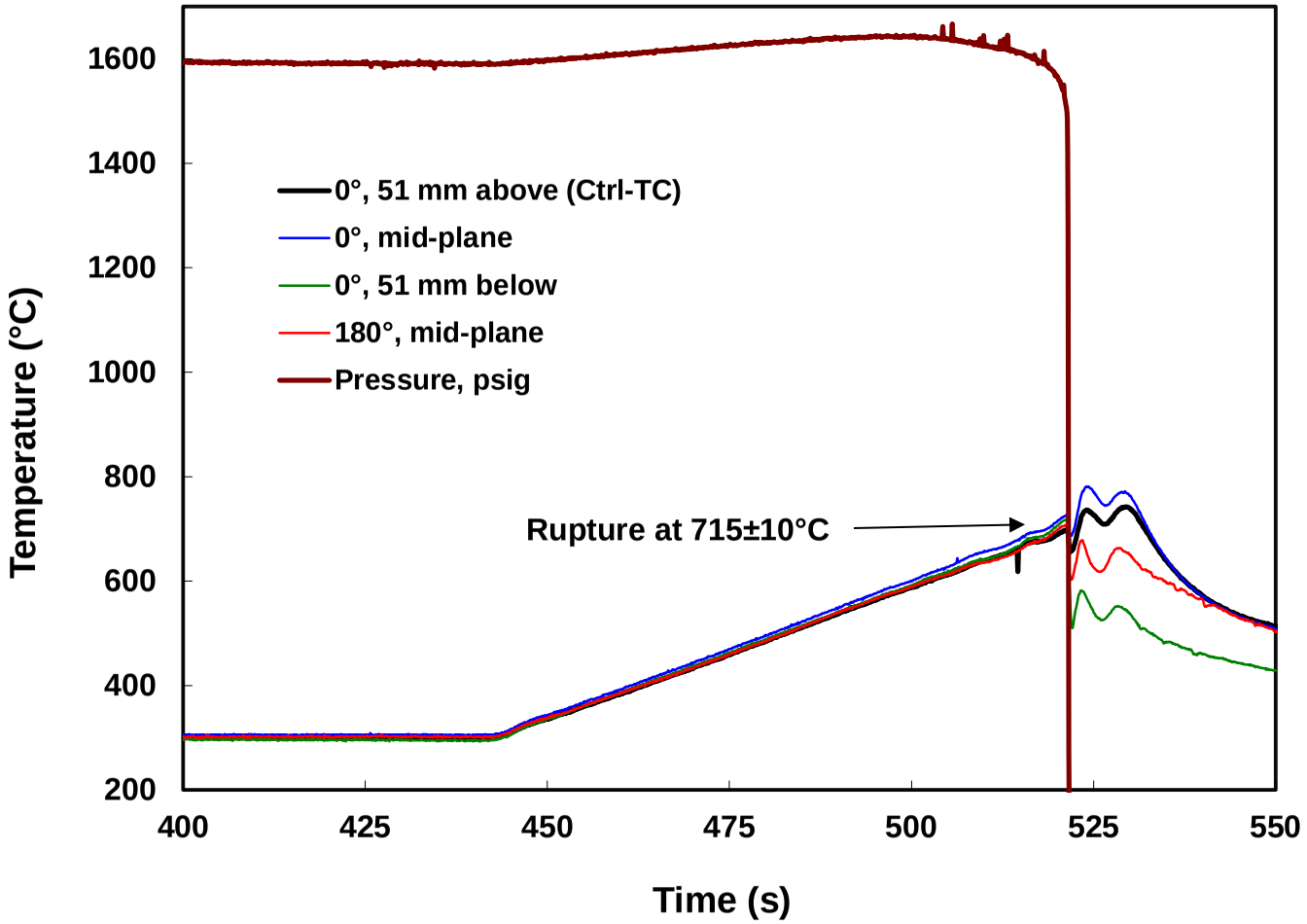

Figure A.6: **Temperature and pressure histories for ramp-to-rupture scoping test OCZL#10 pressurized to 1600 psig and cooled without quench.**

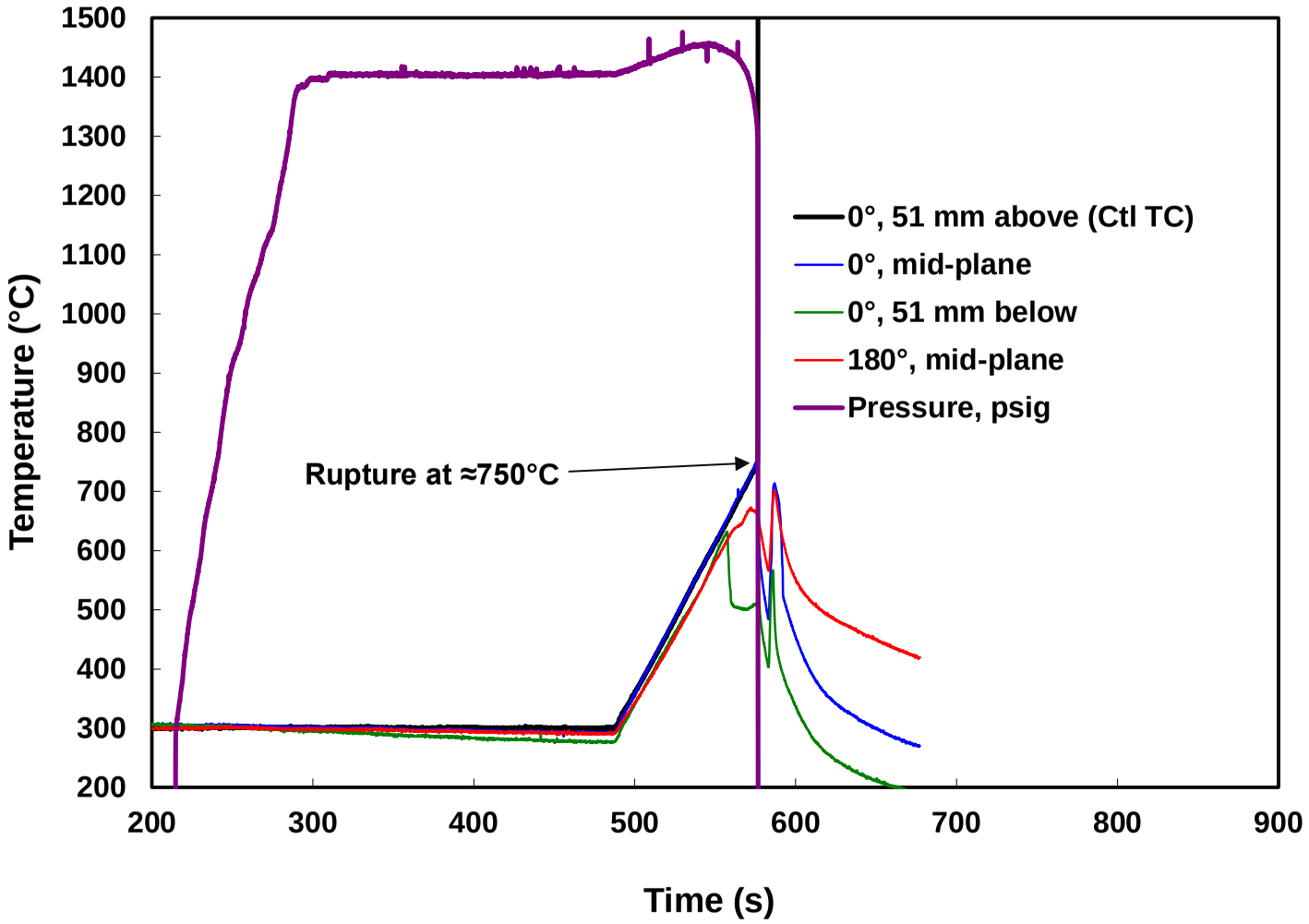

Figure A.7: **Temperature and pressure histories for ramp-to-rupture scoping test OCZL#11 pressurized to 1400 psig and cooled without quench.**

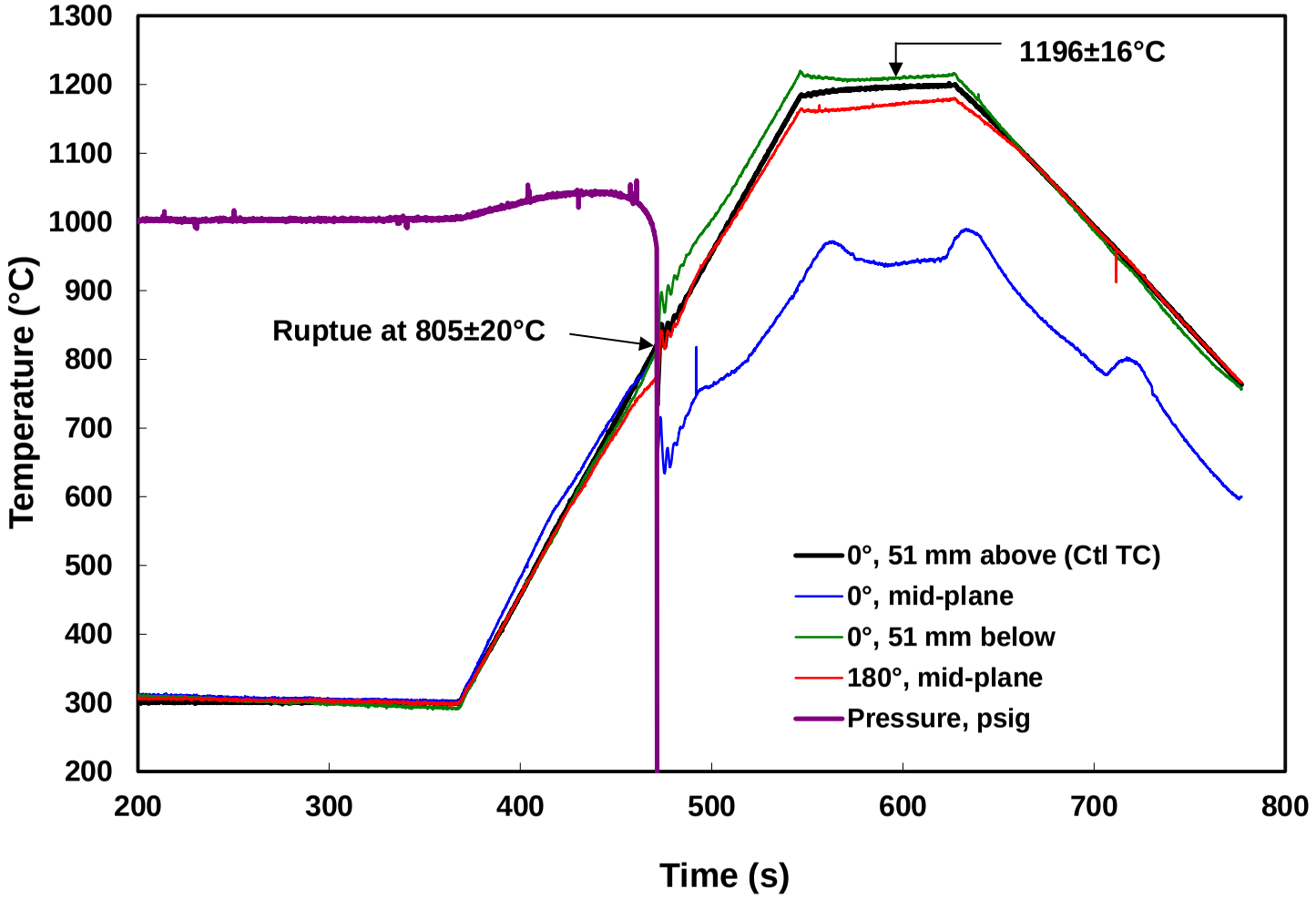

Figure A.8: **Temperature and pressure histories for scoping test OCZL#12 pressurized to 1000 psig, oxidized at 1196°C, and cooled without quench.**

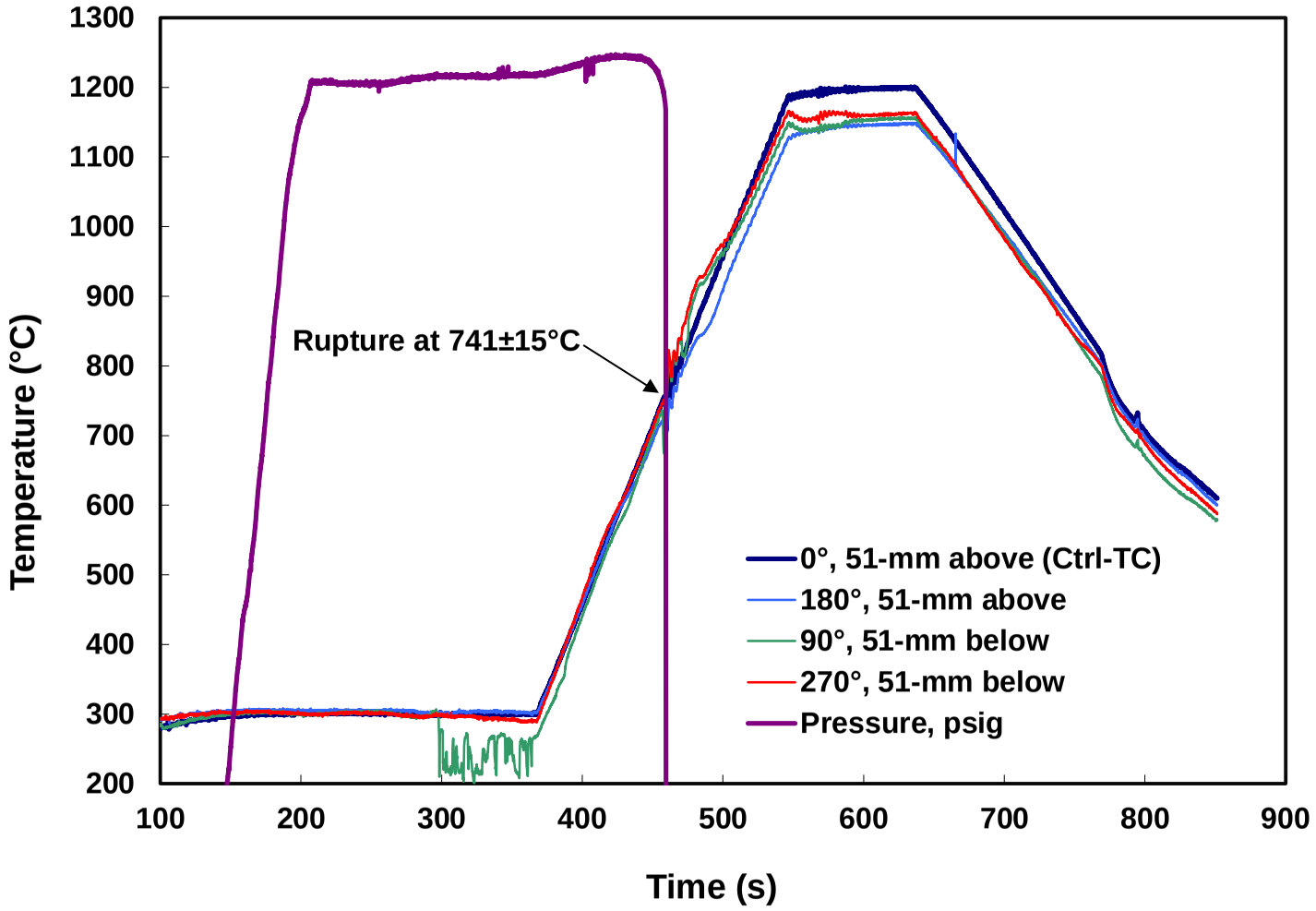

Figure A.9: **Temperature and pressure histories for scoping test OCZL#13 pressurized to 1200 psig, oxidized at ≈1200°C to 15% CP-ECR , and cooled without quench.**

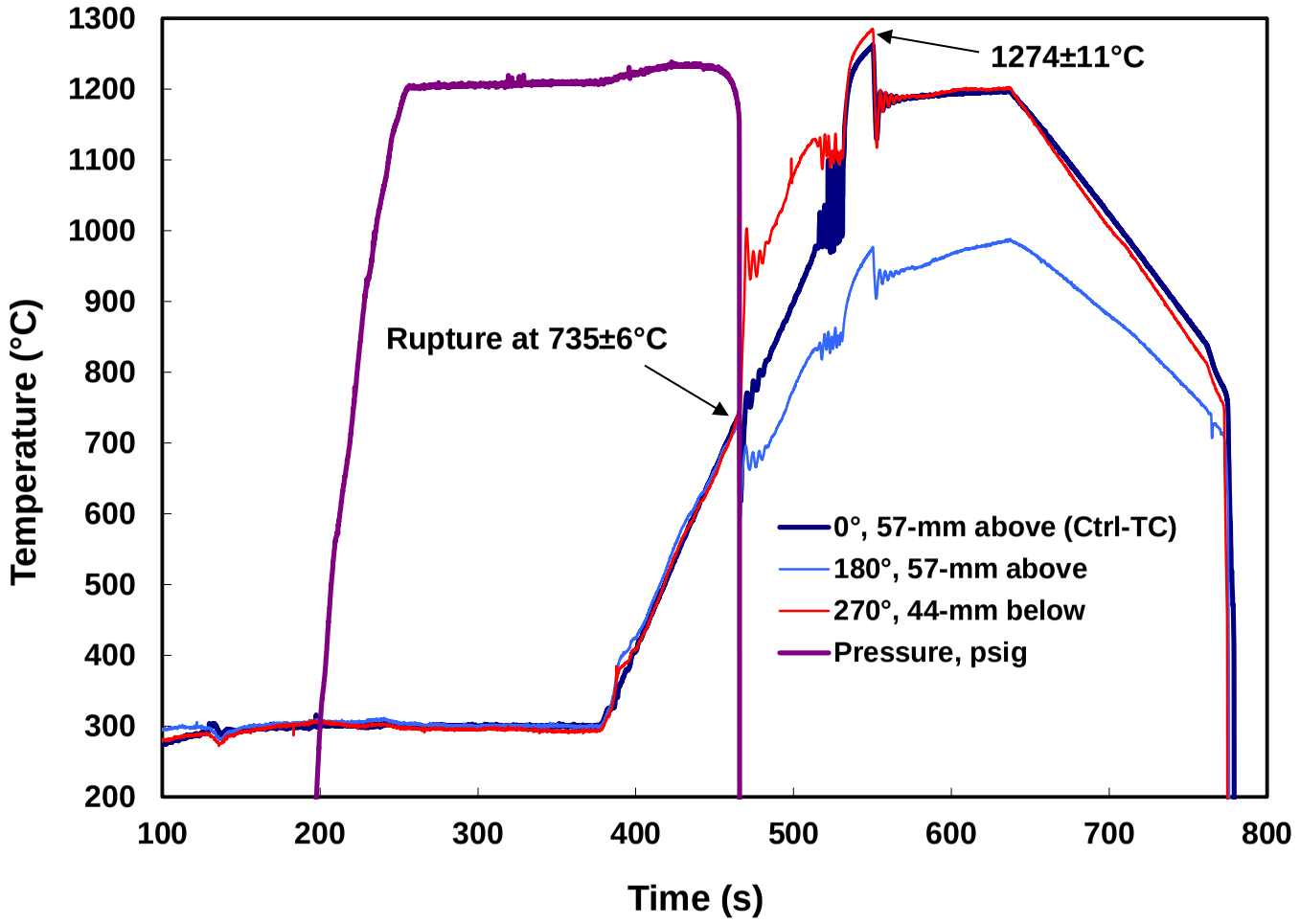

Figure A.10: **Temperature and pressure histories for data-generation test OCZL#14 pressurized to 1200 psig, oxidized at ≈1200°C to 18% CP-ECR, and cooled with quench.**

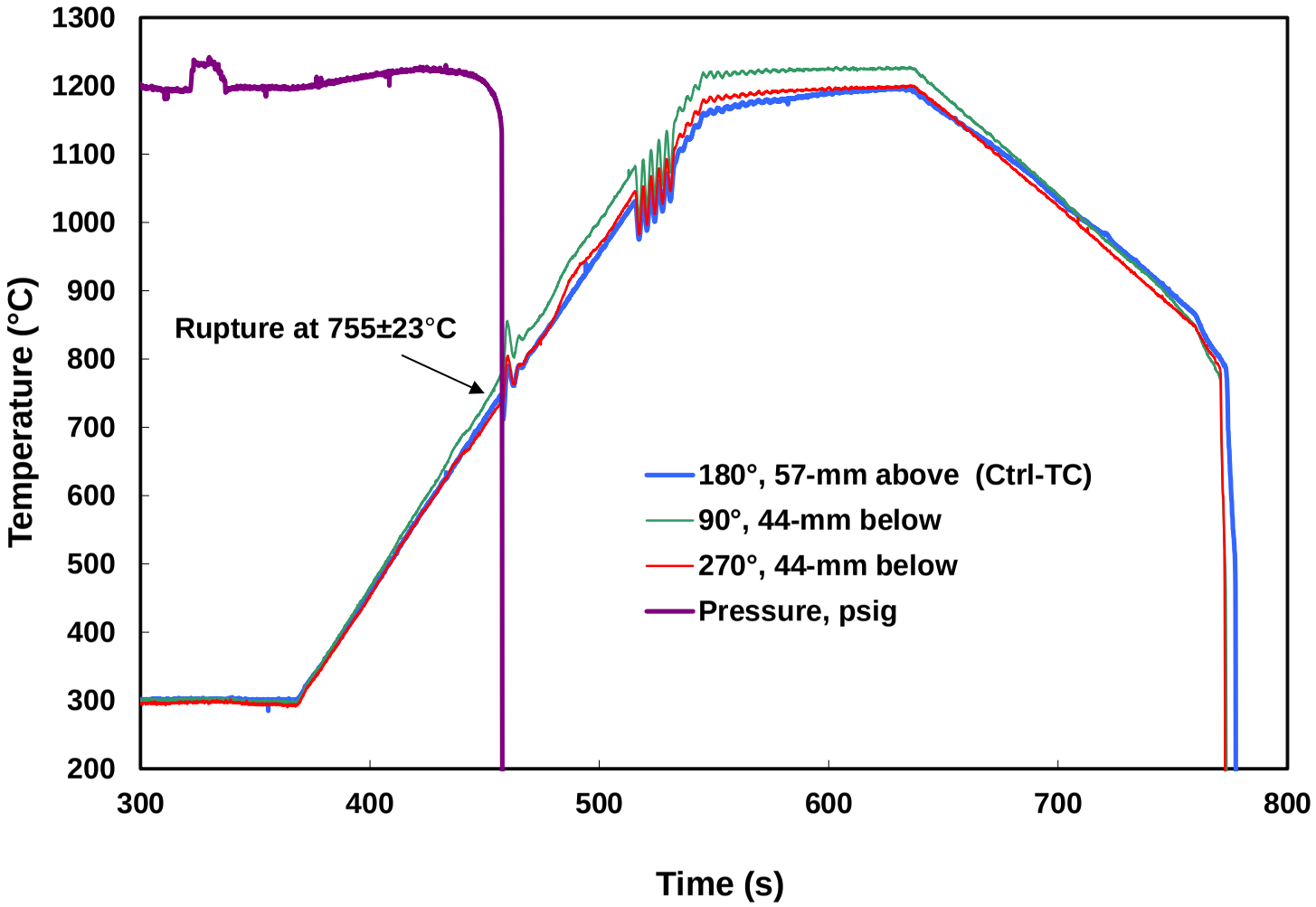

Figure A.11: **Temperature and pressure histories for data-generation test OCZL#15 pressurized to 1200 psig, oxidized at ≈1200°C to 18% CP-ECR, and cooled with quench.**

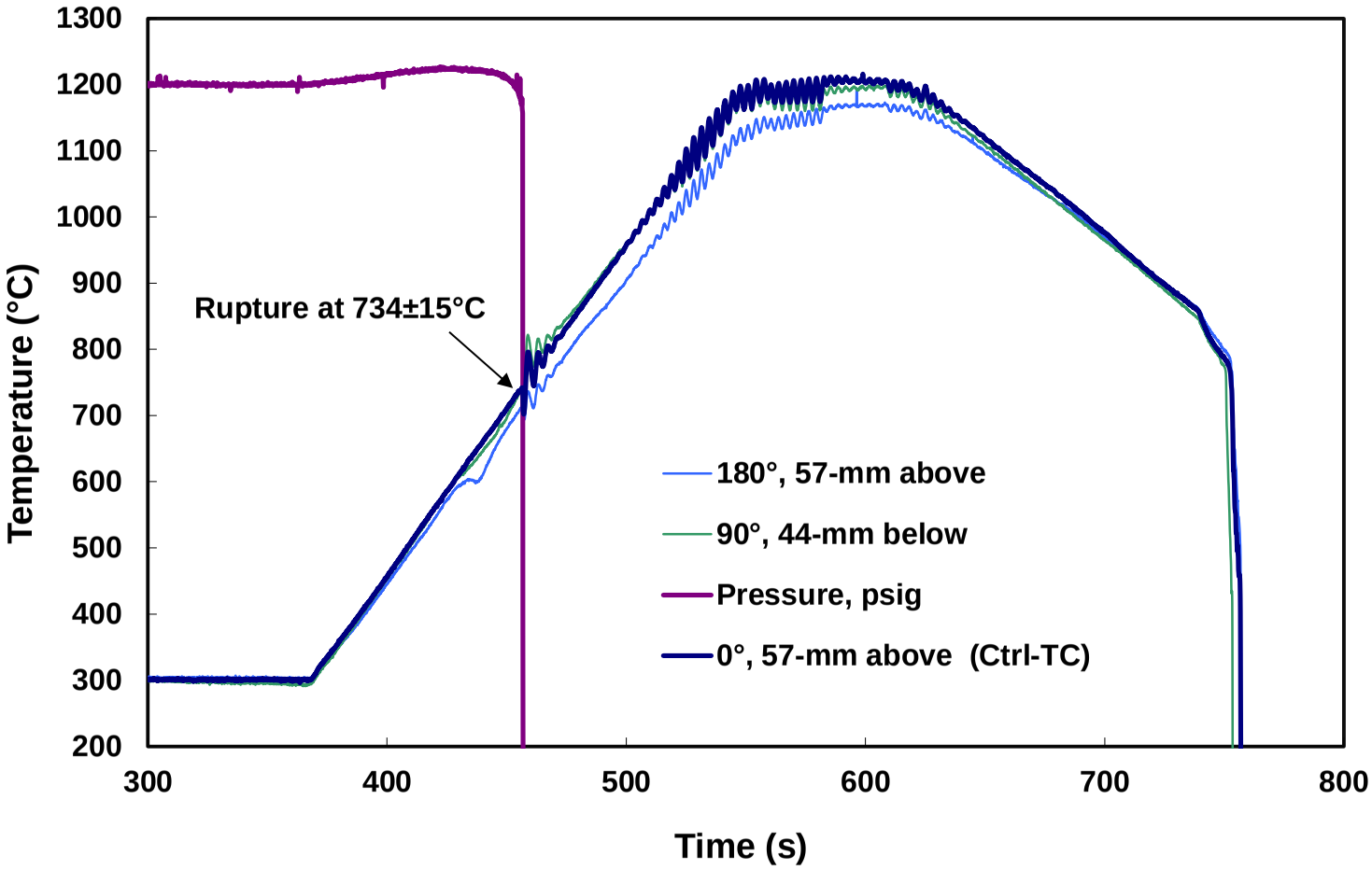

Figure A.12: **Temperature and pressure histories for data-generation test OCZL#16 pressurized to 1200 psig, oxidized at ≈1200°C to 14% CP-ECR, and cooled with quench.**

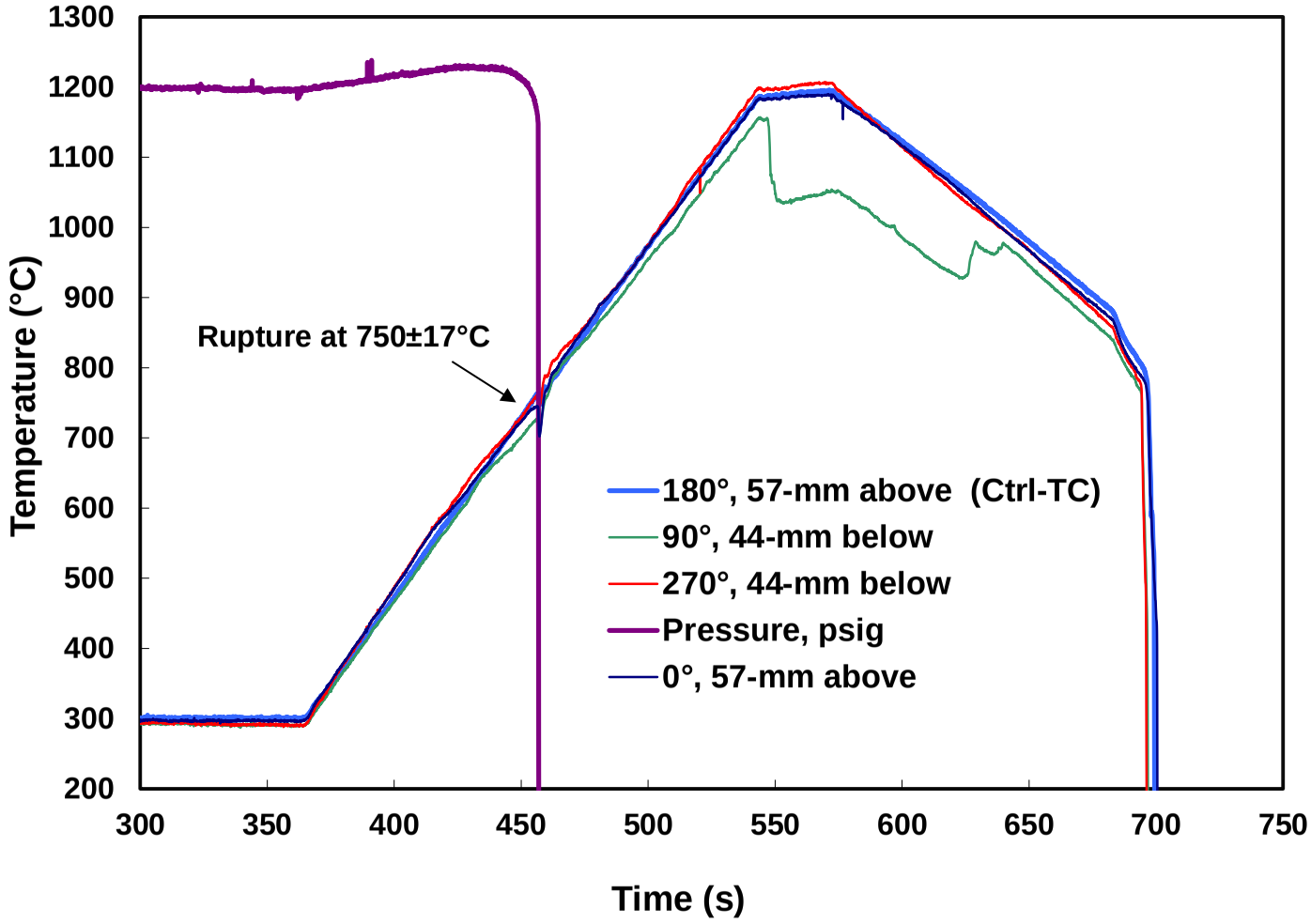

Figure A.13: **Temperature and pressure histories for data-generation test OCZL#17 pressurized to 1200 psig, oxidized at ≈1200°C to13% CP-ECR, and cooled with quench.**

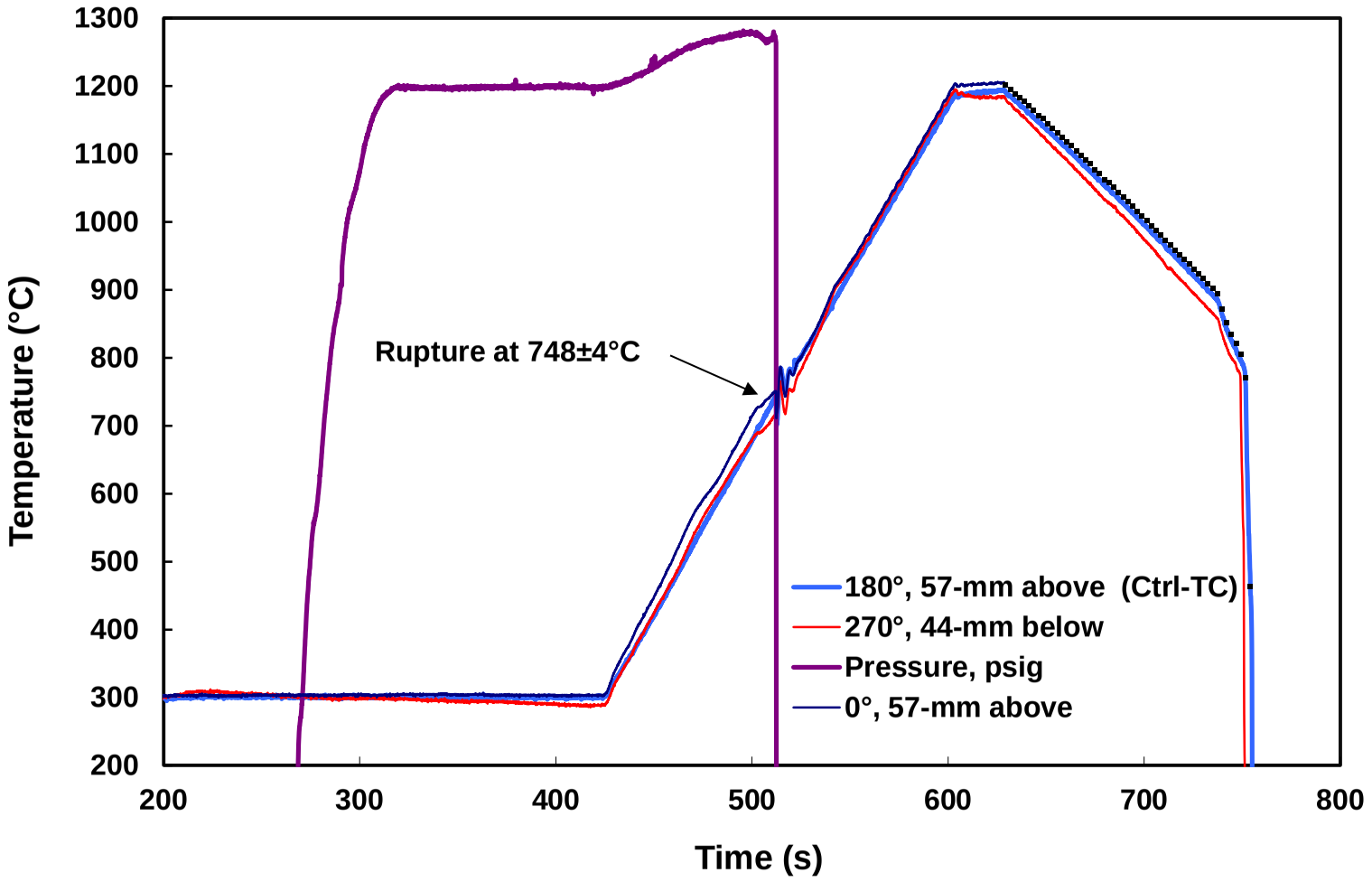

Figure A.14: **Temperature and pressure histories for data-generation test OCZL#18 pressurized to 1200 psig, oxidized at ≈1200°C to 12% CP-ECR, and cooled with quench.**

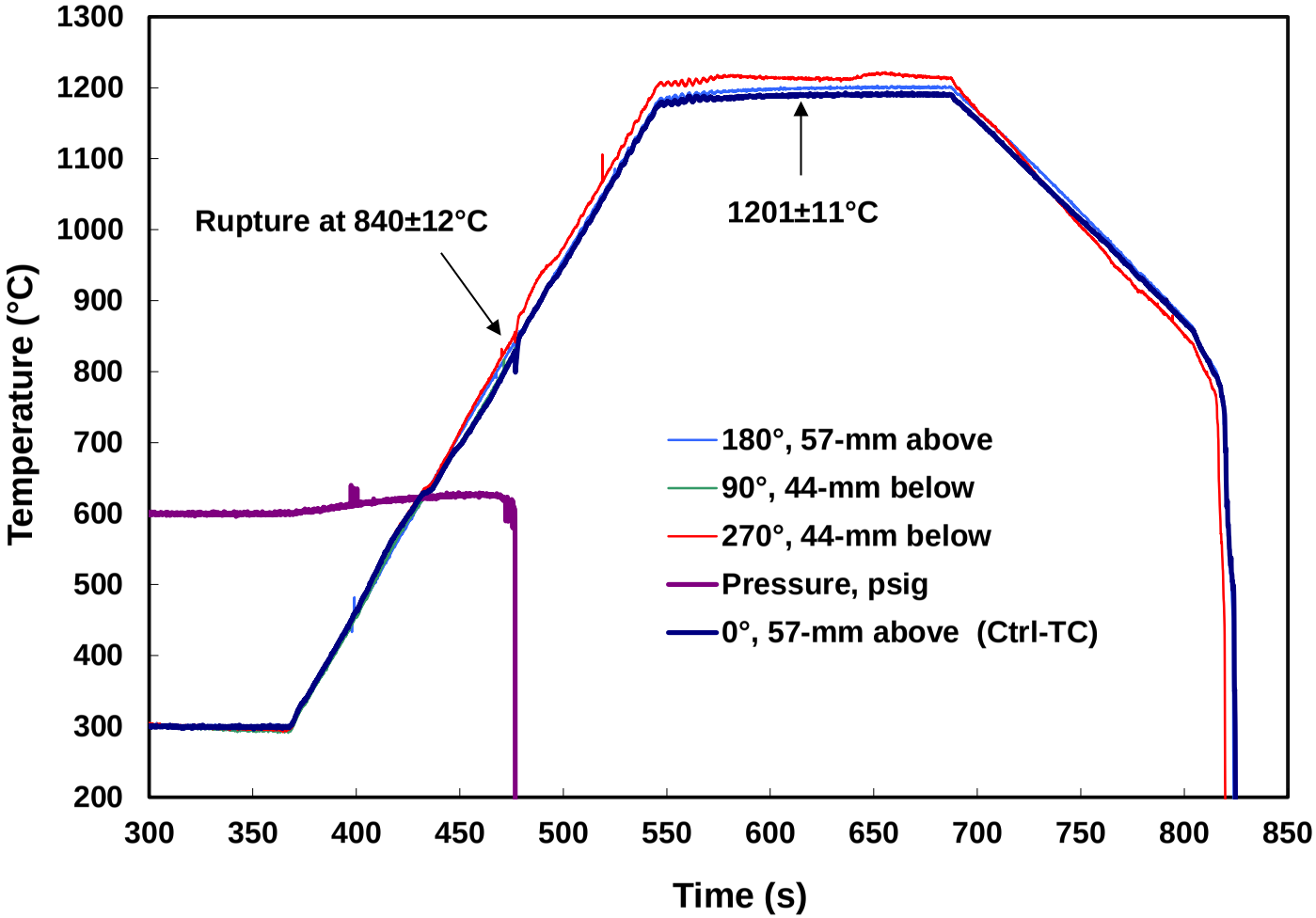

Figure A.15: **Temperature and pressure histories for data-generation test OCZL#19 pressurized to 600 psig, oxidized at ≈1200°C to 17% CP-ECR, and cooled with quench.**

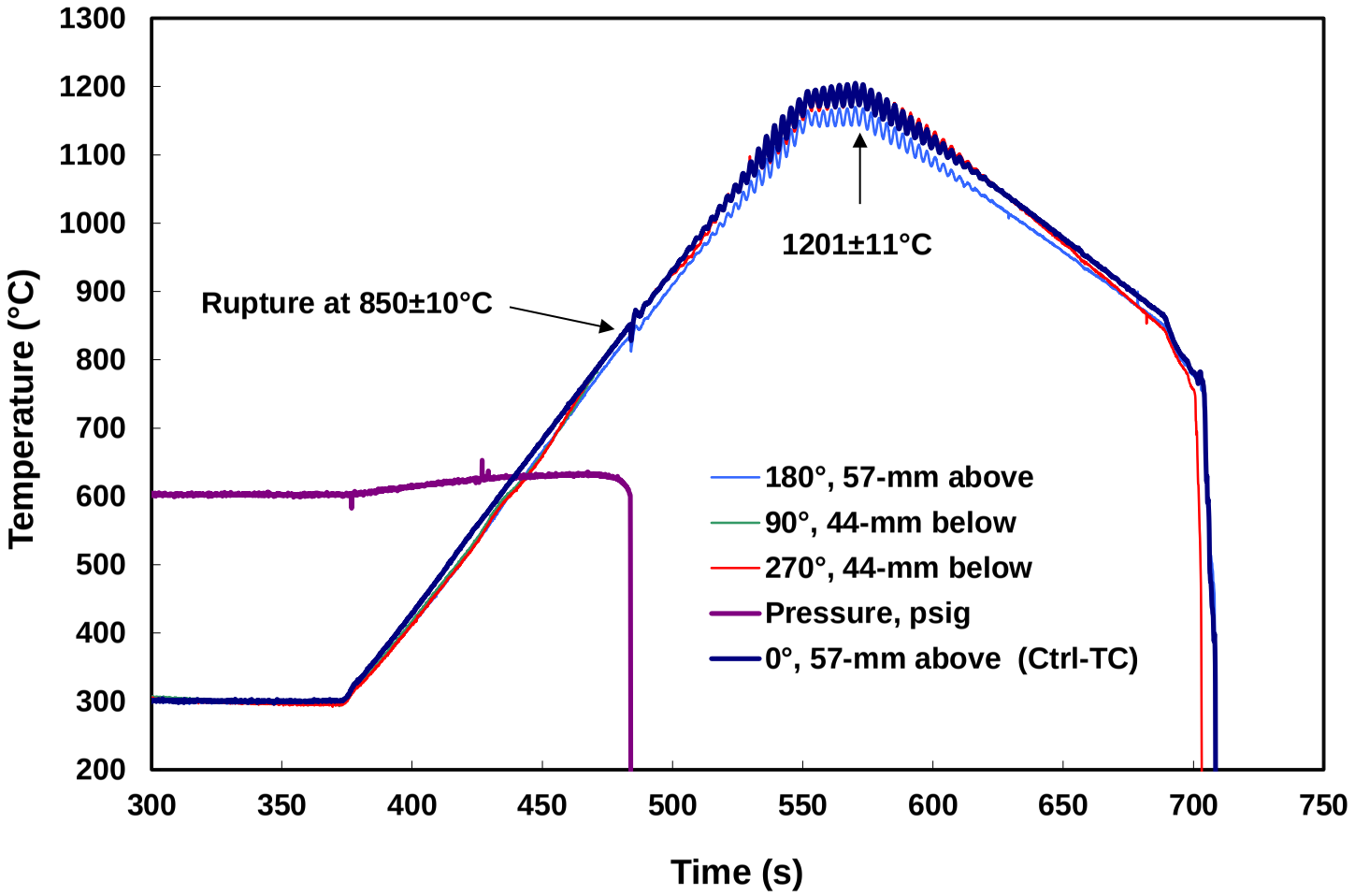

Figure A.16: **Temperature and pressure histories for data-generation test OCZL#21 pressurized to 600 psig, oxidized at ≈1200°C to 11% CP-ECR, and cooled with quench.**

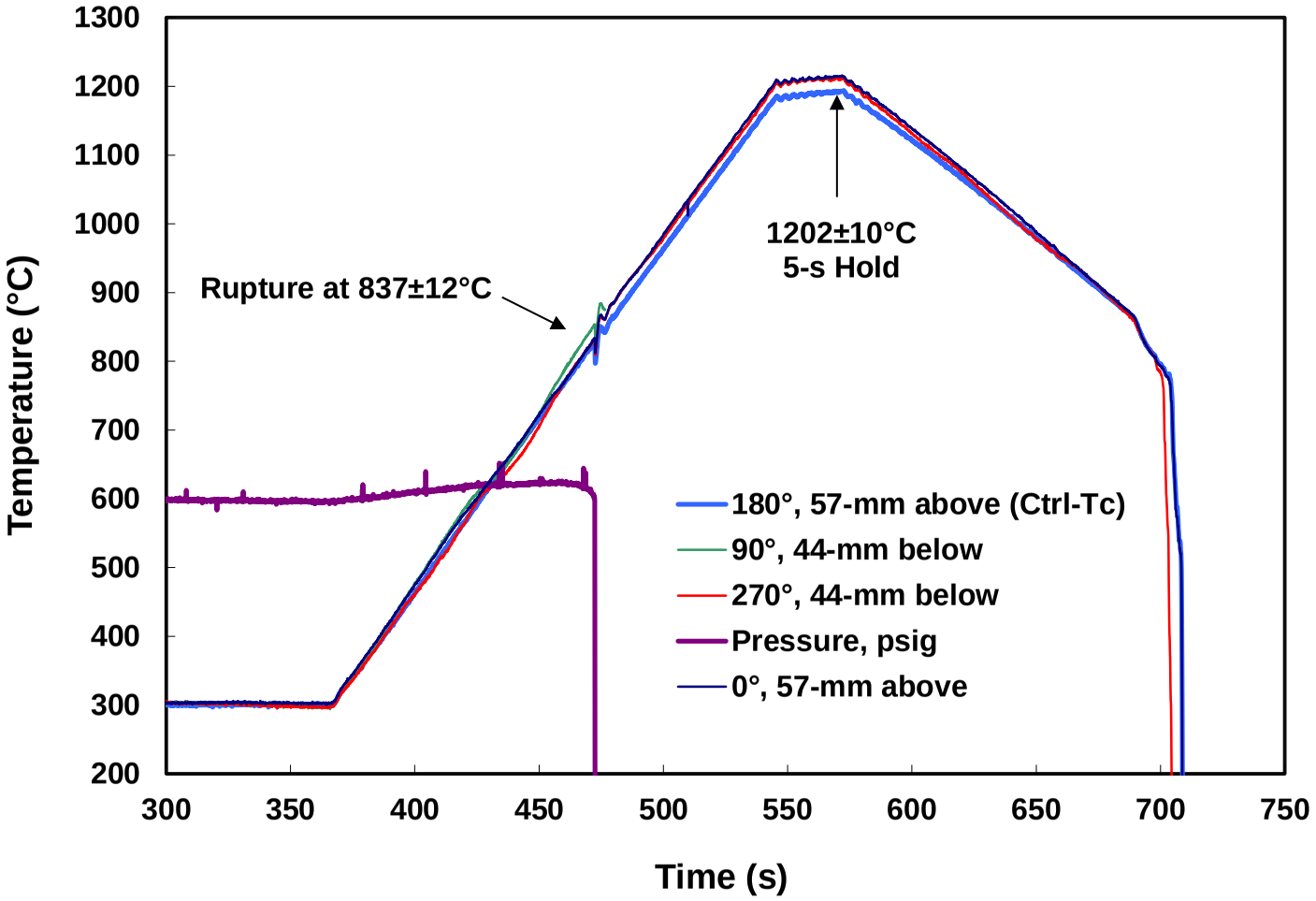

Figure A.17: **Temperature and pressure histories for data-generation test OCZL#22 pressurized to 600 psig, oxidized at ≈1200°C to 12% CP-ECR, and cooled with quench.**

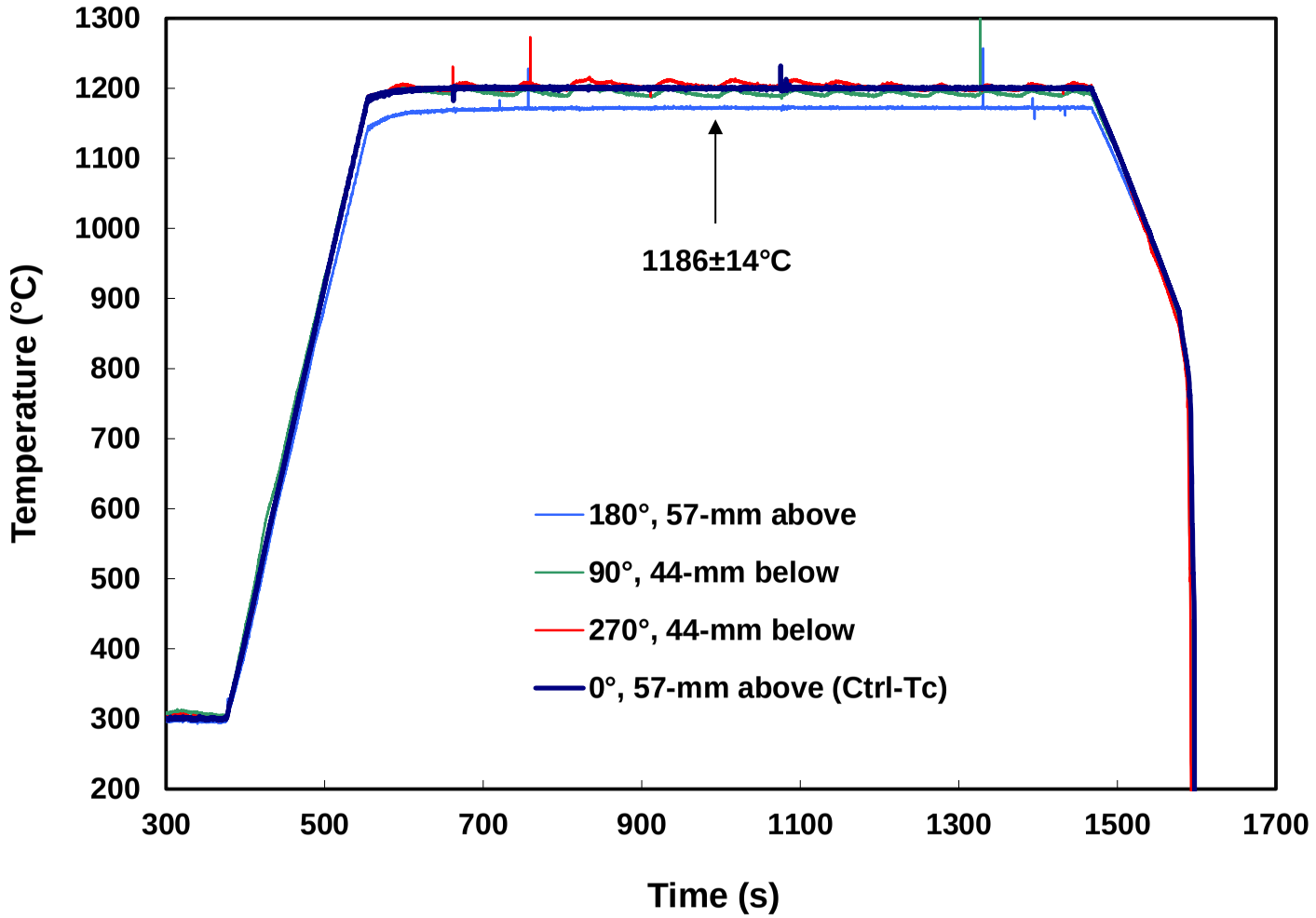

Figure A.18: **Temperature and pressure histories for data-generation test OCZL#24 non-pressurized, one-sided oxidized at ≈1200°C to 17% CP-ECR, and cooled with quench.**

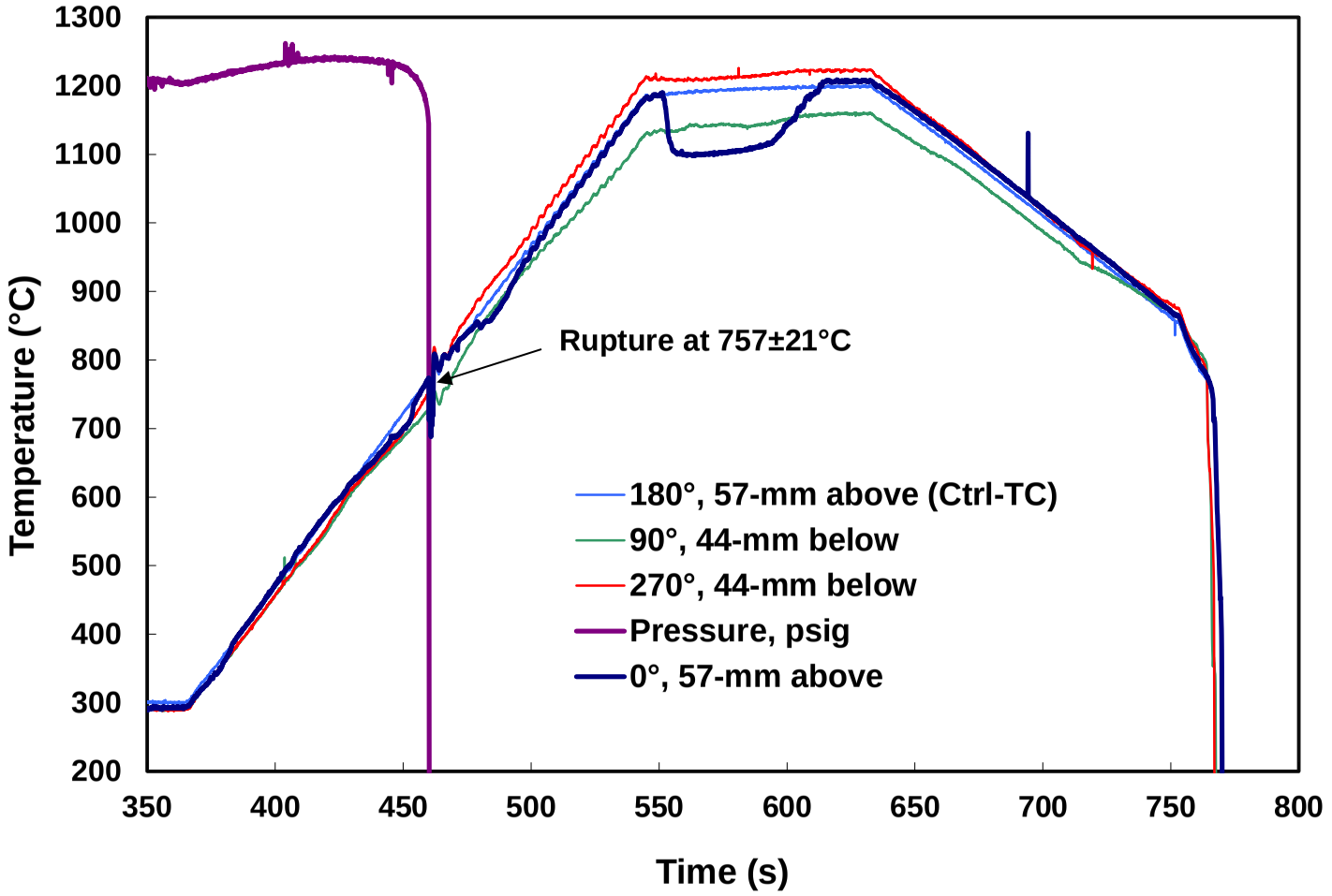

Figure A.19: **Temperature and pressure histories for data-generation test OCZL#25 pressurized to 1200 psig, oxidized at ≈1200°C to 16% CP-ECR, and cooled with quench.**

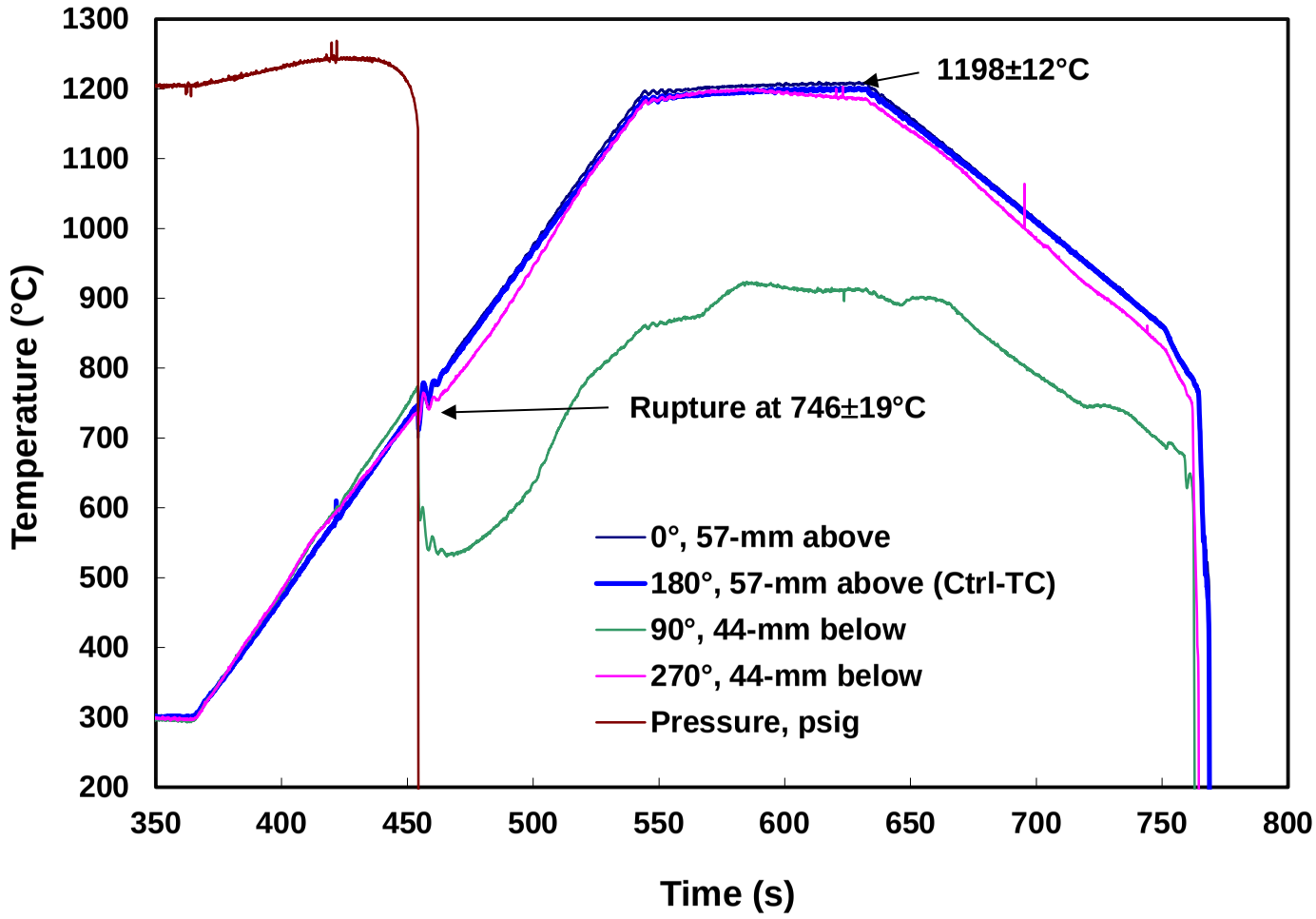

Figure A.20: **Temperature and pressure histories for data-generation test OCZL#29 pressurized to 1200 psig, oxidized at ≈1200°C to 17% CP-ECR, and cooled with quench.**

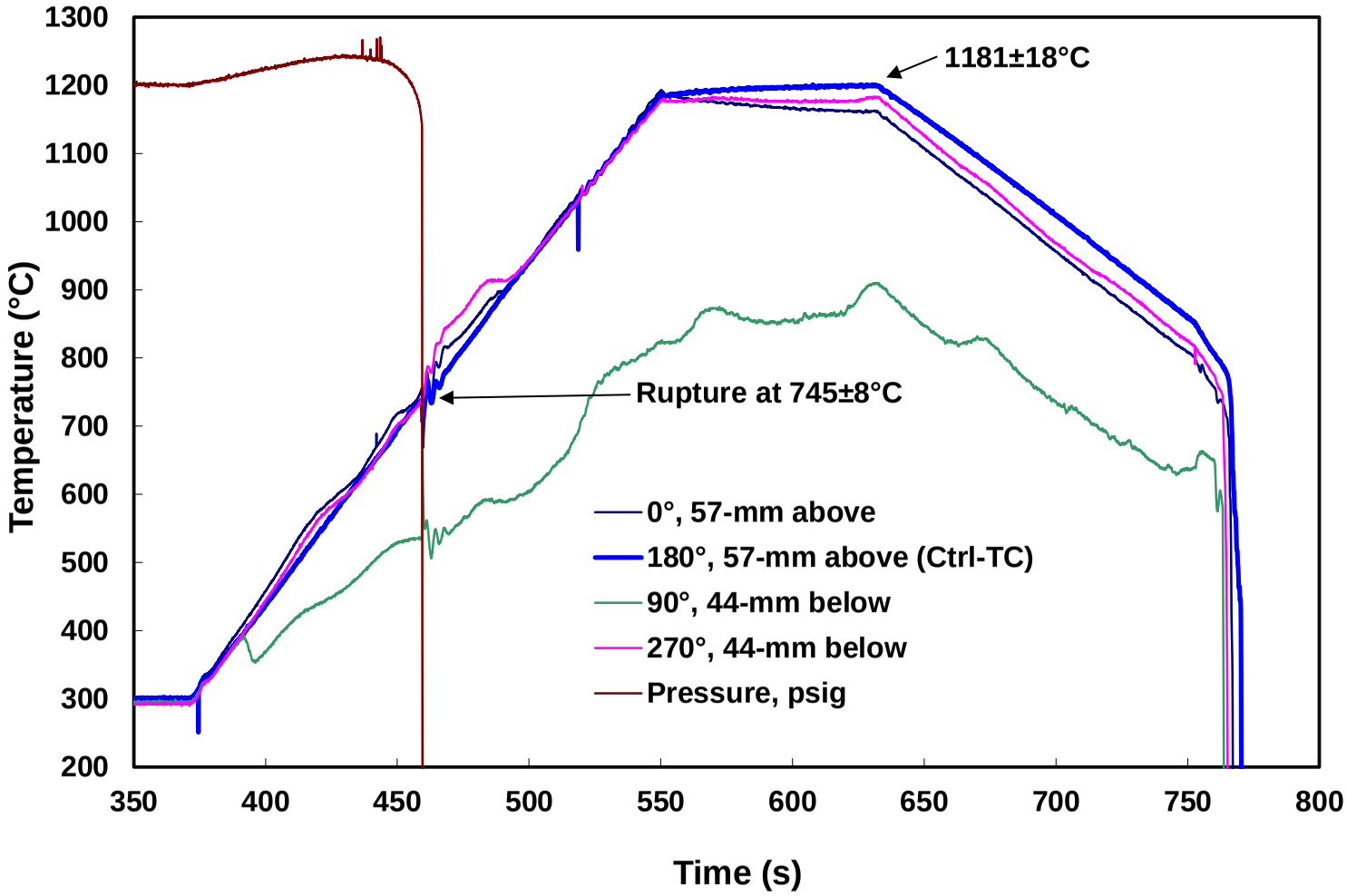

Figure A.21: **Temperature and pressure histories for data-generation test OCZL#32 pressurized to 1200 psig, oxidized at ≈1200°C to 16% CP-ECR, and cooled with quench.**

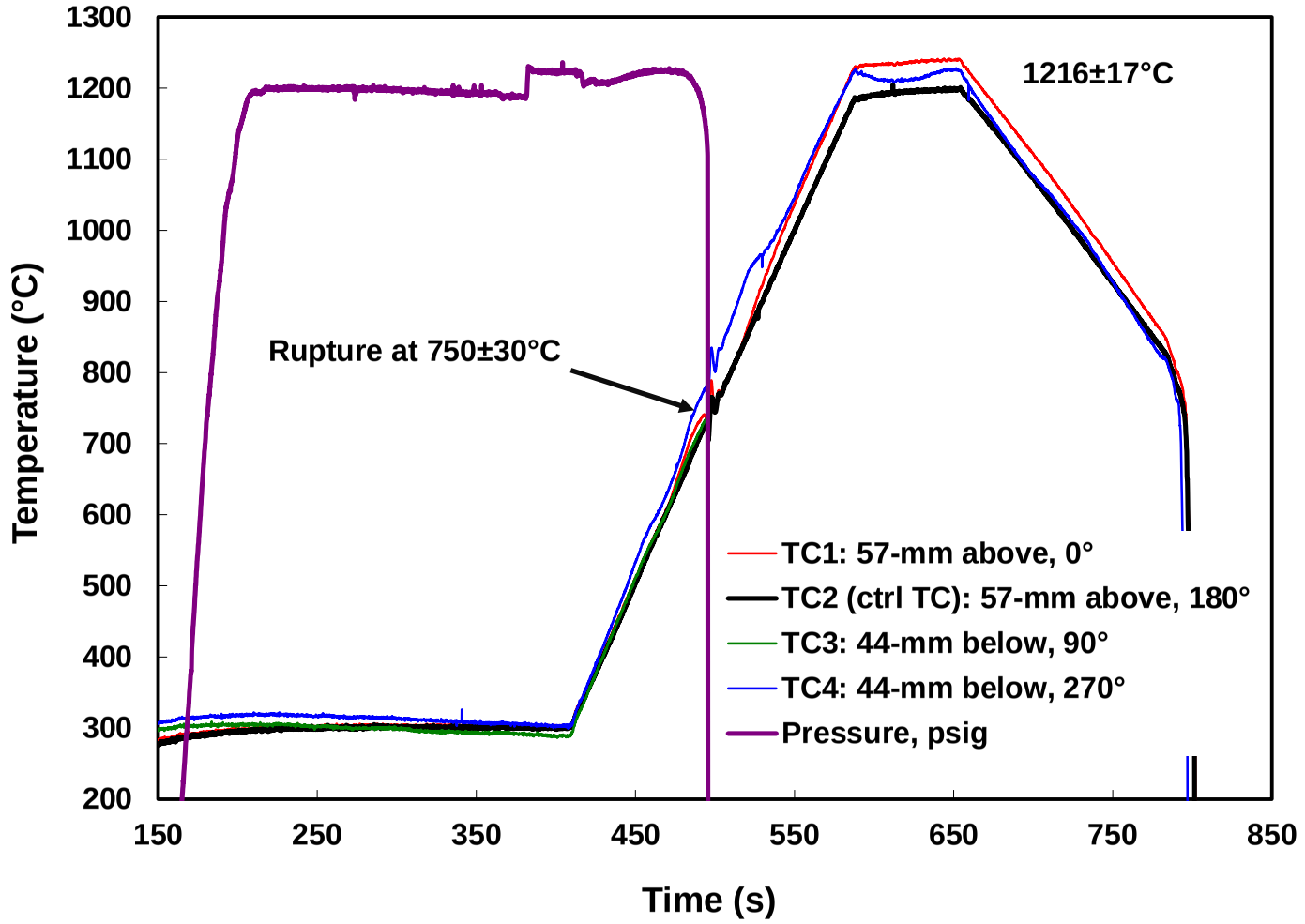

Figure A.22: **Temperature and pressure histories for thermal-benchmark test OCZL#36 pressurized to 1200 psig, oxidized at ≈1200°C to 18% CP-ECR, and cooled with quench.**

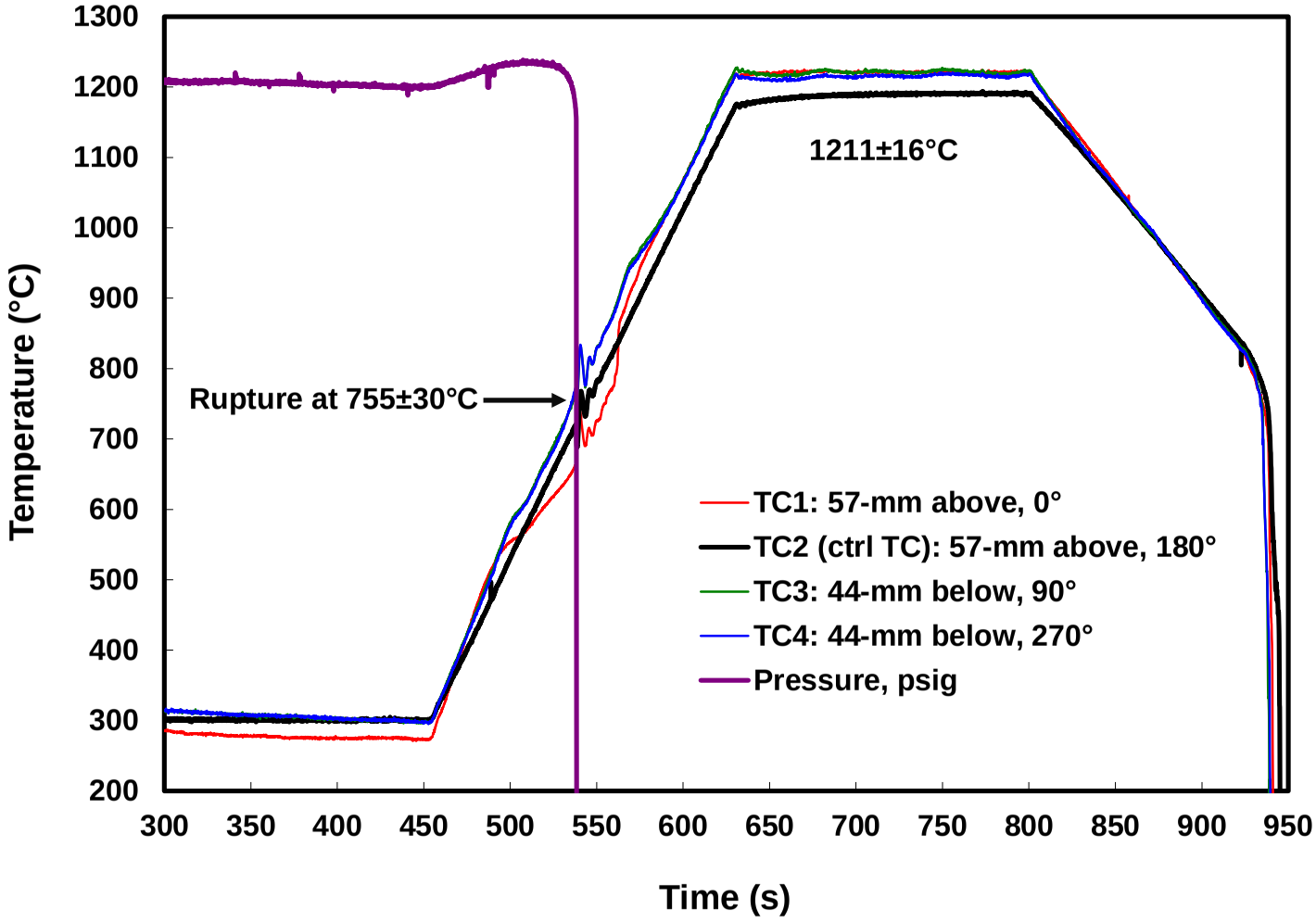

Figure A.23: **Temperature and pressure histories for thermal/4-point-bend benchmark test OCZL#37 pressurized to 1200 psig, oxidized at ≈1200°C to 23% CP-ECR, and cooled with quench.**

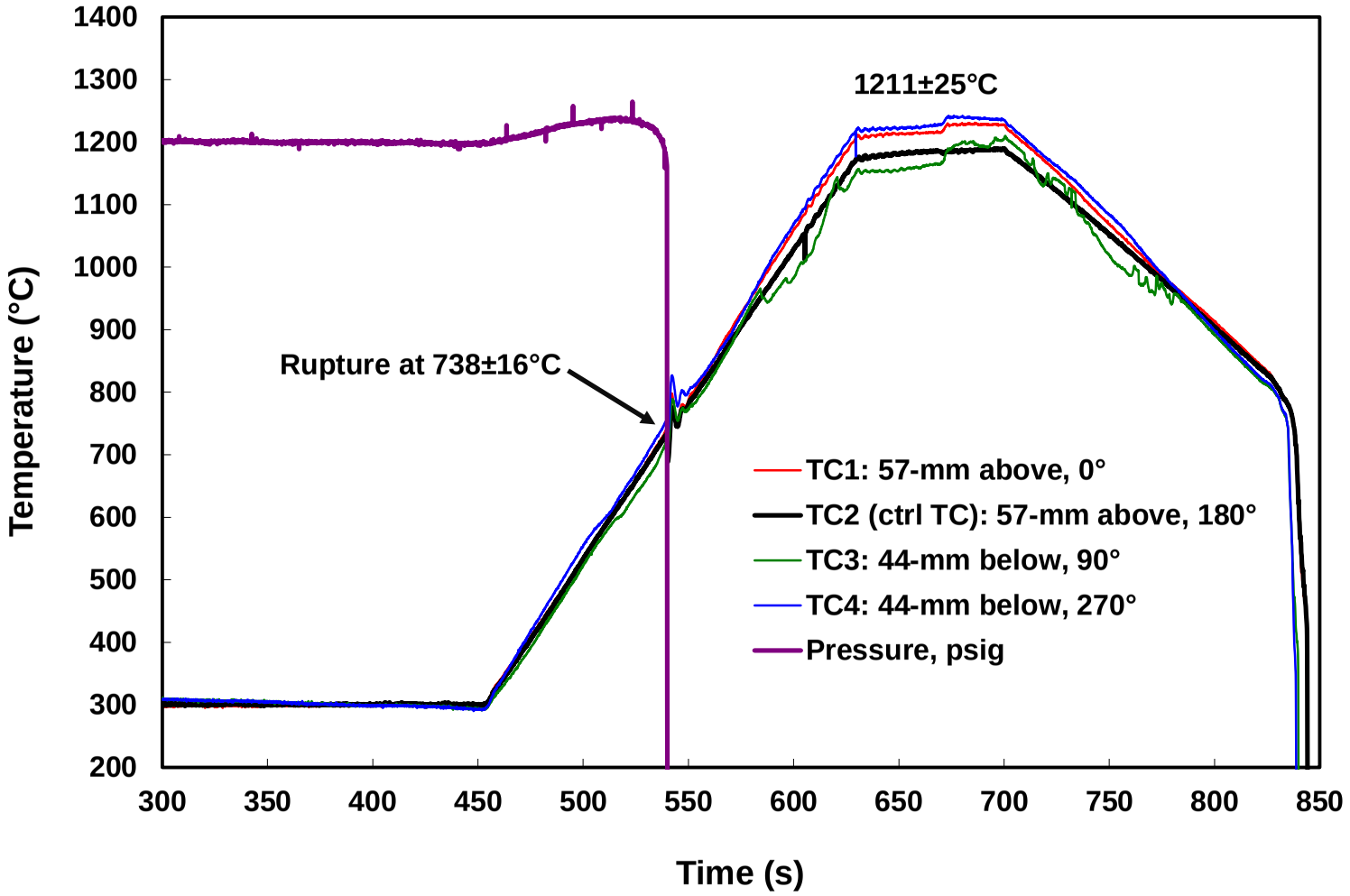

Figure A.24: **Temperature and pressure histories for data-generation test OCZL#43 pressurized to 1200 psig, oxidized at ≈1200°C to 18% CP-ECR, and cooled with quench.**

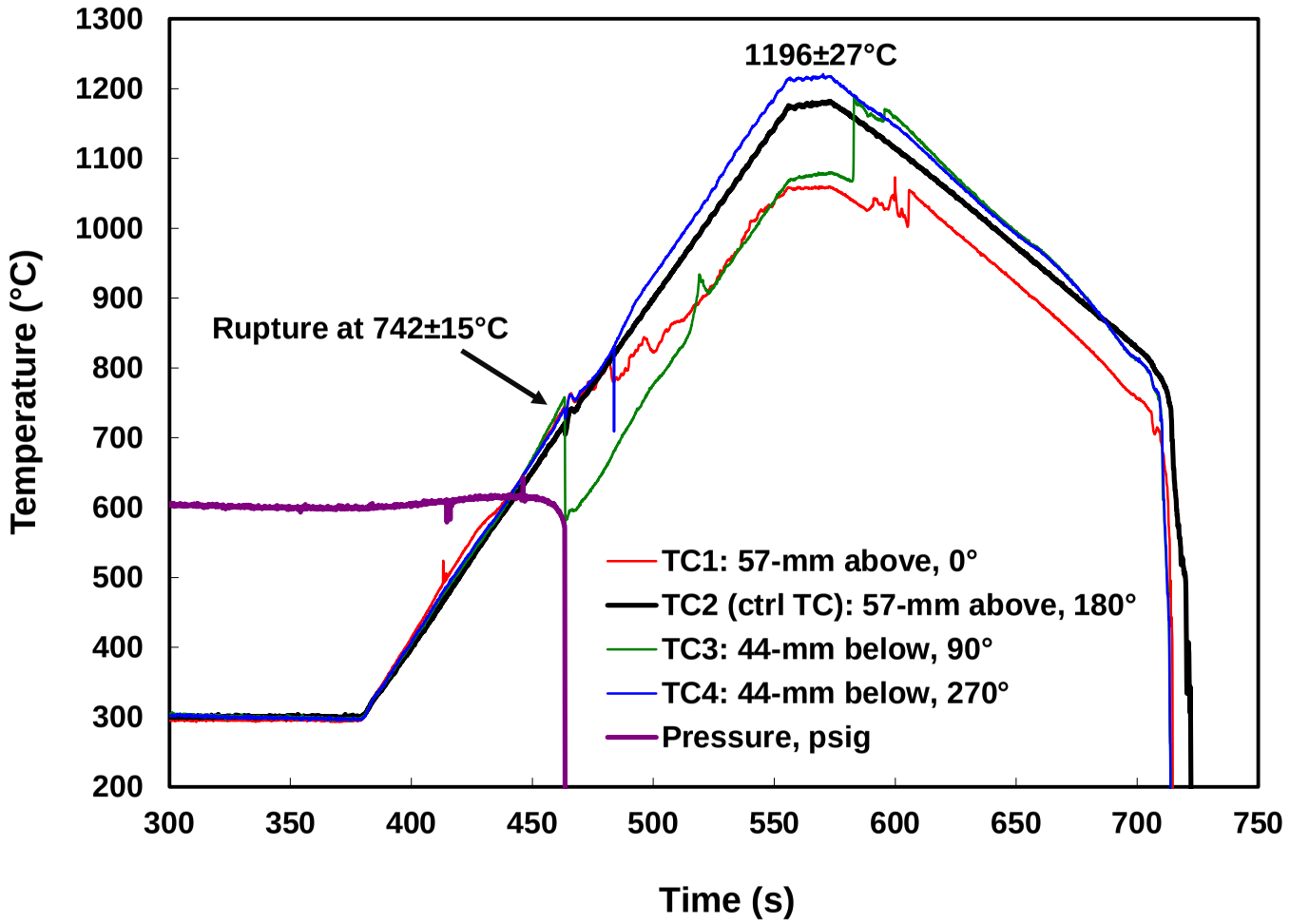

Figure A.25: **Temperature and pressure histories for data-generation test OCZL#39 with pre-hydrided (660 wppm) ZIRLO pressurized to 600 psig, oxidized at ≈1200°C to 13% CP-ECR, and cooled with quench.**

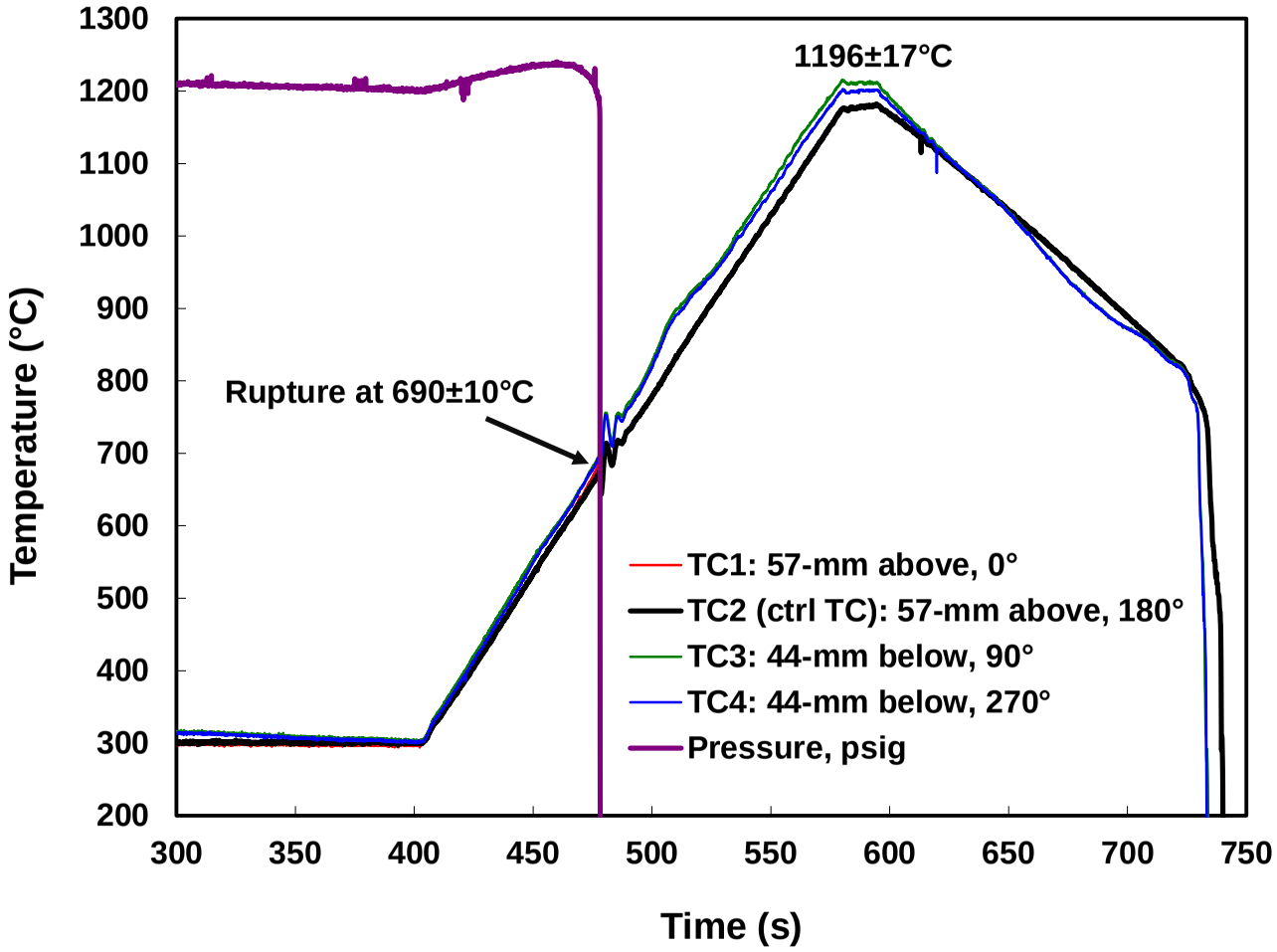

Figure A.26: **Temperature and pressure histories for data-generation test OCZL#40 with pre-hydrided (390 wppm) ZIRLO pressurized to 1200 psig, oxidized at ≈1200°C to 12% CP-ECR, and cooled with quench.**

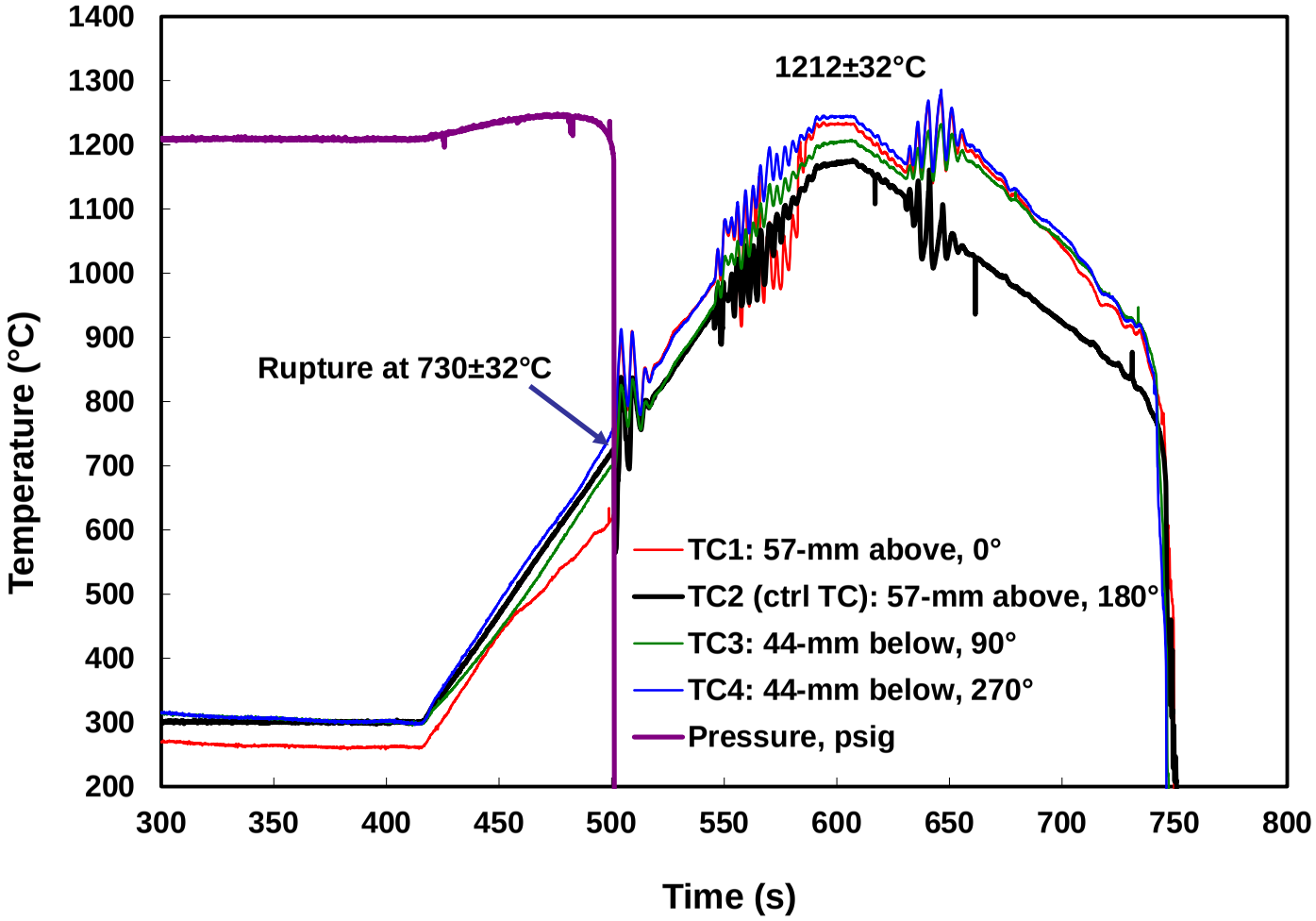

Figure A.27: **Temperature and pressure histories for data-generation test OCZL#41 with pre-hydrided (220 wppm) ZIRLO pressurized to 1200 psig, oxidized at ≈1200°C to 16% CP-ECR, and cooled with quench.**

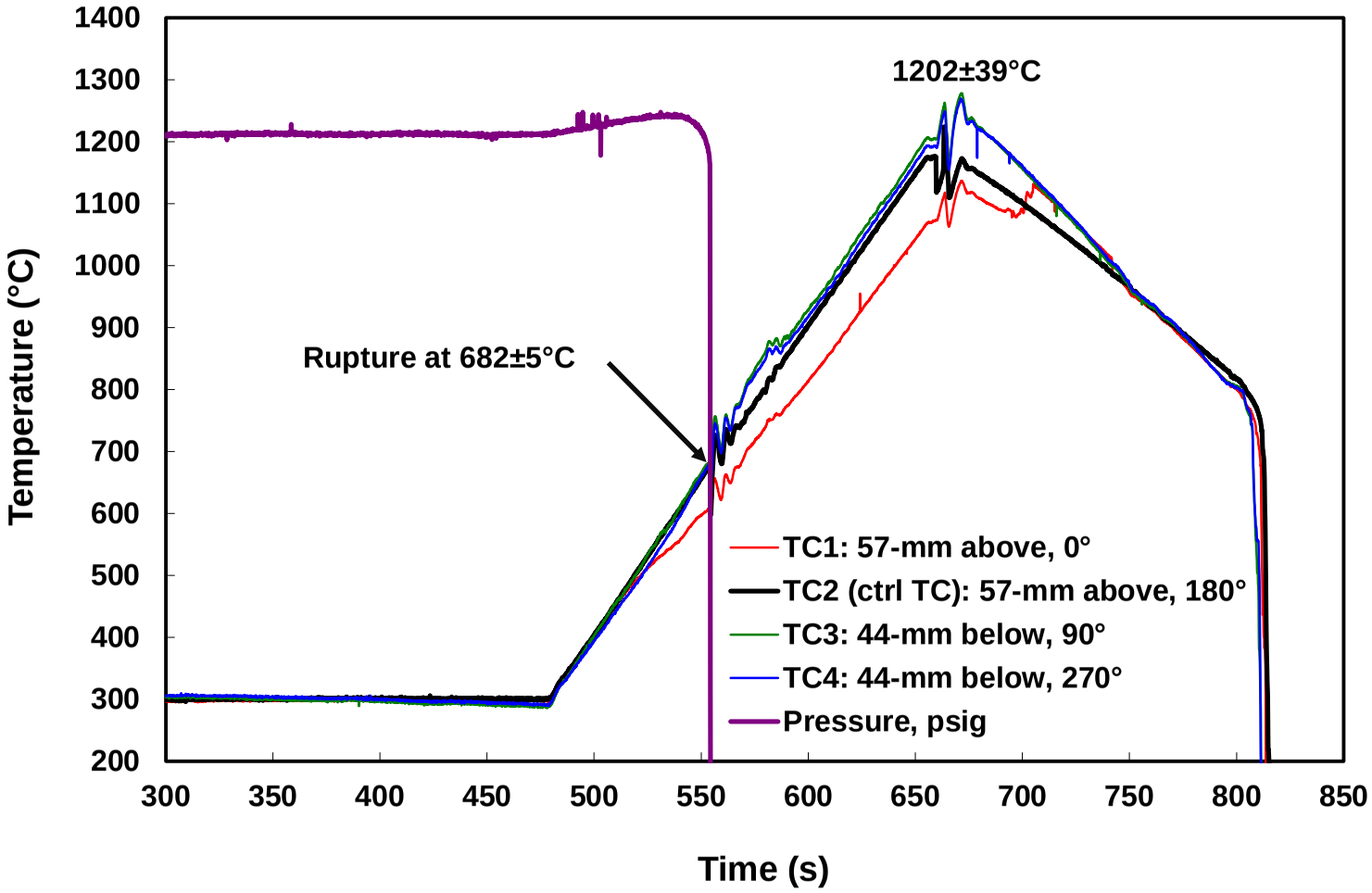

Figure A.28: **Temperature and pressure histories for data-generation test OCZL#42 with pre-hydrided (520 wppm) ZIRLO pressurized to 1200 psig, oxidized at ≈1200°C to 14% CP-ECR, and cooled with quench.**

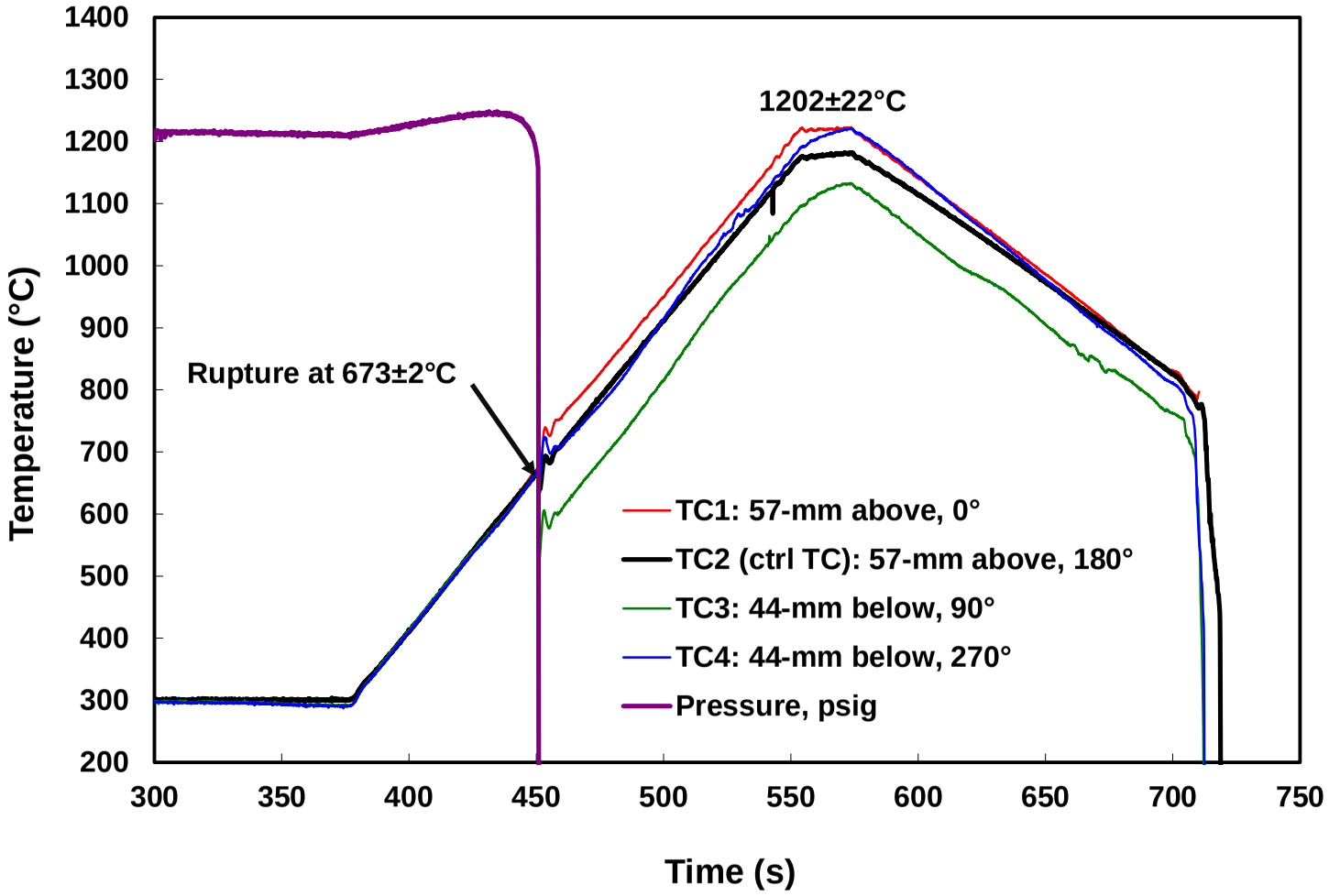

Figure A.29: **Temperature and pressure histories for data-generation test OCZL#44 with pre-hydrided (700 wppm) ZIRLO pressurized to 1200 psig, oxidized at ≈1200°C to 14% CP-ECR, and cooled with quench.**

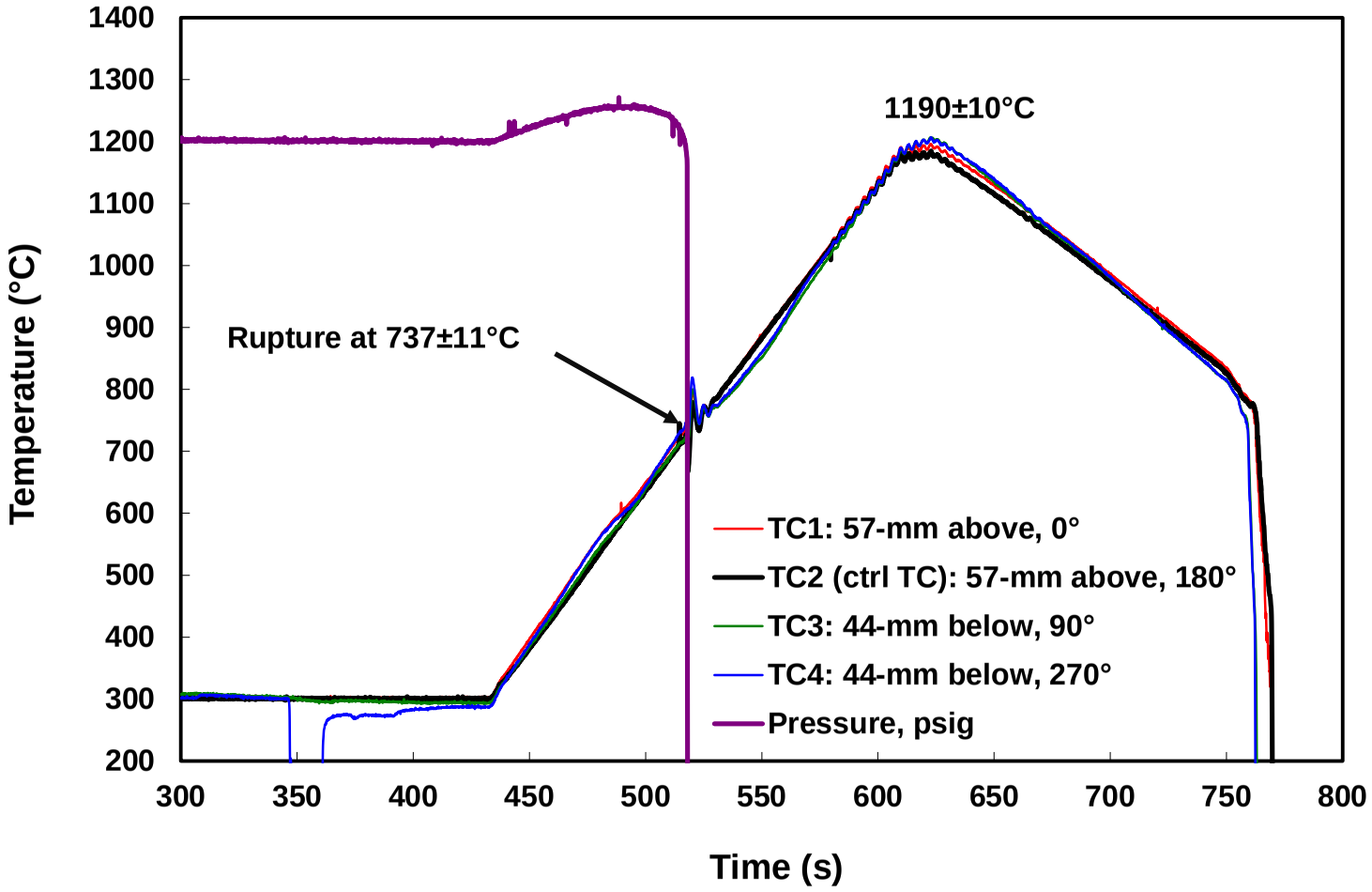

Figure A.30: **Temperature and pressure histories for data-generation test OCZL#45 with pre-hydrided (220 wppm) ZIRLO pressurized to 1200 psig, oxidized at ≈1200°C to 13% CP-ECR, and cooled with quench.**

APPENDIX B: AXIAL PROFILES OF POST-RUPTURE CLADDING STRAINS

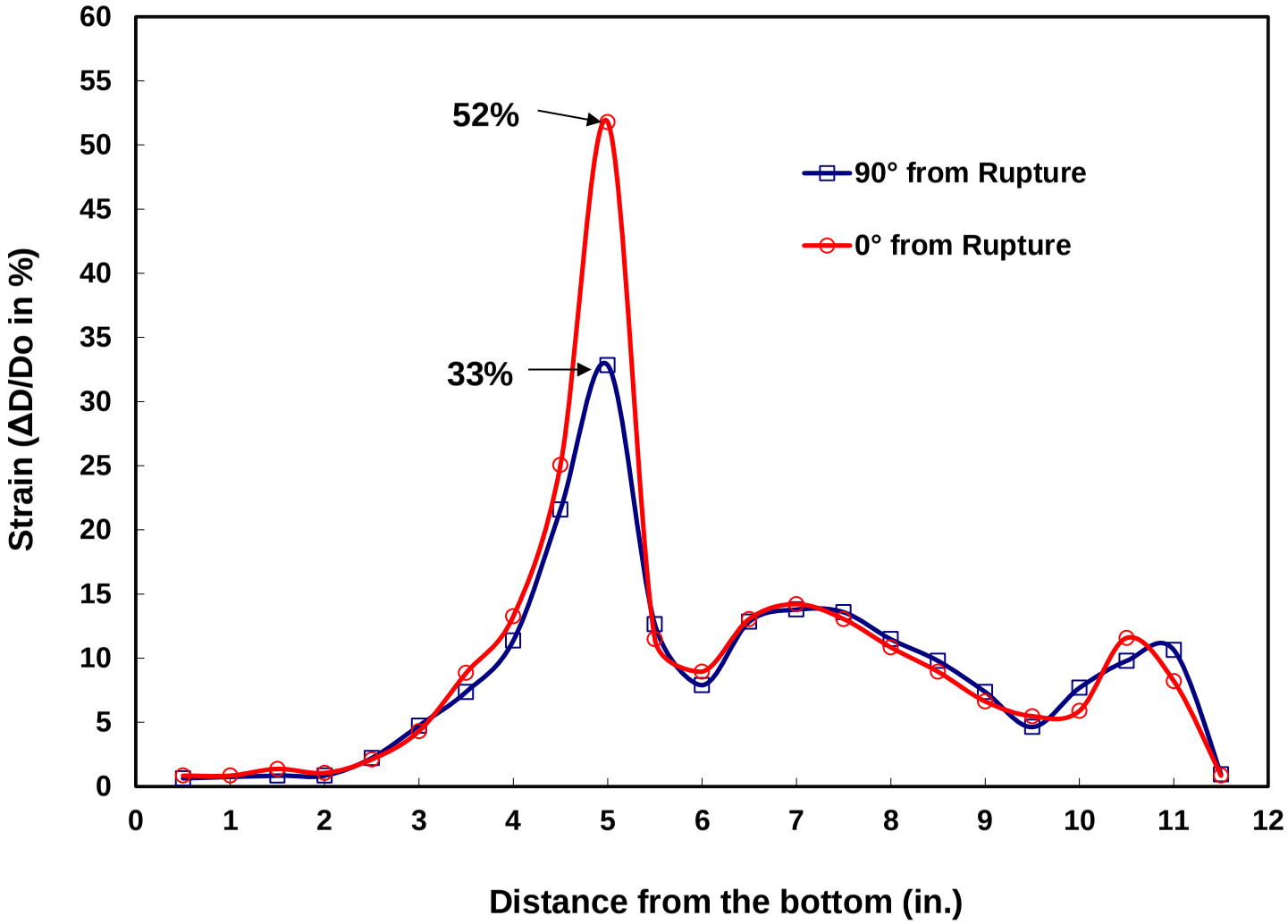

Figure B.1: **Axial profiles for minimum (90°) and maximum (0°) cladding diameters following thermal benchmark test OCZL#6, which was pressurized to 1200 psig, oxidized to 18% CP-ECR at ≈1200°C, and cooled without quench.**

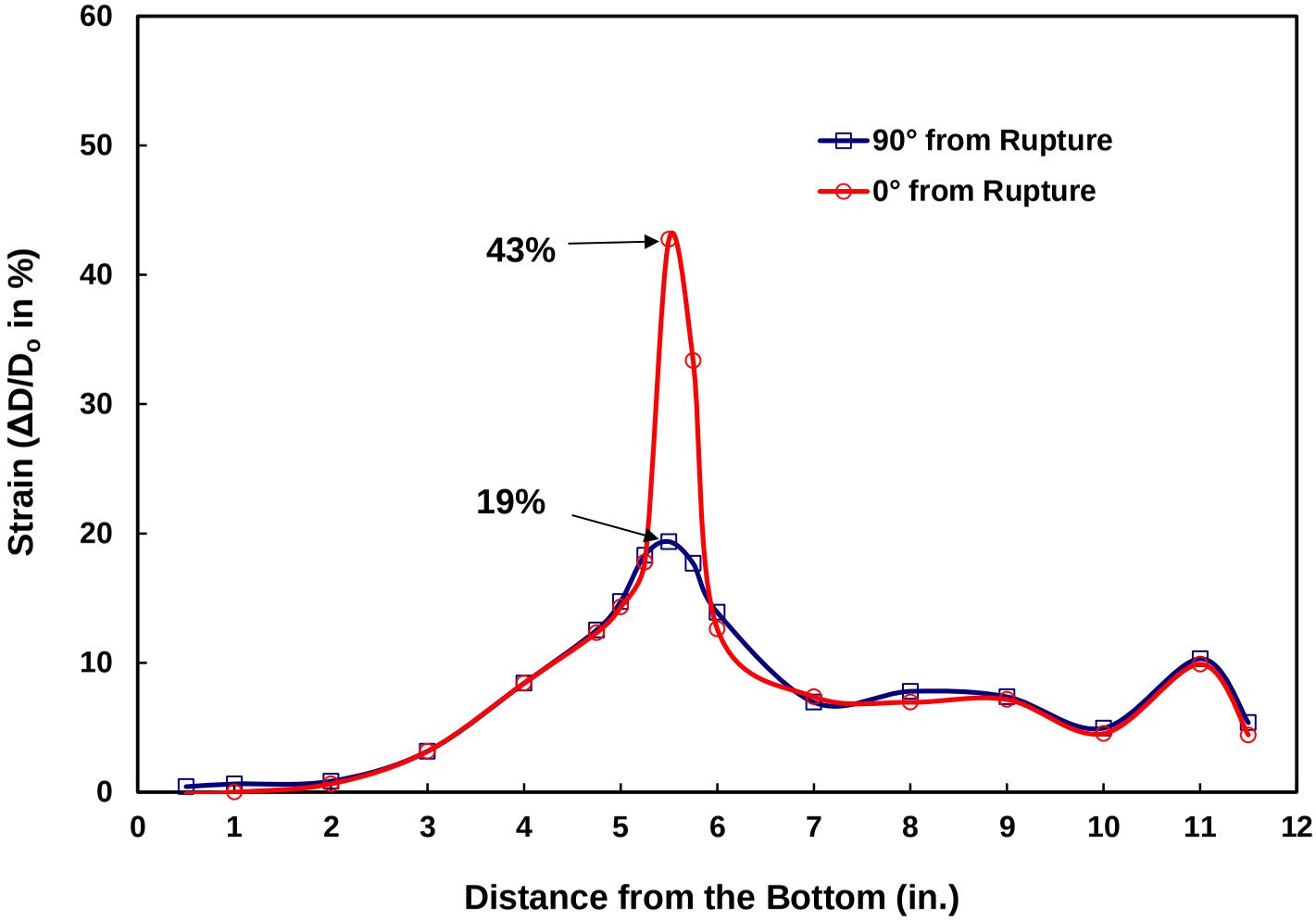

Figure B.2: **Axial profiles for minimum (90°) and maximum (0°) cladding diameters following scoping test OCZL#7, which was pressurized to 800 psig, oxidized to 16% CP-ECR at ≈1200°C, and cooled without quench.**

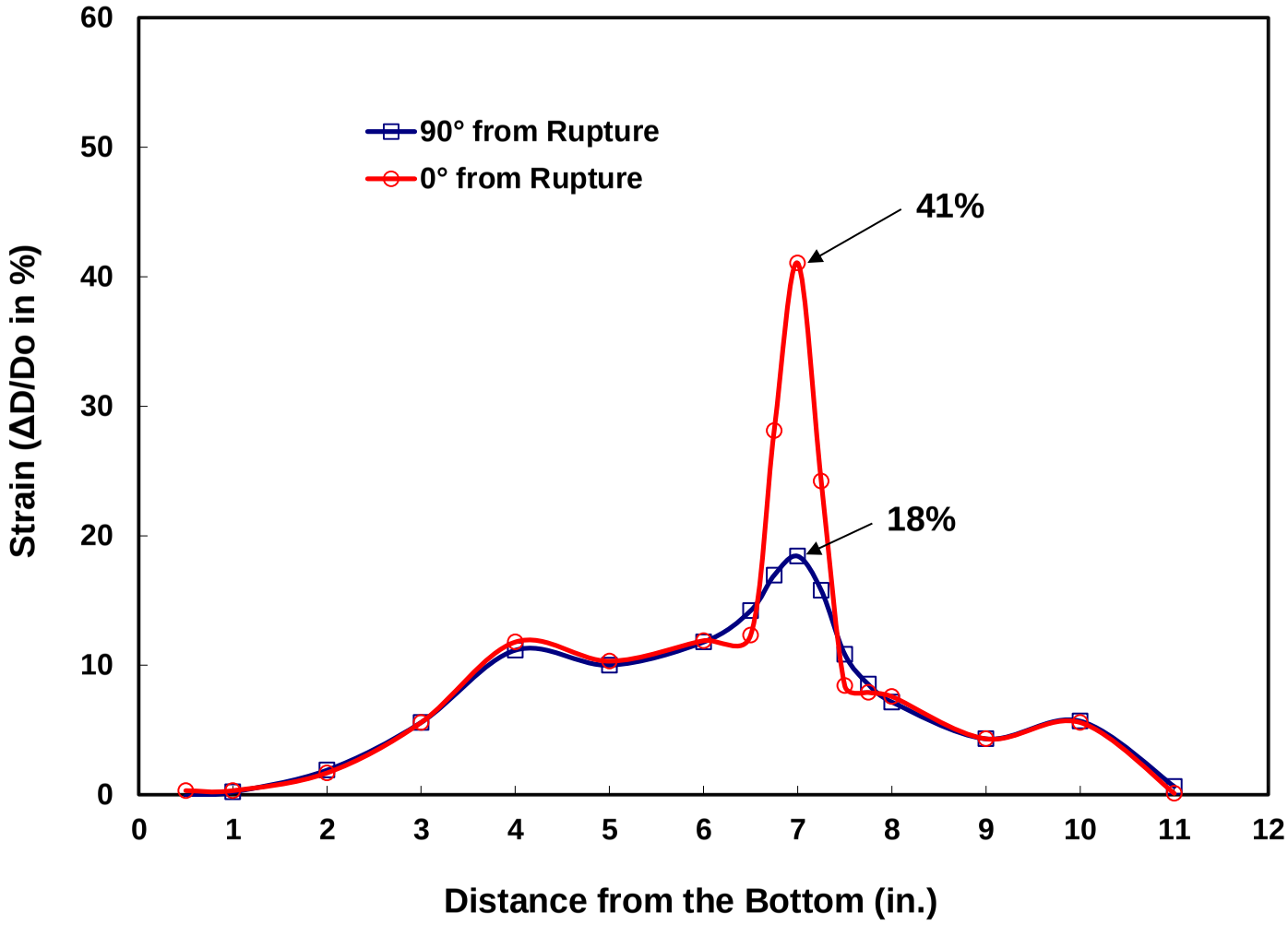

Figure B.3: **Axial profiles for minimum (90°) and maximum (0°) cladding diameters following ramp-to-rupture scoping test OCZL#8, which was pressurized to 600 psig and cooled without quench.**

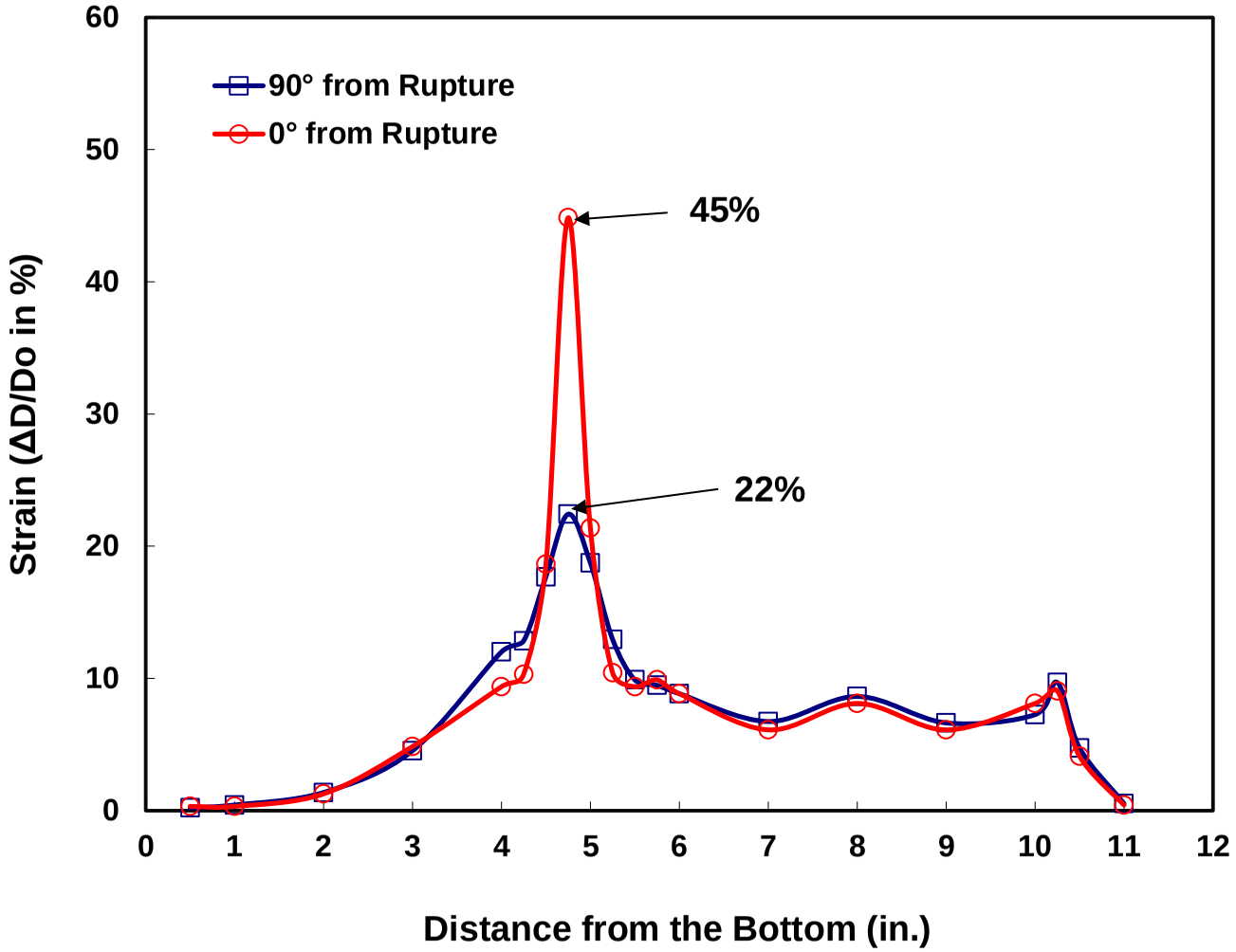

Figure B.4: **Axial profiles for minimum (90°) and maximum (0°) cladding diameters following ramp-to-rupture scoping test OCZL#9, which was pressurized to 400 psig and cooled without quench.**

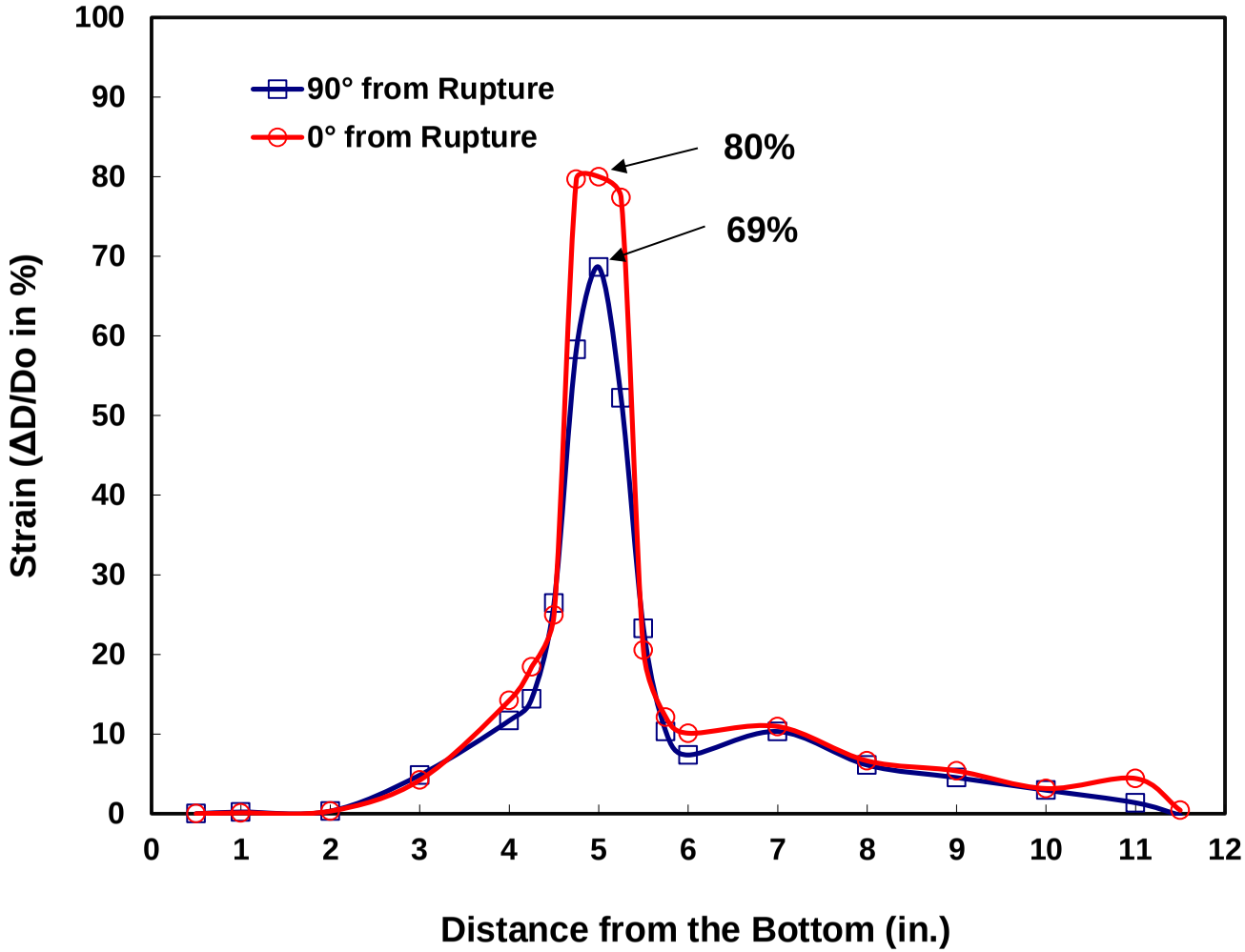

Figure B.5: **Axial profiles for minimum (90°) and maximum (0°) cladding diameters following ramp-to-rupture scoping test OCZL#10, which was pressurized to 1600 psig and cooled without quench.**

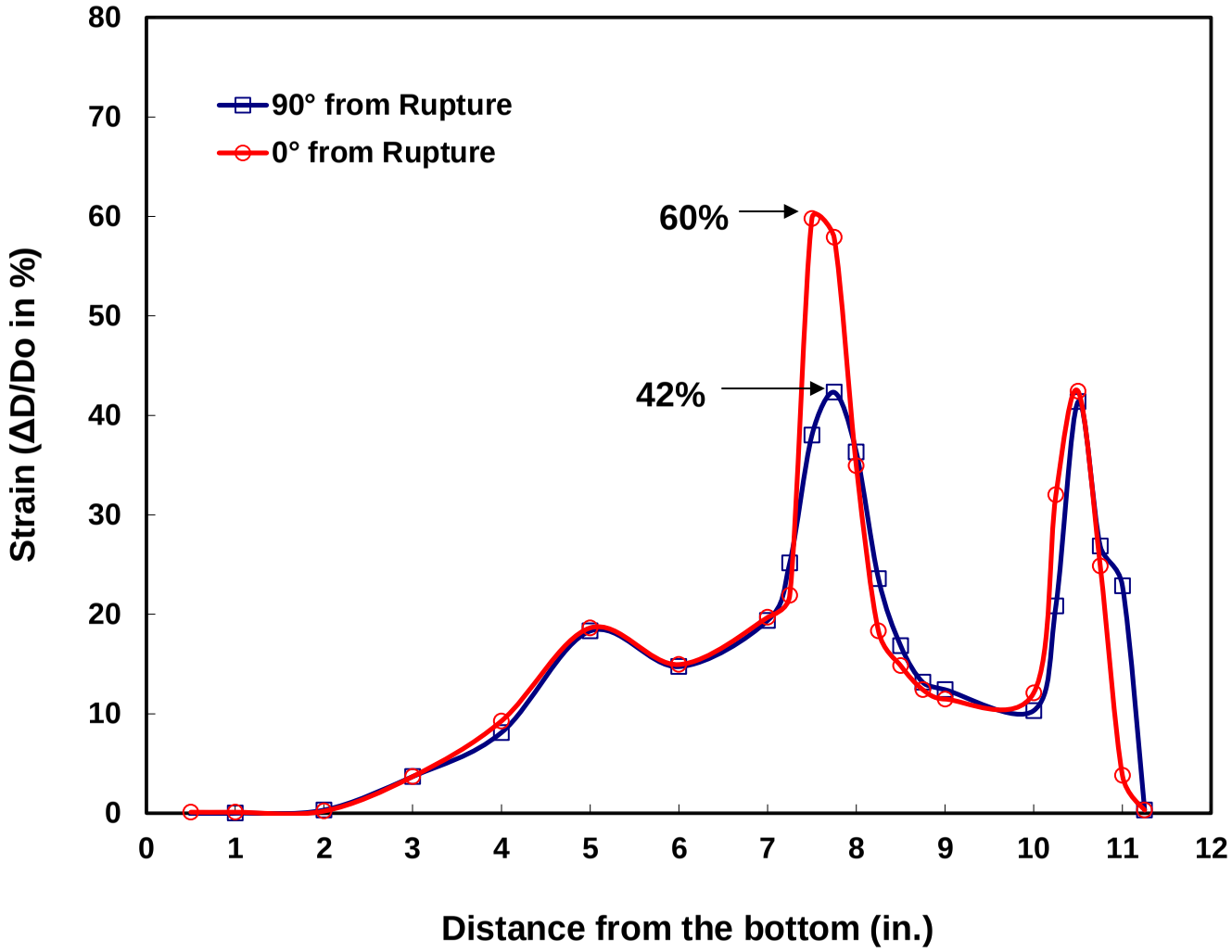

Figure B.6: **Axial profiles for minimum (90°) and maximum (0°) cladding diameters following ramp-to-rupture scoping test OCZL#11, which was pressurized to 1400 psig and cooled without quench.**

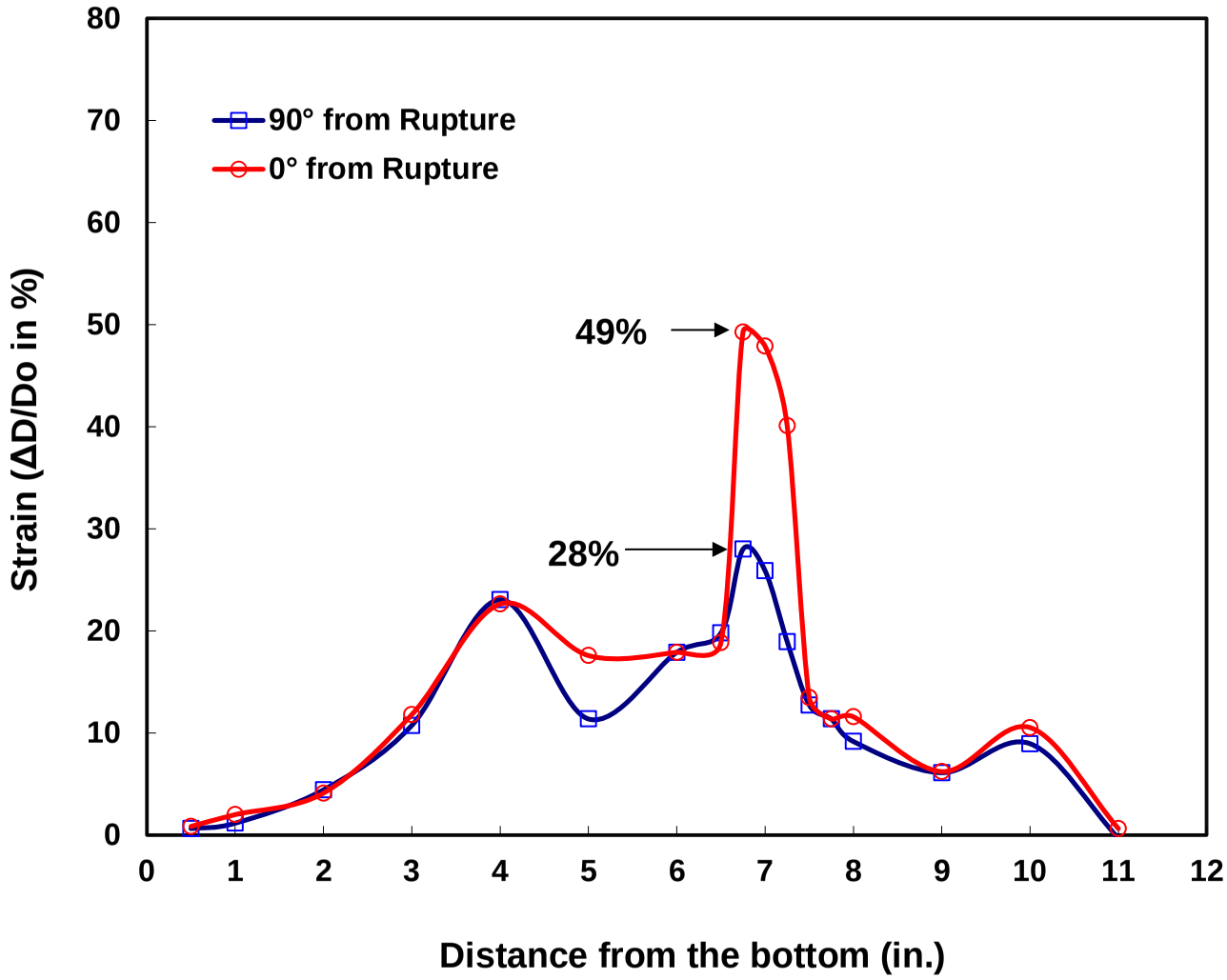

Figure B.7: **Axial profiles for minimum (90°) and maximum (0°) cladding diameters following test OCZL#12, which was pressurized to 1000 psig, oxidized to 15% CP-ECR, and cooled without quench.**

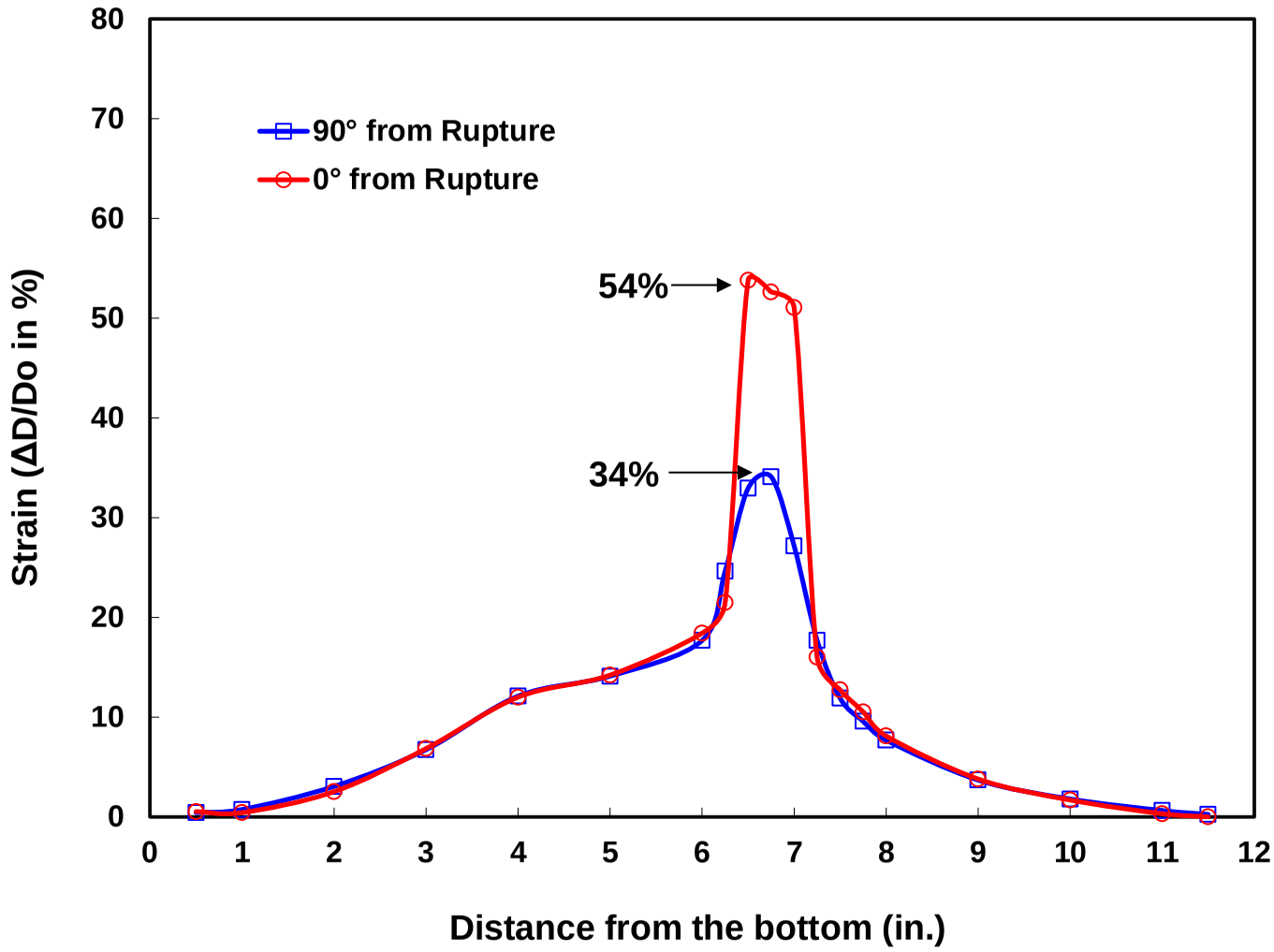

Figure B.8: **Axial profiles for minimum (90°) and maximum (0°) cladding diameters following test OCZL#13, which was pressurized to 1200 psig, oxidized to 14% CP-ECR, and cooled without quench.**

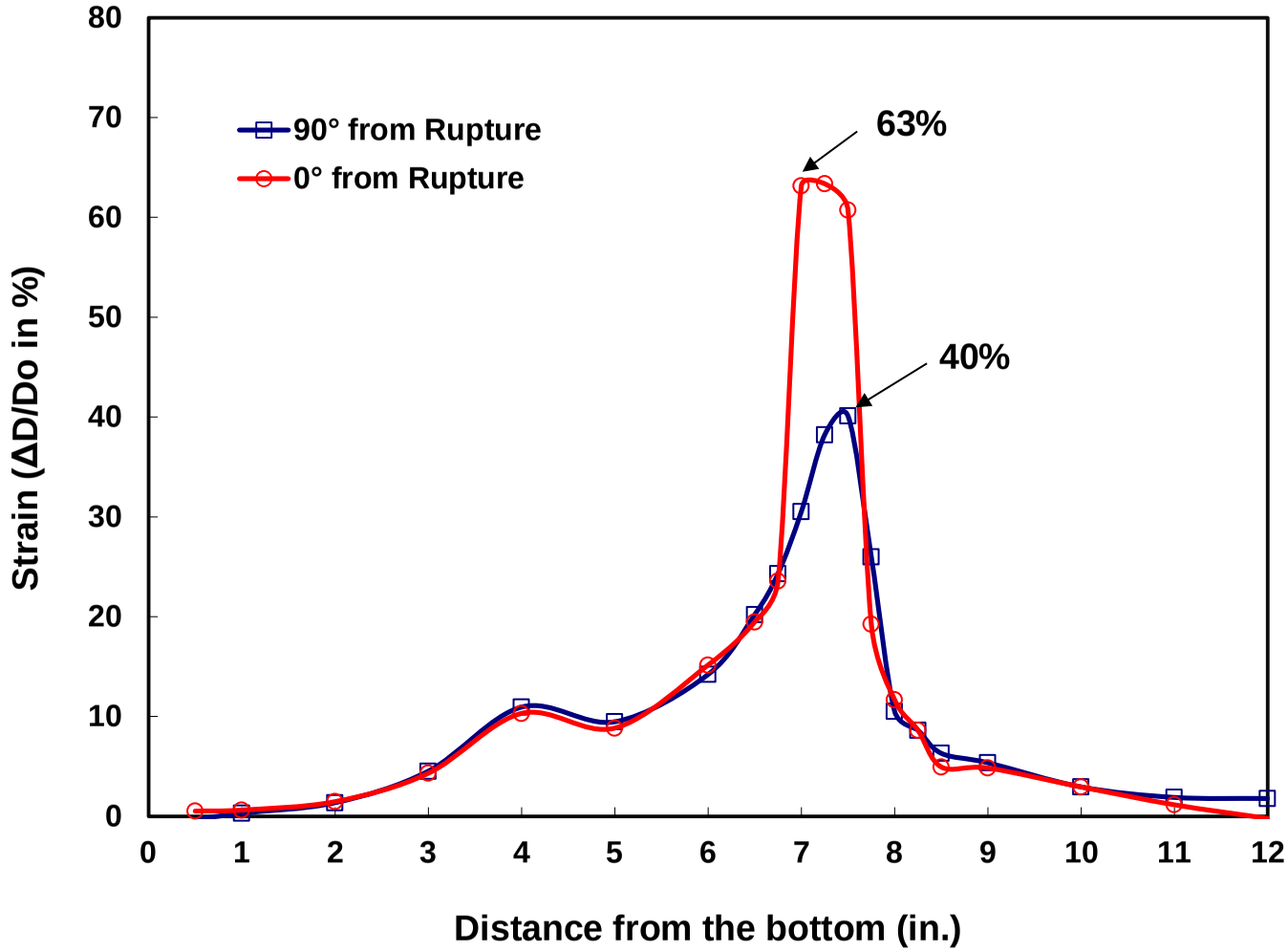

Figure B.9: **Axial profiles for minimum (90°) and maximum (0°) cladding diameters following data-generation test OCZL#14, which was pressurized to 1200 psig, oxidized to 18% CP-ECR, and cooled with quench.**

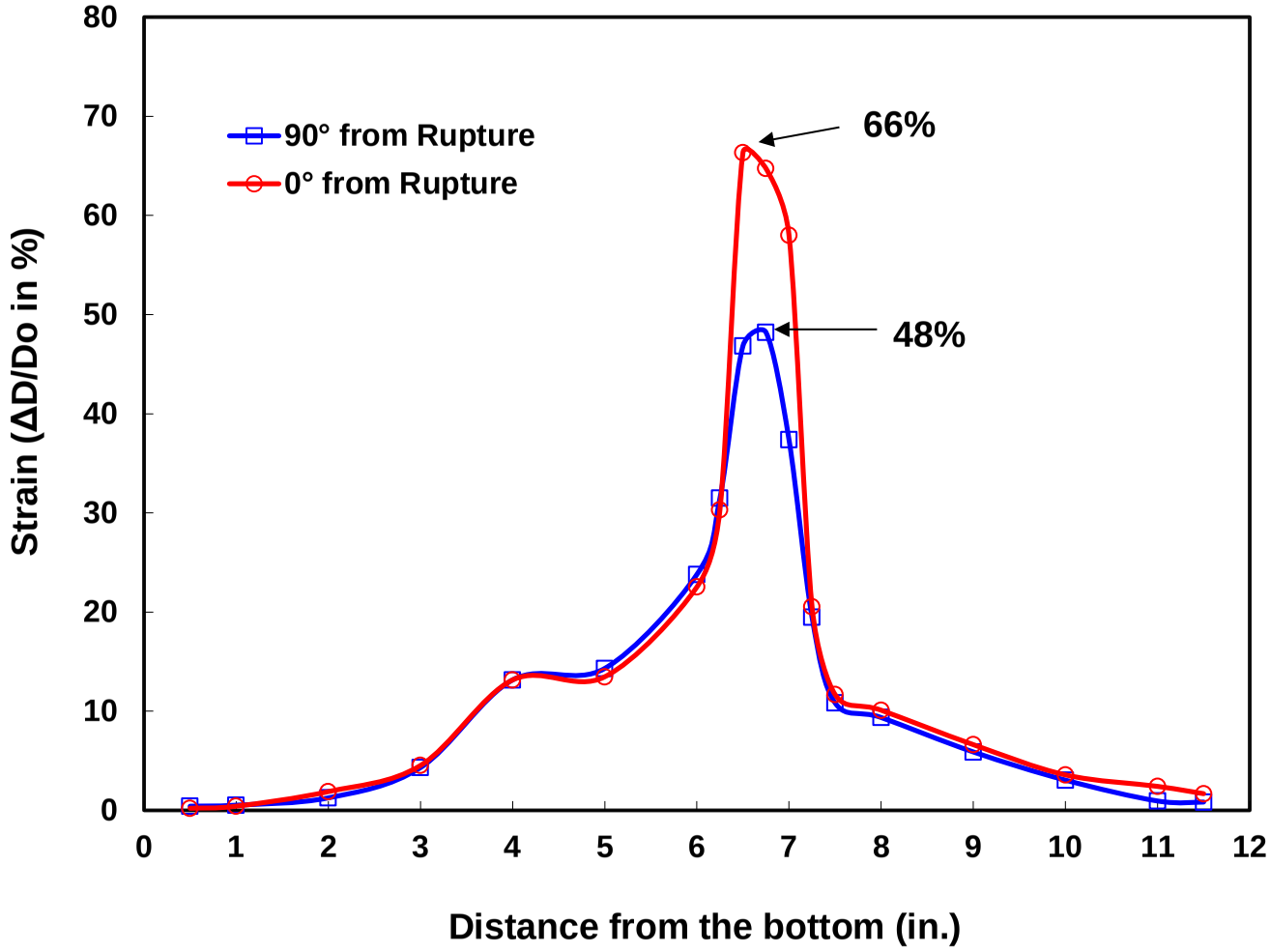

Figure B.10: **Axial profiles for minimum (90°) and maximum (0°) cladding diameters following data-generation test OCZL#15, which was pressurized to 1200 psig, oxidized to 18% CP-ECR, and cooled with quench.**

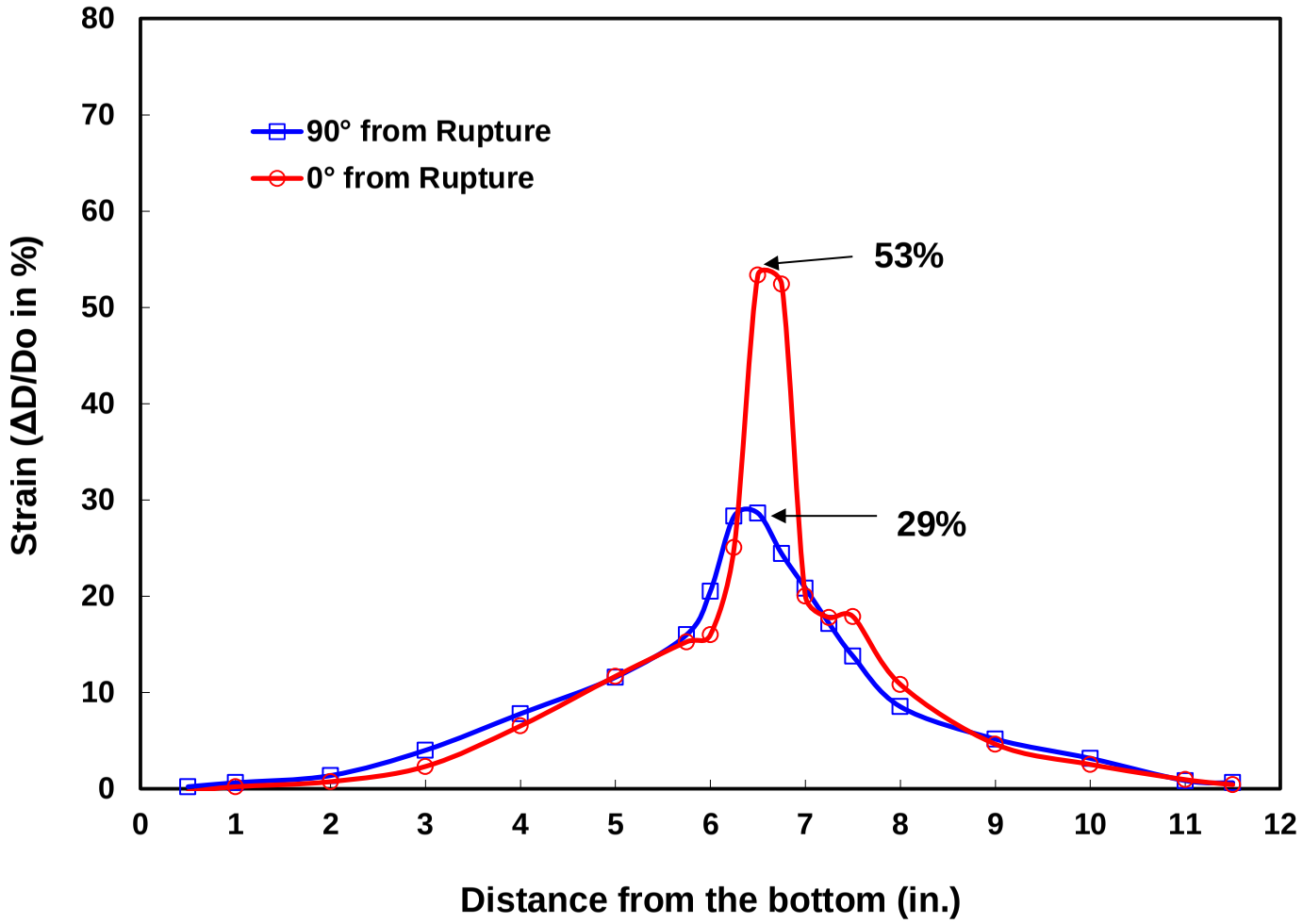

Figure B.11: **Axial profiles for minimum (90°) and maximum (0°) cladding diameters following data-generation test OCZL#16, which was pressurized to 1200 psig, oxidized to 14% CP-ECR, and cooled with quench.**

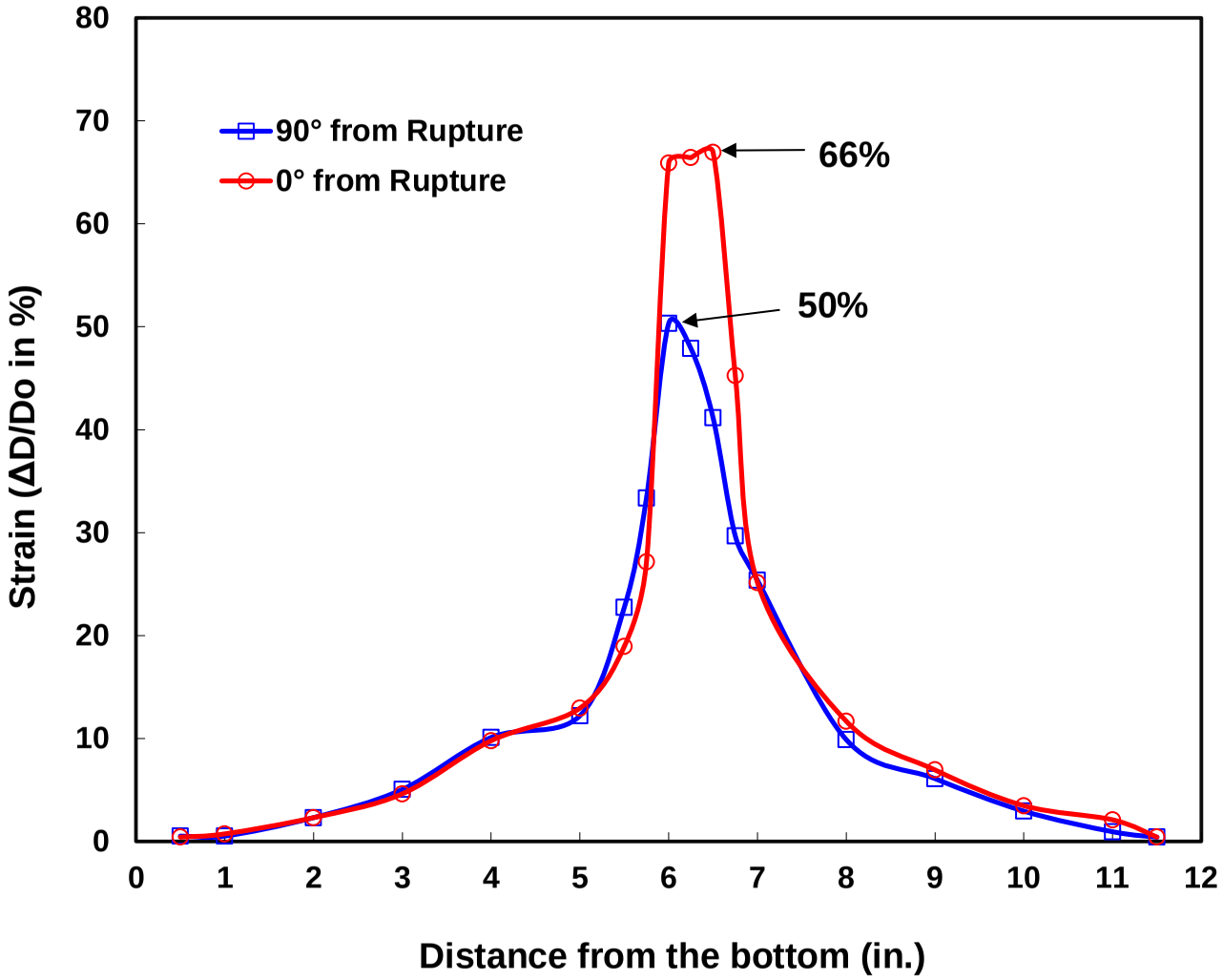

Figure B.12: **Axial profiles for minimum (90°) and maximum (0°) cladding diameters following data-generation test OCZL#17, which was pressurized to 1200 psig, oxidized to 13% CP-ECR, and cooled with quench.**

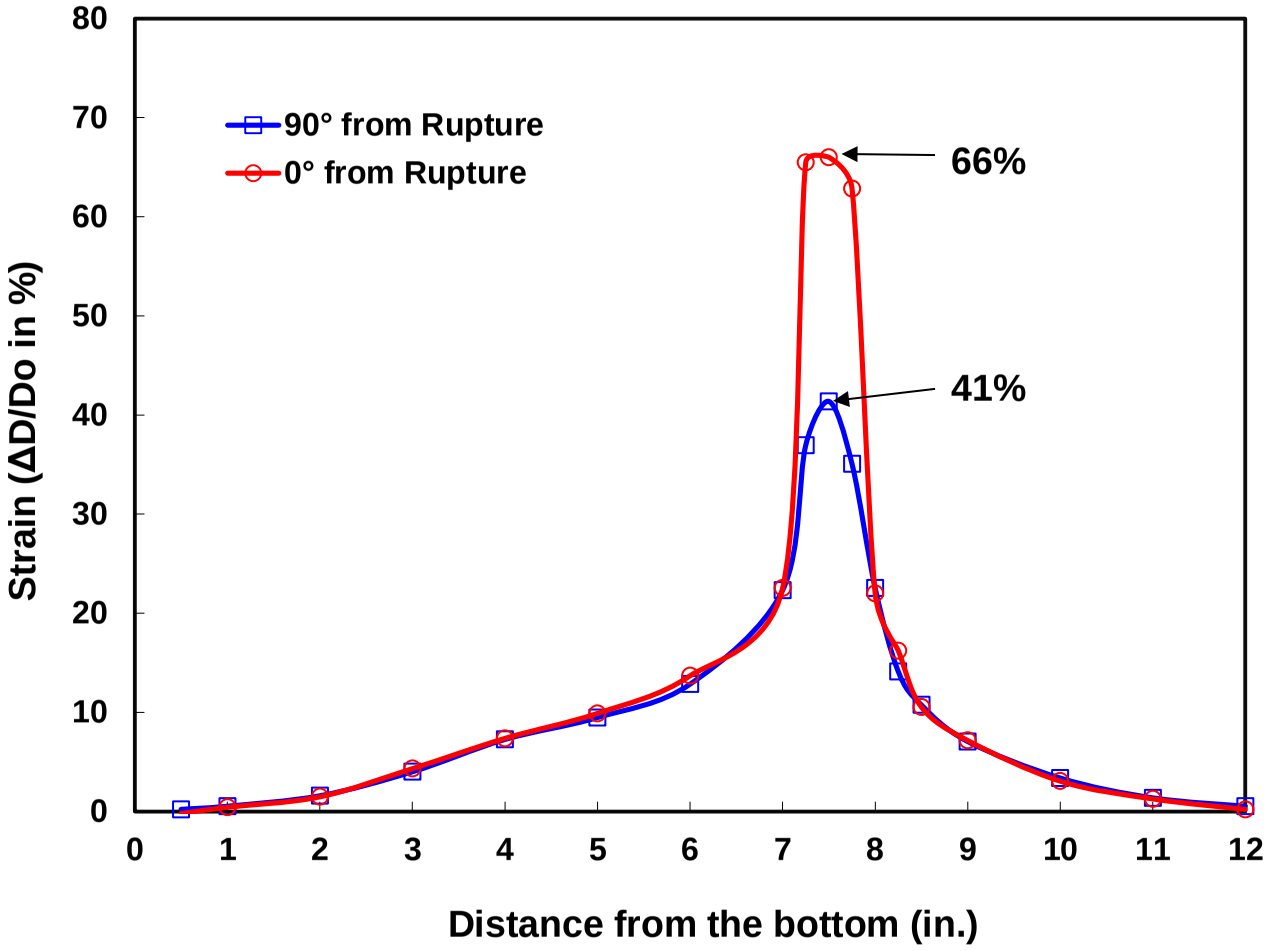

Figure B.13: **Axial profiles for minimum (90°) and maximum (0°) cladding diameters following data-generation test OCZL#18, which was pressurized to 1200 psig, oxidized to 12% CP-ECR, and cooled with quench.**

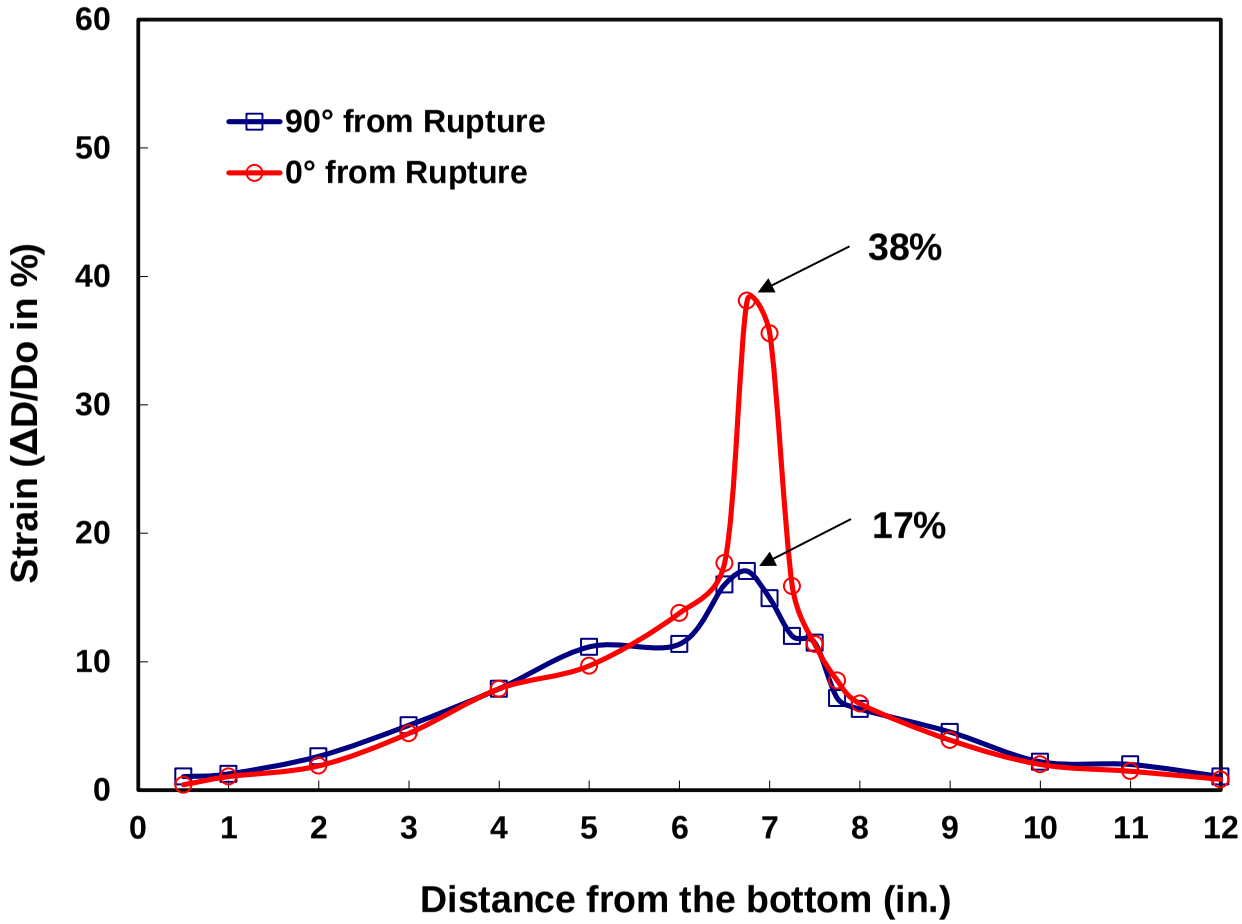

Figure B.14: **Axial profiles for minimum (90°) and maximum (0°) cladding diameters following data-generation test OCZL#19, which was pressurized to 600 psig, oxidized to 17% CP-ECR, and cooled with quench.**

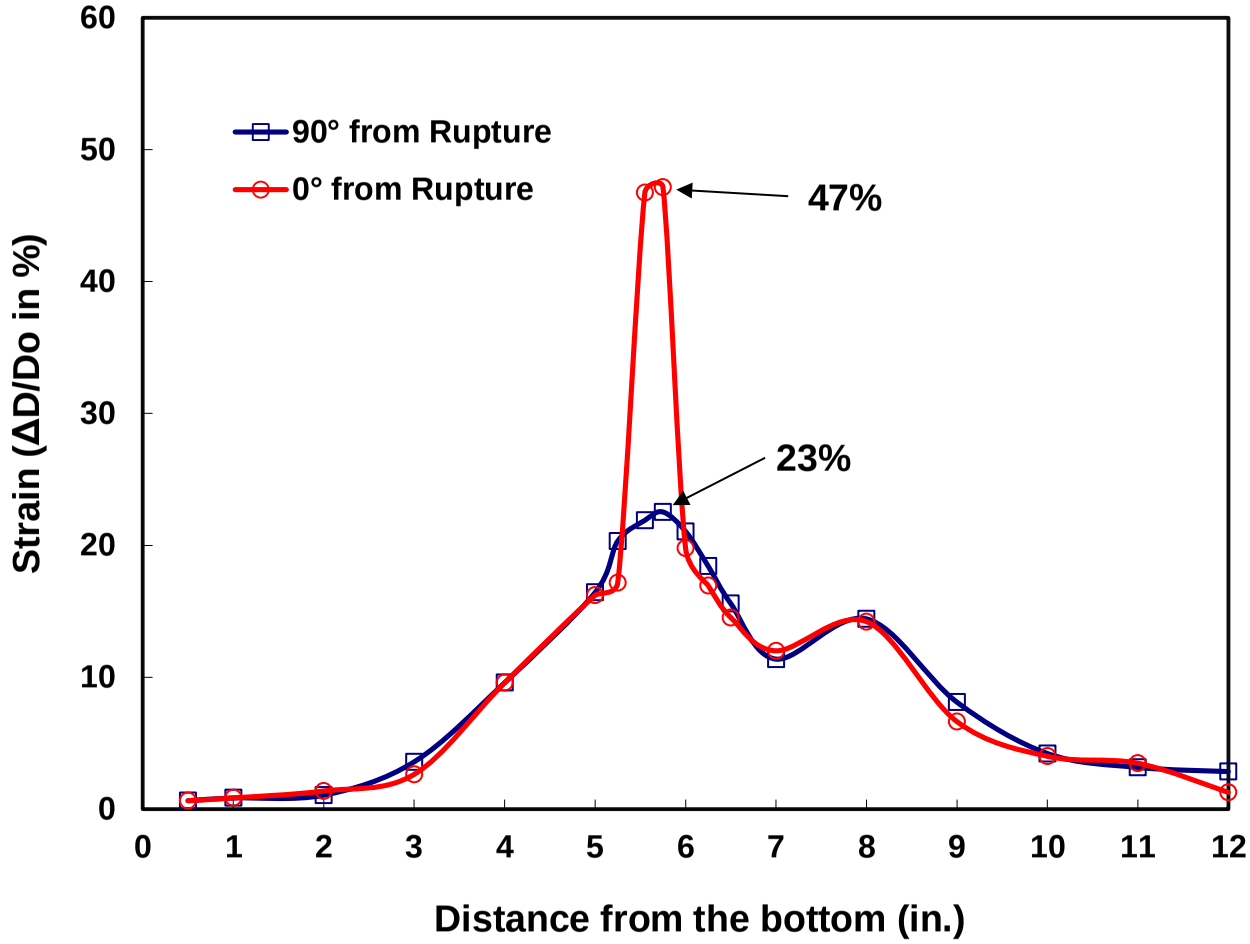

Figure B.15: **Axial profiles for minimum (90°) and maximum (0°) cladding diameters following data-generation test OCZL#21, which was pressurized to 600 psig, oxidized to 11% CP-ECR, and cooled with quench.**

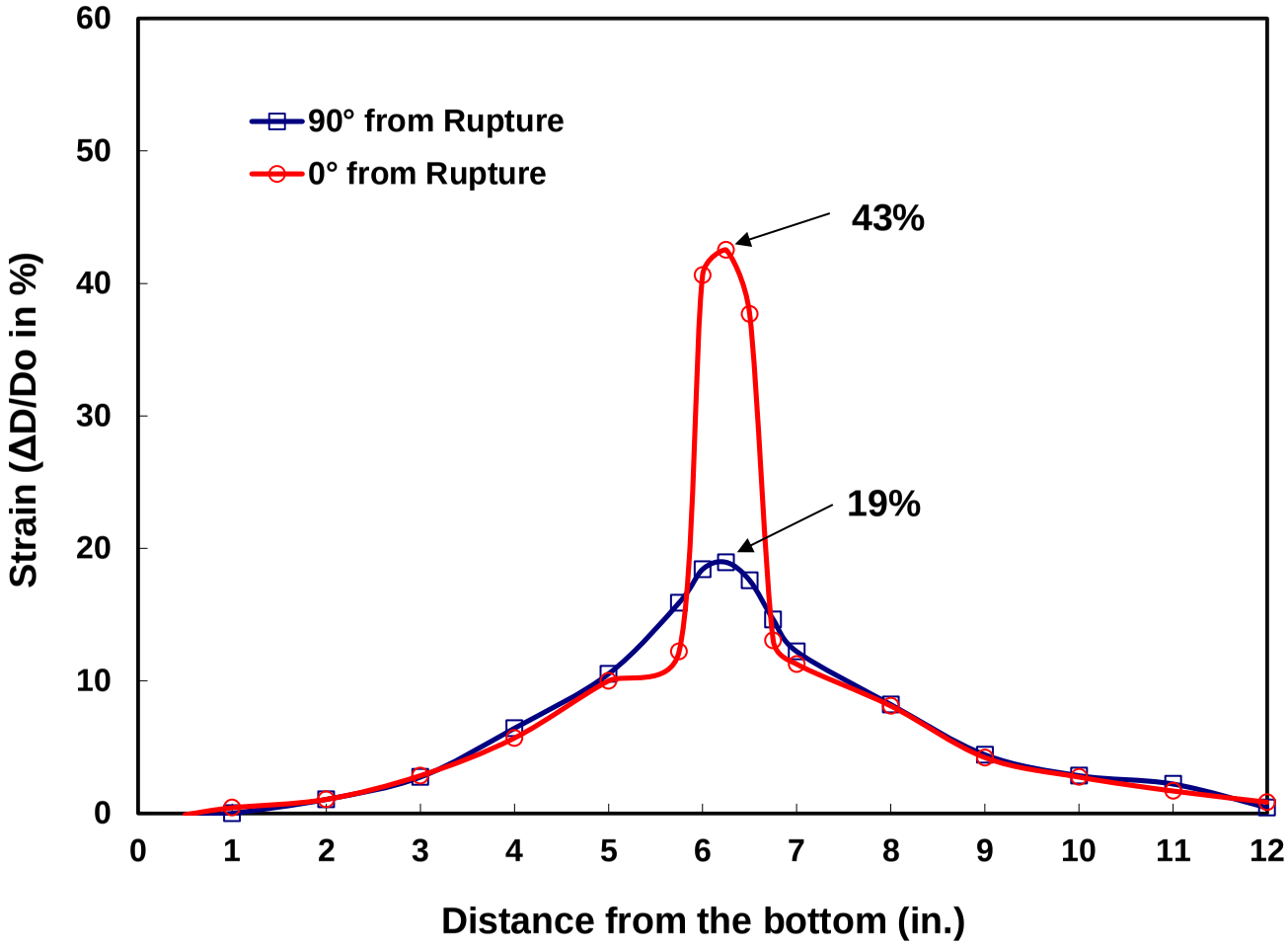

Figure B.16: **Axial profiles for minimum (90°) and maximum (0°) cladding diameters following data-generation test OCZL#22, which was pressurized to 600 psig, oxidized to 12% CP-ECR, and cooled with quench.**

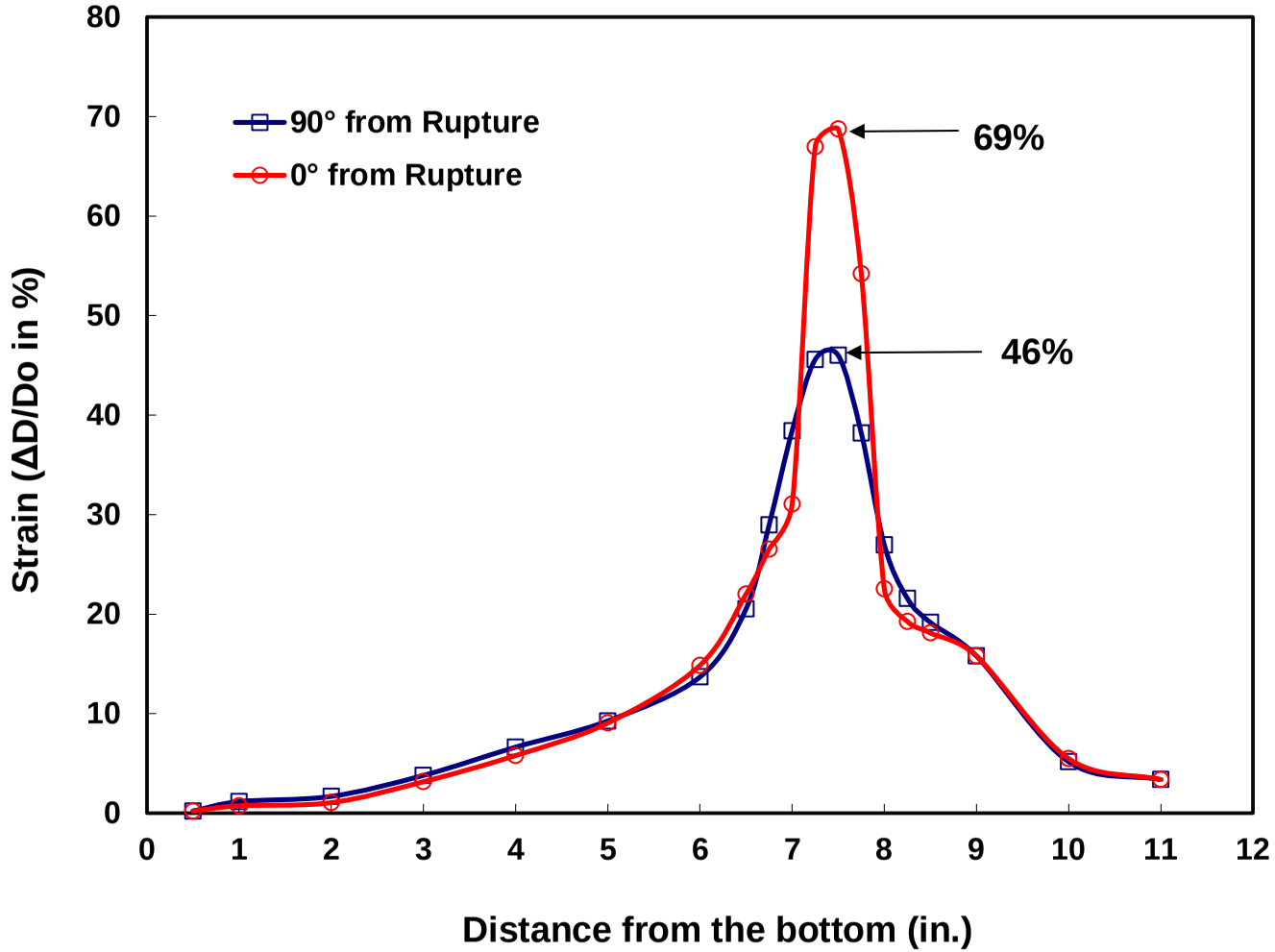

Figure B.17: **Axial profiles for minimum (90°) and maximum (0°) cladding diameters following data-generation test OCZL#25, which was pressurized to 1200 psig, oxidized to 16% CP-ECR, and cooled with quench.**

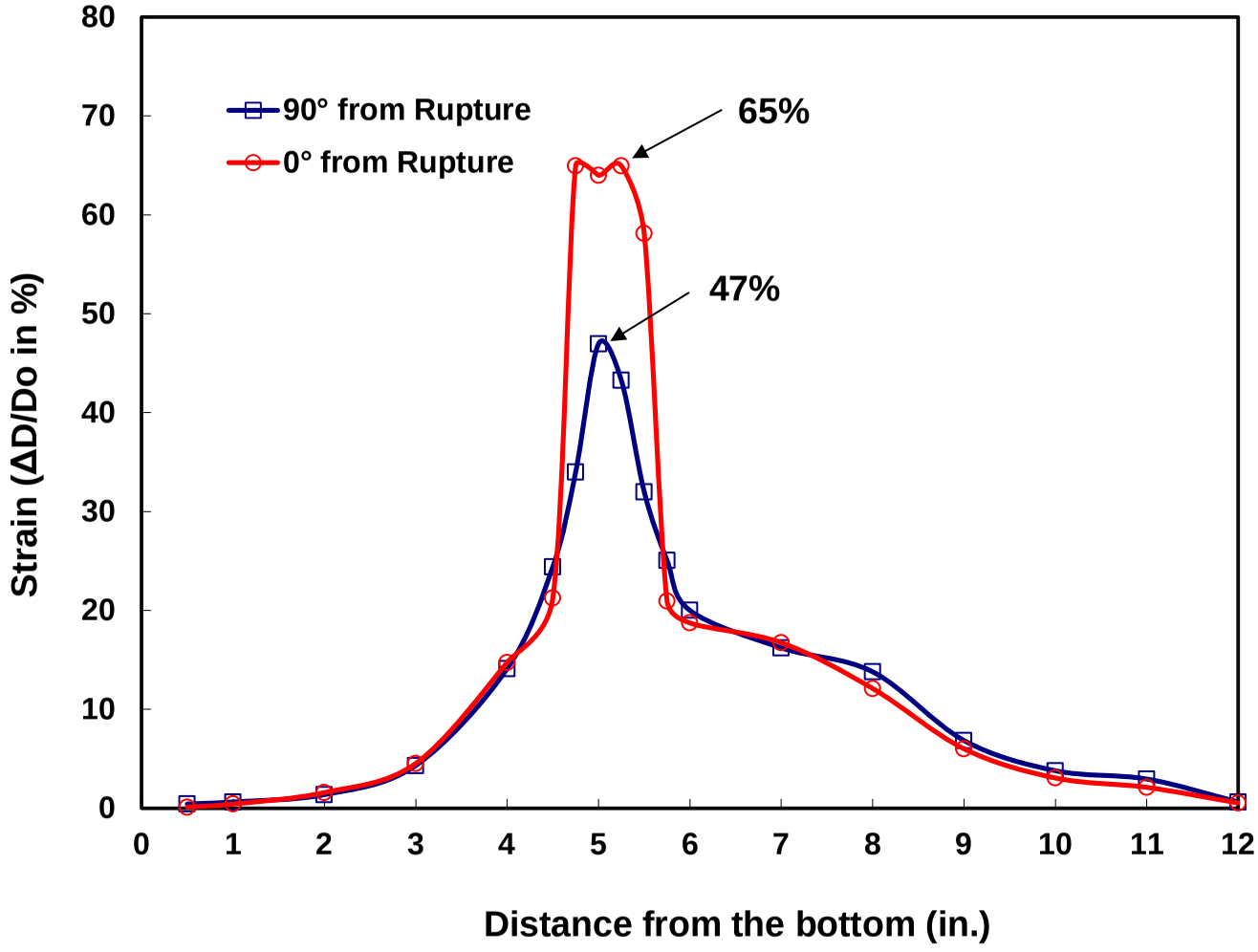

Figure B.18: **Axial profiles for minimum (90°) and maximum (0°) cladding diameters following data-generation test OCZL#29, which was pressurized to 1200 psig, oxidized to 17% CP-ECR, and cooled with quench.**

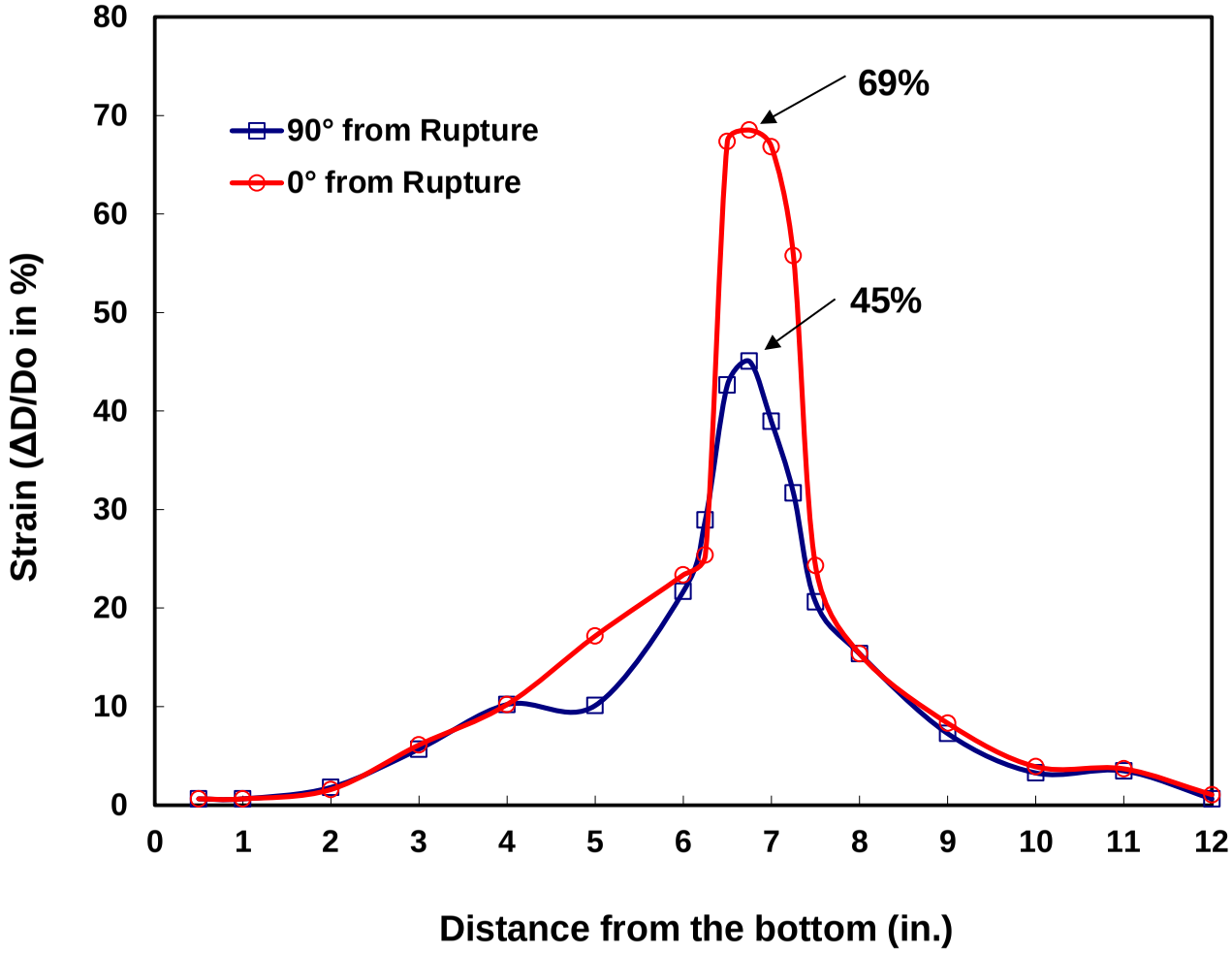

Figure B.19: **Axial profiles for minimum (90°) and maximum (0°) cladding diameters following data-generation test OCZL#32, which was pressurized to 1200 psig, oxidized to 16% CP-ECR, and cooled with quench.**

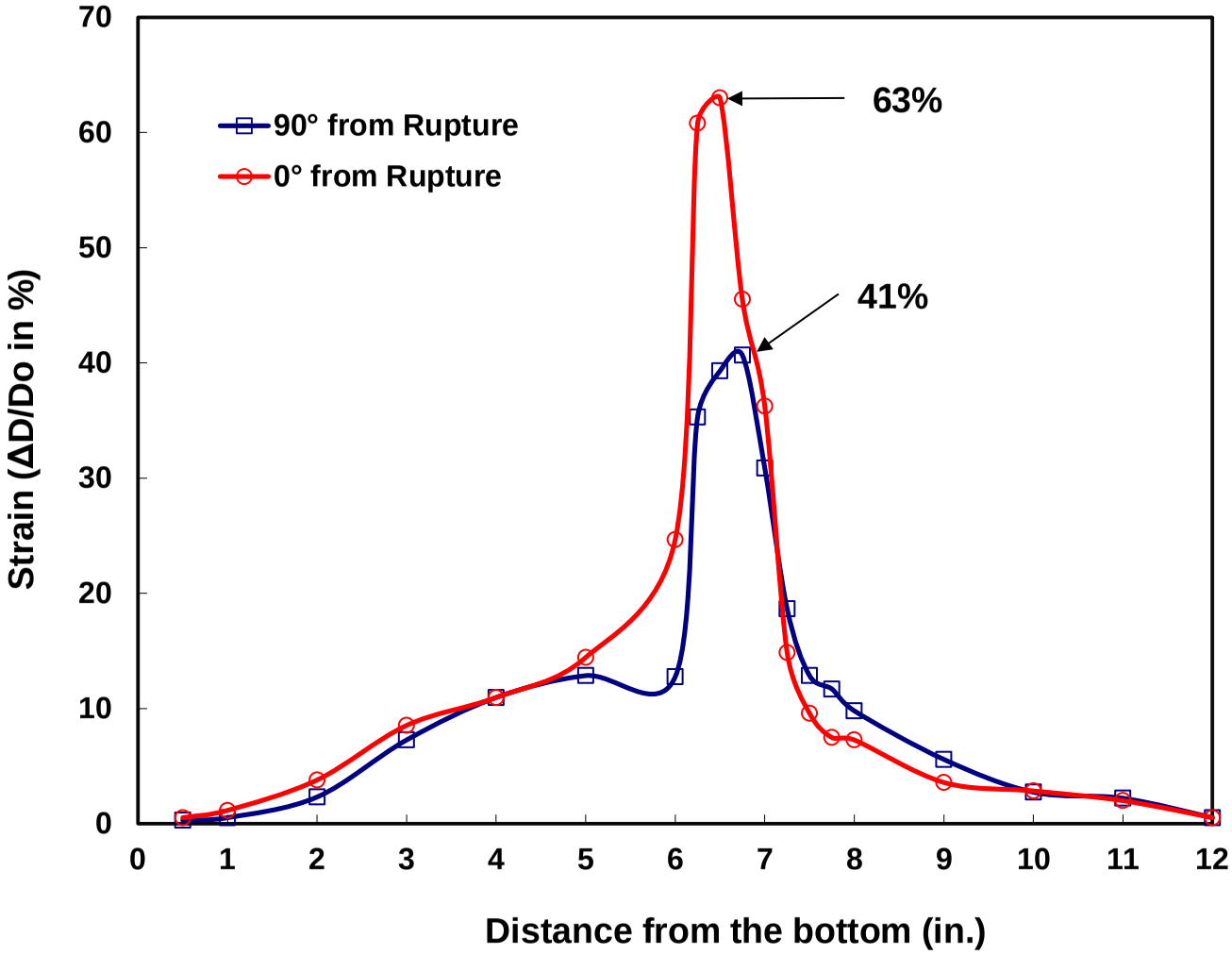

Figure B.20: **Axial profiles for minimum (90°) and maximum (0°) cladding diameters following data-generation test OCZL#37, which was pressurized to 1200 psig, oxidized to 23% CP-ECR, and cooled with quench.**

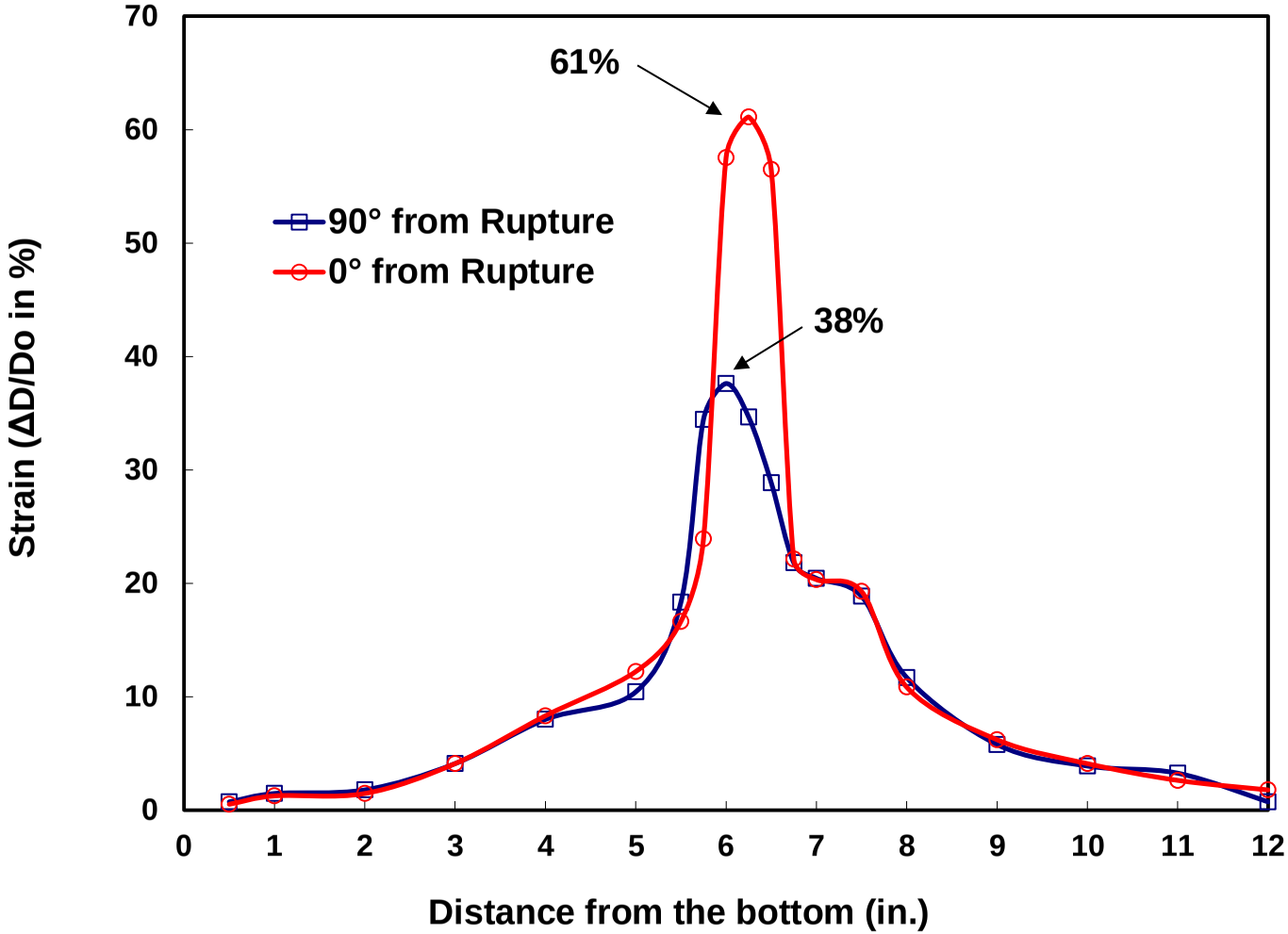

Figure B.21: **Axial profiles for minimum (90°) and maximum (0°) cladding diameters following data-generation test OCZL#43, which was pressurized to 1200 psig, oxidized to 18% CP-ECR, and cooled with quench.**

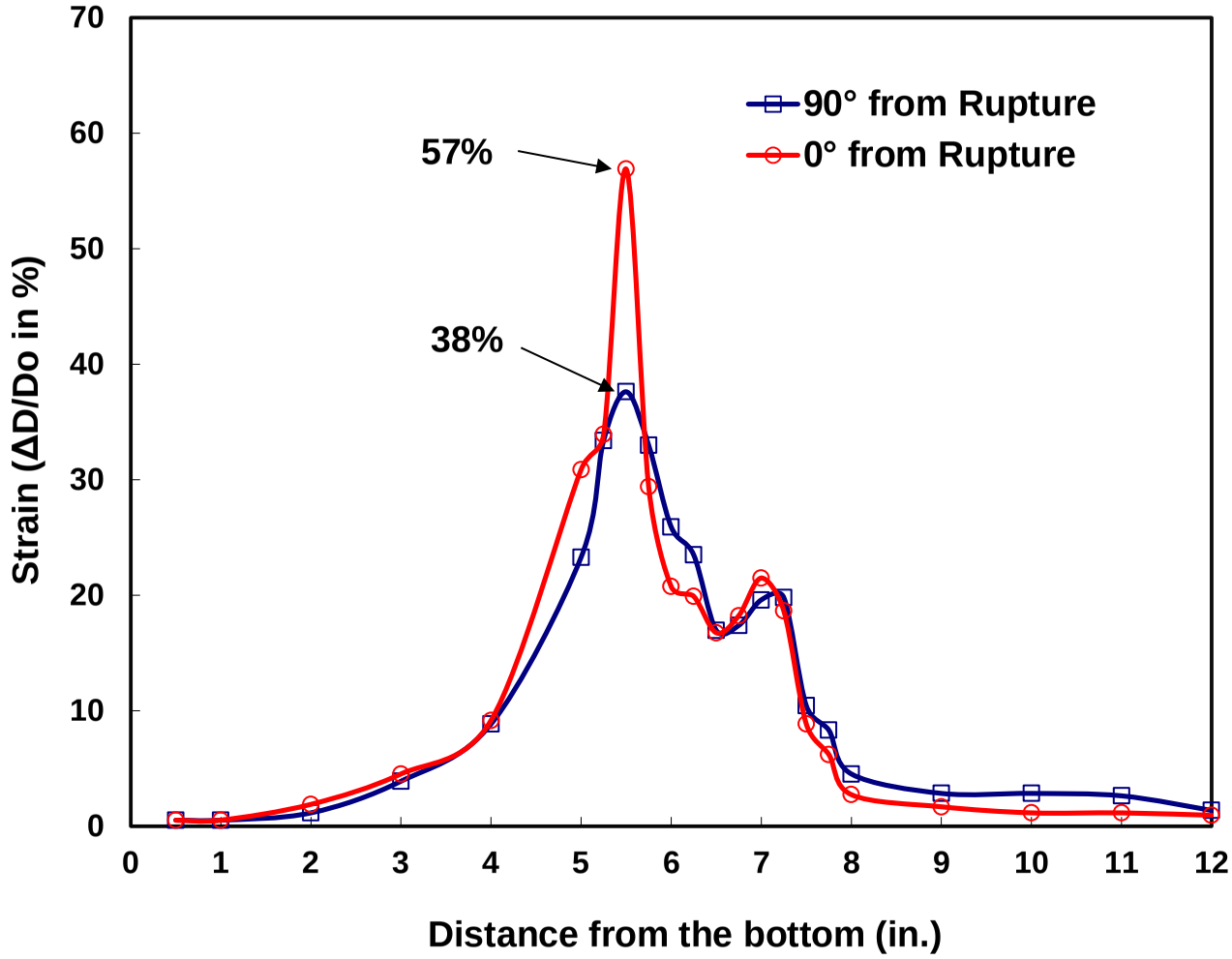

Figure B.22: **Axial profiles for minimum (90°) and maximum (0°) cladding diameters following data-generation test OCZL#39 with 660 wppm pre-hydriding, which was pressurized to 600 psig, oxidized to 13% CP-ECR, and cooled with quench.**

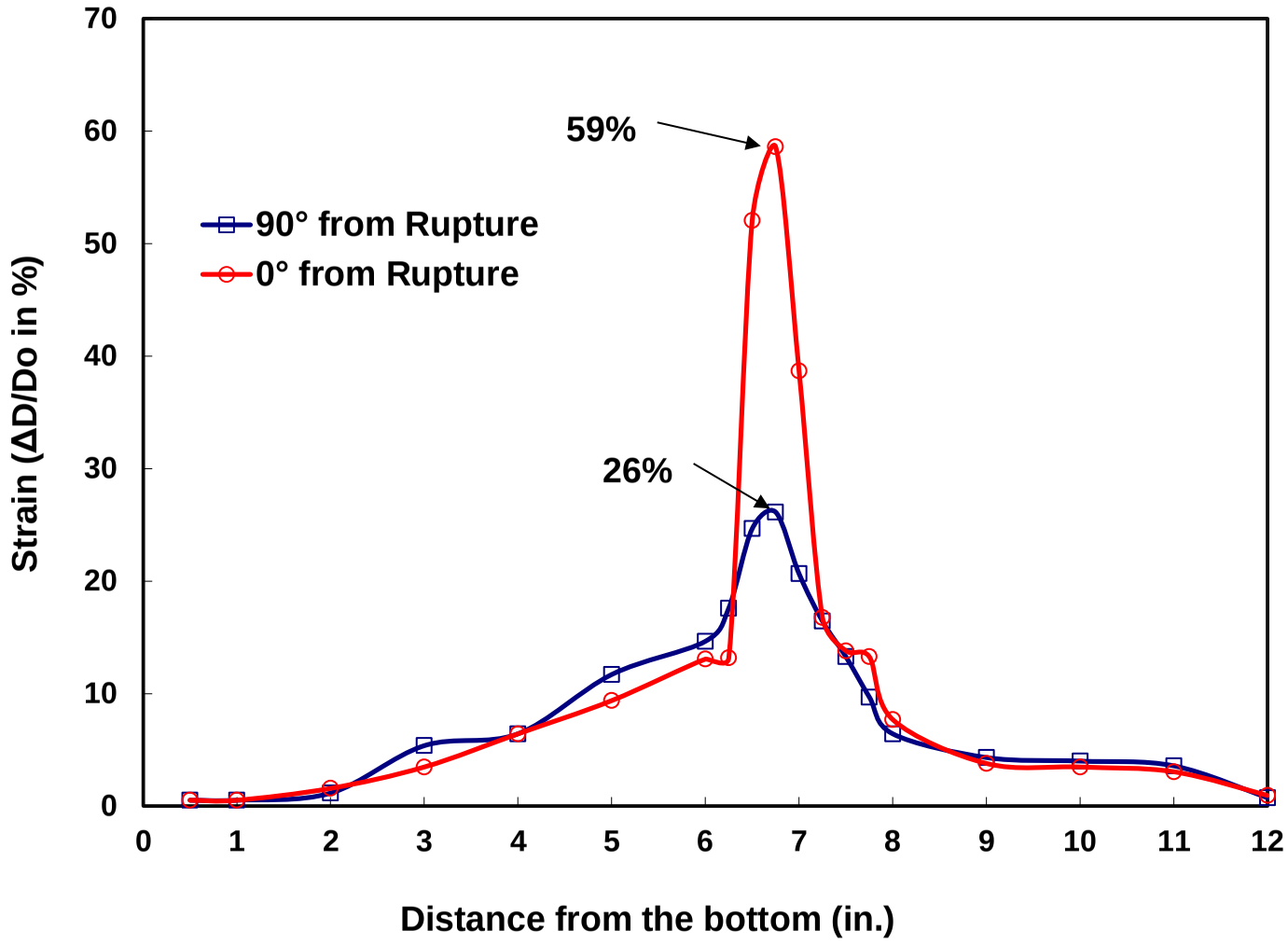

Figure B.23: **Axial profiles for minimum (90°) and maximum (0°) cladding diameters following data-generation test OCZL#40 with 390 wppm pre-hydriding, which was pressurized to 1200 psig, oxidized to 12% CP-ECR, and cooled with quench.**

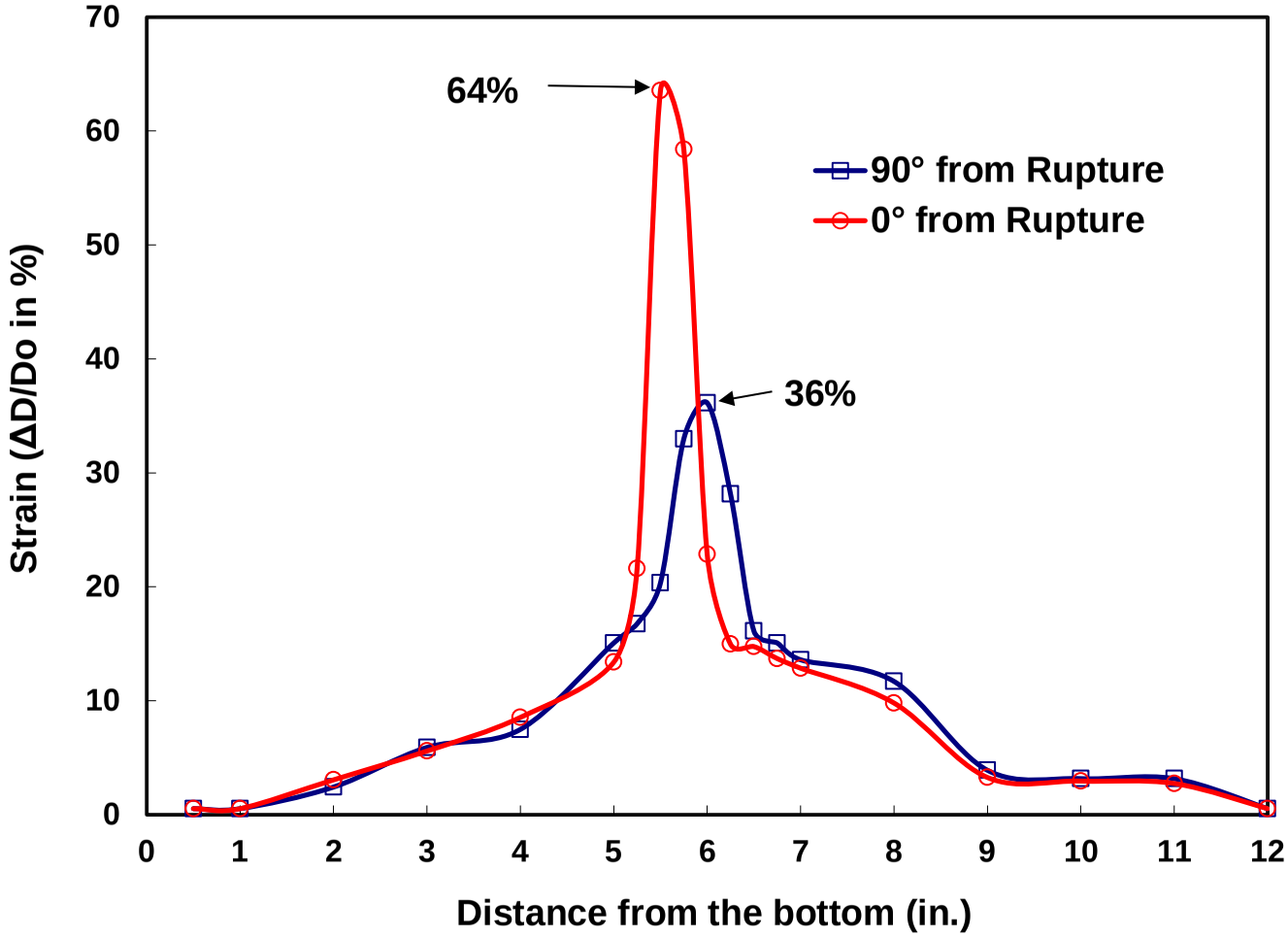

Figure B.24: **Axial profiles for minimum (90°) and maximum (0°) cladding diameters following data-generation test OCZL#41 with 220 wppm pre-hydriding, which was pressurized to 1200 psig, oxidized to 16% CP-ECR, and cooled with quench.**

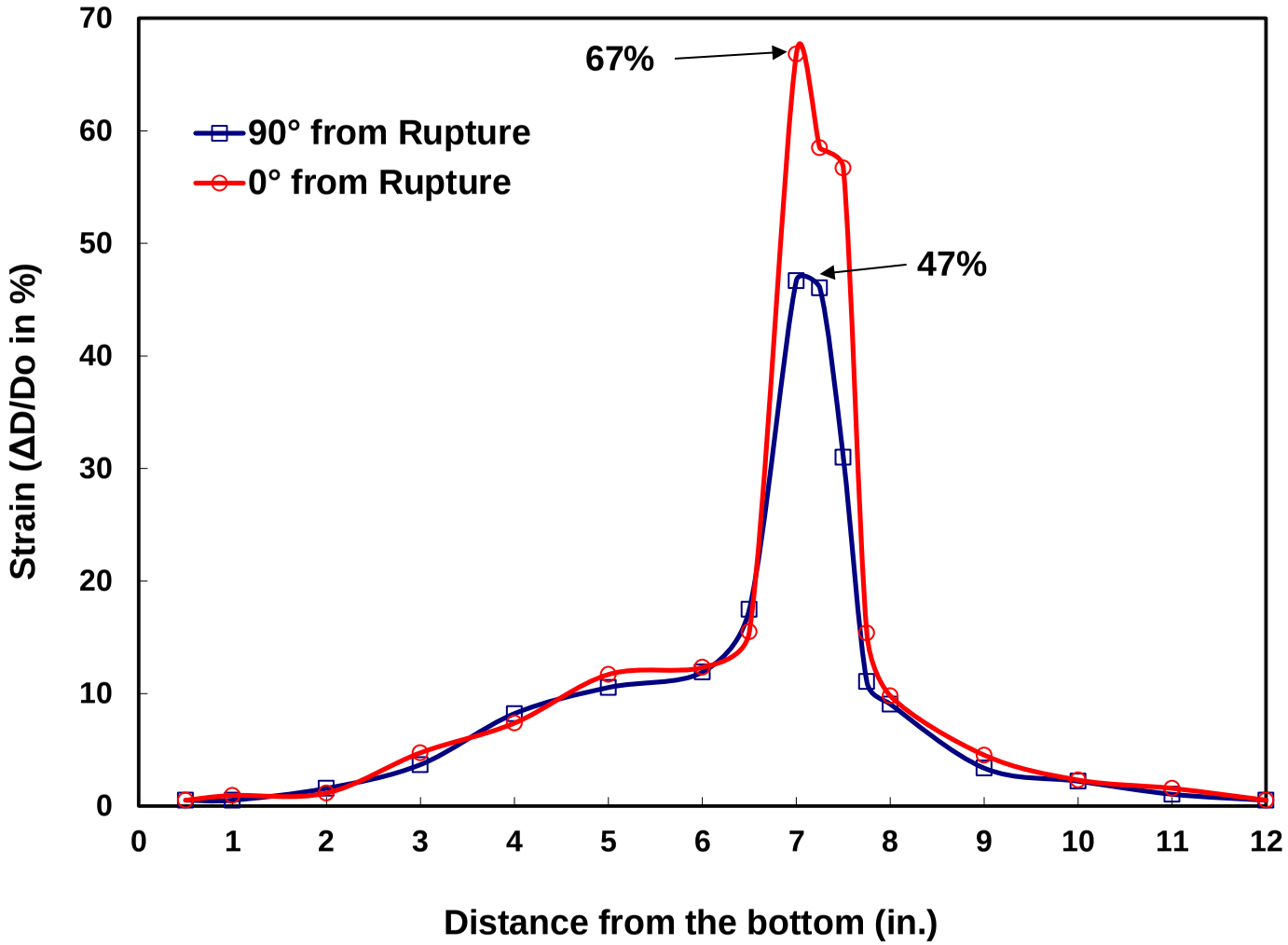

Figure B.25: **Axial profiles for minimum (90°) and maximum (0°) cladding diameters following data-generation test OCZL#42 with 520 wppm pre-hydriding, which was pressurized to 1200 psig, oxidized to 14% CP-ECR, and cooled with quench.**

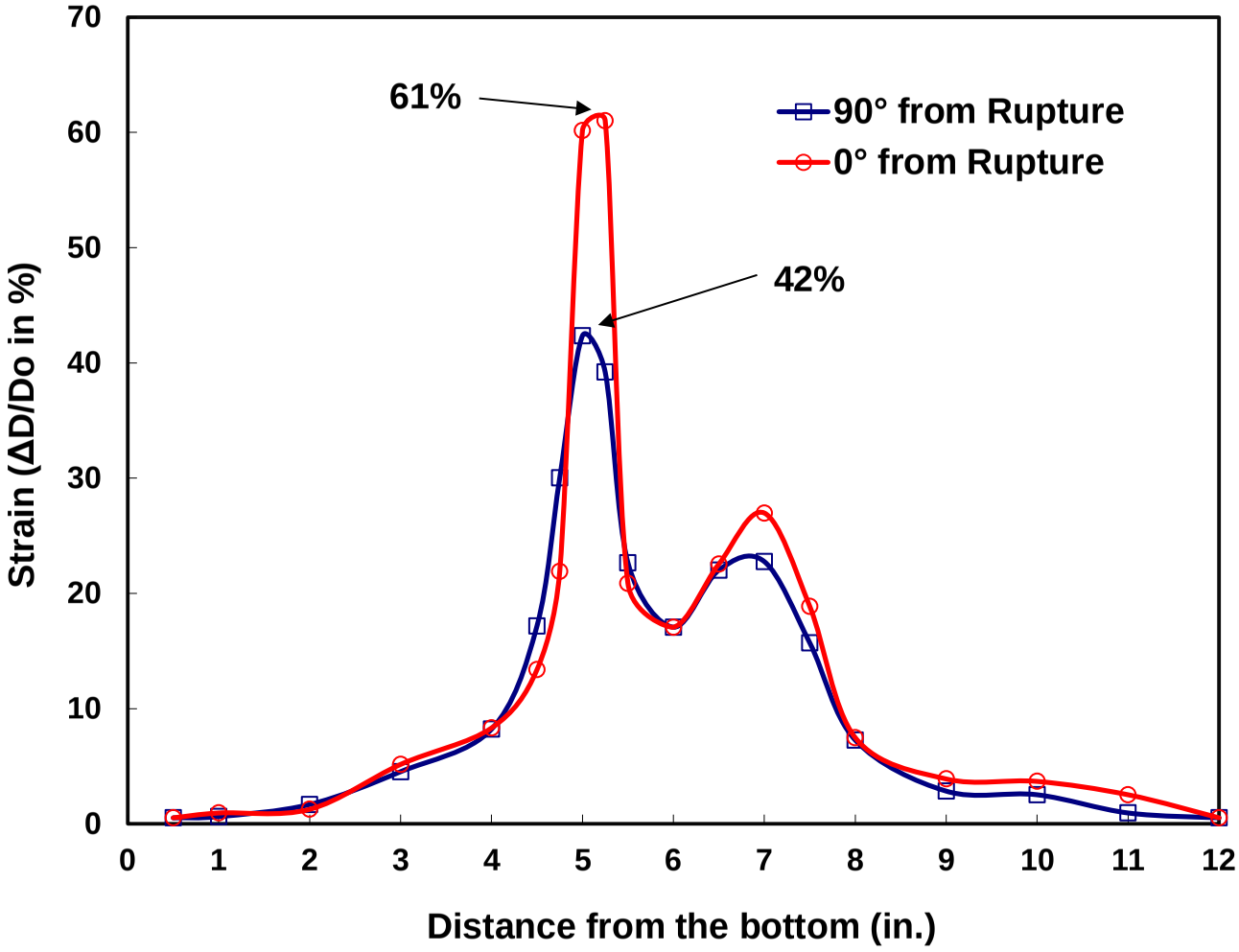

Figure B.26: **Axial profiles for minimum (90°) and maximum (0°) cladding diameters following data-generation test OCZL#44 with 700 wppm pre-hydriding, which was pressurized to 1200 psig, oxidized to 14% CP-ECR, and cooled with quench.**

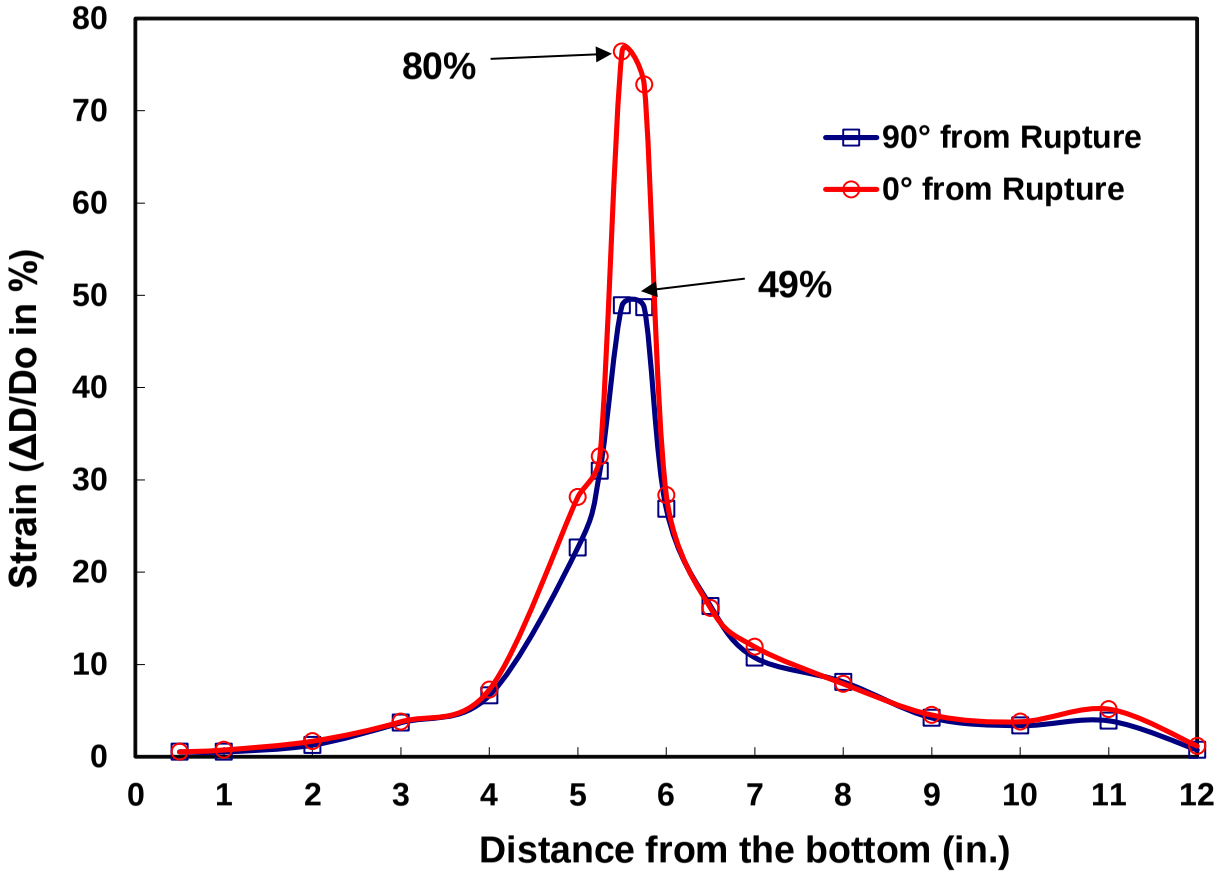

Figure B.27: **Axial profiles for minimum (90°) and maximum (0°) cladding diameters following data-generation test OCZL#45 with 220 wppm pre-hydriding, which was pressurized to 1200 psig, oxidized to 13% CP-ECR, and cooled with quench.**

APPENDIX C: PHOTOGRAPHS OF POST-OXIDATION LOCA INTEGRAL SAMPLES

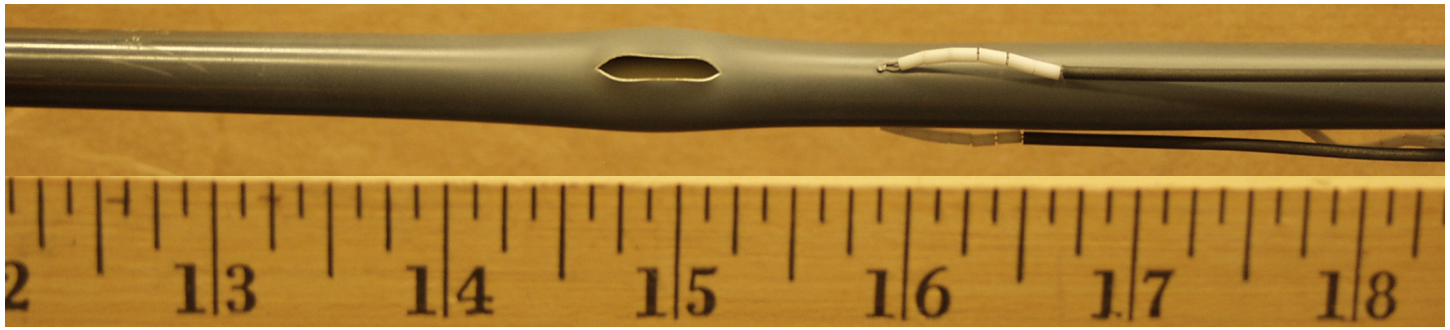

(a)

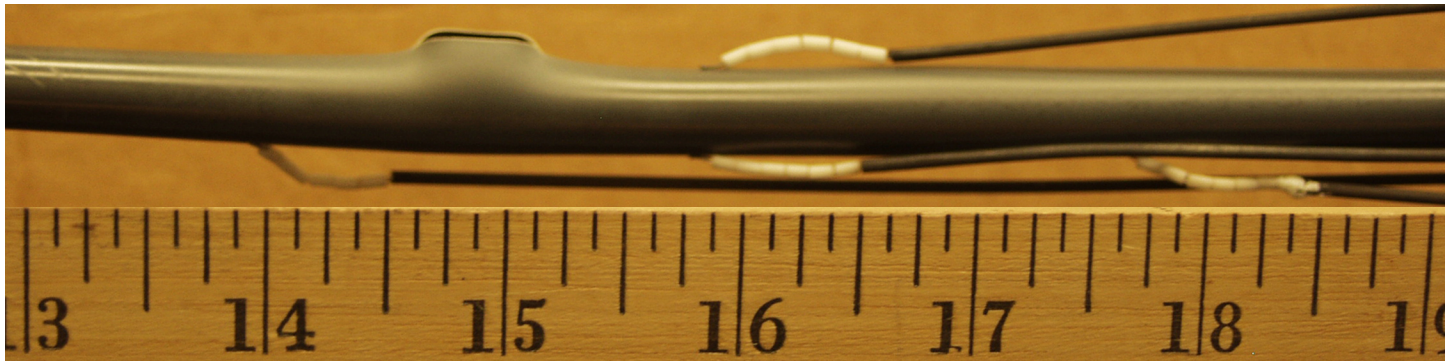

(b)

Figure C.1: **Post-oxidation images of OCZL#6 sample, which was pressurized to 1200 psig, oxidized to 18% CP-ECR at ≈1200°C, and cooled without quench: (a) rupture-opening view and (b) side view.**

(a)

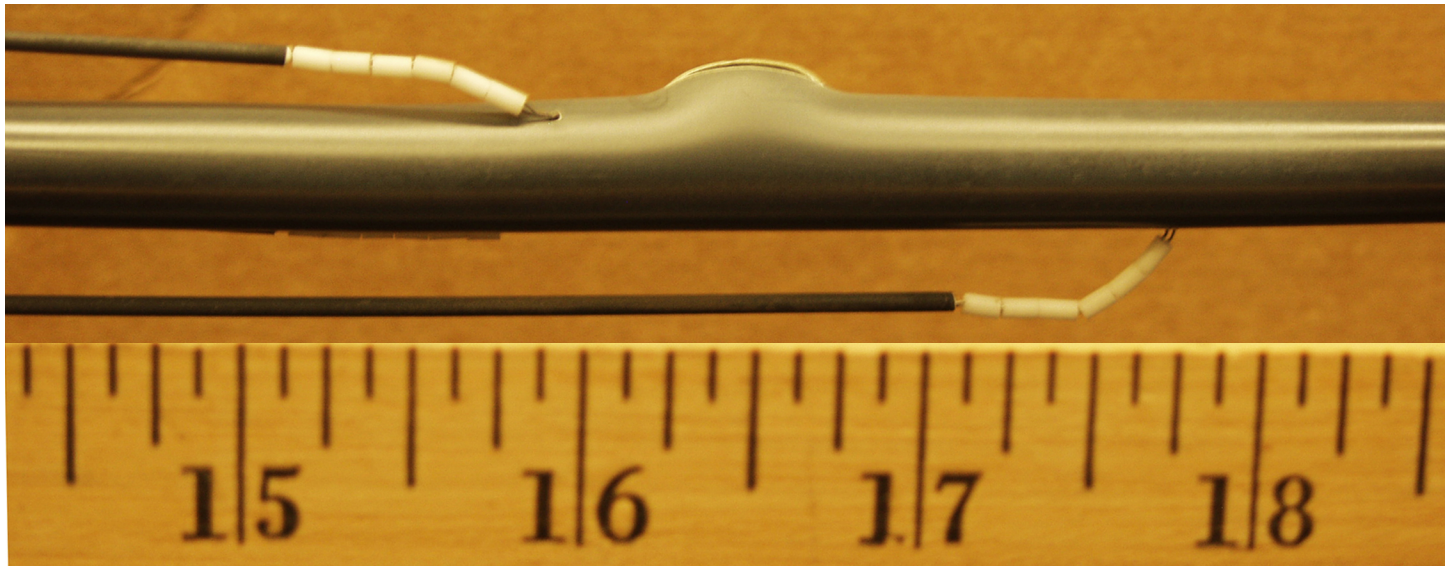

(b)

Figure C.2: Post-oxidation images of OCZL#7 sample, which was pressurized to 800 psig, oxidized to 16% CP-ECR at ≈1200°C, and cooled without quench: (a) rupture-opening view and (b) side view.

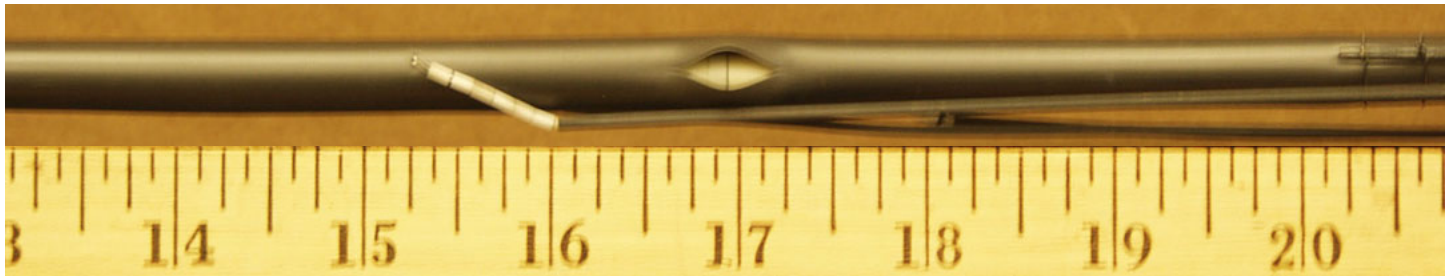

(a)

(b)

Figure C.3: **Post-oxidation images of OCZL#8 sample, which was pressurized to 600 psig, heated to rupture, and cooled without quench: (a) rupture-opening view and (b) side view.**

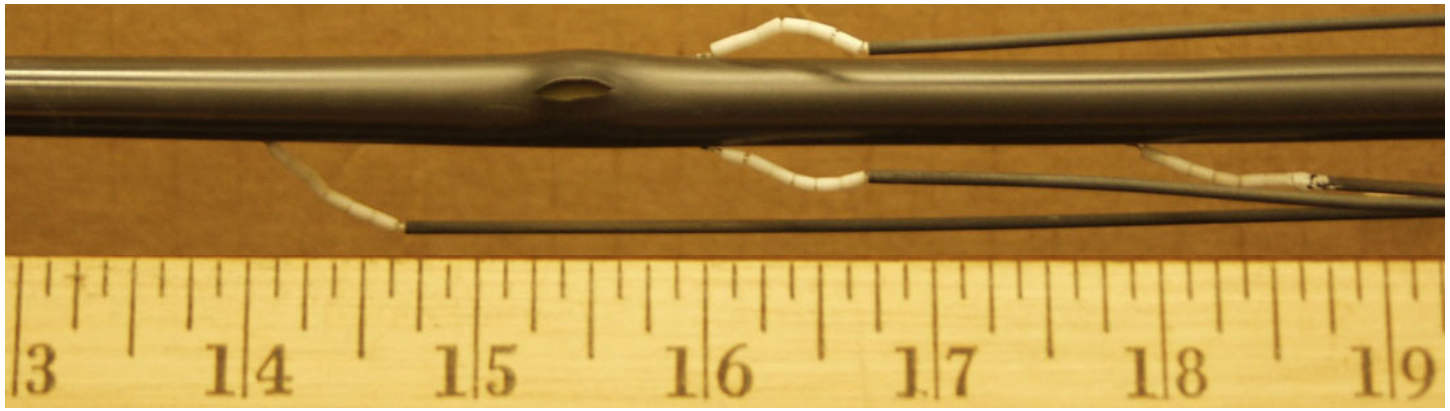

(a)

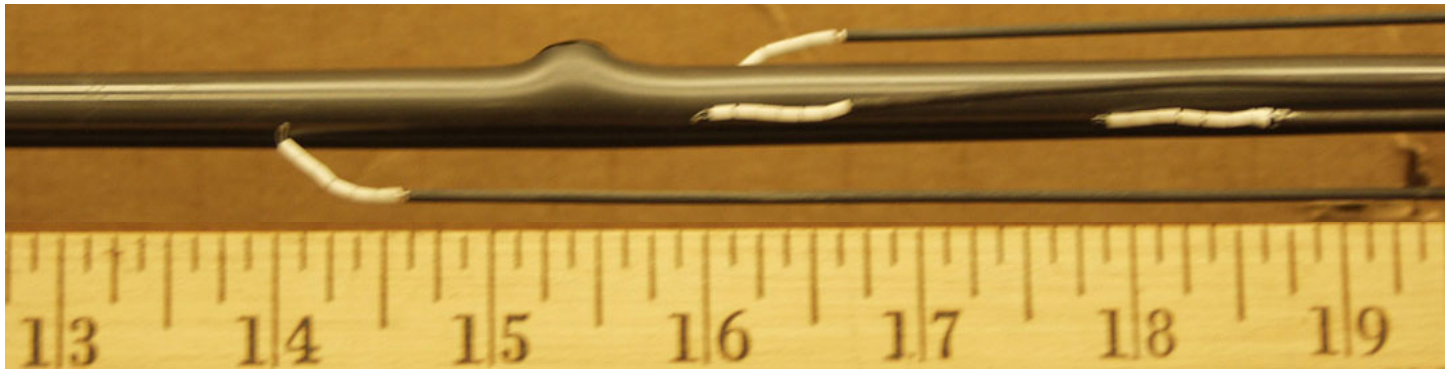

(b)

Figure C.4: Post-oxidation images of OCZL#9 sample, which was pressurized to 400 psig, heated to rupture, and cooled without quench: (a) rupture-opening view and (b) side view.

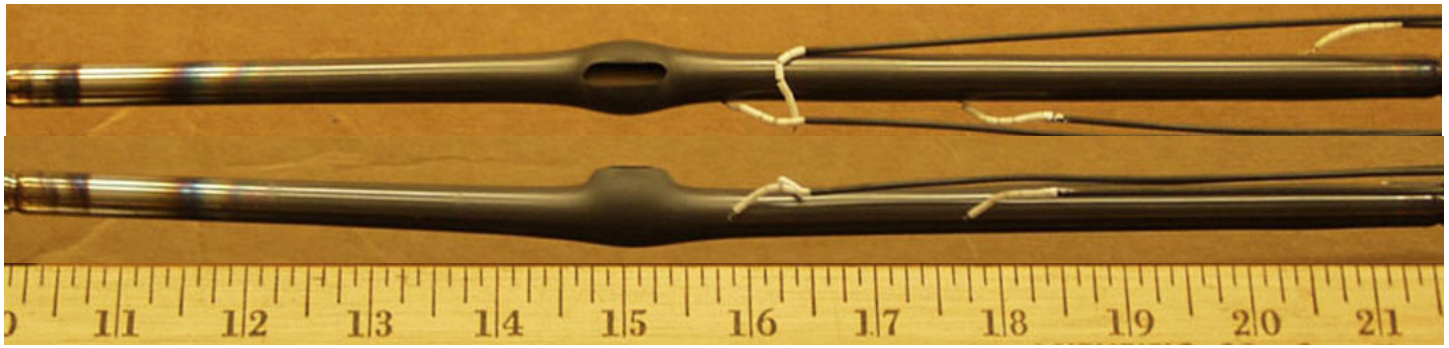

(a)

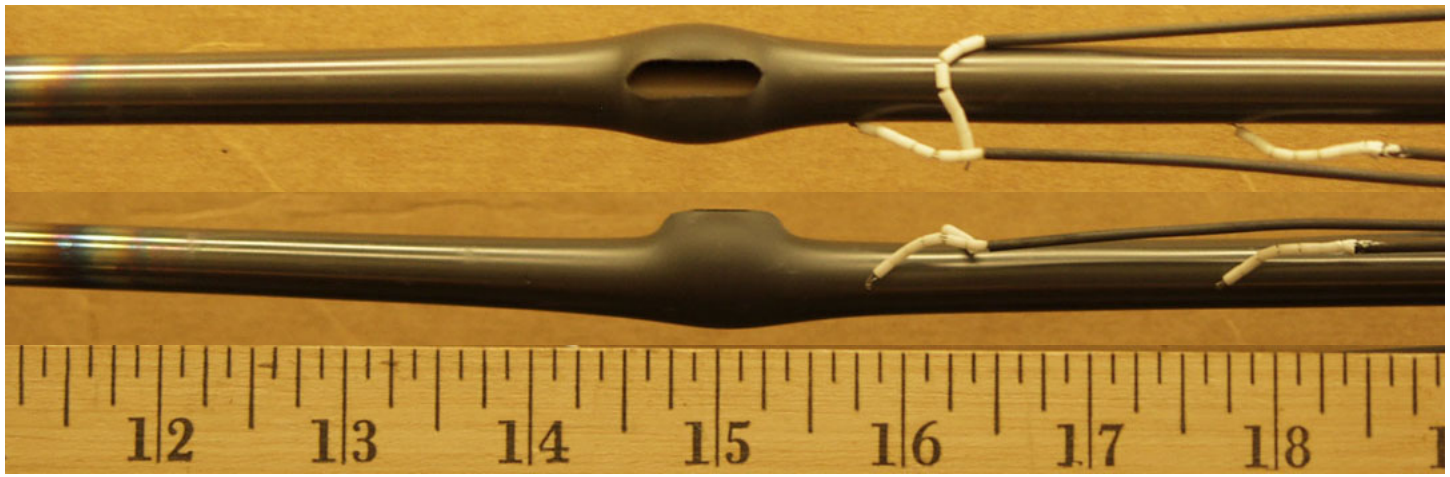

(b)

Figure C.5: Post-oxidation images of OCZL#10 sample, which was pressurized to 1600 psig, heated to rupture, and cooled without quench: (a) low magnification and (b) higher magnification.

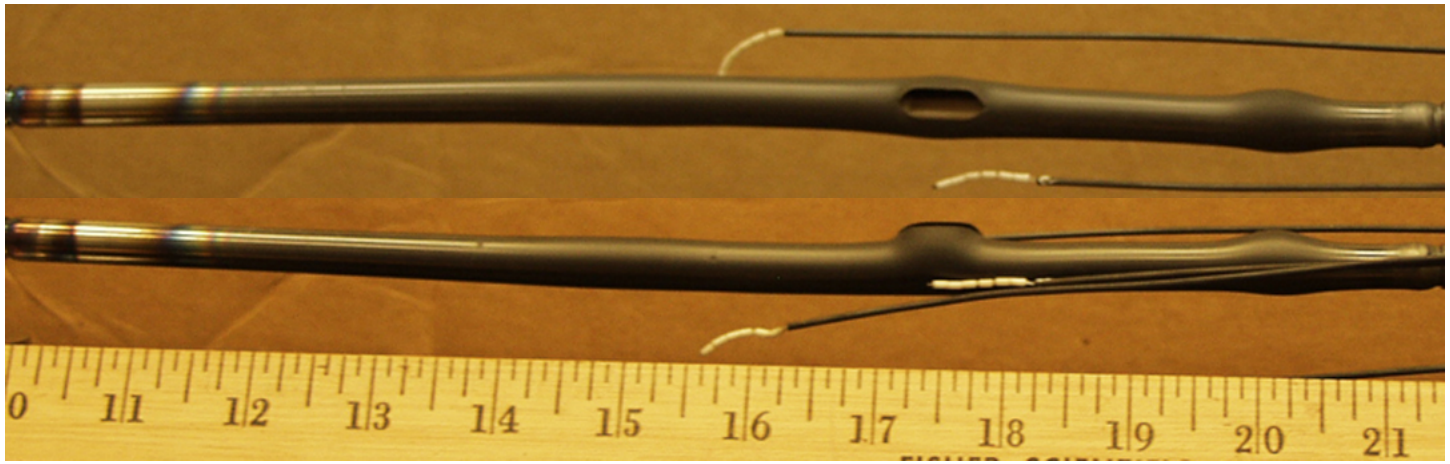

(a)

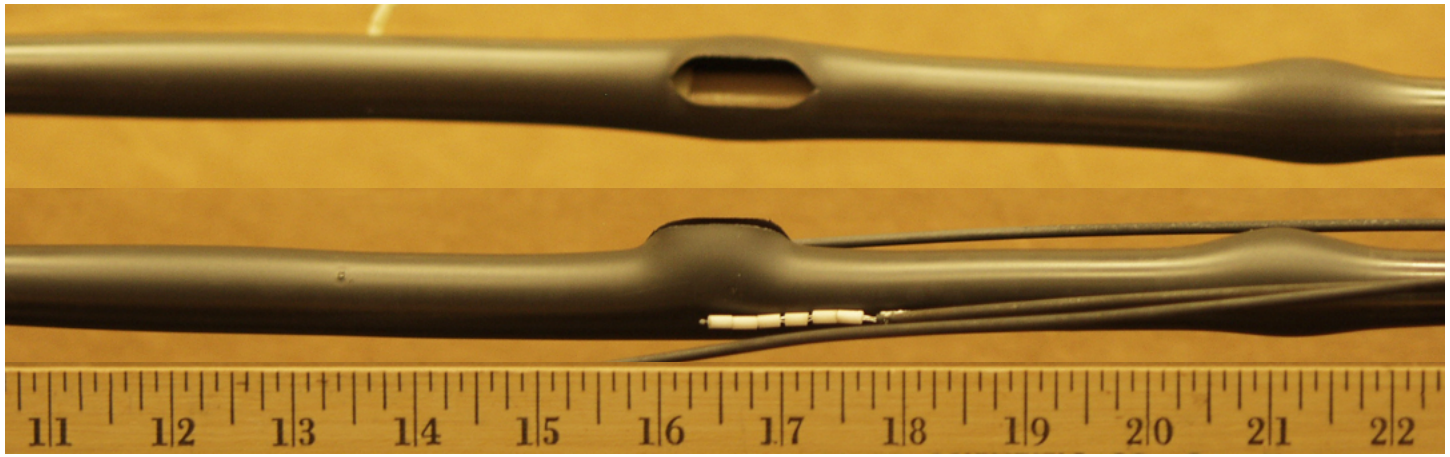

(b)

Figure C.6: Post-oxidation images of OCZL#11 sample, which was pressurized to 1400 psig, heated to rupture, and cooled without quench: (a) low magnification and (b) higher magnification.

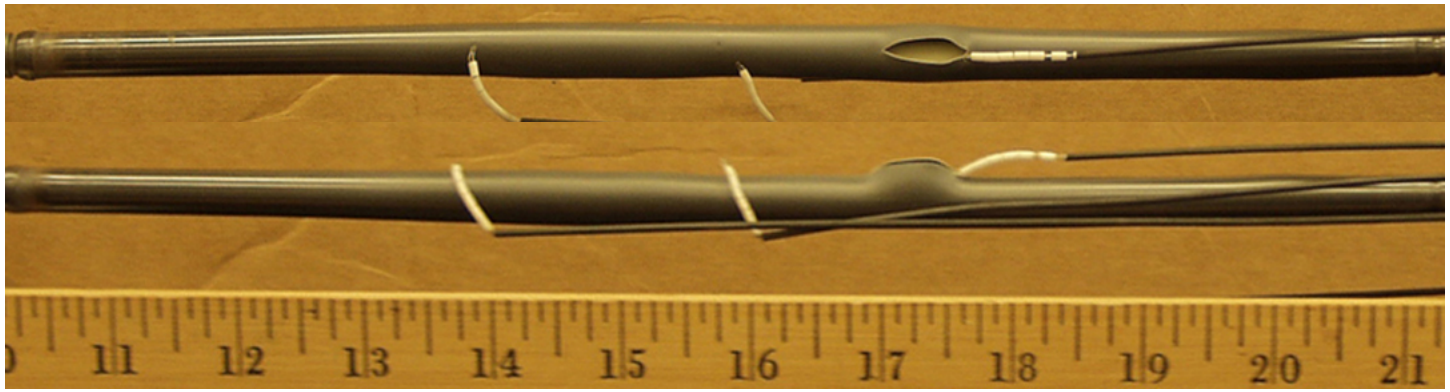

(a)

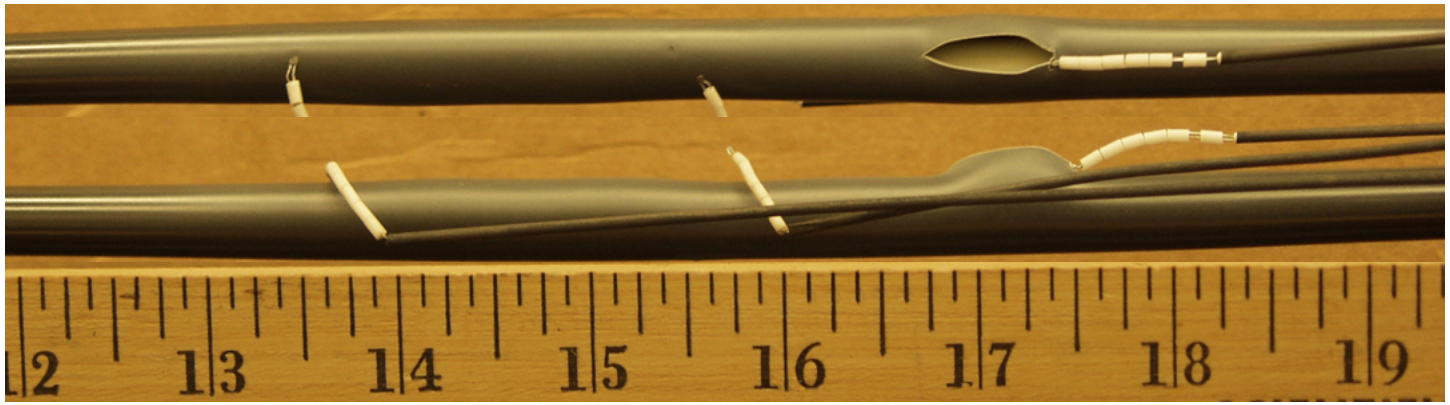

(b)

Figure C.7: Post-oxidation images of OCZL#12 sample, which was pressurized to 1000 psig, heated to rupture to 1200°C, oxidized to 15% CP-ECR, and cooled without quench: (a) low magnification and (b) higher magnification.

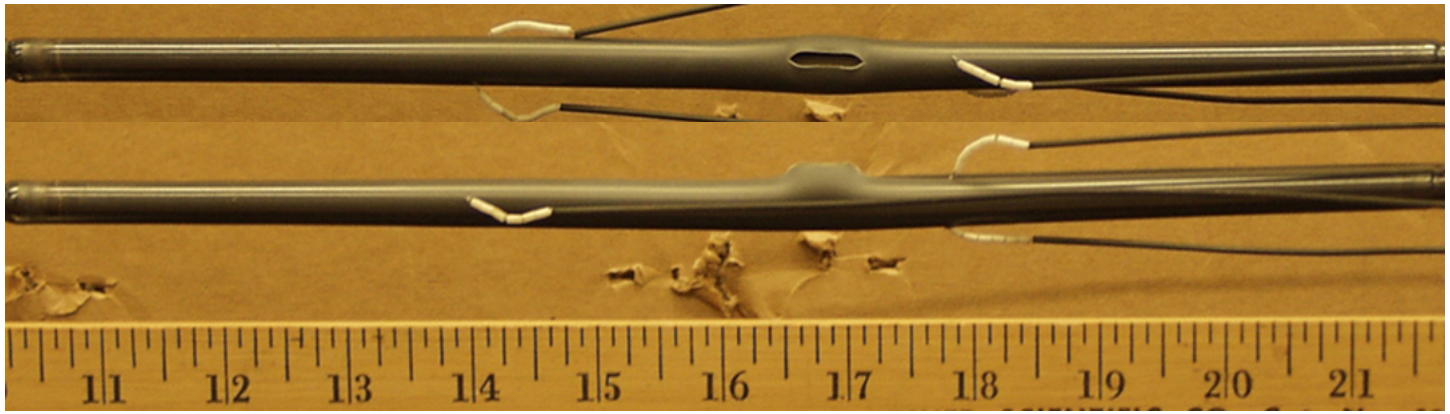

(a)

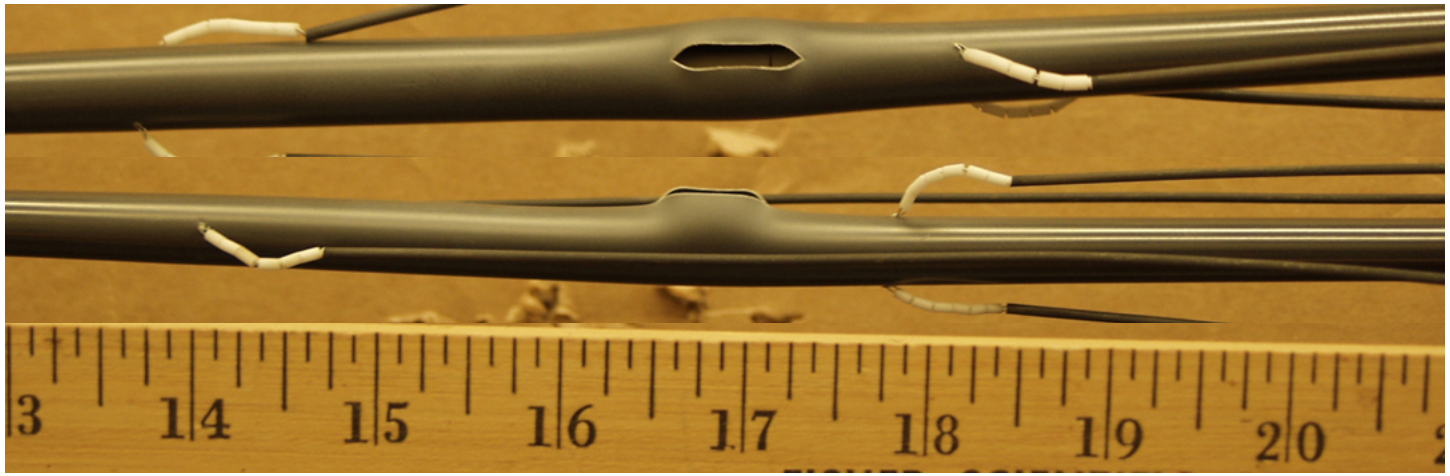

(b)

Figure C.8: Post-oxidation images of OCZL#13 sample, which was pressurized to 1200 psig, heated to 1200°C, oxidized to 14% CP-ECR, and cooled without quench: (a) low magnification and (b) higher magnification.

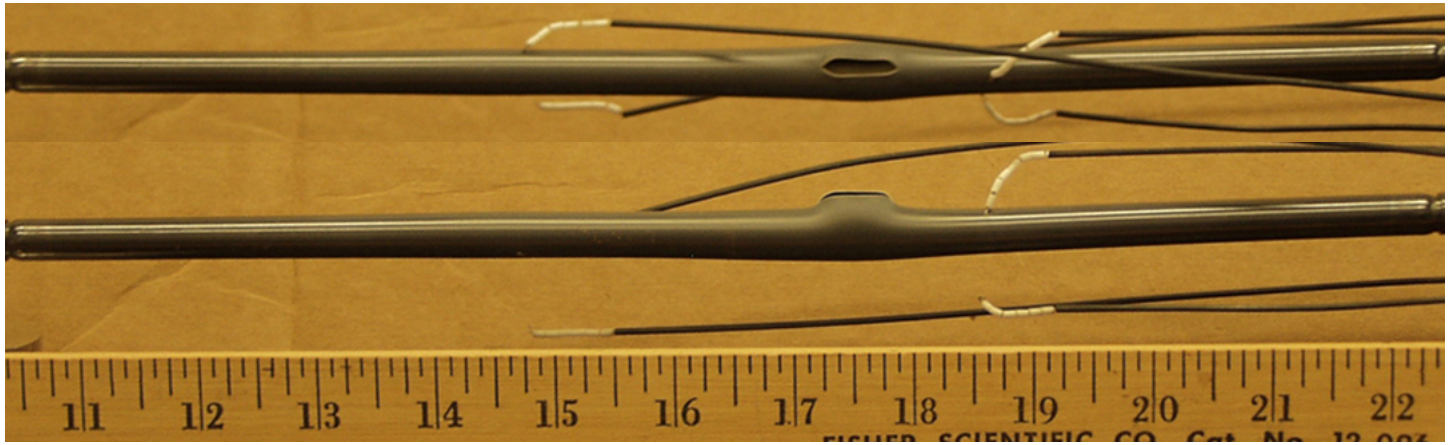

(a)

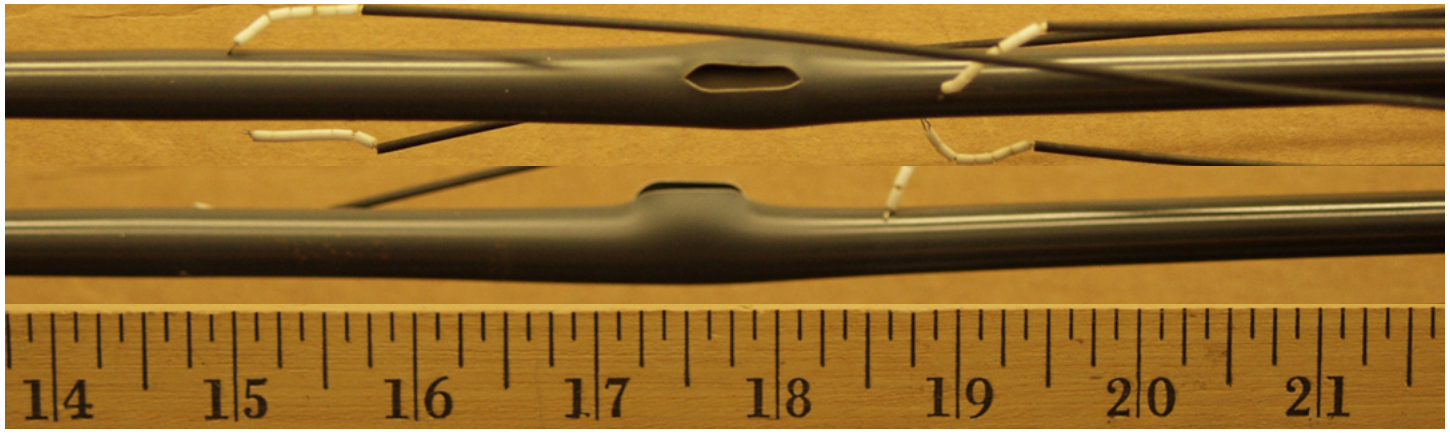

(b)

Figure C.9: **Post-oxidation images of OCZL#14 sample, which was pressurized to 1200 psig, heated to 1200°C, oxidized to 18% CP-ECR, and cooled with quench: (a) low magnification and (b) higher magnification.**

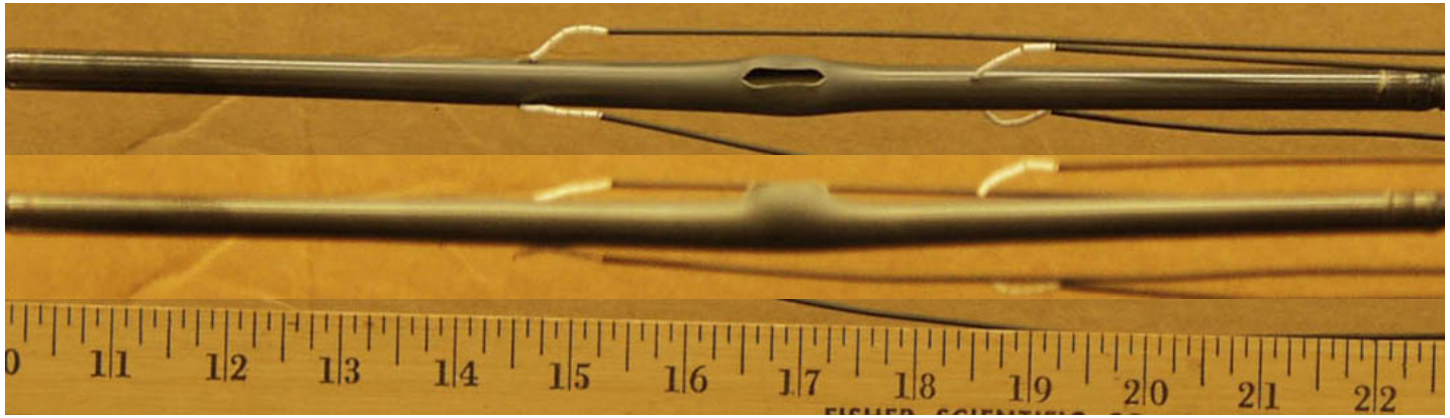

(a)

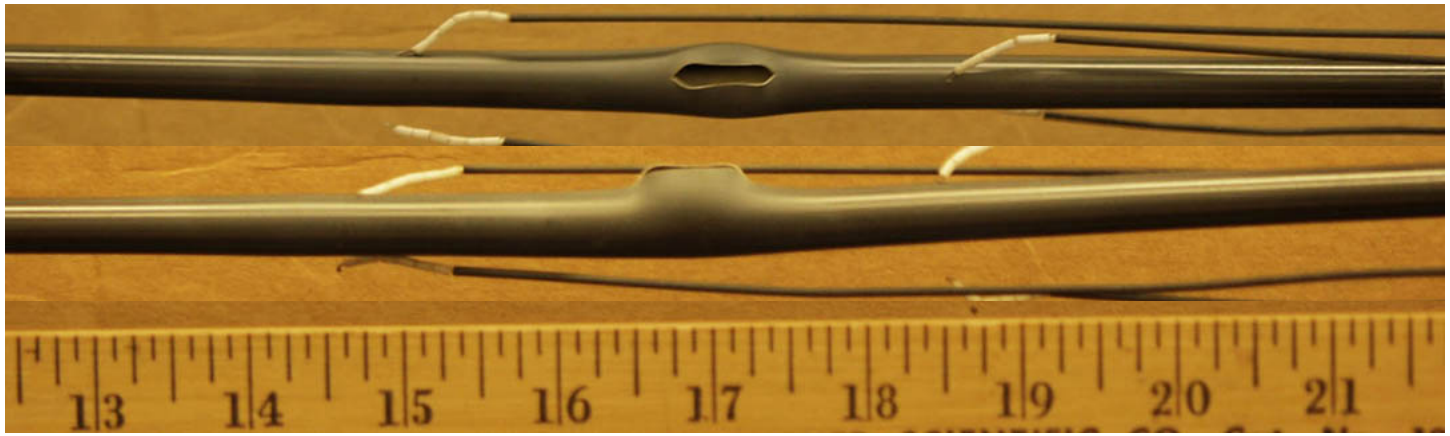

(b)

Figure C.10: Post-oxidation images of OCZL#15 sample, which was pressurized to 1200 psig, heated to 1200°C, oxidized to 18% CP-ECR, and cooled with quench: (a) low magnification and (b) higher magnification.

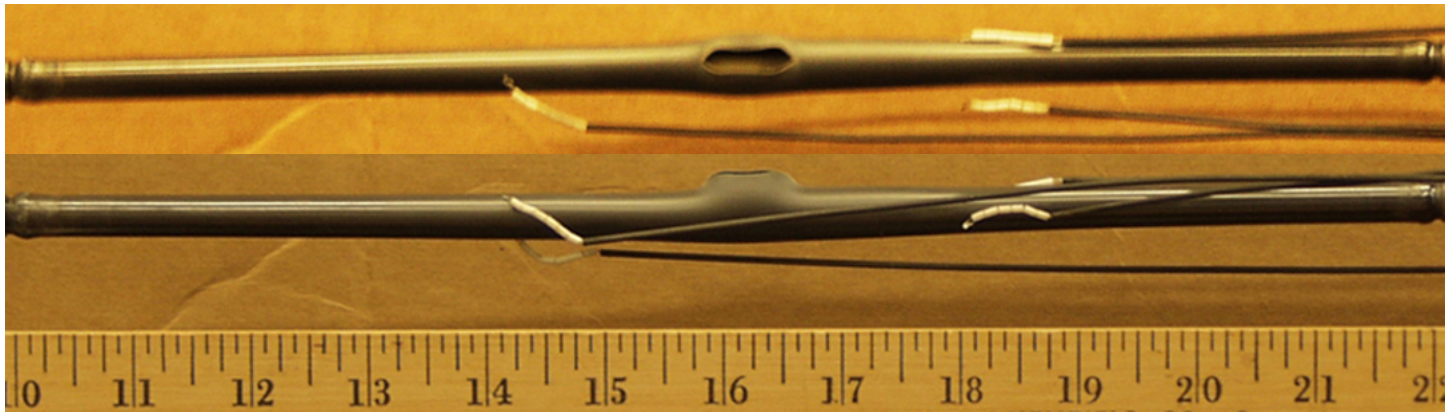

(a)

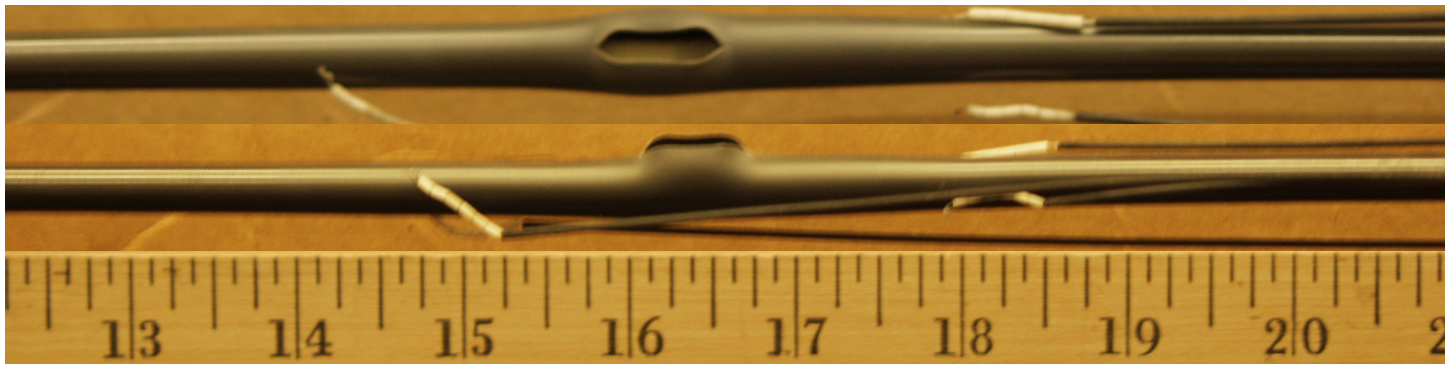

(b)

Figure C.11: Post-oxidation images of OCZL#17 sample, which was pressurized to 1200 psig, heated to 1200°C, oxidized to 13% CP-ECR, and cooled with quench: (a) low magnification and (b) higher magnification.

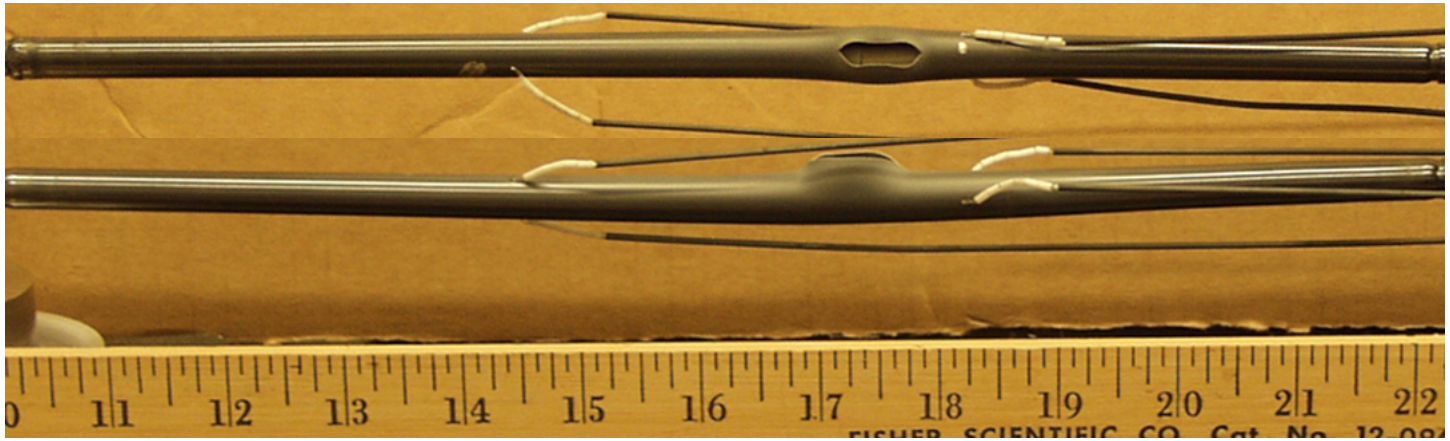

(a)

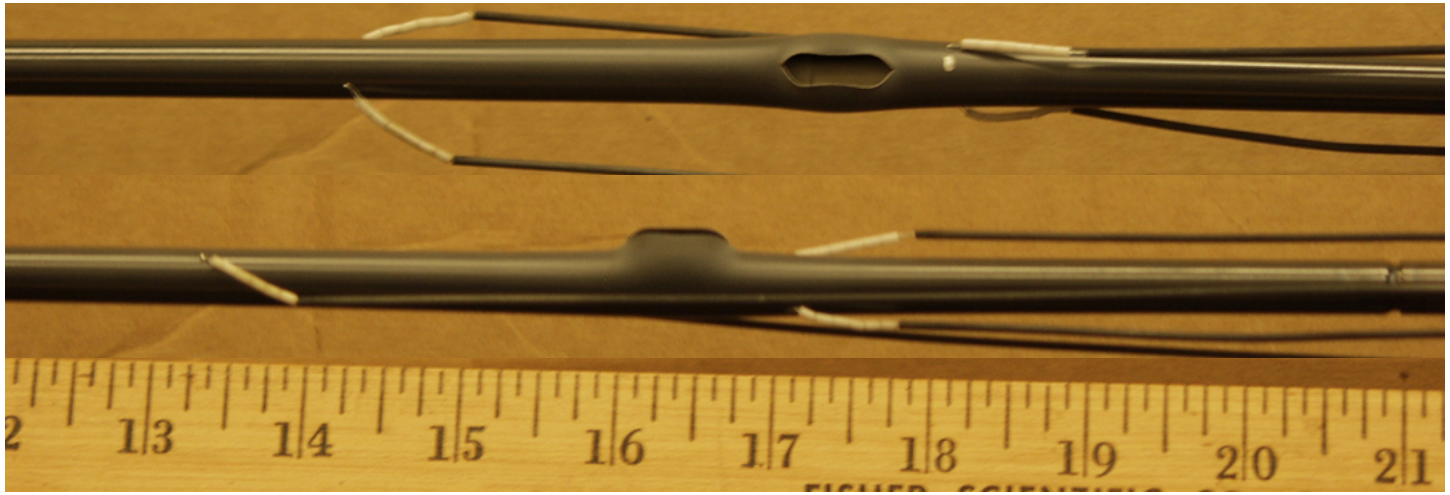

(b)

Figure C.12: Post-oxidation images of OCZL#18 sample, which was pressurized to 1200 psig, heated to 1200°C, oxidized to 12% CP-ECR, and cooled with quench: (a) low magnification and (b) higher magnification.

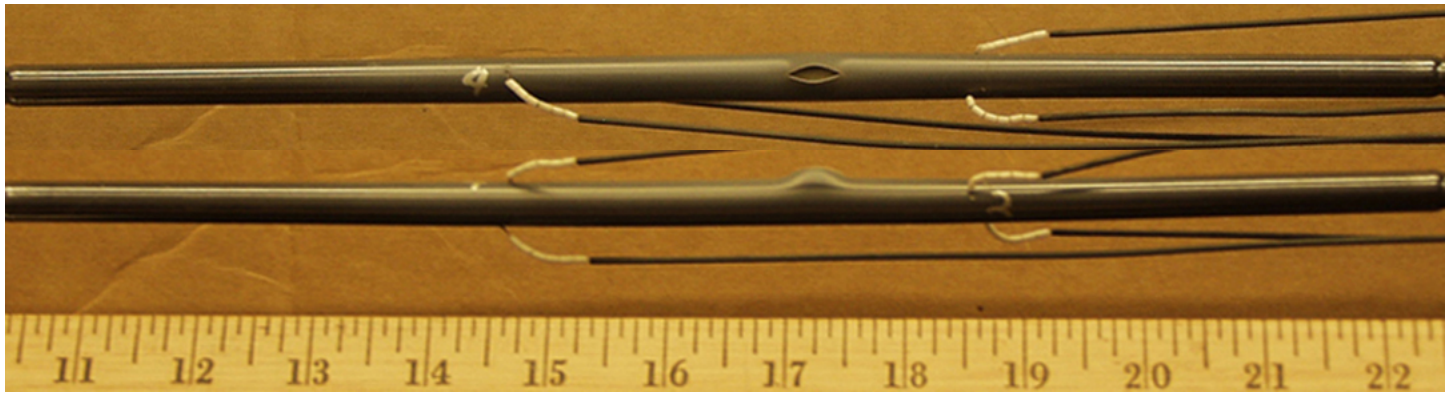

(a)

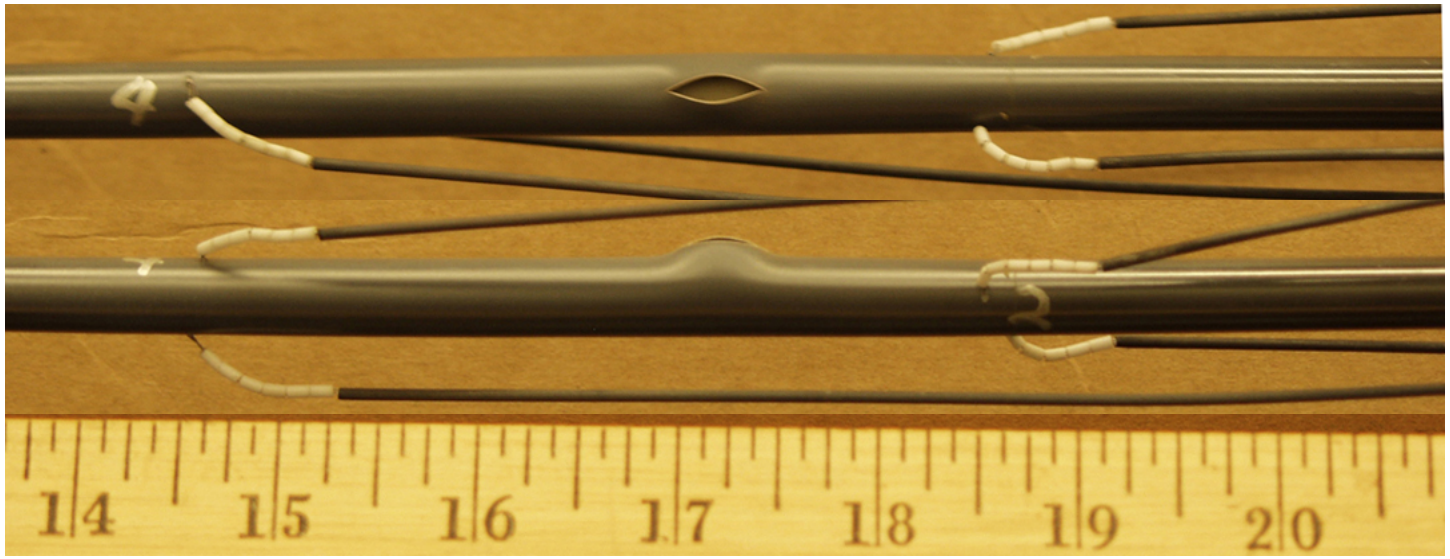

(b)

Figure C.13: Post-oxidation images of OCZL#19 sample, which was pressurized to 600 psig, heated to 1200°C, oxidized to 17% CP-ECR, and cooled with quench: (a) low magnification and (b) higher magnification.

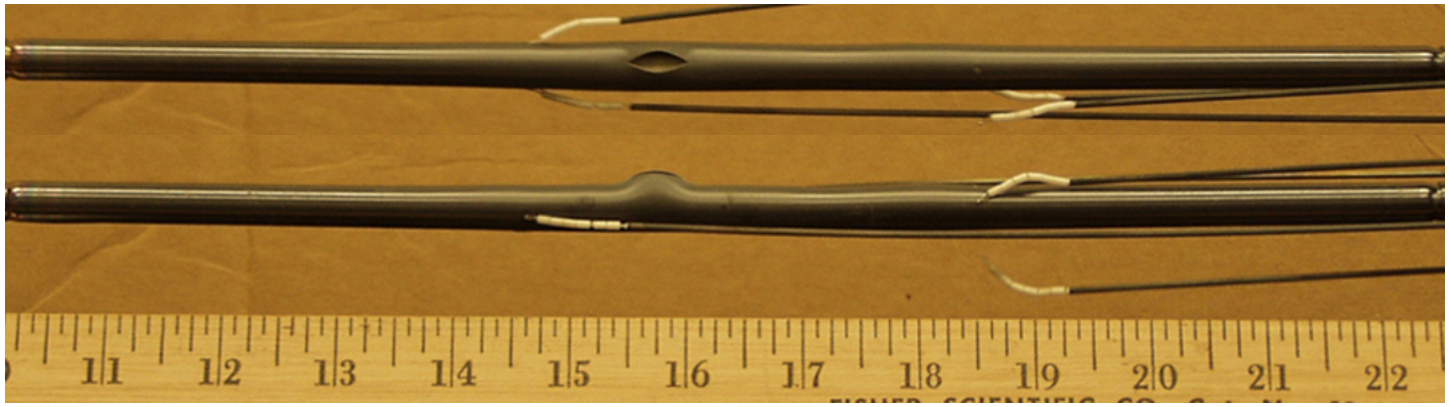

(a)

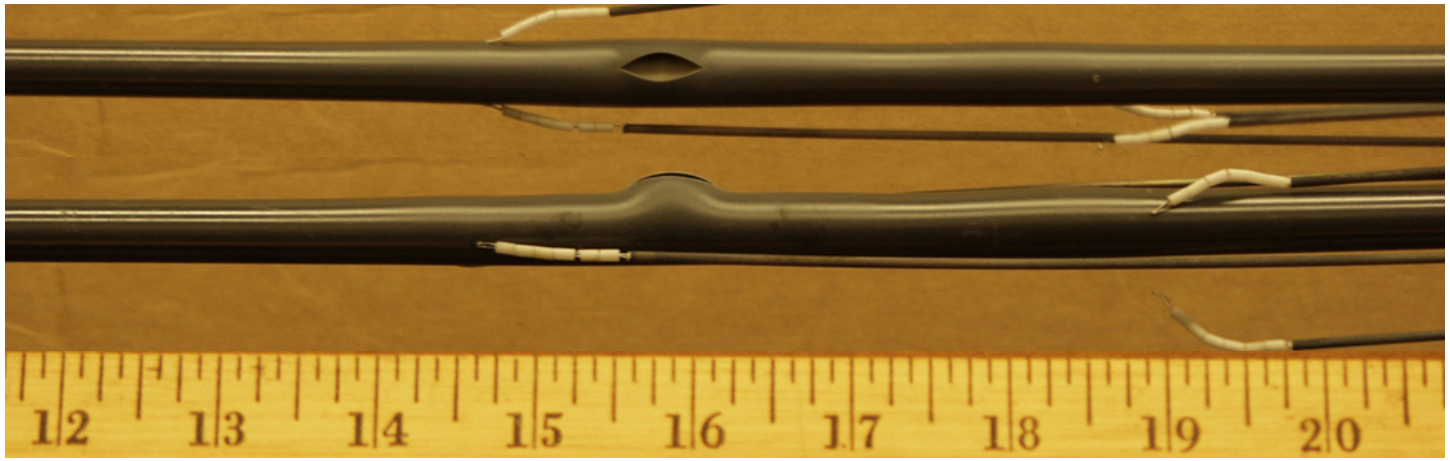

(b)

Figure C.14: Post-oxidation images of OCZL#21 sample, which was pressurized to 600 psig, heated to 1200°C, oxidized to 11% CP-ECR, and cooled with quench: (a) low magnification and (b) higher magnification.

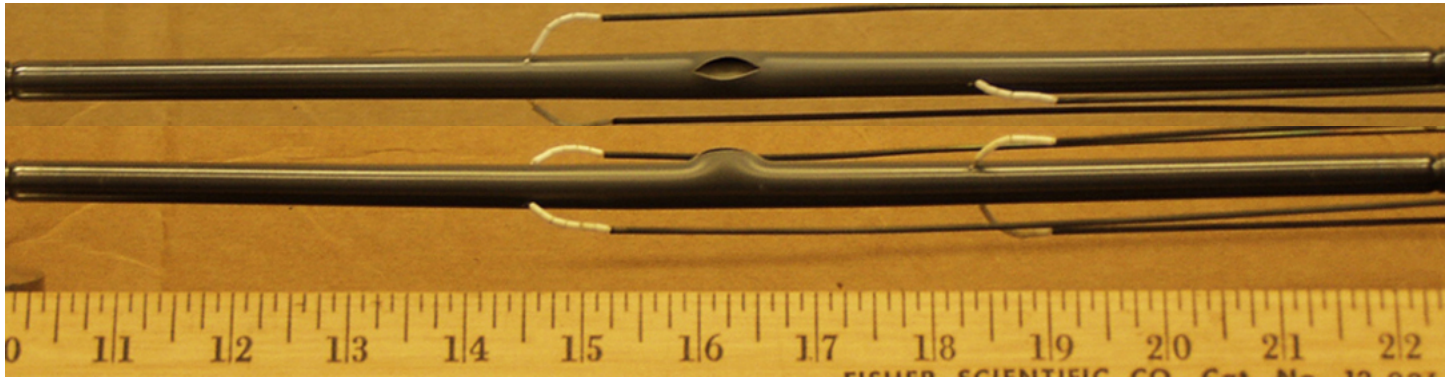

(a)

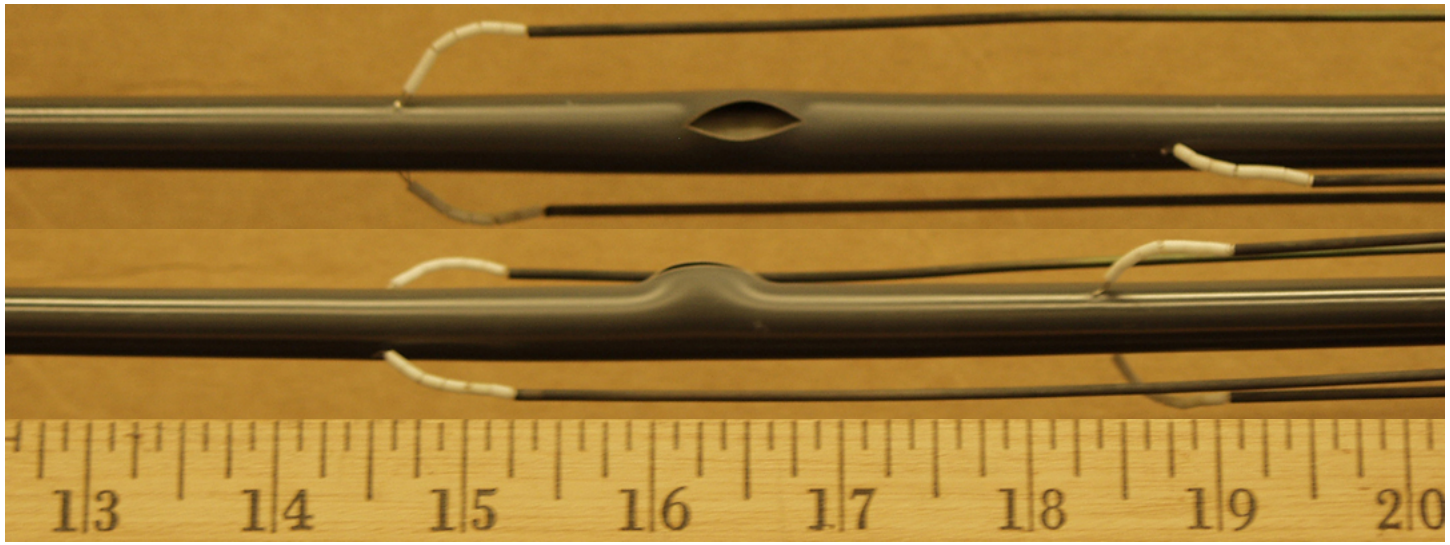

(b)

Figure C.15: Post-oxidation images of OCZL#22 sample, which was pressurized to 600 psig, heated to 1200°C, oxidized to 12% CP-ECR, and cooled with quench: (a) low magnification and (b) higher magnification.

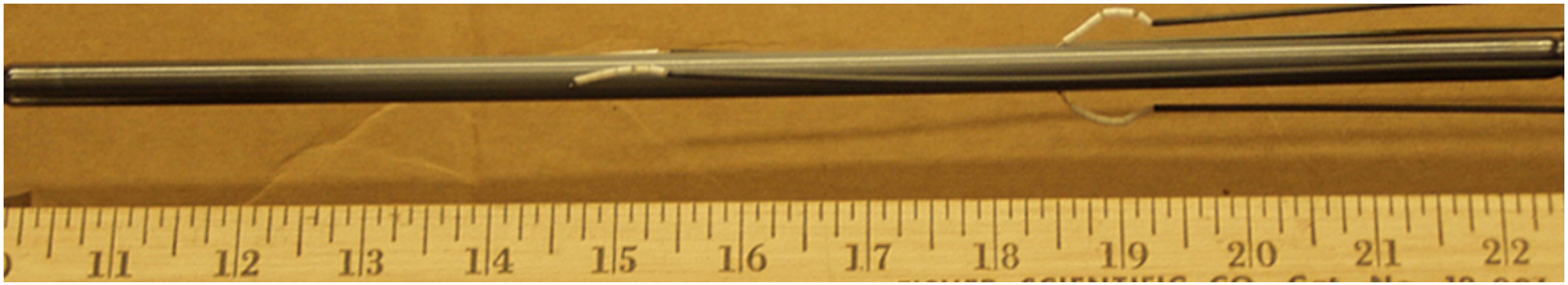

(a)

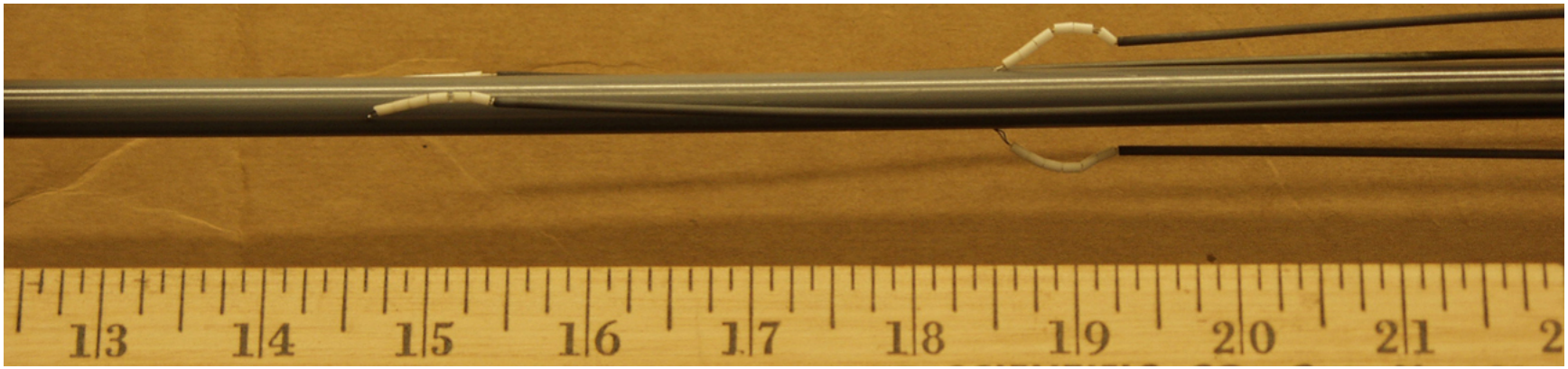

(b)

Figure C.16: Post-oxidation images of OCZL#24 sample, which was non-pressurized, heated to 1200°C, one-sided oxidized to 17% CP-ECR, and cooled with quench: (a) low magnification and (b) higher magnification.

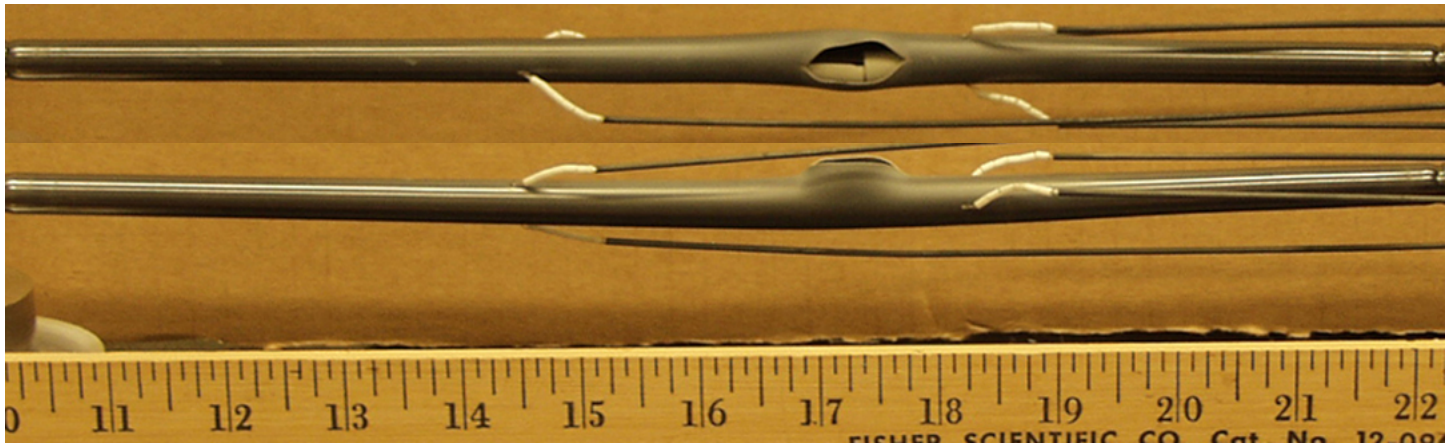

(a)

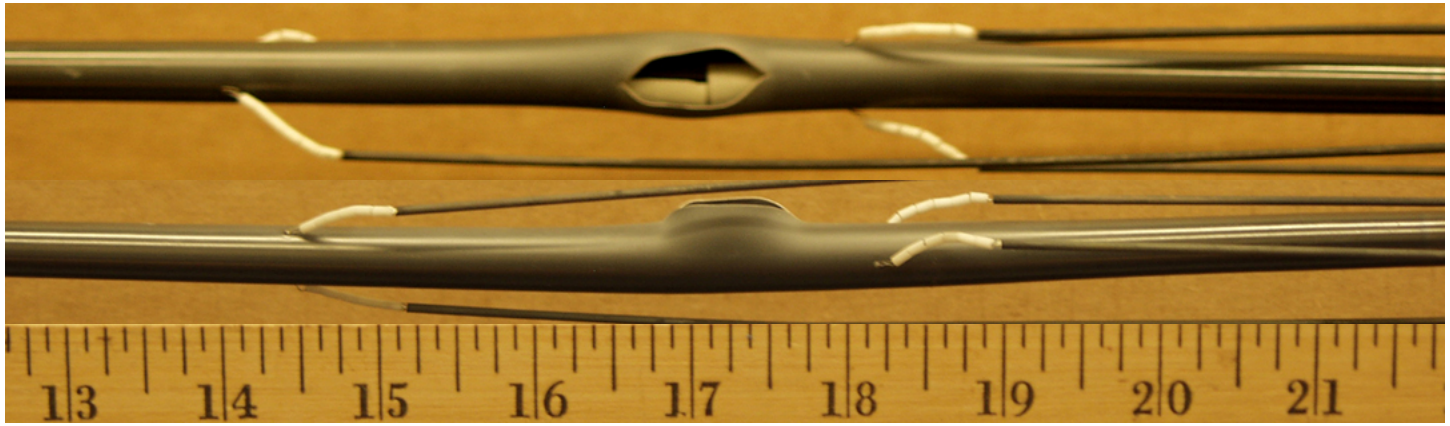

(b)

Figure C.17: Post-oxidation images of OCZL#25 sample, which was pressurized to 1200 psig, heated to 1200°C, oxidized to 16% CP-ECR, and cooled with quench: (a) low magnification and (b) higher magnification.

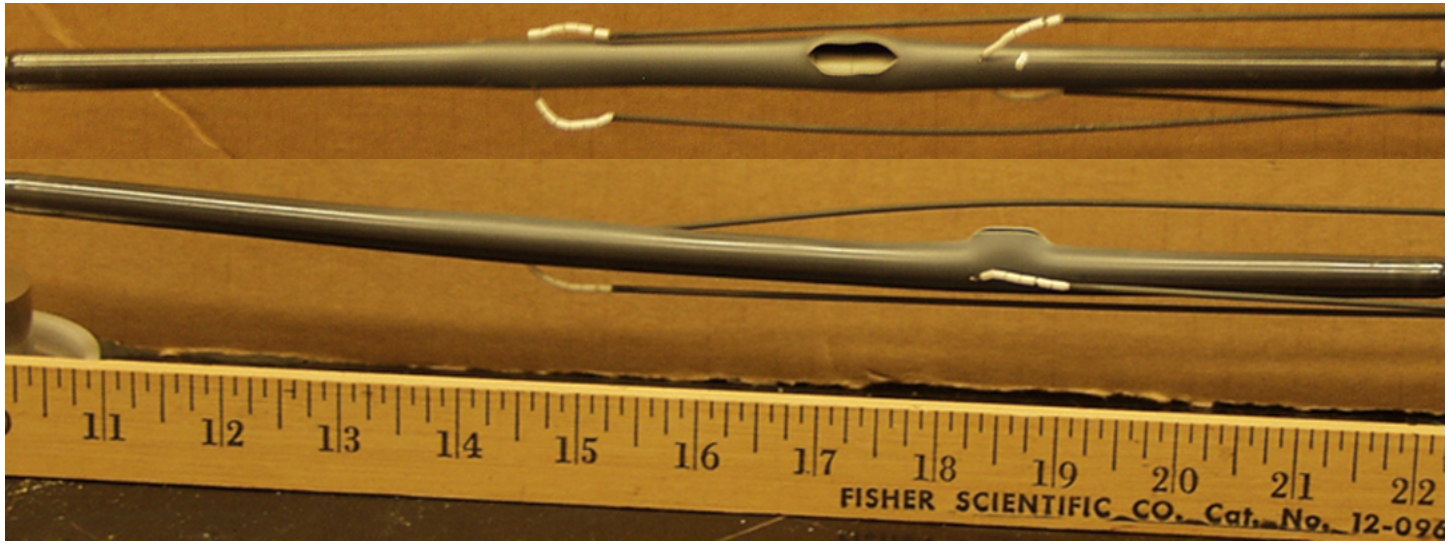

(a)

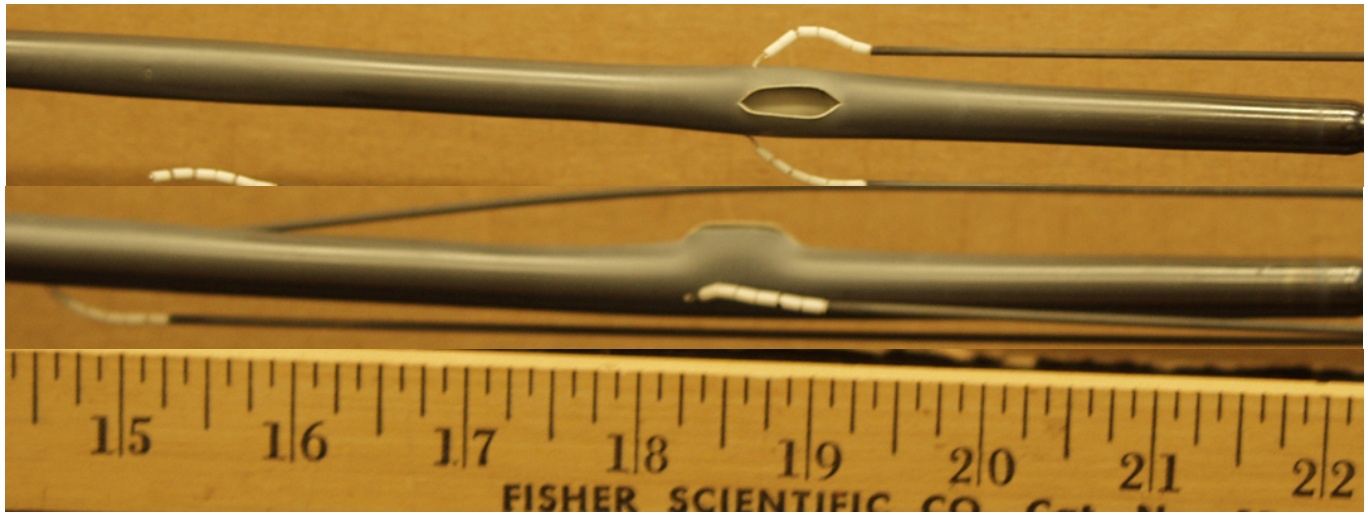

(b)

Figure C.18: Post-oxidation images of OCZL#26 sample, which was pressurized to 1200 psig, heated to 1200°C, oxidized to 16% CP-ECR, and cooled with quench: (a) low magnification and (b) higher magnification.

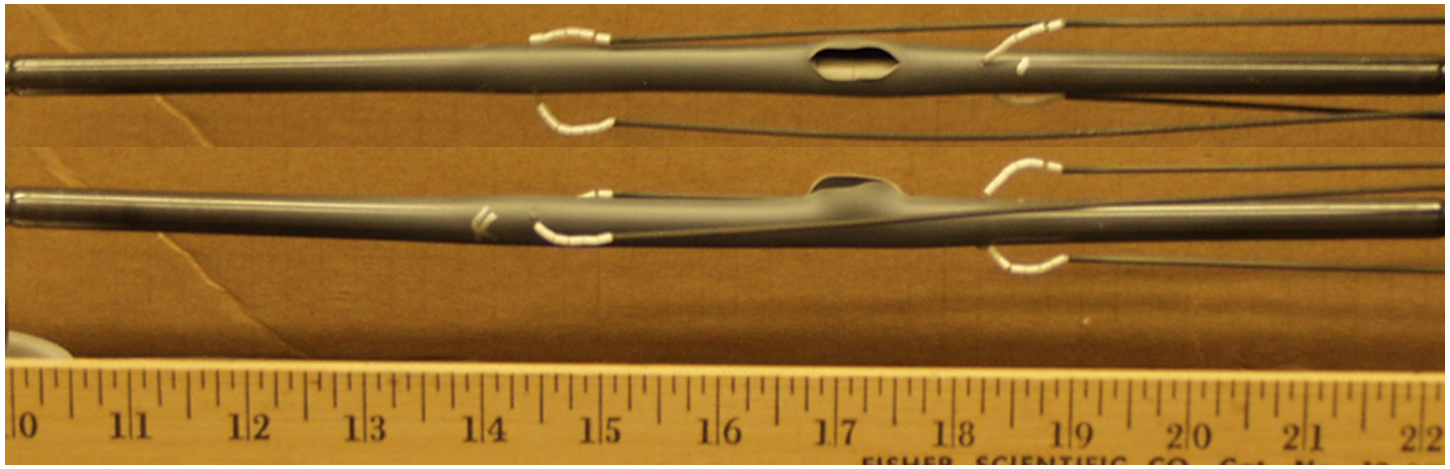

(a)

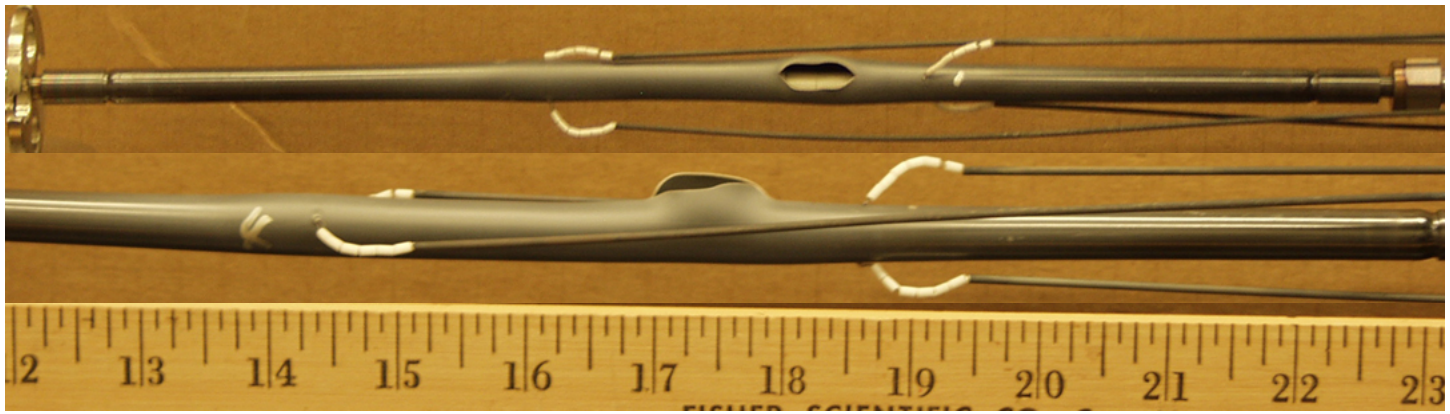

(b)

Figure C.19: Post-oxidation images of OCZL#27 sample, which was pressurized to 1200 psig, heated to 1200°C, oxidized to 18% CP-ECR, and cooled with quench: (a) low magnification and (b) higher magnification.

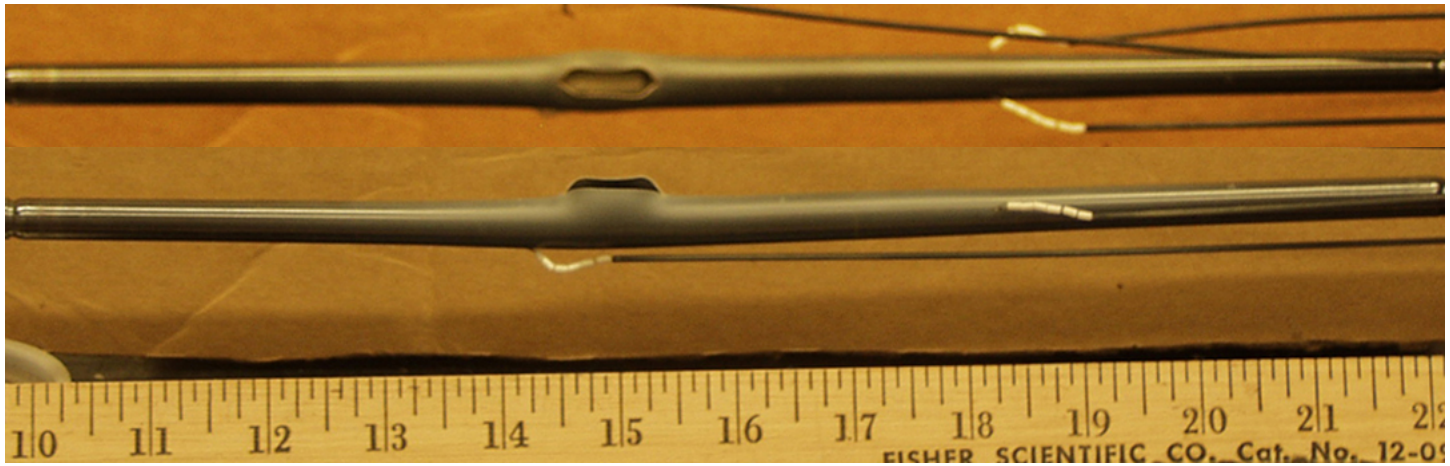

(a)

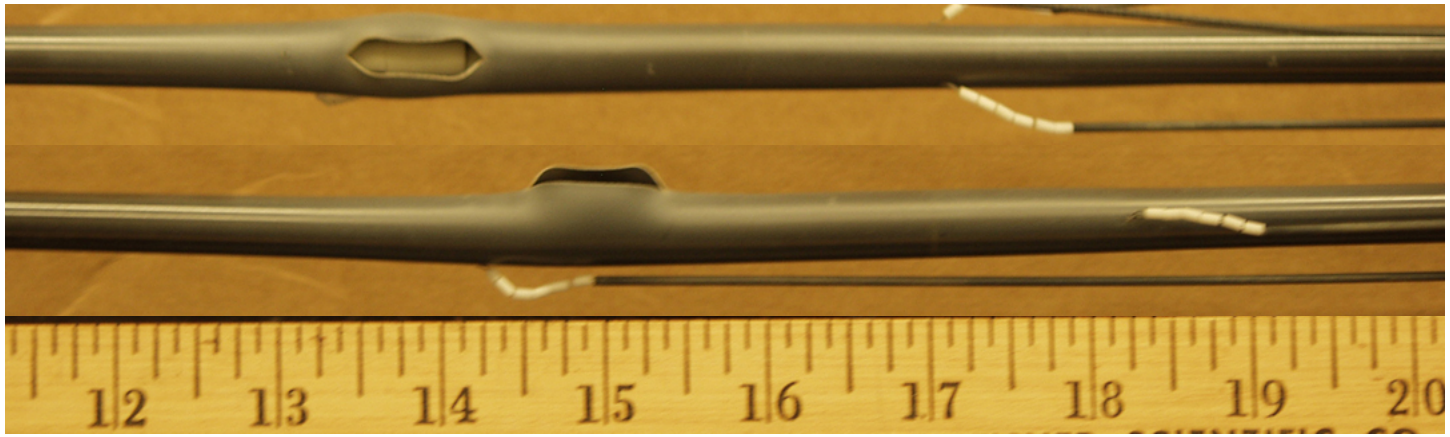

(b)

Figure C.20: Post-oxidation images of OCZL#29 sample, which was pressurized to 1200 psig, heated to 1200°C, oxidized to 17% CP-ECR, and cooled with quench: (a) low magnification and (b) higher magnification.

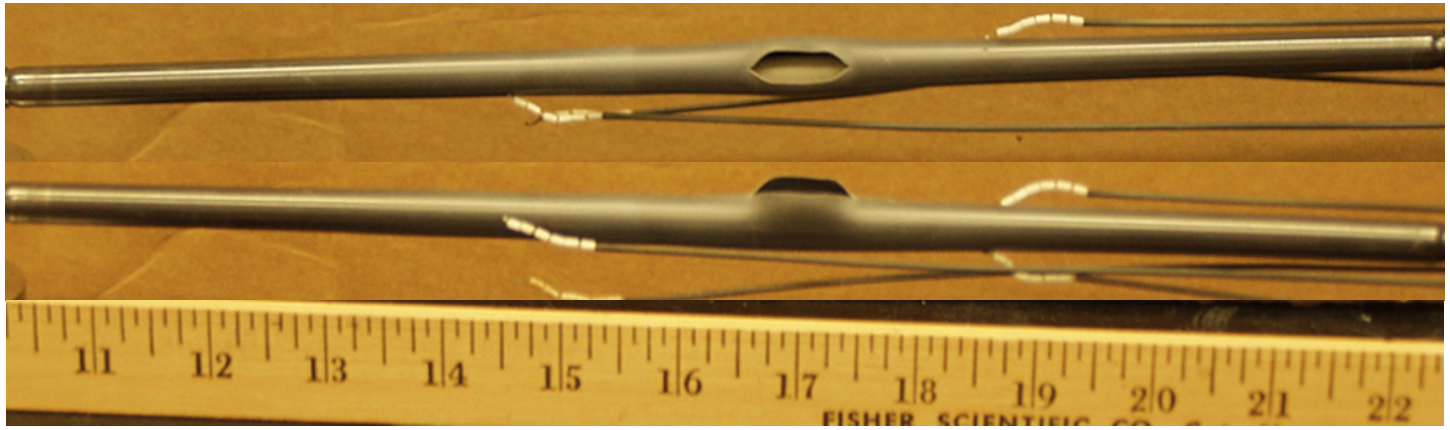

(a)

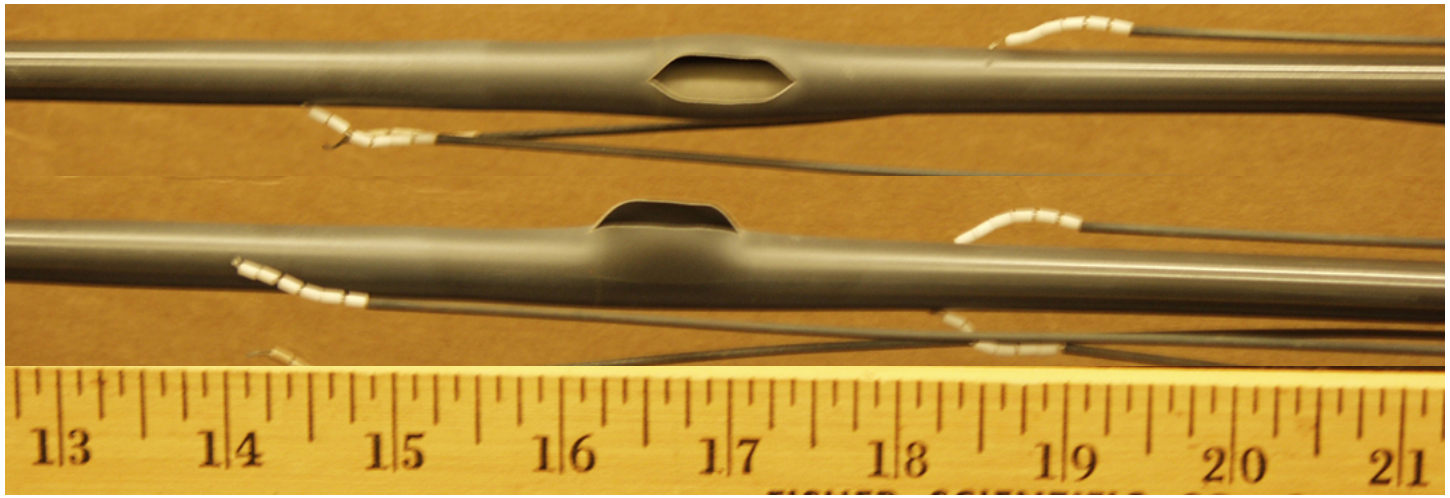

(b)

Figure C.21: Post-oxidation images of OCZL#32 sample, which was pressurized to 1200 psig, heated to 1200°C, oxidized to 16% CP-ECR, and cooled with quench: (a) low magnification and (b) higher magnification.

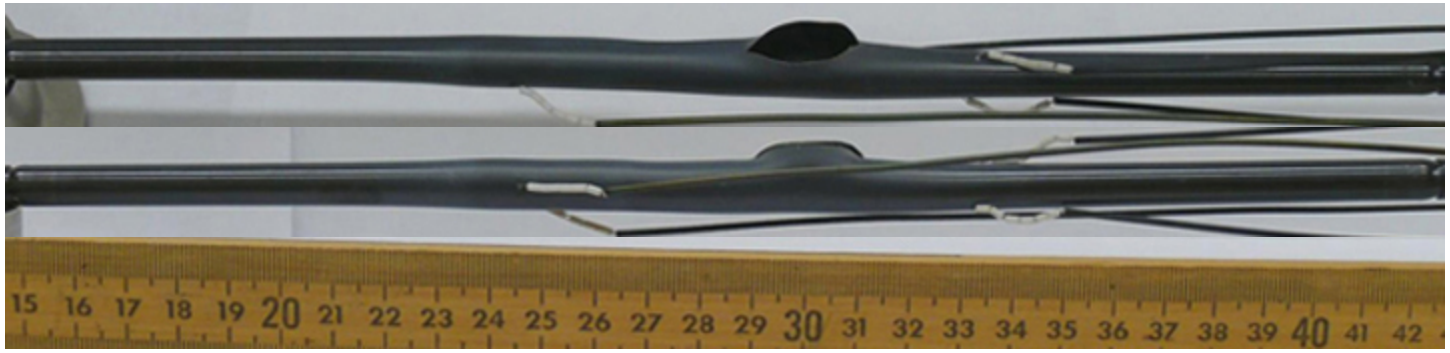

(a)

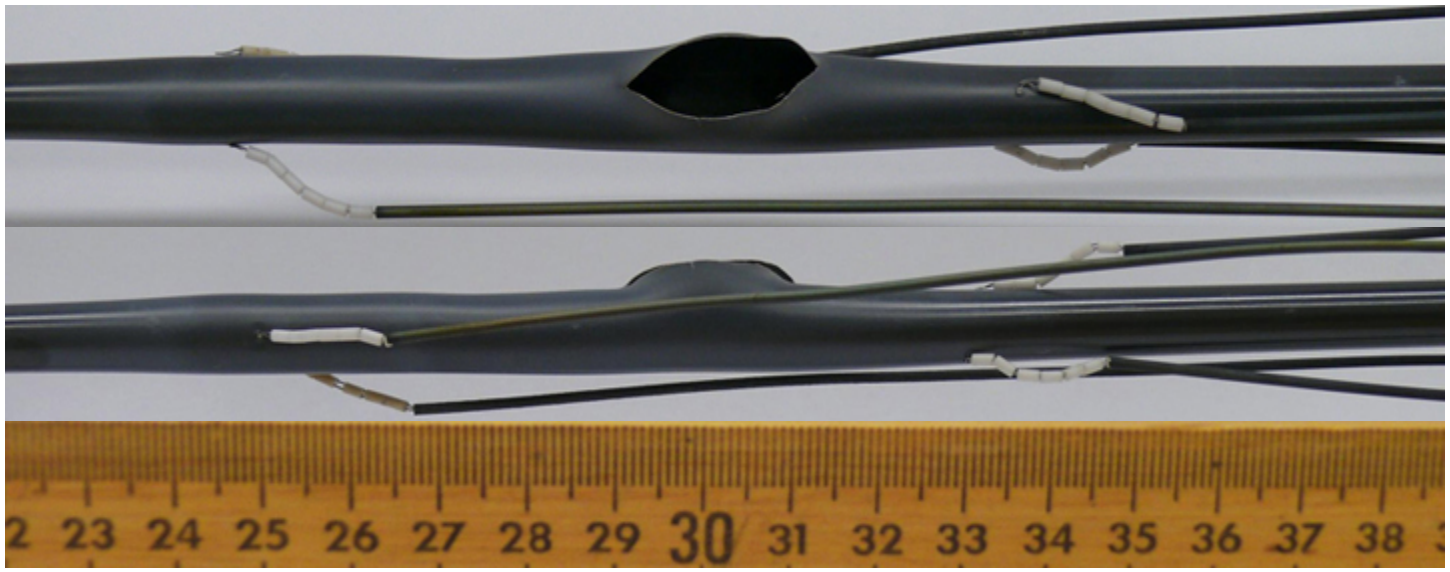

(b)

Figure C.22: Post-oxidation images of OCZL#36 sample, which was pressurized to 1200 psig, heated to 1200°C, oxidized to 18% CP-ECR, and cooled with quench: (a) low magnification and (b) higher magnification.

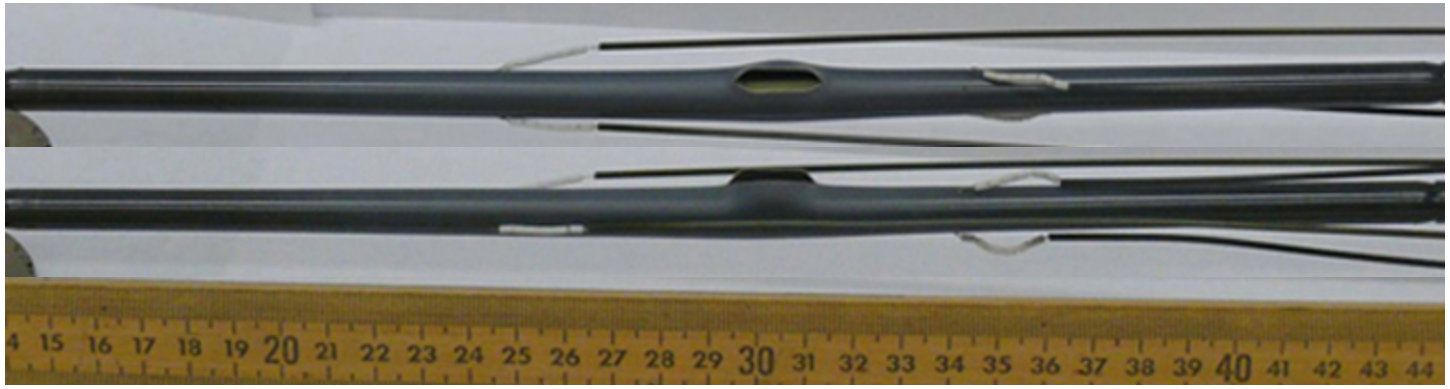

(a)

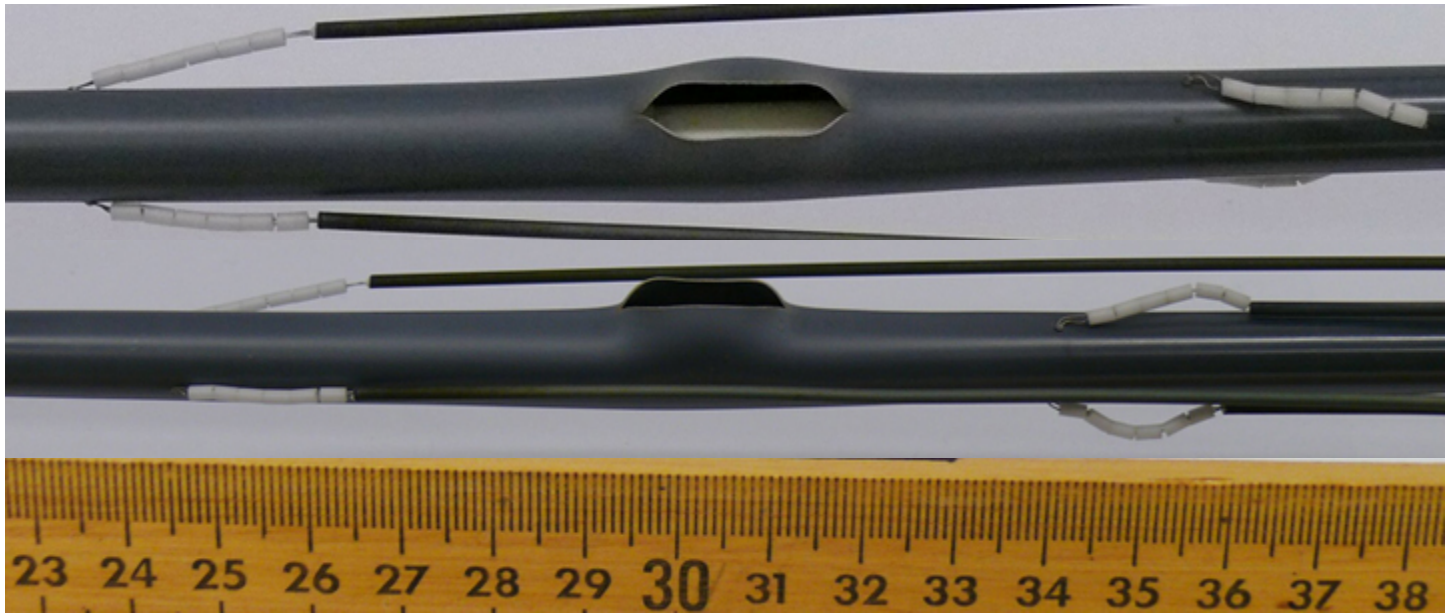

(b)

Figure C.23: Post-oxidation images of OCZL#37 sample, which was pressurized to 1200 psig, heated to 1200°C, oxidized to 23% CP-ECR, and cooled with quench: (a) low magnification and (b) higher magnification.

(a)

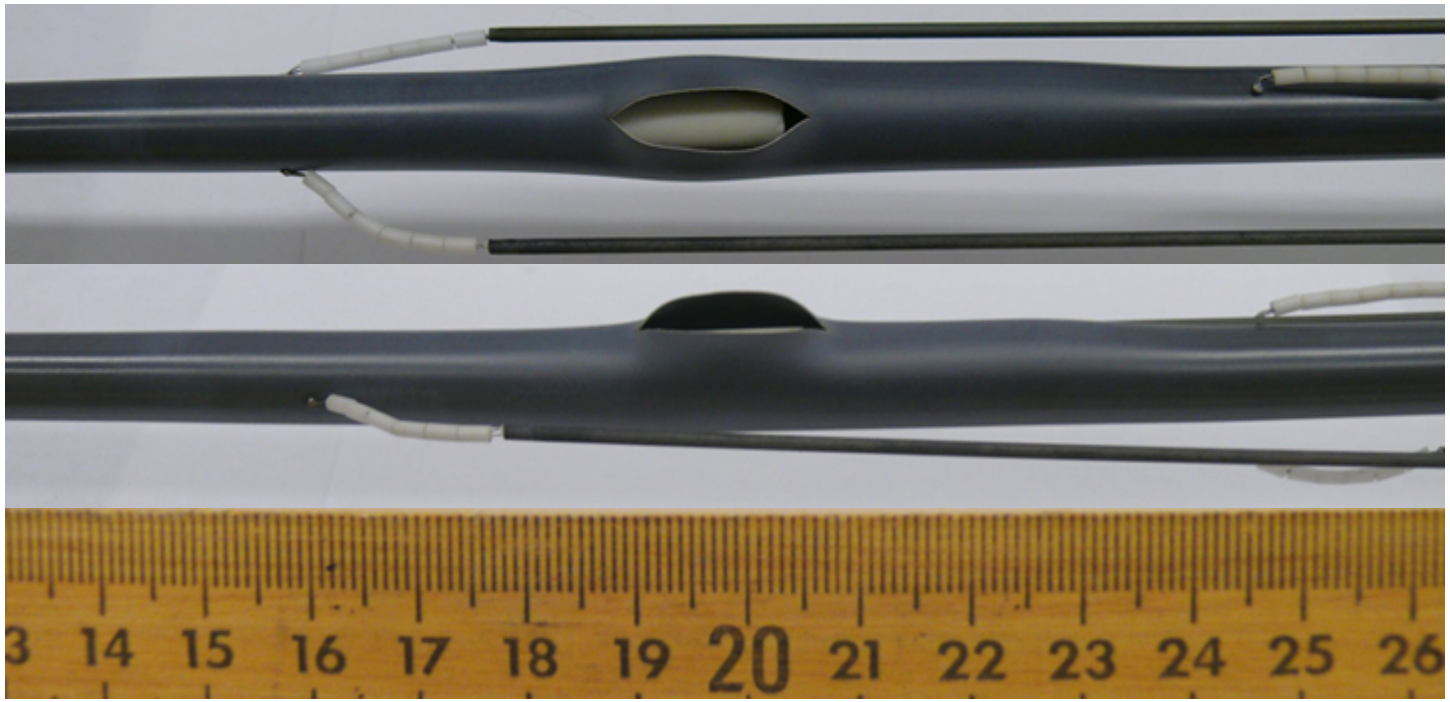

(b)

Figure C.24: Post-oxidation images of OCZL#43 sample, which was pressurized to 1200 psig, heated to 1200°C, oxidized to 18% CP-ECR, and cooled with quench: (a) low magnification and (b) higher magnification.

(a)

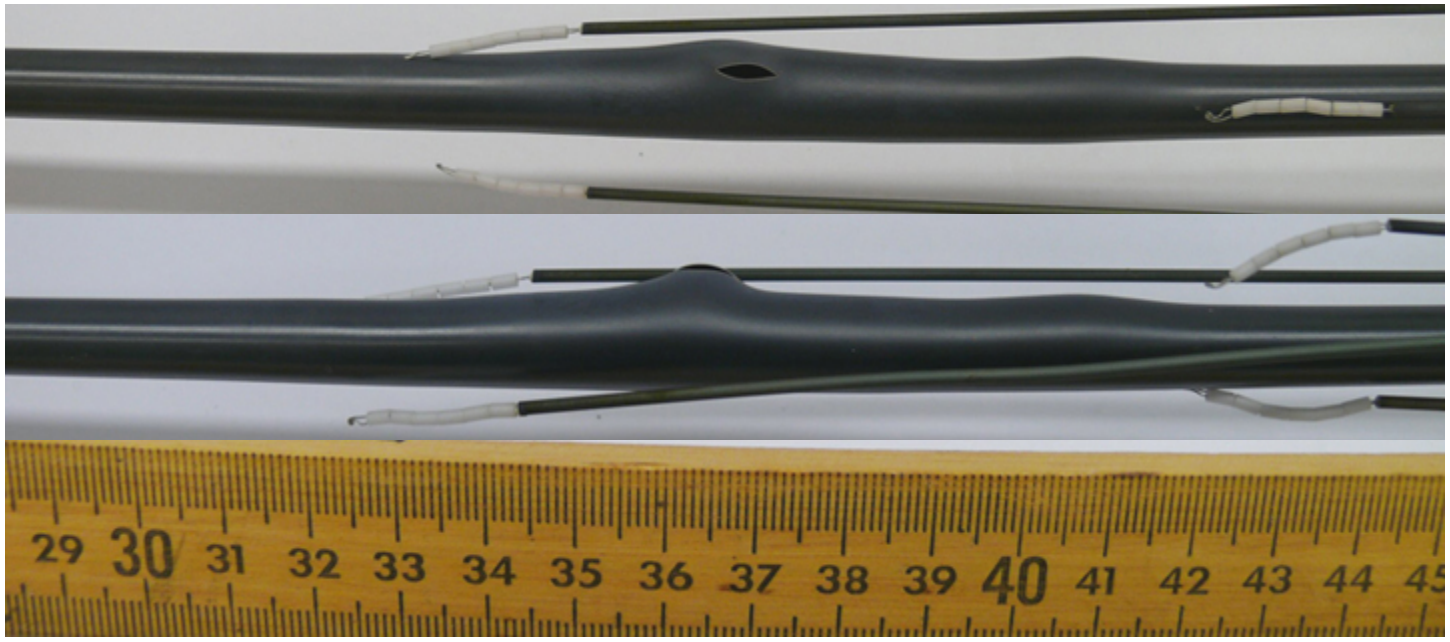

(b)

Figure C.25: Post-oxidation images of OCZL#39PH sample (660 wppm H), which was pressurized to 600 psig, heated to 1200°C, oxidized to 13% CP-ECR, and cooled with quench: (a) low magnification and (b) higher magnification.

(a)

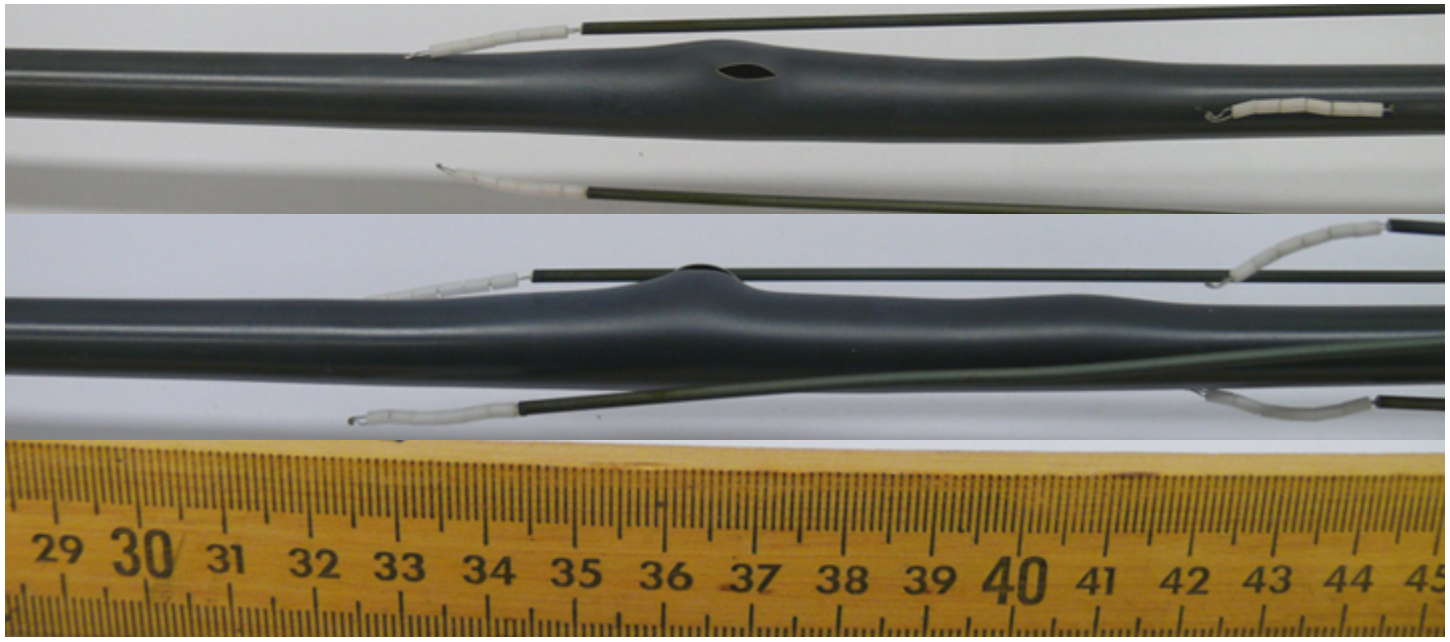

(b)

Figure C.26: Post-oxidation images of OCZL#40 sample (390 wppm H), which was pressurized to 1200 psig, heated to 1200°C, oxidized to 12% CP-ECR, and cooled with quench: (a) low magnification and (b) higher magnification.

(a)

(b)

Figure C.27: Post-oxidation images of OCZL#41 sample (220 wppm H), which was pressurized to 1200 psig, heated to 1200°C, oxidized to 16% CP-ECR, and cooled with quench: (a) low magnification and (b) higher magnification.

(a)

(b)

Figure C.28: Post-oxidation images of OCZL#42 sample (520 wppm H), which was pressurized to 1200 psig, heated to 1200°C, oxidized to 14% CP-ECR, and cooled with quench: (a) low magnification and (b) higher magnification.

(a)

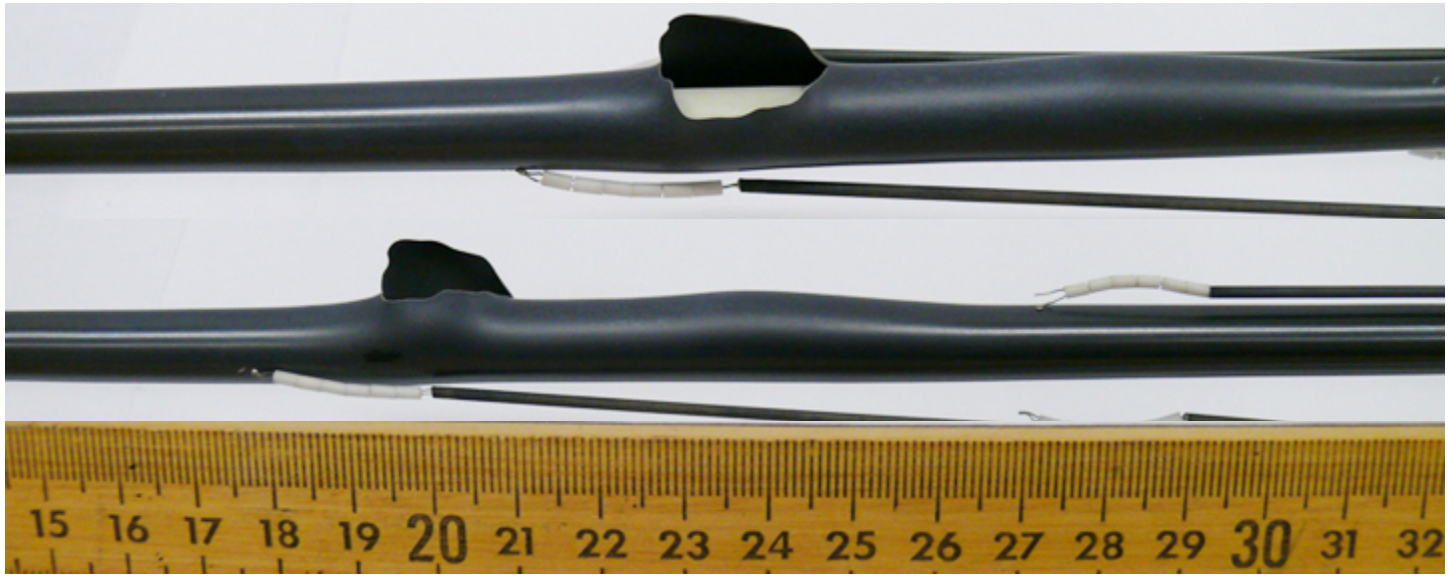

(b)

Figure C.29: Post-oxidation images of OCZL#44 sample (700 wppm H), which was pressurized to 1200 psig, heated to 1200°C, oxidized to 14% CP-ECR, and cooled with quench: (a) low magnification and (b) higher magnification.

(a)

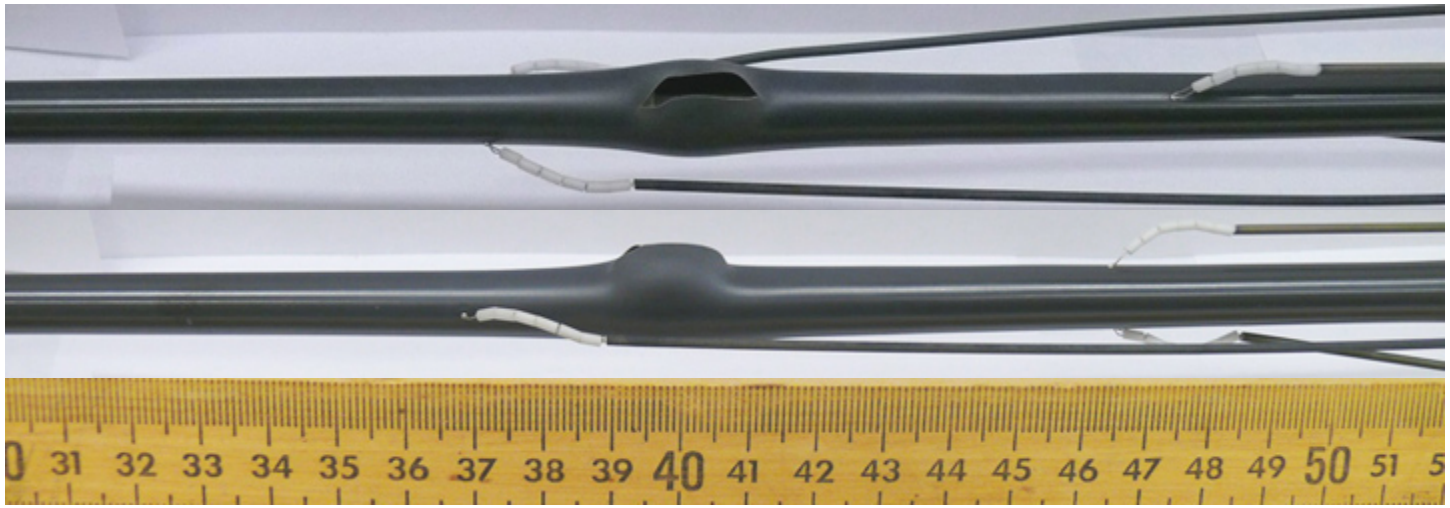

(b)

Figure C.30: Post-oxidation images of OCZL#45 sample (220 wppm H), which was pressurized to 1200 psig, heated to 1200°C, oxidized to 13% CP-ECR, and cooled with quench: (a) low magnification and (b) higher magnification.

APPENDIX D: 4-PBT LOAD-DISPLACEMENT CURVES

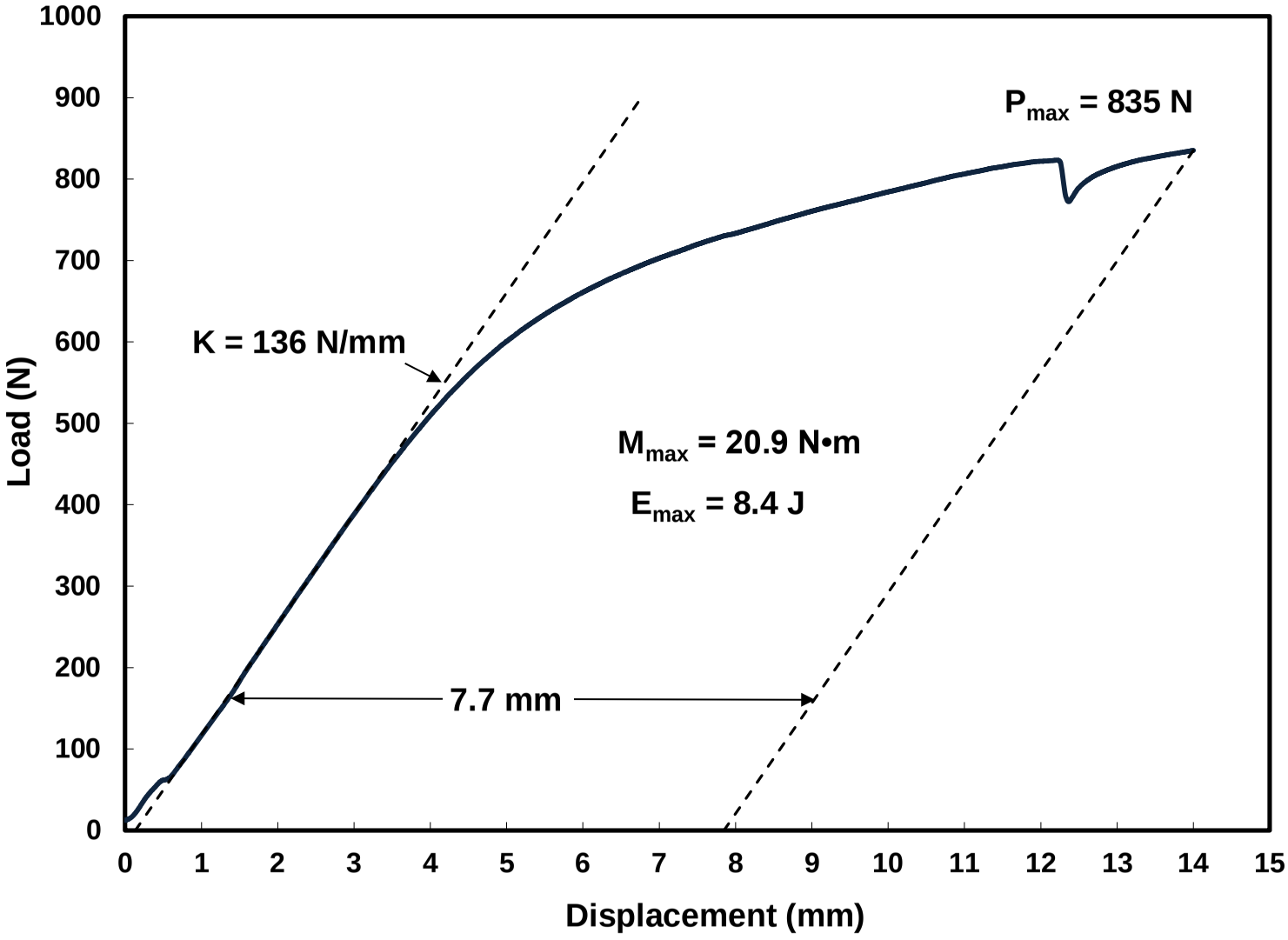

Figure D.1: **4-PBT load-displacement curve for OCZL#8 test sample, which was pressurized to 600 psig, heated to rupture, and cooled without quench.**

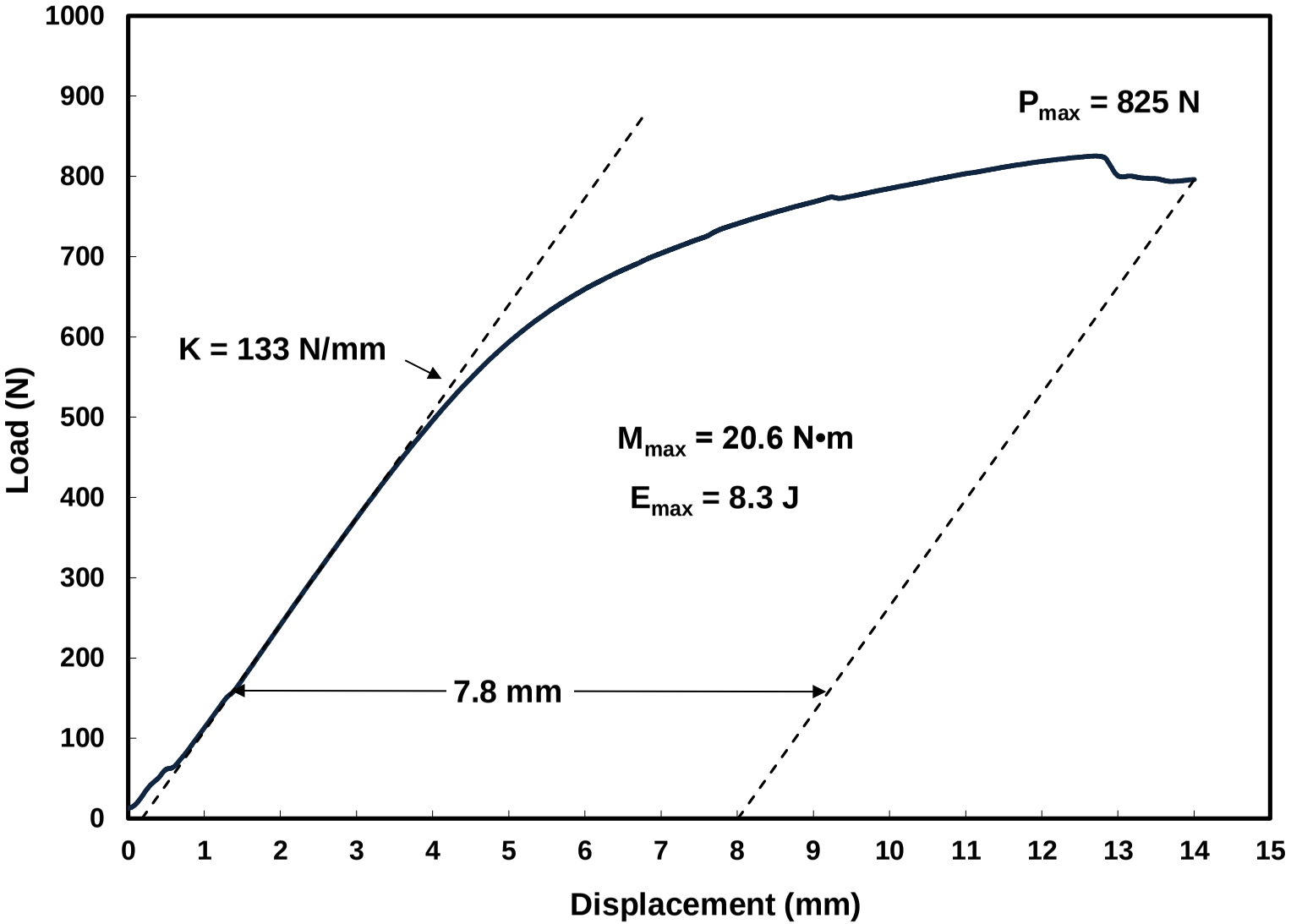

Figure D.2: **4-PBT load-displacement curve for OCZL#9 test sample, which was pressurized to 400 psig, heated to rupture, and cooled without quench.**

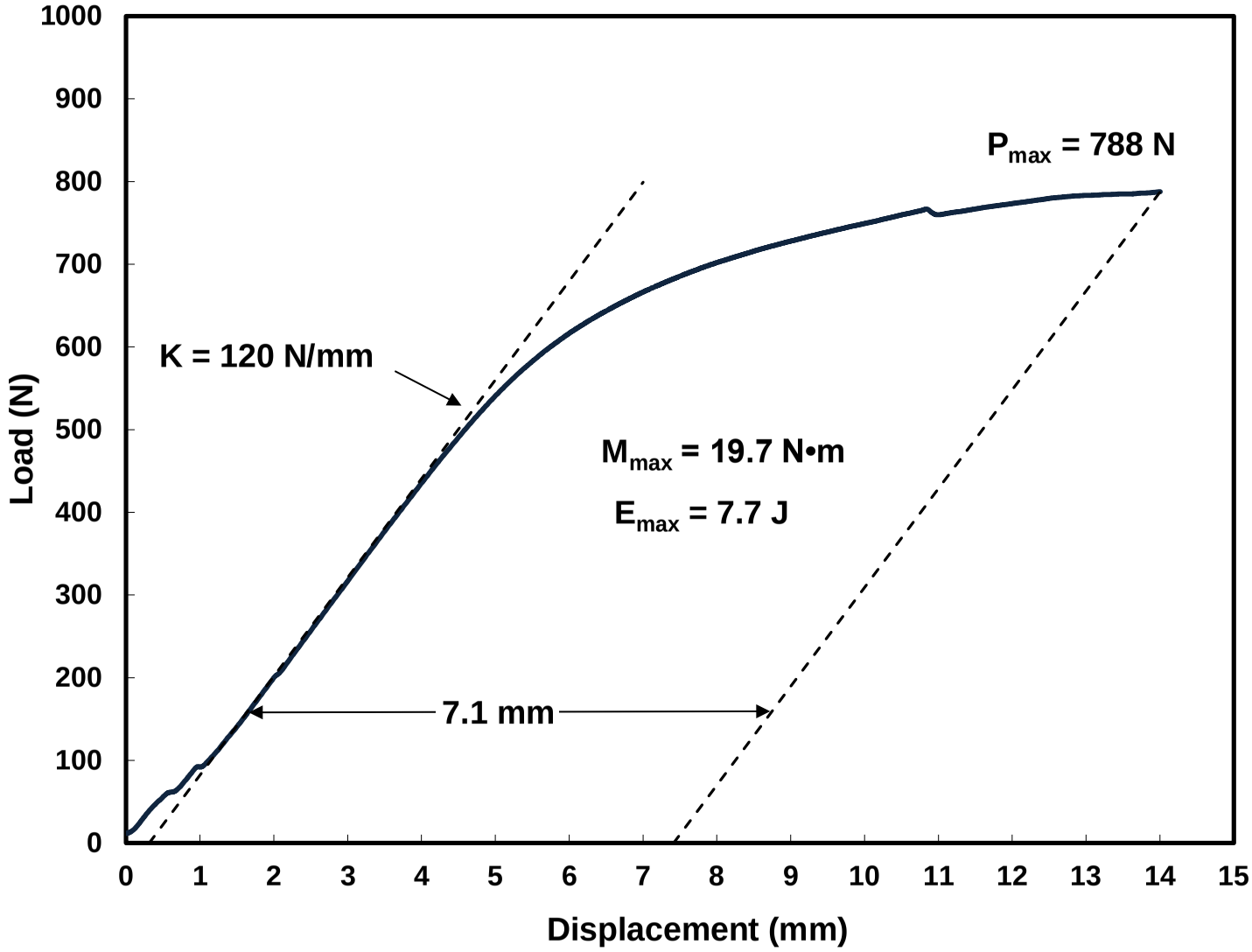

Figure D.3: **4-PBT load-displacement curve for OCZL#10 test sample, which was pressurized to 400 psig, heated to rupture, and cooled without quench.**

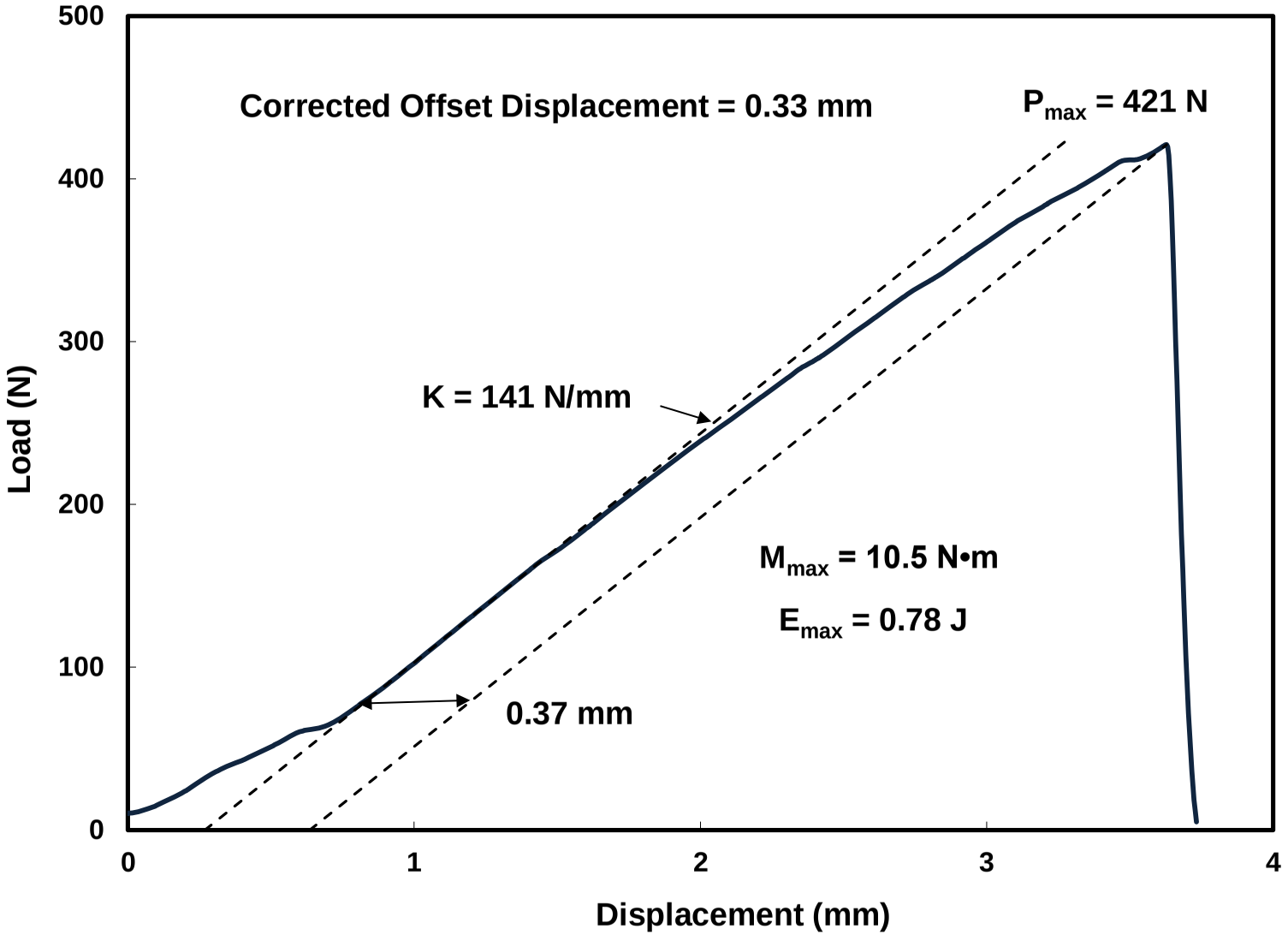

Figure D.4: **4-PBT load-displacement curve for OCZL#12 test sample, which was pressurized to 1000 psig, heated to ≈1200°C, oxidized to 15% CP-ECR, and cooled without quench.**

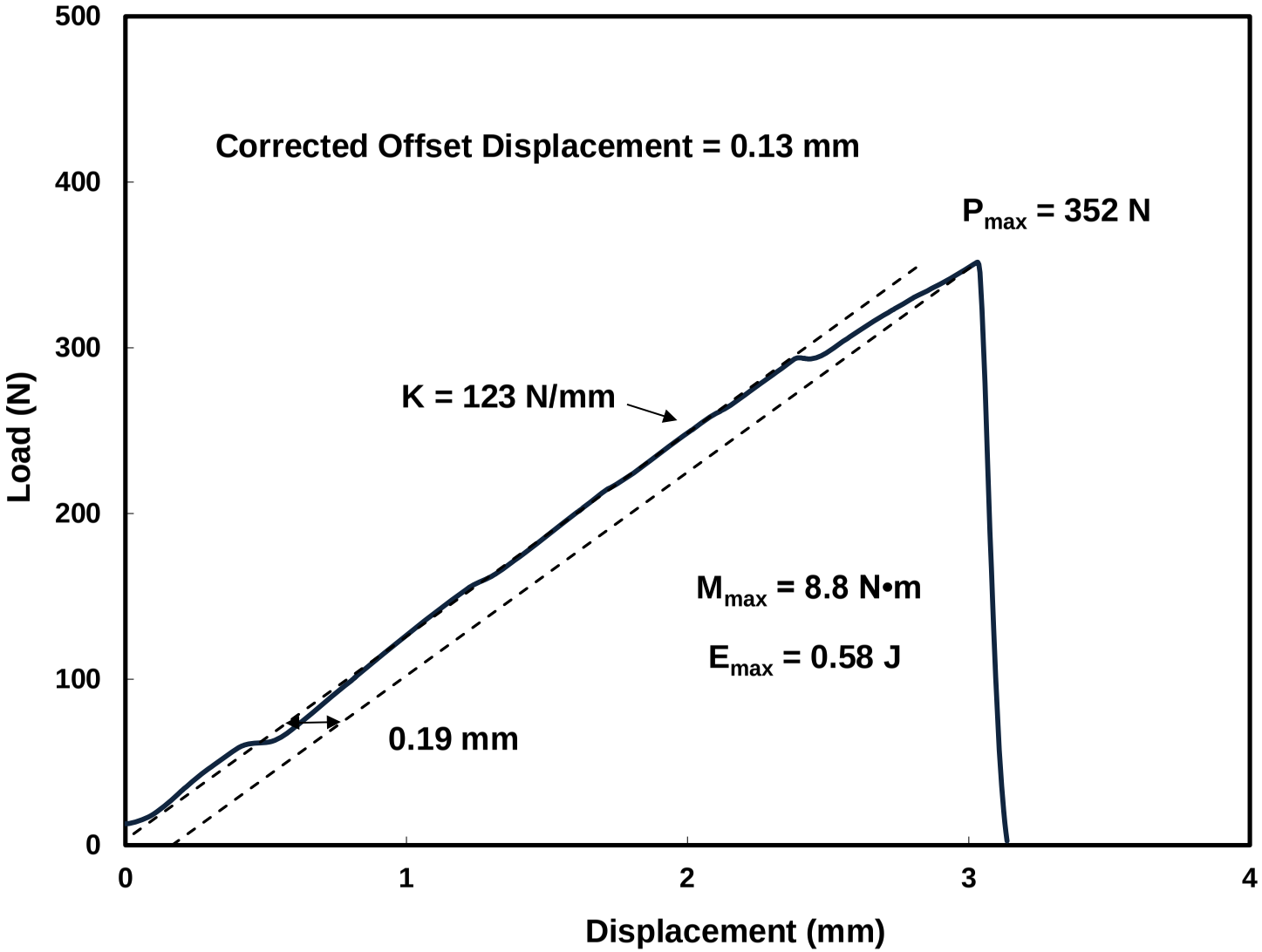

Figure D.5: **4-PBT load-displacement curve for OCZL#13 test sample, which was pressurized to 1200 psig, heated to ≈1200°C, oxidized to 14% CP-ECR, and cooled without quench.**

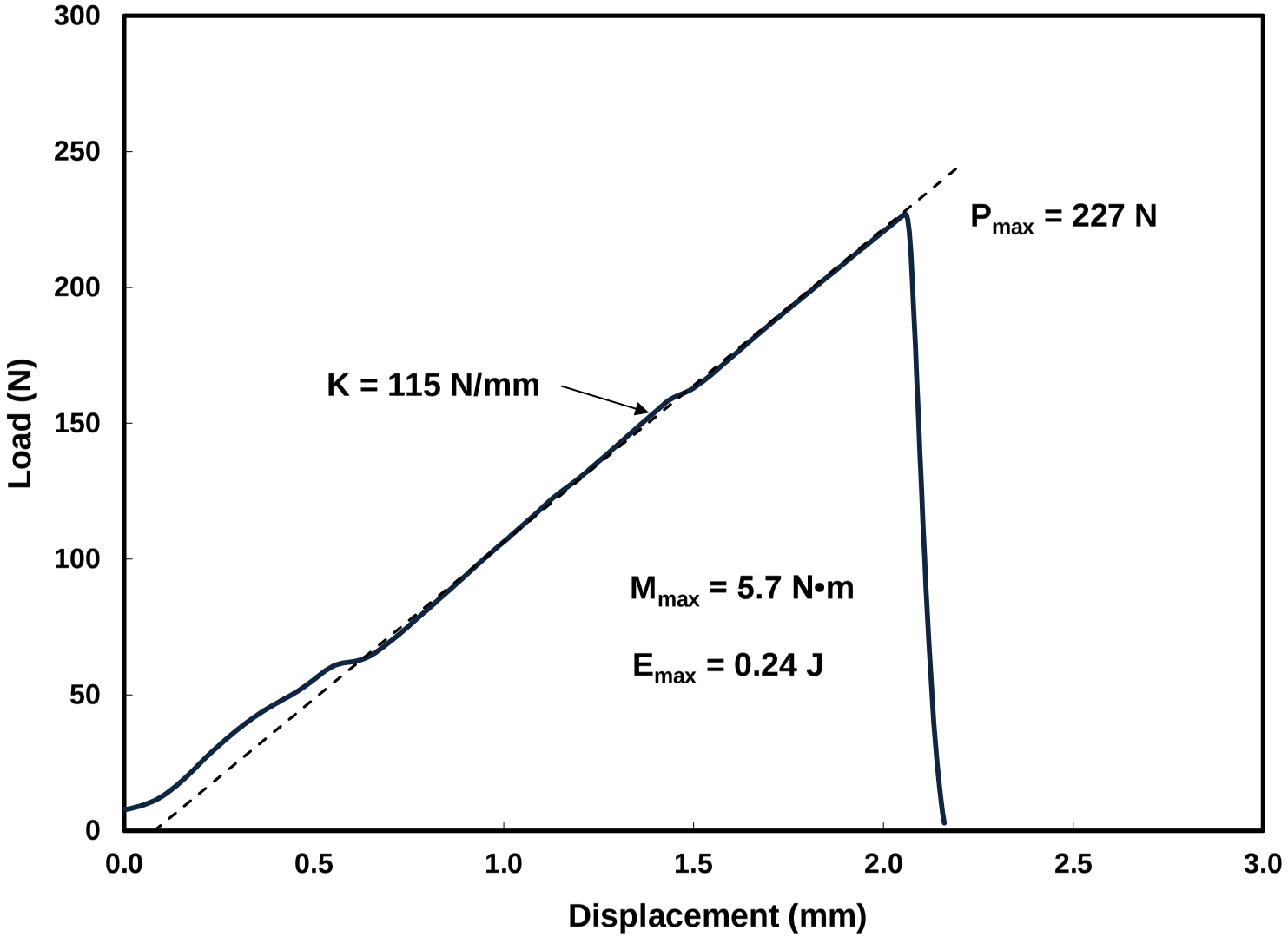

Figure D.6: **4-PBT load-displacement curve for OCZL#14 test sample, which was pressurized to 1200 psig, heated to 1200°C, oxidized to 18% CP-ECR, and cooled with quench.**

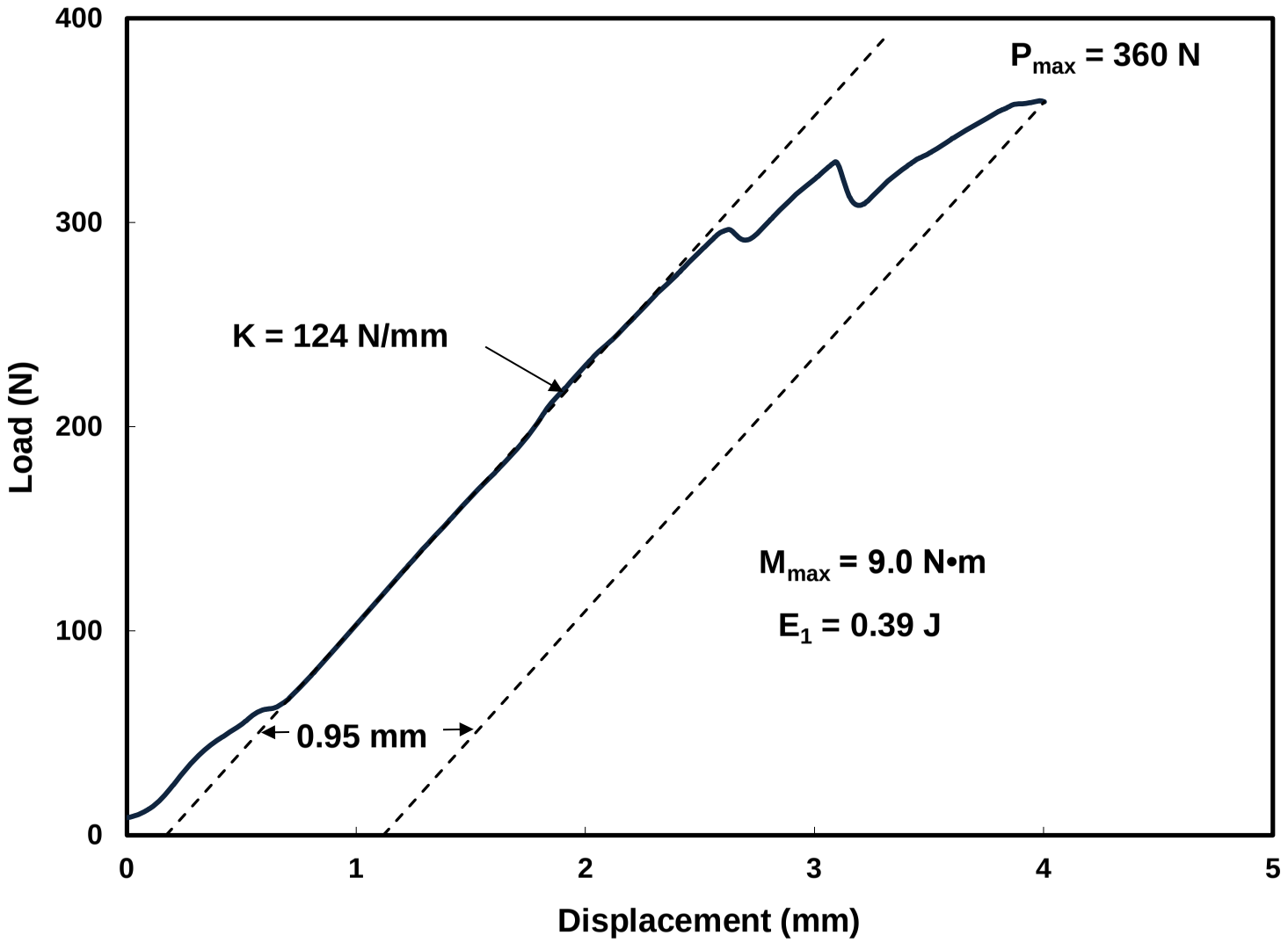

Figure D.7a: **4-PBT load-displacement curve for OCZL#15 test sample, which was pressurized to 1200 psig, heated to 1200°C, oxidized to 18% CP-ECR, and cooled with quench. Sample was subjected to reverse bending with rupture region under maximum compression. Test was interrupted following non-linear displacement to examine sample.**

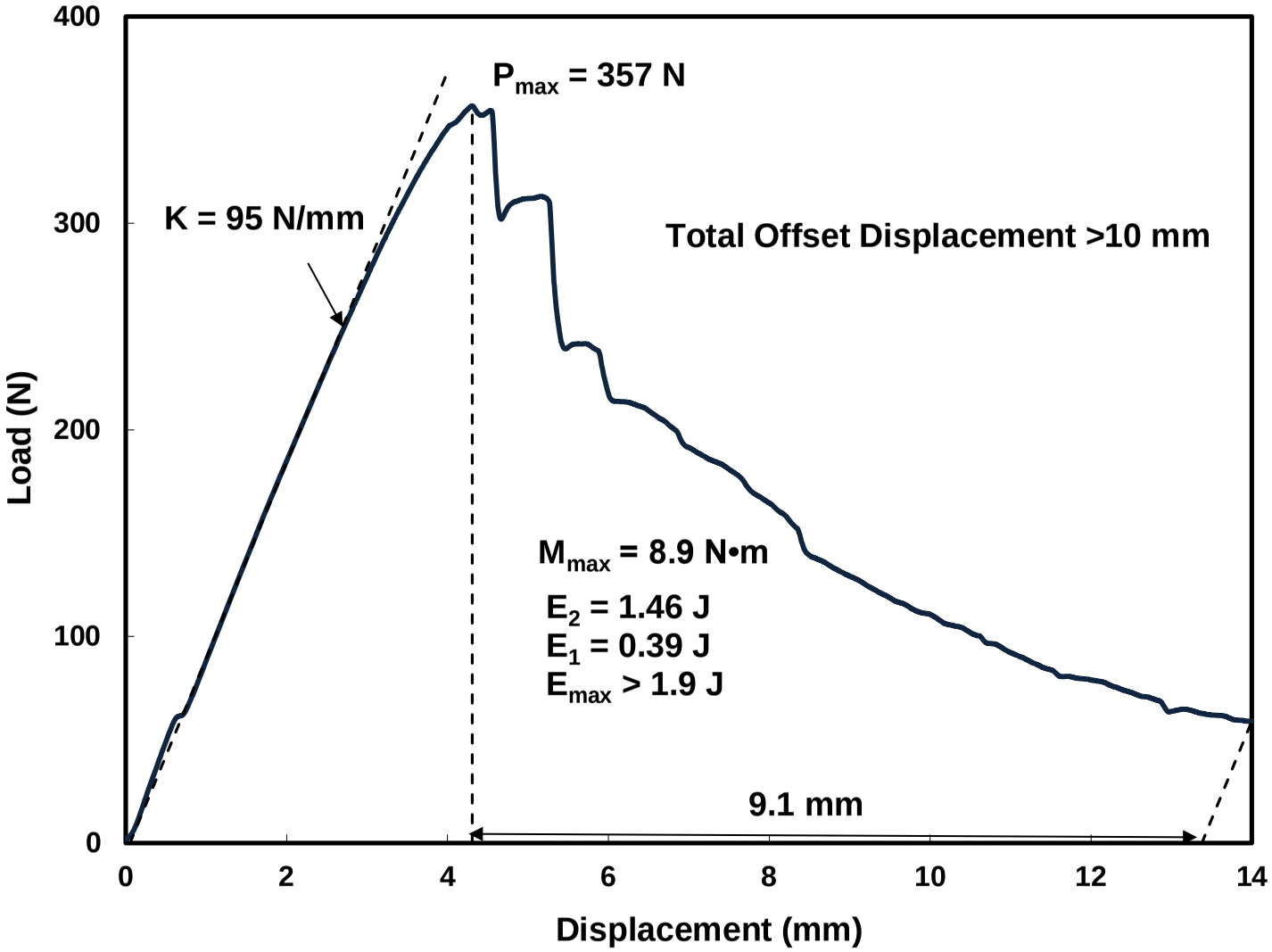

Figure D.7b: **Continuation of 4-PBT load-displacement curve for OCZL#15 test sample, which was pressurized to 1200 psig, heated to 1200°C, oxidized to 18% CP-ECR, and cooled with quench. Sample was subjected to reverse bending with rupture region under maximum compression. Results are for reloading sample.**

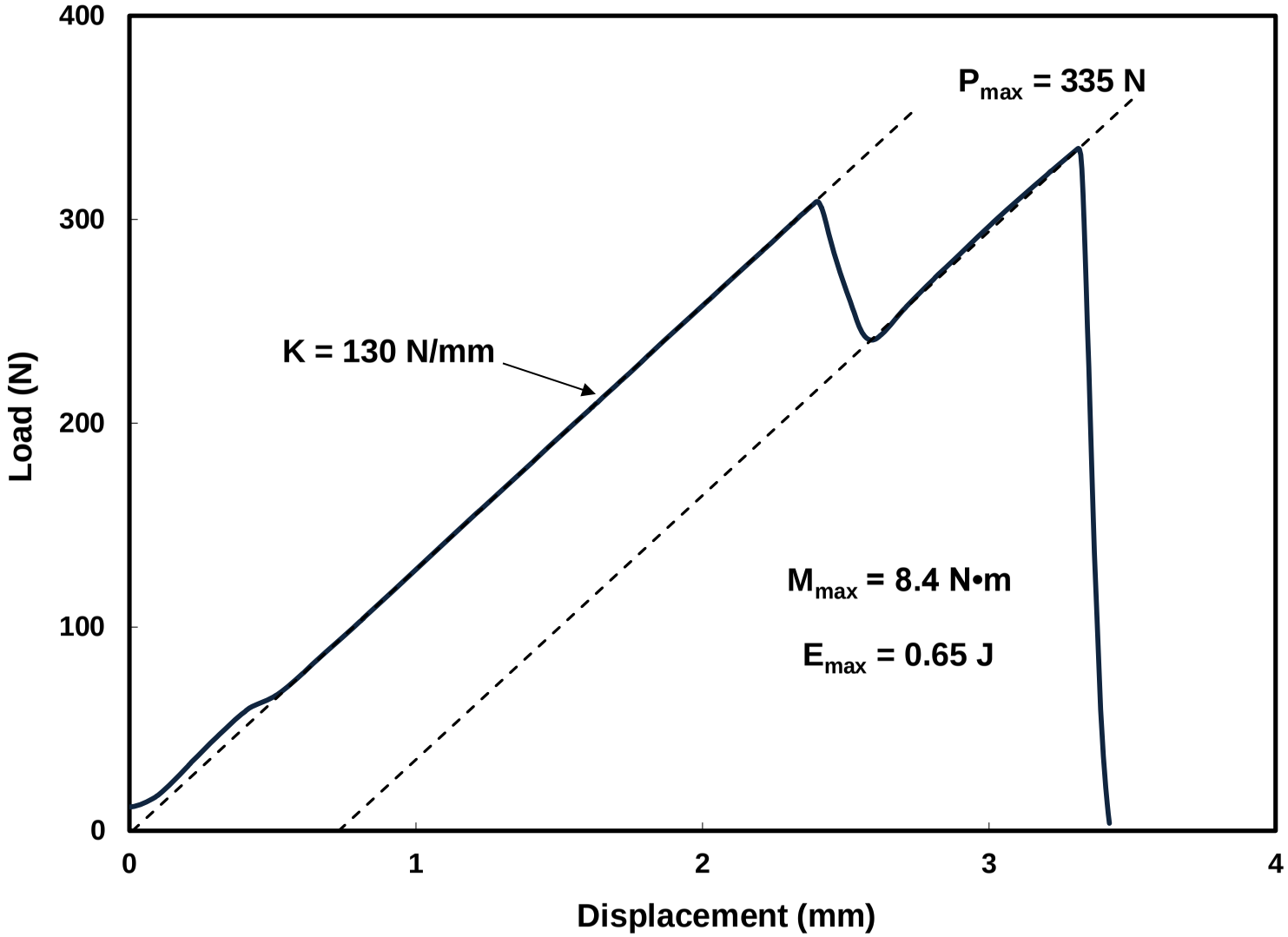

Figure D.8: **4-PBT load-displacement curve for OCZL#17 test sample, which was pressurized to 1200 psig, heated to ≈1200°C, oxidized to 13% CP-ECR, and cooled with quench.**

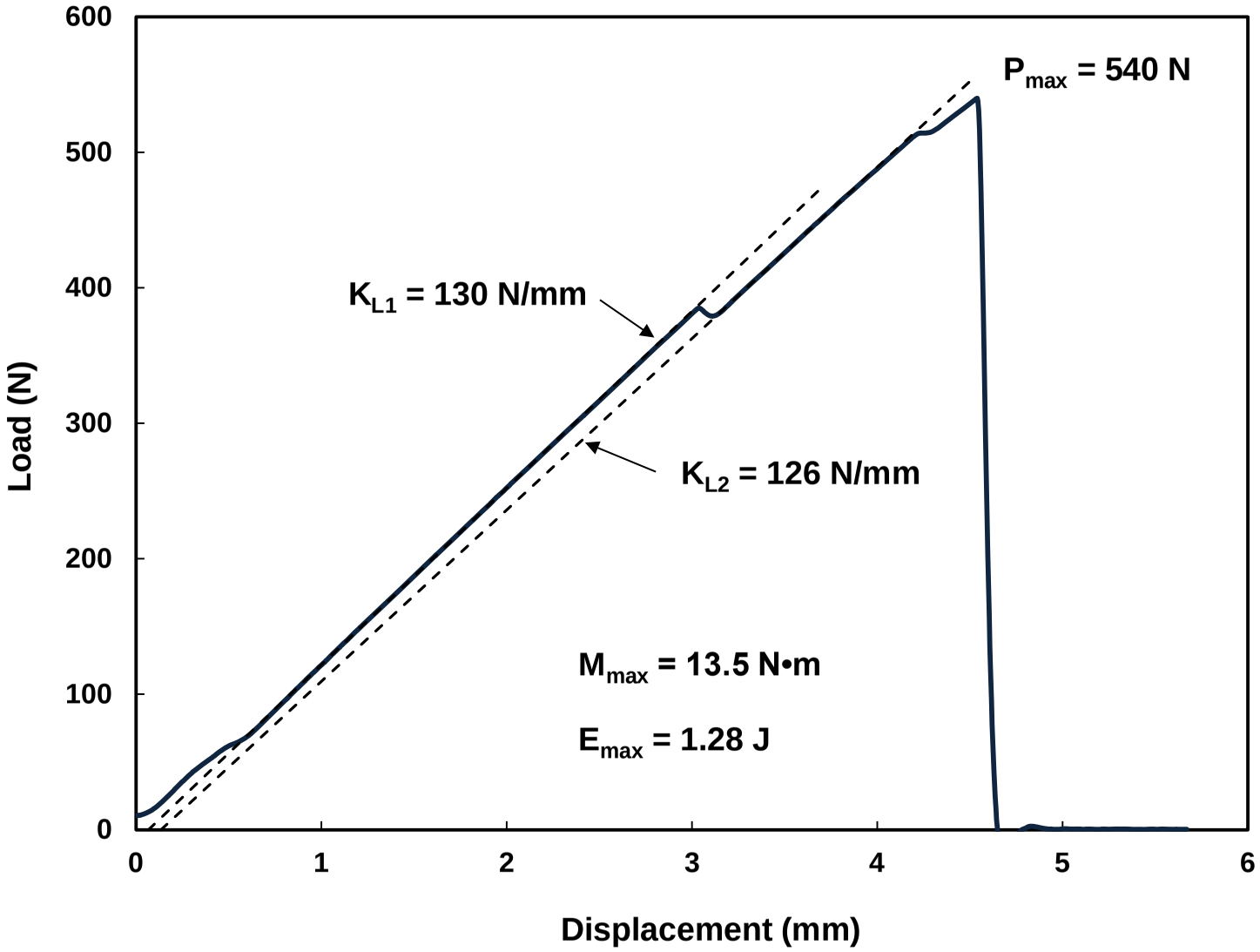

Figure D.9: **4-PBT load-displacement curve for OCZL#18 test sample, which was pressurized to 1200 psig, heated to ≈1200°C, oxidized to 12% CP-ECR, and cooled with quench.**

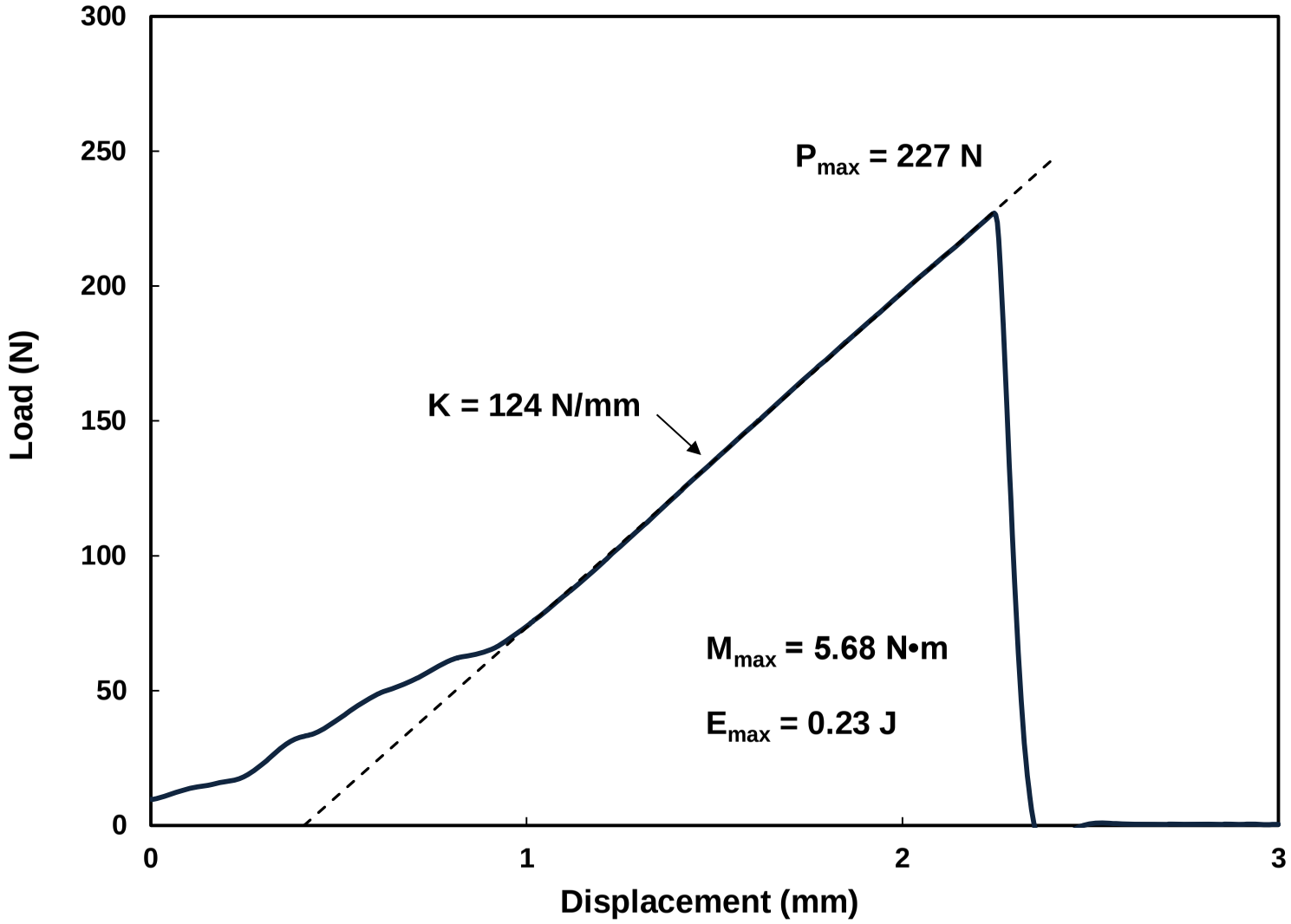

Figure D.10: **4-PBT load-displacement curve for OCZL#19 test sample, which was pressurized to 600 psig, heated to ≈1200°C, oxidized to 17% CP-ECR, and cooled with quench.**

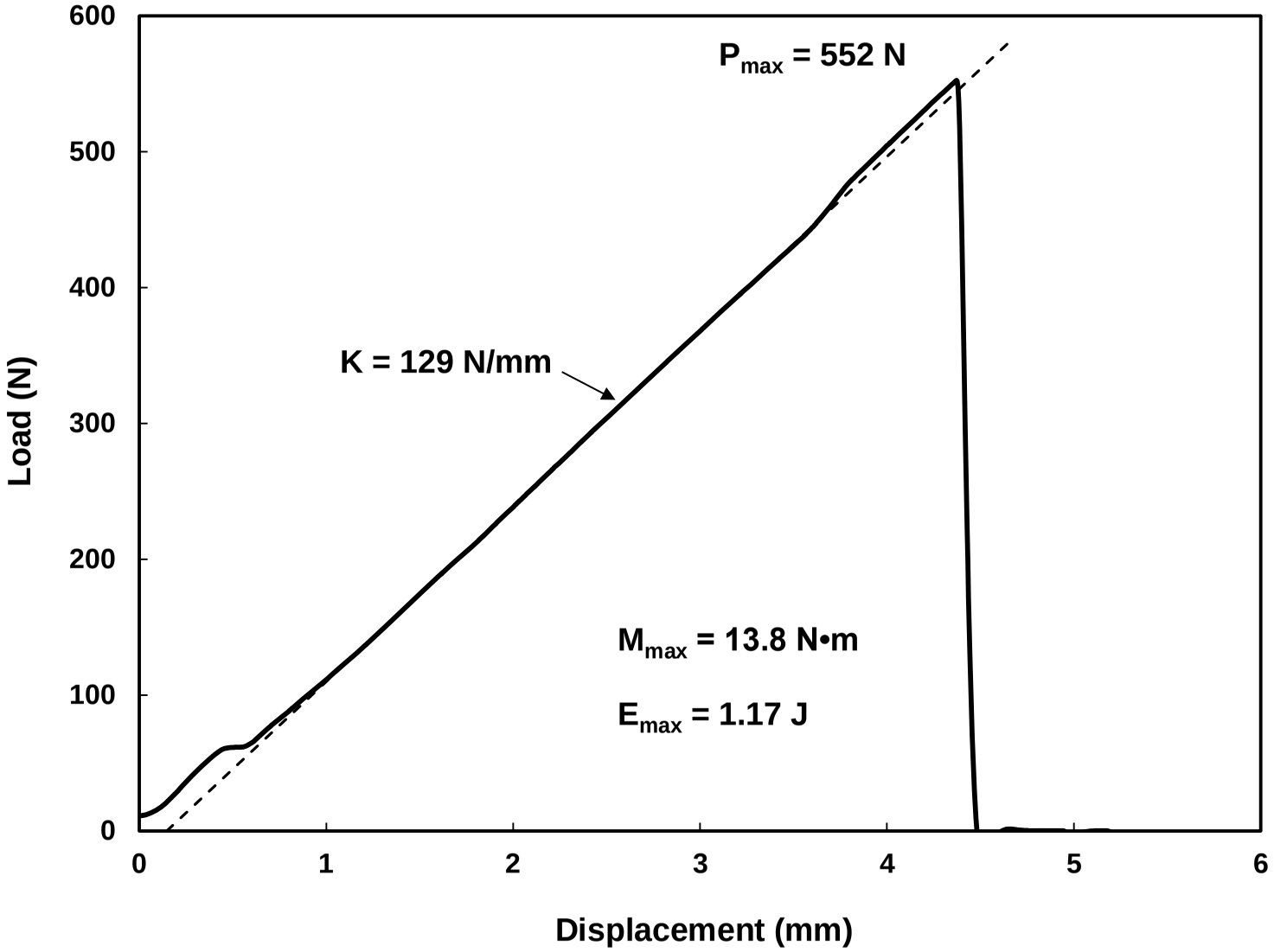

Figure D.11: **4-PBT load-displacement curve for OCZL#21 test sample, which was pressurized to 600 psig, heated to ≈1200°C, oxidized to 11% CP-ECR, and cooled with quench.**

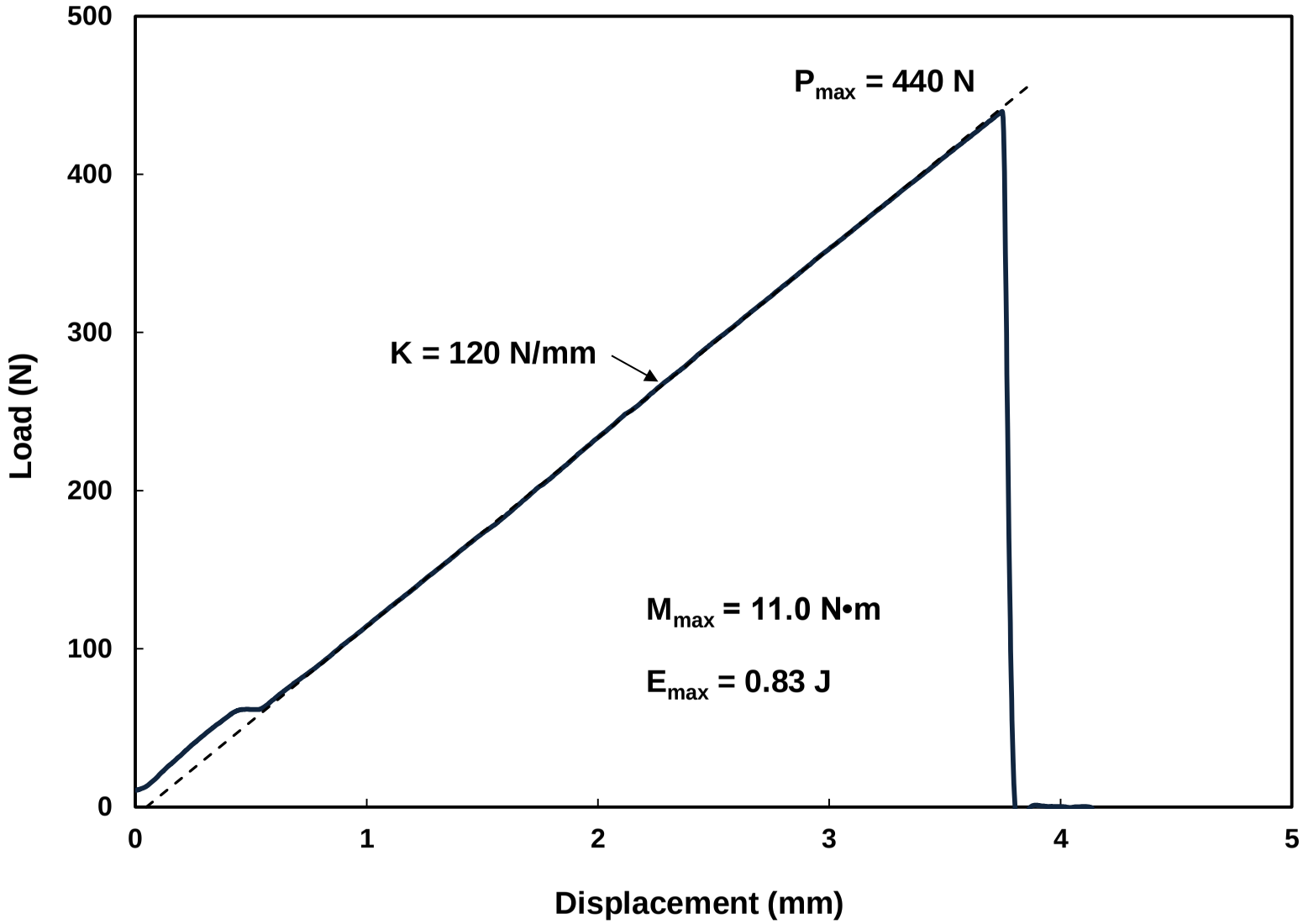

Figure D.12: **4-PBT load-displacement curve for OCZL#22 test sample, which was pressurized to 600 psig, heated to ≈1200°C, oxidized to 12% CP-ECR, and cooled with quench.**

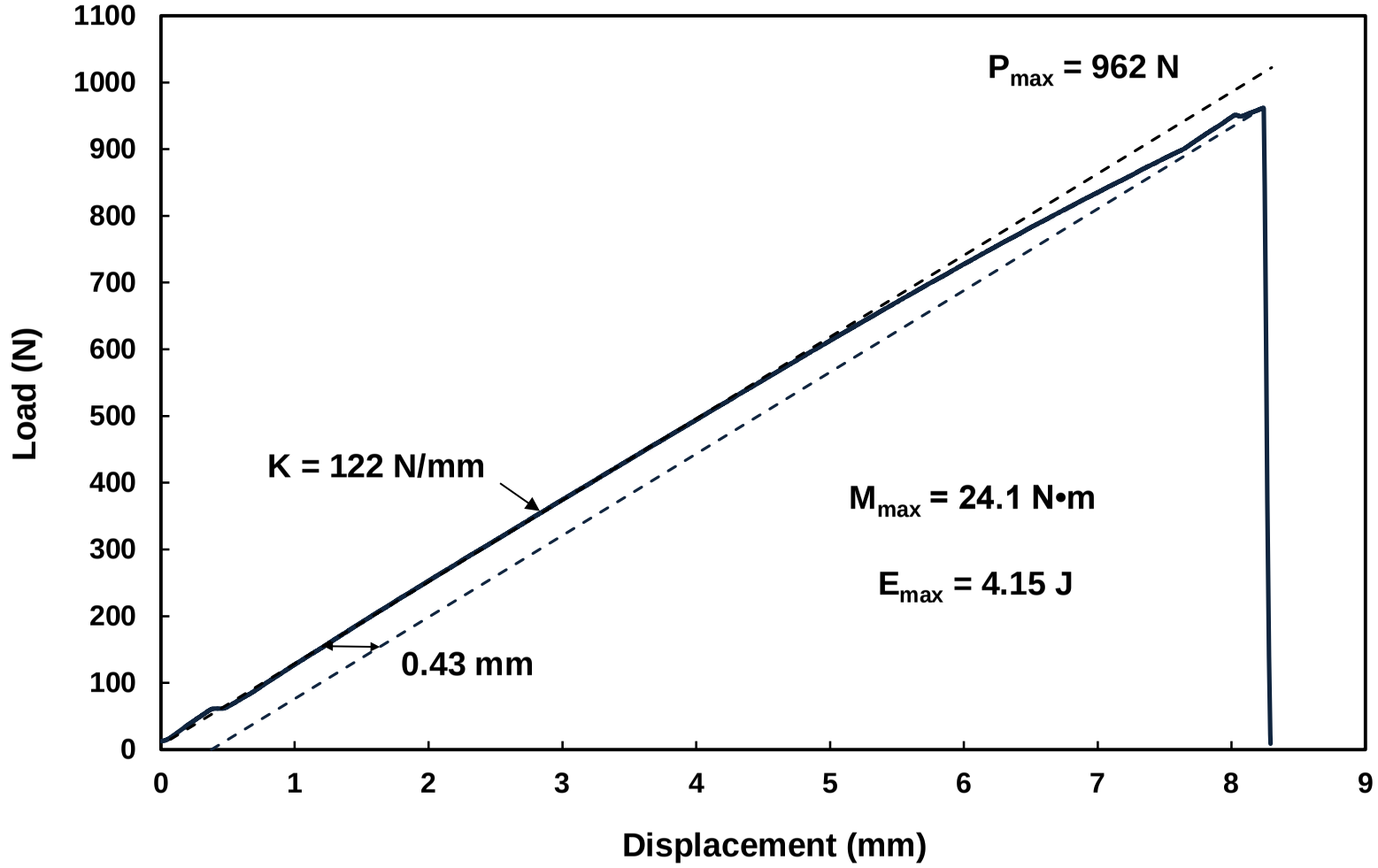

Figure D.13: **4-PBT load-displacement curve for OCZL#24 test sample, which was non-pressurized, heated to ≈1200°C, one-sided oxidized to 17% CP-ECR, and cooled with quench.**

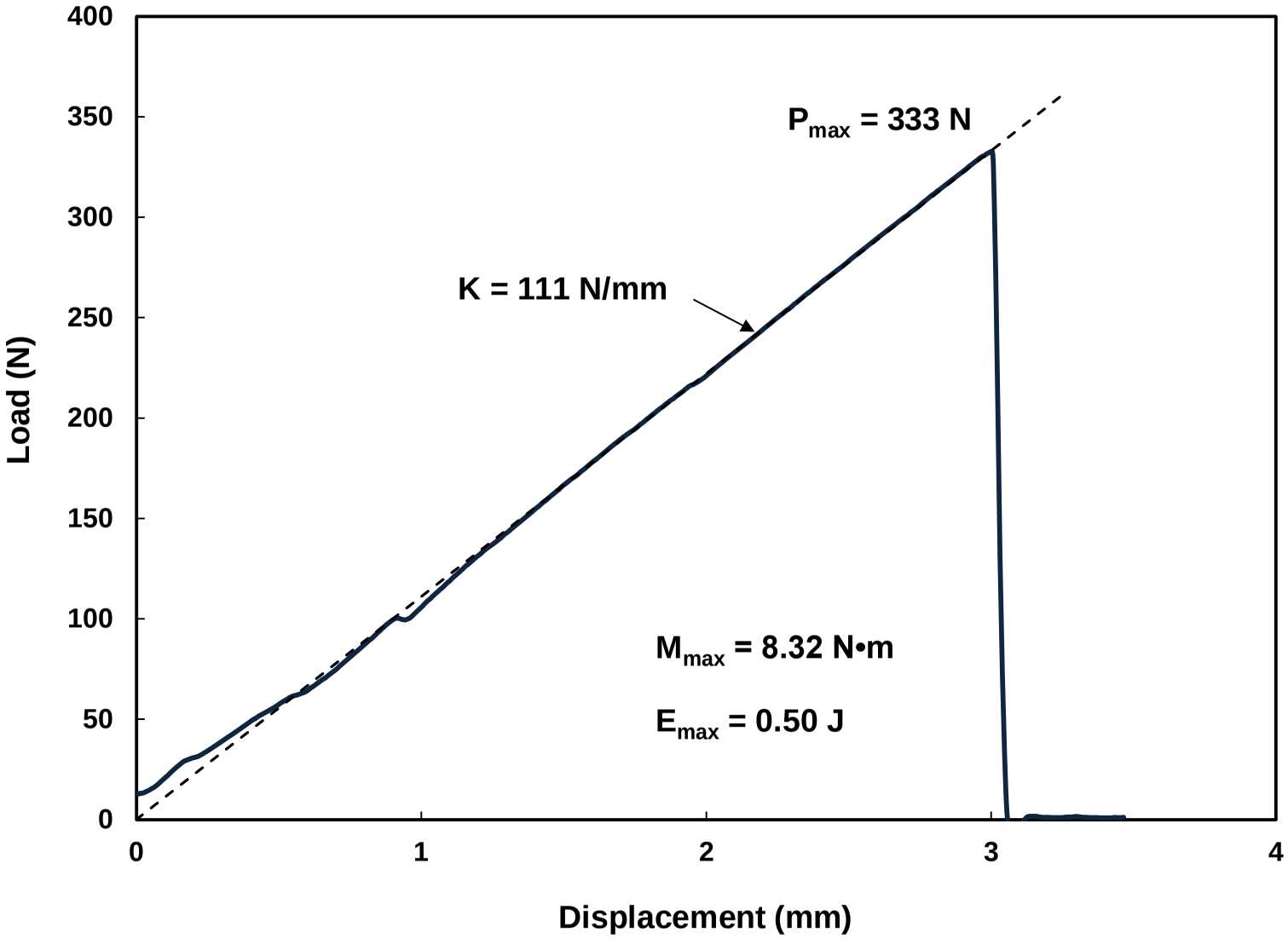

Figure D.14: **4-PBT load-displacement curve for OCZL#25 test sample, which was pressurized to 1200 psig, heated to ≈1200°C, oxidized to 16% CP-ECR, and cooled with quench.**

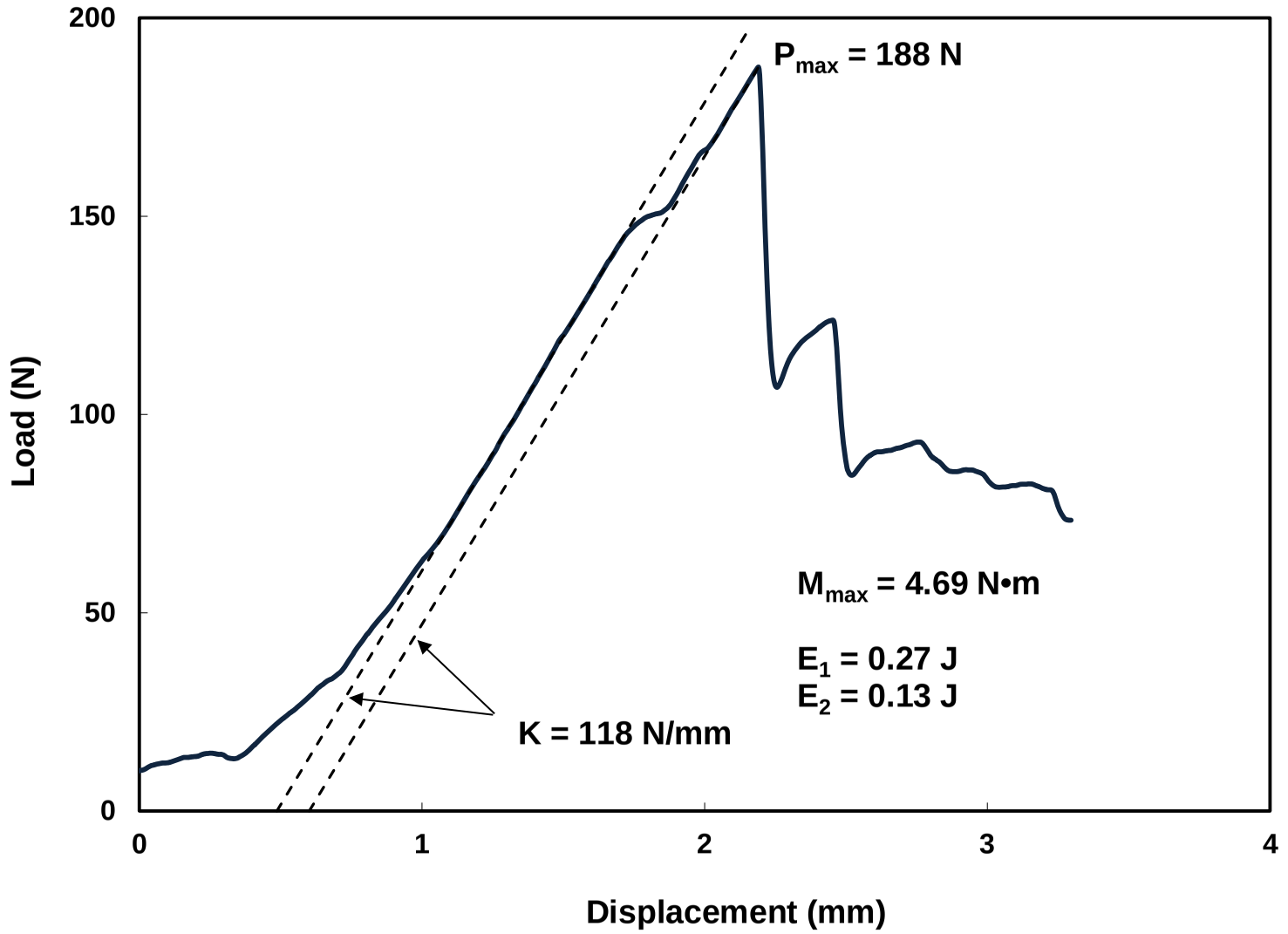

Figure D.15a: 4-PBT load-displacement curve for OCZL#29 test sample, which was pressurized to 1200 psig, heated to ≈1200°C, oxidized to 17% CP-ECR, and cooled with quench. Test was interrupted to allow examination of sample.

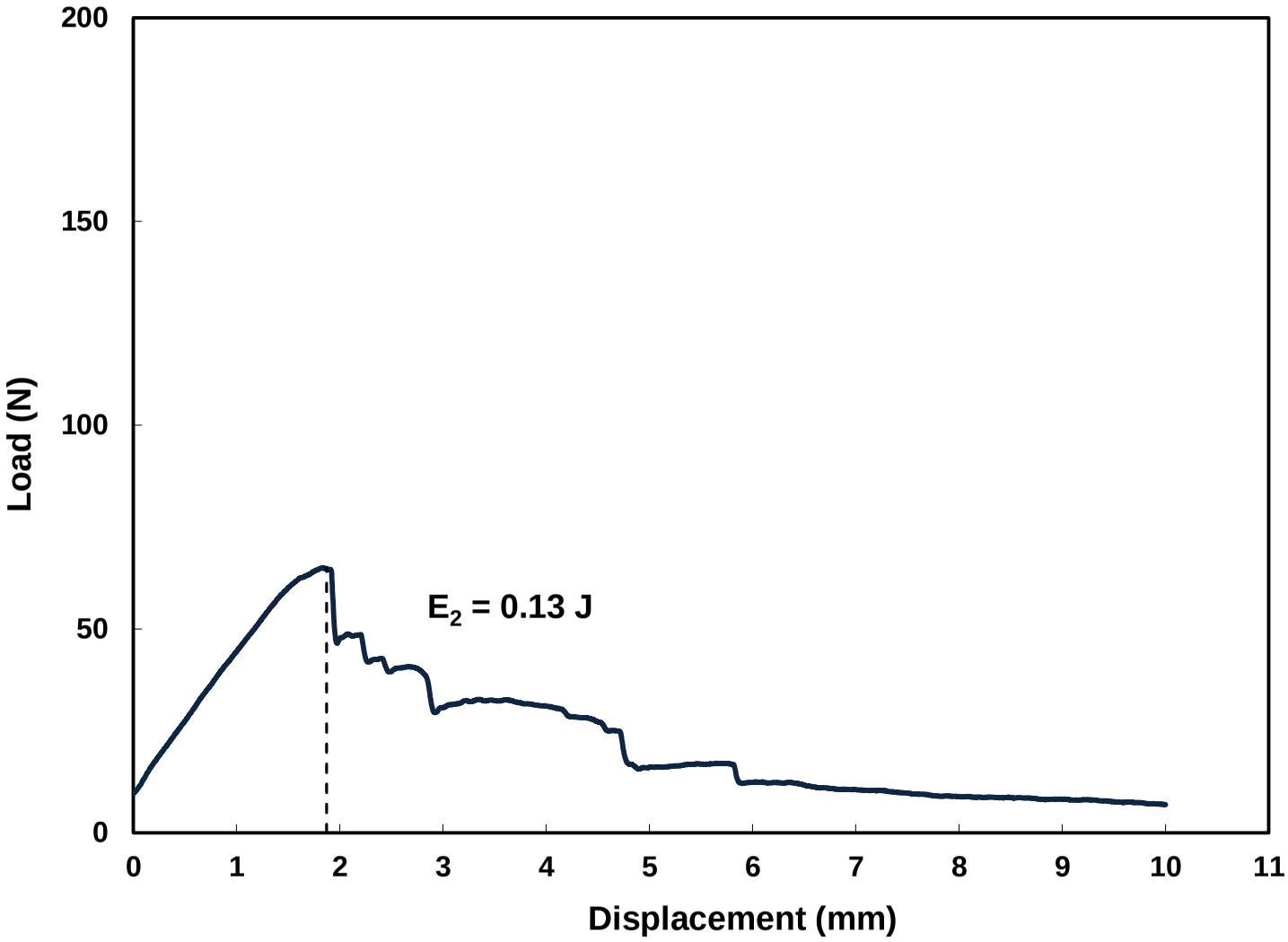

Figure D.15b: 4-PBT load-displacement curve for OCZL#29 test sample, which was pressurized to 1200 psig, heated to ≈1200°C, oxidized to 17% CP-ECR, and cooled with quench. Sample was reloaded after visual examination.

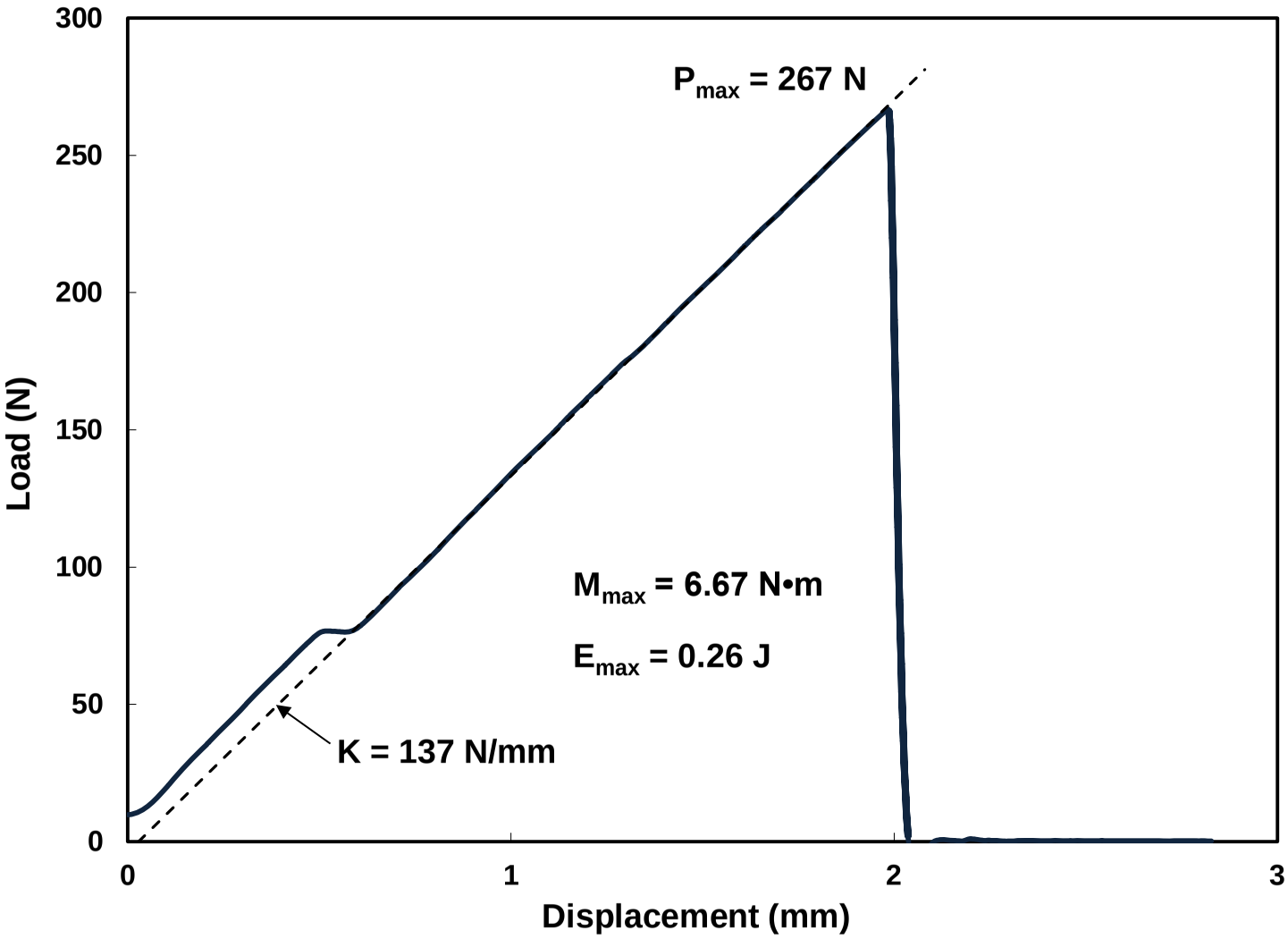

Figure D.16: **4-PBT load-displacement curve for OCZL#32 test sample, which was pressurized to 1200 psig, heated to ≈1200°C, oxidized to 16% CP-ECR, and cooled with quench.**

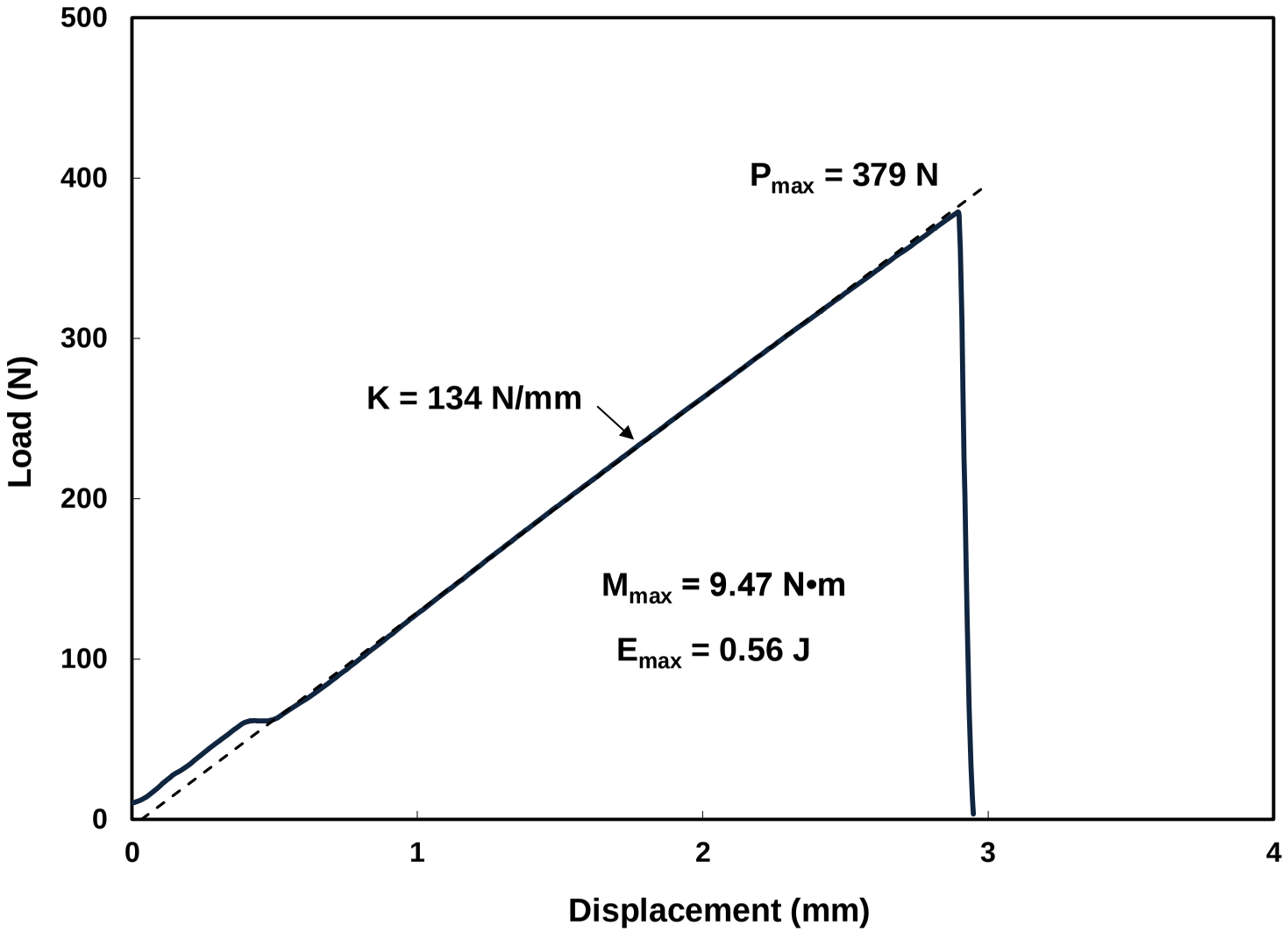

Figure D.17: **4-PBT load-displacement curve for OCZL#36 test sample, which was pressurized to 1200 psig, heated to ≈1200°C, oxidized to 18% CP-ECR, and cooled with quench.**

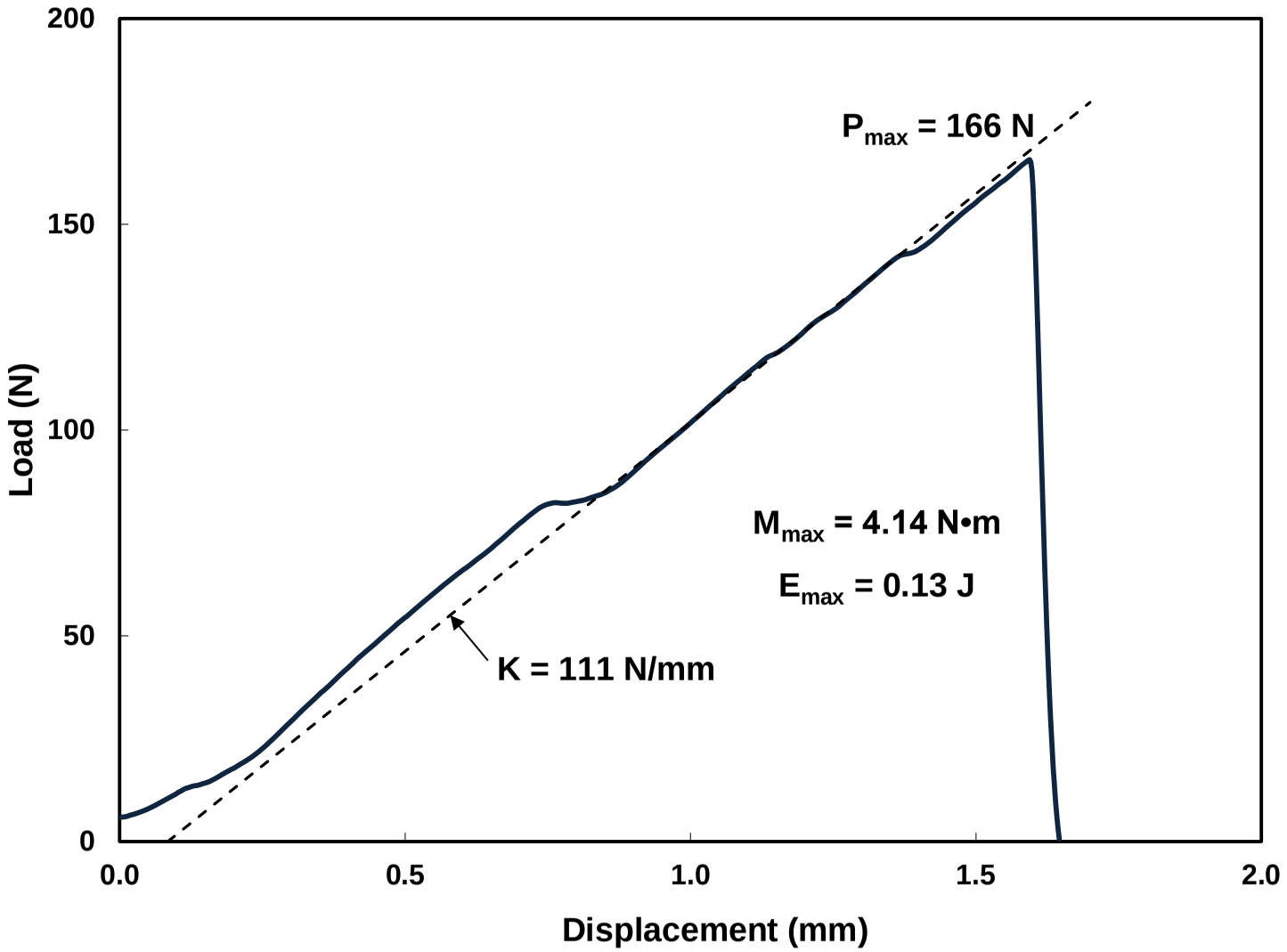

Figure D.18: **4-PBT load-displacement curve for OCZL#37 test sample, which was pressurized to 1200 psig, heated to ≈1200°C, oxidized to 23% CP-ECR, and cooled with quench.**

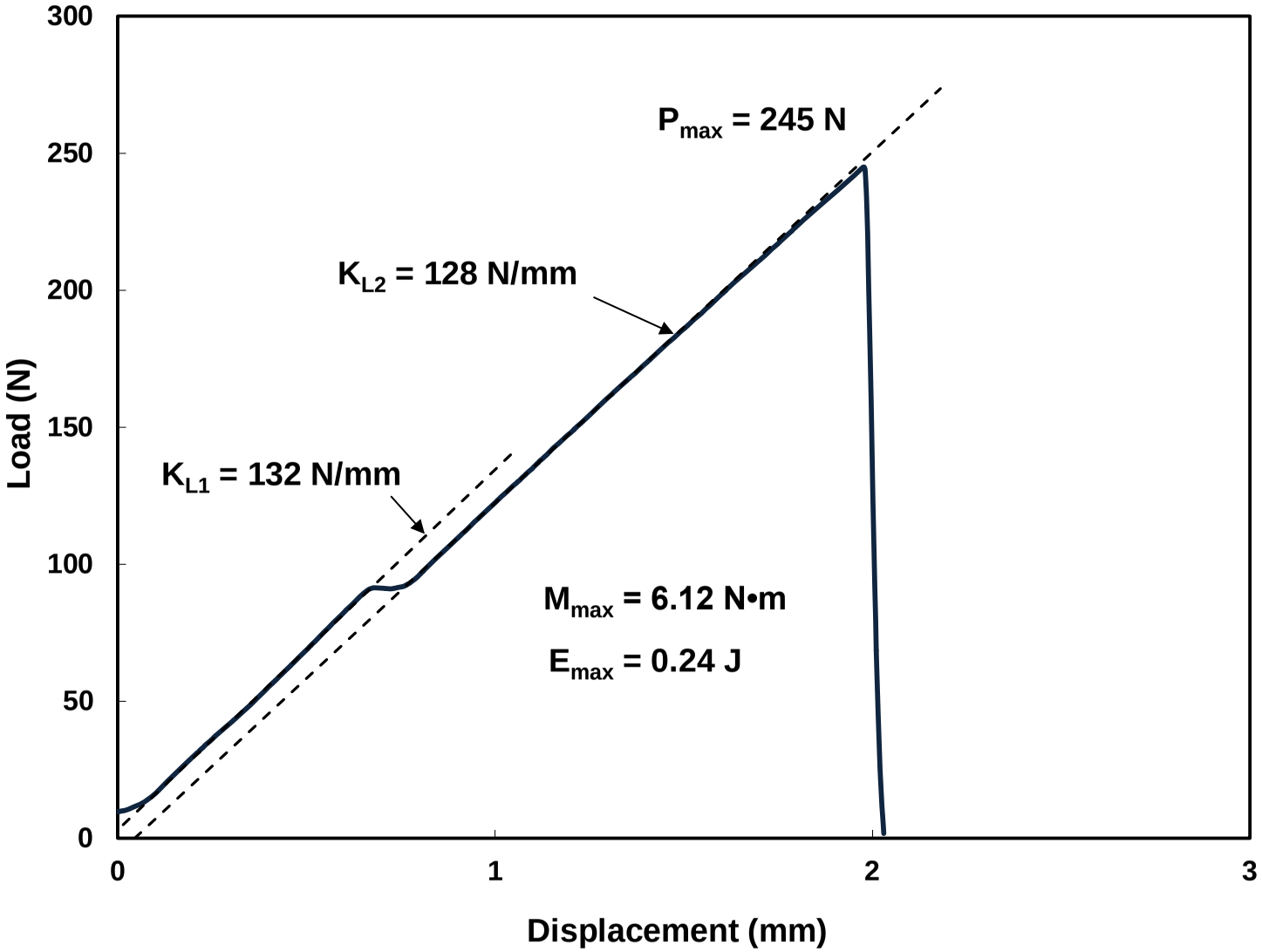

Figure D.19: **4-PBT load-displacement curve for OCZL#43 test sample, which was pressurized to 1200 psig, heated to ≈1200°C, oxidized to 18% CP-ECR, and cooled with quench.**

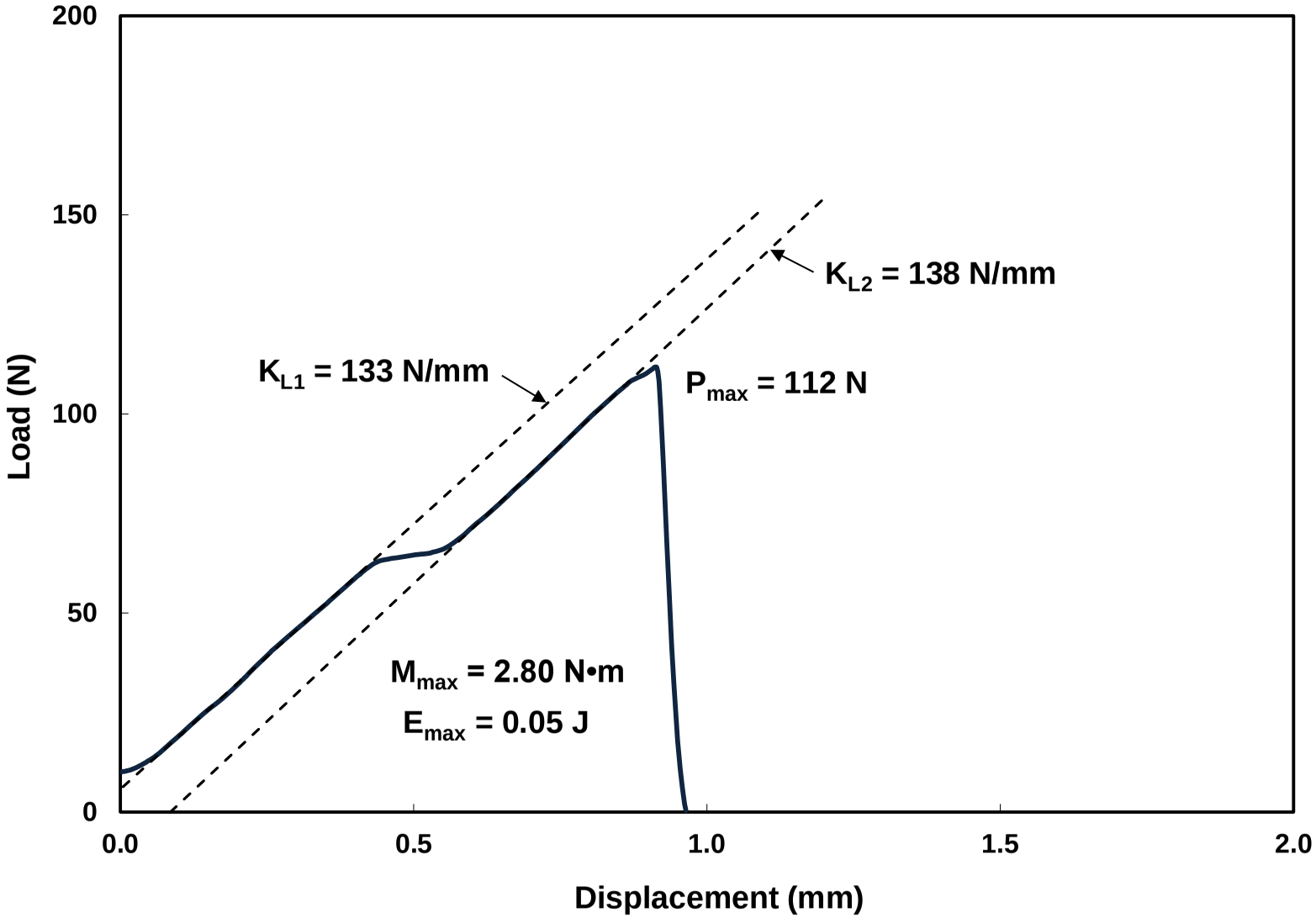

Figure D.20: **4-PBT load-displacement curve for OCZL#39 (660 wppm H) test sample, which was pressurized to 600 psig, heated to ≈1200°C, oxidized to 13% CP-ECR, and cooled with quench.**

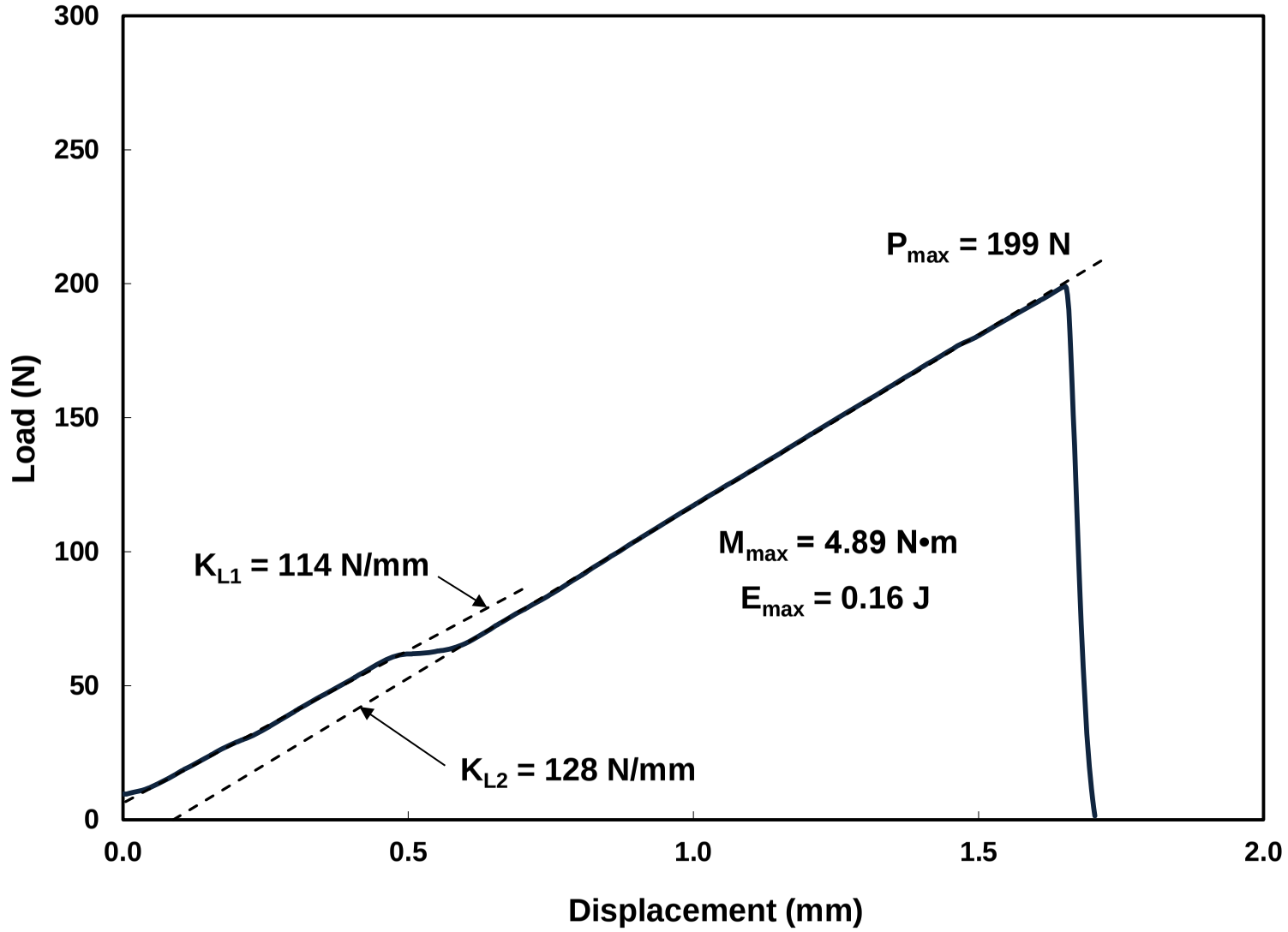

Figure D.21: **4-PBT load-displacement curve for OCZL#40 (390 wppm H) test sample, which was pressurized to 1200 psig, heated to ≈1200°C, oxidized to 12% CP-ECR, and cooled with quench.**

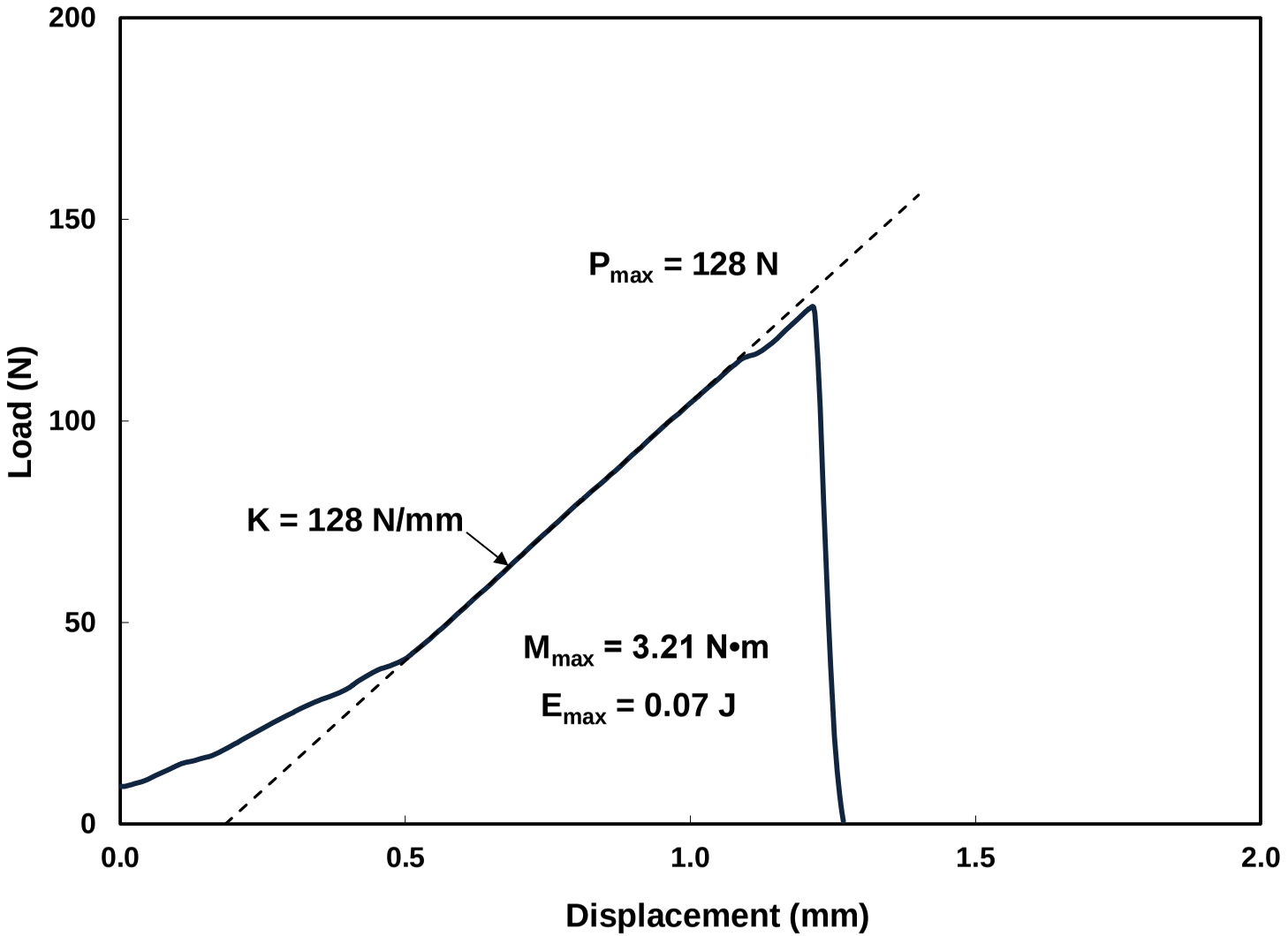

Figure D.22: **4-PBT load-displacement curve for OCZL#41 (220 wppm H) test sample, which was pressurized to 1200 psig, heated to ≈1200°C, oxidized to 16% CP-ECR, and cooled with quench.**

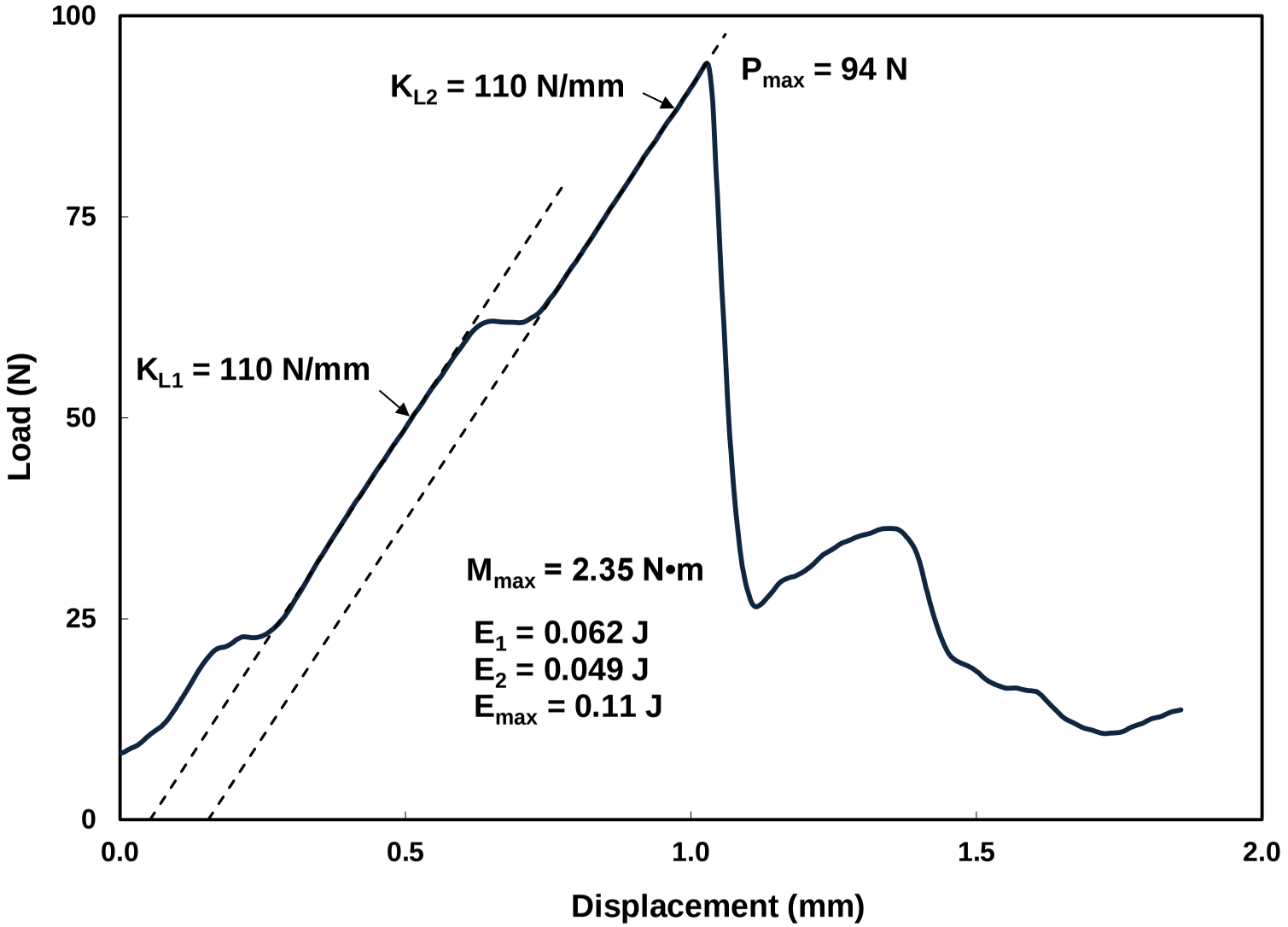

Figure D.23a: 4-PBT load-displacement curve for OCZL#44 (700 wppm H) test sample, which was pressurized to 1200 psig, heated to ≈1200°C, oxidized to 14% CP-ECR, and cooled with quench. Test was interrupted to allow for visual examination.

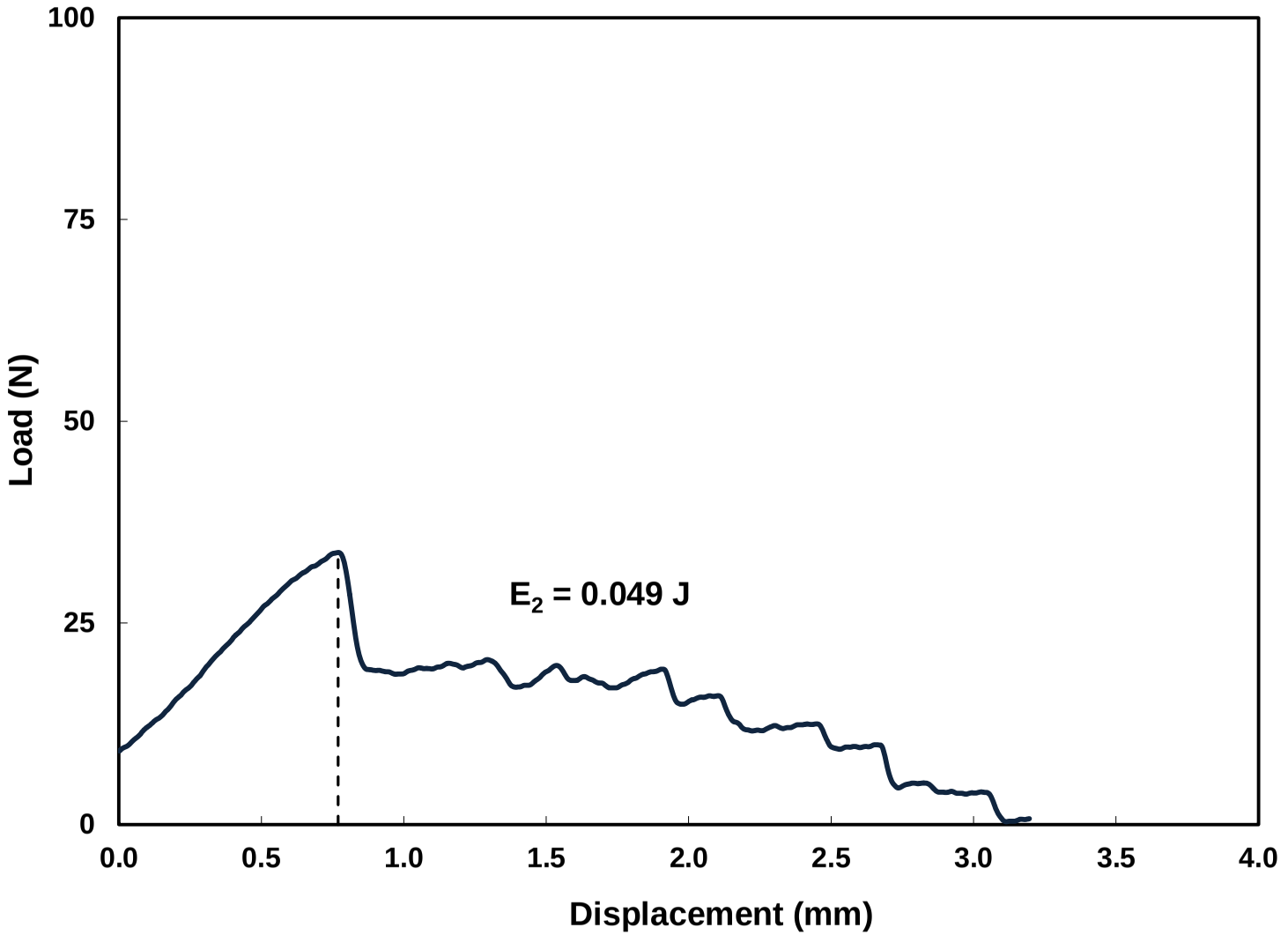

Figure D.23b: 4-PBT load-displacement curve for OCZL#44 (700 wppm H) test sample, which was pressurized to 1200 psig, heated to ≈1200°C, oxidized to 14% CP-ECR, and cooled with quench. Sample was reloaded.

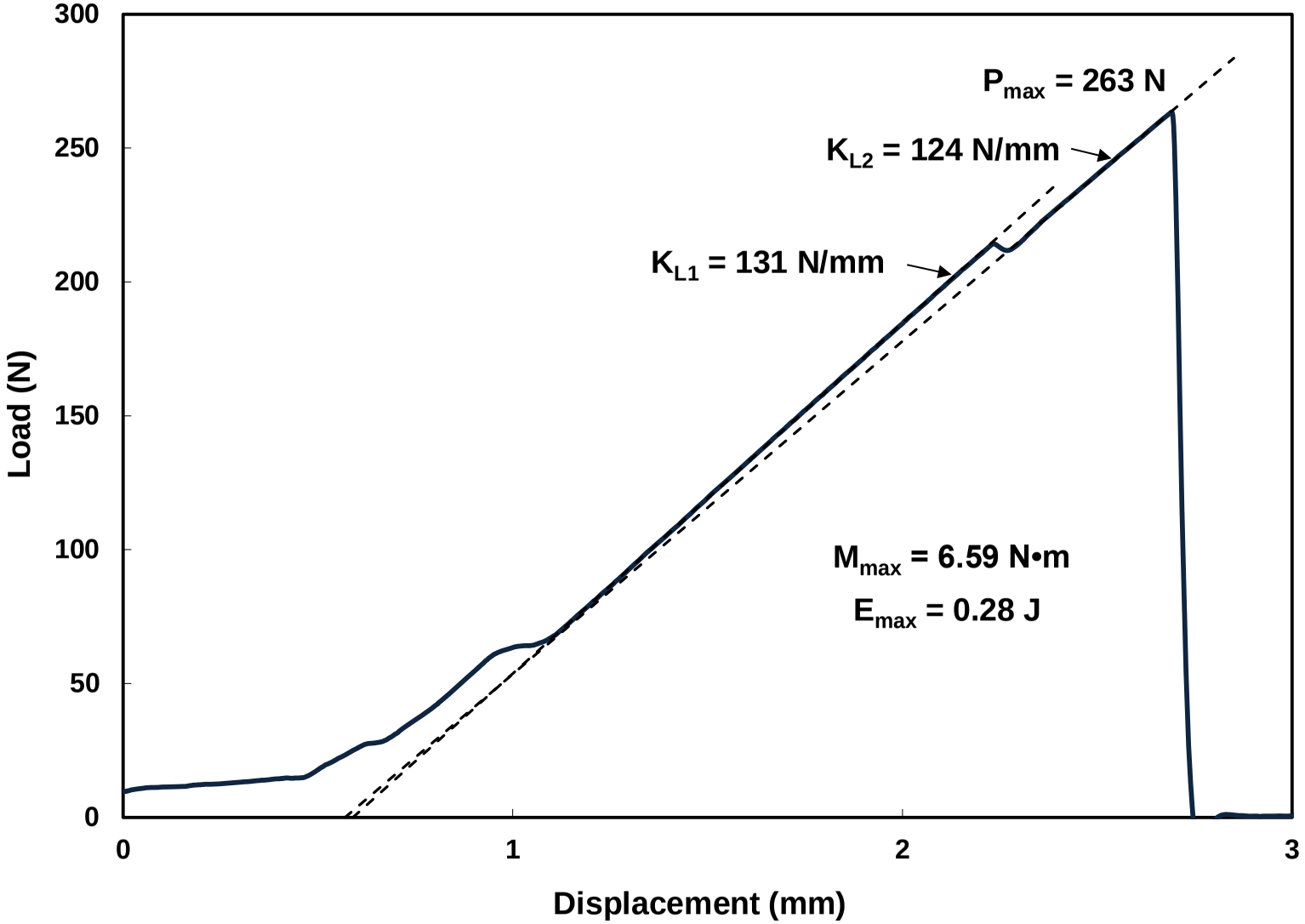

Figure D.24: **4-PBT load-displacement curve for OCZL#45 (220 wppm H) test sample, which was pressurized to ≈1200 psig, heated to ≈1200°C, oxidized to 13% CP-ECR, and cooled with quench.**

APPENDIX E: PHOTOGRAPHS OF POST-BEND LOCA INTEGRAL SAMPLES

Figure E.1: **Post-4-PBT images of ramp-to-rupture samples from OCZL#8, #9, and #10 test samples, which were pressurized at 300°C to 600, 400, and 1600 psig, respectively, heated to rupture, and cooled without quench.**

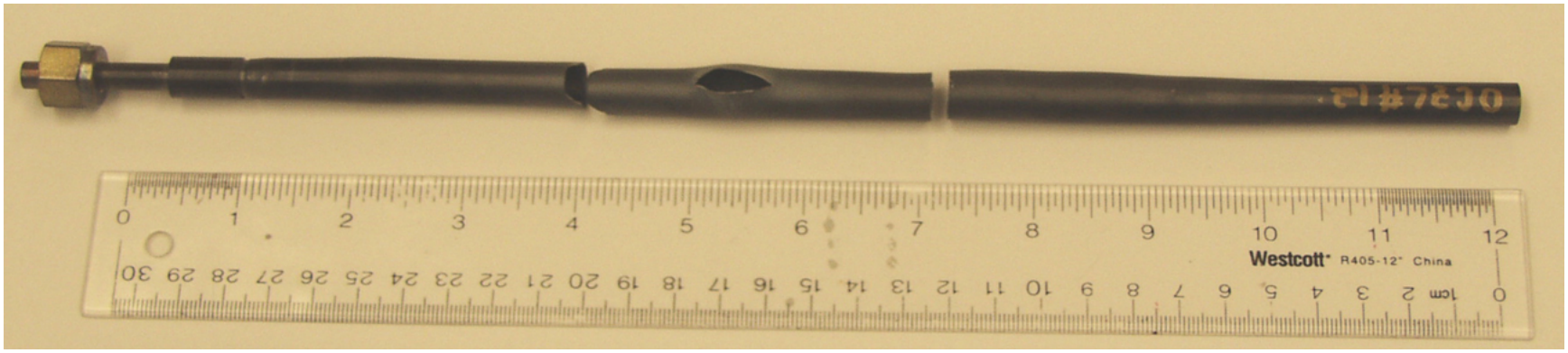

(a)

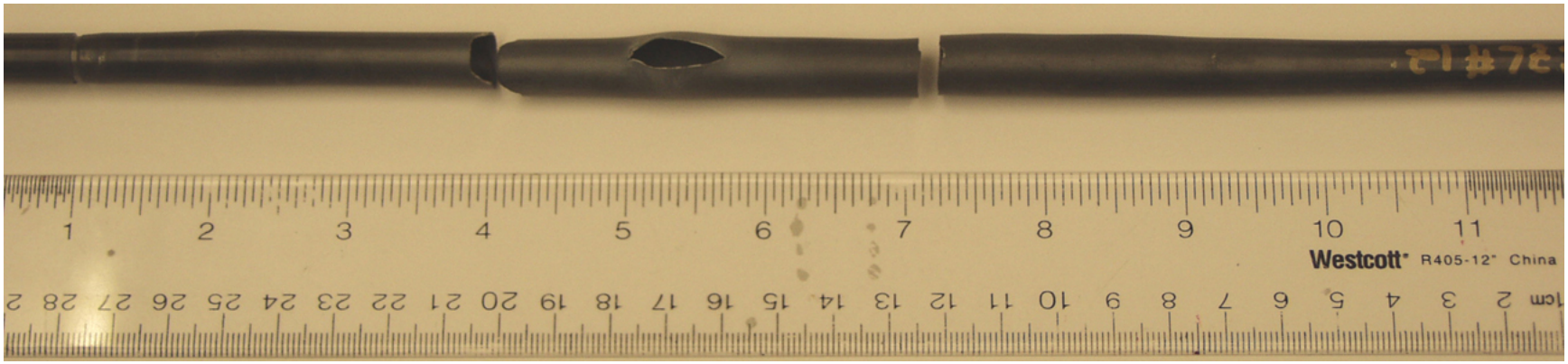

(b)

Figure E.2: Post-4-PBT images of OCZL#12 test sample, which was pressurized to 1000 psig, heated to ≈1200°C, oxidized to 15% CP-ECR, and cooled without quench: (a) low magnification and (b) higher magnification.

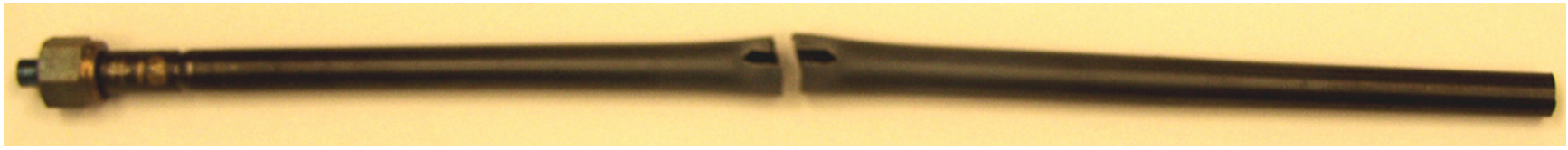

Figure E.3: **Post-4-PBT image of OCZL#13 test sample, which was pressurized to 1200 psig, heated to ≈1200°C, oxidized to 14% CP-ECR, and cooled without quench.**

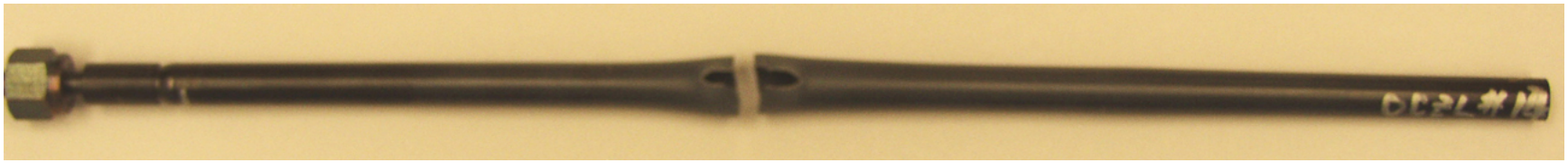

Figure E.4: **Post-4-PBT images of OCZL#14 test sample, which was pressurized to 1200 psig, heated to ≈1200°C, oxidized to 18% CP-ECR, and cooled with quench.**

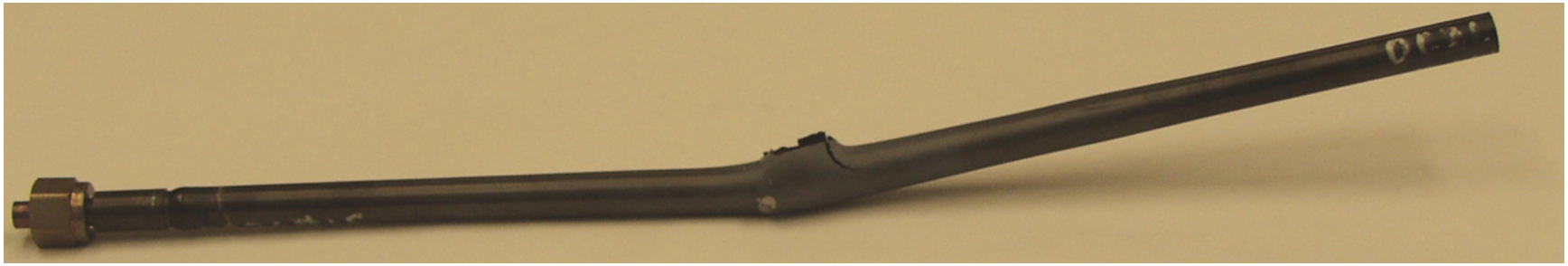

(a)

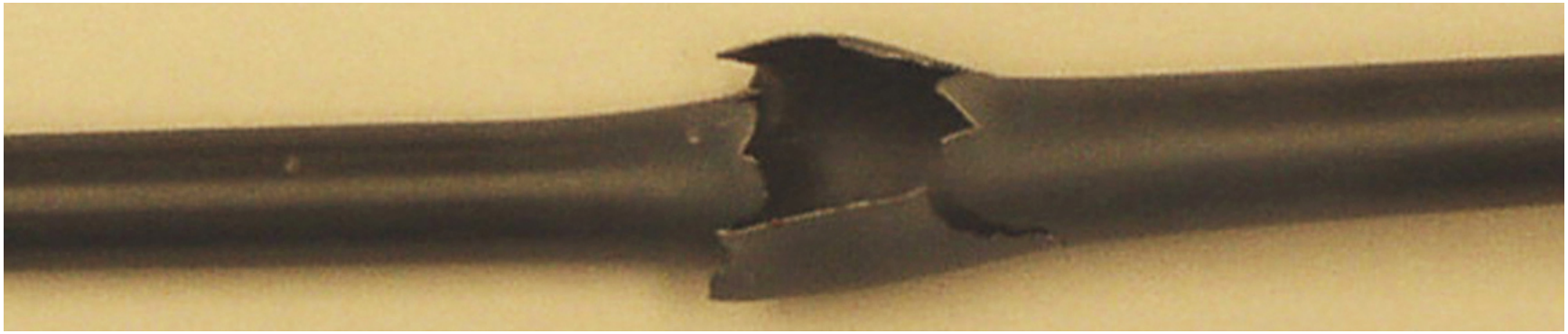

(b)

Figure E.5: **Post-4-PBT images for the OCZL#15 test sample, which was pressurized to 1200 psig, heated to ≈1200°C, oxidized to 18% CP-ECR, cooled with quench, and subjected to reverse bending: (a) low magnification and (b) higher magnification.**

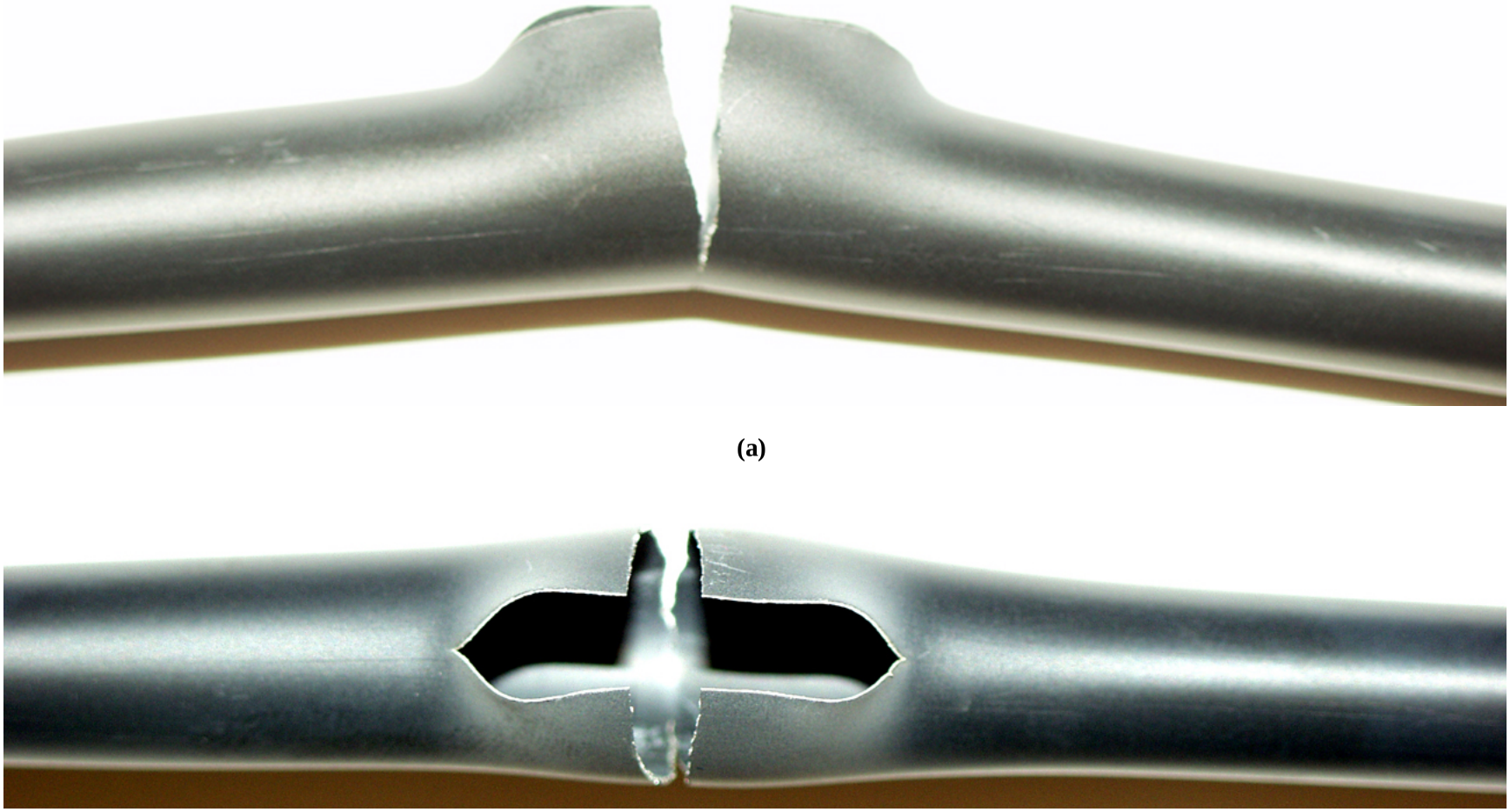

(a)

(b)

Figure E.6: **Post-4-PBT images of OCZL#17 test sample, which was pressurized to 1200 psig, heated to ≈1200°C, oxidized to 13% CP-ECR, and cooled with quench: (a) side view and (b) rupture view.**

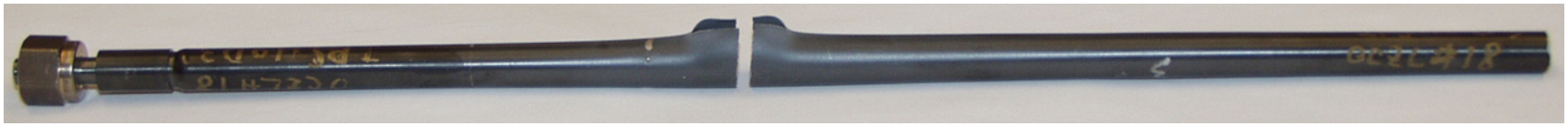

(a)

(b)

Figure E.7: **Post-4-PBT images of OCZL#18 test sample, which was pressurized to 1200 psig, heated to ≈1200°C, oxidized to 12% CP-ECR, and cooled with quench: (a) side view and (b) rupture view.**

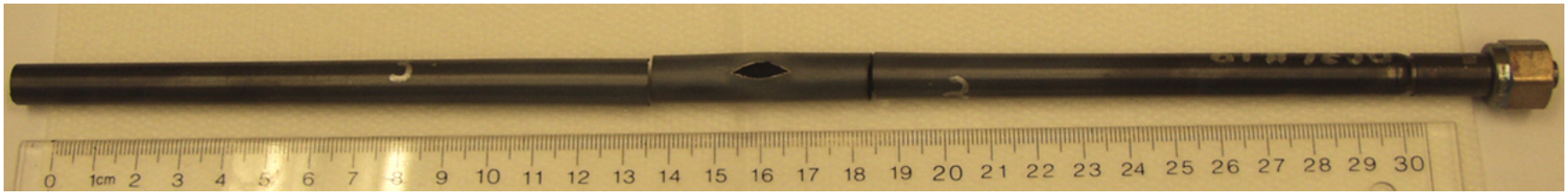

(a)

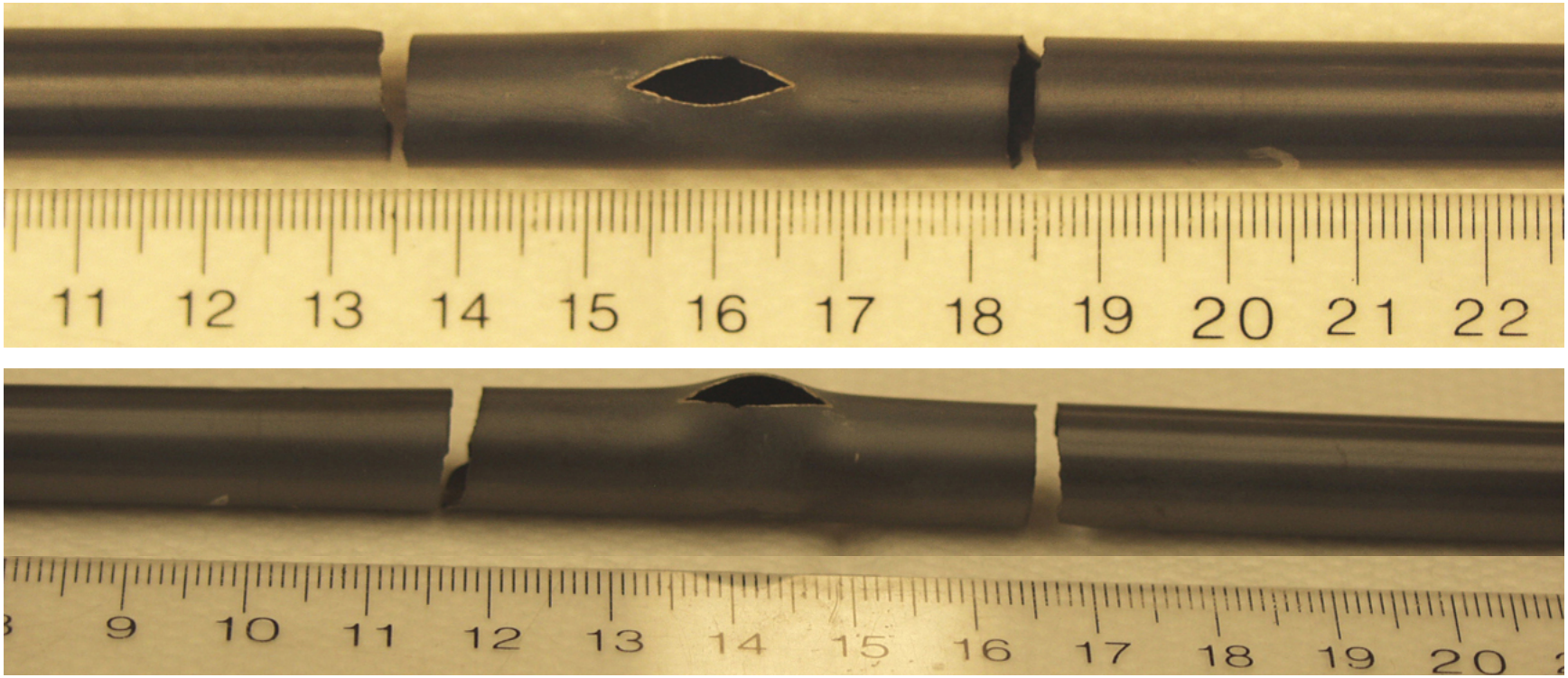

(b)

Figure E.8: **Post-4-PBT images of OCZL#19 test sample, which was pressurized to 600 psig, heated to ≈1200°C, oxidized to 17% CP-ECR, and cooled with quench: (a) low magnification and (b) higher magnification.**

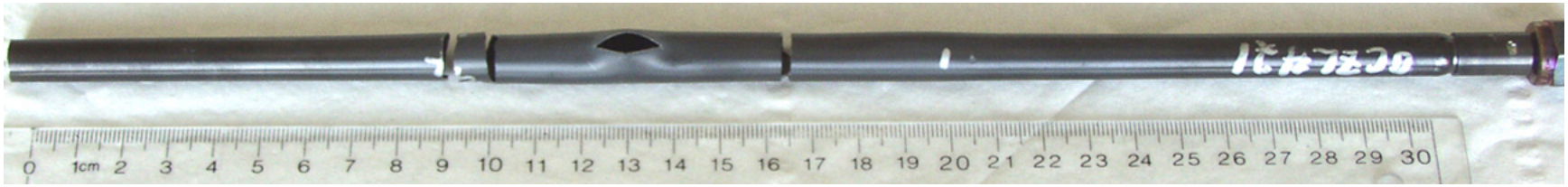

(a)

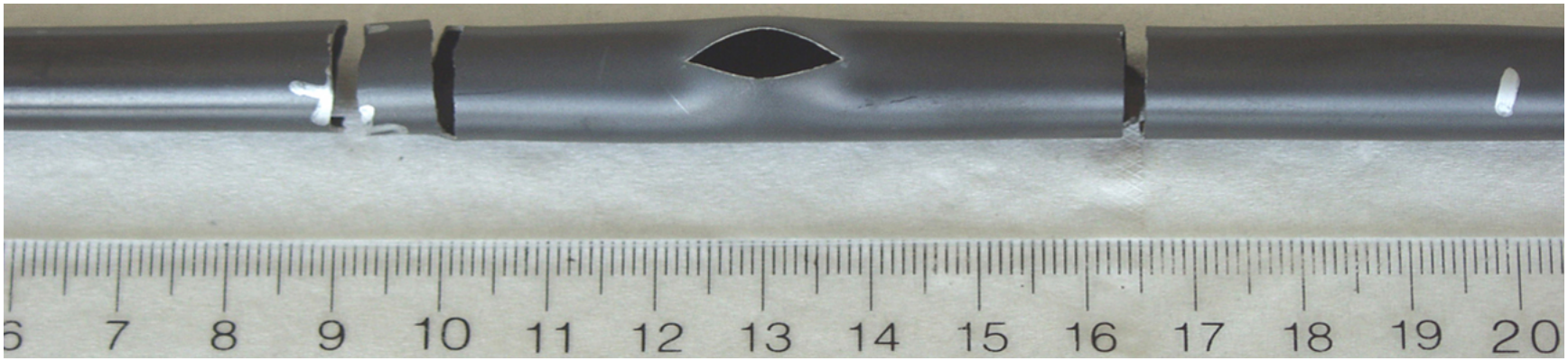

(b)

Figure E.9: Post-4-PBT images of OCZL#21 test sample, which was pressurized to 600 psig, heated to ≈1200°C, oxidized to 11% CP-ECR, and cooled with quench: (a) low magnification and (b) higher magnification.

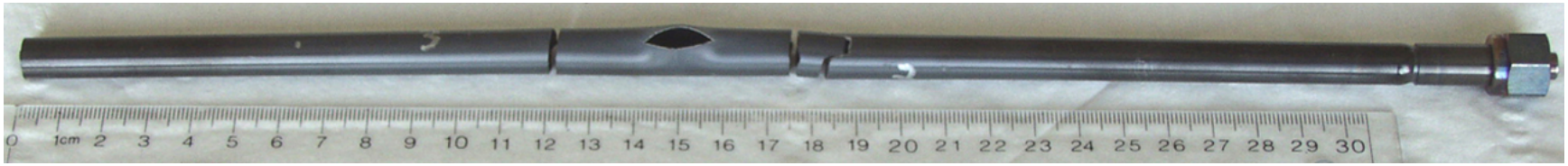

(a)

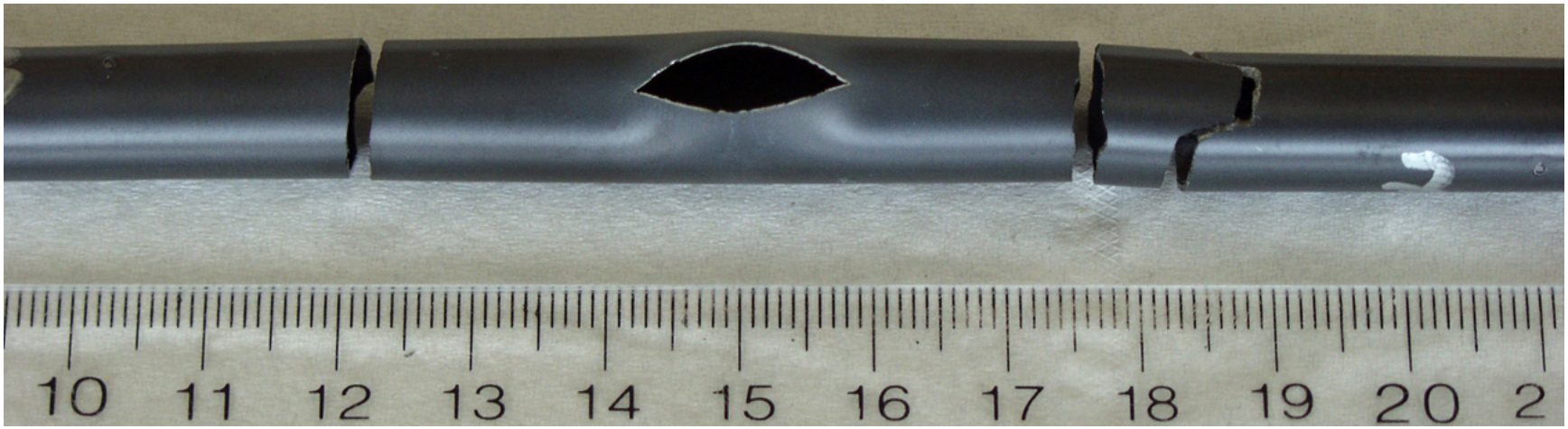

(b)

Figure E.10: Post-4-PBT images of OCZL#22 test sample, which was pressurized to 600 psig, heated to ≈1200°C, oxidized to 12% CP-ECR, and cooled with quench: (a) low magnification and (b) high magnification.

(a)

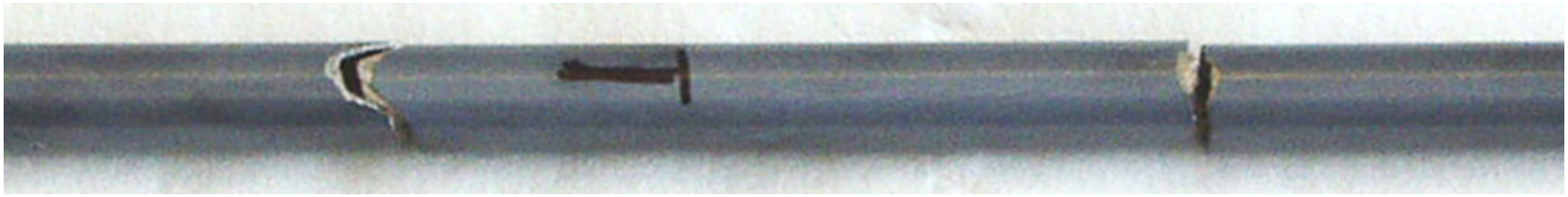

(b)

Figure E.11: Post-4-PBT images of OCZL#24 test sample, which was non-pressurized, heated to ≈1200°C, one-sided oxidized to 17% CP-ECR, and cooled with quench: (a) low magnification and (b) higher magnification.

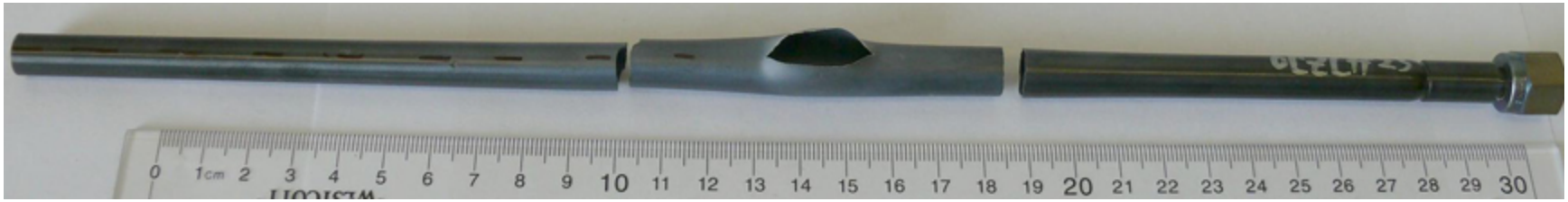

(a)

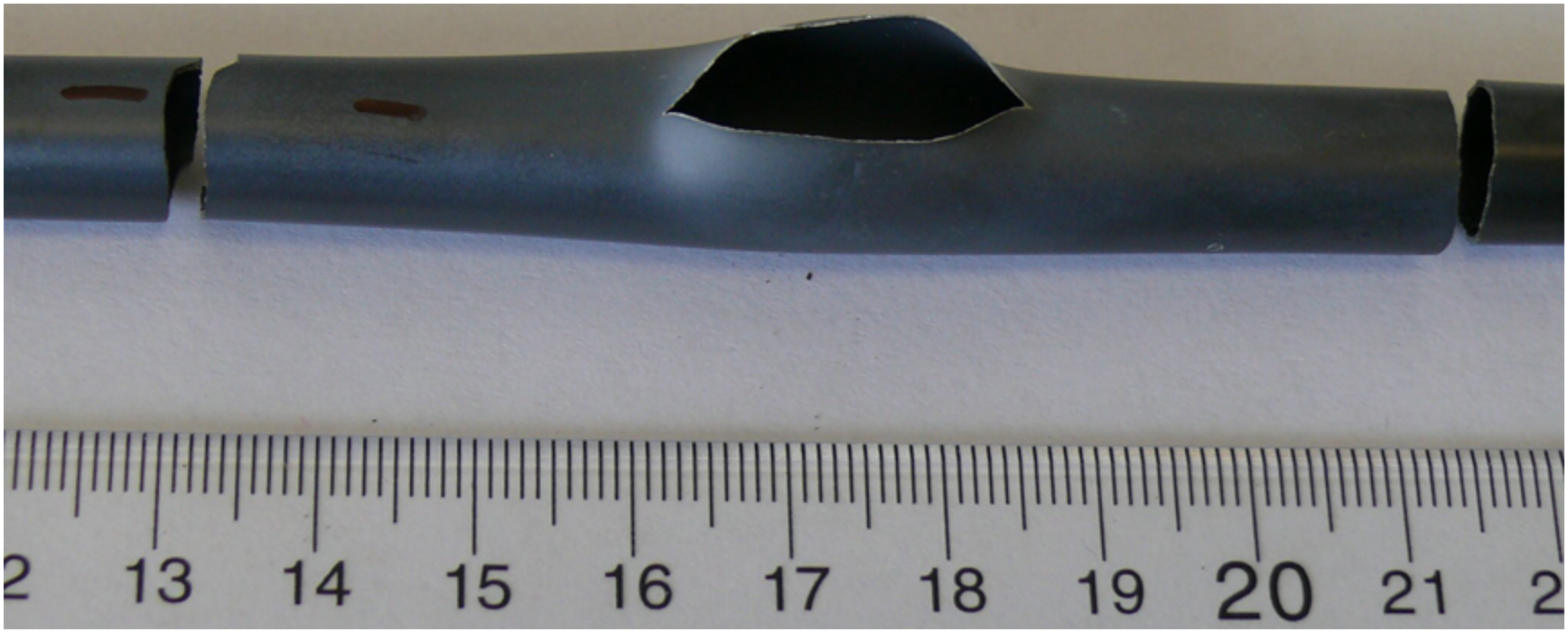

(b)

Figure E.12: Post-4-PBT images of OCZL#25 test sample, which was pressurized to 1200 psig, heated to ≈1200°C, oxidized to 16% CP-ECR, and cooled with quench: (a) low magnification and (b) higher magnification.

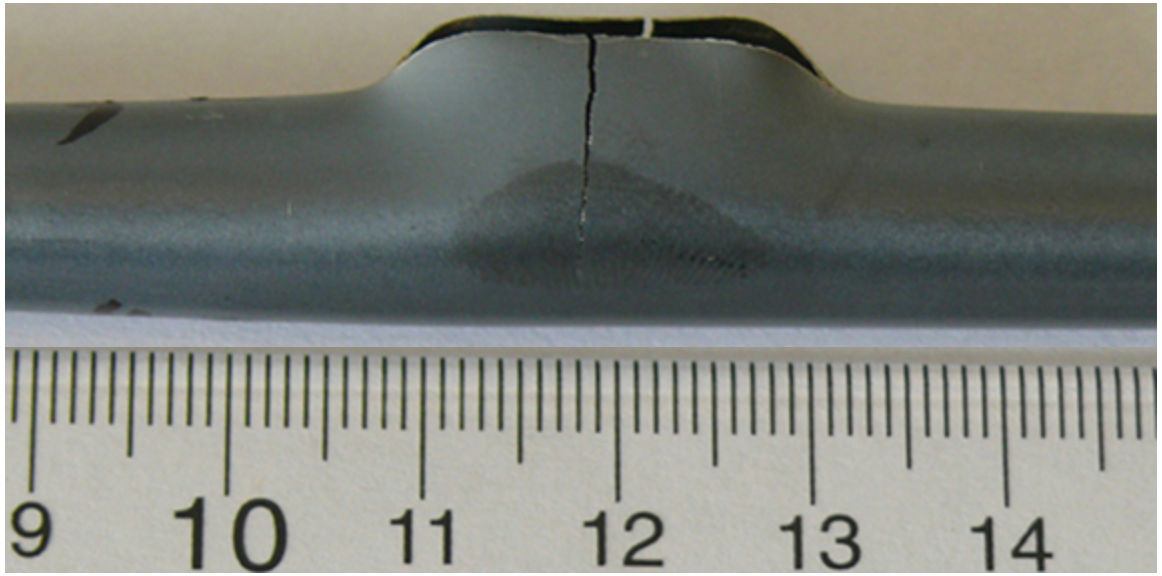

(a)

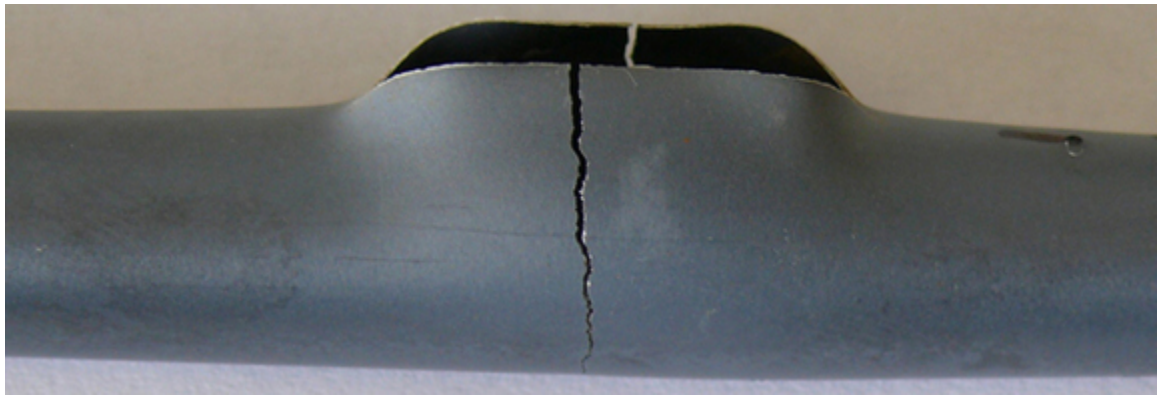

(b)

Figure E.13a: Post-4-PBT images of OCZL#29 test sample, which was pressurized to 1200 psig, heated to ≈1200°C, oxidized to 17% CP-ECR, and cooled with quench. Images were taken after first loading: (a) side A and (b) side B.

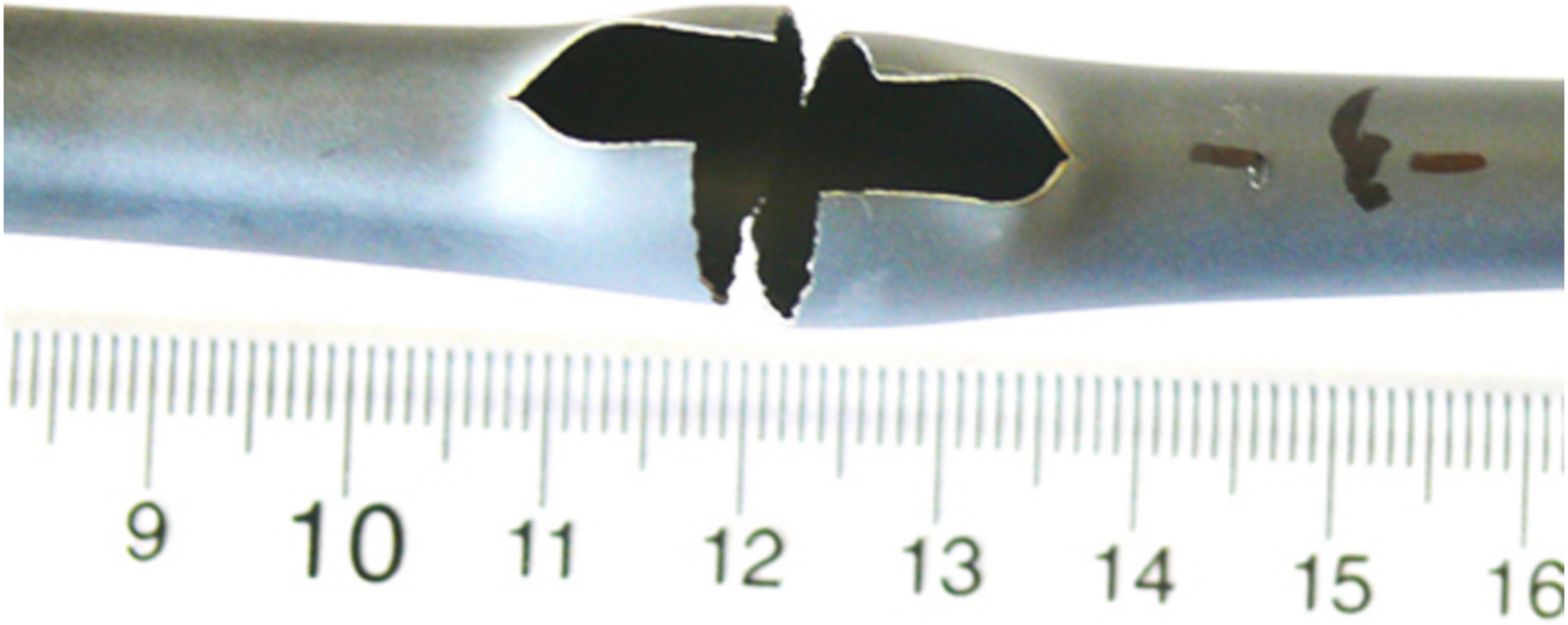

Figure E.13b: Post-4-PBT image of OCZL#29 test sample, which was pressurized to 1200 psig, heated to ≈1200°C, oxidized to 17% CP-ECR, and cooled with quench. Image was taken after second loading.

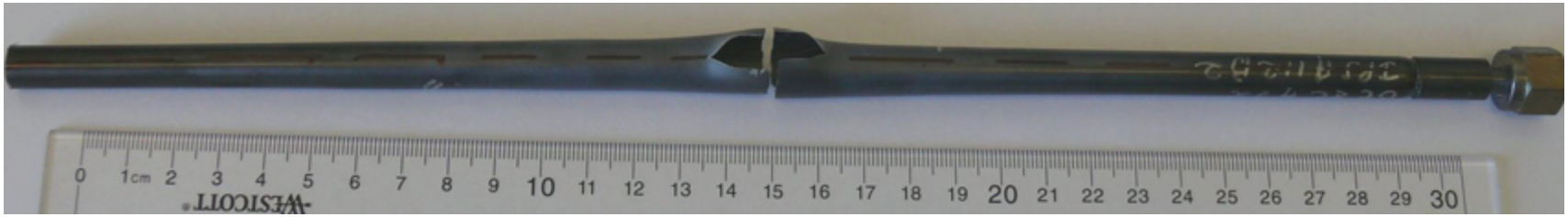

(a)

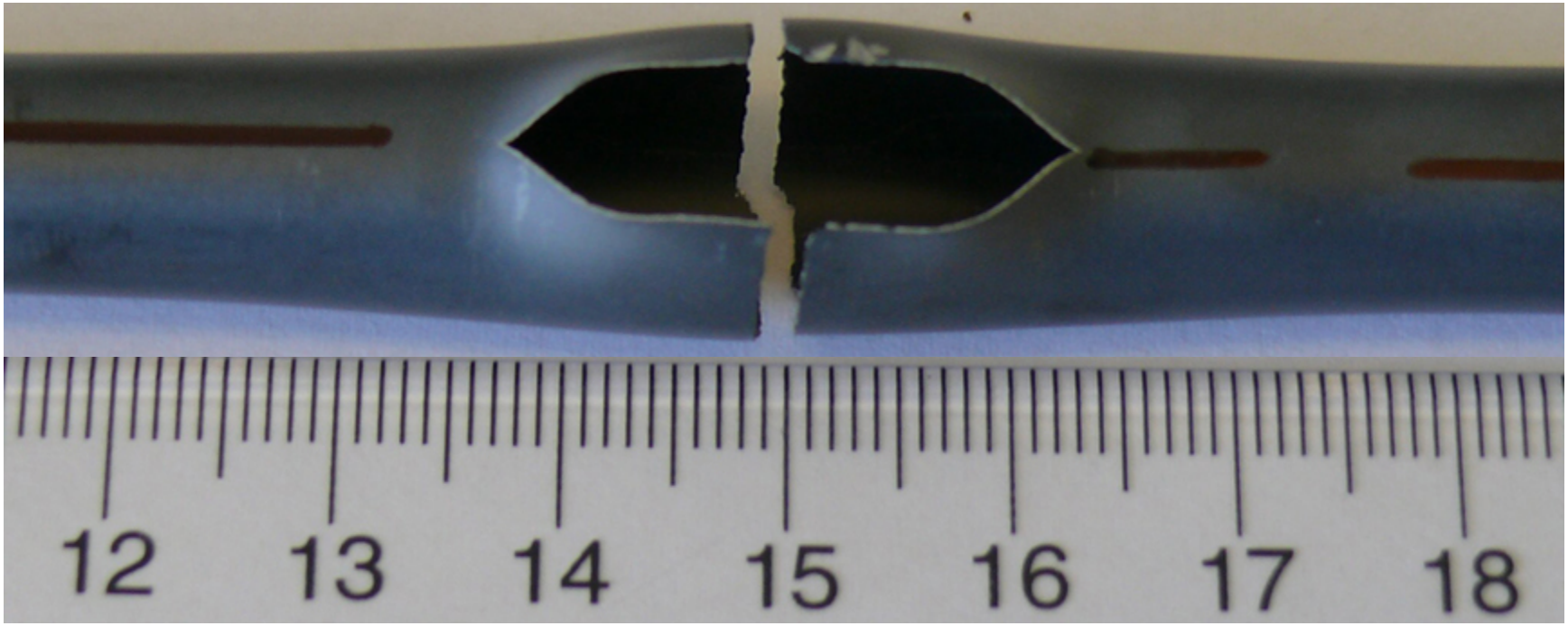

(b)

Figure E.14: Post-4-PBT Images of OCZL#32 test sample, which was pressurized to 1200 psig, heated to ≈1200°C, oxidized to 16% CP-ECR, and cooled with quench: (a) low magnification and (b) higher magnification.

(a)

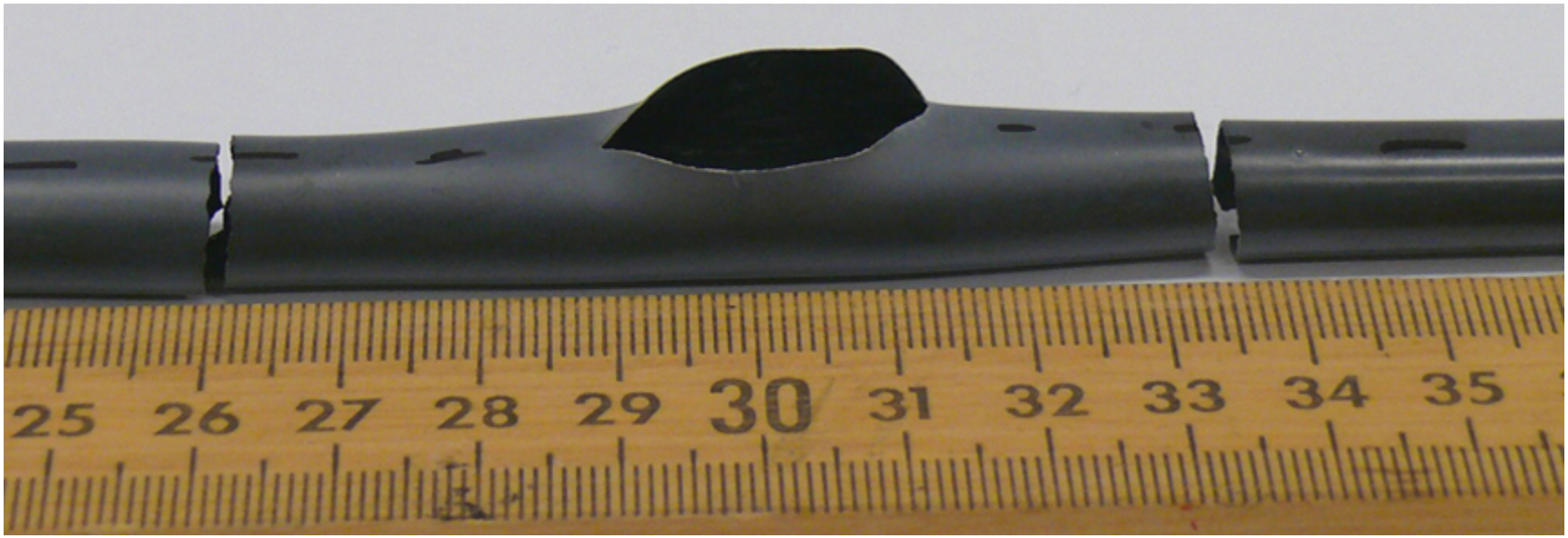

(b)

Figure E.15: Post-4-PBT images of OCZL#36 test sample, which was pressurized to 1200 psig, heated to ≈1200°C, oxidized to 18% CP-ECR, and cooled with quench: (a) low magnification and (b) high magnification.

(a)

(b)

Figure E.16: Post-4-PBT images of OCZL#37 test sample, which was pressurized to 1200 psig, heated to ≈1200°C, oxidized to 23% CP-ECR, and cooled with quench: (a) low magnification and (b) high magnification.

(a)

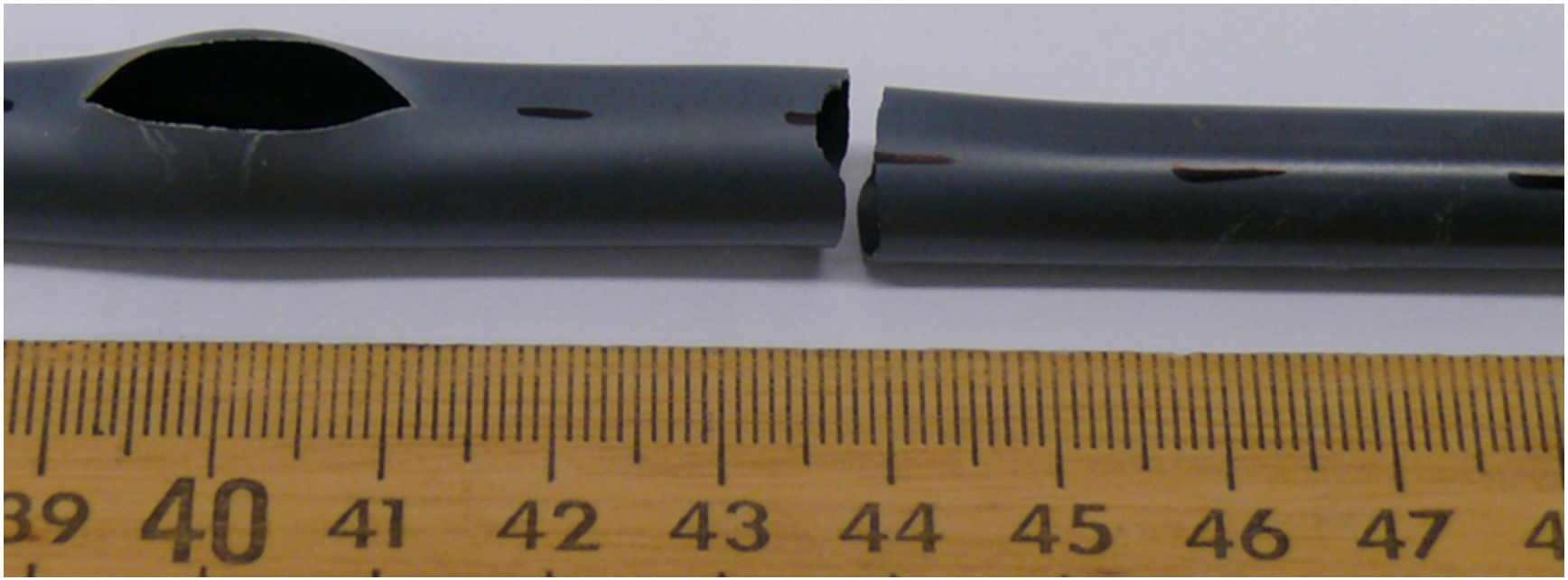

(b)

Figure E.17: Post-4-PBT images of OCZL#43 test sample, which was pressurized to 1200 psig, heated to 1200°C, oxidized to 18% CP-ECR, and cooled with quench: (a) low magnification and (b) higher magnification.

(a)

(b)

Figure E.18: Post-4-PBT images of OCZL#39 (660 wppm H) test sample, which was pressurized to 600 psig, heated to ≈1200°C, oxidized to 13% CP-ECR, and cooled with quench: (a) low magnification and (b) higher magnification.

(a)

(b)

Figure E.19: Post-4-PBT images of OCZL#40 (390 wppm H) test sample, which was pressurized to 1200 psig, heated to ≈1200°C, oxidized to 12% CP-ECR, and cooled with quench: (a) low magnification and (b) higher magnification.

(a)

(b)

Figure E.20: Post-4-PBT images of OCZL#41 (220 wppm H) test sample, which was pressurized to 1200 psig, heated to ≈1200°C, oxidized to 16% CP-ECR, and cooled with quench: (a) low magnification and (b) higher magnification.

(a)

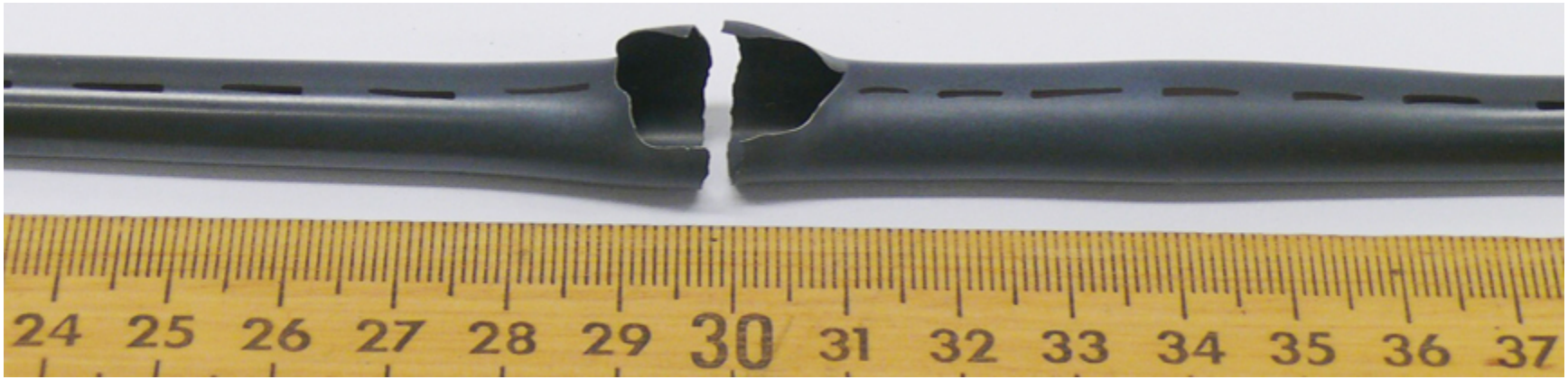

(b)

Figure E.21: Post-4-PBT images of OCZL#44 (700 wppm H) test sample, which was pressurized to 1200 psig, heated to ≈1200°C, oxidized to 14% CP-ECR, and cooled with quench: (a) low magnification and (b) higher magnification.

(a)

(b)

Figure E.22: Post-4-PBT images of OCZL#45 (220 wppm H) test sample, which was pressurized to 1200 psig, heated to ≈1200°C, oxidized to 13% CP-ECR, and cooled with quench: (a) low magnification and (b) higher magnification.

NRC FORM 335
(12-2010)
NRCMD 3.7

U.S. NUCLEAR REGULATORY COMMISSION

BIBLIOGRAPHIC DATA SHEET

(See instructions on the reverse)

1 REPORT NUMBER
(Assigned by NRC, Add Vol., Supp., Rev., and Addendum Numbers, if any.)
NUREG/CR-7219

2 TITLE AND SUBTITLE

Cladding Behavior during Postulated Loss-of-Coolant Accidents

3 DATE REPORT PUBLISHED

MONTH	YEAR
July	2016

4 FIN OR GRANT NUMBER
NRC-HQ-60-11-D-0012

5 AUTHOR(S)

M. C. Billone, Y. Yan,* T.A. Burtseva, and R.O. Meyer

6 TYPE OF REPORT
Technical

7 PERIOD COVERED (Inclusive Dates)

8 PERFORMING ORGANIZATION - NAME AND ADDRESS (If NRC, provide Division, Office or Region, U. S. Nuclear Regulatory Commission, and mailing address, if contractor, provide name and mailing address.)
Nuclear Engineering Division
Argonne National Laboratory
9700 South Cass Avenue
Argonne, IL 60439

9 SPONSORING ORGANIZATION - NAME AND ADDRESS (If NRC, type "Same as above", if contractor, provide NRC Division, Office or Region, U. S. Nuclear Regulatory Commission, and mailing address.)
Division of Systems Analysis
Office of Nuclear Regulatory Research
U.S. Nuclear Regulatory Commission
Washington, DC 20555-0001

10 SUPPLEMENTARY NOTES

11 ABSTRACT (200 words or less)
This report updates results of NUREG/CR-6967, provides additional results in those areas, and adds results of mechanical testing of cladding after ballooning, rupture, oxidation at elevated temperature, and quench. Significant conclusions are as follows. Embrittlement of high-exposure cladding is accelerated by hydrogen that is absorbed during normal reactor operation (i.e., pre-transient) and the acceleration has been quantified as an oxidation limit vs. pre-transient hydrogen content in the cladding metal. Breakaway oxidation, which leads to excessive hydrogen pickup and embrittlement during a LOCA transient, can occur during times that are relevant for these accidents. Conditions that lead to breakaway are only partially understood. Factors that contribute to increased susceptibility to breakaway oxidation – especially surface finish and scratches – have been investigated. Ballooning strains increase as rupture temperature decreases within the temperature range explored in this work. Rupture temperature depends on alloy composition, pre-transient hydrogen level, internal gas pressure, and geometrical factors used to convert gas pressure to hoop stress. Four-point bend tests are effective for measuring post-quench failure limits for ballooned, ruptured, and oxidized cladding. The results indicate that strength and failure energy degrade significantly with increasing pre-transient hydrogen and transient oxygen levels, based on cross-section-average values for these parameters. Further, using the oxidation limit vs. hydrogen content derived for non-ballooned regions would ensure the preservation of strength for ballooned regions.

12 KEY WORDS/DESCRIPTORS (List words or phrases that will assist researchers in locating the report.)
LOCA, fuel performance, breakaway oxidation, cladding embrittlement

13 AVAILABILITY STATEMENT
unlimited

14 SECURITY CLASSIFICATION
(This Page)
unclassified
(This Report)
unclassified

15 NUMBER OF PAGES

16 PRICE

Federal Recycling Program

UNITED STATES
NUCLEAR REGULATORY COMMISSION
WASHINGTON, DC 20555-0001

OFFICIAL BUSINESS